Self-association of complement factor H

in the presence and absence of metals

Thesis Presented for the Degree of

Doctor of Philosophy

By

Ruodan Nan

Department of Structural and Molecular Biology,

University College London.

September 2010

I, Ruodan Nan, confirm that the work presented in this thesis is my own.
Where information has been derived from other sources, I confirm that this has been indicated in the thesis.

Abstract

In the complement system of innate immunity, factor H (FH) is a major regulator of its activation, and is comprised of 20 short complement regulator (SCR) domains. FH is related to age-related macular degeneration (AMD) through a Tyr402His polymorphism, and occurs in drusen deposits that are a key feature of early AMD. High concentrations of zinc are also present in drusen, and the function of FH is inhibited by zinc. In this thesis, FH self-association and its interaction with zinc were investigated. Using X-ray solution scattering and analytical ultracentrifugation, pooled heterozygous FH in physiological conditions self-associated to form 10-15 % of dimer and higher oligomers. Titrations of FH with zinc induced uncontrolled oligomerisation of FH when the zinc concentration was above 20 micromolar, and this correlated with the reduction of FH activity. Structurally distinct large oligomers were also observed for Cu, while Ni, Cd and Fe showed low amounts of oligomers, and Mg and Ca showed no change. These experiments were repeated for the native Tyr402 allotype and the disease-related His402 allotype of FH. X-ray scattering combined with constrained modelling showed that the homozygous Tyr402 and His402 allotypes of FH have indistinguishable folded-back structures in solution. Both homozygous allotypes of full-length FH exhibit similar self-association properties in solution, showing no dependence on heterozygosity. Surface plasmon resonance confirmed these results, but showed that the His402 allotype of SCR-6/8 self-associates more than the Tyr402 allotype. Zinc titrations of the two FH allotypes showed that each allotype formed similar oligomers with zinc. While the major interaction sites of FH with zinc were located within the SCR-6/8 fragment, the surface exposed His402 residue in SCR-6/8 showed no preferential interactions with zinc. Overall, these findings provide insight on the development of drusen deposits in Bruch's membrane and the uncontrolled inflammation associated with AMD.

Acknowledgements

Firstly, I would like to thank my supervisor Professor Stephen J. Perkins, for his help, encouragement and his great enthusiasm about complement factor H, during the course of my PhD.

I also would like to thank my collaborators Dr Imre Lengyel and Professor Alan C. Bird, for useful discussions and insightful suggestions about my projects. I am grateful to Dr Robert B. Sim for providing the monoclonal antibody columns which have performed excellently in the last four years. Thanks to the instrumental experts Dr Theyencheri Narayanan, Dr Pierre Panine, Dr Emanuela Di Cola, Dr Anuj Shukla, Dr Adam McKay and Mr Jayesh Gor for their great supports in data collections.

Thanks to Dr Azubuike Okemefuna for teaching me data analyses and useful discussions, Miss Keying Li and Miss Ami Miller for helps in protein purifications, Miss Irene Farabella and Mr Felix F. Schumacher for their excellent bioinformatics work. Thanks also to all my group-mates who are always friendly and kind to me.

I thank the Biotechnology and Biological Sciences Research Council and the Mercer Fund of the Fight For Sight Charity for a Dorothy Hodgkin Postgraduate Award, and the Henry Smith Charity and the Mercer Fund for other support.

Finally, I would like to thank my mum and dad, and my aunty, for their ever-lasting moral support.

Contents **Page**

Contents – Figures **Page**

Chapter One

Chapter Two

Chapter Three

Chapter Four

Chapter Five

Chapter Six

Chapter Seven

Contents – Tables **Page**

Abbreviations

AD	Alzheimer's disease
aHUS	atypical haemolytic uraemic syndrome
α2M	α2-macroglubulin
AMD	age-related macular degeneration
ANA	anaphylatoxin domain
APS	Advanced Photon Source
AREDS	Age-Related Eye Disease Study
AUC	Analytical ultracentrifugation
AU-FDS	AU Fluorescence Detector System
BM	Bruch's membrane
CCD	charge-coupled device
CCP	complement control protein
CFHR1	factor H-related protein 1
CPN	Carboxypeptidase N
CRIg	complement receptor of the immunoglobulin superfamily
CRP	C-reactive protein
CR1	complement receptor type 1
CR2	complement receptor type 2
CR3	complement receptor type 3
CR4	complement receptor type 4
CUB	complement C1r/C1s, UEGF, BMP1 domain
C1NH	C1 inhibitor
C1qRp	C1q receptor
C3aR	C3a receptor
C4BP	C4b-binding protein
C5aR	C5a receptor
C5L2	C5a receptor-like protein
Da	Dalton
DAF	decay-accelerating factor
DC-SIGN	dendritic cell-specific intercellular adhesion molecule-3-grabbing non-integrin
DDD	dense-deposit disease

dIgA1	dimeric immunoglobulin A
DNA	deoxyribonucleic acid
DSSP	define secondary structure prediction
E. coli	*Escherichia coli*
EDTA	ethylenediaminetetraacetic acid
ELISA	enzyme-linked immunosorbent assay
ESRF	European Synchrotron Radiation Facility
Fc	fragment crystallisable
FFT	fast Fourier transformation
FH	factor H
fHbp	factor H binding protein
FHL1	factor H like protein-1
FI	factor I
FMOD	proteoglycan fibromodulin
FXIIIB	blood-clotting factor XIII B
GABA	γ-aminobutyric acid
GAGs	glycosaminoglycans
GBM	glomerular basement membrane
GeV	gigaelectronvolt
HEPES	4-(2-hydroxyethyl)-1-piperazineethanesulfonic acid
IFN	interferon
IgG	immunoglobulin G
IgM	immunoglobulin M
IL	interleukin
ILL	Institut Laue-Langevin
K_D	dissociation constant
kb	kilobase
kDa	kilo Dalton
LDL	low-density lipoprotein
LNK	linker domain
MAC	membrane attack complex
MASP	MBL-associated serine protease
MBL	mannose-binding lectin
MCP	membrane cofactor protein

mCRP	modified C-reactive protein
MG	macroglobulin
mM	millimolar
μM	micromolar
MPGN II	membranoproliferative glomerulonephritis type II
Mr	relative molecular mass
mRNA	messenger ribonucleic acid
MS	mass spectrometry
MW	molecular weight
m/z	mass to charge ratio
NA	not available
NK	natural killer
NMR	nuclear magnetic resonance
NSB	non-specific binding
PBS	phosphate-buffered saline
PDB	Protein Data Bank
PEG	polyethylene glycol
PIPES	piperazine-N, N'-bis (2-ethanesulphonic acid)
Por1A	porin 1A
ppm	part per millon
RCA	regulators of complement activation
R_G	radius of gyration
RNA	ribonucleic acid
RPE	retinal pigment epithelium
r.p.m	revolutions per minute
r.s.m.d	root mean square deviation
RU	resonance units
R_{XS}	cross-sectional radius of gyration
SANS	small angle neutron scattering
SAXS	small angle X-ray scattering
SC	secretion component
SCR	short complement regulator
SDS-PAGE	sodium dodecyl suphate polyacrylamide gel electrophoresis
SE	sedimentation equilibrium

SIGNR1	specific intercellular adhesion molecule-3-grabbing non-integrin-related protein
SLE	systemic lupus erythematosus
SNS	Spallation Neutron Source
SPICE	smallpox inhibitor of complement enzymes
SPR	surface plasmon resonance
sRPEds	sub-retinal pigment epithelial deposits
SRS	Synchrotron Radiation Source
SV	sedimentation velocity
TED	thioester-containing domain
TNF	tumor necrosis factor
TS2	target station 2 (at ISIS)
UCL	University College London
USAXS	ultra-small-angle scattering
UV	Ultraviolet
WAXS	wide-angle X-ray scattering
2D	two dimensional

Amino Acid Abbreviations

Amino Acid	Three Letter Code	One Letter Code
Alanine	Ala	A
Arginine	Arg	R
Asparagine	Asn	N
Aspartic Acid	Asp	D
Cysteine	Cys	C
Glutamine	Gln	Q
Glutamic Acid	Glu	E
Glycine	Gly	G
Histidine	His	H
Isoleucine	Ile	I
Leucine	Leu	L
Lysine	Lys	K
Methionine	Met	M
Phenylalanine	Phe	F
Proline	Pro	P
Serine	Ser	S
Threonine	Thr	T
Tryptophan	Trp	W
Tyrosine	Tyr	Y
Valine	Val	V

Chapter One

The complement system

1.1 General outline of the complement system

Complement was first discovered by Jules Bordet in late 19th century as a heat-labile component in normal serum (Bordet, 1909). The term 'complement' was introduced by Paul Ehrlich since this component augments the antibacterial activity of antibodies (Morikis & Lambris, 2005; Murphy *et al.*, 2008). Later studies discovered that complement can also be activated in the absence of antibodies (Murphy *et al.*, 2008). Therefore, complement is considered part of the innate immune system as well as part of the adaptive immune system.

The complement system contains more than 30 proteins that interact with one another both in plasma and on cell surface. There is more than 3 g/L of complement proteins in plasma which constitute about 15% of globulin fractions (Walport, 2001). The nomenclature of complement follows the order of discovery of the proteins. The complement system is composed of over 60 components and activation fragments which include the nine central components C1 to C9, activation products such as C3a, C3b, iC3b, C4a and C5a, proteases such as factor I, factor B and factor D, regulators such as factor H, factor H like protein-1 (FHL1), C1q, properdin and complement receptor type 1 (CR1), assembled enzymes in the cascades such as C3 convertases $C\overline{4b2a}$ and $C\overline{3bBb}$, and receptors for the complement effectors such as C3a receptor, C5a receptor and C1q receptor (Zipfel & Skerka, 2009). Several complement proteins exist as zymogens which refer to the inactive proteases that only become activated after being cleaved by another specific protease. Those zymogens can be locally activated by the presence of pathogens including infectious invading organisms and altered host cells. Those activated proteases can trigger a series of enzyme cascades by cleaving other zymogens which then cleave their substrates. In this way, a huge complement response is rapidly generated by successively amplified enzymatic reaction started from the activation of a small number of zymogens (Murphy *et al.*, 2008).

The activation of the complement system results in three biological functions. Firstly, complement protects the host against infections by binding and then opsonising the pathogens for phagocytosis, acting as chemoattractants and activating leukocytes, and attacking and lysing cells and bacteria; secondly, complement plays an important role in activation of the adaptive immune system as the antigen-presenting cells and B-

lymphocytes bear receptors for complement proteins that coat antigens, and therefore this bridges innate and adaptive immunity; thirdly, complement can clear dead, damaged and apoptotic cells and immune complexes from the tissues, and therefore protects the host against immune attacks on the body's own antigens (Goldsby *et al.*, 2000; Walport, 2001).

1.2 Three pathways of complement activation

Complement can be activated by three different pathways, the classical pathway through antibodies, C-reactive protein (CRP) and C1q, the alternative pathway through the low level spontaneous activation of C3, and the lectin pathway through multimeric lectin binding to repeated molecular patterns on pathogens. The final steps which lead to the membrane attack complex are the same in all pathways (Figure 1.1). Component C3 plays a central role in complement system, being common to all three pathways (Law & Reid, 1995).

1.2.1 Classical pathway

The classical pathway usually begins with antibodies complexed with antigens, and therefore it is part of the adaptive immune system. IgM and certain subclasses of IgG can activate the classical complement pathway (Figure 1.1) (Goldsby *et al.*, 2000). The initial steps involve the four central complement component proteins C1, C4, C2 and C3. C1 is a complex consisting of a single molecule C1q and two molecules each of C1r and C1s, held together in a complex ($C1qr_2s_2$), and C1q is composed of six identical subunits (Figure 1.2). The C1q molecules, which contain no enzymatic activity, recognise and bind to the pathogen surface or to the antigen antibody complexes (Figure 1.2). The binding of more than one C1q head to a pathogen surface or to the constant region of antibodies leads to a conformational change in zymogen C1r to an active serine protease enzyme $C\overline{1r}$, which then cleaves the associated zymogen C1s to a similar serine protease enzyme $C\overline{1s}$, and therefore the enzymatic activity of C1 complex is derived (Law & Reid, 1995). $C\overline{1s}$ hydrolyses C4 to an anaphylatoxin C4a and a large fragment C4b, and C4b may bind covalently to the pathogen surface. If C2 zymogen binds to C4b by the neighboring $C\overline{1s}$, C2 is cleaved by $C\overline{1s}$ into a non-

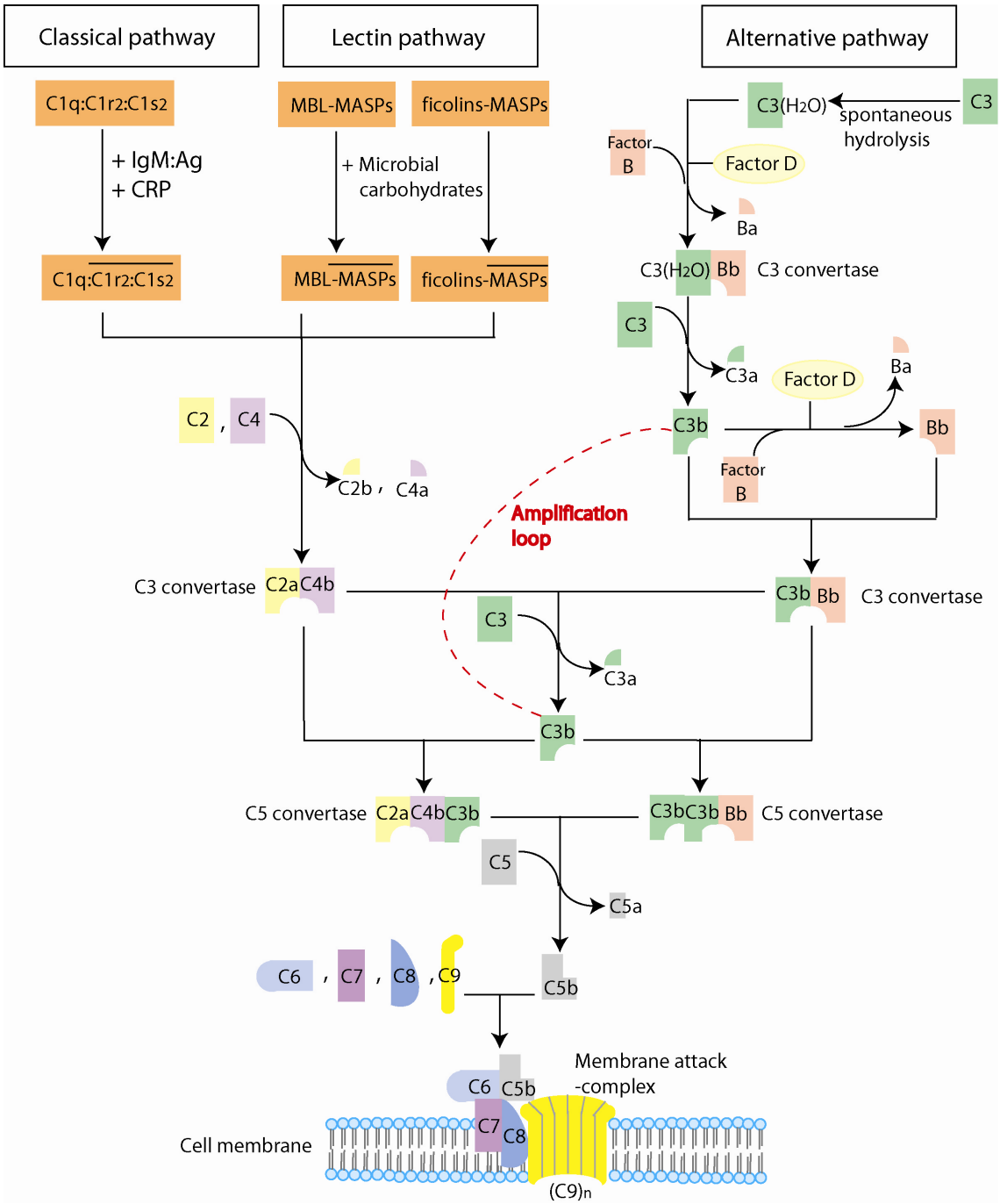

Figure 1.1 Schematic diagram of the complement system cascade.

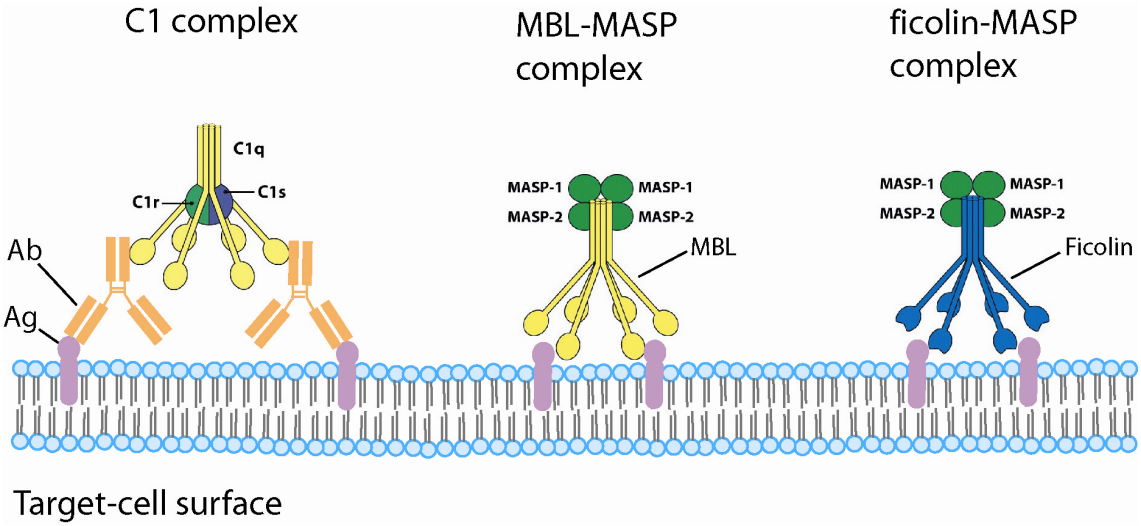

Figure 1.2 The first proteins in the classical pathway of complement activation C1 complex and the first proteins in the lectin pathway including the MBL-MASP complex and the ficolin-MASP complex (adapted from Murphy *et al.*, 2008).

catalytic C2b subunit which then diffuses away and a catalytic C2a subunit which is bound to C4b to form $C\overline{4b2a}$. In the classical pathway, the $C\overline{4b2a}$ complex is the C3 convertase which activates C3 by the proteolytic cleavage of C3 into C3a and C3b. The release of C3a causes a conformational change in C3b, which leads to the exposure of an internal thioester bond which is buried and inaccessible in unactivated C3. This exposed thioester bond reacts with nucleophiles, including water and molecules bearing hydroxyl or amino groups, and therefore leads to C3b covalently bound to the cell which has those molecules on its surface. Some of the C3b molecules bind to $C\overline{4b2a}$ to form $C\overline{4b2a3b}$ which is the C5 convertase in the classical pathway (Law & Reid, 1995; Rother *et al.*, 1998).

The classical pathway also plays a role in the innate immune system. In the innate immune system, natural antibodies are produced in the absence of infections and can react to a broad range of self and microbial antigens. Most natural antibodies produced are of class IgM which can bind to C1q most efficiently, and therefore activate the classical pathway of the complement system. In addition, in the absence of antibodies, C1q can bind to C-reactive protein which binds to phosphocholine on bacterial cell surfaces. Therefore, the classical pathway is part of both the adaptive and innate immune systems (Murphy *et al.*, 2008).

1.2.2 Lectin pathway

The lectin pathway is antibody-independent, and therefore it is one part of the innate immunity. The lectin pathway is homologous to the classical pathway (Figure 1.1). The activation of the lectin pathway is triggered by proteins very similar to C1q including mannose-binding lectin (MBL) and ficolins (Figure 1.2). Like C1q, MBL contains two to four identical subunits, and can forms complexes with two molecules each of the MBL-associated serine protease 1 (MASP-1) and 2 (MASP-2), the equivalent of C1r and C1s in the classical pathway. When MBL binds to the mannose residues on glycoproteins or carbohydrates on the surface of microorganisms, MASP-2 is activated to cleave C4 and then C2, and therefore MBL-MASPs complex mimics the activity of $C1qr_2s_2$ to trigger the formation of the C3 convertase (Goldsby *et al.*, 2000). Similar in shape and function with MBL, ficolins which has a higher concentration in plasma can

also complex with MASP-1 and MASP-2, bind to the oligosaccharides containing *N*-acetylglucosamine on pathogen surfaces, and then trigger the lectin pathway cascade (Murphy *et al.*, 2008).

1.2.3 Alternative pathway

The initiation of the alternative pathway does not have a need for antigen-antibody complex formation, and therefore the alternative pathway is a part of the innate immune system. Activation of this pathway is initiated in the fluid phase with the spontaneous and continuous hydrolysis of C3 (also known as "enzymatic tickover") (Figure 1.1), and the alternative pathway is constantly activated on biological surfaces and in most other body fluids (Zipfel & Skerka, 2009). The native C3 molecule consists of two polypeptide chains, α and β. Without loss of the C3a fragment, a spontaneous hydrolysis of the thioester in the α chain of C3 slowly leads to a formation of C3(H_2O) (also known as C3i or C3u) which has an altered conformation like C3b. In the presence of protease factor D, C3(H_2O) is able to bind factor B which then serves as the substrate for factor D. Factor D cleaves the C3(H_2O)-bound factor B, releasing a small fragment Ba. An unstable fluid-phase C3 convertase $C\overline{3(H_2O)Bb}$ is then formed. All these processes only operate at a low level (Figure 1.1) (Law & Reid, 1995; Rother *et al.*, 1998).

By proteolytic action, C3 convertase $C\overline{3(H_2O)Bb}$ generates the first metastable C3b molecules, much of which are attached to both host and foreign cells. Host cells protect themselves from complement attack with surface-bound sialic acids or other polyanions, and membrane-bound regulatory proteins. Activation proceeds on particles which lack those molecules. On those unprotected particles, a positive-feedback amplification of C3b occurs. C3b binds to Factor B which is then cleaved by factor D. Cleavage of C3b-bound factor B yields the C3 convertase $C\overline{3bBb}$. The activity of C3 convertase $C\overline{3bBb}$ has a half-life of only 5 minutes, unless it binds to properdin, which stabilizes it and extends the half-life of its convertase activity to 30 minutes (Goldsby *et al.*, 2000). C3 convertase $C\overline{3bBb}$ cleaves C3 to generate more C3a and C3b, and thus creates an amplification loop for the cascade (Figure 1.1). C3 convertase $C\overline{3bBb}$ binds to another C3b to form C5 convertase $C\overline{3bBb3b}$, which is analogous to $C\overline{4b2a3b}$ in the classical

pathway (Law & Reid, 1995; Rother *et al.*, 1998). The activation of the alternative pathway is regulated by some plasma-derived regulators including properdin, factor H and factor I, and also by some membrane-bound regulators including decay-accelerating factor (DAF), membrane cofactor protein (MCP) and complement receptor type 1 (CR1) (Rother *et al.*, 1998).

1.3 Membrane attack

C5 is cleaved by the C5 convertase, $C\overline{4b2a3b}$ in the classical pathway and the lectin pathway, or $C\overline{3bBb3b}$ in the alternative pathway. C5 is activated by a mechanism in which a small fragment, C5a, is released from C5b. C5a is the most potent of the anaphylatoxins, and is therefore the most essential complement-derived mediator in inflammation. C5b, the large fragment which is loosely bound to C3b, then initiates the assembly of the membrane attack complex (MAC). C5b binds to C6 to form the C5b6 complex and then to C7 to form the C5b67 complex which is dissociated from C3b. C5b67 has hydrophobic binding sites which enable C5b67 to insert into the phospholipid bilayer. C8 is a complex composed of two protein molecules C8β and C8α-γ. The C8β binds to C5b of the membrane-bound C5b67 complex to form C5b678 complex, and allows the hydrophobic domain of C8α-γ to become inserted into the phospholipid bilayer. The C5b678 complex is able to slowly lyse red blood cells, but the C5b678 complex mainly serves as a receptor for C9 and catalyses C9 polymerization. The final step in the formation of MAC is the binding and polymerization of C9 to the C5b678 complex. The complete MAC has a composition of $C5b678(9)_n$, where n lies from 10 to 16 (Figure 1.1). The MAC has a tubular form 10 nm in diameter, and it forms a transmembrane channel which has a hydrophobic external face that associates with the lipid bilayer but a hydrophilic internal face to allow solutes and water to pass through the lipid bilayer. The disruption caused by MAC finally leads to cell swelling and eventually lysis of the pathogen (Law & Reid, 1995; Murphy *et al.*, 2008).

1.4 Complement component C3

Complement component C3 plays a central role in the proteolytic cascade. Its activation product affects inflammation and both the innate and adaptive immune responses. C3 is a member of the α2-macroglubulin (α2M) family, and two homologous complement proteins C4 and C5 which are 26-30% identical in sequence to C3 also belong to this family. A reactive thioester bond required for association with molecule or cell surface is characteristic for the α2M family proteins, although some members like C5 do not have this thioester bond (Gros *et al.*, 2008). The molecular mechanisms of the function of C3 are better understood as more structural data has been revealed. Crystal structures have been determined for native human C3 (Figure 1.3) (Janssen *et al.*, 2005), the activation fragments C3a (Huber *et al.*, 1980), C3b (Janssen *et al.*, 2006; Abdul Ajees *et al.*, 2006), C3c (Janssen *et al.*, 2005), C3d (Nagar *et al.*, 1998), the C3b and factor H SCR-1/4 complex (Wu *et al.*, 2009), and the C3b and C3c complex with the complement receptor of the immunoglobulin superfamily (CRIg) (Wiesmann *et al.*, 2006). Electron-microscopy images have been obtained for C3(H_2O) and iC3b (Nishida *et al.*, 2006). Mature C3 is composed of a α-chain and a β-chain which contain 13 domains including eight macroglobulin (MG) domains MG1 to MG8, a linker domain (LNK), an anaphylatoxin domain (ANA), a complement C1r/C1s, UEGF, BMP1 domain (CUB), a thioester-containing domain (TED) and a C345c domain (Figure 1.3) (Janssen *et al.*, 2005).

In the complement system cascade, the three activation pathways all lead to the formation of the C3 convertase which then cleaves C3 to release the anaphylatoxin C3a and form C3b. The small fragment C3a can act on certain receptors to produce inflammatory responses. The thioester bond is hidden in the TED-MG8 interface of native C3. The release of the anaphylatoxin domain causes the conformation changes which expose the thioester bond. The exposed thioester bond becomes highly reactive, which results in C3b becoming covalently bound to the cell surface (Figure 1.3). The covalent association of C3b on the pathogen surface (opsonization) is essential for the amplication loop to generate C3b convertase in the alternative pathway. C3b participates in forming C5 convertase which finally leads to pathogen cell lysis. C3b can be cleaved by the protease factor I with the assistance of some regulators such as factor H, complement receptor type 1 (CR1) and membrane cofactor protein (MCP),

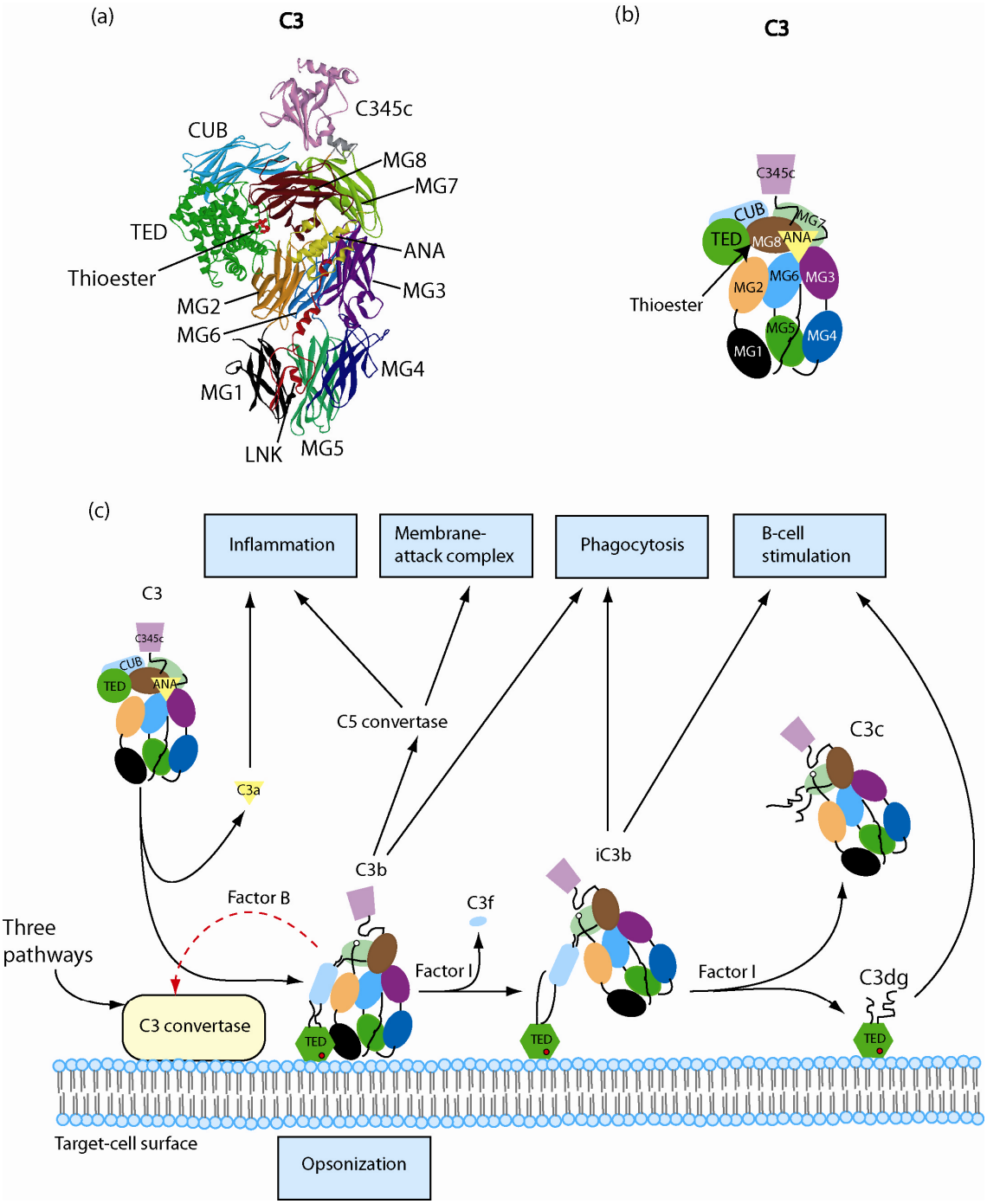

Figure 1.3 Conformational changes of complement component C3 in activation and degradation. (a) An X-ray crystal structure of native human C3 with PDB code 2a73; (b) Schematic representation of the structure of C3; (c) Schematic diagram of the conformational changes of C3 and its activation products in the complement cascade (adapted from Gros *et al.*, 2008).

yielding the fragments C3f, iC3b, C3c and C3dg which can no longer form C3 convertase. C3b and iC3b can bind receptors on macrophages to facilitate phagocytosis, while iC3b and C3dg can bind to receptors on B-cells and stimulate B-cells (Figure 1.3) (Gros *et al.*, 2008).

1.5 Regulation of the complement system

Several mechanisms control the extent of complement activation at different stages of the cascade. Normal host cells are protected from inappropriate complement activation by both positive and negative regulatory proteins both in fluid phase and bound to the membrane (Table 1.1).

At the beginning of the classical pathway, a plasma serine protease inhibitor, C1 inhibitor (C1NH), regulates the activation of C1 complex by dissociating C1r and C1s during complex formation from C1q which remains bound to the pathogen surface, or suppressing spontaneous activation of C1 via a reversible interaction with zymogen C1r and C1s. C1 inhibitor can also regulates the lectin pathway by inactivation of MASP-2 (Davis *et al.*, 2008).

At the formation stage of the C3 convertase, as the thioester bond in C3b and C4b is very reactive and cannot differentiate between the host cell surface and the pathogen surface, several protective mechanisms have developed to minimize the formation of C3 convertase on the normal host cell surface. Firstly, the protease factor I is responsible for cleaving C3b and C4b into inactive fragments, when C3b and C4b are bound to the cofactor proteins (Murphy *et al.*, 2008). For the cleavage of C3b, such cofactor include factor H (Pangburn, 2000), factor H-like protein 1 (FHL1) (Zipfel & Skerka, 1999), membrane cofactor protein (MCP) and complement receptor type 1 (CR1) (Kim & Song, 2006). The C4b-binding protein (C4BP) (Blom *et al.*, 2004) is the cofactor for C4b cleavage by factor I. Secondly, regulators such as factor H, CR1 and the decay-accelerating factor (DAF) can bind to C3b or C4b to displace Bb or C2a and therefore dissociate the C3 convertase $C\overline{3bBb}$ or the C4 convertase $C\overline{4b2a}$ (Pangburn, 2000; Kim & Song, 2006). Thirdly, those regulators that bound to C3b or C4b can accelerate the dissociation of $C\overline{3bBb}$ or $C\overline{4b2a}$ that have already formed. Among those negative

Table 1.1 Regulators in the complement cascade (adapted from Zipfel & Skerka, 2009).

Regulator	Ligands	Phase	Cell surface binding or expression	Function	Regulated pathways
C1 inhibitor	C1r, C1s and MASP2	fluid phase	NA	Blocks serine protease; Acts as a suicide substrate for C1r, C1s, MASP2, coagulation factors and C3b.	Classical pathway; Lectin pathway
Factor I	C3b and C4b	fluid phase	Acquired to surface	Serine protease that cleaves C3b and C4b with aids	All three pathways
Factor H	C3b and C3d	fluid phase	Acquired to surface	Inhibits the assembly of C3 convertase; Acts as the cofactor of factor I to cleave C3b; Accelerates the dacay of C3 convertase in the alternative pathway.	Alternative pathway
Factor H-like protein 1	C3b	fluid phase	Acquired to surface	Simliar to the functions of factor H above	Alternative pathway
Membrane cofactor protein (CD46)	C3b and C4b	membrane-bound	All cells except erythrocytes	Degrades C3; Acts as the cofactor of factor I and factor H and effector for T cell maturation	All three pathways
Complement receptor type 1 (CD35)	C3b, iC3b, C4b and C1q	membrane-bound	Many nucleated cells and erythrocytes, B cells, leukocytes, monocytes and follicular dendritic cells	Clears the immune complexes; Enhances the phagocytosis; Regulates the C3 breakdown	All three pathways
C4b-binding protein	C4	fluid phase	Acquired to surface	Acts as the cofactor of factor I; Accelerates the decay of C3 convertase in the classical pathway.	Classical pathway; Lectin pathway
Complement decay-accelerating factor (CD55)	C3 convertases	membrane-bound	Most cell types including erythrocytes, epithelial cells and endothelial cells	Accelerates C3 convertase dacay	All three pathways
Complement receptor of the immunoglobulin superfamily	C3b, iC3b and C3c	membrane-bound	Macrophages	iC3b-mediated phagocytosis and inhibition of alternative pathway activation	Alternative pathway

Properdin	C3	fluid phase	Binds to apoptotic surface	Stabilizes the alternative pathway convertases	Alternative pathway
Vitronectin	C5b-7 and MAC	fluid phase	NA	Adhesion protein, fibronectin-mediated cell attachment and Arg-Gly-Asp site coagulation in immune defence against *Streptococcus spp*.	MAC formation
Clusterin	C7, C8, C9 and MAC	fluid phase	NA	Inhibits MAC assembly and binds to low density lipoprotein	MAC formation
Factor H-related protein 1	C5 convertase and MAC	fluid phase	Acquired to surface	Inhibits the assembly of C5 convertase and MAC	MAC formation
Protectin (CD59)	C8 and MAC	membrane-bound	Expressed by erythrocytes and most nucleated cells, including renal cells	Inhibits MAC assembly	All three pathways

regulators, factor H, FHL1 and C4BP are plasma regulators that can be attracted to the host cell surface, whereas CR1, DAF and MCP are membrane-bound on the normal host cells (Table 1.1). The regulators FH, FHL1, C4BP, CR1, MCP and DAF all belong to the 'regulators of complement activation' (RCA) family, and the RCA family proteins share one or more copies of a repeating motif of ~60 amino acids called the short complement regulator (SCR), also known as the complement control protein (CCP) repeat or the sushi domain (Morikis & Lambris, 2005). In addition, a newly identified membrane-bound regulator complement receptor of the immunoglobulin superfamily (CRIg) only inhibits the alternative pathway. The mechanism which is different from other established inhibitors is explained in Section 1.6. In contrast, a positive plasma regulator, properdin, can be attracted to the pathogen surfaces or motified host cell surfaces, bind to and stabilize the C3 convertase (Hourcade, 2008).

In addition, there are also mechanisms to prevent inappropriate membrane attack events on host cells. As mentioned in Section 1.3, C5b is produced upon the action of C5 convertase, and then other complement components C6 and C7 bind to C5b to form the C5b67 complex. The plasma protein vitronectin, also known as S-protein, and the plasma protein clusterin, also known as SP-40, can bind to the C5b67 complex thus forming soluble C5b67, to stop the insertion of the complex into the cell membrane. The complement component C8 and C9 can bind to the C5b67 complex to form the $C5b678(9)_n$ complex. The binding of clusterin and vitronectin to nascent amphiphilic $C5b678(9)_n$ complex can make it water-soluble and lytic-inactive (Bhakdi *et al.*, 1988; Tschopp *et al.*, 1993). Factor H-related protein 1 (CFHR1), another plasma protein, is newly identified as inhibitor of the complement cascade, as it may control the C5 convertase activity by contacting the C5 convertase $C\overline{3bBb3b}$ and the substrate C5 at the same time, and it also inhibits assembly of C5b67 complexes and prevents surface attachment (Heinen *et al.*, 2009). The membrane-bound protein protectin on the host cells can inhibit the binding of C9 to the C5b678 complex (Murphy *et al.*, 2008). Some regulators have some other biological functions. For example, clusterin binds to enzymatically modified low-density lipoprotein (LDL) and thus reduces fatty acid-mediated cytotoxicity (Schwarz *et al.*, 2008). Vitronectin is one of the adhesive glycoproteins that functions in the attachment of cells to the matrix, and also plays a role in the blood coagulation and fibrinolytic systems (Table 1.1) (Preissner & Seiffert, 1998).

1.6 Other biological functions mediated by receptors for the complement effectors

The most important result of complement activation is to opsonise the pathogens and to induce phagocytosis by neutrophils and macrophages. As mentioned in Section 1.4, C3b is generated after the action of C3 convertase. Due to the regulation of C3 convertase formation on the normal host cell surfaces, C3b selectively binds to the pathogen surface. C3b and its fragment iC3b therefore act as opsonins, and then induce phagocytosis through specific recognition of C3b or iC3b by complement receptors (CRs) on phagocytes (Table 1.2). Similar to C3b, C4b can act as an opsonin, but to a smaller extent as much more C3b than C4b is generated (Murphy *et al.*, 2008).

Complement receptor types 1 CR1; (CD35) and 2 CR2; (CD21), are multifunctional glycoproteins which belong to the RCA family. CR1 is expressed on both macrophages and neutrophils. In addition to its regulatory role in C3b cleavage, CR1 mediates several other biological functions. Firstly, it can act as a receptor for phagocytosis. Pathogens coated with C3b can be recognized by CR1 molecules on polymorphonuclear cells and monocytes. Fc-γ receptor and CR1 can act together to facilitate the uptake of opsonised pathogens which are then internalized and destroyed in lysosomes. Secondly, it can clear immunecomplexes. CR1 molecules on erythrocytes can bind to the C3b/C4b opsonised immune complexes which are thus localised on erythrocytes and then transferred to the macrophages in the liver and spleen where the immune complexes are engulfed and metabolized. Thirdly, CR1 is also present on B-cells and T-cells. The CR1 molecules present on B-cells appears to control the proliferation of B-cells (Khera & Das, 2009). On the other hand, CR2 is expressed by B lymphocytes, transformed B-cells, follicular dendritic cells, thymocytes and T-cells. It binds to the inactive fragments of C3b including iC3b, C3dg and C3d. CR2 on B-cells can enhance the signal received through the B-cell antigen receptor on binding the pathogen coated with C3d, and in this way the complement activation contributes to a stronger antibody response in adaptive immune system (Isaak *et al.*, 2006).

The complement receptors types 3 (CR3) and 4 (CR4) are transmembrane heterodimers which belong to the β_2 integrin family. CR3 is expressed on phagocytic cells, minor subsets of B and T cells, and natural killer (NK) cells. Most cells that express CR3 also express CR4, but only macrophages express more CR4 than CR3. The binding of CR3

Table 1.2 Distribution and function of receptors for complement effectors (adapted from Zipfel & Skerka, 2009).

Receptor	Ligands	Cell expression	Function
Complement receptor type 1 (CD35)	C3b, iC3b, C4b and C1q	Many nucleated cells and erythrocytes, B cells, leukocytes, monocytes and follicular dendritic cells	Clears the immune complexes; Enhances the phagocytosis; Regulates the C3 breakdown
Complement receptor type 2 (CD21)	C3dg, C3d and iC3b	B cells, T cells and follicular dendritic cells	Regulates B cell functions; Acts like B cell co-receptor; Retents C3d tagged immune complexes
Complement receptor type 3	iC3b and factor H	Monocytes, macrophages, neutrophils, natural killer cells, eosinophils, myeloid cells, follicular dentritic cells, CD4+ T cells and CD8+ T cells	iC3b enhances the contact of opsonized targets, resulting in phagocytosis and adhesion by CR3
Complement receptor type 4	iC3b	Monocytes and macrophages	iC3b-mediated phagocytosis
Complement receptor of the immunoglobulin superfamily	C3b, iC3b and C3c	Macrophages	iC3b-mediated phagocytosis and inhibition of alternative pathway activation
C1q receptor (CD93)	C1q	Endothelial cells, neurons, monocytes and neutrophils	Phagocytosis and cell adhesion
SIGN-related 1	C1q	macrophages	Initiates the classical pathway
C3a receptor	C3a	Neutrophils, monocytes, eosinophils, antigen-presenting cells, T cells, astrocytes, neurons and glial cells	Immune cell recruitment and inflammation
C5a receptor (CD88)	C5a	Myeloid cells, monocytes, neutrophils, dendritic cells, antigen-presenting cells, T cells, endothelial cells and renal tubular cells	Immune cell recruitment and inflammation
C5a receptor-like 2	C5a	Macrophages and neutrophils	Immune cell recruitment and inflammation

and CR4 to iC3b can induce phagocytosis. In addition, they also act as adhesion molecules mediating the diapedesis of leukocytes across the endothelium, and they are both involved in adhesion to the extracellular matrix and synapse formation (Ross, 2000).

The complement receptor of the immunoglobulin superfamily (CRIg; also known as VSIG4) is restrictly expressed by a subset of tissue resident macrophages. CRIg can bind to C3b, iC3b and C3c, and therefore mediates the phagocytosis of C3b or iC3b coated pathogens. CRIg is also a newly identified inhibitor of the alternative pathway. Different from the established regulators such as factor H, CR1 and DAF, CRIg neither competes with Bb to bind with C3b nor acts as a cofactor for factor I. Rather, CRIg inhibits only the alternative pathway by binding to the C3b but not the C4b subunit of the C3 and C5 convertases (Wiesmann *et al.*, 2006; He *et al.*, 2008).

C1q is a subunit of the C1 complex. Beside its role in activating the classical pathway, C1q is able to trigger several other cellular responses mediated by specific receptors. One of these receptors, the C1q receptor (C1qRp), also known as CD93, is a transmembrane glycoprotein which is predominantly expressed on endothelial cells in human tissue and also on phagocytic cells, has been reported to mediate the phagocytosis of C1q coated pathogens (Fonseca *et al.*, 2001). C1qRp molecules are also involved in the C1q-induced Endothelial Cell Adhesion and Spreading (Feng *et al.*, 2002). The dendritic cell-specific ICAM3-grabbing non-integrin (DC-SIGN) homologue SIGN-related 1 (SIGNR1), is a transmembrane C-type lectin which is expressed on splenic marginal zone macrophages and binds to C1q as well as polysaccharides. SIGNR1 is capable to bind to C1q and therefore initiate the classical pathway, and the SIGNR1 mediated classical pathway is crucial in the reorganization of Streptococcus Pneumoniae and defence against this pathogen (Kang *et al.*, 2006).

The small cleavage products of C3 and C5, C3a and C5a generated after complement activation, are often referred to as anaphylatoxins, because of the anaphylactic shock caused by a generalized circulatory collapse induced by large production of those small complement fragments. C5a is more active than C3a. The plasma protein Carboxypeptidase N (CPN), can cleave and partly inactive C3a and C5a and therefore protect the body from excessive accumulation of the anaphylatoxins (Skidgel & Erdos,

2007). The actions of anaphylatoxins are mediated by three members of the seven transmembrane spanning receptor family including C3a receptor (C3aR), C5a receptor (C5aR), and C5a receptor-like 2 (C5L2) (Table 1.2). Those receptors are coupled with intracellular guanine-nucleotide-binding protein called G proteins, through which those receptor signal (Zipfel & Skerka, 2009; Klos *et al.*, 2009). Firstly, C3a and C5a produce local inflammatory response by acting on the receptors on the endothelial cells lining blood vessel to increase vascular permeability and induce adhesion molecules. As a result, fluid leakage from local blood vessels is increased, and antibodies, complement proteins, and phagocytes are more easily recruited to the site of infection. Secondly, the anaphylatoxins can also activate mast cells to release mediators such as histamine and tumor necrosis factor-α (TNF-α) which contribute to the inflammatory responses. The fluid and protein accumulation increase the movement of pathogen-bearing and pathogen-presenting cells to the lymph nodes, and the adaptive immune system is then initiated (Murphy *et al.*, 2008).

1.7 Complement related diseases

The functions and distributions of complement effectors are tightly controlled, and defective regulation and misdirecting of complement effectors lead to various diseases. Some deficiencies in C3 convertase formation and regulation in the alternative pathway can result in host cell damage and accumulation of debris which then cause diseases such as atypical haemolytic uraemic syndrome (aHUS), membranoproliferative glomerulonephritis type II (MPGN II), also known as dense-deposit disease (DDD), age-related macular degeneration (AMD) and Alzheimer's disease (AD). aHUS is a severe kidney disease which is related to gene mutations of factor H, MCP, factor I, factor B and C3 (Saunders *et al.*, 2006; Saunders *et al.*, 2007; Atkinson & Goodship, 2007). MPGN II is characterized by glomerular basement membrane thickening and dense intramembranous deposits. The genetic causes of MPGN II include factor H and CFHR5 gene variations (Abrera-Abeleda *et al.*, 2006). AMD is the most common cause of blindness in the elderly population in the Western world, and it is characterized by the formation of drusen. The Tyr402His polymorphism in factor H is strongly related to AMD (Hageman *et al.*, 2001; Hageman *et al.*, 2005; Klein *et al.*, 2005; Haines *et al.*, 2005; Edwards *et al.*, 2005; Hageman *et al.*, 2006). Other genetically related complement proteins include factor B, C3, and C2 (Gold *et al.*, 2006; Spencer *et al.*,

2007; Yates *et al.*, 2007; Maller *et al.*, 2007). AD is the most common cause of dementia worldwide, and is characterized by the formation of β-amyloid plaques. The factor H Tyr402His polymorphism has also been reported to be associated with AD (Zetterberg *et al.*, 2008).

Deficiencies in the classical pathway cause defective clearance of apoptotic cells, and are associated with an increased risk for developing the autoimmune disease systemic lupus erythematosus (SLE) and SLE-like disease. SLE manifests in multiple organs and is characterized by the presence of auto-antibodies directed against nuclear components. Deficiencies in C1 complex subunits (C1q, C1s, C1r) are strongly associated with SLE, and C4 and C2 are also genetically related to SLE. MBL deficiency has also been suggested to be a factor for SLE (Truedsson *et al.*, 2007).

Carcinoma cells are another type of modified host cells. Increased presence of complement inhibitors on carcinoma cells can result in the escape of carcinoma cells from immune responses. The expression of the membrane-bound complement inhibitors are present on various tumour cell lines. Furthermore, the expression of sialic acid residues is enhanced on certain malignant cells, and thus the binding of soluble inhibitors such as factor H is increased (Donin *et al.*, 2003).

The foreign pathogens such as bacteria and virus have evolved to be able to recruit complement inhibitors from the plasma, and express endogenous regulators that mimic the host complement regulators, and in this way these microbes protect themselves from host innate immune system. For example, *Neisseria gonorrhoeae* can express porin 1A (Por1A) protein which can bind to the complement inhibitor factor H, and weakly bind to FHL1 (Ngampasutadol *et al.*, 2008). The variola virus which causes the disease smallpox can express the smallpox inhibitor of complement enzymes (SPICE) to inactive human C3b and C4b (Rosengard *et al.*, 2002).

Chapter Two

Complement factor H

In the alternative pathway of the innate immune system, factor H (FH) is an important regulator of the amplification cascade. FH consists of 20 globular SCR domains which are linked by 19 potentially flexible peptide links, and FH molecules form folded-back structures in solution. Different functions of FH are located in different domains, and it may form monomers or dimers. Zinc can facilitate the oligomerisation of FH. The polymorphism Tyr402His of FH is a major risk factor for developing age-related macular degeneration (AMD). The concentration of zinc in drusen which is a key feature of AMD is particularly high. How zinc causes FH to oligomerise, especially the Tyr402His variant, needs investigation.

2.1 FH sequence and structure

2.1.1 FH sequence and SCR domains

The complete human FH sequence before secretion contains 1231 amino acid. The SWISSPROT accession number is P08603. The first 18 amino acids at the N-terminus is the signal peptide which is cleaved after the secretion of FH. Therefore, the mature form of human FH after secretion contains 1213 amino acid, and the numbering of the amino acid sequence starts from 19 (Figure 2.1 a) (Ripoche *et al.*, 1988). The molecular weight (MW) of FH is 154 kDa (Aslam & Perkins, 2001; Fenaille *et al.*, 2007). FH belongs to the RCA family which contains the complement regulators FH, FHL1, CFHR1-5, DAF, C4BP, MCP, CR1 and CR2. The RCA family proteins are characterized by the presence of a repeating motif called the SCR domain which contains about 60 amino acids (Section 1.5). SCR domains also exist in some non-RCA proteins such as C1r, C1s, MASP-1, MASP-2, C2, C6, C7, factor B and the blood-clotting factor XIII B subunit (FXIIIB) (Morikis & Lambris, 2005). FH consists entirely of 20 SCR domains arranged in tandem, and 19 flexible linkers between them (Figure 2.1 a). The length of the linkers varies from three to eight residues (Figure 2.1 a). The sequence alignments of the SCR domains show that two cysteines (C^{I} and C^{IV}) are conserved at either end with another two cysteines (C^{II} and C^{III}) located between them. Another highly conserved residue tryptophan is present between C^{III} and C^{IV}, with an exception at SCR-10. There are some other residues such as proline, glycine and tyrosine conserved at different positions in the SCR sequences (Figure 2.1 a) (Aslam &

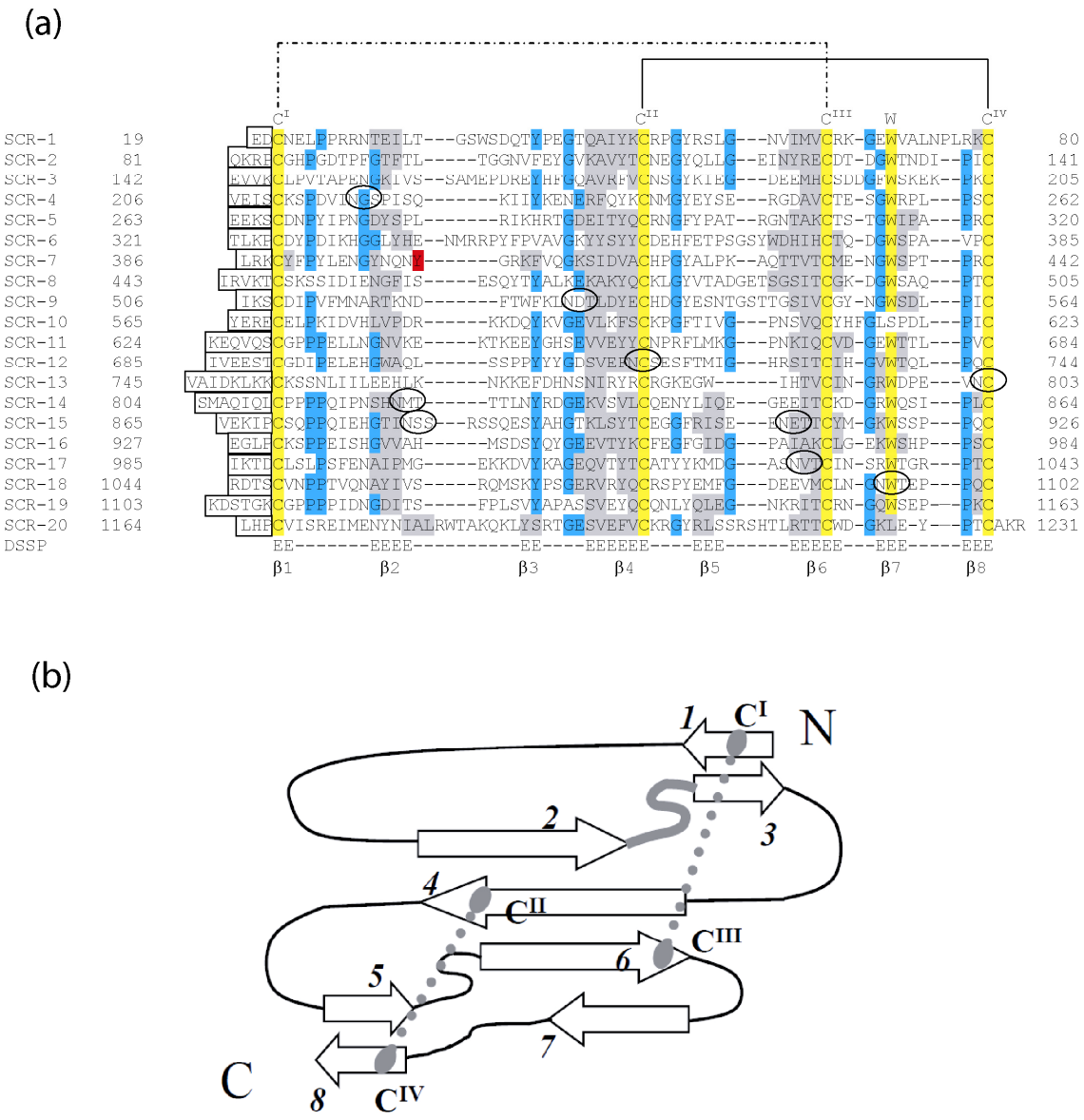

Figure 2.1 FH sequence and SCR domains. (a) Sequence alignment of the SCR domains of FH. The consensus C^{I}, C^{II}, C^{III}, C^{IV} and Trp residues are highlighted in yellow. Other conserved residues are highlighted in blue. The position 402 is highlighted in red. The Define Secondary Structure Prediction (DSSP)-assigned β-strand secondary structure regions are highlighted in grey, and labelled below the alignment. The 19 linkers are boxed. The nine potential glycosylation sites are circled. The disulphide bonds are notified by dashed and straight lines above the alignment. (b) Schematic diagram of the structure of a SCR domain. The β-strands 1-8 are notified by arrows. Disulphide bonds are indicated by thick grey dotted lines, and the hypervariable loop between β2 and β3 is indicated by a thick grey line (adapted from Morikis & Lambris, 2005).

Perkins, 2001; Morikis & Lambris, 2005; Saunders *et al.*, 2006). Two disulphide bonds are formed in the pattern C^{I} - C^{III} and C^{II} - C^{IV}. The solved SCR structures show that there is no α-helix present, and up to eight β-strands in relatively constant positions form a scaffold-like β structure (Figure 2.1 b) (Morikis & Lambris, 2005).

There are nine potential N-glycosylation sites in FH sequence, including Asn217 in SCR-4, Asn529 in SCR-9, Asn718 in SCR-12, Asn802 in SCR-13, Asn822 in SCR-14, Asn882 and Asn911 in SCR-15, Asn1029 in SCR-17, and Asn1095 in SCR-18 (Figure 2.1 a). Except for the site at Asn217, eight sites are occupied. These eight sites are mainly glycosylated by biantennary disialylated glycans of 2204 Da in size (Fenaille *et al.*, 2007).

2.1.2 Structural studies of the SCR domains of FH

Structures of several individual SCR domains or SCR domain groups within FH have been solved over the years by various methods including X-ray crystallography, nuclear magnetic resonance (NMR) and small angle X-ray scattering (SAXS) (Table 2.1). The first FH SCR structure solved was the structure of SCR-16 domain, and the method used was NMR (Norman *et al.*, 1991). Since then, NMR has been used to determine the structures of SCR-15/16 (Barlow, et al, 1993), SCR-19/20 (Herbert *et al.*, 2006), SCR-7 (Herbert *et al.*, 2007), SCR-1/2, SCR-2/3 (Hocking *et al.*, 2008) and SCR-12/13 (Schmidt *et al.*, 2010). Crystal structures have been determined for SCR-19/20 (Jokiranta *et al.*, 2006), SCR-6/7 in complex with sucrose octasulfate (Prosser *et al.*, 2007), the complex between SCR-1/4 and C3b (Wu *et al.*, 2009) and the complex between SCR-6/7 and *Nerisseria meningitidis* FH binding protein (Schneider *et al.*, 2009). SAXS combined with constrained modelling has been used to determine the structures in solution in physiological conditions for SCR-6/8 (Fernando *et al.*, 2007), SCR-1/5, SCR-16/20 (Okemefuna *et al.*, 2008), and SCR-1/20 (Aslam & Perkins, 2001; Okemefuna *et al.*, 2009).

Table 2.1 List of PDB deposited FH structures.

FH domains	PDB entry code	Method of determination	Resolution	Reference	Comments
SCR-1/2	2RLP	NMR		Hocking *et al.*, 2008	
SCR-2/3	2RLQ	NMR		Hocking *et al.*, 2008	
SCR-1/4	2WII	crystallography	2.70 Å	Wu *et al.*, 2009	Complement C3b in complex with FH SCR-1/4
SCR-1/5	2QFG	SAXS		Okemefuna *et al.*, 2008	
SCR-6/7	2W80 / 2W81	crystallography	2.35 Å	Schneider *et al.*, 2009	Structure of a complex between Nerisseria meningitidis FH binding protein and FH SCR-6/7
SCR-7	2JGW	NMR		Herbert *et al.*, 2007	Structure of His402 allotype of FH SCR-7
SCR-7	2JGX	NMR		Herbert *et al.*, 2007	Structure of Tyr402 allotype of FH SCR-7
SCR-6/8	2UWN / 2V8E	crystallography	2.35 Å	Prosser *et al.*, 2007	Structure of FH SCR-6/8 (His402 allotype) in complex with an analogue of glycosaminoglycan.
SCR-6/8	2IC4	SAXS		Fernando *et al.*, 2007	
SCR-12/13	2KMS	NMR		Schmidt *et al.*, 2010	
SCR-15/16	1HFH / 1HFI	NMR		Barlow et al, 1993	
SCR-16	1HCC	NMR		Norman *et al.*, 1991	
SCR-16/20	2QFH	SAXS		Okemefuna *et al.*, 2008	
SCR-19/20	2G7I	crystallography	1.75 Å	Jokiranta *et al.*, 2006	
SCR-19/20	2BZM	NMR		Herbert *et al.*, 2006	
SCR-1/20	1HAQ	SAXS		Aslam & Perkins, 2001	four best fitting models of FH in solution
SCR-1/20	3GAU	SAXS		Okemefuna *et al.*, 2009	Solution structure of FH in 50 mM NaCl buffer
SCR-1/20	3GAV	SAXS		Okemefuna *et al.*, 2009	Solution structure of FH in 137 mM NaCl buffer
SCR-1/20	3GAW	SAXS		Okemefuna *et al.*, 2009	Solution structure of FH in 250 mM NaCl buffer

2.1.3 Structural studies of full-length FH

The large size of FH, the 19 potential flexible peptide links between the 20 SCR domains and the existence of up to nine putative glycosylation sites have hindered the structural studies of full length FH by using X-ray crystallography and NMR (Perkins et al., 1991; Aslam & Perkins, 2001). It is difficult to predict the orientation between two adjacent SCR domains (Lehtinen *et al.*, 2004). Although high resolution crystal or NMR structures have been determined for 13 out of 20 SCR domains so far through the studies of fragment of FH, the whole picture of full-length FH in solution cannot be obtained by simply joining those known SCR domain structures together. As shown by electron microscopy, most intact FH molecules are not extended, and they form different types of folded back structures (DiScipio, 1992). The combination of constrained X-ray solution scattering modelling, analytical ultracentrifugation (AUC) and homology modelling confirmed that the conformation of FH in solution is folded back, and revealed the medium-resolution structures of FH SCR-1/20 in solution for the first time (Aslam & Perkins, 2001; Perkins *et al.*, 2005). This is consistent with the fact that the structures of SCR-1/5, SCR-6/8, and SCR-16/20 in solution also show some degree of folding back (Fernando *et al.*, 2007; Okemefuna *et al.*, 2008). Later, the structures of intact native FH in solution was investigated again using the same methods but with lower FH concentration, improved SAXS and AUC instrumentations, and more high resolution SCR domain structures. Improved medium-resolution structures of FH with a maximum length of 32 nm are then obtained (Figure 2.2 a). Electrostatic interactions contribute to the conformation of FH, as FH molecules become more elongated with increase in ion strength or pH. The oligosaccharides are found not to be significant in determining the conformation of FH (Okemefuna *et al.*, 2009).

2.2 Regulatory role of FH in the alternative pathway

In the alternative pathway, the formation and activity of the amplification C3 convertase $C\overline{3bBb}$ is strictly controlled both in the fluid phase and on the surface of host cells or tissues. The regulator FH is an important and effective inhibitor of the amplification cascade (Zipfel *et al.*, 2006). It acts as an inhibitor in three different ways.

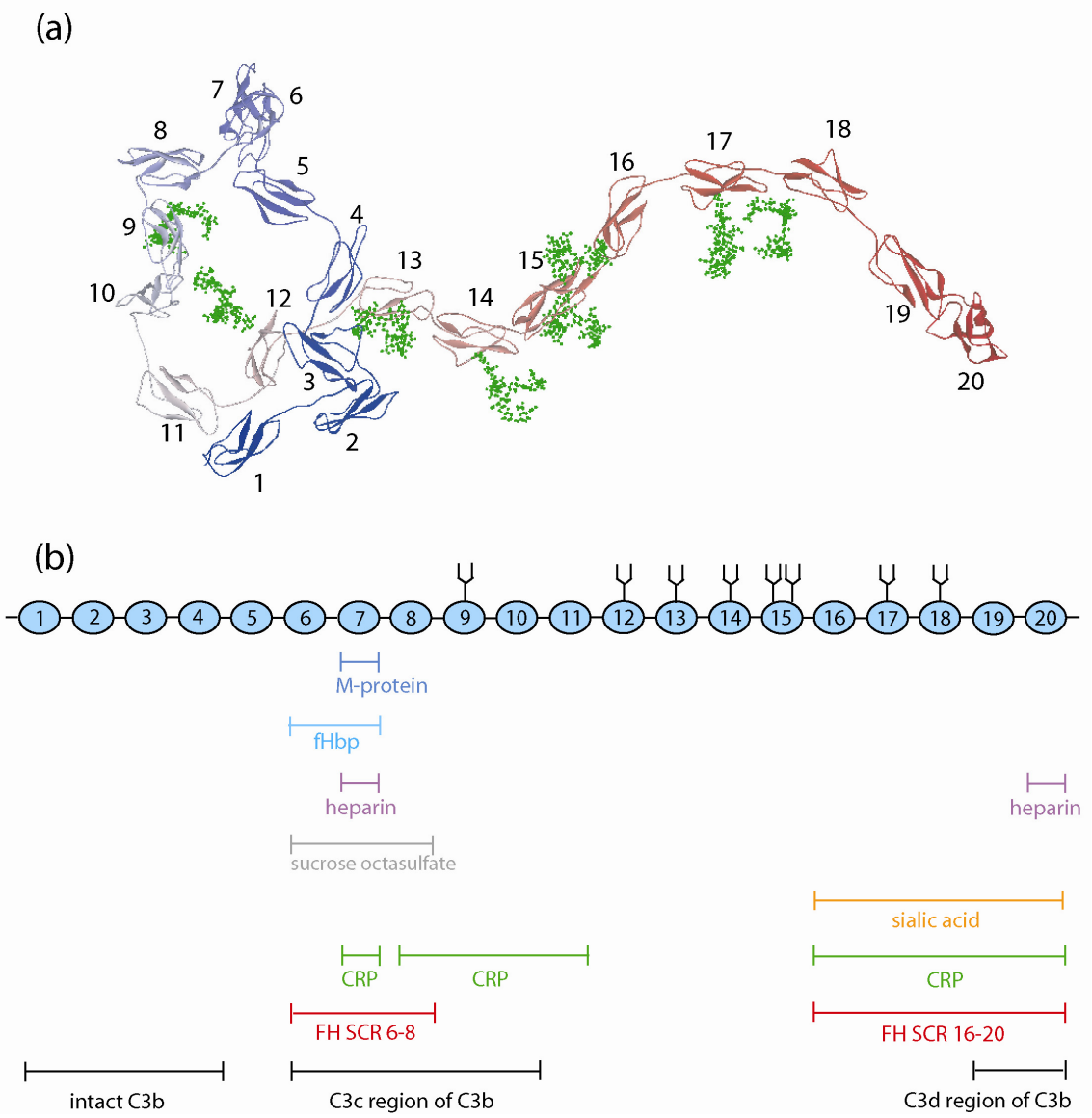

Figure 2.2 Illustration of structure and functional domains of FH. (a) The best fitting solution structure (PDB entry code: 3GAV) of native full-length FH in physiological conditions obtained from X-ray solution scattering combined with constrained modelling (Okemefuna *et al.*, 2009). (b) Mapping of binding sites on the 20 SCR domains for the FH ligands: pathogen expressed proteins such as streptococcal M-protein, FH binding proteins of *N. meningitides* (fHbp); polyanions such as heparin, sucrose octasulfate and sialic acid; C-reactive protein (CRP); potential self-association sites including SCR-6/8 and SCR-16/20; C3b. The eight oligosaccharides are shown as black forks.

Firstly, FH inhibits the assembly of the C3 convertase $C\overline{3bBb}$ by competing with factor B for binding to C3b. The function contributes to the discrimination by the alternative pathway between host cells and foreign cells. On host cells, polyanions such as sialic acids create a high affinity for FH, and therefore the alternative pathway is inhibited. By contrast, on foreign cells, a lack of polyanions results in a low affinity interaction between FH and C3b, and the binding of factor B to C3b is therefore favoured (Giannakis *et al.*, 2001; Zipfel *et al.*, 2006).

Secondly, acting as a cofactor of factor I, FH inactivates C3b molecules. Factor I is a highly specific serine protease which is involved in the regulation of the C3 convertases. Using FH which is bound to C3b on host cells surfaces as a cofactor, factor I cleaves C3b to yield C3f and iC3b which is further degraded to C3c, C3dg and C3d, and thus C3b is permanently inactivated by factor I (Law & Reid, 1995; Zipfel *et al.*, 2006).

Thirdly, FH displays decay accelerating activity to destroy any existing C3 convertase $C\overline{3bBb}$. If C3b forms the C3 convertase $C\overline{3bBb}$, binding of FH together with other complement regulatory proteins will displace Bb from C3b, and therefore the C3b convertase $C\overline{3bBb}$ is destroyed (Rother, 1998; Zipfel *et al.*, 2006).

2.3 Ligands of FH

2.3.1 Binding sites for C3b

FH binds to multiple ligands. The binding sites for various ligands are located on different SCR domains (Figure 2.2 b). The regulation function of FH on the alternative pathway is mediated by the binding between FH and C3b. The first binding site for C3b identified is located in the N-terminal SCR-1/4. Studies have shown that SCR-1/4 is required and sufficient for the decay accelerating and co-factor activities of FH in fluid phase (Alsenz *et al.*, 1984; Kuhn & Zipfel, 1996). The dissociation constant (K_D) between recombinant SCR-1/4 and C3b has been determined to be 11 μM by using surface plasmon resonance (SPR), and the crystal structure of the complex has been solved (Wu *et al.*, 2009). FH SCR-1/4 does not bind to the inactive cleavage products of C3b, C3d and C3c, indicating that the reciprocal binding site on C3b is destroyed by the

cleavage (Jokiranta *et al.*, 2000). The second C3b binding site has been mapped to the C-terminal SCR-16/20 and subsequently SCR-19/20, and the reciprocal binding site on C3b is located on the C3d part (Sharma & Pangburn, 1996; Jokiranta *et al.*, 2000; Hellwage *et al.*, 2002; Bhattacharjee *et al.*, 2010). The K_D of the interaction between FH SCR-19/20 and C3b is determined to be about 4 μM by using SPR (Schmidt *et al.*, 2008b). A third C3b-binding site specific for C3c has been suggested in the middle part of FH. It has been firstly suggested to be within or near SCR-6/10, and then SCR-12/14 (Sharma & Pangburn, 1996; Jokiranta *et al.*, 2000). SCR-10/12, or cooperation between two sub-sites including SCR-10 and the other within SCR-16/18 have also been hypothesised to be the locations (Schmidt *et al.*, 2008a). SCR-6/8 has been suggested to be a weak binding site for C3b by using SPR (Schmidt *et al.*, 2008b). Further evidence such as testing with appropriate constructs is needed for the mapping of the third C3b-binding site.

2.3.2 Binding sites for polyanions

The interaction between FH and polyanion such as sialic acid and glycosaminoglycans (GAGs) is crucial for the surface recognition function of FH. Heparin is the most sulphated GAGs. There are at least two heparin binding sites in intact FH. The first heparin binding site in FH has been found within SCR-6/10, and subsequently been located in SCR-7 (Sharma & Pangburn, 1996; Blackmore *et al.*, 1996). The crystal structure of FH SCR-6/8 with sucrose octasulfate which is an analogue of the GAGs revealed that SCR-6 and the linker between SCR-7 and SCR-8 also participate in glycan binding (Prosser *et al.*, 2007). SCR-13 and SCR-9 have also been suggested to have heparin binding sites (Pangburn *et al.*, 1991; Ormsby *et al.*, 2004), but later studies have suggested the contrary (Blackmore *et al.*, 1996; Schmidt *et al.*, 2008b). Another commonly approved heparin binding site is mapped to SCR-20 (Blackmore *et al.*, 1998). The C-terminal polyanion- and C3b-binding region is necessary for intact FH to recognize and protect normal host cells bearing polyanion on the cell surface (Pangburn, 2000; Pangburn, 2002; Oppermann *et al.*, 2006). Sialic acid on the surface of serum resistant *neisseria gonorrhoeae* was proved to be able to bind SCR-16/20 part of FH, and therefore protect the microbe from complement attack in serum (Ram *et al.*, 1998).

2.3.3 Binding sites for CRP

C-reactive protein (CRP) is an acute phase protein with a MW of 115 kDa. Native CRP is a pentamer composed of 5 subunits, and the assembly is stabilised by the presence of 2.5 mM Ca^{2+} in plasma (Okemefuna *et al.,* 2010). As mentioned in Section 1.2.1, CRP can activate the classical pathway by binding to the C1 complex. CRP has been reported to be able to inhibit the alternative pathway, which might be due to the recruitment of FH by CRP, but the mechanism of inhibition is still not clear (Mold *et al.*, 1999). The removal of Ca^{2+} can cause the CRP pentamer to dissociate to form modified CRP (mCRP) which is denatured and has functions different from the pentamer (Kinoshita *et al.*, 1989). There is no firm evidence for the existence of mCRP *in vivo* (Okemefuna *et al.,* 2010). The binding sites for CRP in FH have been originally located in SCR-7 and SCR-8/11 by using enzyme-linked immunosorbent assay (ELISA) and SPR (Jarva *et al.*, 1999; Giannakis, *et al.,* 2003). However, later studies suggested that there is no such interaction because earlier observed FH-CRP interactions resulted from the use of denatured CRP (Bíró *et al.*, 2007; Hakobyan *et al.*, 2008). The latest study using AUC, SAXS and SPR confirmed the interactions between FH and native CRP, and two independent binding sites for native CRP are mapped in SCR-6/8 with a K_D value of 3.9 μM and SCR-16/20 with a K_D value of 15.3 μM (Okemefuna *et al.,* 2010).

2.3.4 Self-association of FH

The earliest studies of native FH showed that FH exists as monomer in solution (Sim & DiScipio, 1982). The dimerisation of native FH was firstly suggested in 1991. The MW of FH was determined to be 250 – 300 kDa at concentrations between 1 to 11 mg/ml in solution which almost doubled the MW calculated from the FH sequence, by using X-ray solution scattering and neutron scattering. A V-shaped dimer model of two rods joined at an angle of 5° was proposed (Perkins *et al.*, 1991). However, later gel filtration and electron microscopy studies showed no dimer form of native intact FH, although the harsh conditions used for electron microscopy might abrogate the dimerisation of FH (DiScipio, 1992). In 2001, native intact FH was investigated again by using X-ray solution scattering, neutron scattering and analytical altracentrifugation in concentrations from 0.7 to 14 mg/ml. FH was shown to be monomeric with a MW of 147 kDa – 165 kDa in the physiological concentration range between 0.2 – 0.6 mg/ml,

and no concentration dependence of MW has been observed (Aslam & Perkins, 2001). On the other hand, various FH fragments have been demonstrated to self-associate. Fragments SCR-15/18 and SCR-15/20 were found to form some dimers by using non-reducing sodium dodecyl sulfate polyacrylamide gel electrophoresis (SDS-PAGE) and Western blotting analysis (Jokiranta *et al.*, 2000). Fragment SCR-1/7 was observed to bind to intact FH by SPR, and the dissociation profile suggested that the complex is stable (Oppermann *et al.*, 2006). Fragment SCR-6/8 in solution has been found to self-associate weakly from AUC analysis, and a K_D value of 40 μM was determined for the dimerisation of the His402 allotype of SCR-6/8 (Fernando *et al.*, 2007). Also from AUC analysis, SCR-1/5 was found to be monomeric in solution, while SCR-16/20 exhibited a weak monomer-dimer equilibrium with a K_D value of 16 μM (Okemefuna *et al.*, 2008). Some studies suggested that polyanion such as dextran sulphate or heparin can induce FH to form tetramers by size-exclusion gel filtration and AUC, and the site that mediates this polyanion-induced self-association has been mapped in SCR-18/20 (Pangburn *et al.*, 2009). In Chapter 5 and Chapter 7 of this thesis, the evidence for progressive self-association of full-length FH and its implications for complement regulation and disease will be explained.

2.3.5 Metal ligands for FH

Metals have not been commonly considered as FH ligands. In 1980, it was reported that Zn^{2+}, but not Mg^{2+}, Mn^{2+}, Ca^{2+}, Co^{2+}, Ni^{2+}, all at 1000 μM, can inhibit the cleavage of C3b by factor I assisted by FH. This was demonstrated by fluid assays performed with 0.065 mg/ml of C3b, 0.03 mg/ml of FI and 0.045 mg/ml of FH in 150 mM NaCl / 100 mM sodium phosphate buffer, pH 7, incubated at 37 °C (Crossley & Porter, 1980). The inhibition of degradation of C3b by Zn^{2+} was observed again by using fluid phase assays with 0.0014 mg/ml of ^{125}I-labelled C3b, 0.0014 mg/ml of FI, 0.0029 mg/ml of FH and 5000 μM of $ZnCl_2$ in 150 mM NaCl / 2.5 mM Tris-HCl buffer (pH 7.5) incubated at 37 °C. In the same study, it has been suggested that FH and C3b interact with Zn^{2+} with different affinities, whereas FI does not interact with Zn^{2+}, by using affinity chromatography on zinc chelate resin (Day & Sim, 1986). The zinc-induced oligomerisation of FH was firstly reported by X-ray solution scattering analyses of FH at concentrations of 2.7, 5.5, 8.2 and 10.9 mg/ml in 140 mM NaCl / 10 mM PIPES

[piperazine-N, N'-bis (2-ethanesulphonic acid)] buffer (pH 7.0) added with 10 to 500 μM Zn^{2+}, and similar experiments showed that 100 μM Co^{2+}, Hg^{2+}, Mg^{2+}, Mn^{2+} and Ni^{2+} have no effect on FH. This suggested that the inhibitory effect of Zn^{2+} reported originally is a result of zinc-induced rapid oligomerisation of FH (Perkins *et al.*, 1991). However, it has been suggested that Zn^{2+} at 100 – 500 μM enhances the FH activity and abolishes FH activity at 2000 μM and above, while Mg^{2+}, Ni^{2+}, Cu^{2+}, Co^{2+}, Fe^{2+} at 1000 μM or Ca^{2+} at 3000 μM has no effect. This finding was concluded from fluid phase assays using 0.012 mg/ml C3b with trace amounts of ^{125}I-labelled C3b, 0.0051 mg/ml FI and 0.031 mg/ml FH in 150 mM NaCl / 50 mM Tris-HCl buffer (pH 7.4) incubated at 37 °C (Blom *et al.*, 2003). The inhibitory role of zinc was investigated again later by incubating 75 ng/ml of ^{125}I-C3(NH_3), 97 ng/ml of FI and 310 ng/ml of FH in 10 mM potassium phosphate buffer at 37 °C. Zn^{2+} inhibited the breakdown of ^{125}I-C3(NH_3) by FI and FH at 20 or 100 μM, but did not have any effect on FI amidolytic activity without FH (Tsiftsoglou & Sim, 2004). This is consistent with the previous finding that Zn^{2+} binding to FH but not to FI (Day & Sim, 1986; Tsiftsoglou & Sim, 2004). It is noticeable that all the fluid phase assays mentioned above were done with FH concentrations that are far lower than the physiological concentration (0.235 mg/ml - 0.810 mg/ml in serum) (Neumann *et al.*, 2003). The K_D of the interaction between FH and Zn^{2+} has not been obtained, and the zinc binding sites have not been identified.

Four types of zinc binding sites have been identified in proteins: catalytic, cocatalytic, structural and protein interface. In the latter case, zinc sites are formed from ligands supplied by amino acid residues located at the binding surface between the two proteins. Such interactions can induce oligomerisation of the same protein or link two different proteins through intermolecular ligands (Auld, 2001). The most frequently observed coordination geometry of zinc binding sites is tetrahedral, and the sites at protein interfaces often include surface His, Asp, Cys and Glu residues (Rulísek & Vondrásek, 1998). From analysis of zinc binding in known protein structures, the protein interface binding sites are primarily supplied by residues His, Glu and Asp, but sites containing Cys are also found, and β-sheets secondary structure predominately contribute to such ligands (Auld, 2001). Thus, the β-sheet-rich SCR domains of FH with His, Glu and Asp residues that are exposed on the surface could form potential zinc binding sites.

2.3.6 Other ligands of FH

As mentioned in Section 1.7, to avoid complement attack from the host, various microorganisms have developed strategies to minimise the deposition of C3b on the pathogen surface. A streptococci bacterium can express type-specific surface proteins called M proteins which protect the microbes from phagocytosis by binding to FH and therefore down-regulating the opsonization mediated by C3b (Horstmann *et al.*, 1988). The binding site for M protein in FH has been located in SCR-7 (Kotarsky *et al.*, 1998). Site-directed mutagenesis has shown certain residues in SCR-7 that are commonly essential for binding of heparin, CRP and M protein (Giannakis *et al.*, 2003). Another example of such microorganisms is *Neisseria meningitidis*. FH binding protein (fHbp) is a 27 kDa lipoprotein present on the surface of all strains of *N. meningitidis*. The binding site for fHbp is in SCR-6/7 of FH, and the K_D of the interaction is about 5 nM (Schneider *et al.*, 2009). In addition, FH is an adhesion ligand for human neutrophils. The presence of surface bound FH can enhance the neutrophil activities. The specific receptor on neutrophil cell surface for FH has been identified to be integrin alphaMbeta2 (CD11b/CD18) (DiScipio *et al.*, 1998).

2.4 FH expression and genetics

2.4.1 FH biosynthesis

Like the complement components C1r, C1s, C2 to C5, factor B and factor I, both FH and FHL1 are constitutively synthesised and secreted by the liver (Morris *et al.*, 1982; Friese *et al.*, 1999). Various amounts of both proteins are produced by different liver cell types such as hepatocytes and Kuffer cells (Schalf *et al.*, 2001). Both FH and FHL1 can also be synthesised locally at the sites of infection and inflammation by a wide range of extrahepatic cells such as endothelial cells, fibroblasts, myoblasts, mono-nuclear phagocytes, neurons, glomerular mesangial cells, peripheral blood lymphocytes, glial cells and retinal pigment epithelial (RPE) cells (Friese *et al.*, 1999; An *et al.*, 2006; Chen *et al.*, 2007). Depending on the cell type, FH and FHL1 can be synthesised constitutively, and / or induced by cytokine mediators. Their expressions can be regulated differently depending on the cell type. Cytokines and inflammation mediators such as interferon-α (IFN- α), IFN-γ, interleukin-1 (IL-1), IL-2, IL-6, anti-inflammatory

agents (e.g. Dexamethasone), retinoid acid, phorbol myristate acetate and lipopolysaccharide are reported to be able to regulate the expression of FH and FHL1 (Friese *et al.*, 1999). In normal individuals, the concentration of FH varies from 235 to 810 μg/ml in serum (Neumann *et al.*, 2003). The level of FH is influenced by age, genetic and environmental factors (Esparza-Gordillo *et al.*, 2004).

2.4.2 FH gene

As discussed in Section 1.5, FH is a member of the 'regulators of complement activation' (RCA) family. Its gene is located in the RCA gene cluster on chromosome 1q32 (Figure 2.3 a) (Krushkal *et al.*, 2000). The RCA gene cluster contains 60 genes, amongst which 15 genes encode for complement-related proteins. Those 15 genes are arranged within two DNA segments separated by a 14.59 cM long DNA which is not related to complement proteins. One DNA segment contains the genes encoding the FH family proteins including FH, CFHR3, CFHR1, CFHR4, CFHR2 and CFHR5, and the other DNA segments contains the genes encoding C4BPβ, C4BPα, C4BPαL1, C4BPαL2, DAF, CR2, CR1, MCPL1, CR1L1 and MCP. The FH gene is composed of 23 exons and is 94 kb in length. Exon 1 encodes for the un-translated 5' end mRNA region and the 18 amino acid signal peptide of FH. Every other exon encodes for one SCR domain. There are two exceptions. The first one is that exon 3 and 4 together encode SCR-2. The second one is exon 10 which encodes exclusively for FHL-1 rather than FH (de Córdoba & de Jorge, 2008).

2.4.3 FH family proteins

The FH family proteins include FH, FHL1, as well as five FH-related proteins CFHR1, CFHR2, CFHR3, CFHR4 and CFHR5. Those closely related plasma glycoproteins are all mainly synthesised in the liver, and their genes arranged in tandem in the RCA gene cluster on chromosome 1q32 (Figure 2.3 a). Two transcripts, FH and FHL1, have been found for the FH gene, and another two transcripts, CFHR4A and CFHR4B, for the CFHR4 gene, as results of alternative splicing. Deletions within the FH and CFHR1-5 gene region can cause a FH: CFHR1 hybrid gene and / or the deletion of the CFHR3 and CFHR1 genes (Józsi & Zipfel, 2008).

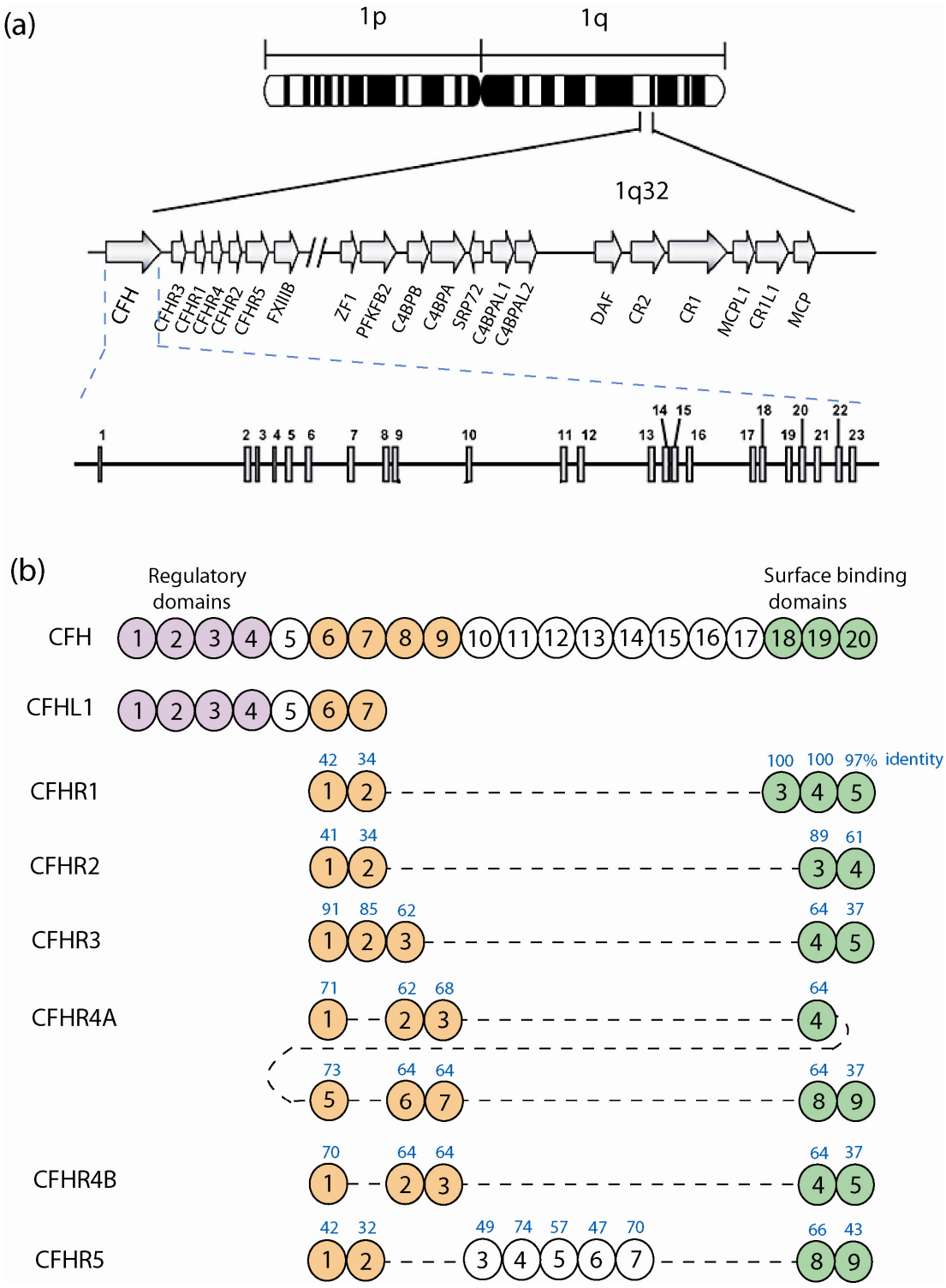

Figure 2.3 Genetics of FH family proteins. (a) Arrangement of the RCA gene cluster and the composition of FH gene (adapted from de Córdoba & de Jorge, 2008). (b) Homology alignment of SCR domains among FH family proteins. Homologous SCR domains are aligned vertically, and the percentages of identity at the protein level to the corresponding FH SCR domain are notified in blue above the domains (adapted from Józsi & Zipfel, 2008).

The FH family proteins are exclusively composed of SCR domains. As discussed in Section 2.3.1 and Section 2.3.2, the functions of acting as a cofactor for factor I and accelerating the decay of C3 convertase are displayed by SCR-1/4 at the N-terminal of FH, whereas the surface binding and recognition functions are displayed by SCR-18/20 at the C-terminal. Other FH family proteins are composed of four to nine SCR domains (Figure 2.3 b). FHL1 is another transcript of the FH gene, and contains SCR-1/7 of FH and a unique extension of four amino acids (Ser-Phe-Leu-Thr) at the C-terminal. Therefore FHL1 can regulate the complement cascades in a similar way as FH does. The homology study of SCR sequences of FH and CFH1-5 revealed that the central region (SCR-6/9) and surface binding region (SCR-18/20) of FH are conserved (Figure 2.3 b). The homology of SCR domains implies similar ligand bindings and overlapping functions. For example, CFHR3, not CFHR4 has a domain homologous to SCR-7 of FH, and thus CFHR3, not CFHR4 can bind to M-protein and heparin. The lack of SCR-1/4 of FH at the N-terminal in all CFHR proteins may explain the fact that CFHR proteins do not have complement cascade regulation functions, and the presence of the similar C-terminal region suggests the similar surface binding and recognition functions. The difference in binding affinities depends on the extent of homology between SCR domains. It is still not clear whether CFHR proteins cooperate or compete with FH in the complement regulation, or perform independent activities (Józsi & Zipfel, 2008).

2.5 FH genetically related diseases

Mutations, polymorphisms and large deletions in FH gene and FH related protein genes (Section 2.4.3) are related to several human diseases. As discussed in Section 1.7, FH is one of the proteins that are genetically related to atypical haemolytic uraemic syndrome (aHUS), membranoproliferative glomerulonephritis type II (MPGN II), age-related macular degeneration (AMD) and Alzheimer's disease (AD). It has been hypothesized that those diseases are caused by the mis-regulation of the complement system.

2.5.1 FH and atypical haemolytic uraemic syndrome (aHUS)

aHUS is a severe kidney disease that is characterized by thrombocytopenia, microangiopathic haemolytic anemia and acute kidney failure. The primary event of this disease is endothelial cell injury (Atkinson & Goodship, 2007). The mutations of FH

related to aHUS prevalently occur in the C-terminal region which is responsible for cell recognition and binding (de Córdoba & de Jorge, 2008). The database http://www.fh-hus.org showed an updated collection of aHUS-related FH mutations (Saunders *et al.*, 2006; Saunders *et al.*, 2007). The mutant FH molecules showed weaker binding affinities to C3d part of C3b, heparin and endothelial cells in several cases (Manuelian *et al.*, 2003; Józsi *et al.*, 2006). In addition, deletion of the CFHR3 and CFHR1 genes and hybrid FH-CFHR1 gene caused by genomic deletion are also related to higher risks for developing aHUS (Zipfel *et al.*, 2007; Venables *et al.*, 2006). There are also five variants in CFHR5 associated with aHUS (Monteferrante at al., 2007).

2.5.2 FH and membranoproliferative glomerulonephritis type II (MPGN II)

MPGN II is a rare kidney disease which is hallmarked by the presence of dense deposits within glomerular basement membrane (GBM) and the thickening of GBM. There are two types of FH mutations that are related to MPGN II. The mutations of the first type can result in impaired FH secretion. Those mutations include those of essential consensus cysteine residues such as Cys431Ser, Cys673Ser and Cys959Tyr, and those of some other residues such as Arg127Leu. The second type includes mutations that cause reduced co-factor and decay accelerating functions of FH in plasma, such as a mutation that result in the deletion of Lys224 in SCR-4 (http://www.fh-hus.org). Further more, three variants on CFHR5 gene have also been reported more frequent in MPGN II patients than in healthy populations (Abrera-Abeleda *et al.*, 2006).

2.5.3 FH and age-related macular degeneration (AMD)

AMD is a leading cause of visual impairment and blindness in the elderly in the Western world (Hageman *et al.*, 2005; Klein *et al.*, 2005). Between 20 and 25 million people are affected worldwide, a figure that will triple with the increase in the ageing population in the next 30-40 years. According to the World Health Organization, due to AMD, 8 million people have severe blindness. Between 182,000 and 300,000 people in the United Kingdom are blind or partially sighted as a result of AMD (Chopdar *et al.*, 2003). AMD is characterised by degenerative and neovascular changes which cause central field visual loss, and occur at the interface between the neural retina and the underlying choroid. At this location are the retinal photoreceptors, the retinal pigmented

epithelium (RPE), Bruch's membrane (BM), which is an extracellular matrix layer interposed between the retinal pigment epithelium (RPE) and the choroidal vasculature, and a network of choroidal capillaries (Hageman *et al.*, 2005; Klein *et al.*, 2005).

A key feature of AMD is the appearance of sub-retinal pigment epithelial deposits (sRPEds) that can be focal (drusen) or diffuse (basal linear and laminar) in the early stages of this disease, and those extracellular deposits accumulate within the BM (Bird, 1992; Bird *et al.*, 1995; Guymer & Bird, 1998). The compositions of drusen include remnants of the RPE, dendric cell processes, oxidized lipids, carbohydrates, and over 200 aggregated proteins such as tissue metalloproteinase inhibitor 3, clusterin, vitronectin, serum albumin, crystallin, immunoglobulins and a range of complement components such as C3 and C9, the membrane attack complex, activators and regulators such as FH (Figure 2.4 a) (Mullins *et al.*, 2000; Crabb *et al.*, 2002; Hageman *et al.*, 2005; Bok, 2005). The PRE is a local source for FH and FHL1 (Hageman *et al.*, 2005). It has been suggested that oxidative injury and local complement activation related inflammation are associated with the formation of drusen (Crabb *et al.*, 2002; Hageman, et al, 2001; Anderson *et al.*, 2002; Hageman *et al.*, 2005). High mM concentrations of zinc have also been found in sRPEds and Bruch's membrane (Lengyel *et al.*, 2007). The function of zinc in the retina and its possible relations to the pathology of AMD will be discussed in Chapter 3. The presence of FH and high concentration of zinc in drusen provides a possibility that the interation between FH and zinc (Section 2.3.5) might be involved in the formation of drusen. The investigations on this possibility will be explained in Chapter 6 and Chapter 8.

Due to the similarity between the manifestations of MPGN II and that of AMD, FH has been investigated as a prime candidate protein which is genetically related to AMD. A common polymorphism of FH, Tyr402His (Figure 2.4 b), was identified as a major risk factor for developing AMD. It is associated with 50 % of AMD cases (Klein *et al.*, 2005; Haines *et al.*, 2005; Hageman *et al.*, 2005; Edwards *et al.*, 2005). The Tyr402His polymorphism is translated from a cDNA variant of FH, T1277C in exon 9 (Goodship, 2006). Residue 402 is located in SCR-7 which contains a binding site for heparin, CRP and for various microbial antigens (Giannakis *et al.*, 2003; Ormsby *et al.*, 2006). The NMR structures of Tyr402 SCR-7 and His402 SCR-7 have been shown to be nearly identical, and the 402 side chain was observed to be solvent-exposed and far from the

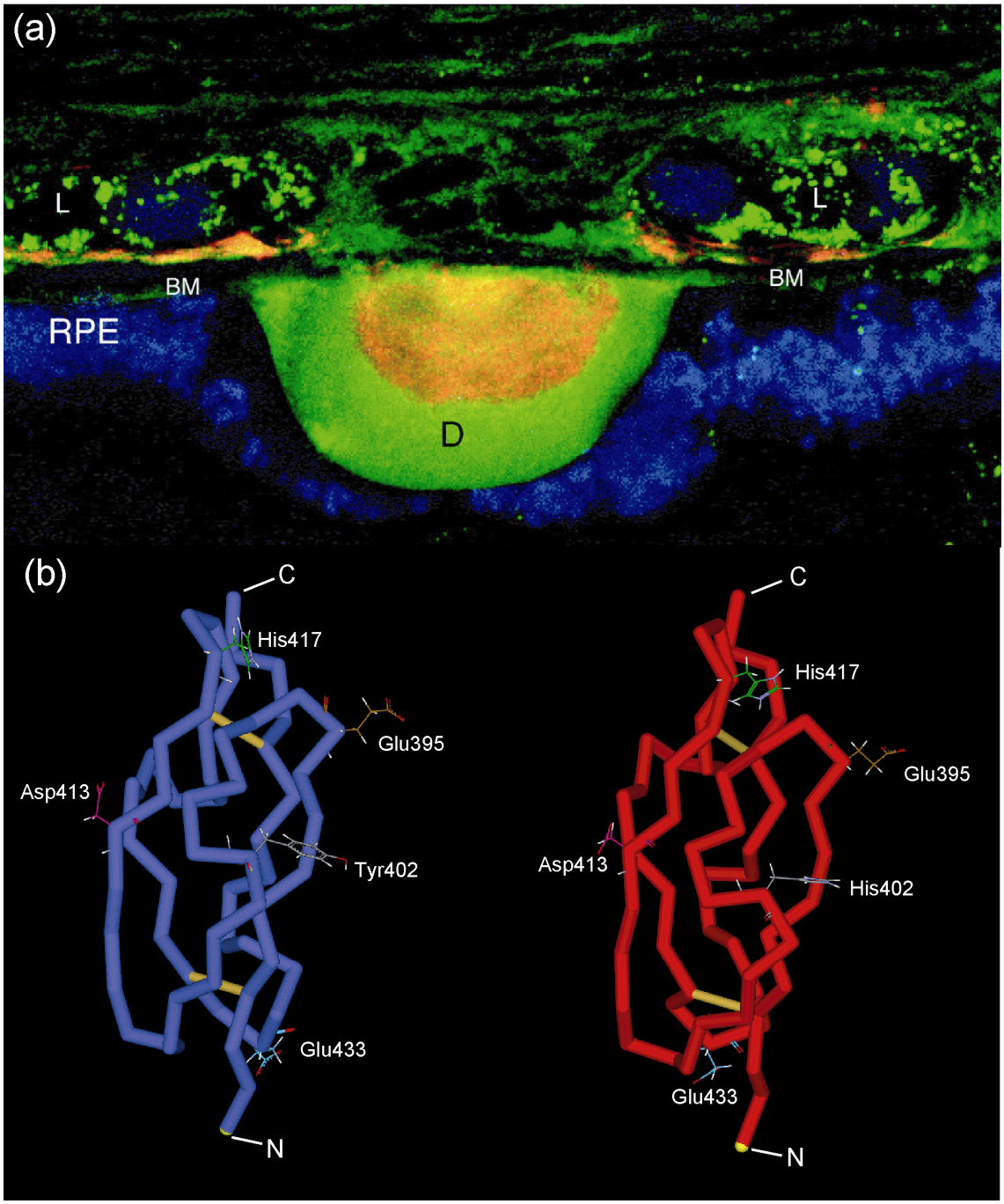

Figure 2.4 FH and AMD. (a) Immunocytochemistry of a drusen (D) stained with antibodies against FH (green), C5b-9 membrane attack complex (orange) and autofluorescent lipofuscin granules (blue). FH staining is also visible in the lumen (L) of the capillaries (Taken from Bok, 2005). (b) NMR structures of FH SCR-7. The structure of Tyr402 SCR-7 is notified in blue (PDB entry code: 2JGX) and that of His402 SCR-7 is notified in red (PDB entry code: 2JGW). The residues including Glu395, Tyr/His402, Asp413, His417 and Glu433 are labelled, as residues His, Glu and Asp exposed on the surface have potential to contribute to form zinc binding sites.

interfaces with the neighbouring SCR-6 or SCR-8 (Herbert *et al.*, 2007). In addition, the solution structure of FH SCR-6/8 in physiological conditions have also been solved by using a combination of solution scattering, analytical ultracentrifugation and modelling studies, and no conformational difference was detected between the Tyr402 and His402 forms of FH SCR-6/8 (Fernando *et al.*, 2007). However, due to the flexibility of the intact FH molecules and their folded back structures in solution, the impact of the change from the surface-exposed tyrosine to histidine at position 402 on the structure of full length FH needs to be studied (Chapter 7).

Since the change from tyrosine to histidine near the binding sites may influence the binding of the ligands and thus leads to a dysfunctional FH, studies have been focused on comparing the binding affinities of the Tyr402 and His402 allotypes of FH with various ligands. The single domain recombinant His402 SCR-7 showed significant weaker binding than Tyr402 SCR-7 did to a heparin affinity column and to defined-length sulphated heparin oligosaccharides employed in gel mobility shifts assays (Herbert *et al.*, 2007). Accordingly, the *Escherichia coli* expressed recombinant His402 FH SCR-6/8 showed weaker binding to a heparin affinity column than Tyr402 FH SCR-6/8 did (Clark *et al.*, 2006). However, equal binding affinities to heparin have been observed for the two forms of FH SCR-6/8 by using similar methods but *Pichia pastoris* expressed recombinant FH fragments, and also for two forms of full-length FH purified from human plasma (Herbert *et al.*, 2007). The difference between the heparin bindings of FH SCR-6/8 and full-length FH might be due to the existence of other GAGs binding sites in the C-terminal SCR-20 domain (Section 2.3.2). In the context of FH binding to CRP, the His402 form of full-length FH, FHL1, recombinant FH SCR-5/7 and FH SCR-6/8 showed reduced affinity to CRP measured by SPR and ELISA (Schmidt *et al.*, 2008a). As mentioned in Section 2.3.3, controversy has been raised by later studies suggested that the FH only interacts with CRP when native CRP pentamers disassociate by removing Ca^{2+} (Bíró *et al.*, 2007; Hakobyan *et al.*, 2008). However, the latest study using AUC, SAXS and SPR confirmed the interactions between FH and native CRP, and that the His402 form of recombinant FH SCR-6/8 is a weaker binder (Okemefuna *et al.*, 2010). Another supporting evidence for this 'FH-CRP hypothesis' is that higher level of CRP is present in the choroid with the risky His402 form of FH, although this could be a result of chronic inflammation which is a by-product of the defect complement regulatory function of FH (Johnson *et al.*, 2006). In the context of C3b

binding, according to a SPR study, the two forms of recombinant FH SCR-6/8 bind to C3b with approximately same weak affinity (Schmidt *et al.*, 2008b). Indeed, in another study both forms of full-length FH and FHL1 showed similar binding to C3b as determined by ELISA (Skerka *et al.*, 2007). The deoxyribonucleic acid (DNA) and the extracellular matrix proteoglycan fibromodulin (FMOD) have also been identified as FH ligands which bind to SCR-6/8 part of FH. In one study the Tyr402 form of FH SCR-6/8 bound stronger to FMOD but weaker to DNA and necrotic cells than the His402 form of FH SCR-6/8 (Sjöberg *et al.*, 2007). The His402 form of both full-length FH and FHL1 exhibited reduced binding to RPE cells and endothelial cells. The two forms of full-length FH and FHL1 showed similar cofactor activity in C3 degeneration in fluid phase, although the His402 form of FHL1 displayed weaker regulatory activity at the Chinese hamster ovary cell surface (Skerka *et al.*, 2007). Although FH itself (Section 2.3.4) and Zn^{2+} (Section 2.3.5) are also FH ligands and abundant Zn^{2+} is present in drusen, very few studies have been focused on comparing these properties between the Tyr402 form and His402 form of FH. In 2007, an AUC study suggested that the His402 form of FH SCR-6/8 can self-associate slightly greater than the Tyr402 form. The effects of the Tyr402His polymorphism on the self-association properties of full-length FH will be discussed in Chapter 7. This polymorphism introduced a surface-exposed histidine residue to SCR-7 which might contribute to form a zinc binding sites (Section 2.3.5), and its effects on zinc binding properties of FH and the implications for AMD will be discussed in Chapter 8.

In addition, other polymorphisms of FH such as c.59-18insTT in intron 2, Ile62Val in SCR-1, Ala307Ala in SCR-5 and Ala473Ala in SCR-8 have also been found to be risk factors for developing AMD (http://www.fh-hus.org). One recent study is focused on comparing the Ile62 and the Val62 form of full-length FH, and it suggested that the Ile62 form binds better to C3b and has stronger cofactor activity in fluid phase and surface bound C3 degeneration, based on ELISA and SPR analyses (Tortajada *et al.*, 2009). It has been suggested that the deletion of CFHR3 and CFHR1 genes contributes to a lower risk for developing AMD (Hughes *et al.*, 2006; Hageman *et al.*, 2006). Until now, the molecular mechanism for the pathology of AMD is not clear.

Chapter Three

Zinc in the retina

3.1 Composition of the retina in the eye

3.1.1 Structure of the eye

The human eye is an approximate sphere which is about 2.5 cm in diameter and has a volume of 6.5 ml, but it actually contains two spheres including the smaller one, cornea, and the larger one, sclera (Figure 3.1). The coat of the eye consists three main layers. The outer layer is the fibrous coat formed by the cornea and sclera. The transparent cornea and associated tear film are responsible for most of the refraction of the eye. The sclera consists of dense irregular connective tissue and elastic tissue which make the sclera strong and flexible enough for protecting the intraocular contents and maintaining the global shape of the eye. The middle layer is the uvea tract which is composed of the choroid, ciliary body and iris. The iris is a thin circular disk which mimics the diaphragm of a camera. The middle opening of iris is the pupil which can change size to regulate the amount of light coming into the eye. The ciliary body functions together with the zonules to change the optic power of the lens (accommodation), and secretes the aqueous humour which fills the space between the lens and the cornea. The choroid is a vascular connective tissue which mainly functions to nourish the retina. The inner layer is the retina which is responsible for detecting lights in the retina image and converting the light energy into neural impulses that are transmitted to the brain. The contents surrounded by the coat contain the lens and the transparent media including the aqueous humour and the vitreous body. The lens can change shape and thus alter the refractive index of the light to focus on the retina and give a clear image. The posterior chamber and the anterior chamber are filled with the transparent aqueous humour which is essential for the transportation of the necessary metabolites to the lens and cornea and for the maintenance of intraocular pressure. The largest cavity in the eye, the vitreous cavity, contains vitreous humour which is a transparent viscoelastic gel. The vitreous humour is almost cell-less, but hyalocytes, the main cell types in the vitreous humour which are active phagocytes, are occasionally present (Oyster, 1999; Forrester *et al.*, 2002).

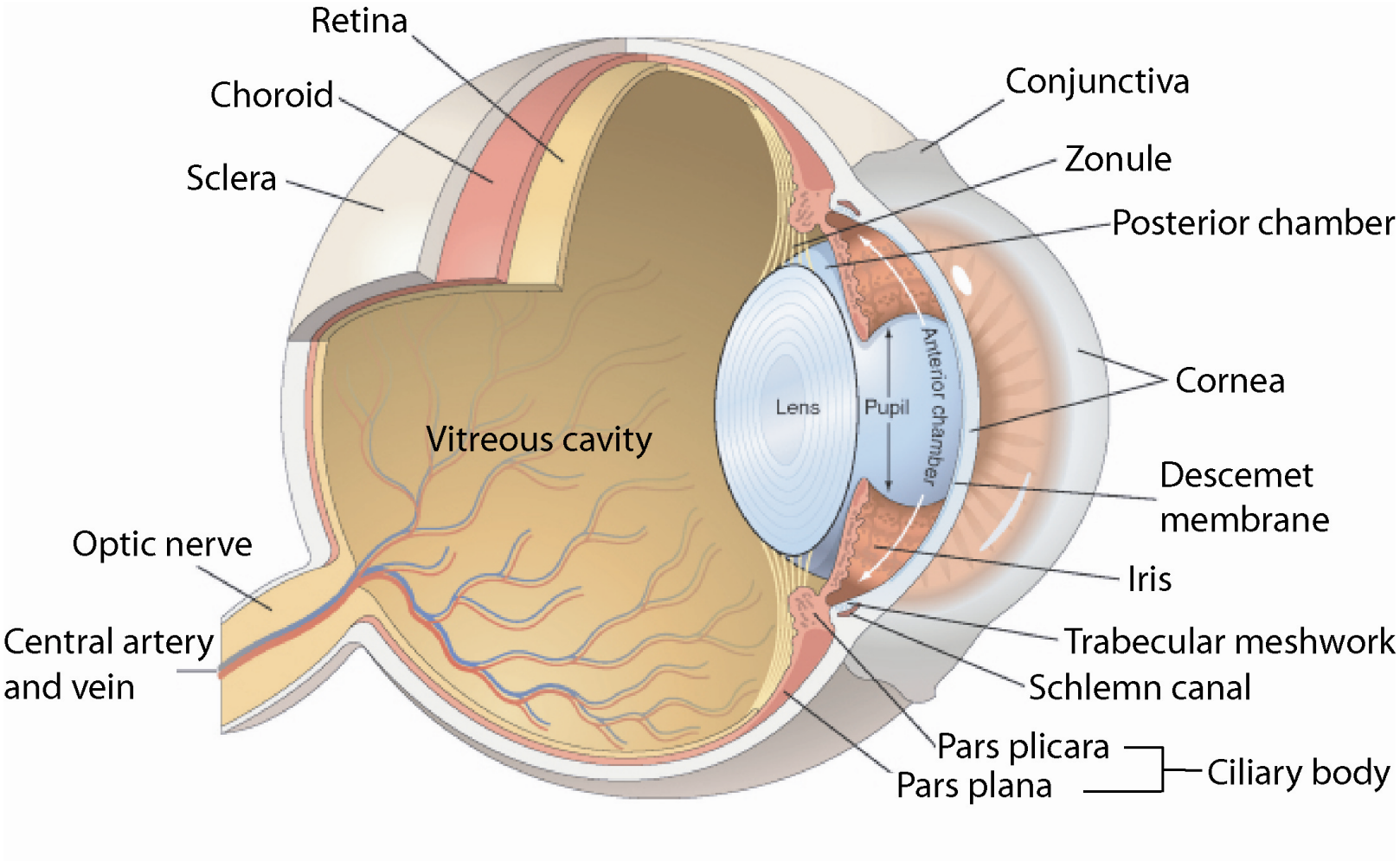

Figure 3.1 Schematic diagram of the human eye. The outer layer formed by the sclera and cornea is notified in light grey, the middle layer, the uvea tract is notified in red, and the inner layer formed by the retina is notified in yellow (adapted from Kumar *et al.*, 2010).

3.2.2 Structure of the retina

The retina consists of two main layers. The outer layer is the retinal pigment epithelium (RPE), and the inner layer is the neurosensory retina. The RPE lies between the outer segments of the photoreceptor layers of the sensory retina and the Bruch's membrane (BM). The BM is a very thin extra cellular matrix (2 μm to 3 μm in thickness). It is formed by the basement membranes of the RPE and choroidal endothelium, and a central layer composed of interlaced elastic fibers sandwiched between two layers of collagen fibers. The BM limits the passing of fluid between the choroid and the RPE, and gradually thickens with age (Oyster, 1999). The RPE is a single continous layer of cuboidal epithelial cells which is not directly involved in the neural events of vision. The RPE forms the blood-retina barrier, a selectively permeable barrier which controls the fluid flow between the neurosensory retina and the choroid. The RPE produces melanin which can absorb excess light energy and thus reduces the scattering of light in the eye. The RPE can also phagocytise the rod outer segments, and transport and store vitamins, especially vitamin A and metabolites. Among any cell layer in the human body, the RPE faces one of the strongest oxidative stresses (Federman *et al.*, 1994).

The neurosensory retina has been shown with nine layers, and it contains several different cell types of which neural cells predominate (Figure 3.2). Photoreceptors form four layers of the neurosensory retina. Two kinds of photoreceptors, rods and cones, are present in the human retina. Their outer and inner segments form the photoreceptor layer, the tight junctions between photoreceptors and Müller's cells form the external limiting membrane, their nuclei form the outer nuclear layer, and their axons and terminals form the outer plexiform layer. The inner nuclear layer consists of the nuclei of the cells including bipolar cells, horizontal cells, most of amacrine cells, displaced ganglion cells, and interplexiform cells. The inner plexiform layer is composed of the interlaced dendrites of ganglian cells and the cells in the inner nuclear layer, and it contains multiple sublayers. The ganglion cell layer consists of the cell bodies of ganglion cells and displaced amacrine cells. Müller's cells are the main cell types of the ganglion cells. The next layer is the nerve fiber layer which is formed by the axons of ganglion cells. The internal limiting membrane contains the terminal expansions of Müller's cells which extend to the photoreceptor layer. Functionally speaking, the photoreceptors contain photopigments such as rhodopsin in the outer segment which

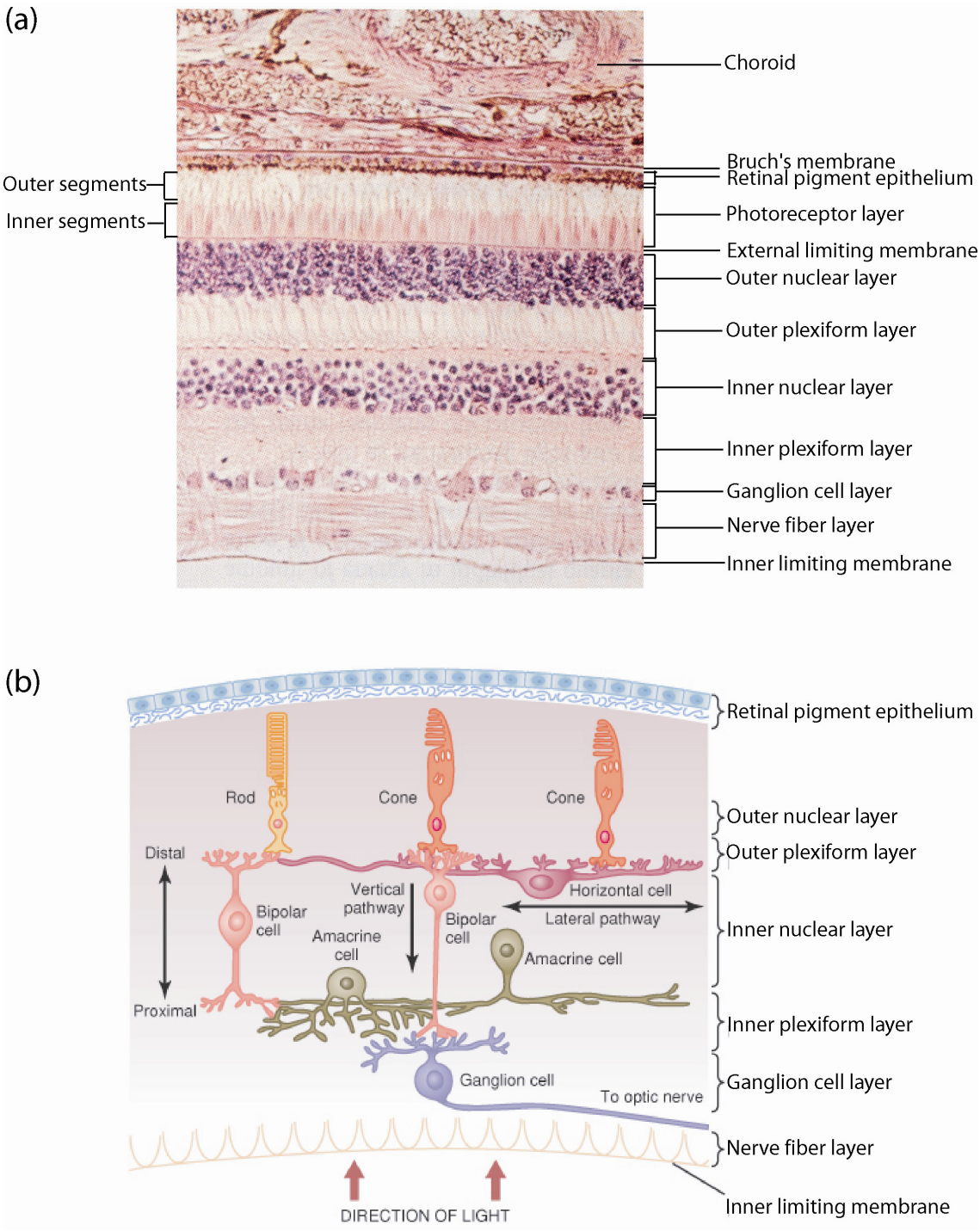

Figure 3.2 Layers of human retina. (a) A section of human retina which shows its organizations. Layers are labelled at the corresponding positions (adapted from Federman *et al.*, 1994). (b) Different functions of neural cells in certain layers of the retina in the phototransduction (Taken from Guyton & Hall, 2006).

can absorb light, and thereafter the photoreceptors produce chemical signals which set off the phototransduction cascades. The signals produced by the photoreceptors are transmitted to the bipolar cells and subsequently to the ganglion cells by making synaptic contacts, and finally the signals are conveyed to the brain. This pathway is defined as the vertical pathway in the retina (Figure 3.2 b). There are also two levels of lateral pathways. The outer level is composed of horizontal cells, and the inner level is formed by amacrine cells. The horizontal cells and the amacrine cells make connections between the vertical pathways, and transform the signal in the vertical pathways from the amount of light to the illumination contrast between photoreceptors and their neighbours. In addition, there is another pathway called the recurrent pathway which is made up of the interplexiform cells which can received input signals from bipolar cells and amacrine cells in the inner retina and give output signals to horizontal cells in the outer retina. The recurrent pathway might play a role in adjusting the sensitivity of the retina (Oyster, 1999).

3.2 Zinc in the eye

3.2.1 Distribution of zinc in the human body

Zinc is an important metal for the growth of plants and animals, and it is the second most abundant trace mineral in the human body. The normal content of zinc in the human body is about 2 g. Most zinc in the human body is intracellular, and the organs that contain relatively high zinc concentrations are the muscle, skin, liver, prostate gland, bones and eye (Karcioglu, 1982; Grahn *et al.*, 2001). The average concentration of zinc in plasma is 12.7 μM (AREDS Research Group, 2002). Most of zinc in plasma is bound to various proteins. For example, 70-85% zinc in plasma is bound to serum albumin which has been considered as the major zinc transporter in plasma (Lu *et al.*, 2008). It has been shown that only 2-8% (0.25 – 1.02 μM) of zinc in plasma is free or chelatable or histochemically reactive (Blom *et al.*, 2003). The RPE and choroid can take up and retain zinc from the blood (Newsome *et al.*, 1992). Ocular tissues contain unusually high concentration of zinc. In human ocular tissues, the zinc concentrations in descending order are 472 μg/g of dry tissue in the RPE and choroid, 464 μg/g in the retina, 227 μg/g in the ciliary body, 132 μg/g in the iris, 113 μg/g in the optic nerves, 49 μg/g in the sclera, 41 μg/g in the cornea and 21 μg/g in the lens (Galin *et al.*, 1962). It has been suggested that if zinc is distributed in retina in the same way it is distributed in

the brain, then only 10 % of retinal zinc is free or loosely bound to proteins (Ugarte & Osborne, 2001).

3.2.2 Putative functions of zinc in the retina

Although zinc is certainly important for the normal function of the retina, the reason for this is not well understood. However, some studies have provided evidence for several putative roles for zinc in the retina. First of all, zinc has been suggested to be able to interact with vitamin A which is taken up by the RPE and is crucial for the activation of rhodopsin and thus the detection of light in the outer segments. Zinc also interacts with taurine, a free amino acid that is an essential neurochemical factor in the visual system, and therefore is involved in the normal functions of the retina. Secondly, zinc is commonly present in the disc membrane which is a component of the outer segment and is developed as obtrusions of the plasma membrane at the outer segment base. Since zinc is important for the normal function of the plasma membrane, it might be involved this way in the function of the photoreceptors. Thirdly, zinc has been reported to interact with rhodopsin and enhance its phosphorylation which initiates the phototransduction of rods. One supporting study found that zinc is mainly located in the photoreceptor perikarya in the outer nuclear layer and the RPE in the dark-adapted retina, but is translocated into the outer and inner segments in the light-adapted retina. The shift of the zinc location may suggest that zinc is involved in primary photochemical events. In addition, zinc might function as a regulator of synaptic transmission, because concentrated zinc has been found in the synaptic terminal regions of photoreceptors. Zinc has also been reported to be capable of modulating the response to the neurotransmitter γ-aminobutyric acid (GABA), a major inhibitory neurotransmitter, in horizontal cells, bipolar cells and ganglion cells. Furthermore, another hypothesised role of zinc is to serve as an antioxidant in the retina which is under intense oxidative stress, since zinc can protect thiol groups from oxidation and inhibit the production of reactive oxygen species by transition metals in some other tissues (Ugarte & Osborne, 2001; Grahn *et al.*, 2001). However, in contrast to all the positive roles that zinc might play, exposure of the retinal tissue to excess amount of free zinc (>20 μM) can induce cell damage, as proved *in vitro* and *in vivo*. The RPE cells can accumulate zinc and prevent extra zinc from entering the neurosensory retina, but under stimuli such as light, the RPE cells can release protein-bound zinc to become

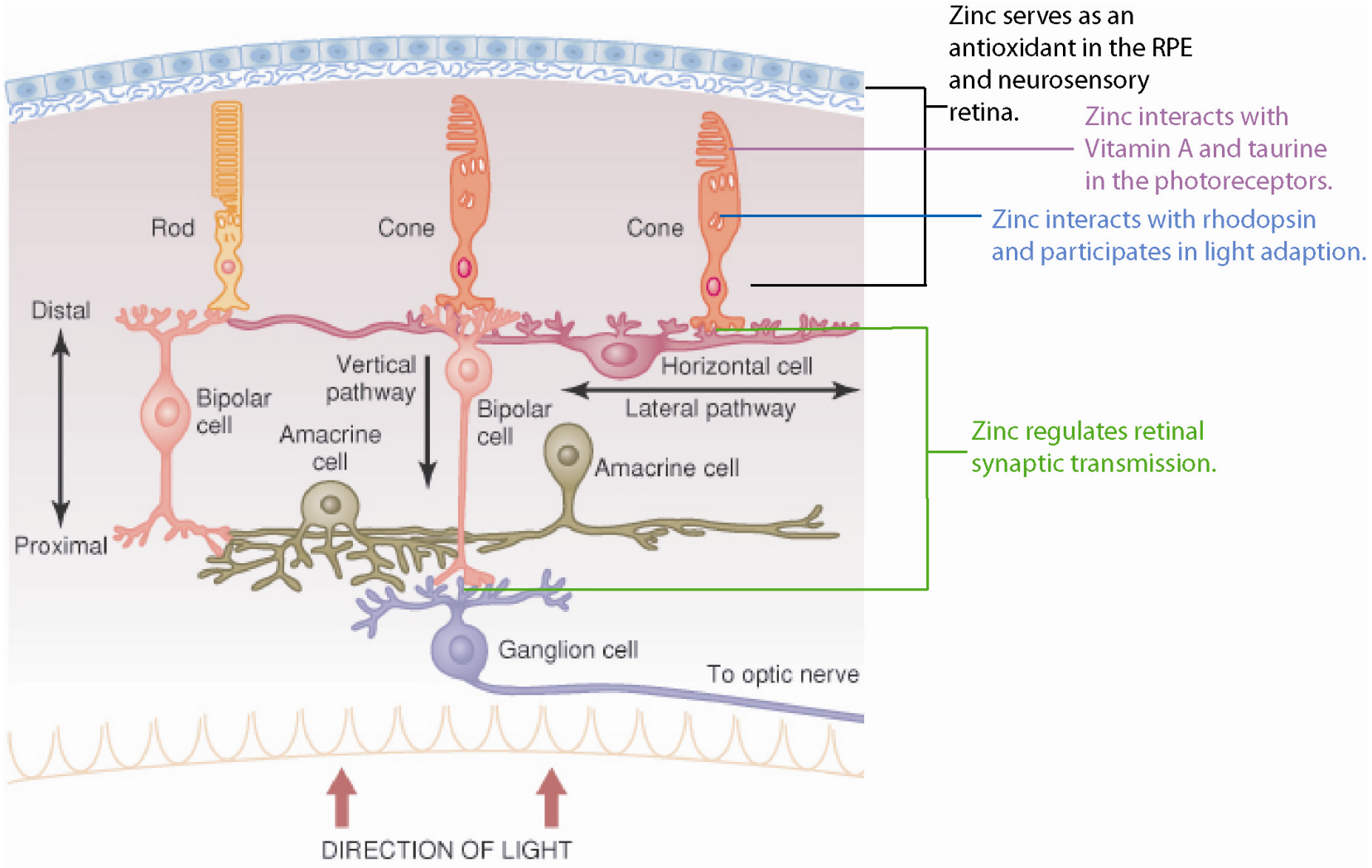

Figure 3.3 Mapping of putative positive functions of zinc in human retina (adapted from Guyton & Hall, 2006).

free zinc into the extracellular space in the neurosensory retina in an exaggerate manner and therefore cause damage (Ugarte & Osborne, 2001).

3.3 Zinc and age-related macular degeneration (AMD)

3.3.1 Main features of AMD

The macula is a clinical term that defies a circular zone with a radius of about 3 mm centred on the fovea, the pit in the central retina which allows for the maximum vision acuity (Forrester *et al.*, 2002). AMD has the worst effects in this central region (Young, 1987). Two different kinds of classification schemes have been developed to classify the severity levels and progression stages of AMD. The first one needs detailed photographic review of the retina (Davis *et al.*, 2005). The second one is a simplified scale which classifies the progression of AMD into early, intermediate and advanced stages based on the size of drusen (Section 2.8) and the level of hypopigmentary and hyperpigmentary changes of the RPE. Early AMD is featured by multiple small drusen (< 63 μm) and intermediate drusen (between 63 μm and 125 μm) with no evidence for advanced AMD. Intermediate AMD is featured by extensive intermediate drusen and large drusen (≥ 125 μm) with no evidence for advanced AMD (Figure 3.4 a). Advanced AMD is characterised by the presence of geographic atrophy (dry AMD) or neovascular AMD (wet AMD). Geographic atrophy involves the retinal depigmentation in a sharp discrete area at least 175 μm in diameter in the centre macula and visible choroid vessels without the features of neovascular AMD in the same eye, and the progression of vision loss is gradual (Figure 3.4 b). Neovascular AMD is characterized by the serous or haemorrhagic detachment of the RPE or the neurosensory retina, the occurrence of subretinal fibrous tissue or fibrosis, and the presence of fluid (exudates or blood) in the extracellular space between the RPE and the neurosensory retina (Figure 3.4 c). The onset of vision loss in neovascular AMD is acute (Ferris *et al.*, 2005). Drusen, a hallmark of early AMD, lie between the RPE and Bruch's membrane, and may be 'hard' or 'soft'. Hard drusen are small and globular, and have discrete margins. Soft drusen are larger with indistinct edges, have a softer consistency, and are able to enlarge, break and spread. While hard drusen are a relatively common feature of retinal senescence (unless becoming numerous), soft drusen are more associated with the

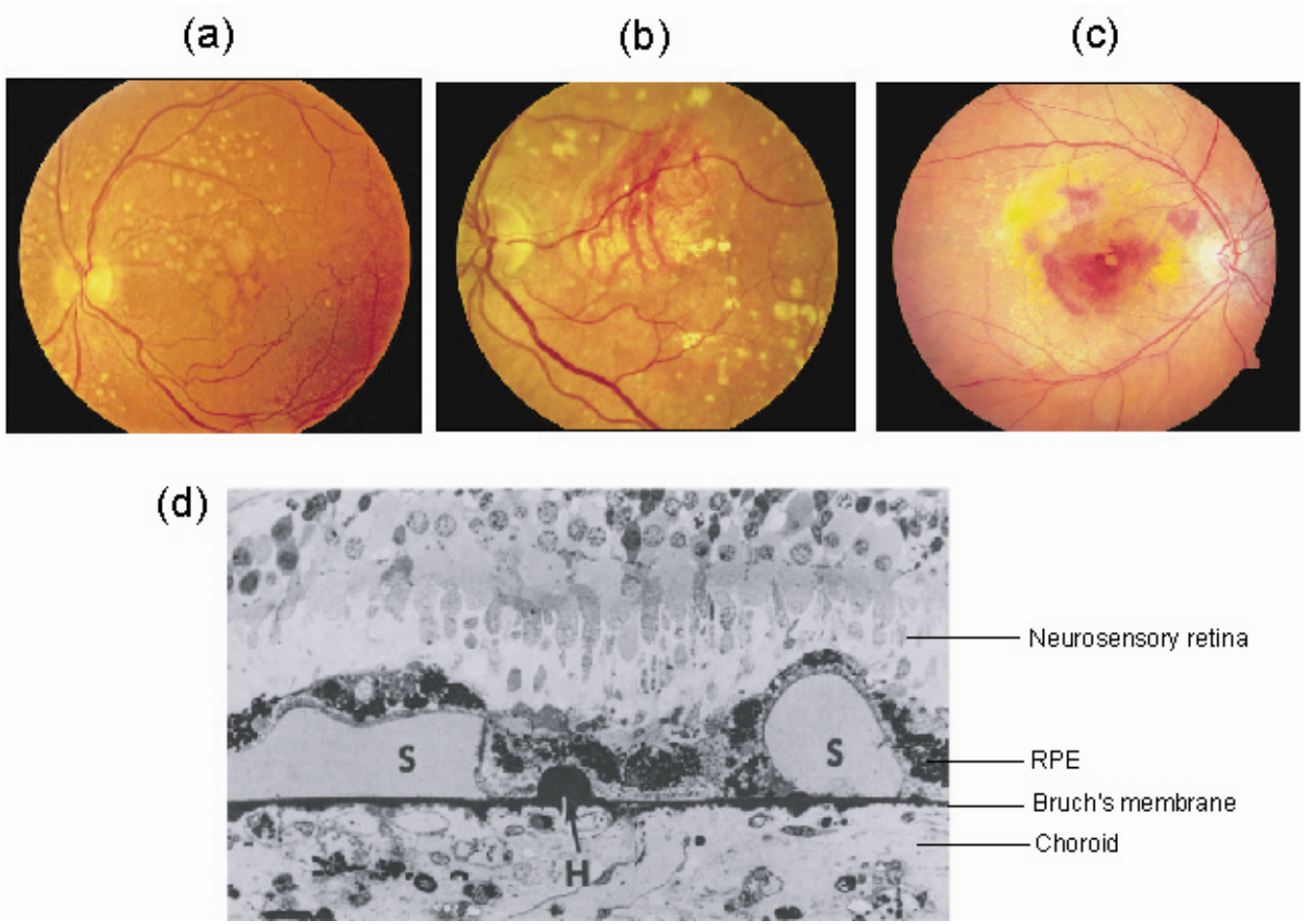

Figure 3.4 Different stages of AMD and two types of drusen. (a) Intermediate AMD with large drusen; (b) Advance drusen with geographic atrophy (dry AMD); (c) Advance drusen with neovascular AMD (wet AMD); (d) Hard (H) and soft (S) drusen (adapted from Young, 1987 and Coleman *et al.*, 2008).

development of advanced AMD (Figure 3.4 d) (Young, 1987; Gehrs *et al.*, 2006). The strongest risk factor for developing AMD is age. Other risk factors such as exposure to sunlight, cigarette smoking, ethnic origin, blue iris colour, and several genetic factors have also been suggested (Coleman *et al.*, 2008).

3.3.2 Zinc supplements and AMD

It is unlikely that systematic concentration change in zinc will lead to a significant change in the extracellular zinc concentration in retina, as only 0.2 % of zinc in blood will have access to the retinal extracellular space (Ugarte & Osborne, 2001). However, because of the possible antioxidant role of zinc in retina, many studies have focused on the relationship between zinc deficiency and AMD. The content of zinc and metallothioneins (which are zinc binding proteins in the RPE cells) are reduced in the human RPE with signs of AMD (Newsome *et al.*, 1995; Tate *et al.*, 1993). In neurosensory retina, the content of zinc showed significant decreases as age increased (Wills *et al.*, 2008). Various studies on the effect of zinc supplement on patients with AMD gave controversial results and have not clarified the issue. Among those studies, the Age-Related Eye Disease Study (AREDS) is a large-scale randomized, placebo-controlled, clinical trial of the effects on AMD of high-dose supplementation with the antioxidants vitamins C and E and β carotene, and zinc with copper, with a 5-year follow-up. According to the findings of AREDS, the average serum zinc level of AMD patients raised from 12.7 μM to 14.7 μM after a 5-year daily supplement with 80 mg of zinc and 2 mg of copper (AREDS Research Group, 2002). A supplement with zinc alone, or with zinc together with vitamins C and E and β carotene reduced the risk for progression to advanced AMD, while supplement with only vitamins C and E and β carotene had no apparent improvement (AREDS Research Group, 2001a; AREDS Research Group, 2001b). Therefore this study recommended that patients with intermediate AMD or advanced AMD in one eye take the supplement with zinc together with vitamins C and E and β carotene. An interesting follow-up study genotyped the AREDS participants for the polymorphism Tyr402His in FH, and found that the treatment response to the AREDS-recommended supplement was influenced by this polymorphism. This supplementation correlated with a smaller reduction to progression of AMD in patients with high-risk homozygous His402 allotype of FH than in patients with the low-risk homozygous Tyr402 allotype of FH (Klein *et al.*, 2008).

3.3.3 Zinc and drusen

Zinc contributes to the formation of deposits in some neurodegenerative diseases such as Alzheimer's disease. A high level of zinc has been detected in drusen in AMD by using microprobe synchrotron X-ray fluorescence (which was used to measure the total zinc concentration), and a zinc specific fluorescence sensor (which can visualize free zinc) (Figure 3.5). The average concentration of the total zinc present was determined to be 494 part per million (ppm) (predicted to be equivalent to 7.6 mM) in drusen in the macula and 252 ppm (3.9 mM) in drusen in the periphery. The fluorescence labelling confirmed the presence of free zinc in drusen, although the concentration of free zinc cannot be measured. The most likely sources of this high level of zinc in drusen are the RPE and the choroid. Considering the beneficial effects of zinc supplementation on the progression of AMD (Section 3.3.2), the increase in zinc concentration in drusen might have various effects on retina affected by AMD. It is of interest that some zinc binding proteins such as β-amyloid, crystallines, serum albumin and FH are also present in drusen (Crabb *et al.*, 2002). The causes and functions behind the accumulation of zinc in the BM and drusen is not clear. The interaction between zinc and FH and its implication for AMD will be discussed in Chapters 6 and Chapter 8.

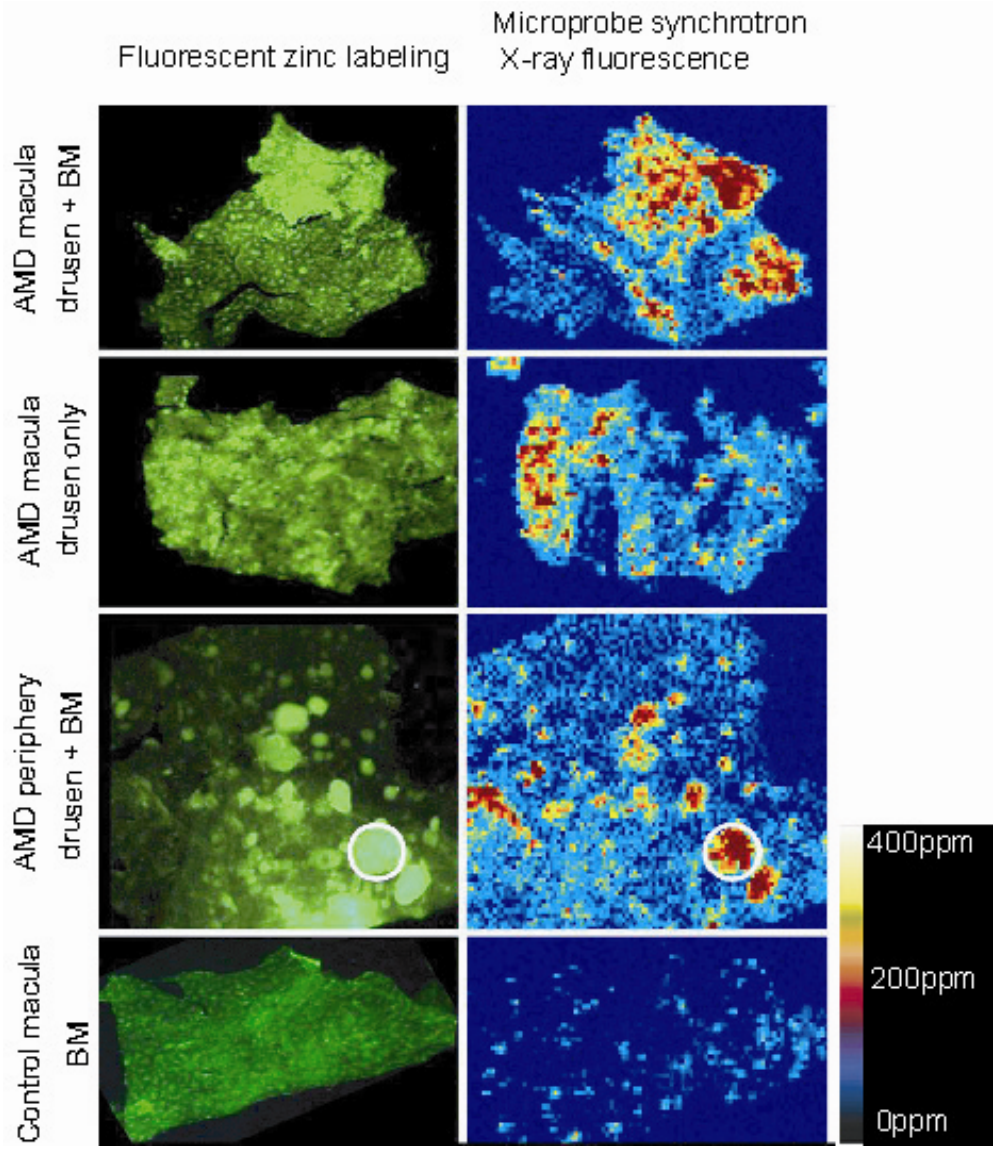

Figure 3.5 Detection of high level of zinc in drusen using fluorescent labelling (left panels) and microprobe synchrotron X-ray fluorescence (right panels). The labelling of free zinc (left panels) correlates well with the presence of total zinc accumulation (right panels) (adapted from Lengyel *et al.*, 2007).

Chapter Four

Methodology:
Analytical ultracentrifugation, solution scattering and surface plasmon resonance

This chapter outlines the background to three major techniques used in this thesis. These are analytical ultracentrifugation (AUC), solution scattering and surface plasmon resonance (SPR).

4.1 Analytical ultracentrifugation (AUC)

Analytical ultracentrifugation (AUC) is a low-resolution technique for characterizing the solution-state behaviour of macromolecules by using the effects of centrifugal forces. It is used to check sample purity, characterise assembly and disassembly mechanisms of macromolecules, determine stoichiometries and conformations of macromolecule, and measure molecular weight, equilibrium constants and thermodynamic parameters (Cole & Hansen, 1999; Harding & Winzor, 2001). The advantages of this method are: i) its ability to study macromolecules in conditions close to physiological conditions; ii) easy access to the instruments within biochemical laboratories; iii) complementing NMR and crystallography for conformational analysis of macromolecules; iv) the ability to apply of constrained structural modelling to clarify the macromolecular structures. Two complementary views of macromolecular behaviour in solution can be obtained by using AUC, sedimentation velocity (SV) and sedimentation equilibrium (SE).

4.1.1 Instrumentation

An XL-A or XL-I analytical ultracentrifuge is composed of an ultracentrifuge and an optical detection system for detecting the sample concentration distribution during sedimentation. An ultracentrifugation rotor has eight (AnTi50 rotor) or four (AnTi60 rotor) holes which accommodate the ultracentrifuge cells. Each cell contains one centrepiece that contains two or six channels that hold the sample solutions and reference buffers. Therefore, several samples can be analysed at once in an analytical ultracentrifuge. The centrepieces can be made of tough materials such as epoxy, anodized aluminium or titanium. The distributions of macromolecules in the sample are monitored in real time by the optical detection system. There are three different kinds of optical measurements, absorbance, interference and fluorescence (Cole & Hansen, 1999). Different optical systems have different characteristics, and thus are suitable for measurements of different samples.

4.1.1.1 Absorbance optical system

In the ProteomeLab XL-A system, the monochromator is based on a scanning UV/VIS absorbance optical system which contains a xenon flashlamp and a spectrophotometer for measuring sample concentration at wavelengths ranging from 190 to 800 nm. The absorbance optical system provides sensitive and selective solute detection, and is especially sensitive to macromolecules containing strong chromophores, such as proteins and nucleic acid, and samples that contain non-dialyzable detergents (Cole & Hansen, 1999; Beckman Coulter$_{TM}$ ProteomeLab^{TM} XL-A/XL-I Protein Characterization System Instruction Manual, 2003). The absorbance value obtained from the spectrophotometer is proportional to the solute concentration under the conditions where the Beer-Lambert law $A = \varepsilon c l$ applies, where A is the absorbance value, ε is the weight extinction coefficient of the solute, c is the weight concentration of the solute, and l is the optical pathlength (1.2 cm for the standard centerpieces). The absorbance optical system is sensitive enough to obtain good quality data from samples which generate no less than 0.1 Optical Density (OD) signal, and the best range of absorbance values is from 0.2 to 1.0 OD for the samples. The wavelength of the monochromator can be set between 190 and 800 nm depending on the properties of the samples, on the condition that the absorbance of the solvent in the samples at the operating wavelength should be less than about 0.5 OD. The signal-to-noise ratio in this system is about 100. The noise is usually random, neither radially-independent nor time-independent. The distance between each obsorbance data point is 20 to 50 μm. The time required for one complete scan is 60 to 300 seconds, which is the longest among the three optical systems. This might be a problem for sedimentation velocity experiments as the long scan times limit the number of scans obtained before the solute reaches complete sedimentation (Cole *et al.*, 2008).

In the scanning UV/VIS absorbance optic system, the light coming from the xenon flashlamp reaches a toroidally curved diffraction grating which varies the wavelength and collimates the light. Then before the light passes through the cell, its intensity is measured by an incident light detector which normalizes the variations of lamp intensity among different flashes. The ultracentrifuge cells house samples and reference buffers. When the rotor spins, the photomultiplier tube, a light detector beneath the

ultracentrifuge, firstly measures the light intensity passing through the reference section in the cell, and then on the next rotation, the light intensity passing through the sample sector is measured. The difference between two signals is then converted into an absorbance value by the system software (Figure 4.1) (Beckman Coulter$_{TM}$ ProteomeLab^{TM} XL-A/XL-I Protein Characterization System Instruction Manual, 2003).

4.1.1.2 Interference optical system

In the ProteomeLab XL-I system, the monochromator comprises a Rayleigh interference optical system added to the XL-A, and therefore the XL-I can obtain data using both kinds of optical measurements. The XL-I Rayleigh interference optical system is composed of a laser diode light source, imaging optics, and a charge-coupled device (CCD) detector. A single beam of collimated light is produced by a laser diode light source which is attached to the absorbance system monochromator. Two separated beams are produced by passing the single beam of light through a pair of parallel slits at the bottom of the laser source and just above the rotor. One beam passes through the sample sector in the cell, and another passes through the reference (buffer) sector. Then a fringe pattern is formed. If the same solutions are present in both sectors, an achromatic fringe will be produced along the optical axis since no refraction of light occurs. In cases that the sample solution contains solute and solvent with different refractive indices while the reference solution only contains solvent, the achromatic fringe will shift. During ultracentrifugation, in the sample sector, both sedimentation and diffusion of solute occur, and the difference of refractive index varies at different radial positions due to different concentrations. Therefore, the achromatic fringe shifts accordingly to the distribution of the concentration of solute, which is known as fringe displacement. The fringe pattern is detected by the CCD detector, via the imaging optics which includes a series of lenses and mirrors in the interference optical system. After a Fast Fourier transformation (FFT) performed by the system software, the digital data from the camera is displayed as a plot of fringe displacement versus radius (Beckman Model XL-A/XL-I Analytical Ultracentrifuge Optima^{TM} Series Training Guide, 1998; Beckman Coulter$_{TM}$ ProteomeLab^{TM} XL-A/XL-I Protein Characterization System Instruction Manual, 2003).

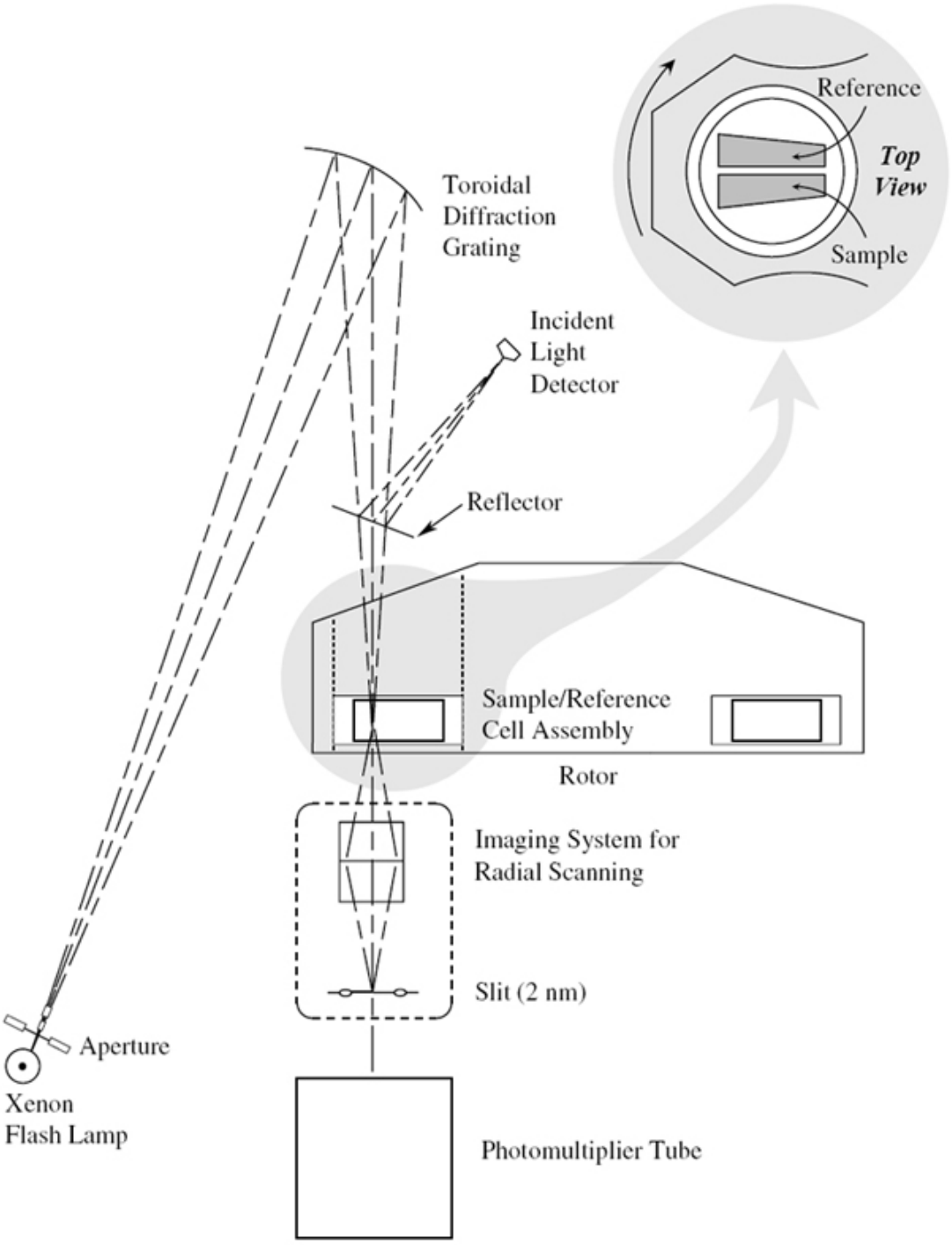

Figure 4.1 Schematic diagram of the scanning UV/VIS absorbance optical system (Taken from Beckman Model XL-A/XL-I Analytical Ultracentrifuge Optima™ Series Training Guide, 1998)

The vertical displacement of the fringes ΔY is dependent on the refractive index difference, Δn ($\Delta n = n_{sample} - n_{reference} = c\frac{dn}{dc}$), according to the equation:

$$\Delta Y = \frac{l\Delta n}{\lambda} = \frac{lc\frac{dn}{dc}}{\lambda}$$

Where l is the optical pathlength (1.2 cm for the standard centerpieces), λ is the wavelength of light (670 nm for the Reyleigh interference optics), c is the weight concentration, and $\frac{dn}{dc}$ is the refractive increment. The value of ΔY is set to be zero at the first measured radical position in one scan, and all the subsequent ΔY readings are relative to the first reading. The refractive increment $\frac{dn}{dc}$ is mainly dependent on the atomic composition of a substance. The average value of $\frac{dn}{dc}$ for proteins is 0.186, and therefore 1 mg/ml of protein can result in a fringe displacement ΔY of about 3.331 fringes (Laue, 1996).

The interference optical system has some advantages. Firstly, the fringe displacement can be obtained from any substance that has a refractive index different from the reference buffer as long as the substances do not absorb at 670 nm. Therefore the interference optical system can produce better results when the solute macromolecules lack strong chromophores such as polysaccharides, and the solvent macromolecules significantly absorb. Furthermore, it is more accurate for characterising samples at very high concentration or high radial resolution. It is also able to track very steep gradients of concentrations (Cole & Hansen, 1999). The interference optical system is more sensitive than the absorbance optical system. The lowest concentration of biological materials that can produce signal with good quality is about 0.1 mg/ml. The time required to complete one scan is 1 to 10 seconds which allows more scans to be obtained over the course of sedimentation velocity experiments. The space between each data point is 10 μm, and the signal noise to ratio is about 1000 which allows more precise measurements. Unlike the absorbance system, the noise of the interference signal is mainly systematic. The systemic noise is caused by optical flaws such as scratches on the lenses or mirrors and oil smears, mechanical stress on the optics, very slight difference between the solvent composition in the sample sector and in the

reference sector, and the alignments of the cells. The windows in the cells have to be made of sapphire for the interference optical system to minimise the changes of refractive index caused by stresses on the optics (Laue, 1996; Arthur *et al.*, 2009; Cole *et al.*, 2008).

4.1.1.3 Fluorescence optical system

The Aviv AU Fluorescence Detector System (AU-FDS) is the newest addition to the ProteomeLab XL-I system, and it is not as well characterized as the absorbance and interference optical system are. The AU-FDS optic box which contains a light source, optics, mirrors and a detector is located over the top of the rotor. The light source is a compact solid state laser which emits excitation light at 488 nm. The light is firstly reflected by a folding mirror to change the direction, and then passes through the beam expander and the first gradium lens to be collimated. After being reflected by a dichroic mirror, the light is then directed vertically downward to pass the focus lens and is focused into a 10 μm spot that is above the cells. The focused light causes the sample to fluoresce, and the emitted fluorescence from the sample travels back through the same focus lens, is transmitted through the same dichroic mirror, passes through a pair of long-pass (> 505 nm) dichroic filters, and is then focused by a gradium lens into a ~100 μm hole in front of the photomultiplier tube which is a very sensitive detector for light. The molecules that are studied by the fluorescence optical system are usually labelled extrinsically. The emission light greater than 505 nm can pass through the filters and be detected by the photomultiplier tube, and this results in a high sensitivity but no selectivity of different labels which have different emission wavelength (Beckman Analytical Ultracentrifuge Fluorescence Detection System and Advanced Operating System User Manual, 2009).

The fluorescence intensity signal F is proportional to the sample concentration: $F = I_o Q \varepsilon c$, where c is the concentration, ε is the extinction coefficient, Q is the quantum yield, the fraction of photons that produce fluorescence signals, and I_o is the incident intensity of the excitation light. The quantum yield Q is largely affected by environmental factors, and therefore, compared to the other two optical systems, it is harder to obtain sample concentrations from the fluorescence intensity. The noise of the

fluorescence signal consists of non-systematic noise which is similar to absorbance noise, and time-dependent systematic noise due to the fluorescent substances that stick to the windows and background fluorescence from the cell components. The signal to noise ratio is about 100. The radial resolution (spacing between each measurement) is 20 to 50 μm. The time required for one scan is 60 to 90 sec (Cole *et al.*, 2008).

4.1.2 Sedimentation velocity

4.1.2.1 Theoretical aspects

Sedimentation velocity is a hydrodynamic technique which is sensitive to the mass and shape of the macromolecules. In a sedimentation velocity experiment, an application of a sufficiently high speed for centrifugation leads to a rapid sedimentation of solute at the top of the cell. During sedimentation, the solute in the region near the sample meniscus is depleted, and then the concentration of the solute reaches a stable stage known as the plateau. Therefore, a solute concentration gradient, the boundary is formed. The sample concentration, c, is measured as a function of radial distance, r, by recording a series of scans at regular intervals, and thus the rate of movement of the boundary as a function of time is determined (Figure 4.2) (Cole & Hansen, 1999; Harding & Winzor, 2001; Perkins *et al.*, 2005).

In a sedimentation velocity experiment, a sedimenting solute molecule is under three forces including the gravitational force, the buoyancy force and the hydrodynamic friction. The gravitational force is $F_{sed} = M_p \omega^2 r$, where M_p is the mass of the solute molecule, and $\omega^2 r$ is the strength of the centrifugal field (ω is the angular velocity, 2π/60 rpm, and r is the radial distance from the centre of rotation). One counterforce, the buoyancy force is $F_b = M_s \omega^2 r$, where M_s is the mass of the solvent displaced by the solute molecule. The mass of solvent displaced is $M_b = M_p \bar{v} \rho$, where $\bar{v}$ is the partial specific volume of the solute, and ρ is the solvent density. Another counterforce caused by the motion of the solute molecule through the solvent is $F_f = fv$, where f is the translational frictional coefficient, and v is the velocity of the solute molecule. Those three forces on the solute molecule are in a balanced relationship:

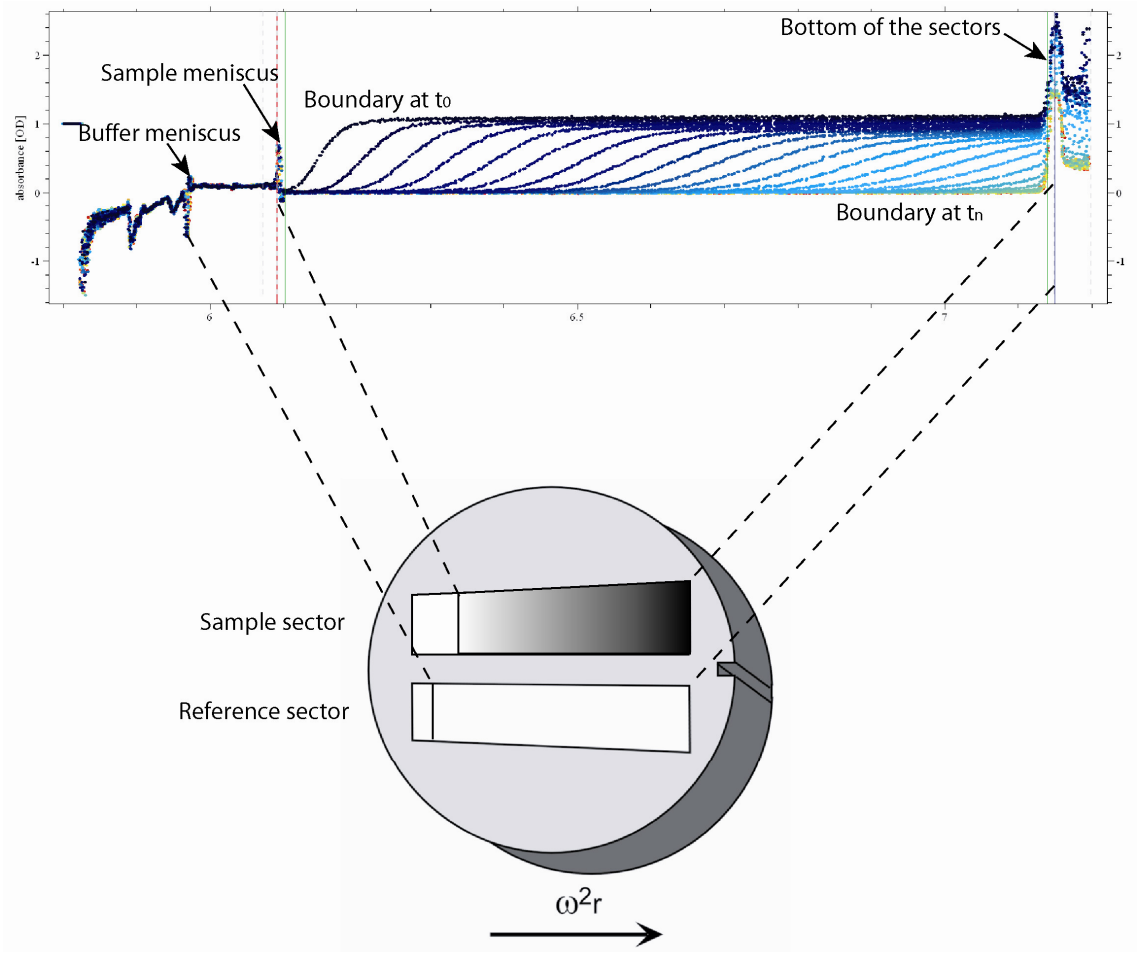

Figure 4.2 Schematic view of a double sector centrifuge cell during a sedimentation velocity experiment.

$fv = M_p\omega^2 r - M_s\omega^2 r = M_p(1-\bar{v}\rho)\omega^2 r = M(1-\bar{v}\rho)\omega^2 r/N$, where M is the molar mass and N is Avogadro's number. The ratio of the velocity of the solute to the strength of the centrifugal field is defined as the sedimentation coefficient s (Cole & Hansen, 1999; Cole *et al.*, 2008):

$$s = v/\omega^2 r = M(1-\bar{v}\rho)/Nf$$

The value of the sedimentation coefficient is dependent on the shape of the macromolecule, and a more compact structure leads to a higher s value (Perkins *et al.*, 2005). As the experimentally observed sedimentation coefficient s varies with temperature and solution density, s is always converted to a standard state of 20 °C in water at infinite dilution ($s^0_{20,w}$) (Scott & Schuck, 2005).

Diffusion, a time-dependent process of the solute molecules, causes the spreading of the sedimenting concentration boundaries. For sedimentation velocity, the diffusion of solute during the sedimentation is defined by the Stokes-Einstein relationship:

$$D = \frac{RT}{Nf}$$

where D is the diffusion coefficient which shows the rate of spreading of a boundary, R is the gas constant ($8.314 \cdot 10^7$ erg/mol K), and T is the temperature in Kelvin. Recalling $s = v/\omega^2 r = M(1-\bar{v}\rho)/Nf$, one can derive the Svedberg equation:

$$\frac{s}{D} = \frac{M(1-\bar{v}\rho)}{RT}$$

Therefore the molar mass of solute, M, can be calculated by :

$$M = RTs/D(1-\bar{v}\rho)$$

(Scott & Schuck, 2005; Beckman Model XL-A/XL-I Analytical Ultracentrifuge Optima™ Series Training Guide, 1998).

The translational frictional coefficient, f, is dependent on the size and shape of the solute macromolecules, as shown by Stokes law:

$$f = 6\pi\eta r_s$$

where η is the viscosity of the solvent, and r_s refers to the radius of the equivalent hydrodynamic sphere, which leads to the dependence of f upon shape of the solute (Harding & Winzor, 2001). For analytical ultracentrifugation, the anisotropy ratio is given by the frictional ratio f/f_0, where f_0 is the frictional coefficient of a sphere of which

the volume is as same as that of the hydrated macromolecule. The degree to which the shape of the macromolecule deviates from that of a sphere which has a same volume is shown by the frictional ratio f/f_0 (Perkins *et al.*, 2005).

The evolution of the complete radial profiles of the solute during the sedimentation velocity in the sector-shaped ultracentrifugation solution column can be described by the detailed sedimentation-diffusion equation, the Lamm equation:

$$\frac{\partial c}{\partial t} = D\left[\frac{\partial^2 c}{\partial r^2} + \frac{1}{r}\frac{\partial c}{\partial r}\right] - s\omega^2\left[r\frac{\partial c}{\partial r} + 2c\right]$$

The radial concentration c distribution as a function of time t, and the radial position r, $c(r,t)$, is recorded by the optical systems. The angular velocity ω is provided by the ultracentrifuge. The diffusion coefficient D and the sedimentation coefficient s are to be determined (Scott & Schuck, 2005; Cole *et al.*, 2008).

4.1.2.2 Data analysis

There are several different approaches to obtain the major parameters, s and D, from raw data. These methods include fitting of the boundaries to the Lamm equations, the integral sedimentation coefficient distributions $G(s)$, the apparent sedimentation coefficient distributions $g(s^*)$ and the sedimentation coefficient distributions $c(s)$ (Scott & Schuck, 2005).

The $g(s^*)$ distributions are obtained by subtracting closely spaced pairs of scans to generate a set of pairwise difference $\Delta c/\Delta t$ data which is taken approximately for the time derivative dc/dt. The subtraction removes systematic noise, and the differences are averaged to improve the signal to noise ratio. The asterisk on s means that the $g(s^*)$ is a distribution of apparent sedimentation coefficients which are the s values of hypothetical non-diffusing ideal particles (Philo, 2000). This method is implemented in the software DCDT+. For single homogeneous species including tightly associated complexes, the $g(s^*)$ distribution can be fitted to a Gaussian function which results in a bell-shaped peak (Figure 4.3 a). The concentration can be derived from the size of the Gaussian peak area. The $s_{20,w}$ value is given by the peak centre of Gaussian function, and the half-width of the bell-shaped peak is related to the diffusion

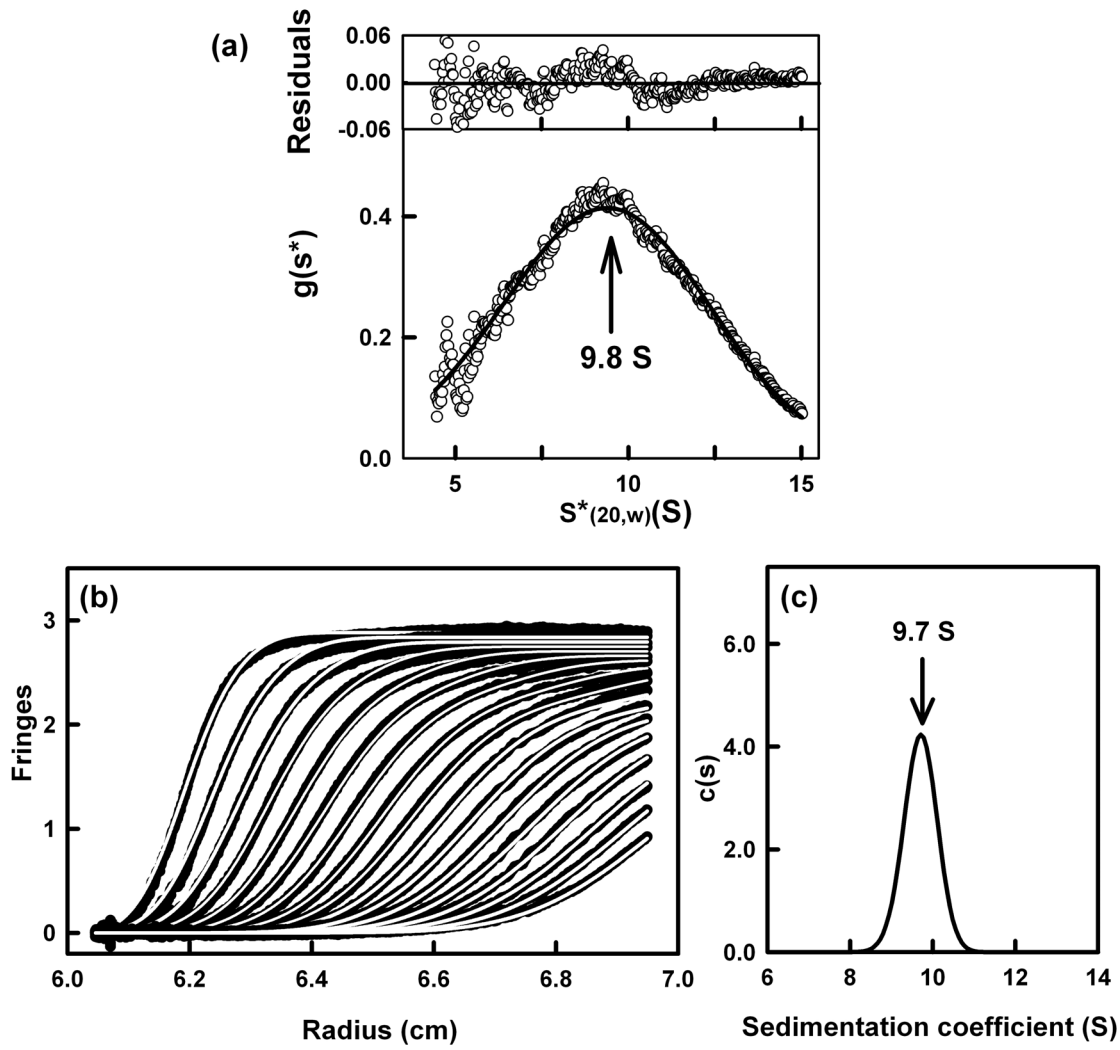

Figure 4.3 Analyses of sedimentation velocity data for human dimeric IgA1 (dIgA1). (a) In a sedimentation experiment for dIgA1, the difference between pairs of sedimentation scans are analysed using g(s*) distributions to result in a Gaussian function. A $s^*_{20,w}$ value of 9.8 S is given by the DCDT+ program which used 4 - 20 scans recorded at 20,000 rpm midway through the sedimentation profile shown in (b). (c) Sedimentation velocity *c(s)* distribution analysis of dIgA1 using SEDFIT by fitting every scans in the sedimentation profile (b) into the Lamm equation. An s value of 9.8 S was derived from the c(s) analysis (taken from Bonner *et al.*, 2008).

coefficient D. Therefore, the molecular weight M is calculated using the Svedberg equation (Cole & Hansen, 1999; Perkins *et al.*, 2005; Scott & Schuck, 2005). Sedimentation coefficients are measured in units called Svedbergs which is equal to 10^{-13} second. More than one Gaussian peaks can be obtained if there are several distinct non-interacting species. The advantages of the *g(s*)* distribution are its simplicity, and no need for any models. The disadvantages of the *g(s*)* distribution caused by the $\Delta c/\Delta t \sim dc/dt$ approximation include the artificial broadening of the Gaussian peaks which may hide the heterogeneity and missing-out of species with small s values. Another disadvantage is the difficulty of analysing heterogeneous samples with a broad range of s values (Scott & Schuck, 2005).

The approach used in this thesis for sedimentation velocity data analysis is the sedimentation coefficient distributions *c(s)*. The observed sedimentation profile of a heterogeneous sample can be described as a superposition of the sedimentation profile of each monodisperse subpopulation:

$$a(r,t) \cong \int c(s)L(s,D,r,t)d(s)$$

where $a(r,t)$ denotes to the observed signal, $c(s)d(s)$ represents the distribution of species at every $d(s)$ value, and $L(s,D,r,t)$ is the solution of the Lamm equation of the monodisperse species with the sedimentation coefficient s. Therefore, using the *c(s)* distribution to analyse the observed profile is like fitting a combination of Lamm equation solutions directly to the data to find the combination that explains the observed sedimentation profile the best. By assuming every single species has the same frictional ratio f/f_0 which means all the species have the same shape, the diffusion coefficient D can be estimated. The *c(s)* distribution method is implemented in the program SEDFIT and SEDPHAT. The *c(s)* analysis using SEDFIT software can fit all obtained scans to numerical Lamm equations using least-squares fitting procedure. The systematic noise can be removed during the fitting. The frictional ratio f/f_0 can be floated during the fitting in order to achieve the best fit. The resulting *c(s)* distribution plot has shape peaks which are not diffusionally broadened (Figure 4.3 b & c). The molar mass distribution *c(M)* can be derived from the sedimentation distribution *c(s)*. However the derived molar mass M of different species is calculated by using the same frictional ratio f/f_0, and therefore the M value can be inaccurate. There are several advantages of this method. Firstly, it is sensitive to trace components. Secondly, all the scans can be

fitted. Thirdly, a broad range of rotor speeds can be used for the fits. Fourthly, multicomponent systems can be analysed. The disadvantage of SEDFIT software is that it does not analyse the back diffusion of the macromolecules, hence high rotor speeds are preferred (Schuck, 2000).

4.1.2.3 Protein interactions in sedimentation velocity

Reversible self-associations and heterogeneous interactions of solute molecules have been observed in sedimentation velocity experiments. It is of importance to determine the stoichiometry of the complex and the strength of the interaction in terms of the association constant *KA* for the biological relevant protein interactions. The equilibrium of the protein interactions can be defined as static (slow) or dynamic (rapid). Static equilibria are very slowly reversible or almost irreversible during the time course of the experiments, and therefore it is possible to separate and characterise the individual reactants and the complex as separating non-interacting species. Different components of the interaction appears as individual peaks that are independent of concentration in the *c(s)* analysis. Dynamic equilibria are rapidly reversible and the interaction takes place in the duration of the experiments. It is impossible to resolve the individual components of the interaction in the *c(s)* analysis, and the interaction appears as a concentration-independent peak of the smaller reactant and a second broad peak with a bigger *s* value which represents a "reaction boundary" rather than the individual species. The *s* value of the "reaction boundary" peak ranges between the values for the bigger reactant and the complex. The weight-average sedimentation coefficient s_w can be obtained by integration of the sedimentation coefficient distribution *c(s)*. The s_w increases as the loading concentration increases, because the complex formed has a higher molar mass than individual reactants. In the case of the dynamic equilibrium, the stoichiometry and *KA* value might be determined by plotting the value of s_w as a function of the loading concentration, if the data is produced from a broad concentration range (eg. 0.1 to 3-fold the K_D value) (Schuck, 2005; Howlett *et al.*, 2006). Recent developments to characterise dynamic equilibria include the programme SEDPHAT which has been designed to allow the global analysis of sedimentation velocity and sedimentation equilibrium experiments, and a computational approach for integrating multiple optical signals into the *c(s)* analysis of the components which combines the

size-dependent separation with discrimination of the distinguishable properties of the components (Schuck, 2003; Balbo *et al.*, 2005).

4.1.3 Sedimentation equilibrium

4.1.3.1 Theoretical aspects

Sedimentation equilibrium is a thermodynamic technique which is sensitive to the mass of solute macromolecules. In sedimentation equilibrium experiments, low rotor speeds are applied, and therefore solute macromolecules do not pellet at the bottom of the cell but are able to diffuse over time. During centrifugation, as the distance from the centre of rotation increases, the concentration of solute is increasing. After a period of time, the effect of sedimentation and that of diffusion on the solute macromolecule are balanced, and no apparent concentration change occurs. This is termed a sedimentation equilibrium experiment (Figure 4.4). The equilibrium distribution depends on the buoyant molecular weight, but not on the shape of the macromolecules, since there is no net transport at equilibrium. (Beckman Model XL-A/XL-I Analytical Ultracentrifuge Optima^{TM} Series Training Guide, 1998; Cole & Hansen, 1999; Harding & Winzor, 2001).

The measured signal for a single component system under ideal conditions generally approaches an exponential, and it can be defined as:

$$a(r) = c(a)\varepsilon l \exp\left[M(1-\bar{v}\rho)\omega^2\left(r^2 - a^2\right)/2RT\right] + \delta$$

where r is the radius, a is the radius of the meniscus, $a(r)$ is the measured signal at the radial position, $c(a)$ is the molar concentration at the meniscus position a, M is the molar mass of the solute molecules, ε is the molar extinction coefficient for the absorbance optics, or the refractive increment multiplied by the molar mass and divided by the wavelength for the interference optics, l is the optical pathlength (1.2 cm for standard centrepieces), $\bar{v}$ is the partial specific volume of the solute, ρ is the solvent density, ω is the angular velocity, R is the gas constant, T is the temperature in Kelvin, and δ is a baseline offset. The *a(r)* and *c(a)* are measured by optical detection systems.

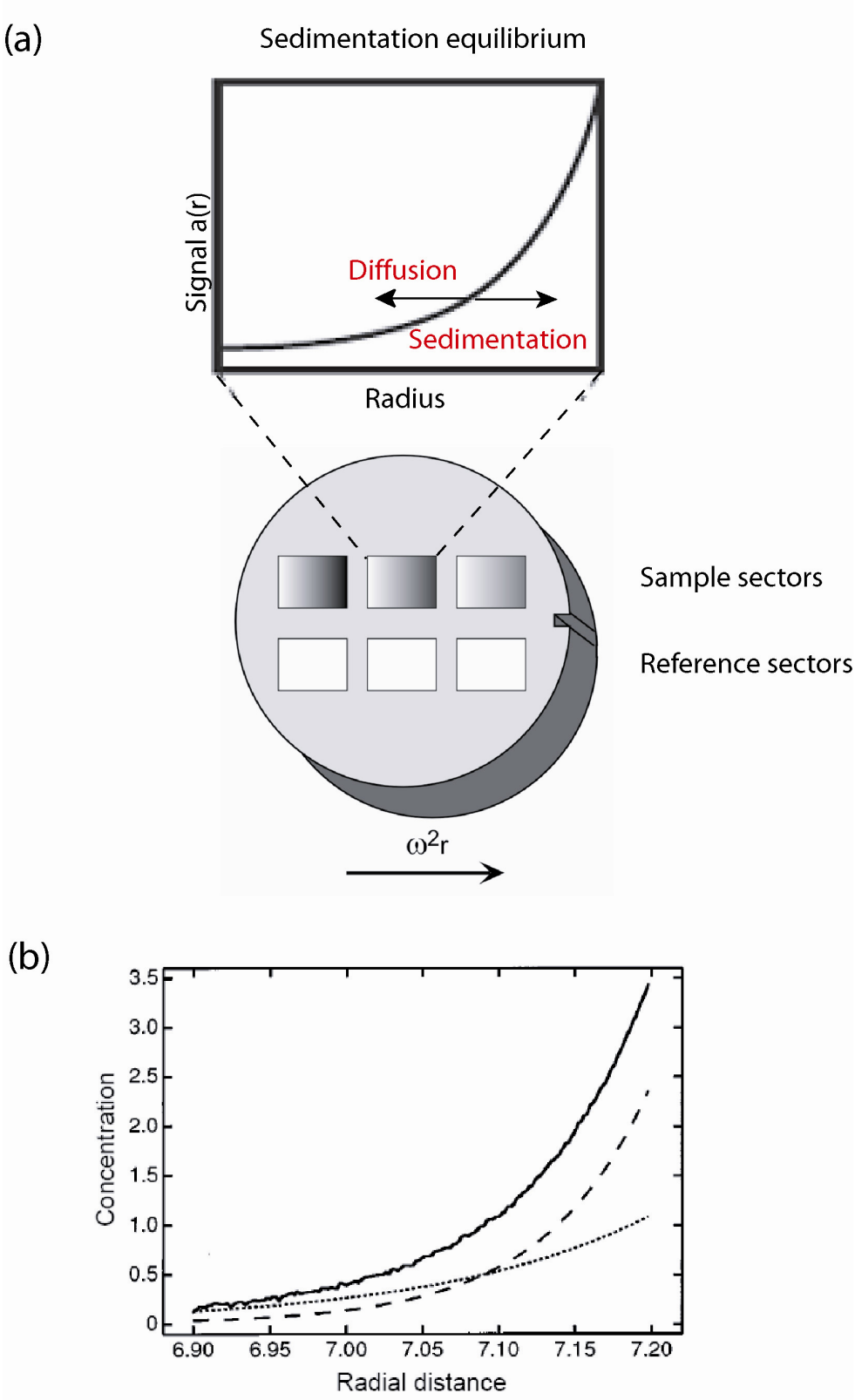

Figure 4.4 Principles of sedimentation equilibrium experiments. (a) View of a six-channel centrifuge cell used during a sedimentation equilibrium experiment. (b) Sedimentation equilibrium data for a reversible monomer-dimer equilibrium: (—) total, (···) monomer, (---) dimer (taken from Cole & Hansen, 1999).

By using known values of ε, l, $\bar{v}$, ρ, and ω, the value for the molecular weight, M, can be calculated (Scott & Schuck, 2005). For a heterogeneous system, the concentration distribution can be described as a sum of the concentration distribution of all n species present (Figure 4.5) (Lebowitz *et al.*, 2002):

$$a(r) = \sum_n c_n(a)\varepsilon_n l \exp[M_n(1-\bar{v}_n\rho)\omega^2(r^2-a^2)/2RT] + \delta .$$

Sedimentation equilibrium can also be used to characterize oligomerisation of a single component (Self-association). The equation for simple component systems can be modified to account for self-association systems. The total concentration distribution is described as:

$$a(r) = \sum_n n\varepsilon_m l K_n c_m(a)^n \exp[nM(1-\bar{v}\rho)\omega^2(r^2-a^2)/2RT] + \delta$$

where $a(r)$ is the total observed signal of the mixture at the radial position r, $c_m(a)$ denotes the concentration of monomer at the meniscus a. The M denotes the molar mass of the monomer. The oligomer that formed by the monomer is defined as n-mer. The ε_m is the molar extinction coeifficient of the monomer, and therefore the value of the molar extinction coefficient of the n-mer is $n\varepsilon_m$. For the monomer-oligomer equilibrium reaction, the association constant, K_n, is defined as: $K_n = c_n/(c_m)^n$, and therefore the concentration of oligomer at the meniscus a equals to $K_n c_m(a)^n$ (McRorie & Voelker, 1993).

For a heterogeneous interaction system in which at least two species reversibly form a complex with a certain stoichiometry, such as an $A + B \Leftrightarrow AB$ interaction, the radial signal of sedimentation equilibrium can be described as:

$$a(r) = c_A(a)\varepsilon_A l \exp[M_{b,A}\omega^2(r^2-a^2)/2RT] + c_B(a)\varepsilon_B l \exp[M_{b,B}\omega^2(r^2-a^2)/2RT]$$
$$+ c_A(a)c_B(a)K_{AB}(\varepsilon_A+\varepsilon_B)l \exp[(M_{b,A}+M_{b,B})\omega^2(r^2-a^2)/2RT] + \delta$$

where the buoyant molar mass is defined as $M_b = M(1-\bar{v}\rho)$, K_{AB} is the association constant, therefore the concentration of the complex AB is $c_{AB} = c_A c_B K_{AB}$, and the molar extinction coefficient of the complex AB is $\varepsilon_{AB} = \varepsilon_A + \varepsilon_B$. The assumption has been made here that the partial specific volume $\bar{v}$ of the complex AB can be calculated

from the respective weight fractions of reactants A and B, $\bar{v}_{AB} = \frac{M_A}{M_{AB}}\bar{v}_A + \frac{M_B}{M_{AB}}\bar{v}_B$, and thus $M_{b,AB} = M_{b,A} + M_{b,B}$ (Lebowitz *et al.*, 2002).

4.1.3.2 Data analysis

It is important to choose the right rotor speed to perform the sedimentation equilibrium experiment, because if the speed is too slow then the curvature of the *a(r)* data is not adequate for curve fitting, and if the speed is too fast then the majority of the solute molecules will sediment to the bottom of the cell. For a certain sample, sedimentation equilibrium needs to be performed at three or four different speeds and at several different concentrations of the solute (Figure 4.5 a), in order to find the optimum speed and concentration for calculation of the molecular weight M (Perkins *et al.*, 2005). For a homogeneous solute with a typical protein $\bar{v}$ value of about 0.74 cm^3/g and a molar mass of M, the recommended lowest speed is $4\times10^6\sqrt{1/M}$, and the higher speeds are increased 1.2-fold to 1.5-fold between each speed. Before using the observed absorbance, interference or fluorescence data, the baseline offset δ has to be subtracted. This can be achieved by increasing the rotor speed to 40,000 r.p.m at the end of the experiment to pellet the solutes and then using the final *a(r)* data as the offset δ. Another way is to treating the baseline offset as a fitting parameter when *a(r)* data is fitted by various programmes (Cole *et al.*, 2008).

The method used in this thesis for analysing the sedimentation equilibrium data is the nonlinear least squares analysis. The fitting programmes such as SEDPHAT directly fit the experimental data into the equations of certain models such as single component model, self-association of a single component model and heterogeneous interaction system model, to determine the molar mass M of the solute molecules. In SEDPHAT, the scan data can be loaded as single sedimentation equilibrium files or multi-speed equilibrium file. For a single component system, the buoyant molar mass M_b can be readily obtained, since only one exponential distribution is present in the system. If the value of the partial specific volume $\bar{v}$ is known, then the molar mass of the solute M can be easily calculated. For a self-association system, an association model should be selected, and a global nonlinear regression fitting of multiple scans at different

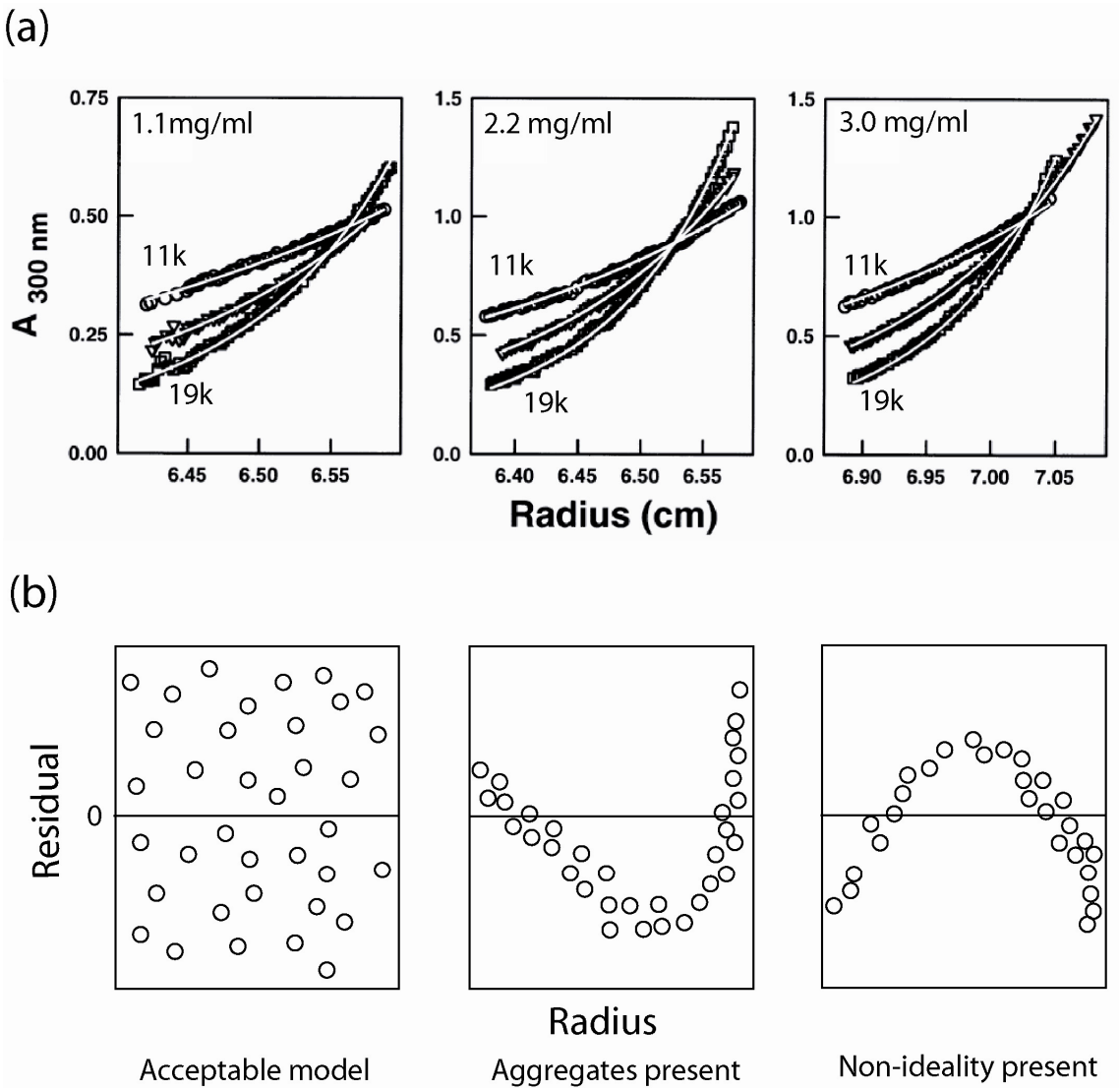

Figure 4.5 Analyses of sedimentation equilibrium data. (a) Sedimentation equilibrium analysis of the single-chain Fv fragment MFE-23. The curves were obtained at three concentrations of 1.1, 2.2 and 3.0 mg/ml, and three angular velocities of 11,000, 15,000 and 19,000 r.p.m. The continuous white line is the result of the simultaneous fit using non-linear least-squares regression analysis (adapted from Perkins *et al.*, 2005). (b) Residuals from desired fit. The patterns of residuals indicate good fit in the left panel, aggregation in the middle panel, and nonideality in the right panel (adapted from Beckman Model XL-A/XL-I Analytical Ultracentrifuge OptimaTM Series Training Guide, 1998).

concentrations and different rotor speeds should be performed to determine the M of the monomer, the association constant K_n, and the stoichimetries n of the best fitted association model. For heterogeneous interactions, the buoyant molar mass of the reactants $M_{b,A}$ and $M_{b,B}$ can be determined in advance by performing sedimentation equilibrium experiments on reactants A and B seperately, and a heterogeneous interaction model and a global fitting are needed for scans required at multiple concentrations and rotor speeds. If the difference between the molar mass of the reactant A and B is less than 20% or more than a factor of 5, it is very difficult to fit the data. However, if A and B have significant distinguishable absorbance properties (eg. a protein-DNA interaction), an absorbance optical system which allows for multi-wavelength scans can make the analysis possible. In addition, if the total concentration of the solute remains the same during the course of the sedimentation equilibrium experiments, the data fitting of self-association model and heterogeneous interaction model can be easier (Lebowitz *et al.*, 2002; Cole *et al.*, 2008).

The residual plot is very sensitive to the goodness of model fit, and it can also indicate possible alternative models. The difference between each experimental data point and the corresponding point on the curve calculated from the model equation is the residual. After curve fitting, the residuals should be examined by plotting these as a function of radius (Figure 4.5 b). For a good fit, the residuals should be randomly distributed near the zero (McRorie & Voelker, 1993; Beckman Model XL-A/XL-I Analytical Ultracentrifuge Optima™ Series Training Guide, 1998).

4.1.4 AUC in constrained modelling

Like solution scattering (see below: Section 4.2), a unique structure for the macromolecule cannot be determined by analytical ultracentrifugation in that the orientations of the macromolecule in solution are random. In addition, only a single parameter is fitted. Therefore, the constrained scattering modelling approach is applicable to model $s^o_{20,w}$ values. The best-fit structures with $s^o_{20,w}$ values within an acceptable error range are selected by performing an automated trial-and-error fit procedure (Section 4.2.5.4; Perkins *et al.*, 2005).

4.2 Solution scattering

Solution scattering is a low resolution diffraction technique suitable for studying the overall structure features of biological macromolecules in solution state in random orientations (Glatter & Kratky, 1982; Perkins, 1988). It can complement high-resolution techniques such as crystallography and nuclear magnetic resonance (NMR).

4.2.1 Theoretical aspects

4.2.1.1 Physical principles of solution scattering

X-rays are diffracted by electrons and neutrons are diffracted by nuclei, but the physical principles are the same. A macromolecular sample is irradiated with a collimated, monochromatic beam of X-rays or neutrons. All of the electrons (or nuclei) in a molecule scatter Xrays or neutrons as waves which can constructively or destructively interfere with each other (Figure 4.6 a). If the waves scattered from two electrons (or nuclei) are out of phase by $n\pi$ while n is zero or an even integer, the interference is constructive. If n is an odd integer, the interference is destructive. At very small angles longe range structure is probed, which at low resolution, allows in many cases the precise details of the atomic coordinates to be ignored, and regions of locally uniform scattering density to be considered instead. Equations can be derived for the small angle scattering of, for example, spheres, cylinders or Gaussian coils of uniform scattering density. Some universal equations appear such as the Guinier Law for the form of the small Q (scattering vector) scattering for any shape of dilute object. The larger the object the faster the scattering falls off in the scattering vector Q.

As a result of all the interference, a circularly-symmetric diffraction pattern is observed on a two dimensional (2D) area detector placed behind the sample (Figure 4.6 b). The radically averaged intensities $I(Q)$ are measured in a small angular range as a function of the magnitude of the scattering vector Q, where $Q=4\pi \sin\theta/\lambda$ (2θ is the scattering angle and λ the wavelength). The $I(Q)$ decreases as the Q increases. Radial integration of this two-dimensional pattern yields the scattering curve $I(Q)$ in one dimension. Classical solution scattering views structures at a low structural resolution about 2-4 nm from data obtained in a Q range between 0.05 to over 2 nm^{-1}. Analyses of

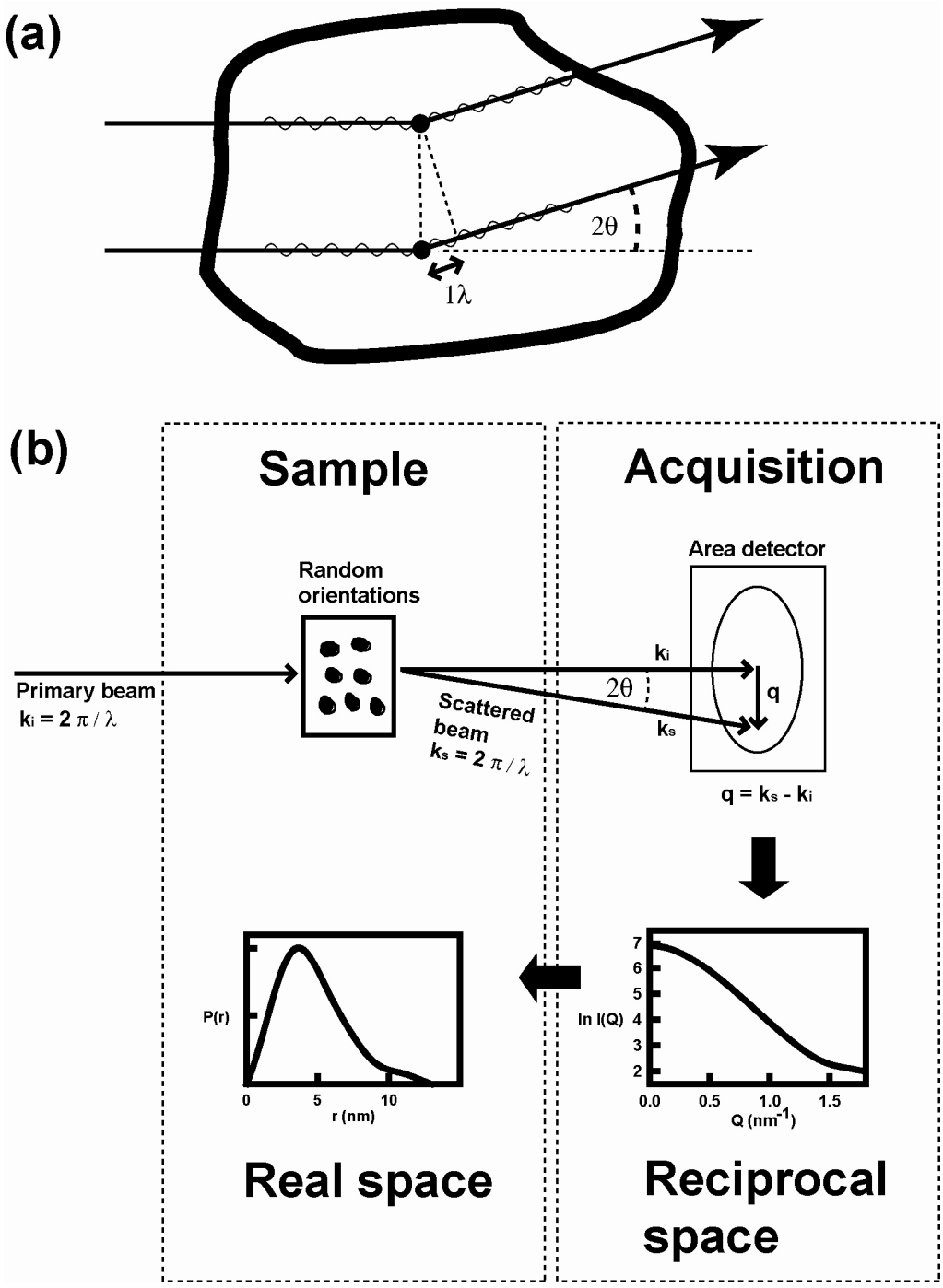

Figure 4.6 Schematic diagram of a complete scattering experiment (taken from Perkins *et al.*, 2009). (a) Scattering from two electrons (or nuclei) in a globular molecule to an angle 2θ which have a scattering angle of 2θ and a path difference of 1λ. (b) The diffraction pattern of a sample of macromolecules at random orientations in solution is recorded on a 2D detector. The scattering vector is $q = k_s - k_i$, and Q is the magnitude of the scattering vector $Q = |q| = 4\pi \sin\theta/\lambda$. The diffraction pattern gives the scattering curve *I(Q)* in reciprocal space, and transforming *I(Q)* into the real space gives the distance distribution *P(r)*.

I(Q) lead to the overall molecular weight, the degree of oligomerization, the radius of gyration R_G (and in certain cases, those of the cross-section and the thickness), the dimension and the shape of the macromolecules (Perkins, 1994; Perkins, 2001a; Perkins *et al.*, 2005). The Fourier transformation of $I(Q)$ from the reciprocal space into the real space gives the distance distribution *P(r)* which provides the maximum dimension and information about the shape of the particles. A powerful method of constrained solution scattering has been developed, in which automated curve fit procedures based on known crystal structures are able to extract structural information to a precision of 0.5-1.0 nm, corresponding to medium resolution structures (Perkins, 2001a; Perkins, 1998).

4.2.1.2 Comparison between X-ray scattering and neutron scattering

X-rays are diffracted by electrons. The intensity of scattering *I(Q)* by an electron is proportional to the X-ray scattering length *f* of the electron, which has a value of 2.81 fm. The X-ray scattering length for small angle scattering studies of an atom is the atomic number multiplied by the electron scattering length (Table 4.1 a). Therefore, the hydrogen isotopes, ^{1}H and ^{2}H, both have the scattering length of an electron of 2.81 fm (Perkins, 1988). The scattering intensity *I(Q)* of a sample of molecules at random orientations in solution can be described by the Debye equation, when the value of Q is not zero:

$$I(Q) = \sum_p \sum_q f_p f_q \frac{\sin(rQ)}{rQ}$$

where p and q are two different points within a molecule, r is the distance between them, and f_p and f_p are the scattering length of the electrons at the point p and q respectively.

The physical principles of neutron scattering are the same as for X-ray scattering. However, there are some significant differences between those two types of scattering experiments. Unlike X-rays which are scattered by electrons, neutrons are scattered by the nuclei of atoms. The nuclear atomic scattering length b, which is equivalent to and replaces the X-ray scattering length f in the Debye equation, is usually positive and similar between different nuclei. There is an important exception in that the ^{1}H isotope, has a large, negative b value of –3.742 fm (Table 4.1 a). Some other atoms or isotopes have negative scattering lengths but ^{1}H is the most important. The large difference in

(a) Scattering lengths of biological important nuclei (adapted from Perkins, 1988)

		Atomic number	f (2θ=0˚) (fm)	b (fm)
Hydrogen	^{1}H	1	2.81	-3.742
	^{2}H	1	2.81	6.671
Carbon	^{12}C	6	16.9	6.651
Nitrogen	^{14}N	7	19.7	9.40
Oxygen	^{16}O	8	22.5	5.804
Phosphorus	^{31}P	15	42.3	5.1

(b) Scattering densities of solvents and macromolecules (adapted from Perkins, 1988)

	X-ray ($e.nm^{-3}$)	Neutrons (% $^{2}H_2O$)
H_2O	334	0
$^{2}H_2O$	334	100
50% (w/w) sucrose in H_2O	402	13
Lipids	310-340	10-14
Detergents	300-430	6-23
Proteins	410-450	40-45
Carbohydrates	490	47
DNA	590	65
RNA	600	72

the neutron scattering properties of the two hydrogen isotopes is very important in neutron scattering experiments, as this made the contrast variation experiments possible to study the internal structure of the macromolecule, if it is heterogeneous in its scattering properties (Perkins, 2001a). The scattering density ρ is the total of scattering lengths, f for X-ray scattering and b for neutron scattering, within the molecule divided by the molecular volume. The contrast $\Delta\rho$ is defined as the difference between the mean scattering density of the macromolecule ρ_v and that of its buffer ρ_s: $\Delta\rho = \rho_v - \rho_s$ (Perkins, 1988). Since different biological macromolecules have different proportion of non-exchangeable protons, different macromolecules such as lipids, proteins, carbohydrates and nucleic acids possess distinct neutron scattering densities which fall between the very different neutron scattering densities of H_2O and ^2H_2O (Table 4.1 b). Variation of the ratio of H_2O and ^2H_2O in neutron scattering experiments alters the contrast $\Delta\rho$, and thus reveals the internal structure of the components within the macromolecules such as protein-RNA and protein-lipid complexes. In principle, ^{1}H- ^{2}H exchange processes will mean that there will be internal regions where the macromolecule appears to be hollow ($\Delta\rho$=0). The contrast $\Delta\rho$ variation in X-ray scattering can be achieved by varying the percentage of sucrose, but the scattering density range is limited (Perkins, 2001a).

Another difference between X-ray scattering and neutron scattering is that the hydration shell surrounding the macromolecules such as protein and carbohydrate is visible by X-ray scattering but much less so by neutron scattering in ^2H_2O. In solution, a macromolecule has a surrounding hydration shell which has an electron density similar to that of protein and higher than that of bulk water, and therefore hydration shells are visualised as part of the macromolecular structures by X-ray scattering. The dynamic properties of these hydrated structures can be studied in sedimentation velocity experiments by analytical ultracentrifugation. In the case of neutron scattering, the hydration shells are not significant in ^2H_2O. At other neutron contrasts the water shell may be more visible than that in ^2H_2O. Glycoproteins in solution are assumed to have 0.3 g H_2O / g protein of hydration shell which contributes approximately 33% of the total structure volume. Another difference is that neutron scattering does not cause radiation damages to the proteins which happen frequently in X-ray scattering experiments (Perkins, 2001b).

Solution scattering is usually applied to proteins that are bigger than 10 kDa in size including glycosylated proteins. Nucleic acids such as DNA and RNA are difficult to study by solution scattering due to their extended polyelectrolyte structure and their less optimal scattering density. Biological complexes such as protein-protein, protein-nucleic acid and protein-lipid complexes can also be studied. Since protein-protein complexes have scattering densities that are uniform throughout complex molecules, they are suitable to be studied by both X-ray and neutron scattering. Neutron scattering has advantages in studying protein-nucleic acid and protein-lipid complexes, because the scattering densities of the complexes vary significantly between the protein, nucleic acids and lipid components (Perkins *et al.*, 2008).

4.2.3 Instrumentation

A scattering camera is designed to irradiate a solution which has a path thickness of 1-2 mm with a collimated, monochromatized beam of X-ray photons or neutrons, and to record the resulting circularly-symmetric scattering pattern by using a two-dimensional area detector interfaced to a computer (Perkins, 2001a). The use of high-flux sources such as the European Synchrotron Radiation Facility (ESRF), the Institut Laue-Langevin (ILL) both based in Grenoble, France, and Diamond (Oxfordshire, UK) greatly facilities the study of biological samples (Perkins *et al.*, 2008).

4.2.3.1 Instruments for X-ray scattering

There are about 70 X-ray synchrotron sources in the world, of which the most powerful ones are currently the 'third-generation' machines such as the 6 gigaelectronvolt (GeV) ESRF in France, the 8 GeV Super Photon Ring (Spring8) in Japan, and the 7 GeV Advanced Photon Source (APS) in America (Perkins, 2001a). At ESRF, electrons are emitted by an electron gun. Then electrons are accelerated in a linear accelerator (linac), and transmitted to a booster synchrotron which is a circular accelerator to be accelerated to 6 GeV energies. The 6 GeV electrons are then injected into the main storage ring where they circulate in vacuum at a constant energy for many hours. The storage ring is refilled several times a day, as the lifetime of the electron beam is 12 to 24 hours. Electrons circulating in the storage ring emit white radiation tangentially into various

beamlines which contains all the wavelengths including X-rays from the storage ring (Figure 4.7 a). There are 49 different beamlines at ESRF that are designed for different purposes. A typical beamline consists of an optics cabin which contains the optical systems used to select and optimise the radiation to the desired properties (eg. X-ray wavelength), an experimental cabin where samples and the detector are housed and the interactions between samples and the X-ray beam are recorded, and a control cabin where scientists control the experiments and collect the data (Figure 4.7 b). The beamline ID02 at the ESRF was designed for small-angle X-ray scattering (SAXS) combined with wide-angle X-ray scattering (WAXS) and ultra-small-angle scattering (USAXS), using a highly monochromatic beam with very low divergence and small cross-section. The emitted white beam provides a high photon flux with a low divergence. The high photon flux then passes through the ID02 optical system. The optical system consists of a cryogenic crystal Si-111 monochromator which provides a monochromatic X-ray beam with a wavelength of 0.1 nm, a toroidal focusing mirror to focus the X-ray beam, and the primary, secondary and guard slits to collimate the beam to a cross section of 0.2 mm x 0.4 mm. There are two experimental cameras inside the ID02 beamline, namely a Bonse-Hart camera for USAXS and a pin-hole camera for SAXS and WAXS (Figure 4.8 a). The pin-hole camera is located in Experimental hutch 2. In the pin-hole camera, two guard slits are located directly before the sample holder. After the sample holder, there is an image-intensified charged coupled device (CCD) detector inside a 12-m-long detector tube in a vacuum which is movable and is responsible for recording SAXS curves. The sample-detector distance for this detector can be varied between 1 m to 10 m and therefore the Q range for this detector is between 0.006 nm^{-1} and 6 nm^{-1}. Outside this 12 m detector tube, there is a second detector which records the WAXS curves. This second detector covers a Q range between 5 nm^{-1} and 60 nm^{-1} (Figure 4.8 b). Thus, by combining the two different detectors in the pin-hole camera, both SAXS and WAXS curves in a broad Q range, 0.006 nm^{-1} to 60 nm^{-1}, can be recorded. The Bonse-Hart camera is located in Experimental hutch 1, and is used to perform USAXS experiments. The Bonse-Hart camera is composed of one Si-220 triple-bounce crystal before the sample holder as a conditioning monochromator, another Si-220 triple-bounce crystal after the sample holder as a horizontal analyzer, a Si-111 double reflection vertical analyzer, and an avalanche photo diode detector (Figure 4.8 a). The Bonse-Hart camera can extend the low Q limit to 0.0008 nm^{-1}. At ID02 beamline, the operating energy is 12.4 KeV, and

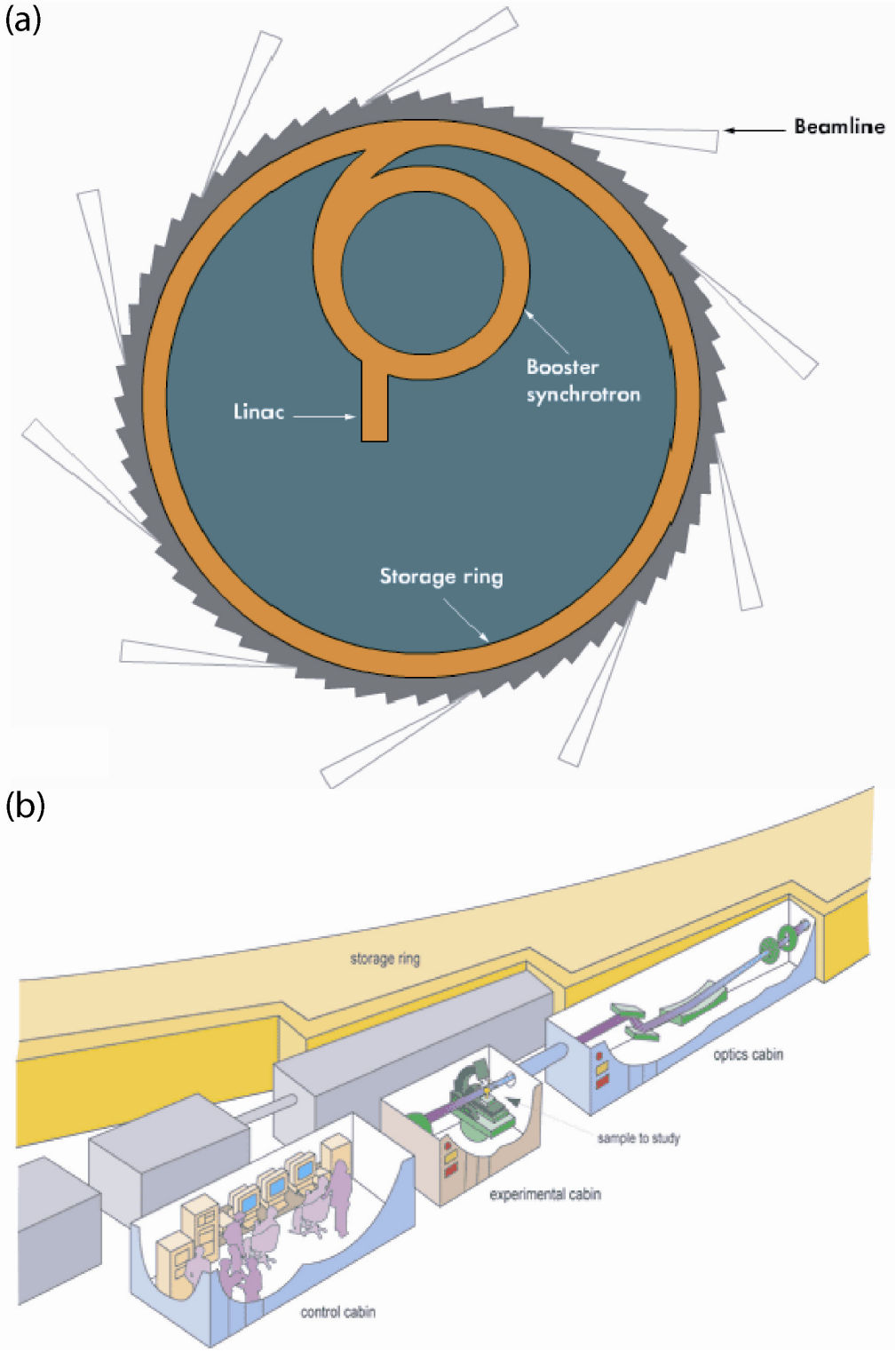

Figure 4.7 Schematic layout of the ESRF, Grenoble. (a) How synchrotron light is produced. Electrons emitted from an electron gun are accelerated in the linac first, then in the booster synchrotron, and then transmitted into the storage ring where they circulate and emit synchrotron light beams into various beamlines (taken from http://www.esrf.eu). (b) layout of a typical beamline at the ESRF (taken from http://www.esrf.eu).

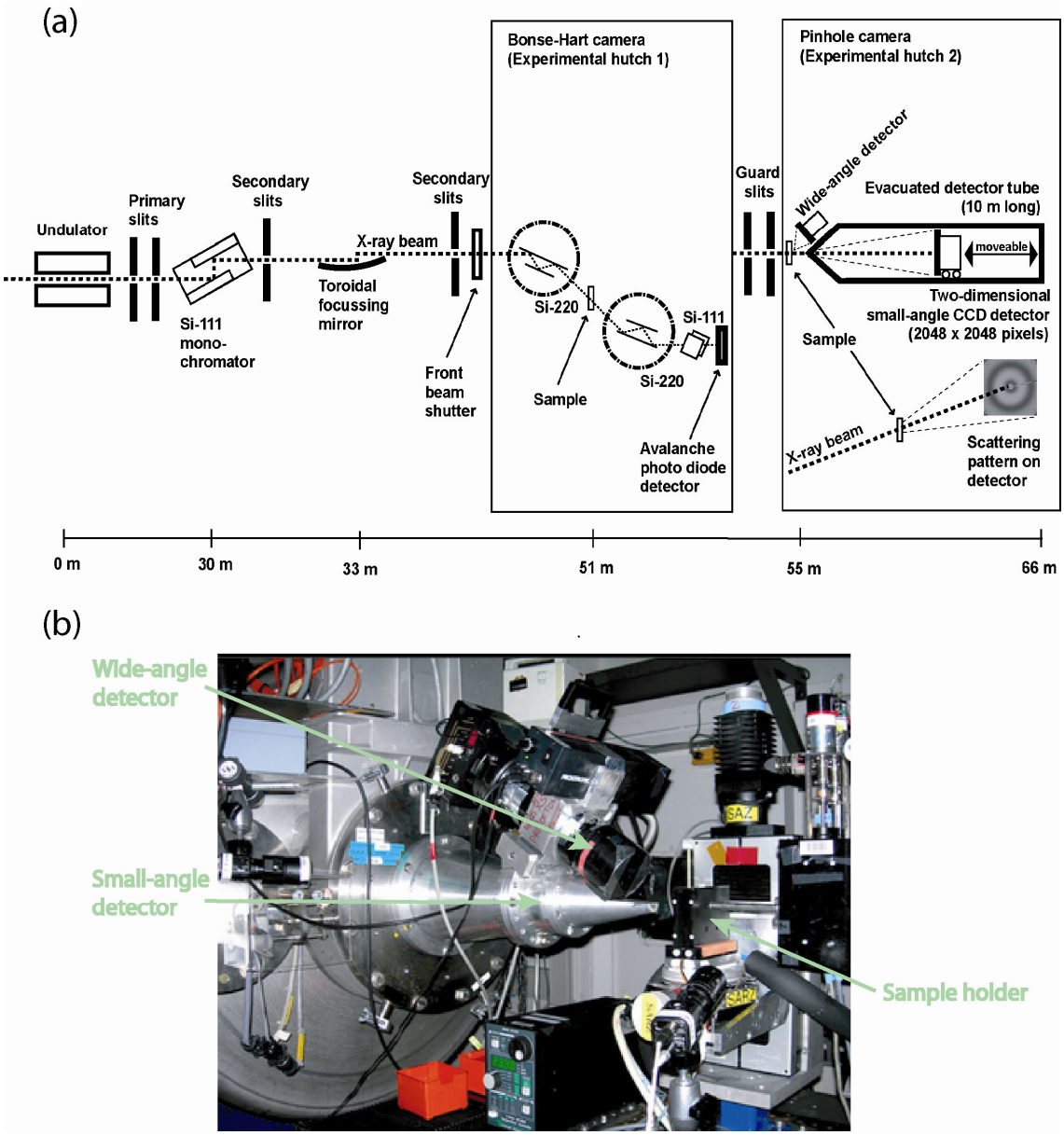

Figure 4.8 Composition of the beamline ID02 at the ESRF, Grenoble. (a) Schematic layout of the beamline ID02 which contains two cameras, the Bonse-Hart camera and the pin-hole camera (taken from Perkins *et al.*, 2008). (b) A front view of the combined SAXS/WAXS detection configuration of the pin-hole camera in Experimental hutch 2 (taken from http://www.esrf.eu).

the frame rate can reach 10 images per second (http://www.esrf.eu). Typical photon flux routinely obtained at the sample position is nearly 10^{13} photons/s (Narayanan & Bosecke, 2001). The optimum sample thickness is 1 mm for dilute protein solutions. In order to reduce the radiation damage to protein solutions, a 1-mm-wide quartz capillary is used as a flow cell which allows each protein solution to pass through the capillary at a controlled speed, and therefore the X-ray beam always pass across a fresh protein solution. The exposure time of the sample to the beam is also monitored to minimise the radiation damage, and it can be as short as 0.001 sec (Perkins *et al.*, 2008).

4.2.3.2 Instruments for neutron scattering

There are about 35-40 neutron sources in the world. Most of them are reactor sources, but five of them are spallation sources. A neutron reactor is a category of nuclear devices which initiate, control and substain a nuclear chain reaction called nuclear fission. In a nuclear fission event, a neutron is absorbed by a ^{235}U atom which then becomes a heavy ^{236}U atom. The heavy atom then splits into two lighter atoms, and release free neutrons and other fission products. The released neutrons can be absorbed by other ^{235}U atoms to initiate more nuclear reactions which can release more neutrons. A neutron spallation source is a device in which a particle accelerator is used to generate a beam of neutrons. A highly accelerated beam of protons hit onto a target composed of heavy metal such as mercury or tantalum. As a result, 20 to 30 neutrons are expelled from a heavy metal nucleus hit by a proton. Presently, the most powerful reactor source is the 58 MW High Flux Reactor at the ILL in Grenoble, and the most powerful spallation source is that of the Spallation Neutron Source (SNS) in Oak Ridge, Tennessee, USA (Perkins, 2001a). The new station TS2 at ISIS near Oxford in the UK, offers world-class facilities.

The most powerful instrument used for neutron scattering at the ILL with a high-flux reactor in Grenoble is the camera D22. The camera D22 is designed to maximize the incident flux at a sample by the use of physical large designs and large samples. The fission of ^{235}U in a specially-designed reactor core produces fast high-energy neutrons. A cold source (liquid $^{2}H_2$) moderates the neutrons and enhances the number of neutrons in a wavelength range of 0.1-1 nm. A velocity selector based on a rotating drum with a helical slot is used for beam monochromatization. The wavelengths of the neutrons that

can pass the velocity selector range between 0.45 nm to 4 nm. The suitable wavelength for biological samples is 1.0 nm. A beam collimation employs a series of movable segments of beam guides. An aperture defines the beam size. A two dimensional ^{3}He detector which has a size of 102 cm x 100 cm with 128 × 128 cells can be moved within a 20-m-long evacuated tube, which makes the sample-detector distance ranges between 1.35 m and 18 m (Figure 4.9 a). This detector can be moved sideways in order to access bigger *Q*. The accessible *Q* range is between 0.004 nm^{-1} to 4.4 nm^{-1}. The progress of the experiments, data collection and storage are controlled by computers (Perkins, 2001a; Perkins *et al.*, 2008).

At the spallation neutron source at ISIS, Rutherford Appleton Laboratory, a 200 mA, 800 MeV, proton synchrotron is used to accelerate a proton beam to strike a target made of depleted uranium or tantalum which then emits 50 pulses/sec of neutron beams, rather than a continuous beam as with a reactor source. A cold source (liquid H_2) is used again to make each neutron pulse contains wavelengths between 0.2 nm and 1.0 nm. The camera LOQ is designed for small angle neutron scattering (SANS). Inside LOQ, a spinning double-disk chopper is used to remove every other pulse to prevent frame overlapping between consecutive pulses. Two apertures define the size of the beam. The sample holder is an automatic sample changer which can house 20 different samples in quartz cells. Unlike the ILL, both the collimation and the sample-detector distance on the LOQ camera are fixed. The sample-detector distance is fixed at 4.1 m. Monochromatization of the neutron beam is achieved by time-of-flight techniques which are based on the time required for each pulse travels from the uranium target to the two dimensional ORDELA detector. The size of the ORDELA detector is 64 cm x 64 cm (Figure 4.9 b). The major advantage of the LOQ camera design is that the entire scattering curve in the *Q* range of 0.06-2.2 nm^{-1} can be measured simultaneously, and this is ideal for *P(r)* calculation and kinetic experiments (Perkins, 1988; Perkins, 2001a; Perkins *et al.*, 2008). Recently, a new camera SANS2D has been commissioned at ISIS and offer even higher performance.

4.2.4 Data collection

Before the scattering experiments are performed, a proper *Q* range must be chosen for the sample. The minimum *Q* required for a R_G determination of protein molecule with a

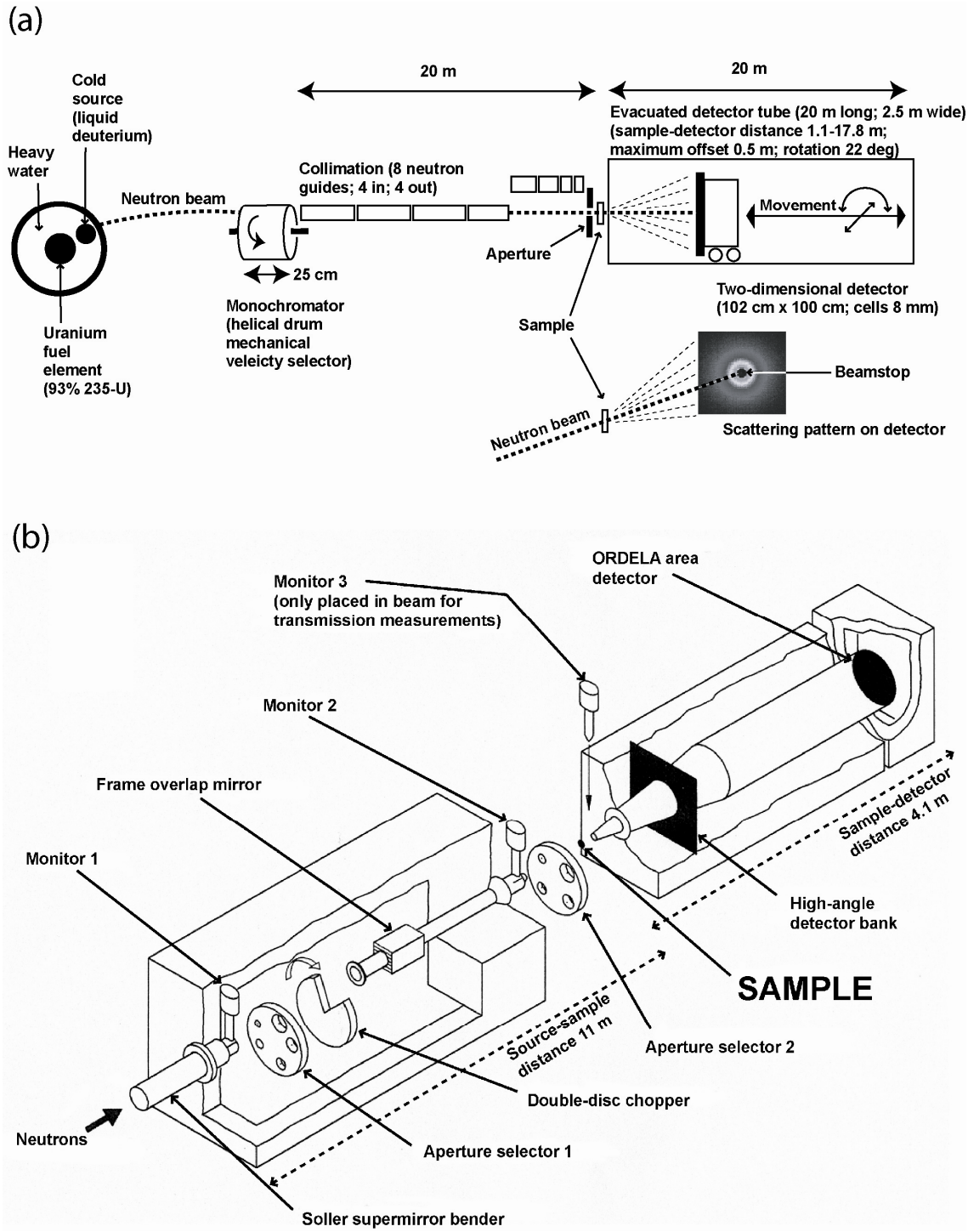

Figure 4.9 Examples of SANS cameras. (a) Schematic layout of the neutron camera D22 at the ILL (taken from Perkins *et al.*, 2008). (b) Schematic layout of the neutron camera LOQ at ISIS (taken from Perkins *et al.*, 2008).

dimension L can be decided by using the relationship (Perkins, 1988):

$$Q_{\min} L \leq \pi .$$

The value of L can be estimated in advance from electron microscopy or calculated from the sedimentation coefficient from analytical ultracentrifugation experiments assuming that the shape of the molecule is a rigid rod (Perkins, 1988). The variation of the Q range can be achieved by altering the sample-detector distance. The longer the sample-detector distance is, the smaller the Q_{min} and Q_{max} values will be (http://www.esrf.eu). However, the counting rates must be taken into consideration, because they decrease proportionally as the square value of sample-detector distance increase.

For X-ray scattering, radiation damage of the protein sample caused by the interactions with X-ray is shown as a systematic increase or in some cases decrease of *I(Q)* at low *Q* as a result of the exposure to X-rays. Thus, radiation damage has to be eliminated to obtain reliable *I(Q)* curves. At the ESRF, X-ray beams with reduced intensity such as single-bunch mode beam with a current of 16 mA or 16-bunch mode beam with a current of 90 mA are used for the work in this thesis, instead of the uniform fill mode at 200 mA which is more suited for stopped-flow work. In addition, a flow sample cell connected with a motorised syringe which can push fresh sample solution across the X-ray at a controlled speed causes the X-ray beam to continuously interact with fresh sample that have not been irradiated. Radiation damage tests must be perform before data collection, by exposing the sample to X-rays for 0.1 – 2 sec and choosing the maximum exposure time that does not cause systematic change of the *I(Q)* curve (Perkins *et al.*, 2008).

To avoid the effect of time-dependent changes of the sample cell such as accumulation of protein on the capillary wall, it is necessary to check the overlapping of the *I(Q)* curves of the same buffer throughout the beamtime. If the latter *I(Q)* curve of the buffer is higher in intensity than the curve of the same buffer at the beginning of the beamtime, then the capillary cell needs to be cleaned. Buffers must be measured immediately before the corresponding samples, and the *I(Q)* curves of the sample must be subtracted with the buffer curve just before the sample run, to minimise the effects from the time-dependent changes of the sample cell. For sample preparations, sufficient buffer

exchange is needed, and concentration series are important to detect any concentration-dependent change of the *I(Q)* curves.

4.2.5 Data analyses

4.2.5.1 Guinier analyses

At sufficiently low Q values, Guinier analyses (Figure 4.10 a, b) of the scattering curves In *I(Q)* as a function of Q^2 give the radius of gyration, R_G, and the forward scattered intensity *I(0)*:

$$\text{In } I(Q) = \text{In } I(0) - R_G^2 Q^2/3$$

R_G characterizes the degree of structural elongation, and corresponds to the mean square distance of scattering elements from their centre of gravity. R_G should be measured in a Q range in which $Q_{\min} \cdot R_G \geq 0.5$ and $Q_{\max} \cdot R_G \leq 1.5$. The anisotropy ratio is determined by R_G / R_O, where R_O is the R_G of the sphere of volume equal to that of the protein, to show the degree to which the shape deviates from that of a perfect sphere. The anisotropy ratio of globular protein molecules is about 1.28. *I(0)* is the intensity at zero Q which is determined by the intercept of the linear plot with the Y axis. *I(0)* is proportional to M_r^2, where M_r represents the relative molecular mass. *I(0)*/c (c = sample concentration in mg/ml) is proportional to M_r. M_r values can be deduced from *I(0)*/c, either as relative values from the X-ray scattering data, or as absolute values from neutron data by referencing *I(0)* to the incoherent scattering of water as a standard. Thus, concentration-dependent change of the M_r value of the sample can be checked by plotting *I(0)*/c as a function of concentration c (Perkins, 1988; Perkins, 1994; Perkins, 2001a).

For elongated macromolecules such as rod-like macromolecules, the corresponding cross-sectional radius of gyration, R_{XS}, and the cross-sectional intensity at zero angle $[I(0)Q]_{Q\to 0}$ are obtained from curve analyses in a Q range which is larger than and does not overlap with the one used for the R_G determination (Figure 4.10 c,d) (Perkins, 1988; Perkins, 1994; Perkins, 2001a) :

$$\text{In } [I(Q)Q] = \text{In } [I(0)Q]_{Q\to 0} - R_{XS}^2 Q^2/2$$

The combination of the R_G and R_{XS} analyses gives an estimate of the macromolecular

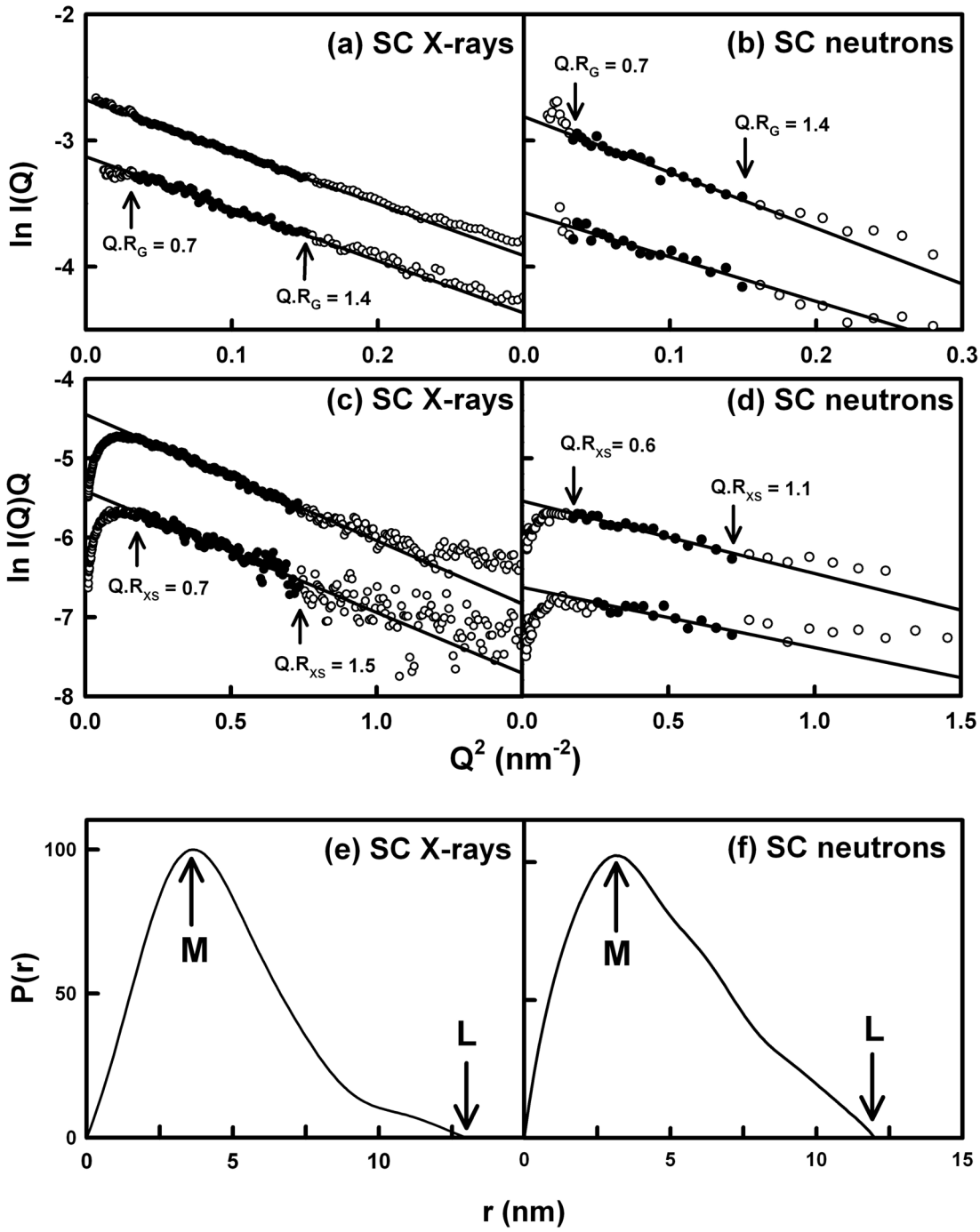

Figure 4.10 X-ray and neutron data analyses for human secretory component (SC) (adapted from Bonner *et al.*, 2007). (a to d) Guinier R_G (a, b) and R_{XS} (c, d) fits of X-ray (a, c) and neutron (b, d) data for SC. Filled circles between the $Q{\cdot}R_G$ and $Q{\cdot}R_{XS}$ ranges show the data points used to determine the R_G and R_{XS} values. (e,f) Distance distribution functions *P(r)* of X-ray (e) and neutron data (f) for SC.

dimension L assuming the structure of the molecule is an elliptical cylinder (Perkins, 2001a):

$$L = \sqrt{12 \cdot (R_G^2 - R_{XS}^2)} \text{ and } L = \pi \cdot I(0) / [I(Q) \cdot Q]_{Q \to 0}$$

In neutron scattering experiments in which the solute-solvent contrast Δρ is varied, the R_G depends on $\Delta\rho$, if the macromolecules that are measured do not have uniform scattering densities within the molecule (Perkins, 1988). Stuhrmann analyses (Ibel & Stuhrmann, 1975) of the R_G^2 as a function of $\Delta\rho^{-1}$ give information about the internal structure of the macromolecule:

$$R_G^2 = R_C^2 + \alpha \cdot \Delta\rho^{-1} - \beta \cdot \Delta\rho^{-2}$$

R_C is the R_G at infinite contrast ($\Delta\rho^{-1} = 0$). The term α is the radial distribution of scattering density fluctuations within the macromolecule. The term β is the curvature of the Stuhrmann parabola, and measures the effect on R_G from the $\Delta\rho$ dependent change of the centre of gravity (Perkins, 1988). A similar analysis can be made using the R_{XS}^2 values. For protein-protein complexes and two-component centro-symmetric complexes with two different scattering densities, β is negligible, and therefore the Stuhrmann analyses should give linear R_G^2 plots as a function of $\Delta\rho^{-1}$, and the slope of the plots can give the valued of α. For macromolecules which have two asymmetrically distributed centres of scattering densities, such as macromolecules with two asymmetrically distributed components, one of which has been heavily deuterated, the Stuhrmann plot is a parabola, and β, the curvature, provides the distance between those two centres of gravity (Perkins, 2001a).

4.2.5.2 Distance distribution function analyses

The scattering curve $I(Q)$ represents the macromolecular structure in reciprocal space. By using Fourier transformation over $0 \leq Q \leq \infty$, the scattering curve $I(Q)$ can be converted into the distance distribution function $P(r)$ (Figure 4.10 e, f), which reveals the particle shape in real space:

$$P(r) = \frac{1}{2\pi^2} \int_0^\infty I(Q) Qr \sin(Qr) dQ$$

where $P(r)$ corresponds to the distribution of distances r between any two volume elements within one particle weighted by the product of their respective scattering

densities. In general, $P(r)$ termination errors occur, because data points are missing at low Q values because of the beam stop, or are truncated at large Q at the edge of the detector. This problem can be dealt with by using the Indirect Transform Procedure which fits the experimental curve to B-splines that are then transformed to give *P(r)*. This was performed using the GNOM program which does this semi-automatically (Semenyuk & Svergun, 1991).

Several important results can be obtained from $P(r)$ analyses. First of all, $P(r)$ analyses give an alternative calculation of the R_G and *I(0)* values based on the whole scattering curve, which complements the Guinier analyses made at low Q values. Secondly, at the point at which the P(r) becomes zero, the r value gives the dimension L of the macromolecule. Thirdly, the r value of one or more maxima M corresponds to the most common distance between any two volume elements within the macromolecule.

Experimentally, $P(r)$ curves are finalized according to several criteria: Firstly, the $P(r)$ curve should exhibit positive values. Secondly, the R_G value from the $P(r)$ curves should agree with the R_G value from Guinier analyses. Thirdly, when r is zero, $P(r)$ should be zero. Fourthly, $P(r)$ should be stable for different experimental $I(Q)$ curves when the trial L value is varied over a reasonable range (Perkins, 1988; Perkins, 1994; Perkins, 2001a).

4.2.6 Modelling of scattering curves

4.2.6.1 Generation of atomic coordinates

To generate trial structures for a multi-domain protein, first of all, atomic models for each domain are created. A search for any known atomic structures from crystallography or NMR deposited in PDB is needed. If there is an atomic structure available for the domains of the protein, this atomic structure provides the basis for the models created by the automated modelling procedures. The structures from crystallography and NMR for individual domains provide the main constraint for the sphere modelling. If there is not any, the individual domains are modelled using the known sequences and structures of similar domains as templates to create homology models, and these homology modelling can be done by using a package such as

MODELLER. For glycosylated proteins, all the oligosaccharide chains need to be added onto the glycosylation sites on the atomic structures. Secondly, if the domains are connected by flexible linker peptide, then a library contains thousands randomised conformations is generated for each linker by using molecular dynamic methods. Finally, a full unhydrated trial atomic coordinate for the protein molecule is created by joining one of the randomised conformations of each linker with atomic structures of the domains. A large number of these unhydrated trial coordinates, typically in a range of 2,000 -10,000, are generated to be able to produce best-fit models for the experimental data. The generation of random trial coordinates, the "search", can be carried out in other different ways such as translational search and rotational search. A translational search does not change the domains' rotational position, but optimise the relative distances between each domain. On the contrary, a rotational search keeps the inter-domain distance constant, but optimises the rotational position of each domain (Chamberlain *et al.*, 1998; Perkins *et al.*, 2009).

4.2.6.2 Generation of sphere models

The full trial atomic structure of the protein molecule is then converted into a sphere model which consists of hundreds of spheres of the same total volume as the original atomic model. Spheres are less power demanding for the processors than atoms. To do this, the coordinates of an atomic model are converted to spheres by putting the full coordinates in a three-dimensional grid of cubes of side about 0.55 nm in length, which is much less in length than the resolution $2\pi/Q_{max}$ of the scattering curves (Figure 4.11). A cube was included as a sphere in a model if it contained sufficient coordinates above a self-defined cut-off value, so that the total volume of all the cubes included in the model was close to the unhydrated volume calculated for the protein. The unhydrated sphere models can be used for neutron scattering curve calculations. X-ray scattering curves require hydrated models because of the hydration shell (Section 4.2.1.2). To create hydrated models, the hydration shell of a protein is added by assuming a hydration of 0.3 g water/g protein and an electrostricted volume of 0.0245 nm^3 per bound water molecule, and spheres corresponding to water molecules are added over the surface of the unhydrated sphere. The duplicated and excess water spheres are removed to match the calculated hydrated volume of the spheres with that calculated from the sequence (Perkins, 1998; Perkins, 2001b).

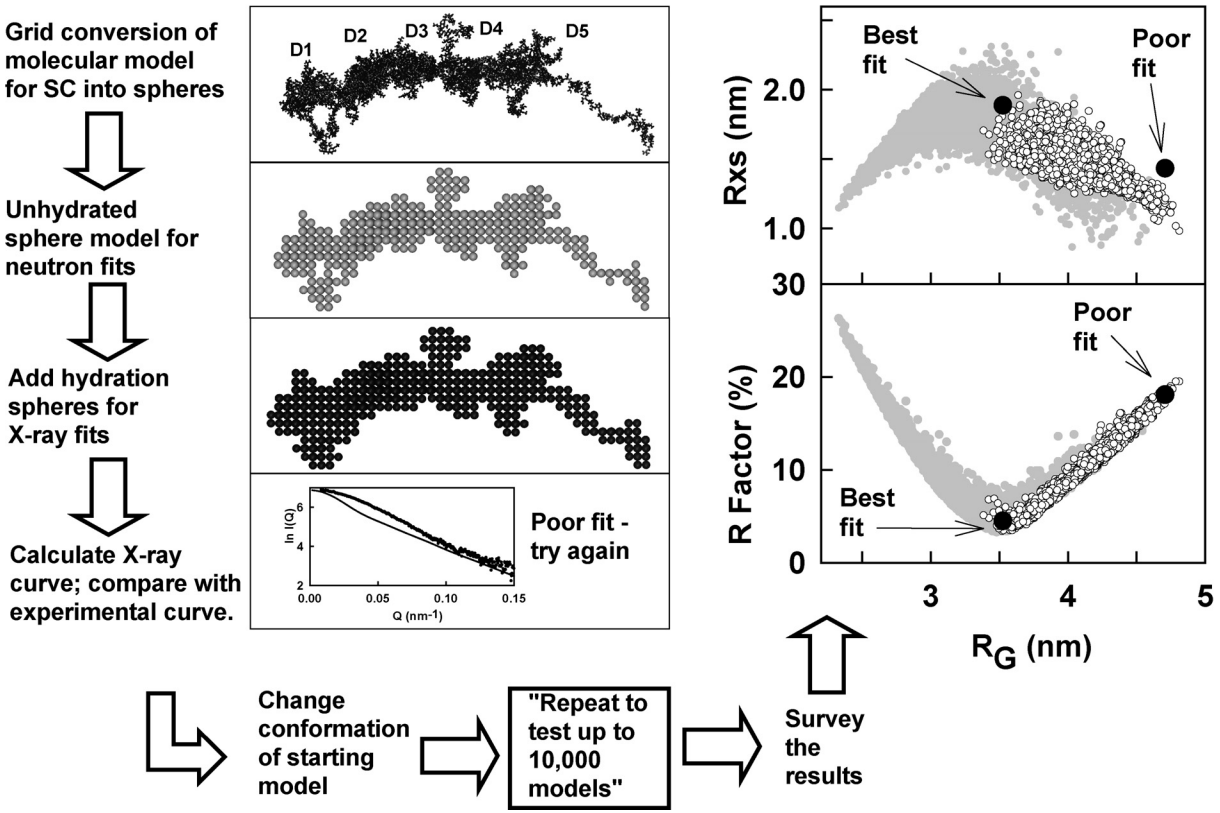

Figure 4.11 Constrained modelling process and outcome (taken from Perkins *et al.*, 2009). A randomly selected atomic coordinate of human secretion component (SC) which contains five domains is converted into a sphere model. The hydration shell is then added. A theoretical X-ray scattering curved is generated from the hydrated sphere model, and compared with the experimental X-ray scattering curve to give a goodness-of-fit *R*-factor. The scattering parameters such as R_G, R_{XS} and *R*-factor are calculated for 10,000 theoretical scattering curves. Best fit models are elected from two different searches by comparing the theoretical R_G, R_{XS} with experimental values and the lowest *R*-factors.

4.2.6.3 Generation of theoretical scattering curves

The next step is to generate theoretical scattering curves of thousands of the sphere models. The scattering curve *I(Q)* is calculated using Debye's Law adapted to spheres, by computing all the distances r from each sphere to the remaining spheres and summing the results. For macromolecules of a single density:

$$\frac{I(Q)}{I(0)} = g(Q)\left(n^{-1} + 2n^{-2}\sum_{j=1}^{m} A_j \frac{\sin Qr_j}{Qr_j} \right)$$

$$g(Q) = \left(3\left(\sin QR - QR\cos QR\right)\right)^2 / Q^6R^6$$

where *g(Q)* is the squared form factor for the sphere of radius *R*, *n* is the number of spheres filling the body, A_j is the number of distances r_j for that value of *j*, r_j is the distance between the spheres and m is the number of different distances r_j. This equation is suitable for proteins and for glycoproteins with low carbohydrate contents, if equally good scattering curve fits to the same model can be obtained with the X-ray data in positive contrasts and the neutron data in negative contrasts (Perkins, 2001a). If not, the equation has to be adapted for different densities (eg: protein-DNA complex).

4.2.6.4 Identification of best-fit models

The 2,000 – 10,000 theoretical scattering curves from the sphere models are then compared with the best experimental scattering curve (Figure 4.11). The unhydrated sphere models should be fitted to neutron scattering curves, whereas the hydrated sphere models should be fitted to X-ray scattering curves. The models are then selected by a trial-and-error process which uses three generous filters to remove unsatisfactory full models: Firstly, sterical overlap between the subunits can result during the creation of models. So the number of spheres in each model was compared to that expected from the volume calculated from the molecular sequence and composition. The model was retained if it has at least 95% of the total spheres expected. Secondly, the scattering parameters R_G and R_{XS} are calculated from each theoretical scattering curve. Models were retained if the modelled R_G and R_{XS} values were within 5% or ±0.3 nm from the experimental values. Thirdly, models were then assessed using a goodness-of-fit R-factor $\left(100 \cdot \sum \left| I(Q)_{\exp} - I(Q)_{cal} \right| \Big/ \sum \left| I(Q)_{\exp} \right| \right)$ to measure the agreement between calculated and observed scattering curves. If *I(0)* is set as 1000, good R-factor values

are less than 10%, and preferably less than 5%. A comparison between R-factor and R_G values should show that the sphere models that give the lowest R-factors also give R_G values close to the experimental R_G value (Perkins, 2001a; Perkins, 2005). The identified best-fit models are double-checked by comparing the experimental sedimentation coefficient value with the calculated values from the models by using the HYDRO and HYDROPRO programme (Section 4.1.4). The difference between the experimental sedimentation coefficient value and the calculated values from the best-fit models should be within 0.21 S (Perkins *et al.*, 2009).

4.2.7 Advantages of solution scattering

There are two essential advantages of solution scattering. Firstly, it can describe a protein structure in near-physiological conditions, for comparison with the structures seen in high or low salt obtained by crystallography. Secondly, using known atomic structure, modelling of the scattering curves can be largely constrained to produce structures that are deposited in PDB and can be visualised. Compared to X-ray crystallography, solution scattering can provide information about large-scale conformational changes of macromolecular interactions and the oligomerization of the macromolecule. It can also study macromolecules which cannot be crystallized. Unlike 2D-NMR spectroscopy which has a macromolecular size limitation about 25,000 Da, solution scattering can study macromolecules of mass 10,000 Da upwards (Perkins, 2001a). To sum up, solution scattering is a multi-parameter diffraction method which can provide very useful information about the overall structure of biological macromolecules.

4.3 Surface plasmon resonance

4.3.1 Principles underlying surface plasmon resonance

Surface plasmon resonance (SPR) is a phenomenon based on the excitation of surface plasmons (electromagnetic waves which propagates along the interface between media of different refractive indexes such as a dielectric and a metal) by incident light (Homola, 2003). The electromagnetic field of surface plasmons is confined at the interface and deceases exponentially with the distance from the interface. The effective

penetration depth is about 20% of the wavelength of the incident light. The Biacore™, manufactured by GE Healthcare, is the most widely used SPR-based system which exploits the SPR phenomenon to monitor interactions between molecules in real time. A SPR sensor chip in a Biacore™ system contains a glass surface covered with a thin gold film. In Biacore™ systems, the excitation of surface plasmons is achieved by means of prism coupling (Figure 4.12 a). Light waves (wavelength about 800 nm for Biacore™) with a range of incidence angles pass through a high refractive index prism, and are then reflected at the interface between the glass and the gold film. The incident light can excite surface plasmons along the interface between the gold film and the glass only at a certain combination of incidence angle and wavelength of the light (Homola, 2003). As a result, the intensity of reflected light waves drops at certain angle which is called the "SPR angle" (Figure 4.12 b). At the SPR angle, the energy of the incident light is absorbed to generate electromagnetic waves. The changes to the refractive index of the solution at the surface of the sensor chip within the effective penetration depth (150 nm for Biacore™ system) of the electromagnetic field can lead to the shifts of the SPR angle which are detected in real time by the Biacore™ system. Therefore the refractive index on the sensor chip surface is monitored in real time (Biacore® Sensor Surface Handbook, 2003).

The interactions between two different molecules are monitored by attaching one molecule onto the sensor chip surface, and passing the other molecule in solution over the sensor chip surface. In SPR assays, the reactant immobilised on the sensor chip surface is termed as the ligand, whereas the reactant in solution is termed as the analyte. The interaction between the ligand and the analyte leads to changes in mass in the aqueous layer (150 nm in thickness) close to the sensor chip surface, which then leads to changes in the refractive index that are detected by the Biacore™ system (Figure 4.12 b) (Torreri *et al.*, 2005).

4.3.2 Sensorgram

In Biacore™ systems, the sample solution which contains analyte is injected over the sensor chip surface in a continuous, pulse-free fashion at a controlled speed. The mass close to the sensor chip surface increases when the analytes bind to the ligands immobilised on the surface, and decreases when the analytes disassociate from the

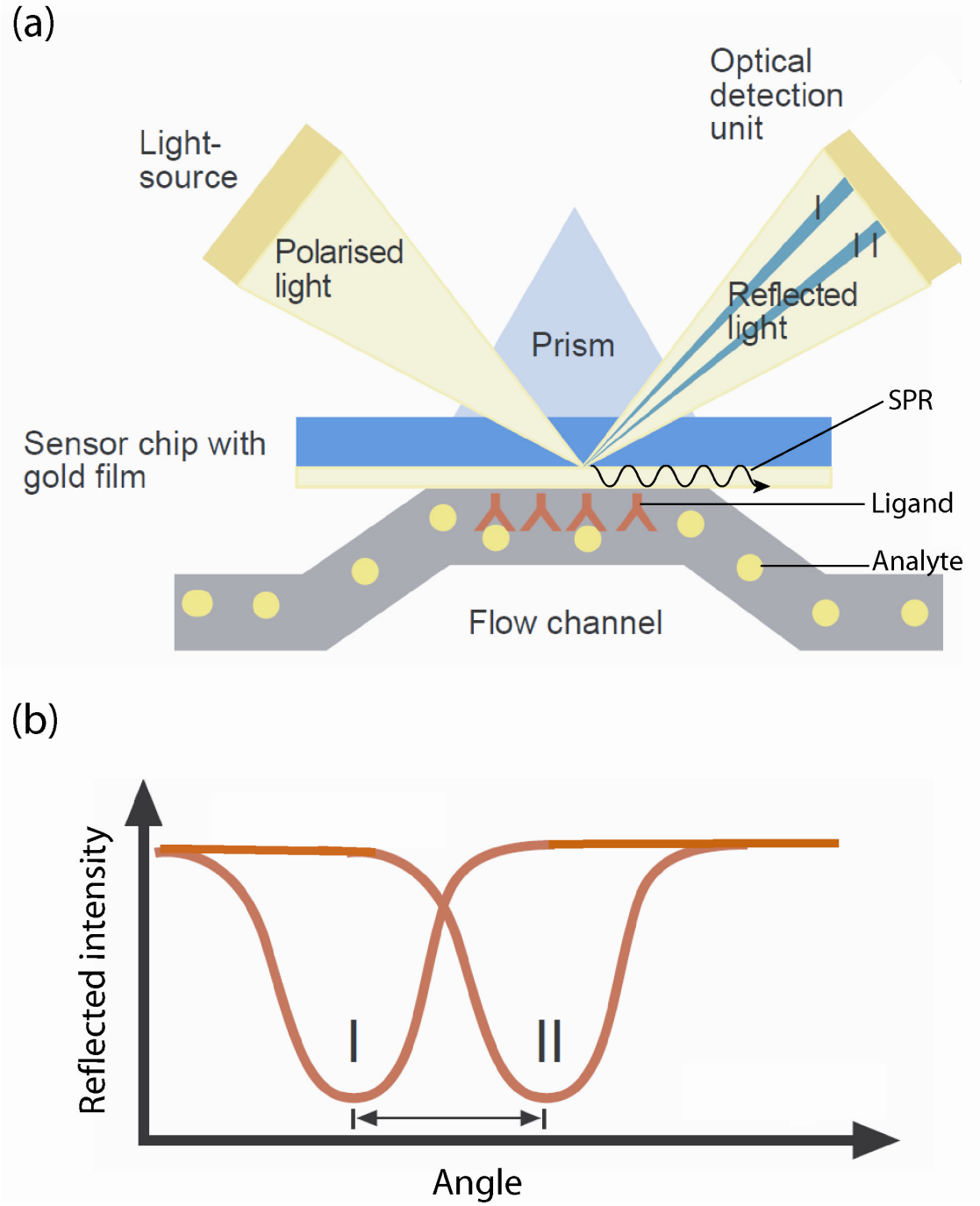

Figure 4.12 Surface plasmon resonance principles (Adapted from An introduction to Biacore®'s SPR technology, 2002). (a) Excitation of surface plasmons. (b) At the SPR angle, the intensity of the reflected light drops. The change of mass close to the sensor chip surface leads to the shift of the SPR angle.

ligands. A SPR signal response caused by the surface mass change is proportional to the concentration of bound analytes, and is measured in resonance units (RU). One RU represents approximately 1 pg of bound protein /mm^2 (Van der Merwe, 2001). A sensorgram shows the change of the response as a function of time which shows the progress of the interaction. The sensorgram of an SPR assay is generated in real time and directly displayed on the computer screen during the course of the experiment. A typical SPR assay contains five different stages (Figure 4.13). At the first stage, the running buffer is flowing over the sensor chip surface, and the response value at this stage is considered to be the baseline. The baseline should be stable to obtain reliable measurements. The second stage is the sample injection which shows the association phase of the interaction. During the sample injection, the observed upward slope of the sensorgram shows that the association rate is bigger than the dissociation rate. The binding rate decreases as more ligand sites are occupied by the analyte. If the sample injection stage lasts long enough, a steady state of the sensorgram should be reached when the association rate is equal to the dissociation rate. The next stage after sample injection is when the sample solution is replaced by the running buffer flowing over the sensor chip surface. At this stage, the slope of the sensorgram is downward, as the analyte disassociate from the ligand and are washed away by the continuous flow of the running buffer. At the fourth stage, the regeneration buffer is flowed over the surface to disassociate any remaining analyte on the sensor chip surface. At the final stage after regeneration, the regeneration buffer is replaced by the running buffer, and the response should be back to the baseline if the regeneration is successful (http://www.biacore.com; Torreri *et al.*, 2005).

4.3.3 Applications

SPR assays have been used to study many biosystems: proteins, oligonucleotides, oligosaccharides, lipids, small molecules (as small as 100 Da), phage, viral particles and cells (Rich & Myszka, 2000). There are three types of SPR assays including binding analysis, equilibrium analysis and concentration analysis that can be performed depending on what characters of the interactions need to be determined.

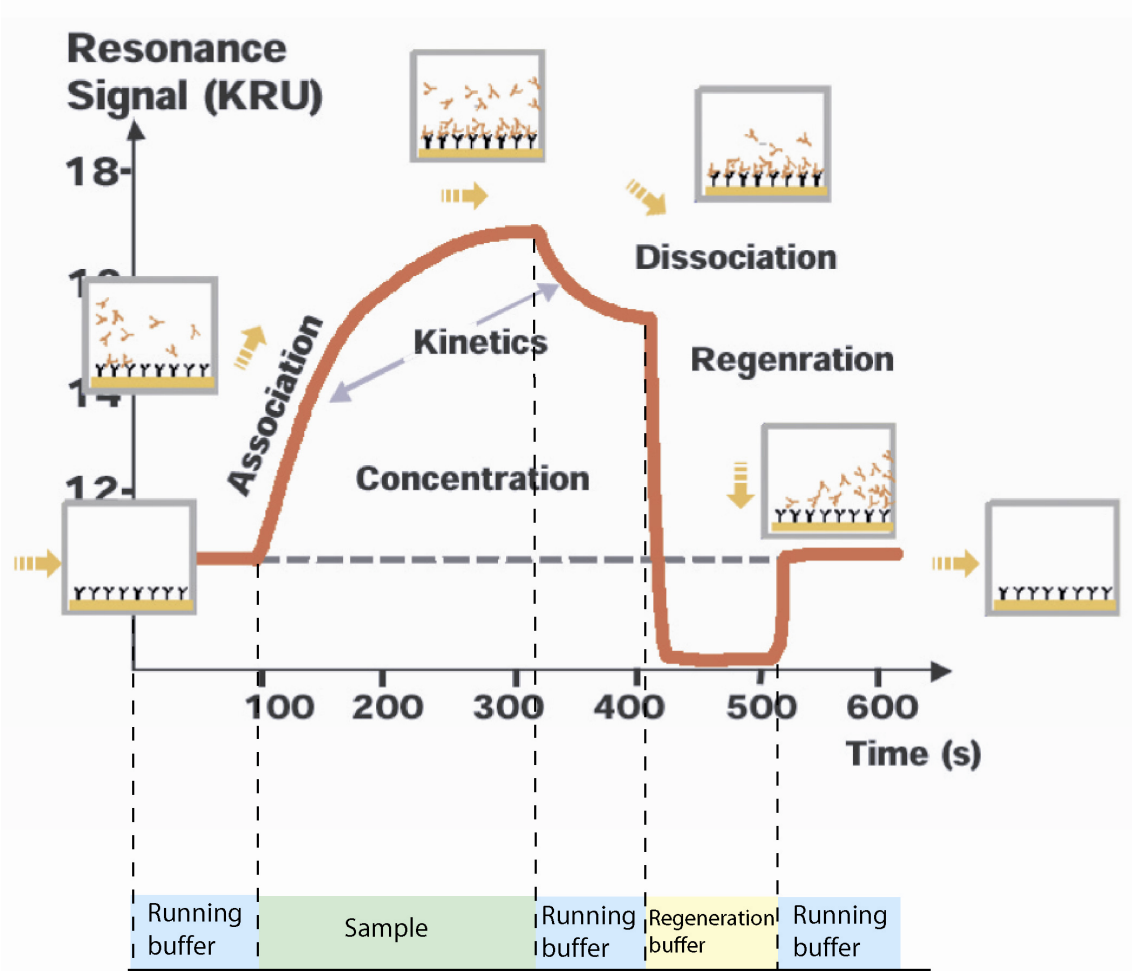

Figure 4.13 Typical sensorgram of a surface plasmon resonance assay (Adapted from An introduction to Biacore®'s SPR technology, 2002).

4.3.3.1 Binding analysis

The easiest SPR assay is the binding analysis which is used to characterise the specificity of biomolecular interactions, and measure the degree of binding between different molecules. The results from such analyses are evaluated by using maximum binding report point values or bar charts, and the information from the association and dissociation phase of the interaction is not needed. A typical example of the binding analysis application is to evaluate the correct folding of recombinant proteins. The binding site of a protein molecule to its natural ligand involves multiple residues that are usually far apart in the sequence. Therefore, if a recombinant protein molecule is correctly folded to have the same structure as its native counterpart, then it should be able to bind to its natural ligands. The binding of recombinant protein to its natural ligands or to the monoclonal antibodies of its native counterpart can be easily checked by performing binding analyses in the Biacore™ system (Van der Merwe, 2001; Biacore® Sensor Surface Handbook, 2003).

4.3.3.2 Equilibrium analysis

An equilibrium analysis is used to determine the kinetics and affinity of an interaction, by interpreting the sensorgrams of sequential injections of an analyte at different concentrations in terms of molecular interaction models. Each concentration of the analyte is run in a separate cycle, and the analyte should be completely removed from the sensor chip surface after the regeneration stage in each cycle. The dissociation constant K_D of an interaction can be determined from the steady state affinity measurements and from the kinetic rate constants. The change of steady-state response (R_{eq}) is plotted as a function of the analyte concentrations (C). In the Biacore X100 evaluation software (version 1.1), this function is fitted into a model of a 1:1 interaction which can be expressed in the equation:

$$R_{eq} = \frac{CR_{\max}}{K_D + C} + RI$$

where R_{max} is the maximum binding capacity of the sensor chip, and RI is the bulk refractive index which represents the contribution of buffer to the signal. Other use-defined models can also be used. For the K_D values determined from the steady-state affinity measurements to be reliable, most of the sequential sensorgrams should reach

the steady state, and the response value should be measured at or close to steady-state binding levels. The concentration range of the analyte needs to be wide enough to give a good curve fitting. Ideally, the highest concentration of analyte should be higher than twice of the K_D value (Biacore™ X100 Handbook, 2008).

The K_D value can also be derived from the kinetic constants which describe how fast the ligand and analyte associate and dissociate. The association rate constant ($M^{-1}s^{-1}$) is defined as k_a, and the dissociation rate constant (s^{-1}) is defined as k_d. The value of K_D can be determined by $K_D = k_d / k_a$. In the Biacore X100 evaluation software (version 1.1), there are several predefined mathematical models used to interpret the sensorgram of an interaction. The default model is the 1:1 interaction model: $A + B \leftrightarrow AB$ in which the association of the reactants can be expressed by

$$\frac{d[AB]}{dt} = k_a \cdot [A] \cdot [B],$$

and the disassociation of the complex can be expressed by

$$\frac{-d[AB]}{dt} = k_d \cdot [AB].$$

Therefore the concentration changes in the interaction can be described in the equation:

$$\frac{d[AB]}{dt} = k_a \cdot [A] \cdot [B] - k_d \cdot [AB]$$

The concentration of the complex [AB] is given by the response value R. The concentration of the free analyte [A] over the surface is known and is constant in each cycle. The [A] is expressed as C here. The concentration of the free ligand [B] can not be measured directly, but can be expressed as $R_{max} - R$. The equation above can be transformed as:

$$\frac{dR}{dt} = k_a C(R_{max} - R) - k_d R.$$

In the disassociation phase in a sensorgram, since the free analyte is washed away by the running buffer, the value of C is zero, and therefore

$$\frac{dR}{dt} = k_d R.$$

The values of k_a and k_d, and thus K_D, can derived from analysing the association phase and the disassociation phase in a sensorgram. Global fitting of sequential sensorgrams of different analyte concentrations gives more reliable kinetic constants values.

However, if the interaction associates and dissociates so fast that the k_a value is outside the range of 3 x 10^2 $M^{-1}s^{-1}$ to 3 x 10^7 $M^{-1}s^{-1}$ and the k_d value is outside the range of 10^{-5} s^{-1} to 10^{-1} s^{-1}, then the kinetic rate constants cannot be measured accurately (Biacore™ X100 Handbook, 2008).

4.3.3.3 Concentration analysis

Concentration analysis is used to determine the concentration of specific molecules present in a sample, by comparing the observed response value with a calibration curve of known samples. The calibration curves may be linear or curved. Compared with the conventional interaction-based methods such as ELISA which only provide end-point measurements, the concentration analysis by using Biacore monitors the binding in real time, and therefore can provide both rate-based and end-point measurements. In addition, there is no need to use labels for the detection (Biacore® Concentration Analysis Handbook Version AA, 2001).

4.3.4 Sensor surface

As mentioned in Section 4.3.1, a sensor chip in Biacore™ system contains a glass surface covered with a thin layer of gold. The unmodified gold surface is not suitable for interaction in biosystems, and therefore the gold surface of most of the Biacore sensor chips is coated with a layer of molecules that are covalently bound. This extra molecule layer prevents the biomolecules from contacting the gold, and can be designed to suit different ligand-immobilisation chemistry.

CM-series sensor chips have gold layers covalently bound with a matrix of carboxymethylated dextran. The CM-series sensor chips are designed for covalent attachment of biomolecules used as the ligands to the surface by using a variety of chemical methods exploiting amino groups, aldehyde groups of the ligands, or thio-disulfide exchanges between the ligands and the surface matrix. The carboxymethylated dextran matrix provides a hydrophilic environment for the attached molecules, and preserves them in a non-denaturated state. In addition, the flexibility of the matrix allows relatively free movements of the attached ligands. The sensor chip CM5 used in Chapter 7 is the most common used chip for general purposes. It has a

carboxymethylated dextran layer that extends about 100 nm from the gold surface in physiological buffer conditions, and provides a high capacity for immobilisation of a wide variety of biomolecules. The sensor chip CM4 also used in Chapter 7 is similar to CM5 chip but has only 30% of the degree of carboxymethylation, which leads to reduced immobilisation capacity and surface charge density. The non-specific binding of positive charged molecules to the surface is reduced as a result of the lower surface charge density (Biacore® Sensor Surface Handbook, 2003).

Chapter Five

Implications of the progressive self-association of heterozygous human factor H for complement regulation and disease

5.1 Introduction

In the human innate immune defence system, the central complement component C3 is activated to C3b by the cleavage and removal of the small anaphylatoxin C3a to initiate the alternative pathway in serum. C3b is regulated by factor H (FH) in order to prevent complement-mediated host cell damage, in which FH acts as a cofactor for factor I cleavage of C3b to form iC3b, accelerating the decay of the C3 convertase C3bBb, and competing with factor B for binding to C3b (Whaley & Ruddy, 1976; Weiler *et al.*, 1976; Pangburn *et al.*, 1977; Farries *et al.*, 1990; Law & Reid, 1995). FH is comprised of 20 short complement regulator (SCR) domains, each of length about 61 residues. SCR domains, also known as short consensus repeats, Sushi or complement control protein domains (Soares and Barlow, 2005), constitute the most abundant domain type in complement proteins. There are multiple binding sites for C3b within the 20 SCR domains (Sharma & Pangburn, 1996; Jokiranta *et al.*, 2000), and likewise there are multiple binding sites for heparin (Blackmore *et al.*, 1996; Blackmore *et al.*, 1998; Ormsby *et al.*, 2006; Prosser *et al.*, 2007). FH regulates surface-bound C3b activity by recognising charge (anionic) clusters on the surfaces of host cells that are mimicked by heparin. The initial contact with host cells is made through its C-terminal end, which is followed by N-terminal regulatory activity (Oppermann *et al.*, 2006; Ferreira *et al.*, 2006). Polymorphisms and mutations in FH have been associated with age-related macular degeneration (AMD) (Klein *et al.*, 2005; Haines *et al.*, 2005; Edwards *et al.*, 2005; Hageman *et al.*, Saunders *et al.*, 2007), the most common cause of blindness in the elderly in the Western world, and also with atypical haemolytic uraemic syndrome (aHUS) (Saunders *et al.*, 2007; Dragon-Durey & Frémeaux-Bacchi, 2005), a rare disease leading to renal failure that affects all ages but primarily children and young adults (http://www.fh-hus.org). The involvement of FH indicates that complement activation and regulation in the retina and the kidney endothelium has been impaired.

Intact FH has not been crystallised to date for reason of its size, glycosylation and inter-SCR flexibility. Thus solution scattering and electron microscopy methods have been applied to show that the FH SCR domain structure is not fully extended in solution (Perkins

et al., 1991; DiScipio, 1992; Aslam and Perkins, 2001). X-ray scattering and ultracentrifugation data in combination with constrained scattering modelling is a powerful approach that resulted in the first molecular structures for FH and its SCR-6/8, SCR-1/5 and SCR-16/20 fragments (Perkins *et al.*, 1998; Aslam & Perkins, 2001; Fernando *et al.*, 2007; Perkins *et al.*, 2008; Okemefuna *et al.*, 2008). Homology models for the SCR domains provided many of the first structural explanations for AMD and aHUS (Aslam & Perkins, 2001; Perkins & Goodship, 2002; Saunders *et al.*, 2006). AMD was associated with a common Tyr402His polymorphism which is located at the surface of SCR-7 and close to a heparin binding site. The aHUS related mutations cluster at the surface of SCR-20 and to a lesser degree in SCR-16 to SCR-19, and are associated with another heparin binding site. The distribution of over 100 genetic alterations (http://www.fh-hus.org) showed that the observed clinical phenotype is correlated with their structural location (Saunders *et al.*, 2007). NMR and crystal structures, starting with those for SCR-5 and SCR-15/16, and more recently extended to those for SCR-6/8 and SCR-19/20, have confirmed and extended these predictions (Soares & Barlow, 2005; Prosser *et al.*, 2007; Barlow *et al.*, 1992; Barlow *et al.*, 1993; Jokiranta *et al.*, 2006; Herbert *et al.*, 2007). Even with these structures, there are no clear indications of a molecular mechanism involving FH that leads to AMD.

One of the hallmarks of AMD is the appearance of drusen, an amyloid plaque-like deposition in Bruch's membrane, a layer interposed between the retinal pigment epithelium and the choroidal vasculature (Bird, 1992; Bird, 1995). These deposits contain oxidized lipids and many aggregated proteins including FH (Hageman *et al.*, 2001). The self-association properties of FH are thus relevant to drusen formation. FH was originally shown to be monomeric by ultracentrifugation (Sim & DiScipio, 1982). Dimeric FH was demonstrated by scattering, but this observation could not be subsequently replicated (Perkins *et al.*, 1991; Aslam & Perkins, 2001). Partial FH SCR-15/18 and SCR-15/20 dimers were however observed by non-reducing SDS-PAGE, and SCR-1/7 was observed to interact with SCR-1/20 by surface plasmon resonance (Jokiranta *et al.*, 2000; Oppermann *et al.*, 2006). Ultracentrifugation and scattering studies showed that SCR-6/8 and SCR-16/20 (but not SCR-1/5) exhibit weak monomer-dimer associations (Fernando *et al.*, 2007;

Okemefuna *et al.*, 2008). These studies indicate at least two potential dimerisation sites in FH. In combination, the two sites would constitute a mechanism for its continual self-association that would lead ultimately to aggregate formation. In this chapter, the re-investigation of the oligomerisation properties of native heterozygous FH is explained. Due to the use of improved scattering and ultracentrifugation instrumentation and analyses, a monomer-dimer equilibrium of heterozygous FH at physiological concentrations and multiple oligomers of heterozygous FH at higher concentrations have been observed. The implications of this result for complement regulation and AMD is also discussed in this chapter. This chapter is a preliminary study which sets up the basis for the studies in Chapter 6, 7 and 8.

5.2 Results and discussion

5.2.1 X-ray scattering of FH oligomers

The X-ray scattering radius of gyration (R_G) of FH monitors its degree of elongation. FH prepared two days beforehand was studied on Instrument ID02 at the ESRF in eight concentrations between 8.7 mg/ml to 0.43 mg/ml in HEPES buffer (Figure 5.1) (Narayanan & Bosecke, 2001). Here improved Guinier R_G fits were obtained at lower Q values compared to the previous X-ray measurements at the SRS at Daresbury ($Q = 4\pi \sin\theta / \lambda$ where 2θ = scattering angle, and λ = wavelength) (Perkins *et al.*, 1991; Aslam & Perkins, 2001). Due to the higher beam intensities at ESRF, improved signal-noise ratios were obtained (Figure 5.1 a, b). There is better control of radiation damage on Instrument ID02 as this is monitored on-line during data acquisition. The Guinier R_G and its cross-sectional radius of gyration $R_{XS\text{-}1}$ parameters but not its $R_{XS\text{-}2}$ parameter and the associated intensity $I(0)/c$ parameters showed small but visible concentration dependences (Figure 5.2 a, b, c, d). The $R_{XS\text{-}2}$ parameter differs from SCR protein to protein, and generally monitors the averaged short-range degree of bend between two or three adjacent SCR domains along the length of the protein (Aslam & Perkins, 2001). An additional medium-range proximity relationship between non-neighbouring SCR domains that are further apart in the sequence leads to the observation of the $R_{XS\text{-}1}$ region (Aslam & Perkins, 2001). This weak

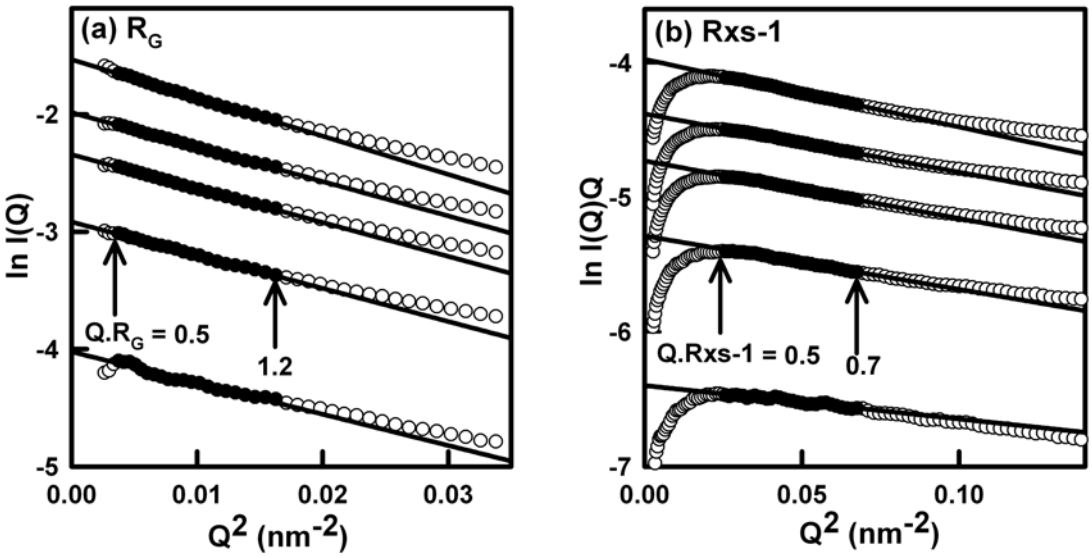

Figure 5.1 Guinier analyses for heterozygous FH at a series of concentrations.

(a) Guinier R_G plots of ln $I(Q)$ vs. Q^2 at low Q values for heterozygous FH at concentrations of 8.69 mg/ml, 6.08 mg/ml, 4.34 mg/ml, 2.61 mg/ml and 0.87 mg/ml. The Q fit range was 0.06 - 0.13 nm^{-1} The filled circles correspond to the *I(Q)* data used to determine the R_G values, and the straight line correspond to the best fit through those points. The $Q.R_G$ ranges used in the fits are arrowed.

(b) The corresponding Guinier cross-sectional R_{XS-1} fits of ln $I(Q).Q$ vs. Q^2 for the same five scattering curves in a Q range of 0.16 - 0.26 nm^{-1} are shown The R_{XS-2} fits in a Q range of 0.4 - 0.8 nm^{-1} are not shown.

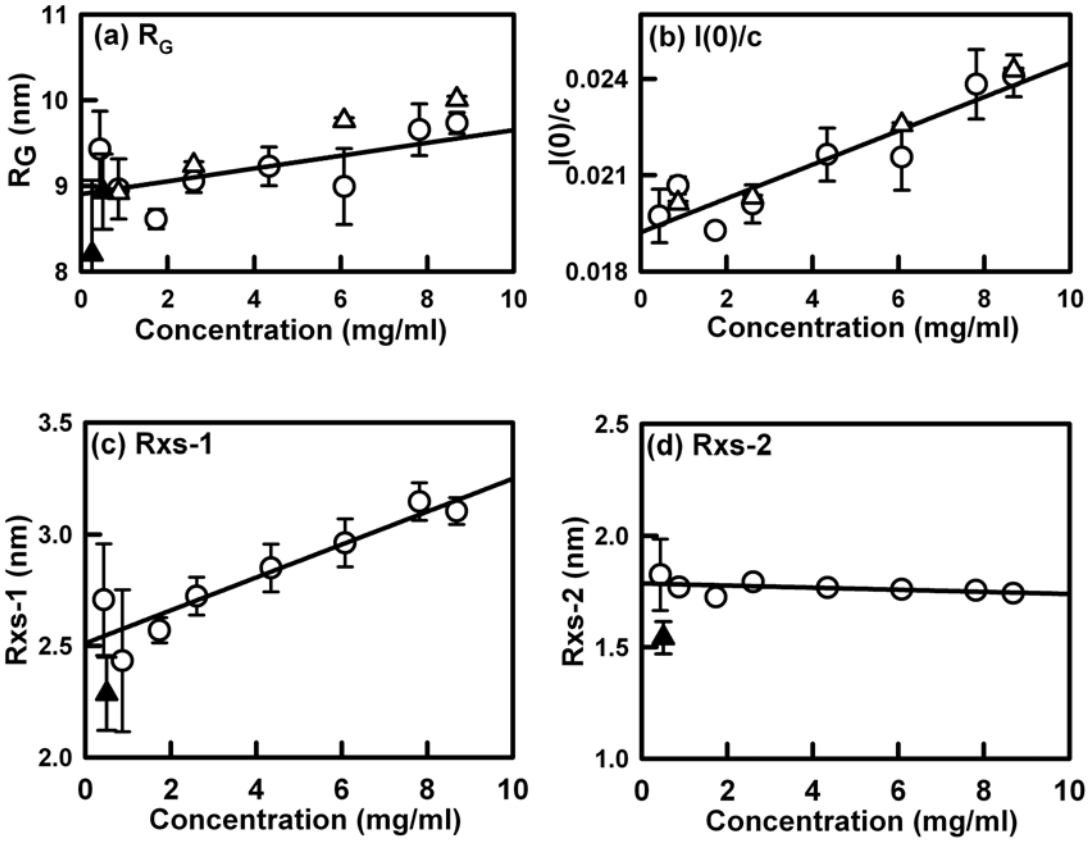

Figure 5.2 Dependence of Guinier parameters on FH concentrations. Concentration dependence of the R_G in (a), *I(0)/c* in (b) R_{XS-1} values in (c) and R_{XS-2} values in (d) (O). Each value was measured in quadruplicate and averaged. Statistical error bars are shown where visible. These data were fitted by linear regression. The open triangles (Δ) correspond to the R_G and *I(0)/c* parameters from the distance distribution function. The filled triangles (▲) correspond to data measured in PBS buffer.

concentration dependence showed that FH oligomerisation had occurred. Data obtained using phosphate buffered saline (PBS: 137 mM NaCl, 2.7 mM KCl, 8.1 mM Na_2HPO_4, 1.15 mM KH_2PO_4, pH 7.4) were consistent with the HEPES data (Figure 5.2 a, c). The R_G value extrapolated to zero concentration is 8.90 (± 0.19) nm, while $R_{XS\text{-}1}$ is 2.51 (± 0.06) nm and $R_{XS\text{-}2}$ is 1.79 (± 0.01) nm. If the slope of the $I(0)/c$ parameter as a function of FH concentration (Figure 5.2 b) corresponds to a monomer-dimer equilibrium, the resulting dissociation constant K_D is estimated to be about 100 μM. This is comparable with the K_D values of 40 μM and 16 μM observed for the SCR-6/8 and SCR-16/20 fragments respectively (Fernando *et al.*, 2007; Okemefuna *et al.*, 2008).

The present R_G values for FH are lower than previous. This was shown by comparisons of Figure 5.1 here with Figure 3 of the 2001 analysis (Aslam & Perkins, 2001) and Figure 2 of the 1991 analysis (Perkins *et al.*, 1991). From 2001, the apparent R_G value was 11.4 (± 0.4) nm, $R_{XS\text{-}1}$ was 4.4 (± 0.2) nm and $R_{XS\text{-}2}$ was 1.7 (± 0.1) nm. From 1991, the apparent R_G value was 12.4 (± 0.4) nm, $R_{XS\text{-}1}$ was 3.6 (± 0.4) nm and $R_{XS\text{-}2}$ was 1.8 (± 0.3) nm. These earlier values were confirmed by reanalyses of the earlier data files retrieved from archives. The difference is attributed to the presence of minor aggregation in 2001 and a greater level of aggregation in 1991, together with worsened signal-noise ratios in 2001 and 1991. These issues may have masked the presently observed concentration dependence in FH. Previously it was thought that alkaline pH values would cause FH to self-associate (Aslam & Perkins, 2001). This was not confirmed after sample dialysis for 2 days at pH 11.9, followed by X-ray measurement.

The *P(r)* function summarises all the distances between pairs of atoms within FH, and gives an independent calculation of the R_G and *I(0)* values that is based on the full scattering curve, and gives the maximum length of FH, denoted *L*. The *P(r)* R_G and *I(0)/c* values were in good agreement with the Guinier R_G values (Figure 5.2 a, b). The eight *P(r)* curves show a concentration-independent peak *M1* at r = 4.8 ± 0.3 nm. A second peak *M2* was observed at r = 10.2 ± 0.6 nm, and, as the concentration increased, peak *M2* increases in its relative intensity. *L* increased from 32 nm at 0.9 mg/ml to 38 nm at 8.7 mg/ml (Figure 5.3). These changes are attributed to oligomer formation in FH. The value of *L* between 32-38 nm is

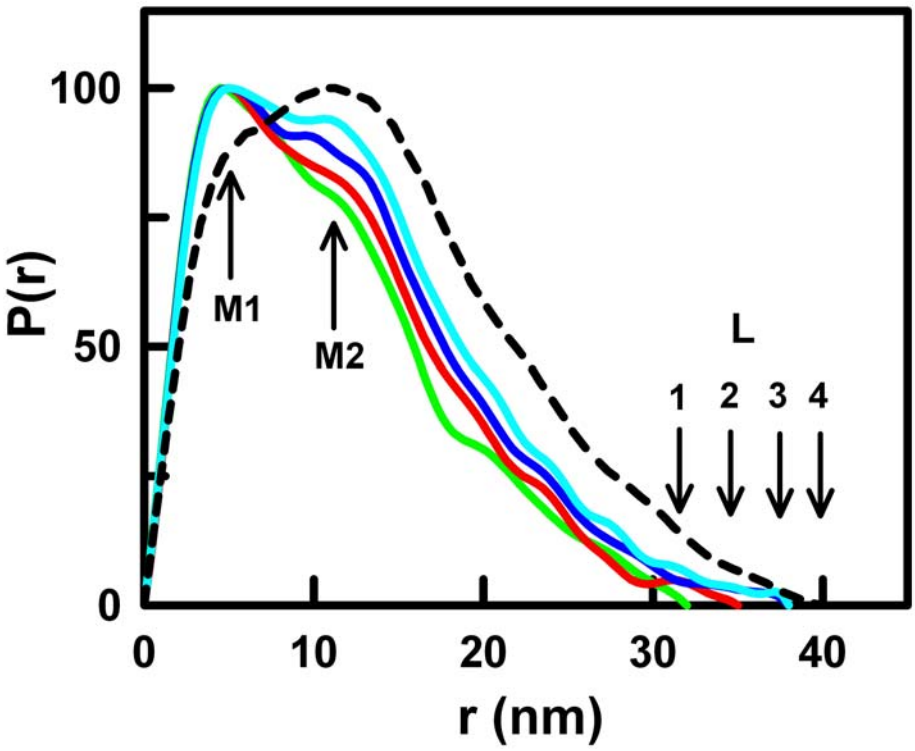

Figure 5.3 Dependence of distance distribution *P(r)* analyses on FH concentrations. The four *P(r)* curves correspond to concentrations of 0.87 mg/ml (green), 2.61 mg/ml (red), 6.08 mg/ml (blue), and 8.69 mg/ml (cyan). The peaks in the *P(r)* curves are denoted as *M1* at 4.9 nm and *M2* at 10.3 nm. The maximum length *L* was determined to be 32 nm, 35 nm and 38 nm (numbered 1, 2 and 3). The intensities of the four *P(r)* curves are normalised using the peak *M1* in order to show the concentration dependence of peak *M2* and *L* more clearly. The dashed line corresponds to the *P(r)* curve obtained in 2001 for FH at 3.56 mg/ml in Tris-HCl buffer (Aslam & Perkins, 2001), for which *L* was determined to be 40 nm (numbered 4).

about half the length of 73 nm expected if the 20 SCR domains in FH are in a fully extended arrangement. When compared with the *P(r)* curve from 2001 at 3.6 mg/ml in 25 mM Tris-HCl, 140 mM NaCl, 0.5 mM EDTA buffer, pH 7.4, the intensity of peak *M2* is now greater than *M1*, and *L* is 40 nm (Figure 5.2 d) (Aslam & Perkins, 2001). This difference is consistent with the presence of minor aggregation in FH from 2001. The superimposition of the *I(Q)* curves from 1991 and 2001 upon the current ones shows increased intensities at low *Q* that are consistent with aggregation (Figure 5.4). The *P*(*r*) curves show that the SCR domains in FH are bent or folded back upon themselves in solution, both for the monomer and its oligomeric and aggregated forms (Figure 5.3).

5.2.2 Sedimentation equilibrium of FH oligomers

Sedimentation equilibrium experiments were performed on heterozygous FH samples in HEPES buffer prepared 16 days beforehand. Data were acquired at 4°C, 20°C and 37°C at concentrations between 0.07 mg/ml to 7.11 mg/ml and four rotor speeds between 8k r.p.m. and 20k r.p.m. Data were fitted using SEDPHAT v4.10b software both individually and globally (Schuck, 2003). Similar fit outcomes were obtained with the data at three different temperatures. In the individual fits, the fitting of a monomer-dimer model to the 11k data at 1.32 mg/ml gave a reduced χ^2 value of 3.7 compared to that of 34.8 from a monomer model using the same data. In global fits up to 1.32 mg/ml, and based on a fixed molecular weight of 145 kDa, the monomer-dimer model (reduced χ^2 of 11) gave significantly improved fits compared to a monomer model that gave a high molecular weight of 187 kDa and an increased reduced χ^2 of 22. Low random residuals were obtained (upper nine fits in Figure 5.5). This showed that a monomer-dimer equilibrium existed in a physiological concentration range.

At higher FH concentrations, the formation of higher oligomers was detected. Between 2.86 – 7.11 mg/ml, the monomer-dimer model did not result in good fits. Large deviations in the residuals were consistent with aggregate formation (lowest three fits in Figure 5.5) (McRorie & Voelker, 1993). Tests with other fit models based on the inclusion of trimers or tetramers gave no improvement in the residuals or reduced χ^2 values. The reduced χ^2

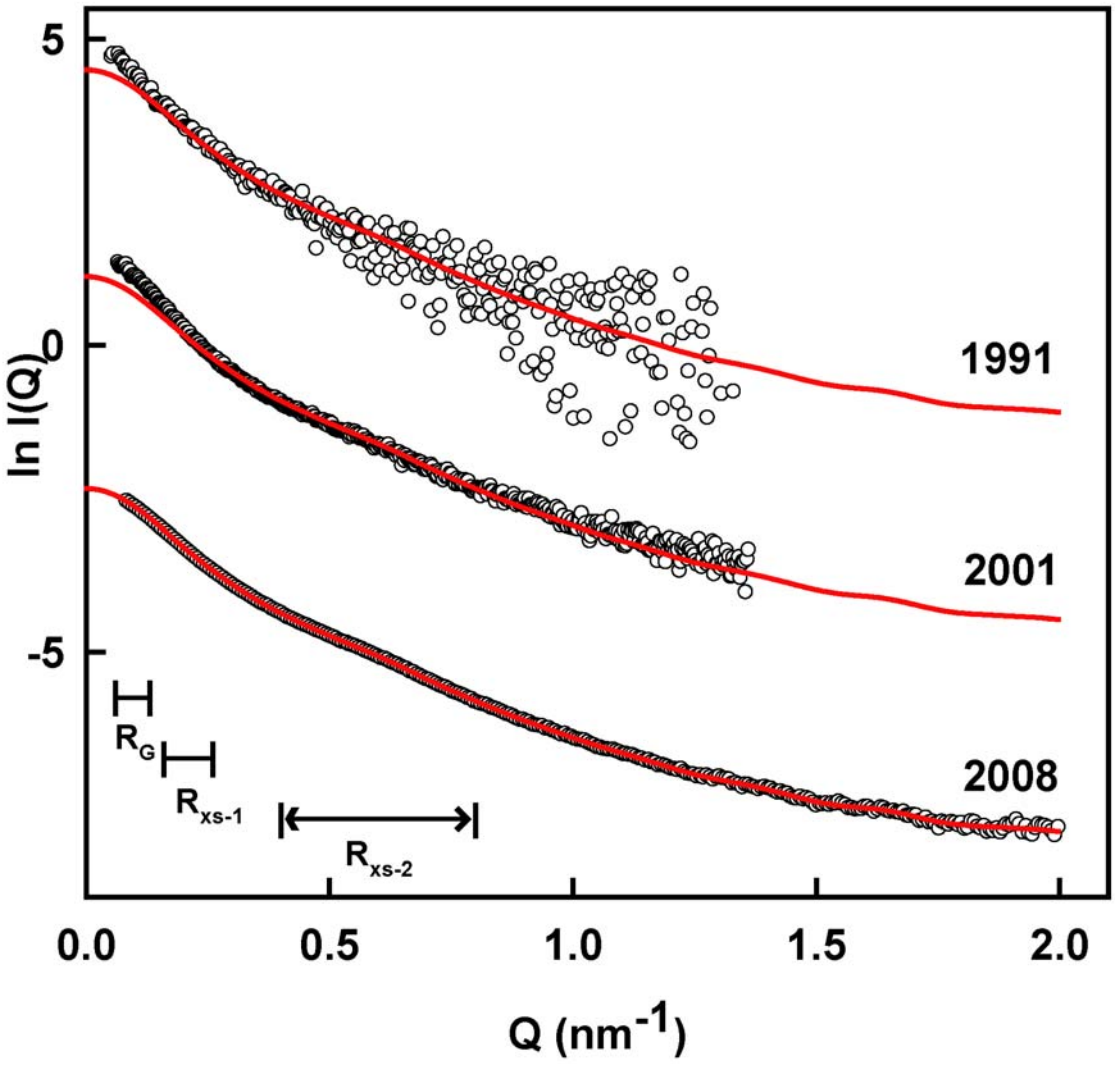

Figure 5.4 Comparison of current and previous X-ray scattering data of heterozygous FH. The X-ray scattering curves for FH used in this chapter (Section 5.2.1; Nan *et al.*, 2008) are compared with the previous published X-ray scattering curves in 1991 (Perkins *et al.*, 1991) and in 2001 (Aslam & Perkins, 2001). Both the previous mesurements were done at the Daresbury synchrotron, and the concentrations of heterozygous FH used were 2.0 mg/ml in 1991 and 3.6 mg/ml in 2001. The X-ray scattering curve in this chapter was obtained at the ESRF synchrotron, and the concentration was 4.3 mg/ml. The continuous line corresponds to the distance distribution function $P(r)$ fitted curve in this chapter, which is then compared with the 1991 and 2001 curves. The Q ranges used to report the R_G, R_{XS-1} and R_{XS-2} values from the scattering data are indicated as arrowed.

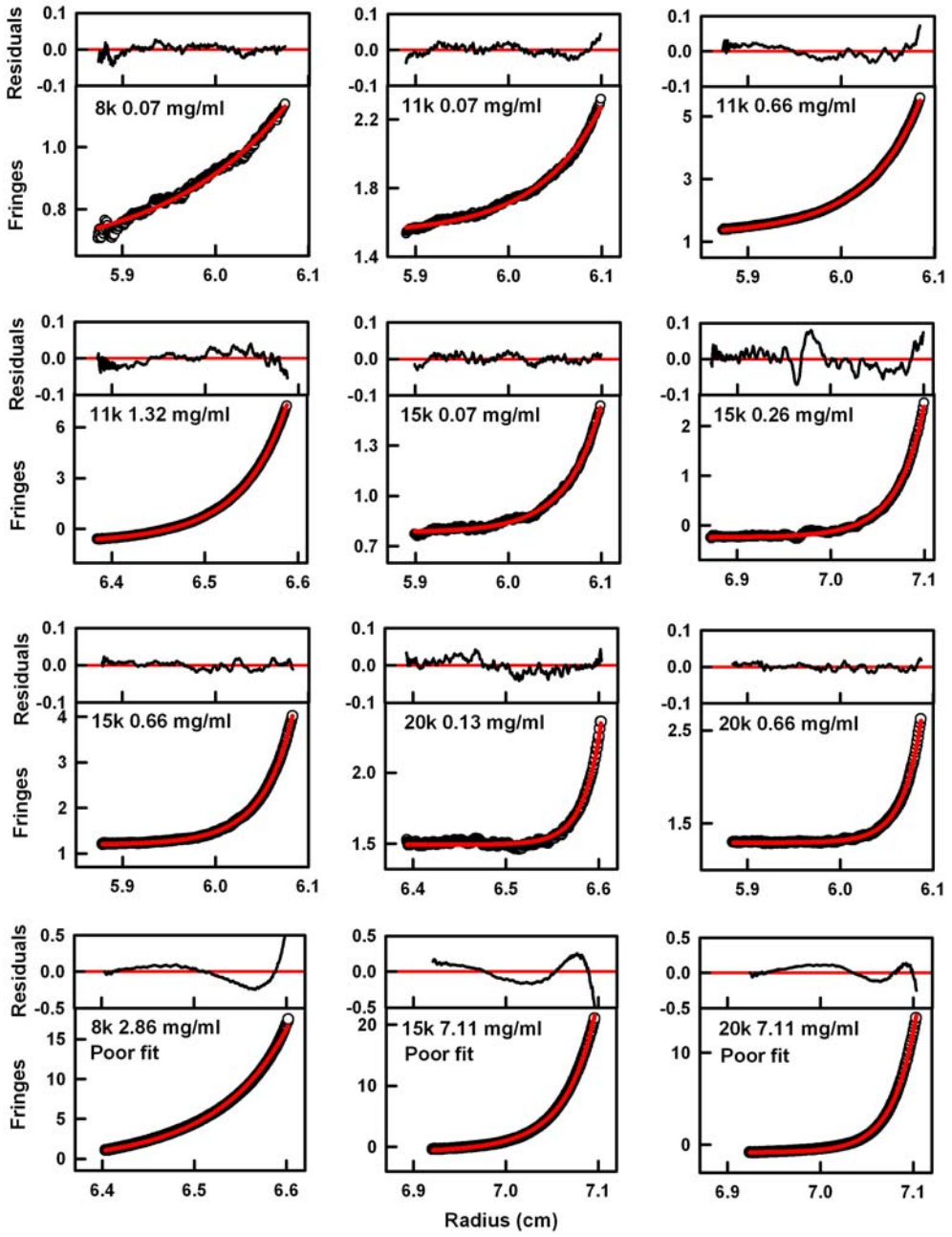

Figure 5.5 Sedimentation equilibrium of heterozygous FH. The upper nine panels show the outcome of a global fit using SEDPHAT when the equilibrium curves of five concentrations between 0.07 mg/ml to 1.32 mg/ml of FH at 20^{o}C were fitted to the "monomer-dimer self-association" model using the "M and s" fitting routine. The fit residuals are shown above each panel. The lower three panels show the poor fits to the monomer-dimer self-association model when higher concentrations of FH (2.86 mg/ml, 7.11 mg/ml) were fitted.

values of between 269 to 980 for these fits at higher concentrations showed that neither monomer-dimer, monomer-dimer-trimer or monomer-dimer-tetramer self-association models would fit. Hence these data do not correspond to an equilibrium between monomers and higher oligomers.

5.2.3 SDS-PAGE and size-exclusion gel filtration of FH oligomers

Non-reducing SDS-PAGE of the samples at three concentrations including 0.16 mg/ml, 1.42 mg/ml and 2.74 mg/ml after ultracentrifugation showed that a dimer band was observed at the higher concentrations used, and fainter bands corresponding approximately to trimers and tetramers could be observed (Figure 5.6 b). There are no unpaired Cys residues in FH that would explain this. The size-exclusion gel filtration of heterozygous FH in the original purification showed the single homogenous peak between 65 ml and 75 ml of FH and a small peak at about 80 ml corresponds to residual human serum albumin which was then removed (Figure 5.6 a). The size-exclusion gel filtration of the equilibrium FH samples 78 days after their original purification showed that the single homogenous peak of FH between 65 ml and 75 ml was supplemented by additional peaks that eluted between 50 ml and 65 ml (Figure 5.6 a). This showed that oligomers had formed during the ultracentrifugation experiment and the subsequent sample storage at 4°C.

5.2.4 Sedimentation velocity of FH oligomers

The sedimentation coefficient $s_{20,w}$ monitors macromolecular elongation, and provides an independent monitor of the scattering data through its ability to detect sample polydispersity. Sedimentation velocity experiments were performed at four rotor speeds between 25k r.p.m. and 60k r.p.m. using three FH preparations at nine concentrations between 0.07-5.9 mg/ml in HEPES buffer and between 0.05-0.35 mg/ml in PBS buffer. Data analyses utilised size-distribution *c(s)* analyses in SEDFIT v9.3b in order to identify species other than monomeric FH (Schuck, 1998; Schuck, 2000). At all concentrations, monomeric FH was observed to sediment at $s_{20,w}$ = 5.65 (± 0.05) S. This is in good agreement with previous determinations of the $s_{20,w}$ value of 5.5 S to 5.6 S and 5.3 ± 0.1 S

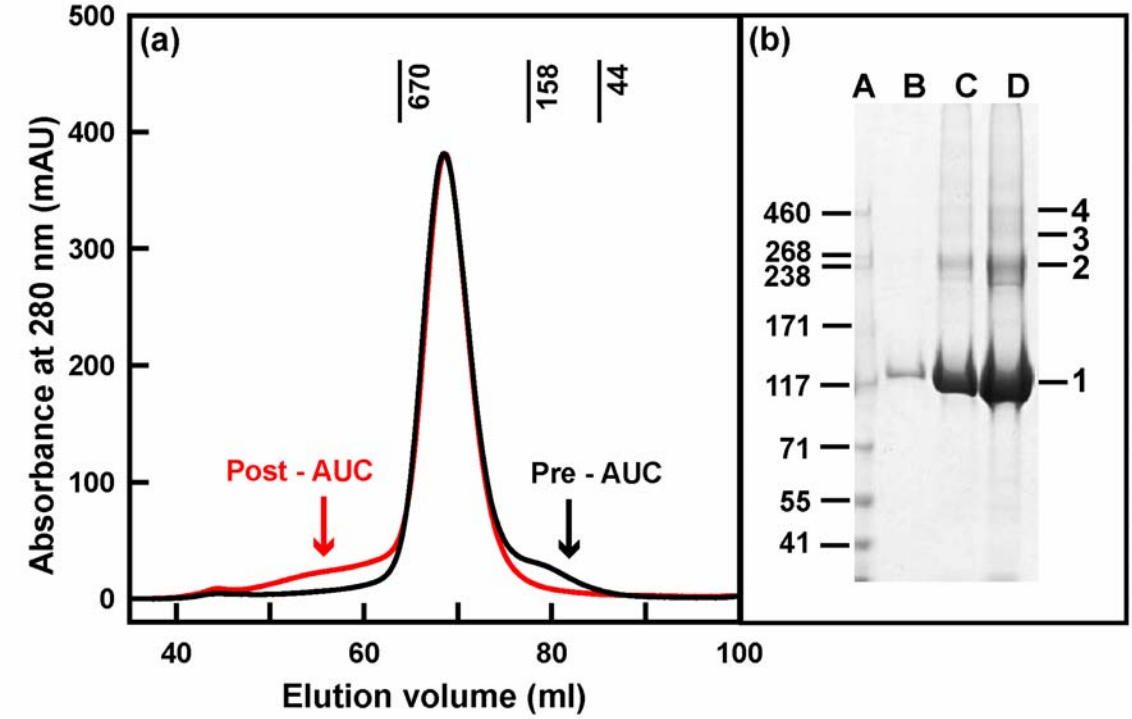

Figure 5.6 Size-exclusion gel filtration and non-reducing SDS-PAGE analyses of heterozygous FH.

(a) FH samples at 3 mg/ml were loaded onto a Superose^{TM} 6 prep grade XK 16/60 column following purification (black) and 78 days after purification (red). The elution positions of three molecular mass standards are shown.

(b) Non-reducing SDS-PAGE analyses of FH after ultracentrifugation. Lane A: Himark^{TM} Prestained High Molecular Weight Standard, labelled to the left; Lane B: 0.16 mg/ml FH; Lane C: 1.42 mg/ml FH; Lane D: 2.74 mg/ml FH. The higher molecular weight bands seen in FH are labelled on the right by 1, 2, 3 and 4 to denote monomer, dimer, trimer and tetramer.

(Whaley & Ruddy, 1976; Aslam & Perkins, 2001; Fernando *et al.*, 2007).

A concentration dependence of the *c(s)* distributions was observed. At 0.17 mg/ml, the shape of the sedimentation boundaries indicated a predominantly single sedimentation species (Figure 5.7 b). For 0.17 mg/ml and 0.63 mg/ml of heterozygous FH in either HEPES or PBS buffer, a second peak was observed in the *c*(s) analyses at 9.2 ± 0.5 S and its relative intensity increased with concentration (Figure 5.7 c). The *c*(*M*) size distribution plots showed that the major peak at 5.56 S corresponds to a molecular weight of 142 ± 2 kDa. This is consistent with the global fit of the sedimentation equilibrium data (Figure 5.5). At higher FH concentrations and using a one-day old FH preparation, the sedimentation boundaries of heterozygous FH at 5.92 mg/ml indicated a more complex sedimentation profile (Figure 5.7 a), and the peak at about 7.3 S is 7% of the intensity of the major peak at 5.56 S. As the concentration of FH increased from 1.53 mg/ml to 5.92 mg/ml, six smaller sedimentation species were consistently observed at *s* values of 7.3 (± 0.2) S, 9.2 (± 0.2) S, 11.3 (± 0.4) S, 13.4 (± 0.06) S, 15.4 (± 0.2) S and 17.2 (± 0.4) S at 50k r.p.m. This suggested that FH formed not only dimers but also trimeric to heptameric oligomers in small but significant amounts of about 15% in total.

This interpretation was verified starting from the four best-fit glycosylated FH models previously generated by constrained scattering modelling done in 2001 (Aslam & Perkins, 2001). The present R_G value of 8.9 nm for monomeric FH (Figure 5.2 c), meant that these previous models with a R_G value of 9.9 nm in 2001 were now too elongated. Thus linkers in one of the previous four best-fit FH models were adjusted in order to generate a more compact SCR arrangement. In satisfactory agreement with the experimental *s* value of 5.65 S, a $s_{20,w}$ value of 5.2 S was obtained from this glycosylated model using HYDROPRO v7c (Garcia de la Torre *et al.*, 2000), using the default value of 0.31 nm for the atomic element radius for all atoms in order to represent the hydration shell. The $s_{20,w}$ calculations were insensitive to the presence or absence of six biantennary oligosaccharide chains at Asn511, Asn784, Asn804, Asn864, Asn893 and Asn1011 (mature protein numbering) (Aslam & Perkins, 2001). If a FH monomer became spherical in its shape, the maximum possible $s_{20,w}$ value would be 9.4 S. Hence postulating the occurrence of conformational changes in

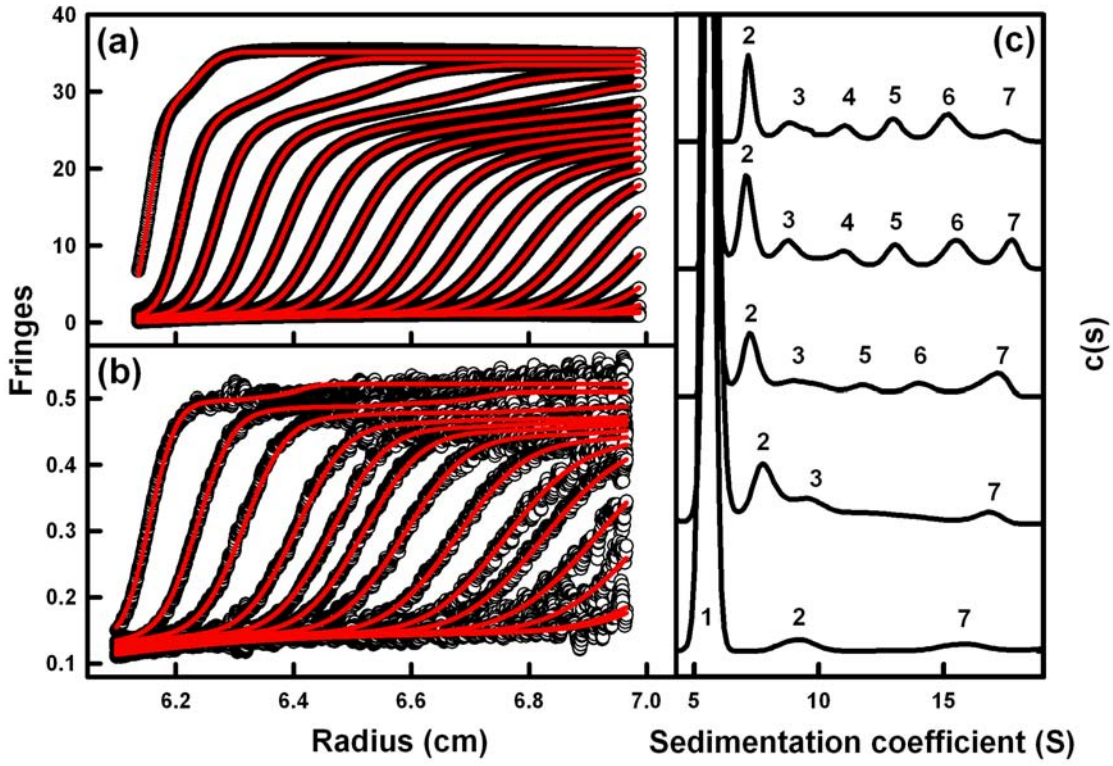

Figure 5.7 Sedimentation velocity of heterozygous FH.

(a) The 200 scan boundaries for FH at 5.92 mg/ml at 50k r.p.m. were fitted using Lamm equation fits with SEDFIT. Only every tenth scan is shown for reason of clarity.

(b) The corresponding boundary fits are shown for FH at 0.17 mg/ml at 40k r.p.m.. Other details follow (a).

(c) In the five *c(s)* size-distribution analyses, the major sedimentation species at 5.56 S is labelled as 1. Its intensity was normalised in all five analyses for clarity. From bottom to top, the FH concentrations were 0.17 mg/ml, 0.63 mg/ml, 1.53 mg/ml, 2.99 mg/ml and 5.92 mg/ml. The oligomeric FH peaks in increasing order of S values are labelled from 2 to 7. The five analyses are displaced by 10% of the intensity of peak 1.

monomeric FH is unable to explain the discrete peaks seen at the larger *s* values in the *c*(*s*) analyses for heterozygous FH at concentrations above 1.53 mg/ml (Figure 5.7 c).

Modelling to account for oligomer formation was arbitrarily created from dimerisation sites at opposite ends of the FH monomer model. Oligomers were created using INSIGHT II 98.0 molecular graphics software (Accelrys, San Diego, CA, USA) on Silicon Graphics OCTANE Workstations (Figure 5.8). The predicted $s_{20,w}$ value for a dimer model in an extended conformation was 7.5 S, in good agreement with the observed peak at 7.3 S. The addition of a third monomer to this dimer model resulted in a predicted $s_{20,w}$ values of 9.2 S, in good agreement with the observed peak at 9.2 S. Starting with the tetramer, it was found necessary to add further monomers in a more compact arrangement to give models with predicted $s_{20,w}$ values that agreed within error of the experimental values. The movement of monomer 1 in the tetrameric model towards the centre of the model gave a predicted value of 11.3 S, in good agreement with the observed peak at 11.3 S. The pentamer, hexamer and heptamer models gave predicted values of 13.5 S, 15.2 S and 16.9 S respectively, which agreed well with the experimental values of 13.4 S, 15.4 S and 17.2 S respectively. These agreements support the assignment of the six additional peaks at high S values in the *c(s)* plots to a series of FH oligomers.

5.3 Material and Methods

5.3.1 Protein purification

The purification of heterozygous FH for X-ray scattering and analytical ultracentrifugation experiments utilised a 3 litre pool of just-outdated anonymised human plasma from the Royal Free Hospital Blood Bank with an anti-FH monoclonal antibody Sepharose MRC-OX23 column as described (Aslam & Perkins, 2001; Sim *et al.*, 1993). About 50ml of mixed human plasma, made 5 mM with EDTA, was made 0.5 mM with protease inhibitor Pefabloc-SC[70], and then dialysed against Tris buffer (25 mM Tris-HCl, 140 mM NaCl, 0.5 mM EDTA, pH 7.4). To deplete proteins which bind to Sepharose or to IgG, the plasma was passed through a column of non-immune IgG immobilized on Sepharose.

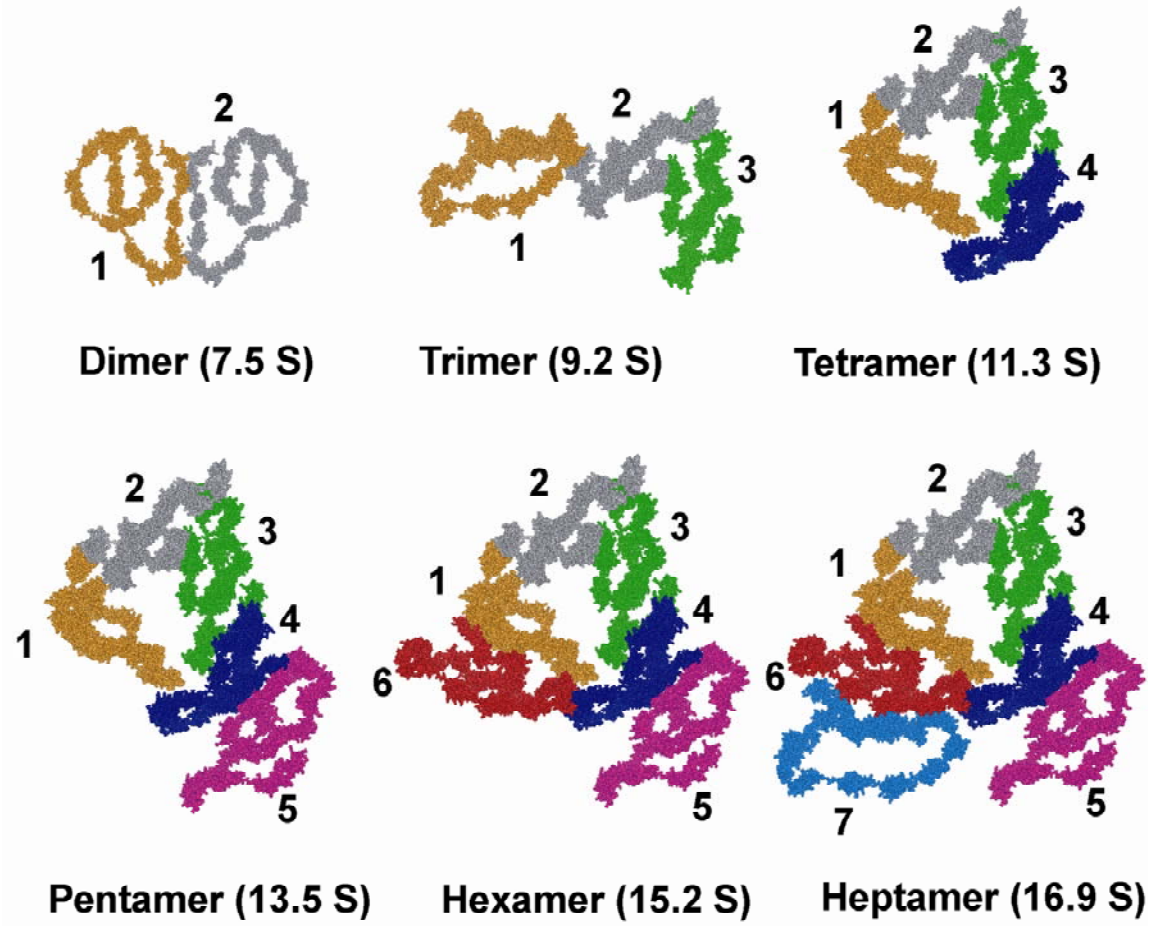

Figure 5.8 Schematic models for FH oligomers observed in the sedimentation coefficient distribution analyses for sedimentation velocity data. Six schematic models for oligomers of FH are shown that yield the predicted $s_{20,w}$ values shown in brackets. The monomers are denoted by different colours and numbered. Monomers 2 and 3 are viewed in the same orientation in all the models except for the dimer.

Plasminogen/plasmin was then removed by passing the plasma through a lysine-sepharose column. After that, the plasma was passed through a monoclonal antibody column, MRC OX23-Sepharose specific for FH, at a rate less than 1ml/min. FH was then eluted with about 40ml of the chaotrope, 3 M $MgCl_2$, pH 6.9. The material was dialysed against HEPES buffer (10 mM HEPES, 137 mM NaCl, pH 7.4) in the presence of 0.5 mM EDTA. The material was then passed through Hitrap Protein G HP column to remove any contaminant IgG. The FH concentration step at 4°C employed a gentle centrifugation approach without stirring (Amicon® Ultra-15 centrifugal filter devices with a molecular weight cut-off of 50 kDa at 2500 g). Non-specific aggregates of FH and human serum albumin were removed by gel-filtration on a Superose™ 6 prep grade XK 16/60 column, at a flow rate of 1 ml/min and the HEPES buffer with 0.5 mM EDTA as the running buffer. The purified FH sample was reconcentrated by centrifugation. All FH samples were checked using SDS-PAGE before and after scattering and ultracentrifugation experiments. The electrophoresis was performed by using NuPAGE® Novex 3-8% Tris-Acetate Mini Gel and the standard protocol. An absorption coefficient of 16.7 (1%, 280 nm, 1 cm path length) was used to determine concentrations (Aslam & Perkins, 2001). Note that this value will be revised in Chapter 7 and 8 below.

5.3.2 X-ray scattering data collection and analysis

X-ray scattering data were obtained in three beam time sessions on the Beamline ID02 at the European Synchrotron Radiation Facility (ESRF), Grenoble, France operating with a ring energy of 6.0 GeV (Sim *et al.*, 1993). Storage ring currents ranged from 63 mA to 65 mA and 66 mA to 91 mA (two sessions in 16-bunch mode) and from 170 mA to 172 mA (one beam session in uniform fill mode). Samples were measured in flow cells to reduce radiation damage by moving the sample continuously during beam exposure in 10 time frames of duration 0.1 sec or 0.2 sec each (uniform fill mode), or 1.0 or 2.0 sec each (16-bunch mode), together with on-line checks for the absence of radiation damage, after which the frames were averaged. Heterozygous FH prepared two days beforehand was studied at eight concentrations including 0.43 mg/ml, 0.87 mg/ml, 1.74 mg/ml, 2.6 mg/ml, 4.3 mg/ml, 6.1 mg/ml, 7.8 mg/ml and 8.7 mg/ml in HEPES buffer. The Guinier analyses were

performed to obtain the values of R_G, R_{XS-1} and R_{XS-2} using a PERL script program SCTPL7 (J. T. Eaton & S. J. Perkins, unpublished software) on Silicon Graphics O2 Workstations. The indirect transformation of the scattering data $I(Q)$ in reciprocal space in the Q range between 0.08 nm^{-1} to 2.1 nm^{-1} into real space gives the distance distribution function $P(r)$. Other details about data collection and Guinier and *P(r)* analyses are described in Section 4.2.4 and 4.2.5.

5.3.3 Sedimentation equilibrium data collection and analysis

Analytical ultracentrifugation experiments were performed on two Beckman XL-I instruments using an eight-hole rotor AnTi50 and a six-hole rotor AnTi60. Sedimentation equilibrium experiments were conducted using six-sector cells with solution column heights of 2 mm at rotor speeds of 8k r.p.m., 11k r.p.m., 15k r.p.m. and 20k r.p.m. and temperatures of 4 °C, 20 °C and 37 °C on heterozygous FH samples at 20 concentrations between 0.07 mg/ml and 7.1 mg/ml. Both absorbance and interference optical systems were used. Absorbance data at 280 nm above 0.7 mg/ml were not fitted because of the saturation of the optics, thus interference data were fitted. Data at 20 °C were fitted using SEDPHAT v4.10b software initially using individual fits of 80 equilibrium curves, and subsequently followed by global fits of between nine to 20 curves (Schuck, 2003). Both a monomer model and a "monomer-dimer self-association" model were used. The global fitting of the interference data at concentrations between 0.07 mg/ml to 1.32 mg/ml utilised the "monomer-dimer self-association" model with the "M and s" fitting routine. In this fitting, the molecular weight of FH monomer was fixed at 145 kDa, while the baseline and the dissociation constant K_D were floated. Other details about sedimentation equilibrium experiments are explained in Section 4.1.3.

5.3.4 Sedimentation velocity data collection and analysis

Sedimentation velocity experiments were performed at 20 °C for heterozygous FH at various concentrations in HEPES buffer and PBS buffer at rotor speeds of 25k r.p.m., 40k r.p.m, 50k r.p.m and 60k r.p.m. on two Beckman XL-L analytical ultracentrifuges equipped

with AnTi60 rotors and two-sector cells with a column height of 12 mm. The sedimentation coefficient distribution *c*(*s*) analyses of the data were performed using the programme SEDFIT (version 9.3b) (Schuck, 1998; Schuck, 2000). The fits were based on a resolution of 200 and a fixed frictional coefficient ratio *f/fo* of 1.78, while allowing both the meniscus and the cell bottom to float within a narrow range of 0.01 cm until the overall root mean square deviation (r.m.s.d) and fitting residuals were satisfactory. Other details about *c*(*s*) analyses are explained in Section 4.1.2.

5.4 Conclusions

Knowledge of the oligomeric state of FH is crucial for understanding its immunological function in complement regulation and its likely roles in AMD and aHUS disease. The new data collection in this study clarified that heterozygous FH exhibits oligomeric forms after all, as originally proposed (Perkins *et al.*, 1991). A monomer-dimer equilibrium was identified at the lowest concentrations. Partial FH dimerisation has been reported by two other laboratories (Jokiranta *et al.*, 2000; Jokiranta *et al.*, 2006; Oppermann *et al.*, 2006). As the concentration increases, higher oligomeric structures that can be as large as heptamers and are not in equilibrium with each other were identified. The studies of heterozygous FH in 2001 and 1991 had reported R_G values that were stated to be approximate for reason of the need to access the lowest Q values, which is difficult to measure with highly elongated proteins. Under these conditions, the aggregation of a highly elongated protein can be hard to identify. Here, the use of freshly-purified FH resulted in a lower R_G value of 8.90 nm in place of the apparent R_G values of 11.4 nm and 12.4 nm before. The sequence-calculated molecular weight of FH is 150,000 Da assuming six N-linked oligosaccharides. In 2001, the molecular weight of FH was determined as 148,000-182,000 Da, as the result of which FH was deduced to be monomeric (Aslam & Perkins, 2001). In 1991, its molecular weight was determined to be 250,000-320,000 Da, leading to the deduction that FH was dimeric (Perkins *et al.*, 1991). The new data suggest that the 1991 result is best explained in terms of the presence of monomeric FH together with sufficient FH oligomers to double its averaged observed molecular weight. Oligomerisation

in the 1991 study was favoured by the higher FH concentrations that were necessary for the X-ray data collection.

This study of FH oligomerisation resulted from the unexpected observation of weak monomer-dimer equilibria for two fragments of FH. One for the SCR-6/8 fragment of FH has a K_D of about 40 μM. Detailed ultracentrifugation equilibrium and velocity measurements were required to establish this, as the compact structure of this SCR-6/8 dimer meant that dimerisation was not readily detected by X-ray scattering (Fernando *et al.*, 2007). However the presence of the SCR-6/8 dimer was requisite for good X-ray modelling fits to its structure. The second weak monomer-dimer equilibrium with a K_D of 16 μM for the SCR-16/20 fragment was readily detected by both X-ray scattering and ultracentrifugation because this dimer has an extended structure (Okemefuna *et al.*, 2008). Both these K_D values are comparable with that of 28 μM for heterozygous FH from the SEDPHAT global fits below 1.36 mg/ml (Figure 5.5). This suggests that the dimerisation of SCR-6/8 and SCR-16/20 is physiologically relevant, even though both were recombinant proteins. FH concentrations range between 0.235-0.810 mg/ml in blood (Saunders *et al.*, 2007). Therefore so long as no other factors require consideration, this K_D value of 28 μM indicates that about 5% to 15% of FH in blood will be dimeric. The complement regulatory function of FH will be affected by dimer formation in serum. Thus ligands may be sterically blocked from approaching their binding sites if they are proximate to either of the two presumed FH dimer sites, or may not bind because of aggregate formation. Alternatively ligand binding may be enhanced if their binding sites are distant from the FH dimer sites, because in that case FH would become multivalent. Future studies of FH-ligand binding will be complicated by the observation of dimerisation. Thus FH-ligand binding studies that disregard dimerisation are open to misinterpretation, as exemplified by a recent SEDPHAT sedimentation equilibrium study of SCR-6/8 (Prosser *et al.*, 2007). Alternative approaches are required to establish 1:1 complex formation with ligands in the presence of dimers, such as that described in Figure 3 of the original ultracentrifugation study of the SCR-6/8 complex with heparin, where titrations with a range of heparin-protein ratios were analysed using SEDFIT *c(s)* size distribution plots (Fernando *et al.*, 2007).

A mechanistic pathway for oligomer formation is suggested from this work. At higher concentrations, the existence of two different weak self-association sites in FH suggests that FH can self-associate continuously by intermolecular contacts that occur alternately through both these sites to form large oligomers. These higher oligomers were indeed directly observed above 2 mg/ml in fresh FH samples by velocity experiments (Figure 5.7). At low FH concentrations, the modelling of the species observed in the c(s) analyses suggests that extended dimer structures were formed, which would explain its reversibility. At higher concentrations, the formation of higher oligomers is predicted to involve more compact associations of the monomer (Figure 5.8), and this would explain its lack of reversibility (Figure 5.5). The storage of FH samples may facilitate the formation of more stable higher oligomers. Further studies of this are in progress. These results suggest that the use of freshly gel-filtrated FH samples stored below 1 mg/ml concentrations may be required for complement regulatory functional studies. The aggregation of FH is relevant for AMD, for which a risk factor is the observation of drusen deposits at the retinal surface. Currently there is no detailed knowledge of the mechanism of drusen formation in AMD. It is possible that the localised accumulation of higher FH concentrations within the eye may facilitate the slow formation of protein precipitates within drusen during the course of a lifetime. For such a mechanism to operate, any FH precipitation in drusen would appear to necessitate much higher concentrations of FH than those seen physiologically in serum, and this would occur in the presence of a number of other components that are present. The latter would alter the kinetics and thermodynamics of deposit formation when compared to a mechanism based only on FH self-association. In this context, it is intriguing that the His402 genetic polymorphism that is a risk factor for AMD showed a slightly higher propensity to self-associate than the lower-risk Tyr402 form when the SCR-6/8 fragment was studied by X-ray scattering and ultracentrifugation (Fernando *et al.*, 2007).

Chapter Six

Uncontrolled zinc- and copper-induced oligomerisation of heterozygous human factor H and its possible implications for function and disease

6.1 Introduction

In the innate immune response, C3 is activated to C3b by the cleavage of the small anaphylatoxin C3a, thereby initiating the alternative complement pathway. To prevent complement-mediated host cell damage, C3b is regulated by factor H (FH) amongst other proteins, in which FH acts as a cofactor for the factor I-mediated cleavage of C3b to form iC3b, C3c and C3dg (Law & Reid, 1995; Whaley & Ruddy, 1976; Pangburn *et al.*, 1977). FH also accelerates the decay of the C3 convertase C3bBb and competes with factor B for binding to C3b (Whaley & Ruddy, 1976; Weiler *et al.*, 1976; Farries *et al.*, 1990). FH is comprised of a linear arrangement of 20 short complement regulator (SCR) domains, each of length about 61 residues, and 19 linkers between the domains (Soares & Barlow, 2005). FH possesses multiple binding sites for C3b and heparin, the latter being an analogue of heparan sulphate that is found on host cell surfaces, and FH also binds to other proteins such as C-reactive protein (Ormsby *et al.*, 2006; Sharma & Pangburn., 1996; Jokiranta *et al.*, 2000). FH protects host cells by binding to heparin-like negatively-charged clusters on their surfaces through its C-terminal end, which is then followed by N-terminal regulatory activity against C3b (Oppermann *et al.*, 2006; Ferreira *et al.*, 2006). FH involvement in uncontrolled inflammation is associated with disease, namely atypical haemolytic uraemic syndrome (aHUS) and membranoproliferative glomerulonephritis type II (MPGN) and age-related macular degeneration (AMD) (Saunders *et al.*, 2007; Klein *et al.*, 2005; Haines *et al.*, 2005; Edwards *et al.*, 2005; Hageman *et al.*, 2005). AMD is the most common cause of blindness in the elderly in the Western world. In several groups identified a Tyr402His FH polymorphism that increased the risk of developing AMD over seven-fold (Klein *et al.*, 2005; Haines *et al.*, 2005; Edwards *et al.*, 2005; Hageman *et al.*, 2005). Since then, other FH variants have been shown to modify the risk for AMD (Li *et al.*, 2006; Maller *et al.*, 2006; Hughes *et al.*, 2006). Even with the analysis of over 100 genetic alterations in FH, no clear molecular mechanism for diseases based on the involvement of defective forms of FH has been proposed so far (Saunders *et al.*, 2007).

An early hallmark of AMD is the appearance of sub-retinal pigment epithelial deposits (sRPEds) that can be focal (drusen) or diffuse (basal linear and laminar). These deposits contain oxidized lipids and over 120 aggregated proteins including FH and other

complement components that are secreted by RPE cells or delivered by the choroidal blood circulation (Crabb *et al.*, 2002; Hageman *et al.*, 2001). These deposits develop within Bruch's membrane, an extracellular matrix layer interposed between the retinal pigment epithelium (RPE) and the choroidal vasculature (Bird, 1992; Bird *et al.*, 1995). Recently, millimolar concentrations of zinc have been found in sRPEds and Bruch's membrane, suggesting that the pathological release of zinc from surrounding tissues like the zinc-rich RPE choroid complex might be involved in sRPEd formation (Galin *et al.*, 1962; Lengyel *et al.*, 2007). In the context of AMD the presence of FH and zinc in sRPEd is of interest, firstly because zinc inhibits the factor I-mediated cleavage of C3b leading to uncontrolled inflammation, and secondly an initial X-ray scattering study showed that FH aggregates in the presence of high zinc concentrations (Crossley & Porter, 1980; Perkins *et al.*, 1991).

The molecular basis of the self-associative interaction between FH and zinc is unknown. The overall structure of native FH is not straightforward to characterise by methods such as crystallisation or NMR for reason of its large size, glycosylation and inter-SCR flexibility between its 20 domains, although several crystal and NMR structures have been published for small domain fragments of FH (Section 2.1.2). Solution structural methods such as X-ray and neutron scattering and analytical ultracentrifugation have been applied to demonstrate that native FH possesses a partially-folded back SCR structure in solution (Perkins *et al.*, 2008; Cole *et al.*, 2008). Recently we showed that native FH is predominantly monomeric and partly dimeric at physiological concentrations in serum, and forms higher oligomers as its concentration increases if no other factors require consideration (Chapter Five; Nan *et al.*, 2008a). The original X-ray scattering study of FH-zinc complexes was limited by a requirement for relatively high FH concentrations at that time, consequently only Guinier analyses at low scattering angles were measured, and the resulting averaged FH structure was mostly dimeric (Perkins *et al.*, 1991). Since that time, the availability of monomeric FH at low concentrations and improvements in X-ray scattering instrumentation at the ESRF synchrotron facility permits a more detailed investigation of the role of zinc and FH in a physiological concentration range (Chapter Five; Nan *et al.*, 2008a). Following the study of the self-association properties of heterozygous FH in Chapter Five, in this chapter, by performing quantitative titration studies of FH with a range of different

metals by X-ray scattering, supplemented by analytical ultracentrifugation, aggregations of heterozygous FH in the presence of zinc was observed. Other transition metals such as copper induce different degrees of uncontrolled FH oligomer formation. The aggregation of heterozygous FH in the presence of zinc and copper correlated with the reduction of FH activity. Whether the high zinc concentrations associated with Bruch's membrane may drive the aggregation of FH in the environment of the retina, and the molecular implications of our results for complement regulation and sRPEd formation are discussed in this chapter.

6.2 Results and Discussion

6.2.1 Guinier X-ray scattering analyses of FH-metal complexes

Freshly-purified heterozygous FH for scattering and ultracentrifugation studies resulted in a homogeneous peak by gel-filtration, and the purity of FH was verified by SDS-PAGE (Figure 5.6 in Chapter Five; Nan *et al.*, 2008a). FH concentrations were generally maintained at 1 mg/ml or less with storage at 4^{o}C to avoid irreversible oligomer formation, and studied at this concentration or less to be comparable with physiological FH concentrations between 0.235-0.810 mg/ml in serum (Saunder *et al.*, 2007). The effect of metals on FH was studied by synchrotron X-ray scattering and analytical ultracentrifugation in HEPES buffer (Section 6.3.1). Phosphate buffer was not used because zinc precipitates with phosphate.

Solution scattering enabled the overall structure and size of FH to be studied (Section 4.2; Perkins *et al.*, 2008). FH samples at 0.42 mg/ml (2.8 μM) and 1.05 mg/ml (7.0 μM) were titrated with 0 μM, 0.2 μM, 0.6 μM, 2 μM, 6 μM, 20 μM, 60 μM and 200 μM $ZnSO_4$. Excellent signal-noise ratios were obtained with the improved instrument at ESRF, and no detectable effect was observed from radiation damage. Linear Guinier analyses at low Q values (where $Q = 4\pi \sin\theta / \lambda$; 2θ = scattering angle; λ = wavelength) gave the radius of gyration R_G in satisfactory $Q.R_G$ ranges below 1.1 (Figure 6.1). The data obtained at 0.42 mg/ml FH was relatively nosier than that at 1.05 mg/ml. The R_G of FH corresponds to its degree of elongation. For heterozygous FH without zinc, the mean R_G value was 8.45 (± 0.14) nm at 1.05 mg/ml and 8.28 (± 1.18) nm at 0.42 mg/ml. Both

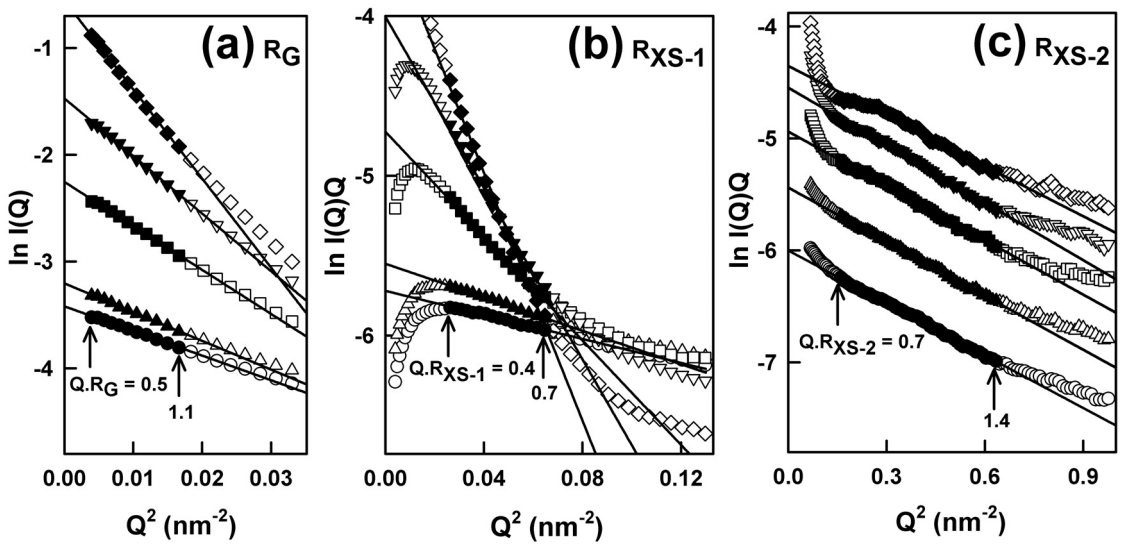

Figure 6.1 Guinier analyses for heterozygous FH titrated with zinc. The filled symbols correspond to the Q range used to determine the R_G and R_{XS} values. The symbols ○, Δ, □, ∇, ◊ represent [Zn] of 2 μM, 6 μM, 20 μM, 60 μM and 200 μM in that order. The filled symbols represent the data points used to determine R_G or R_{XS} values, and the straight lines represent the best linear fits through those data points. The $Q.R_G$ and $Q.R_{XS}$ fit ranges are arrowed.

(a) R_G plots of ln I(Q) vs. Q^2 for 1.05 mg/ml heterozygous FH using a Q range of 0.06 - 0.13 nm^{-1}.

(b,c) The corresponding cross-sectional R_{XS-1} and R_{XS-2} plots of ln $I(Q).Q$ vs. Q^2 for the same five scattering curves in a Q range of 0.16 - 0.26 nm^{-1} and 0.4 - 0.8 nm^{-1} are shown. In (c), the five curves are successively displaced in steps of 0.5 ln units for reason of clarity.

values were consistent with the recently determined R_G value of 8.89 (± 0.19) nm for heterozygous FH monomers (Chapter Five; Nan *et al.*, 2008a). The present R_G values starting from a monodisperse preparation of FH were consistently lower than the old R_G values for FH which had partially self-aggregated (Perkins *et al.*, 1991). Here, the R_G values stayed stable when [Zn] ≤ 6 μM, and increased significantly when [Zn] ≥ 20 μM (Figure 6.1 a and Figure 6.2 a). The associated intensity *I(0)/c* parameters which are derived from R_G fits, are proportional to relative molecular weights *Mr* of the FH macromolecules. The *I(0)/c* value of heterozygous FH also showed a large increase at [Zn] ≥ 20 μM (Figure 6.2 b). Hence these changes are attributable to strong FH oligomer formation previously seen for dimeric FH (Perkins *et al.*, 1991). To investigate the effects of SO_4^{-2} on FH, heterozygous FH prepared two days beforehand at 0.93 mg/ml added with 200 μM $ZnSO_4$ or $ZnCl_2$ in HEPES buffer was studied using synchrotron X-ray scattering. No significant difference in the Guinier parameters has been observed, hence ruling out any anion effects on the oligomerisation of FH induced by zinc. The present experiments extend the previous X-ray work by demonstrating that zinc chloride causes monomeric FH to aggregate (Perkins *et al.*, 1991).

The cross-sectional Guinier analyses monitor the structural proximity relationships between non-neighbouring SCR domains (R_{XS-1}) and neighbouring SCR domains (R_{XS-2}) (Aslam & Perkins, 2001). Linear fits for both parameters were obtained within satisfactory Q.R_{XS} ranges (Figure 6.1 b, c). Without zinc, the R_{XS-1} value of heterozygous FH was determined to be 2.68 (± 0.08) nm at 1.04 mg/ml and 2.40 (± 0.16) nm at 0.42 mg/ml, in good agreement with the previously determined R_{XS-1} value of 2.51 (± 0.06) nm for the heterozygous FH monomer (Chapter Five; Nan *et al.*, 2008a). The R_G and R_{XS-1} values without the presence of zinc were consistent with the fact that heterozygous FH is mainly monomer (85% to 95%) in physiological concentration range (Nan *et al.*, 2008). The R_{XS-1} values significantly increased when [Zn] was 20 μM or greater (Figure 6.2 c). This change showed that the FH oligomers associated in a side-by-side manner, and not end-to-end. Without zinc, the R_{XS-2} value was determined to be 1.78 (± 0.03) nm, in good agreement with the previous value of 1.79 (± 0.01) nm (Perkins *et al.*, 1991; Chapter Five; Nan *et al.*, 2008a; Aslam & Perkins, 2001). When zinc was added, the R_{XS-2} value did not alter significantly (Figure 6.2 d), indicating that the linear arrangement of neighbouring SCR domains was unchanged.

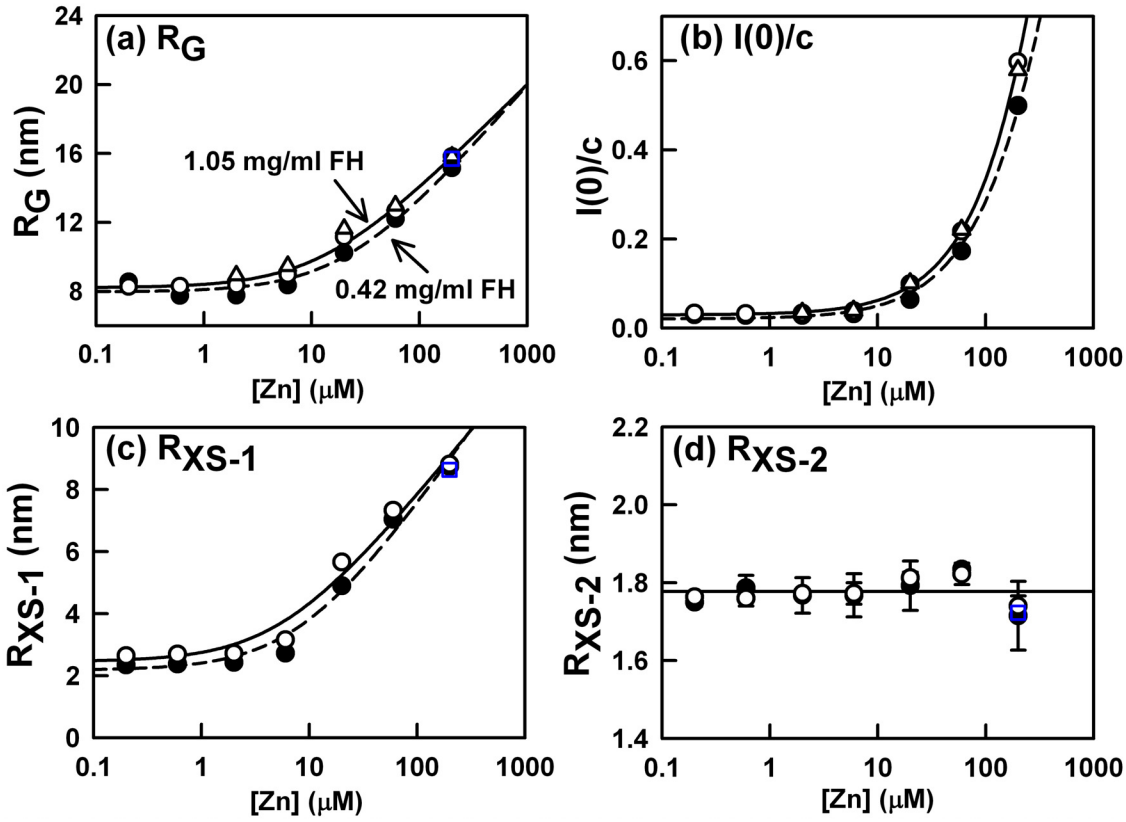

Figure 6.2 Dependence of the Guinier parameters of heterozygous FH on the $ZnSO_4$ concentration. Each value was measured in quadruplicate and averaged. The two titrations correspond to 1.05 mg/ml FH titrated with $ZnSO_4$ (○, solid line), and 0.42 mg/ml FH titrated with $ZnSO_4$ (●, dashed line). The R_G and $I(0)/c$ values calculated from the distance distribution function are denoted as Δ in (a) and (b). (a,c) The data were fitted to a three-parameter function $y = y_0 + a\ln(x - x_0)$. (b) The lines correspond to a two-parameter function $y = \ln(a + bx)$. (d) A straight line indicates the averaged R_{XS-2} values for FH at 0.42 mg/ml, with statistical error bars shown where visible. In (a, b and c), the Guinier values of heterozygous FH at 0.93 mg/ml titrated with 200 μM $ZnCl_2$ are denoted as blue squares.

The effect of copper on the oligomerisation of heterozygous FH was studied by synchrotron X-ray scattering (see Materials and Methods). Copper had not previously been tested (Crossley & Porter, 1980; Perkins *et al.*, 1991). Freshly prepared heterozygous FH was studied at 0.93 mg/ml in HEPES buffer, and titrated with 0.2 µM to 200 µM copper sulphate. For heterozygous FH at 0.93 mg/ml without copper, a similar R_G value of 9.00 (± 0.23) nm, $R_{XS\text{-}1}$ value of 2.76 (± 0.13) nm, and $R_{XS\text{-}2}$ value of 1.78 (± 0.01) nm were obtained. The values of R_G, $I(0)/c$, $R_{XS\text{-}1}$ parameters of FH showed a significant concentration dependence of copper. Different from the effect of zinc, the large increases of the R_G, $R_{XS\text{-}1}$ and $I(0)/c$ parameters were observed after the concentration of copper reached 60 µM (Figure 6.3 a, b, c). No concentration dependence of copper has been observed for the $R_{XS\text{-}2}$ parameter of FH (Figure 6.3 d).

The reversibility of complex formations with zinc and copper were tested by studying the 0.93 mg/ml FH samples with 200 µM $ZnSO_4$ or $ZnCl_2$ which were diluted two folds by addition of 1.5 mM EDTA using X-ray scattering. After adding with EDTA, the R_G, $R_{XS\text{-}1}$ and $I(0)/c$ parameters decreased to the values agreeable with those of the FH at 0.93 mg/ml without any metals. Thus, the complex formations of FH with zinc and copper were reversible.

Control experiments with other metals were performed with 200 µM $CaCl_2$, $MgCl_2$, $NiCl_2$, $CdCl_2$ and $FeSO_4$ with FH at 0.93 mg/ml. No change was detected for $CaCl_2$ and $MgCl_2$. Small increases in the R_G, $R_{XS\text{-}1}$ and $I(0)/c$ values compared to zinc were observed for $NiCl_2$, $CdCl_2$ or $FeSO_4$ (Table 6.1). The result for nickel was unexpected, as previously 100 µM Ni^{2+} had showed no effect, and the difference is attributed to the improved signal-noise ratio available at ESRF (Perkins *et al.*, 1991).

6.2.2 X-ray distance distribution function FH-metal complexes

The distance distribution function $P(r)$ is calculated from the full scattering curve and reports the distances between all pairs of atoms within FH. The calculation of the R_G and $I(0)$ values from the $P(r)$ curve agreed well with the Guinier R_G and $I(0)$ values above, showing that the scattering curve is self-consistent across the observed Q range (Figure 6.2 a, b and Figure 6.3 a, b). The intensity of the $P(r)$ curve increased

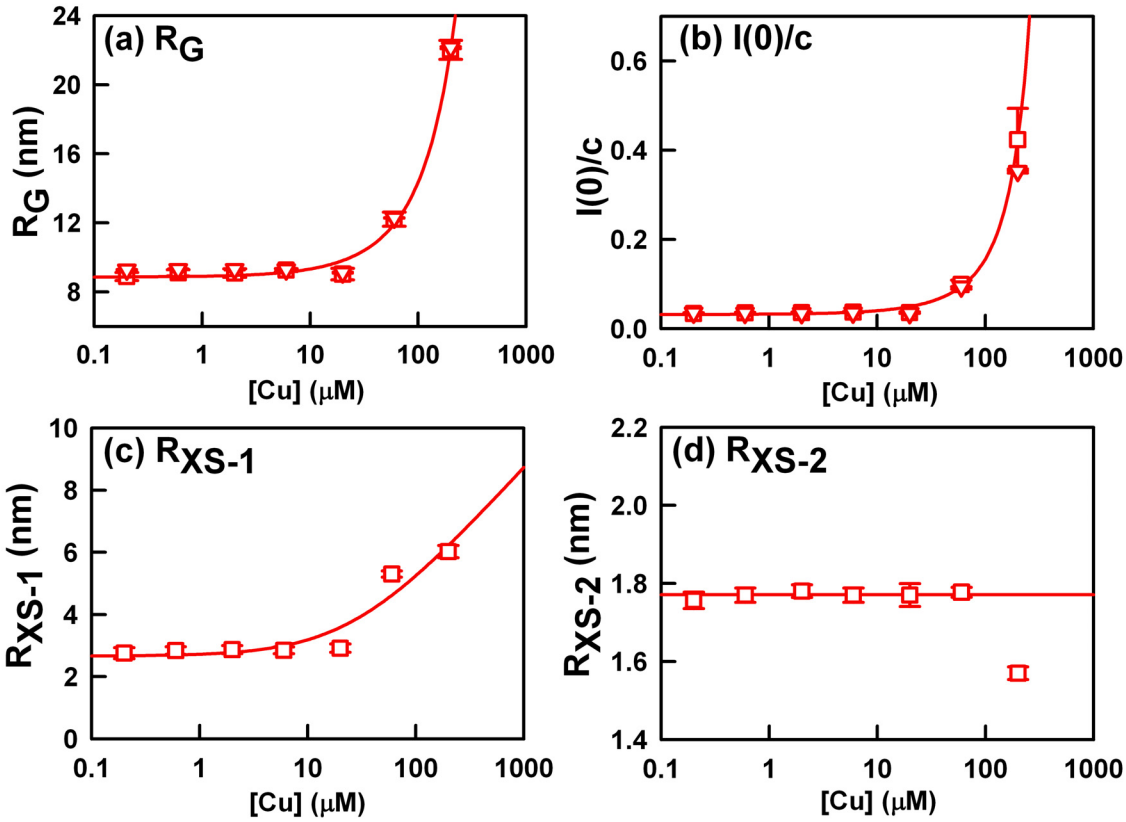

Figure 6.3 Dependence of the Guinier parameters of heterozygous FH on the copper concentration. Each value was measured in quadruplicate and averaged. The Guinier parameters of 0.93 mg/ml FH titrated with copper are denoted as squares in (a), (b), (c) and (d), and the R_G and $I(0)/c$ values calculated from the distance distribution function are denoted as triangles in (a) and (b). (a,c) The data were fitted to a three-parameter function $y = y_0 + a\ln(x - x_0)$. (b) The lines correspond to a two-parameter function $y = \ln(a + bx)$. (d) A straight line indicates the averaged R_{XS-2} values for heterozygous FH. Statistical error bars are shown where visible.

Table 6.1 Guinier parameters of heterozygous FH at 0.93 mg/ml added with 200 μM of various metals.

Metal / Parameter	No metal	Mg	Ca	Ni	Cd	Fe	Cu	Zn
R_G (nm)	9.00±0.23	9.38±0.12	9.64±0.05	14.99±0.25	12.78±0.07	11.76±0.04	22.02±0.55	15.32±0.04
I(0)/c	0.0347±0.0010	0.0424±0.0022	0.0440±0.0018	0.1223±0.0061	0.1103±0.0069	0.1298±0.0012	0.4236±0.0700	0.5163±0.0054
R_{XS-1} (nm)	2.76±0.13	2.93±0.21	2.89±0.17	4.39±0.03	5.04±0.14	4.37±0.06	6.02±0.20	9.02±0.05

significantly with increase in [Zn] (Figure 6.4 a). The maximum dimension *L* is determined when *P(r)* = 0 at large *r*. For 1.05 mg/ml heterozygous FH, when [Zn] was between 0 μM and 2 μM, the *L* value of FH was 32 nm, in good agreement with previous for metal-free heterozygous FH (Chapter Five; Nan *et al.*, 2008a). When [Zn] increased from 2 μM to 200 μM, *L* increased to 50 nm (Figure 6.4 a, b). The *r* value of the maximum *M* in the *P*(*r*) curve gives the most commonly occurring distance within the macromolecule. Peak *M1* at *r* = 5.2 ± 0.6 nm was observed for [Zn] up to 6 μM, which agrees with the previous *M1* determination of 4.8 ± 0.3 nm for metal-free heterozygous FH (Figure 5.3 in Chapter Five; Nan *et al.*, 2008a). Peak *M2* was previously observed for metal-free heterozygous FH at 10.2 ± 0.6 nm (Figure 5.3 in Chapter Five; Nan *et al.*, 2008a), but here its position shifted from a starting value of 10.8 nm at [Zn] = 6 μM up to 17.0 nm at [Zn] = 200 μM (Figure 6.4 b). The changes in the *P*(*r*) curves with increase in [Zn] showed that zinc formed relatively compact FH oligomers with maximum dimensions not much larger than that for monomeric metal-free FH. No difference between the *P*(*r*) curves for heterozygous FH added with 200 μM $ZnSO_4$ and with 200 μM $ZnCl_2$ has been observed, which ruled out the effects any anion effects. For heterozygous FH at 0.93 mg/ml titrated with 0.2 μM to 200 μM copper, the changes of *P*(*r*) curve differed from those seen with zinc. The intensity of the *P(r)* curve increased significantly with [Cu] ≥ 60 μM (Figure 6.5 a), which indicates the copper induced oligomerisation of heterozygous FH. The *L* value of FH was 32 nm with 0.2 μM to 20 μM copper, and increased to 62 nm when the [Cu] increased to 200 μM (Figure 6.5 a, b). The position of M2 shifted to 26 nm when [Cu] increased to 200 μM (Figure 6.5 a, b). The *P*(*r*) curves of heterozygous FH with 200 μM zinc or copper reverted to the metal-free *P(r)* curve after being diluted two folds by addition 1.5 mM EDTA was added, and the *L* value decreased to 30 nm after adding EDTA (Figure 6.6).

Other metals showed divergent effects. The addition of $CaCl_2$ and $MgCl_2$ had no effect (Figure 6.7). The *P*(*r*) intensities increased in the presence of 200 μM $NiCl_2$, $CdCl_2$, $FeSO_4$, $CuSO_4$ and $ZnSO_4$ in that order. The *L* values however increased in the presence of 200 μM $FeSO_4$, $CdCl_2$, $NiCl_2$, $ZnSO_4$ and $CuSO_4$ in that order, which is different and showing that different metals caused different structural effects on FH.

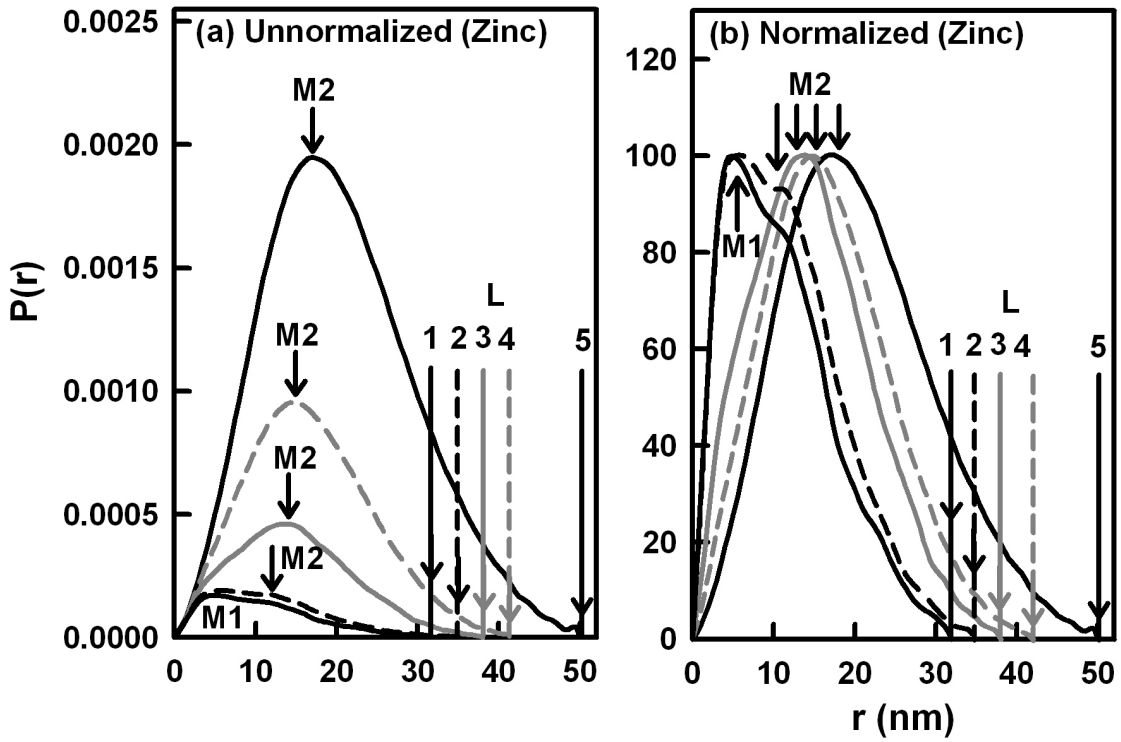

Figure 6.4 Dependence of the distance distribution function *P(r)* on zinc.

(a) The unnormalised *P(r)* curves were calculated from the five scattering curves in Figure 6.1. From bottom to top, [Zn] are 2 μM, 6 μM, 20 μM, 60 μM and 200 μM, represented by alternate solid and dashed lines in grey and black. The two maxima occur at *M1* and *M2*. The maximum length *L* was determined to be 32 nm, 35 nm, 38 nm, 42 nm and 50 nm (numbered 1, 2, 3, 4 and 5) with increase in [Zn].

(b) The five *P(r)* curves in (a) are normalised to 100 to show that *M1* is unchanged at 5.2 ± 0.6 nm while *M2* increases from 10.8 nm to 17.0 nm with increase in [Zn]. The alternate solid and dashed lines correspond to those in (a).

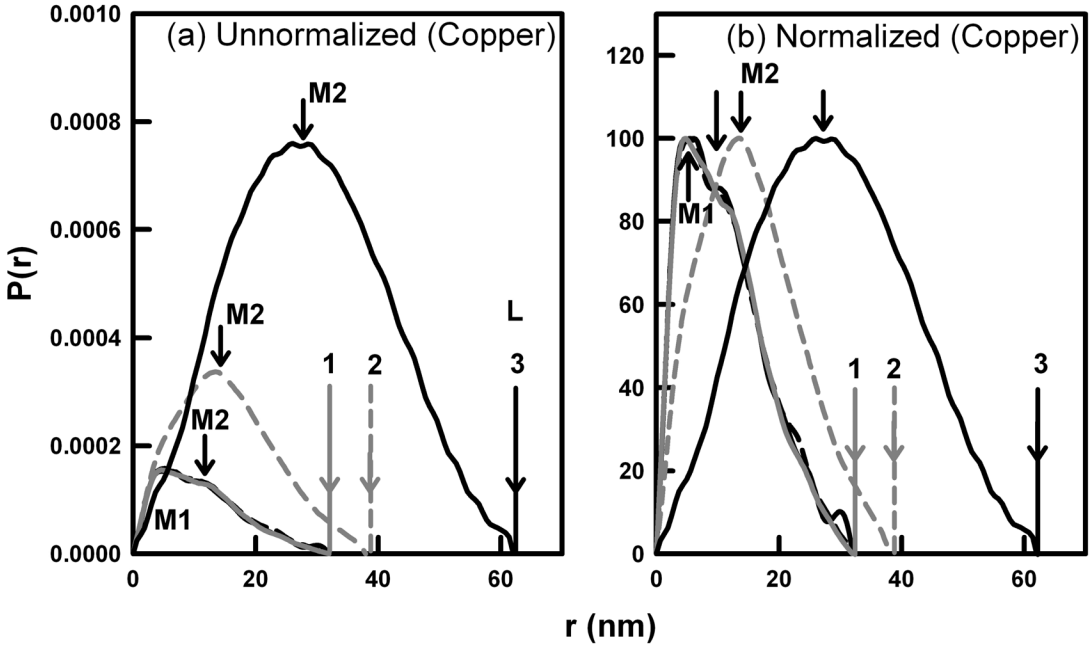

Figure 6.5 Dependence of the distance distribution function *P(r)* on copper.

(a) The unnormalised *P(r)* curves were calculated from the five scattering curves of 0.93 mg/ml of heterozygous FH titrated with 2 μM to 200 μM copper. From bottom to top, [Cu] are 2 μM, 6 μM, 20 μM, 60 μM and 200 μM, represented by alternate solid and dashed lines in grey and black. The two maxima occur at *M1* and *M2*. The maximum length *L* of heterozygous FH was determined to be 32 nm (numbered 1) with [Cu] of 2 μM, 6 μM and 20 μM, 38 nm (numbered 2) with [Cu] of 60 μM, and 62 nm (numbered 3) with [Cu] of 200 μM.

(b) The five *P(r)* curves in (a) are normalised to 100 to show the increase of *M2* with [Cu] ≥ 60 μM. The alternate solid and dashed lines correspond to those in (a).

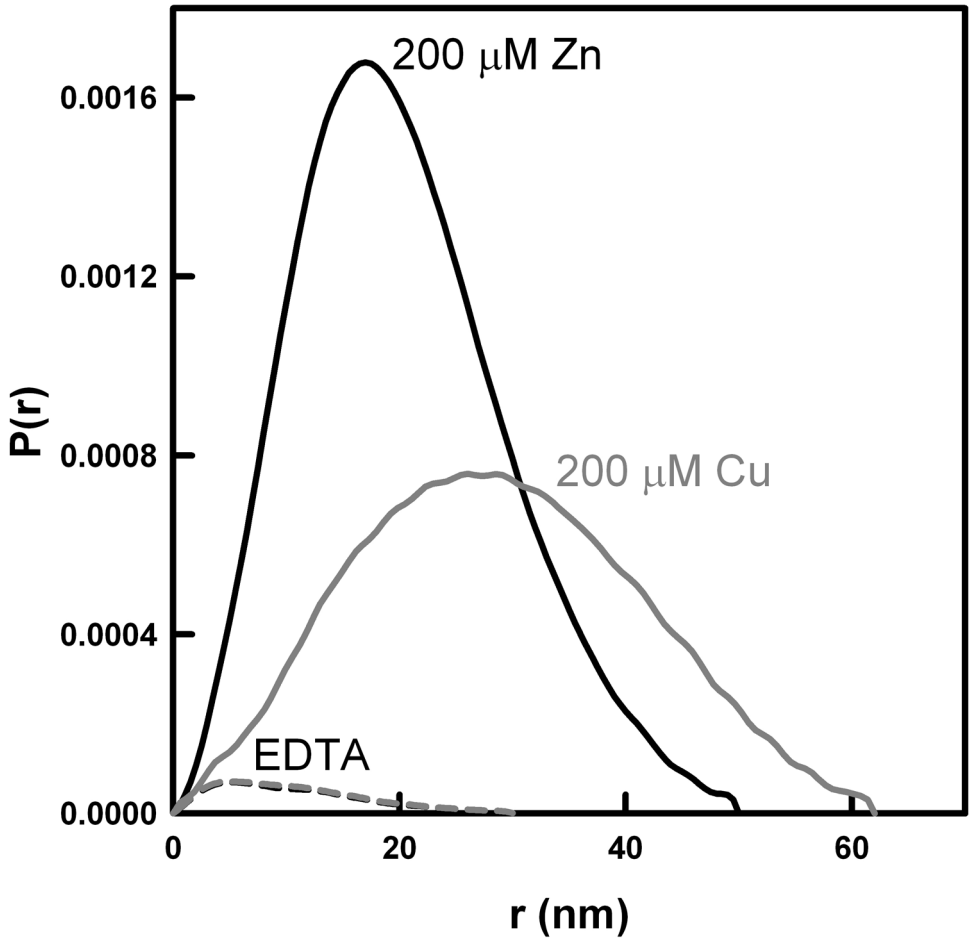

Figure 6.6 Effects of EDTA on the distance distribution function $P(r)$ of heterozygous FH added with zinc or copper. The $P(r)$ curve of heterozygous FH added with 200 mM zinc is denoted as solid black line, and that of the same sample after being added EDTA is denoted as dashed black line. The corresponding $P(r)$ curves for heterozygous FH with copper are denoted in grey.

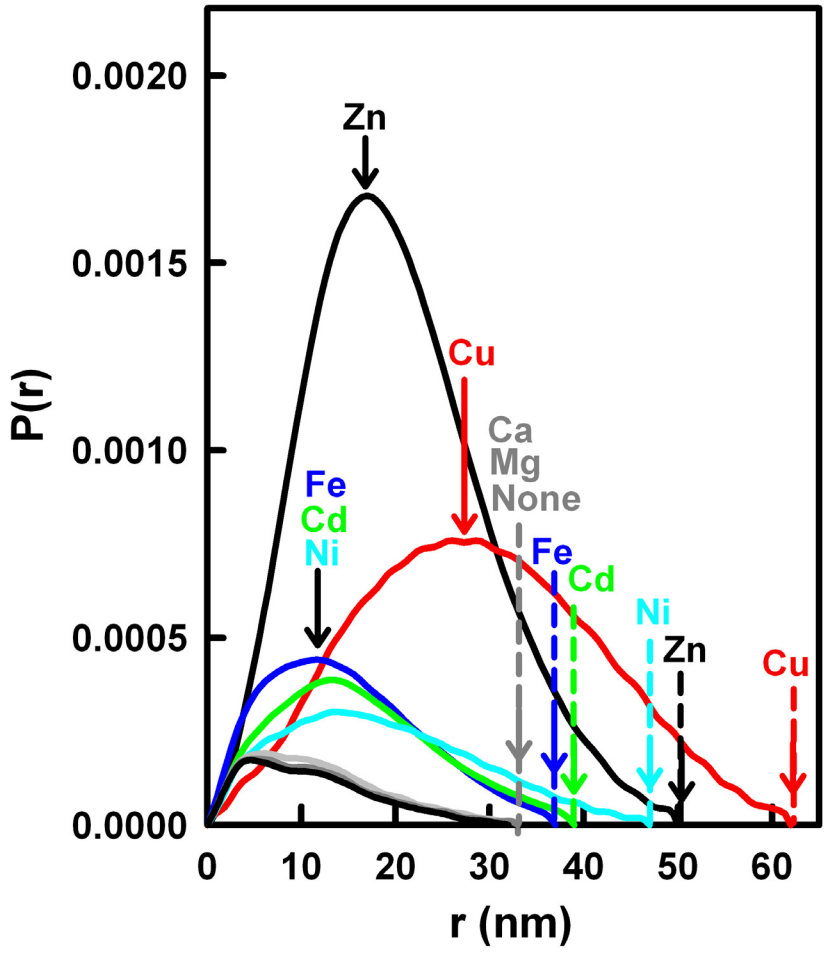

Figure 6.7 Eight *P(r)* curves for 0.93 mg/ml FH in the presence of seven metals at 200 μM. The *M2* and *L* values are arrowed for each curve. The *L* values were 32 nm (no metal, Mg, Ca), 37 nm (Fe, blue), 39 nm (Cd, green), 47 nm (Ni, cyan), 50 nm (Zn, black) and 62 nm (Cu, red).

6.2.3 Sedimentation velocity analyses of FH-metal complexes

Sedimentation velocity experiments by analytical ultracentrifugation follow the sedimentation behaviour of FH on subjecting this to a high centrifugal force (Section 4.1; Cole *et al.*, 2008). The sedimentation coefficient $s_{20,w}$ monitors macromolecular elongation, and is analogous to the R_G value. Velocity experiments were performed at four rotor speeds up to 60,000 r.p.m. for FH at 0.35 mg/ml and 0.87 mg/ml, each titrated with zinc at eight concentrations between 0 µM to 200 µM. In comparison to the run at 6 µM zinc, rapidly-sedimenting species were observed at 60 µM of zinc, and even more so at 200 µM zinc (Figures 6.8 a, b, c). The observed sedimentation boundaries were fitted using size-distribution analyses *c(s)* in which the frictional ratio *f/fo* was held fixed (Materials and Methods), and good fits were obtained in all cases (Figures 6.8 a, b, c).

The sedimentation coefficient distribution *c(s)* analyses revealed the presence of distinct FH oligomers through the appearance of resolved stable multiple peaks (Figures 6.9 a, b). At all zinc concentrations, a FH monomer peak was observed at $s_{20,w}$ = 5.57 (± 0.12) S (Figure 6.9 b). A *c(M)* mass distribution plot showed that this corresponded to a molecular weight of 138 ± 7 kDa. This value agreed well with the sequence-determined molecular mass of 155 kDa and also with previous $s_{20,w}$ determinations of 5.65 (± 0.12) S and 5.3 ± 0.1 S, and mass determinations of 142 ± 2 kDa by c(M) size distribution analyses and 145 kDa by sedimentation equilibrium experiments for FH monomers (Chapter Five; Nan *et al.*, 2008a; Aslam & Perkins, 2001). At all zinc concentrations, the *c(s)* distributions showed additional peaks that correspond to larger FH oligomers as [Zn] increased. For [Zn] between 0 µM and 20 µM, dimers were visible at a $s_{20,w}$ value of 7.7 (± 0.3) S. In addition, smaller amounts of trimers to nonamers of FH were consistently observed at $s_{20,w}$ values of 10.0 (± 0.6) S, 11.8 (± 0.7) S, 14.2 (± 0.7) S, 16.1 (± 0.8) S, 18.5 (± 0.9) S, 22.6 (± 1.5) S and 27.0 (± 0.5) S (Figure 6.9 b), and this agrees with the progressive self-association properties of FH observed previously (Chapter Five; Nan *et al.*, 2008a). At 0 µM zinc, 12% oligomers were seen in agreement with previous observation (Chapter Five; Nan *et al.*, 2008a). At [Zn] = 60 µM, sizeable amounts of larger FH oligomers with $s_{20,w}$ values up to 50 S and increased intensities

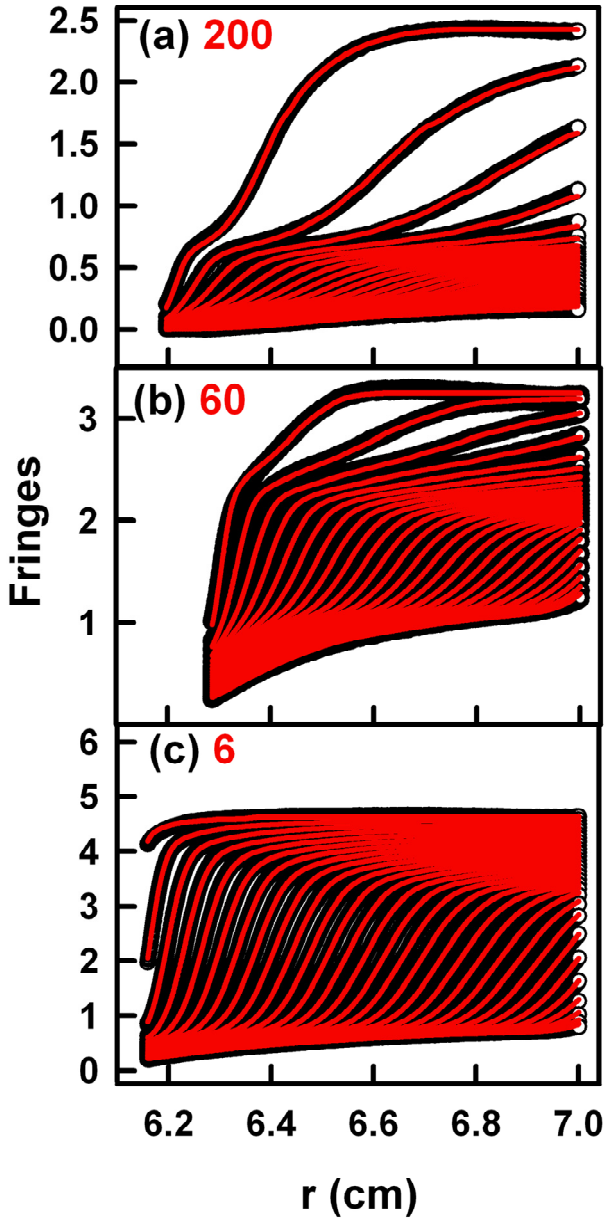

Figure 6.8 Fittings of sedimentation boundaries of heterozygous FH titrated with zinc by size-distribution analyses *c(s)*. The [Zn] values in μM are denoted by red numbers. The experimental runs were performed at 50k r.p.m. with 0.87 mg/ml FH (black), and the boundary fits are shown in red. (a) Every sixth scan boundary for 200 μM zinc was fitted; (b) Every fifteenth scan boundary for 60 μM zinc was fitted; (c) Every sixth scan boundary for 6 μM zinc was fitted.

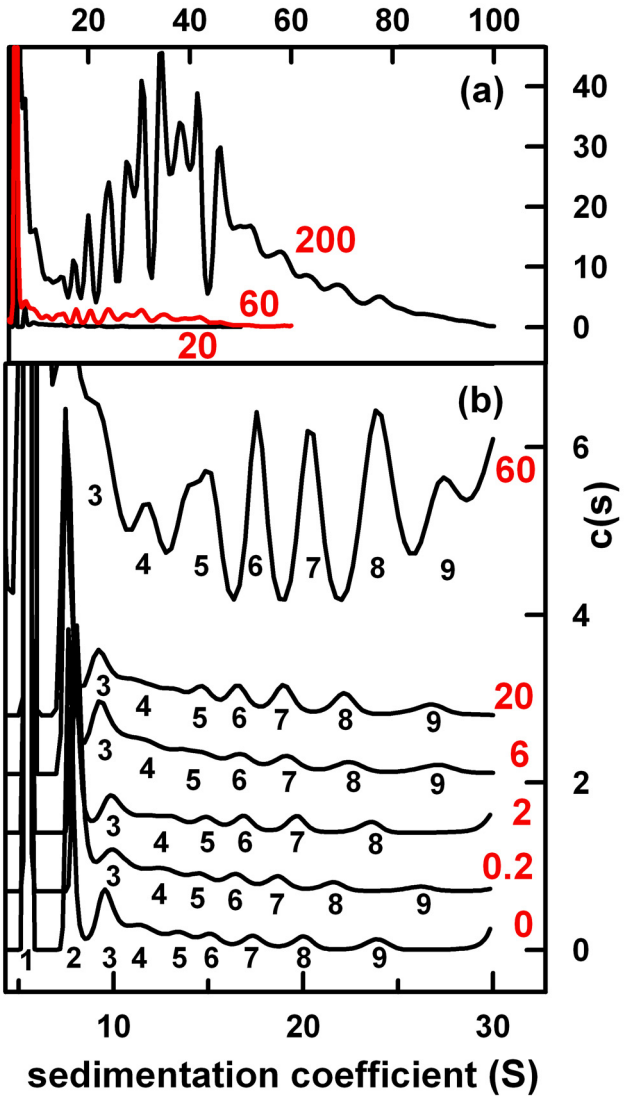

Figure 6.9 Size-distribution *c(s)* analyses for heterozygous FH titrated with zinc. The [Zn] values in μM are denoted by red numbers.

(a) The *c(s)* size-distribution analyses for 20 μM, 60 μM and 200 μM zinc are shown. Here and in (b), the intensity of the monomer peak at 5.57 S was set to 100 for clarity.

(b) The *c(s)* size-distribution analyses for 0 μM, 0.2 μM, 2 μM, 6 μM, 20 μM, and 60 μM zinc are shown. The FH oligomers are numbered from 2 to 9 in increasing order of S values (Chapter Five; Nan *et al.*, 2008a).The six analyses are displaced vertically in steps of 0.7 units for reason of clarity.

were observed in the *c(s)* distribution (Figures 6.9 a, b). At [Zn] = 200 μM, the size of the FH oligomers reached 100 S, together with a significant increase in their intensities (Figure 6.9 b).

The effect of copper on heterozygous FH was also investigated by performing sedimentation velocity experiments on 0.81 mg/ml heterozygous FH titrated with 0.2 μM to 200 μM $CuSO_4$ (Materials and Methods). Similar to the heterozygous FH titrated with zinc, the sedimentation coefficient distribution *c*(*s*) revealed that small amount of oligomers was observed for heterozygous FH with 0.2 μM to 20 μM copper, and rapidly-sedimenting species were observed at 60 μM of copper, and even more so at 200 μM copper (Figures 6.10 a, b, c and Figure 6.11). However, the sedimentation boundaries and therefore the *c*(*s*) analyses for heterozygous FH with 200 μM copper were different from those for 200 μM zinc (Figure 6.10 a and Figure 6.11).

To gain a quantitive understanding of the effect of zinc concentration change on the oligomerisation of heterozygous FH in sedimentation velocity experiments, the integration function for *c(s)* size-distribution analyses were used to determine the percentages of FH monomer and oligomers (Materials and Methods). For heterozygous FH at 0.35 mg/ml and 0.87 mg/ml, the percentage of monomer decreased while the percentage of oligomers increased, as a result of increasing of zinc concentration (Figure 6.12). Here, 50% oligomer formation occurred with approximately 35 μM zinc for 0.35 mg/ml FH, and with 50 μM zinc for 0.87 mg/ml FH (Figure 6.12). The slight difference is attributed to the larger zinc:FH ratio at the lower FH concentration, meaning that more FH oligomers were formed at 0.35 mg/ml FH for a given zinc concentration. The effect of 0.2 μM to 200 μM $CuSO_4$ on 0.81 mg/ml FH caused significant oligomer formation to take place, for which 50% oligomer formation occurred at approximately 150 μM [Cu] (Figure 6.12).

To test the reversibility of the oligomerisation of heterozygous FH induced by zinc, sedimentation velocity experiments were performed on the sample of 0.87 mg/ml FH with 120 μM zinc which was diluted four folds by the addition of 1.5 mM EDTA. The *c(s)* distribution analyses showed that after added with EDTA, the oligomeric species with high $s_{20,w}$ decreased significantly both in intensities and the number of species (Figure 6.13 a, b),

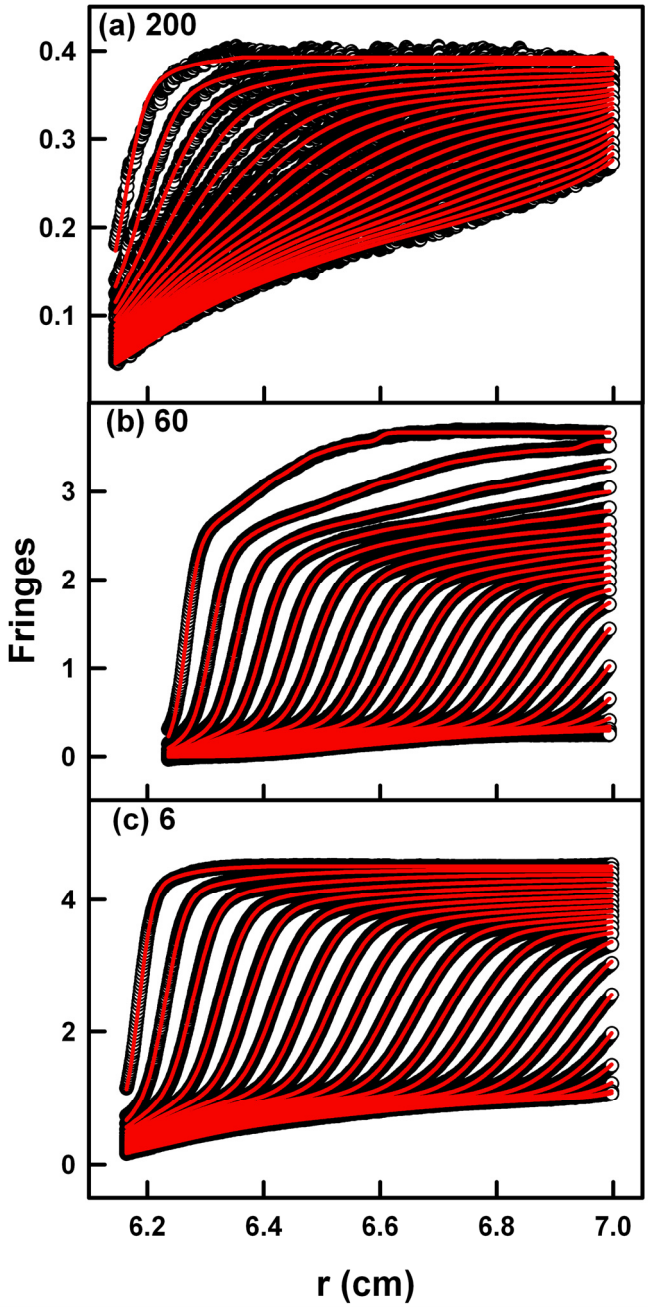

Figure 6.10 Fittings of sedimentation boundaries of heterozygous FH titrated with copper by size-distribution analyses *c(s)*. The [Cu] values in μM are denoted in each panel. The experimental runs were performed at 50k r.p.m. for 200 μM and 6 μM copper and at 60k r.p.m. for 60 μM copper with 0.81 mg/ml FH (black), and the boundary fits are shown in red. (a) Every eighth scan boundary for 200 μM copper was fitted; (b) Every tenth scan boundary for 60 μM copper was fitted; (c) Every eighth scan boundary for 6 μM copper was fitted.

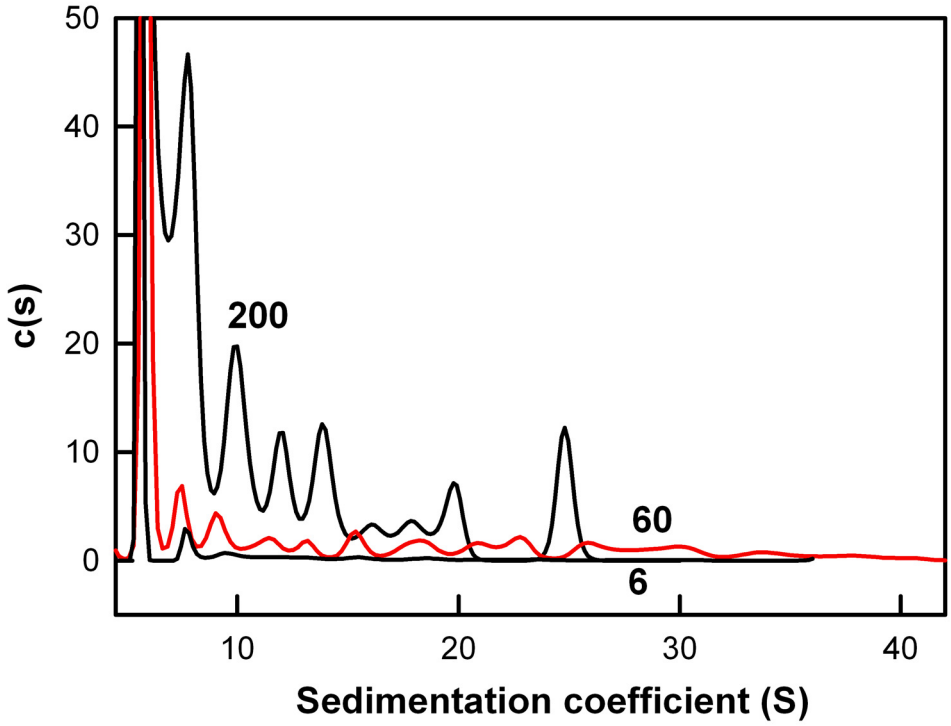

Figure 6.11 Size-distribution *c(s)* analyses for heterozygous FH titrated with copper. The [Cu] values in μM are denoted near the corresponding *c*(*s*) analysis. The *c(s)* size-distribution analyses for 20 μM, 60 μM and 200 μM copper are shown. The intensity of the monomer peak at 5.57 S was set to 100 for clarity.

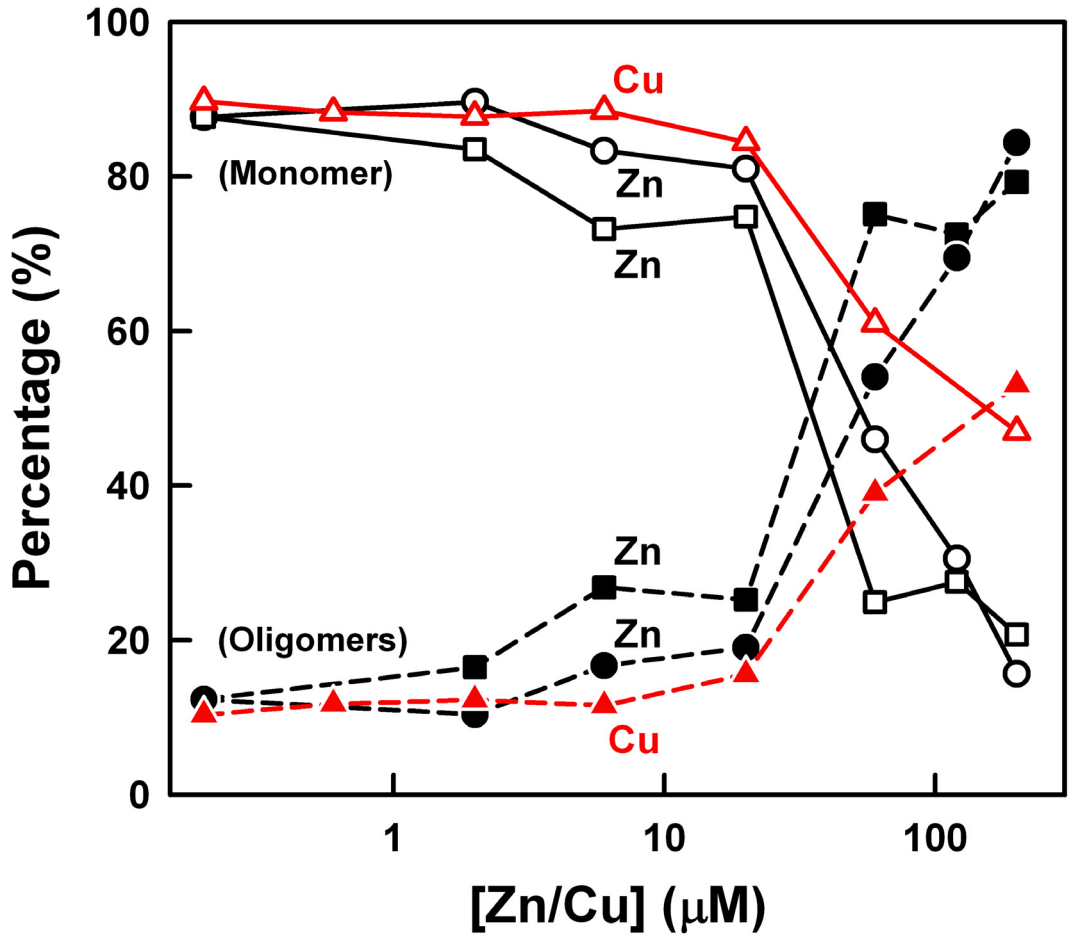

Figure 6.12 Comparison of the proportion of heterozygous FH monomer and oligomers in titrations with zinc and copper. The percentages were derived by integration of the *c(s)* analyses, and correspond to the mean value obtained at 50,000 r.p.m. and 60,000 r.p.m.. Monomers are denoted by filled symbols and oligomers by open symbols (0.87 mg/ml FH with zinc, black ●, ○; 0.35 mg/ml FH with zinc, black ■, □; 0.81 mg/ml FH with copper, red ▲, Δ).

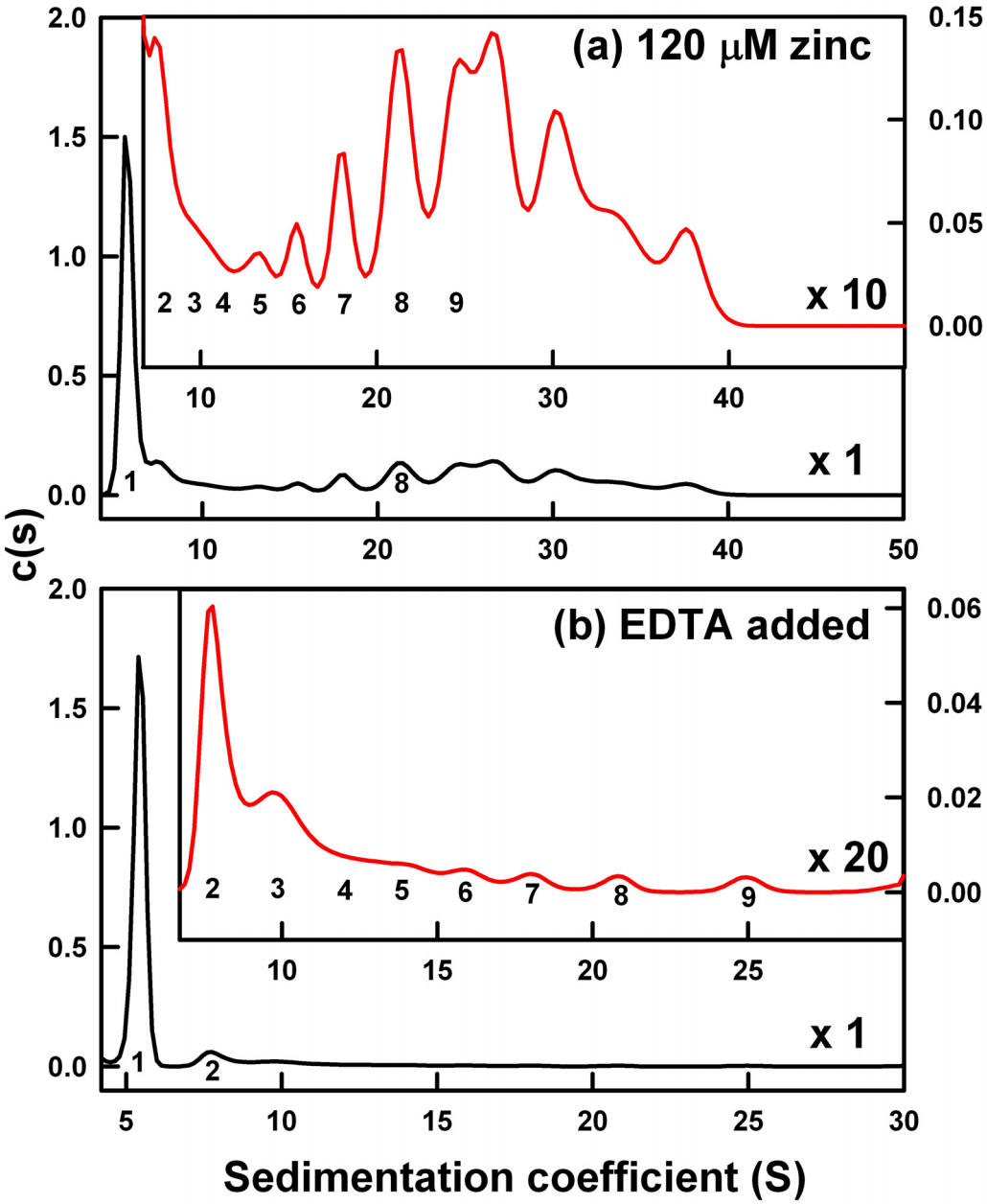

Figure 6.13 Effects of EDTA on the sedimentation coefficient distribution *c*(*s*) of heterozygous FH added with zinc. The sedimentation velocity data was obtained at 50,000 r.p.m.. The oligomer peaks are labelled from 2 to 9 to follow Figure 6.9.

(a) The *c(s)* distribution analyses for 0.87 mg/ml FH with 120 μM zinc. The inserted panel shows the 10 times zoomed in view of the *c*(*s*) distribution from 7 S to 50 S.

(b) The *c(s)* distribution analyses after the addition of EDTA to a final concentration of 0.22 mg/ml FH, 30 μM zinc and 1.5 mM EDTA. The inserted panel shows the 20 times zoomed in view of the *c(s)* distribution from 7 S to 30 S.

and the *c(s)* plot was identical to that of 0.87 mg/ml FH without zinc. After adding of EDTA, the percentage of oligomers decreased from 62% to 16% which is very near to that of 0.87 mg/ml FH without zinc. These changes indicate that the oligomerisation of heterozygous FH induced by zinc is reversible.

Control experiments were performed. The comparison of 200 μM $ZnSO_4$ and $ZnCl_2$ on 0.93 mg/ml FH showed no difference in the *c(s)* distributions, hence oligomer formation is not dependent on the anion. FH at 0.93 mg/ml was also studied with 200 μM $CaCl_2$, $MgCl_2$, $NiCl_2$, $CdCl_2$, $FeSO_4$, $CuSO_4$ and $ZnSO_4$. The *c(s)* plots for $NiCl_2$, $CdCl_2$ or $FeSO_4$ showed an increase in oligomer formation from 12% to 20% when compared with that of FH alone or with $CaCl_2$ or $MgCl_2$ (Figures 6.14 a, b). Oligomer formation increased even further with $CuSO_4$ and $ZnSO_4$ (Figure 6.14 b).

6.2.4 Fluid-phase activity assays of FH-metal complexes

In order to test whether the formation of heterozygous FH oligomers is correlated with the regulatory cofactor role of heterozygous FH, assays of fluid-phase ammonium-inactivated C3 cleavage by factor I were performed in the presence and absence of metals (Crossley & Porter, 1980). As mentioned in Section 2.3.5, complement functional assays routinely employed heterozygous FH concentrations that were significantly lower than the 0.235-0.81 mg/ml (1.6–5.4 μM) observed *in vivo* (e.g. 45 μg/ml, 3 μg/ml, 31 μg/ml and 0.31 μg/ml) (Crossley & Porter, 1980; Day & Sim, 1986; Blom *et al.*, 2003; Tsiftsoglou & Sim, 2004). Accordingly assays in this thesis were performed at 0.3 mg/ml FH (2 μM) for direct comparison with the AUC data and to be more comparable with serum levels. SDS-PAGE showed that the α-chain of haemolytically inactive C3 was cleaved by factor I in the presence of heterozygous FH to produce two major degradation fragments at apparent sizes of 45 kDa and 75 kDa (Figure 6.15 a and Figure 6.16 a). The influence of zinc or copper on this reaction was investigated at concentrations of 0 μM, 2 μM, 20 μM, 60 μM, 120 μM and 200 μM. The cleavage rate was decreased by both metals, and this became noticeable with zinc at 120 μM and 200 μM (Figure 6.15 b, c and Figure 6.17 a) and to a lesser extent with copper at 200 μM (Figure 6.16 b, c and Figure 6.17 b). This matched the growth of oligomers in Figure 6.12, indicating that the oligomerisation of FH is able to account for the decrease of activity of FH

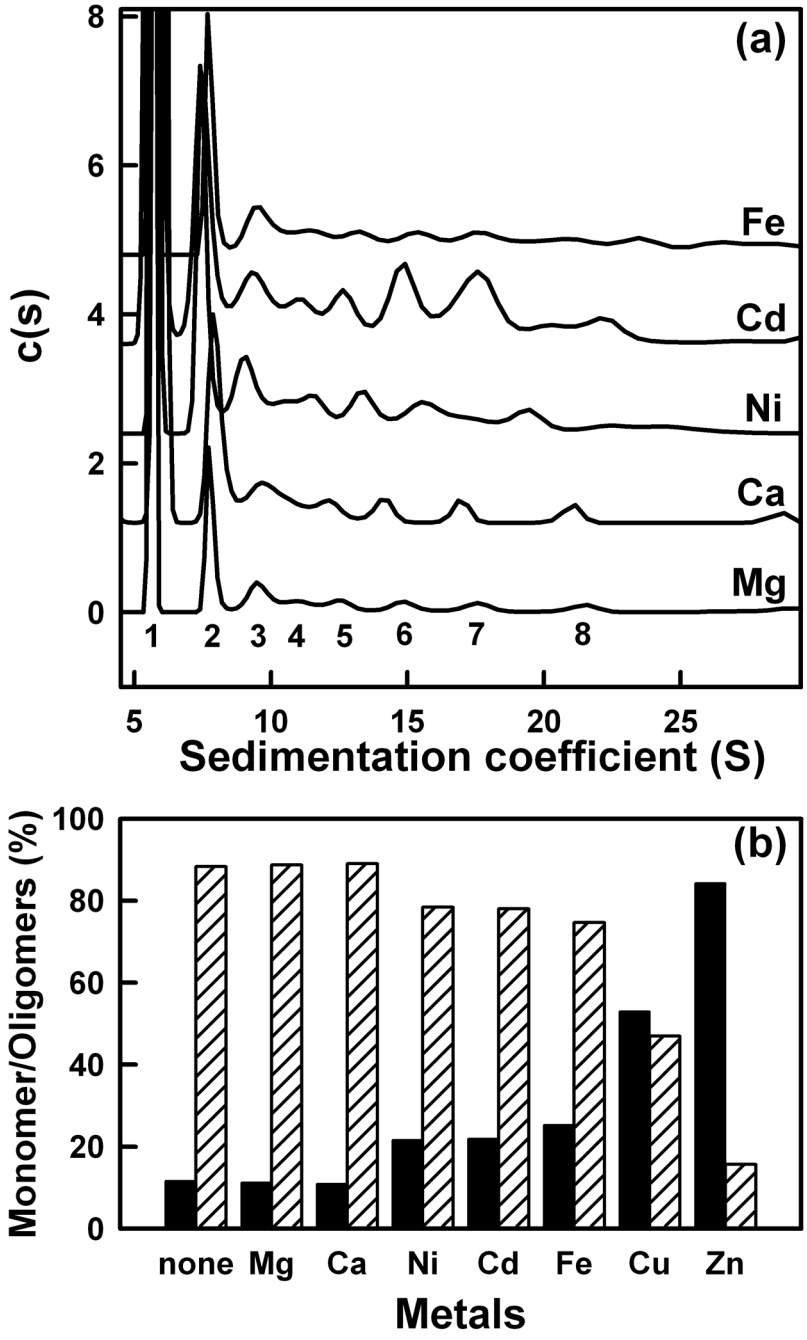

Figure 6.14 Comparative effects of different metals on heterozygous FH oligomerisation. The sedimentation velocity data was obtained at 50,000 r.p.m.. The intensity of the monomer peak at 5.57 S was set to 100 for clarity. The oligomer peaks are labelled from 2 to 9 to follow Figure 6.9. (a) The *c(s)* distribution analyses for 0.93 mg/ml FH for five metals at 200 μM (labelled). (b) Proportion of FH monomer and oligomer in the presence of different metals at a concentration of 200 μM. The hatched columns correspond to FH monomer, and the solid columns correspond to FH oligomers.

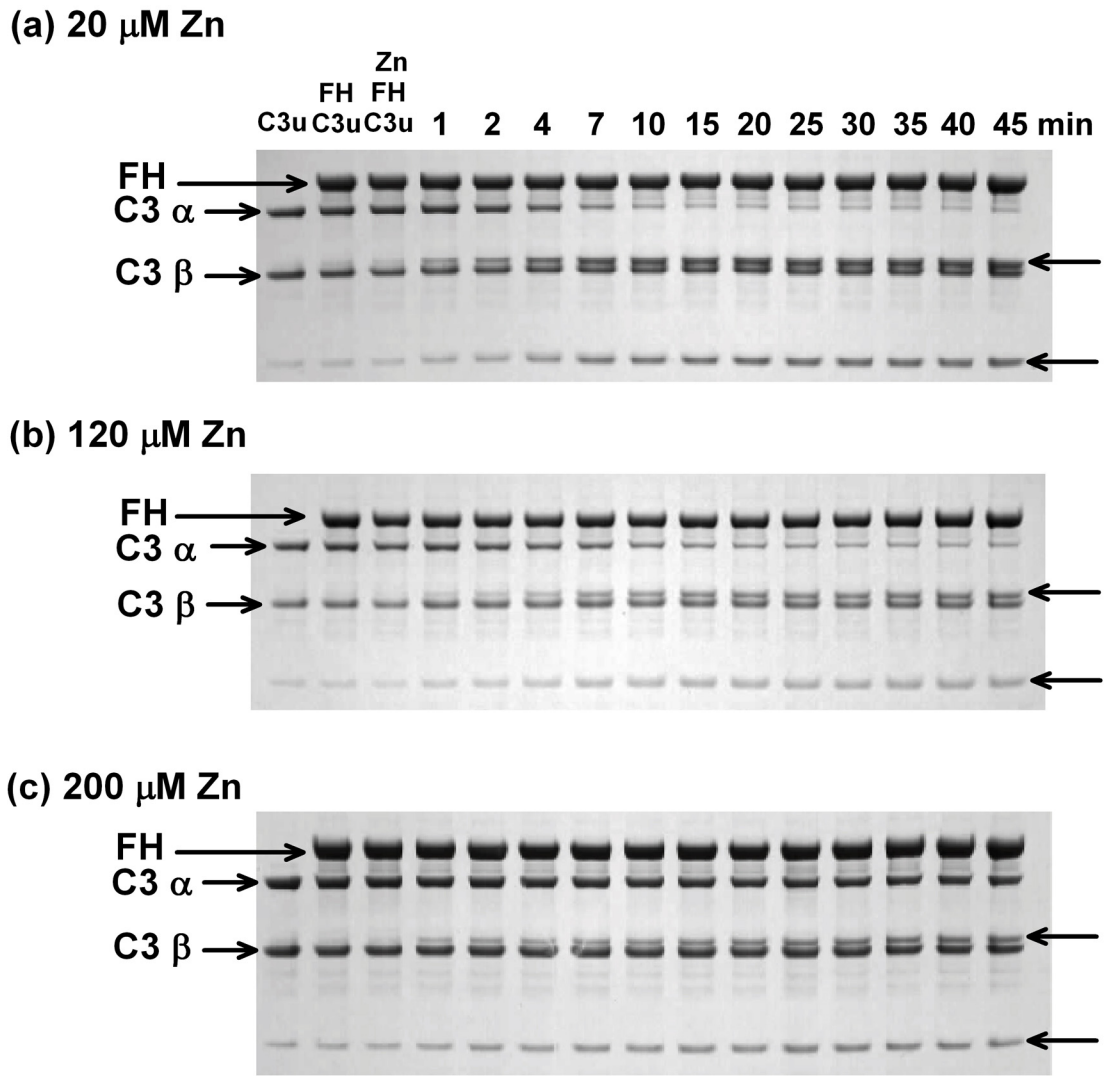

Figure 6.15 Cleavage of fluid phase inactive C3 (C3u) in the presence of zinc. (a) Reducing SDS-PAGE analysis of C3u cleavage in 20 μM zinc (lanes 4 – 15 correspond to the reaction times in min as labelled). Lane 1, 0.3 mg/ml C3u; Lane 2, 0.3 mg/ml C3u and 0.3 mg/ml FH; Lane 3, 0.3 mg/ml C3u, 0.3 mg/ml FH and zinc. FH, C3 α-chain and C3 β-chain are arrowed on the left, and the C3 α-chain cleavage products are arrowed on the right. Reducing SDS-PAGE analysis of C3u cleavage in 120 μM zinc is shown in (b) and that in 200 μM zinc is shown in (c). Other details in (b,c) follow (a).

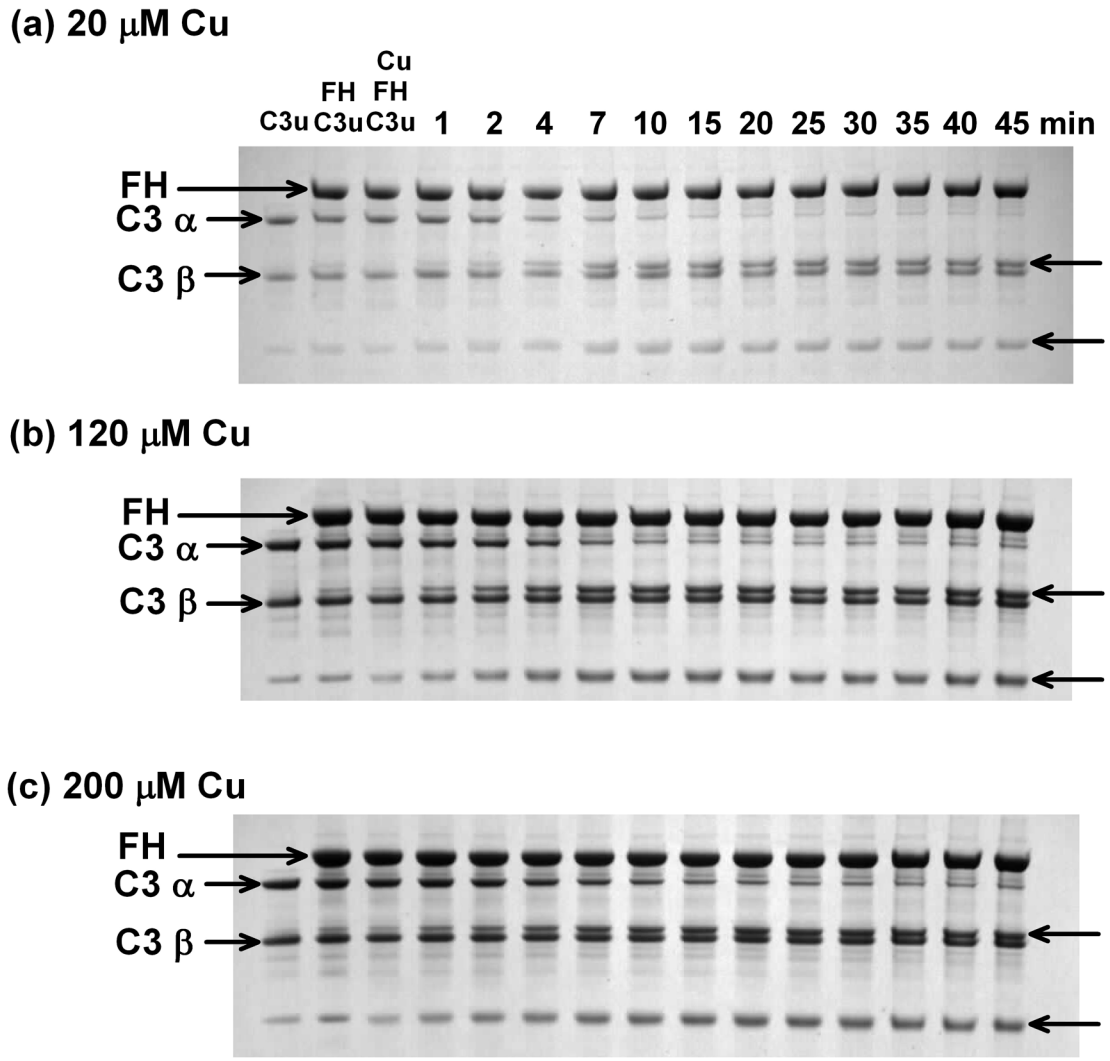

Figure 6.16 Cleavage of fluid phase inactive C3 (C3u) in the presence of copper. Reducing SDS-PAGE analysis of C3u cleavage by FI and heterozygous FH with 20 μM Copper in (a), with 120 μM Copper in (b), and with 200 μM Copper in (c). Other details follow Figure 6.15 except the metal used here is copper.

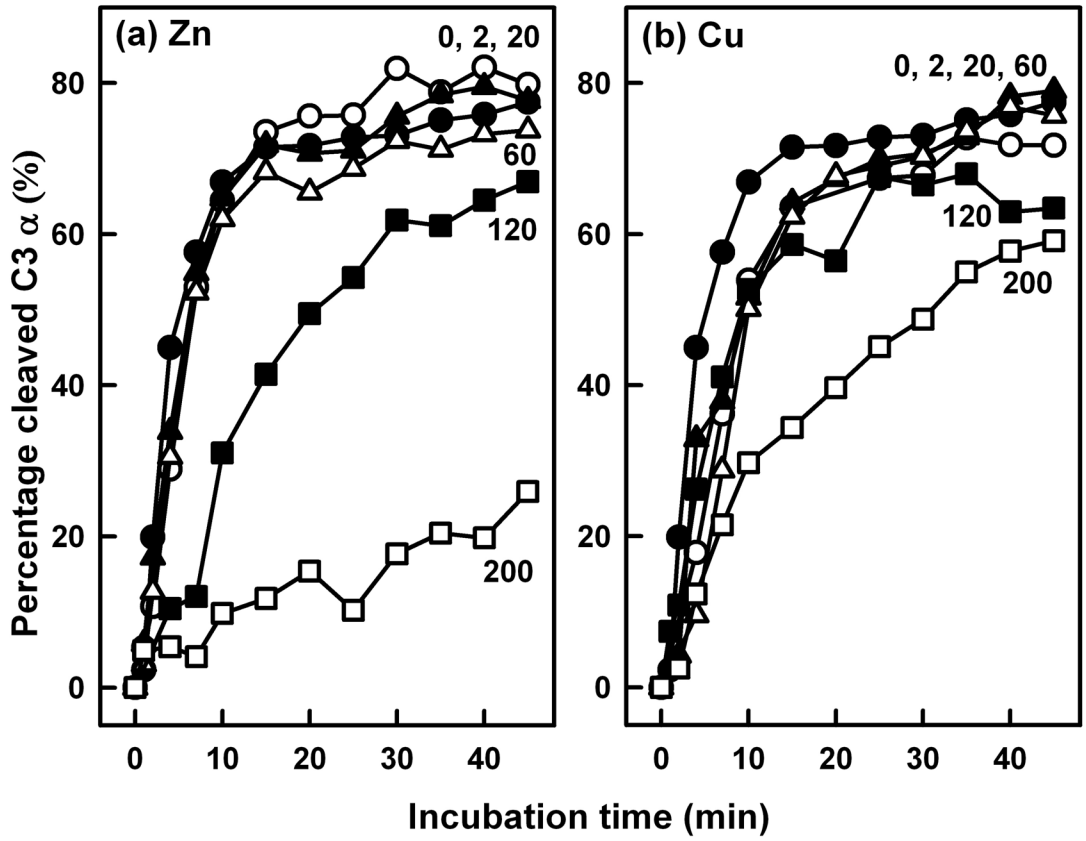

Figure 6.17 Quantification of the cleavage of fluid phase inactive C3 (C3u) in the presence of zinc (Figure 6.15) or copper (Figure 6.16).

(a) The percentage cleavage of C3 α-chain is shown as a function of [Zn], with their values shown as labels (0 μM, ●; 2 μM, ○; 20 μM, ▲; 60 μM, Δ; 120 μM, ■; 200 μM, □).

(b) As for (a) except that copper is used instead of zinc.

by blocking FH access to C3u and/or factor I. Factor I activity is unaffected by zinc, while C3b binds to zinc with little change in activity (Day & Sim, 1986; Blom *et al.*, 2003; Tsiftsoglou & Sim, 2004).

6.3 Materials and Methods

6.3.1 Protein purification

Heterozygous FH and factor I were purified from a 3 litre pool of just-outdated anonymised human plasma from the Royal Free Hospital Blood Bank, using an anti-FH monoclonal antibody MRC-OX23 Sepharose column, and an anti-FI monoclonal antibody MRC-OX21 Sepharose column (Aslam & Perkins, 2001; Sim *et al.*, 1993). Both monoclonal antibody columns were kindly provided by Dr R. B. Sim in Oxford University. About 50 ml of mixed human plasma with 5 mM EDTA and protease inhibitor Pefabloc-SC[70], was first dialysed into Tris buffer (25 mM Tris-HCl, 140 mM NaCl, 0.5 mM EDTA, pH 7.4). After the dialysis, the plasma was passed through a Sepharose column immobilised with non-immune IgG to remove the proteins that bind to Sepharose or IgG, then a lysine-sepharose column to remove plasminogen/plasmin. After these two columns, the plasma was passed through the MRC-OX23 column specific for FH, and then through the MRC-OX21 column specific for FI. Repeating passing the plasma through these two monoclonal antibody columns significantly improved the yields of FH and FI. Bound FH and factor I were each eluted from the column using 3 M $MgCl_2$, pH 6.9, then each was dialysed into HEPES buffer (10 mM HEPES, 137 mM NaCl, pH 7.4) in the presence of 0.5 mM EDTA to remove Mg^{2+}, then each was passed through a Hitrap Protein G HP column to remove contaminant IgG. Non-specific aggregates and human serum albumin were removed using Superose^{TM} 6 gel filtration (Section 5.3.1).

Native C3 was purified from the author's own fresh plasma using slightly modified methods described previously (Dodds *et al.*, 1993). 20 ml fresh plasma made 5% with polyethylene glycol (PEG) 3500 MWCO was centrifuged, and the supernatant then made 12% with PEG 3500 MWCO was centrifuged again. The final pellet was resuspended in the starting buffer (20 mM HEPES, 50 mM NaCl, 50 mM ε-aminocaproic acid, 5 mM EDTA, 0.5 mM Pefabloc-SC, pH 7.5) for ion-exchange chromatography. The suspension was then filtered before loading onto a 20 ml Q-Sepharose^{TM} fast flow anion-exchange column (Amersham Biosciences, GE Healthcare, Uppsala, Sweden). The Q-Sepharose^{TM} fast flow column was

then washed with the washing buffer (20 mM HEPES, 100 mM NaCl, 50 mM ε-aminocaproic acid, 5 mM EDTA, 0.5 mM Pefabloc-SC, pH 7.5) to remove the unbound proteins, and then a linear salt gradient to 300 mM NaCl was used to elute C3 which was eluted with about 210 mM NaCl to 240 mM NaCl. The elution fractions were checked by reducing SDS-PAGE. The C3 fractions were pooled together and then diluted to reduce the salt concentration to 100 mM NaCl, and then loaded onto a MonoQ 5/50 GL column (Pharmacia GE Healthcare, Uppsala, Sweden) to improve the purity of C3. The MonoQ 5/50 GL column is also an anion-exchange column but with better resolution. Using a linear salt gradient to 300 mM NaCl, and the C3 was eluted with about 210 mM NaCl to 240 mM NaCl. The purity of the eluted C3 was checked again by using SDS-PAGE. Haemolytically inactive C3 (C3u) was prepared by incubating native C3 in 200 mM hydrazine at 37°C for 1 h (Dodds *et al.*, 1993).

The purified FH, FI and C3u were dialysed into HEPES buffer (10 mM HEPES, 137 mM NaCl, pH 7.4). Protein concentrations were determined from absorption coefficients of 16.7 for FH, 12 for FI and 9.4 for C3u (1%, 280 nm, 1 cm path length) which were calculated from protein compositions (Perkins & Sim, 1986; Ullman *et al.*, 1998; Aslam & Perkins, 2001; Li *et al.*, 2010). The absorption coefficient value for FH will be revised in Chapter Seven and Chapter Eight. The protein concentration preps utilised a gentle centrifugation approach with Amicon® Ultra-15 centrifugal filter devices. Protein integrities were routinely checked by SDS-PAGE before and after scattering, ultracentrifugation and assays.

6.3.2 X-ray scattering data collection and analysis

X-ray scattering is a diffraction method used to study solution structures of macromolecules in random orientations (Section 4.2; Perkins *et al.*, 2008). The X-ray data $I(Q)$ as a function of the scattering vector Q were acquired in two beam sessions on Beamline ID02 at the European Synchrotron Radiation Facility (Grenoble, France) with a ring energy of 6.0 GeV and operating in 4-bunch and 16-bunch modes to reduce the incident flux. Storage ring currents ranged from 22 mA to 41 mA (4-bunch mode), and from 67 mA to 92 mA (16-bunch mode). Potential radiation damage was eliminated by continuous movement of the sample in a flow cell during beam exposure, the use of 10 time frames of duration 0.2 sec or 0.5 sec each during each acquisition, and on-line checks for the absence of radiation damage at low Q. FH was studied at concentrations of 1.05 mg/ml (7.0 μM) and 0.42 mg/ml (2.8 μM)

respectively with $ZnSO_4$ concentrations between 0 µM to 200 µM, and 0.93 mg/ml (6.2 µM) with $CuSO_4$ in the same concentration range as well as 200 µM of $ZnCl_2$, $CaCl_2$, $MgCl_2$, $NiCl_2$, $CdCl_2$ and $FeSO_4$. Other details including the data reduction are described elsewhere (Section 4.2.4; Fernando *et al.*, 2007; Okemefuna *et al.*, 2008).

In a given solute-solvent contrast, Guinier analyses of ln $I(Q)$ vs Q^2 at low Q give the radius of gyration R_G and the forward scattering at zero angle $I(0)$ (Section 4.2.5):

$$\text{In } I(Q) = \text{In } I(0) - R_G^2 Q^2/3$$

The R_G is the root mean square radius of scattering density, and $I(0)/c$ (c = concentration) is a measure of its molecular weight. For elongated structures, the cross-sectional radius of gyration R_{XS} and cross-sectional intensity at zero angle $[I(Q).Q]_{Q\rightarrow 0}$ is obtained from analyses at larger Q ranges:

$$\ln [I(Q)Q] = \ln [I(Q)Q]_{Q\rightarrow 0} - R_{XS}^2 Q^2/2.$$

These provide information on the structural relationship between adjacent SCR domains. Indirect transformation of the scattering data $I(Q)$ in reciprocal space to give the distance distribution function $P(r)$ in real space was carried out using GNOM (Section 4.2.5):

$$P(r) = \frac{1}{2\pi^2}\int_0^\infty I(Q)Qr\sin(Qr)dQ$$

The $P(r)$ curve reports the distribution of distances r between all volume elements within the protein. This offers an alternative calculation of the R_G and $I(0)$ values that is based on the full scattering curve $I(Q)$, and not that at low Q. It also gives the maximum dimension of the macromolecule L. The X-ray curve utilised up to 211 data points for Q between 0.06 nm^{-1} and 1.50 nm^{-1} for 0.42 mg/ml FH, 309 data points for Q between 0.06 nm^{-1} and 2.10 nm^{-1} for 1.05 mg/ml FH, and up to 599 data points for Q between 0.09 nm^{-1} and 2.10 nm^{-1} for 0.93 mg/ml FH. Other details are described elsewhere (Nan *et al.*, 2008a; Aslam & Perkins, 2001; Fernando *et al.*, 2007; Okemefuna *et al.*, 2008).

6.3.3 Sedimentation velocity data collection and analyses

Analytical ultracentrifugation studies the sedimentation behaviour of macromolecules on subjecting these to a high centrifugal force in order to determine their sizes and shapes (Cole *et al.*,2008). Data were obtained on a Beckman XL-I instrument using AnTi50 or AnTi60 rotors at 20°C. Sedimentation velocity experiments were performed at rotor speeds up to

60,000 r.p.m. in two-sector cells with column heights of 12 mm. for 0.87 mg/ml and 0.35 mg/ml FH titrated with $ZnSO_4$ at eight concentrations between 0 μM and 200 μM, 0.81 mg/ml FH titrated with $CuSO_4$ at eight concentrations from 0 μM to 200 μM, and 0.93 mg/ml FH with 200 μM of $ZnCl_2$, $CaCl_2$, $MgCl_2$, $NiCl_2$, $CdCl_2$ and $FeSO_4$. Data analyses were performed using SEDFIT (version 9.4). The size-distribution analyses *c(s)* that provided size and shape data were based on a fixed resolution of 200 and frictional ratio *f/fo* of 1.78, and floated the meniscus, the bottom of the cell, and the baseline until the overall root mean square deviation and fits between the observed and calculated sedimentation boundaries were satisfactory. The percentage fraction of oligomers in the total loading concentration was derived using the *c(s)* integration function. Other details are described elsewhere (Section 4.1.2; Nan *et al.*, 2008a; Okemefuna *et al.*, 2008).

6.3.4 Fluid-phase activity assays

The reaction mixtures contained 0.3 mg/ml FH, 0.3 mg/ml C3u and 0.003 mg/ml factor I in six concentrations of $ZnSO_4$ or $CuSO_4$ (0 μM, 2 μM, 20 μM, 60 μM, 120 μM and 200 μM) and were incubated in a water bath at 37 °C. At timed intervals, 5 μl aliquots were removed for reducing SDS-PAGE analyses. Three controls were used, namely 0.3 mg/ml C3u; 0.3 mg/ml C3u and 0.3 mg/ml FH; and 0.3 mg/ml C3u, 0.3 mg/ml FH and zinc or copper. The C3 α-chain band densities from SDS-PAGE were measured using the gel analysis system SYNGENE (Synoptics Ltd., Cambridge, UK). The C3 α-chain cleavage was referenced to the averaged density of the uncleaved bands in the controls. Electrophoresis was performed by using NuPAGE® Novex® 4-12% Bis-Tris Mini Gel according to manufacturer's standard protocol.

6.4 Conclusions

Metals have not generally been considered as FH ligands. In distinction to the original study of the interaction between heterozygous FH with zinc (Perkins *et al.*, 1991), the study in this thesis has shown that five transition metals cause monomeric heterozygous FH to form large oligomers at the FH concentration seen in human serum. By performing X-ray solution scattering and analytical ultracentrifugation experiments, heterozygous FH at 2.8 – 7.0 μM was shown to be unaffected with [Zn] ≤ 20 μM, but formed a series of large oligomers with

[Zn] ≥ 60 μM. Structurally distinct large oligomers were also observed for Cu, while Ni, Cd and Fe showed low amounts of oligomers, and Mg and Ca showed no changes. The increased oligomer formation of heterozygous FH induced by zinc or copper matched with reduced FH activities shown by fluid-phase assays. Therefore zinc and copper should be considered as newly-identified inhibitory FH ligands at pathological metal concentrations above 60 μM. Not only do zinc and copper promote uncontrolled oligomer formation of heterozygous FH, but the pre-formed oligomers can be disassembled by chelation using EDTA.

FH is a major complement regulator in blood, and is expressed and secreted by many different cell types including the RPE (An *et al.*, 2006). Many functional studies of FH binding to its major ligand C3b, and to others such as heparin and C-reactive protein, have been performed. In distinction, surprisingly little attention has been paid to FH self-association and its effect on its regulatory function. The originally-reported inhibition of C3b cleavage in 1000 μM zinc could be explained in terms of the non-specific aggregation of FH first reported by X-ray scattering, because the protein aggregates would block the accessibility to the functionally-active regions in FH (Crossley & Porter, 1980; Perkins *et al.*, 1991). While FH is often considered to be monomeric, several groups have reported its ability to dimerise (Jokiranta *et al.*, 2000; Oppermann *et al.*, 2006; Jokiranta *et al.*, 2006). There are two dimerisation sites that have been located within the FH SCR-6/8 and SCR-16/20 fragments with K_D values of about 40 μM and 16 μM respectively (Fernando *et al.*, 2007; Okemefuna *et al.*, 2008). Ultracentrifugation showed that heterozygous FH exists in a reversible monomer-dimer equilibrium with a K_D of 28 μM up to 1.36 mg/ml, indicating that about 5% to 15% of FH in serum is reversibly dimeric, and that nonreversible higher oligomers form at higher concentrations, presumably through a alternating chain of dimerisation events at the two dimer sites (Chapter Five; Nan *et al.*, 2008a). The effect of dimerisation on regulatory function is not known. Here, using physiological concentrations of heterozygous FH from pooled serum, our scattering data showed the formation of large but compact oligomers of heterozygous FH in the presence of zinc and copper, while our ultracentrifugation data show that heterozygous FH is 85% oligomeric in 200 μM zinc and 50% oligomeric in 200 μM copper. FH activity was proportionately reduced by oligomer formation (Figure 6.17).

In a physiological scenario, because this metal binding is weak, the zinc- (or copper-) induced uncontrolled oligomerisation of FH can only occur in tissues where a sufficient amount of zinc (or copper) is present. For example, the total zinc concentration of 12.5 μM in serum is clearly too low to induce FH oligomerisation according to our data (Figure 6.2 and Figure 6.12). This level remains low at 14.7 μM even after a daily diet supplement with 80 mg zinc in the AREDS trials (AREDS Research Group, 2001b; AREDS Research Group, 2002). Few tissues have high enough total zinc concentrations to release biologically reactive zinc in the range of 20-200 μM (Frederickson *et al.*, 2006). The retina appears to be an exception, as this has the highest concentration of zinc per gram of tissue (Ugarte & Osborne, 2001). Retinal zinc is concentrated mostly in the RPE-choroidal complex, where sRPEds are formed, bound to melanin, metallothionein and other zinc binding proteins (Galin *et al.*, 1962; Newsome *et al.*, 1992). Cellular damage to the RPE which may occur through stress factors such as excessive light, smoking, or oxidative processes during ageing, is one of the first pathological events that lead to AMD. Damage to RPE cells may trigger the release of pathological levels of zinc from protein complexes into extracellular regions, and the local bioavailable zinc level may reach >60 μM which will be sufficient to initiate FH oligomerisation (Figure 6.2 and Figure 6.12) and its precipitation into sRPEds (Frederickson *et al.*, 2006). The concept that zinc might be involved in the initiation of AMD appears to contradict the clinical observation that zinc supplements are able to slow the development of blindness in patients (AREDS Research Group, 2001b; AREDS Research Group, 2002). However, AMD is a progressive disease, and decades elapse between the appearance of sRPEds and the degeneration that eventually lead to blindness. Therefore, it is possible that too much bio-available zinc in the early stages of the disease can trigger the problem by facilitating the formation of sRPEds, while decades later zinc supplementation can be beneficial if most of the zinc in the tissues is trapped in sRPEds and the surrounding tissues are relatively depleted (Lengyel & Peto, 2008).

At present, there is no simple mechanistic understanding of the formation of sRPEds and the slow progression to AMD over several decades of a lifespan. In the absence of metal, FH self-association involving probably SCR-7 and SCR-20 may lead to the formation of higher oligomers of FH through a set of alternating dimeric interactions between FH molecules (Chapter Five; Nan *et al.*, 2008a; Fernando *et al.*, 2007; Okemefuna *et al.*, 2008). It is intriguing that the SCR-6/8 fragment with the His402 allotype that is a risk factor for AMD

shows a slightly higher propensity to self-associate than the wild-type Tyr402 allotype (Fernando *et al.*, 2007), and this by itself could enhance the deposition of FH into sRPEds over several decades. A detailed comparison of the self-association properties between the Tyr402 and His402 allotype of FH is explained in Chapter Seven. However, if the alternative pathway is involved in AMD, as suggested from the involvement of FH polymorphisms (Klein *et al.*, 2005; Haines *et al.*, 2005; Edwards *et al.*, 2005; Hageman *et al.*, 2005) (and not the classical pathway which is regulated by membrane-bound regulators including membrane cofactor protein and decay-acceleration factor), and if FH-metal complexes contribute to the onset of AMD, a pathway for zinc-induced oligomer formation is suggested by the results in this chapter. Zinc is tetrahedrally coordinated in proteins (Auld, 2001). Given that zinc ligands at protein interfaces often include pairs of surface Asp and His residues, and Tyr402 is exposed at the surface of SCR-7 (Fernando *et al.*, 2007), it is also intriguing that the AMD-risk Tyr402His polymorphism involves the introduction of a His residue (Klein *et al.*, 2005; Haines *et al.*, 2005; Edwards *et al.*, 2005; Hageman *et al.*, 2005). This raises the possibility that an Asp-His pair on the surface of an SCR domain forms half a zinc binding site, and zinc may pair these two SCR domains together in a symmetric arrangement. The comparison of the zinc-binding properties of the Tyr402 and His402 allotypes of FH and the prediction of possible zinc-binding sites within FH are reported in Chapter Eight. Other scenarios based on other metal coordinations are possible. Irrespective of whether zinc interacts with specific residues on the surface of SCR domains, or whether zinc promotes the previously-observed self-association dimer sites in SCR-6/8 and SCR-16/20, it is clear that, in the presence of zinc, FH will form indefinite oligomers more readily than in its absence. Different metals will cause different oligomerisation properties, depending on their relative affinity for different self-association sites. For example, the more compact zinc-promoted oligomers (Figure 6.7) may be formed through a stronger pairing of two central SCR domains of FH, while the more extended copper-induced oligomers may result from a stronger pairing of SCR domains at one end of FH (Figure 6.18). As zinc is more abundant in sRPEds than any other metal (Flinn *et al.*, 2008; Scholl *et al.*, 2008), a compact association mechanism might be more relevant. While such an aggregation mechanism may be directly relevant to AMD, it is not known whether this proposed aggregation mechanism may act as a trigger for sRPEd formation, or facilitates the growth of sRPEd into larger and clinically relevant sizes over several decades of a lifespan. An aggregation mechanism will be distinct from that in which excessive complement activation and uncontrolled inflammation caused by reduced FH regulation will generate the slow build-up of protein and lipids after complement attack of host cells (Klein

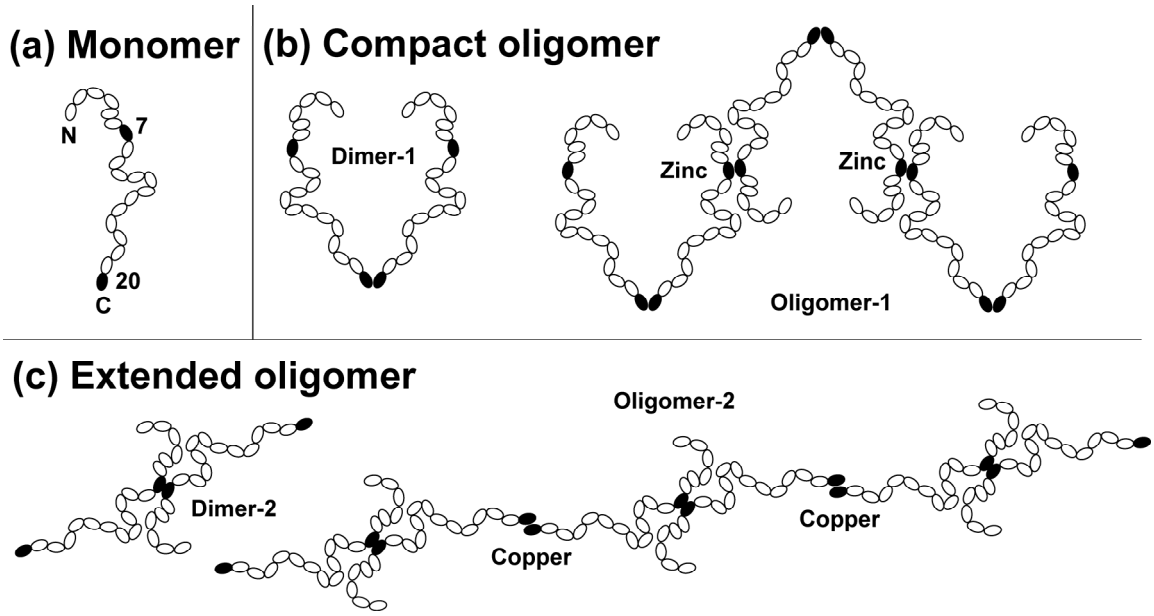

Figure 6.18 Hypothetical cartoon of the differential effect of metals on FH oligomerisation.

(a) A partially folded-back FH monomer structure is depicted, with SCR-7 and SCR-20 highlighted in black as possible dimerisation sites in native FH. It is stressed that the FH monomer is more compact in its folded-back structure than that shown, which is drawn for reason of clarity.

(b) A putative compact oligomer is formed, initially as a dimer through contacts in the region near SCR-20. The presence of zinc promotes further dimerisation in a central region of FH near to but not necessarily at SCR-7, and this leads to a set of compact oligomers (Figure 6.7).

(c) More extended oligomers can be formed if a different metal promotes a different pattern of oligomer formation. In the schematic view shown, dimers are initially formed near SCR-7, and the presence of copper leads to further dimerisation near to one end of FH, not necessarily at SCR-20. More extended oligomers are formed in the presence of copper (Figure 6.7).

et al., 2005; Haines *et al.*, 2005; Edwards *et al.*, 2005; Hageman *et al.*, 2005; Lengyel *et al.*, 2004).

The molecular effect of dimerisation on FH function is not presently known, but Figure 6.17 indicated that complement regulation by FH will be diminished by oligomer formation. The C3b or factor I ligands may be sterically blocked from interaction with FH aggregates by zinc. Alternatively, or simultaneously, zinc may enhance the deposition of FH-binding proteins, together with FH, into sRPEds contributing to the accelerated protein built up in the Bruch's membrane. This process might be slow, given that it could be triggered by the gradual decline of RPE cells that may happen without relevant visual impairment of the peripheral retina (Jager *et al.*, 2008). However, the process might be accelerated by the several environmental, cellular and genetic factors associated with AMD, especially when the damage affects the macula (Wills *et al.*, 2008). If FH-metal complexes contribute to the onset of AMD, a pathway for zinc-induced oligomer formation is suggested by analogy with the two FH dimerisation site, SCR-6/8 and SCR-16/20 (Fernando *et al.*, 2007; Okemefuna *et al.*, 2008). By this, two weak dimer sites will initiate FH dimer formation at either site. As shown in Figure 6.18 a, these are arbitrarily postulated to be in the vicinity of SCR-7 and SCR-20. In the absence of metal, these sites will lead to higher oligomers of FH at high concentration through a set of alternating dimeric interactions between FH molecules (Chapter Five; Nan *et al.*, 2008a). If the process of self-association at two dimer sites is enhanced by the presence of zinc (not necessarily at SCR-7 and SCR-20), FH will form indefinite oligomers more readily (Figure 6.18 b). The varied effect of different transition metals on the FH oligomer structure is explained schematically in Figure 6.18 depending on which of the two dimer sites is more strongly promoted by metal. For example, the more compact zinc-promoted oligomers of Figure 6.7 may be formed through a stronger dimerisation effect at a central SCR domain of FH (Figure 6.18 b), while the more extended copper-induced oligomers may result from a stronger effect at a C-terminal region of FH (Figure 6.18 c). Note that zinc is more abundant in the retina than copper (Flinn *et al.*, 2008; Wills *et al.*, 2008). While such an aggregation mechanism for FH may be directly relevant to AMD, it is possible that the high bioavailability of zinc in the retina may exert a pathogenic effect by this route. Given that zinc ligands at protein interfaces often include surface Asp and His residues, and Tyr402 is exposed at the surface of SCR-7 (Fernando *et al.*, 2007), it is also intriguing that the AMD-risk polymorphism in FH replaces Tyr402 with His402 (Klein *et al.*, 2005; Haines *et al.*, 2005; Edwards *et al.*, 2005; Hageman *et al.*, 2005).

Given the unambiguous association between complement activation and AMD, the presence of FH and other complement related proteins in sRPEds (Hageman *et al.*, 2001), and the indication that FH plays a role in the age-related thickening of the Bruch's membrane (Coffey *et al.*, 2007), an improved understanding of the role for FH may lead to novel therapies for AMD. For example, if a metal-induced aggregation mechanism or metal-induced complement dysregulation proves to be significant, the reversibility of FH oligomerisation with EDTA offers the possibility to capture this oligomerisation before the irreversible cross linking of proteins with photo-oxidised lipids takes place (Crabb *et al.*, 2002). Similar arguments may be relevant to other deposit-forming diseases in which trace metals are involved, such as Alzheimer's disease in which a zinc buffering compound is already in clinical trials (Ritchie *et al.*, 2003).

Chapter Seven

Self-association and folded-back solution structure of the wild-type Tyr402 and the disease-related His402 allotypes of homozygous complement factor H

7.1 Introduction

The alternative complement pathway is a crucial component of the innate immune system. Its activation is initiated by the spontaneous hydrolysis of C3 to form C3u, also known as C3(H_2O), which leads to a positive-feedback amplification of C3 cleavage to form the activated form C3b which is deposited on pathogenic cell surfaces. To prevent complement-mediated host cell damage, complement factor H (FH) regulates the alternative pathway by acting as a cofactor for factor I (FI) to cleave C3b (Law & Reid, 1995; Whaley & Ruddy, 1976; Pangburn *et al.*, 1977), competing with factor B to interfere with the formation of the C3 convertase C3bBb (Farries *et al.*, 1990), and accelerating the decay of the C3bBb complex (Whaley & Ruddy, 1976; Weiler *et al.*, 1976). FH is genetically associated through a common Tyr402His polymorphism with age-related macular degeneration (AMD), the most common cause of blindness in the elderly in the Western population (Klein *et al.*, 2005; Haines *et al.*, 2005; Edwards *et al.*, 2005; Hageman *et al.*, 2005). FH is also involved with kidney diseases including atypical haemolytic uraemic syndrome and membranoproliferative glomerulonephritis type II, and with dementia, including Alzheimer's disease (Strohmeyer *et al.*, 2002; Saunders *et al.*, 2007; Zetterberg *et al.*, 2008). Even with the analysis of over 100 genetic alterations in FH (Saunders *et al.*, 2007), molecular mechanisms leading to these four diseases based on the involvement of altered forms of FH are still not clear. In the context of AMD, the early stages of this disease involve the appearance of sub-retinal pigment epithelial deposits that develop in the extracellular matrix interposed between the retinal pigment epithelium (RPE) and the choroidal vasculature, called Bruch's membrane (Bird, 2010). Sub-RPE deposits have been long recognized as a hallmark of AMD. They contain oxidized lipids, carbohydrates, cellular materials and over 200 proteins including FH and other complement components (Hageman *et al.*, 2005; Crabb *et al.*, 2002; Bok, 2005). Based on these co-localizations, complement activation-related inflammation was proposed to be associated with sub-RPE deposit formation (Hageman *et al.*, 2005; Anderson *et al.*, 2002). The studies in Chapter Five and Chapter Six proposed that the propensity of heterozygous FH to form oligomers may contribute to sub-RPE deposits (Nan *et al.*, 2008a; Nan *et al.*, 2008b), thus it becomes necessary to understand how the individual homozygous FH allotypes form oligomers.

FH is constructed from 20 short complement regulator (SCR) domains, each of length about 61 residues, with 19 linkers of lengths composed of three to eight residues between the domains (Soares & Barlow, 2005). There are nine potential N-glycosylation sites in FH, of which eight are occupied by biantennary disialylated glycans (Fenaille *et al.*, 2007). FH binds to three major physiological ligands via comparatively weak interactions at multiple sites (Perkins *et al.*, 2010a; Perkins *et al.*, 2010b). Three binding sites have been proposed for C3b, including SCR-1/4 that binds to intact C3b, SCR-6/10 that binds to the C3c fragment of C3b and SCR-16/20 that binds to the C3d fragment (Sharma & Pangburn, 1996; Jokiranta *et al.*, 2000; Schmidt *et al.*, 2008b). At least two binding sites for heparin have been proposed at SCR-7 and SCR-20, where heparin is an analogue of heparan sulphate that coats the host cell surface (Blackmore *et al.*, 1996; Blackmore *et al.*, 1998; Ormsby *et al.*, 2006). At least two major binding sites have been proposed for C-reactive protein (CRP) at SCR-7 and SCR-8/11, and also at SCR-16/20 (Okemefuna *et al.*, 2010). The FH-CRP interaction has been controversial for reason of the strong affinity of denatured CRP for FH which complicated earlier analyses (Hakobyan *et al.*, 2008), however the most recent study reconciled observations based on inappropriate buffers and denatured CRP to confirm that native CRP interacts with FH at two different sites (Okemefuna *et al.*, 2010). The FH Tyr402His polymorphism was recognized as a risk factor for AMD (Klein *et al.*, 2005; Haines *et al.*, 2005; Edwards *et al.*, 2005; Hageman *et al.*, 2005), and residue 402 is located in SCR-7 which interacts with heparin and CRP. The SCR-6/8 His402 allotype exhibits reduced binding to CRP than the Tyr402 allotype (Okemefuna *et al.*, 2010), while variable results have been obtained in binding studies of FH to heparin (Clark *et al.*, 2006). The Val62Ile polymorphism is protective against AMD (Hageman *et al.*, 2005; Hocking *et al.*, 2008), and this is located in SCR-1 which interacts with C3b. FH also forms oligomers through self-association sites at each of SCR-6/8 and SCR-16/20 (Chapter Five; Nan *et al.*, 2008a; Fernando *et al.*, 2007; Okemefuna *et al.*, 2008). Dimer formation at SCR-7 may affect FH-ligand interactions that involve SCR-7.

To date, the structure of full-length FH has not been determined by crystallography or NMR methods for reason of its large size and the glycosylation of its 20 domains. Crystal and NMR structures have been published for small domain fragments of FH (Hocking *et al.*, 2008; Wu *et al.*, 2009; Schmidt *et al.*, 2010; Okemefuna *et al.*, 2009).

FH self-association is not always considered in these crystal and NMR studies. FH dimers in solution at high concentrations were reported by X-ray and neutron scattering (Perkins *et al.*, 1991), while other studies showed that heterozygous FH possesses a partially folded-back and largely monomeric domain structure in solution that is affected by ionic strength (Okemefuna *et al.*, 2009; DiScipio, 1992; Aslam & Perkins, 2001). The recombinant SCR-6/8 and SCR-16/20 fragments of FH each showed dimeric properties (Fernando *et al.*, 2007; Okemefuna *et al.*, 2008). The sequential daisy-chaining of these dimer sites in FH would lead to the formation of a series of FH oligomers, and this hypothesis was verified by ultracentrifugation of heterozygous FH (Chapter Five; Nan *et al.*, 2008a; Okemefuna *et al.*, 2009). Given the involvement of the Tyr402His polymorphism at one of the two dimerisation sites with AMD, more detailed knowledge of how dimers and higher oligomers are formed in the two homozygous FH allotypes is essential to understand the relation of FH to AMD. Previously, ultracentrifugation suggested that the His402 allotype of SCR-6/8 showed a greater self-association than the Tyr402 allotype (Fernando *et al.*, 2007). Following the study in Chapter Five, the self-association of the Tyr402 and His402 allotypes of full-length homozygous FH and its SCR-6/8 fragment are characterised in this chapter. The study in this chapter shows that the His402 allotype of SCR-6/8 exhibits significantly greater self-association than the Tyr402 allotype when immobilised at surfaces, and that both forms of full-length FH self-associate by similar amounts to form oligomers. Improved similar folded-back solution structures are determined for both FH allotypes by constrained scattering modelling, and two different mechanisms for FH self-association are proposed. The implications of these results for complement regulation and the formation of protein aggregates in the development of AMD are also discussed in this chapter.

7.2 Results and discussion

7.2.1 Surface plasmon resonance of the two FH allotypes and FH SCR-6/8

Both the full-length FH Tyr402 and FH His402 allotypes were purified from the plasma of genotyped healthy volunteers without known eye disease (Table 7.1) from the major peak in size-exclusion chromatography. Both gave clean single bands by SDS-PAGE as in Figure 5.6 b (Chapter Five; Nan *et al.*, 2008a). The seven Tyr402 samples were

Table 7.1 Genotyped FH samples used in this chapter.

FH source	Tyr402His	Ile62Val	Experiment [a]
002CW	Tyr402	heterozygous	Gel filtration; AUC
004EE	Tyr402	heterozygous	Gel filtration; AUC
026II	Tyr402	Ile62	Gel filtration; AUC
020FM	Tyr402	heterozygous	AUC; SAXS; Modelling
022LM	Tyr402	Val62	AUC; SAXS; Modelling
013HH	Tyr402	Val62	MS
018DK	Tyr402	heterozygous	SPR
011KY	His402	Val62	Gel filtration; AUC
027BA	His402	Val62	Gel filtration; AUC
023SK	His402	Val62	AUC
028EL	His402	Val62	AUC; SAXS; Modelling
032KO	His402	Val62	AUC; SAXS; Modelling
015LT	His402	Val62	MS
030TJ	His402	Val62	SPR

[a] Abbreviations: AUC, analytical ultracentrifugation; SAXS, small angle X-ray scattering; Modelling, constrained scattering modelling; MS, mass spectrometry; SPR, surface plasmon resonance.

homozygous or heterozygous for the Ile62Val polymorphism (Table 7.1), another AMD-asscoiated polymorphism. All seven AMD-risk His402 samples were homozygous for the Val62 polymorphism. Fluid-phase activity assays using C3u and factor I with both FH allotypes showed that both demonstrated similar C3u cleavage rates (Nan *et al.*, 2008b).

Surface plasmon resonance (SPR) studies of protein in the solution phase binding to an immobilised protein surface enabled FH self-association to be studied in terms of the Tyr402His polymorphism and their dissociation constant K_D values (Tanious *et al.*, 2008). A total of 150 RU (resonance unit) of heterozygous FH was immobilised on a CM5 chip. Equilibrium experiments were performed by flowing FH Tyr402 over the chip at concentrations between 0.1-1.5 mg/ml (0.65-9.74 μM) (Figure 7.1 a), and FH His402 over the chip at concentrations between 0.1-1.8 mg/ml (0.65-11.69 μM) in HEPES buffer (Figure 7.1 b). The binding of both FH allotypes to heterozygous immobilised FH was observed at all concentrations (Figure 7.1 a, b), indicating that FH oligomerisation proceeded in physiological relevant conditions. In equilibrium analyses, the individual sensorgrams could not be fitted to a 1:1 binding kinetic model, suggesting that FH binding is more complicated that that provided by a 1:1 model, in agreement with the conclusion from ultracentrifugation that at least two self-association sites exist on FH (Chapter Five; Nan *et al.*, 2008a). However, the maximum binding response from each sensorgram can be well fitted to a steady state affinity model which assuming the binding is 1:1. Therefore if assuming 1:1 binding, a K_D value of 8.04 μM with a χ^2 value of 2.58 RU^2 was determined for FH Tyr402, while a similar K_D value of 6.72 μM with a χ^2 value of 6.53 RU^2 was determined for FH His402 from a steady state affinity model (Figure 7.1 c). Both these K_D values were smaller than the K_D value of 28 μM determined for heterozygous FH in solution by sedimentation equilibrium ultracentrifugation (Nan *et al.*, 2008a). The stronger self-association of FH seen by SPR than by ultracentrifugation may result from its immobilisation on a surface, at which local concentration effects will amplify the strength of binding. Overall, these experiments with one pair of FH allotypes show that the binding of FH His402 and FH Tyr402 to immobilised FH are similar.

Earlier analytical ultracentrifugation experiments showed that the His402 allotype of FH SCR-6/8 self-associated slightly more than the Tyr402 allotype in solution (Fernando et

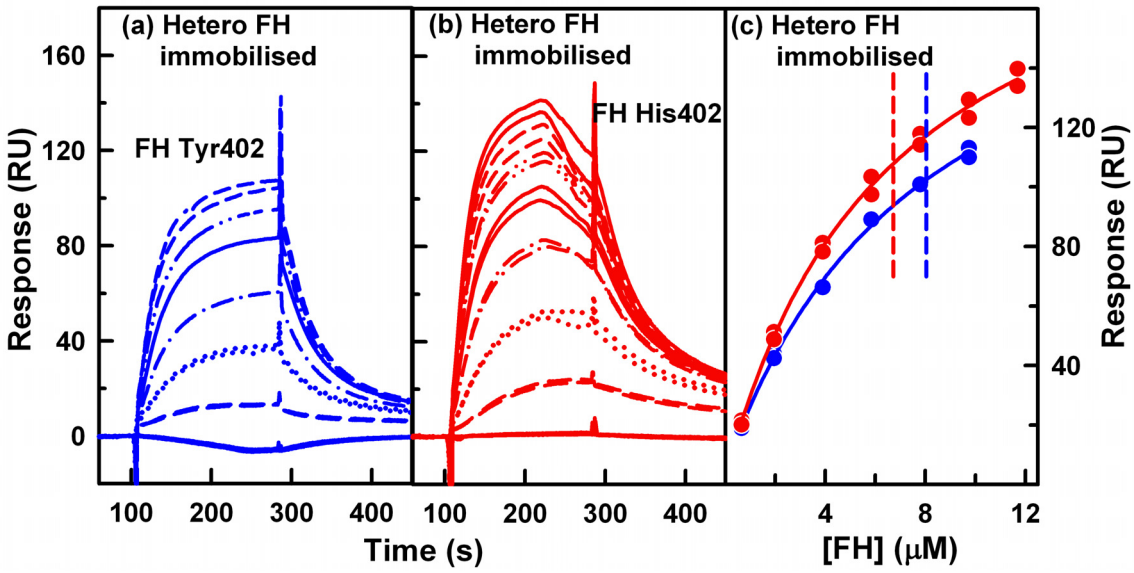

Figure 7.1 Surface plasmon resonance analysis of the FH self-association. 150 RU of wild-type heterozygous FH was immobilised on a CM5 chip; The Tyr402 allotype is denoted by blue; the His402 allotype is denoted by red.

(a) A FH Tyr402 sample 018DK was analysed at seven concentrations of 0 μM (measured twice), 0.65 μM, 1.95 μM (twice), 3.90 μM, 5.84 μM, 7.79 μM and 9.74 μM (twice) from bottom to top;

(b) A FH His402 sample 030TJ was analysed at eight concentrations of 0 μM, 0.65 μM, 1.95 μM, 3.90 μM, 5.84 μM, 7.79 μM, 9.74 μM and 11.69 μM from bottom to top, each measured in duplicate;

(c) Binding affinities were fitted using the maximum response values in (a) and (b). The K_D values were determined as 8.04 μM (Tyr402) with a χ^2 value of 2.58 RU^2 and 6.72 μM (His402) with a χ^2 value of 6.53 RU^2 (vertical dashed straight lines).

al., 2007). Accordingly further SPR studies were made using both allotypes of the FH SCR-6/8 fragment. Each allotype was separately successfully immobilised to a CM4 chip up to a total response of 150 RU (Figure 7.2), and the His402 allotype was also immobilised up to 400 RU on a third chip (Figure 7.3). The binding of FH SCR-6/8 Tyr402 was studied at concentrations between 0.04-0.8 mg/ml (2-40 μM) over CM4 chips immobilised with either FH SCR-6/8 Tyr402 (Figure 7.2 a) or FH SCR-6/8 His402 respectively (Figure 7.3 a). The binding of FH SCR-6/8 His402 was studied at concentrations between 0.04-0.6 mg/ml (2-28 μM) over CM4 chips immobilised with either FH SCR-6/8 Tyr402 (Figure 7.2 b) or FH SCR-6/8 His402 (Figure 7.3 b) respectively. Binding was observed in all cases, and therefore both allotypes of FH SCR-6/8 self-associate with each other. The two allotypes of FH SCR-6/8 showed the same binding affinities on the surface immobilised with FH SCR-6/8 Tyr402 allotype (Figure 7.2 c), and this indicates that the affinity of the self-association of FH SCR-6/8 Tyr402 allotype is similar to that of the self-association of the heterozygous FH SCR-6/8. On the other hand, the FH SCR-6/8 His402 allotype showed significantly higher binding affinity than the Tyr402 allotype did to the surface immobilised with the His402 allotype (Figure 7.3 c), and this indicates that the affinity of the self-assocation of FH SCR-6/8 His402 allotype is higher than that of the heterozygous FH SCR-6/8. From the two comparions, one can derive that the FH SCR-6/8 His402 allotype self-associates more than the FH SCR-6/8 Tyr402 allotype does, and the His402 residue is participating in the binding. The K_D values could not be determined from steady state affinity fits because both K_D values were larger than 40 μM, which indicate that the binding is weak. This is consistent with the K_D value of approximately 40 μM determined by ultracentrifugation for the His402 allotype (Fernando *et al.*, 2007). Given that the self-association of the two FH SCR-6/8 allotypes is weaker than the self-association of the two full-length FH allotypes, for which the K_D value is 28 μM for heterozygous full-length FH in solution (Chapter Five; Nan *et al.*, 2008a) and 7-8 μM by SPR above for the full-length FH allotypes, this also indicates that other self-association sites exist in FH as well as that in SCR-6/8.

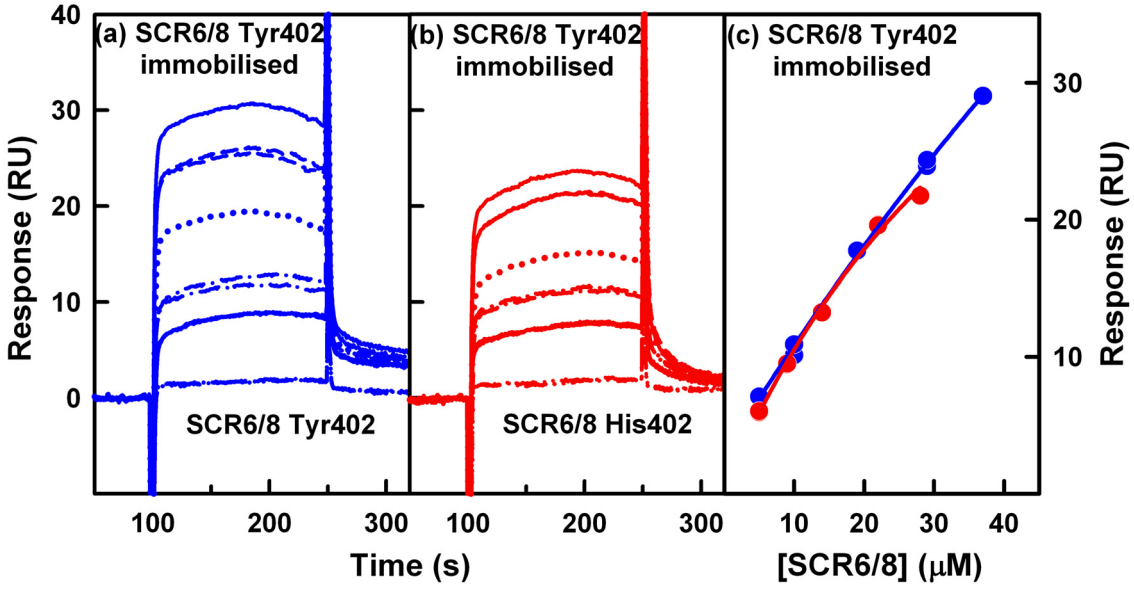

Figure 7.2 Surface plasmon resonance analysis of the FH SCR-6/8 self-association with 150 RU of the Tyr402 allotype of FH SCR-6/8 immobilised on a CM4 chip. The Tyr402 allotype is denoted by blue; the His402 allotype is denoted by red.

(a) A FH SCR-6/8 Tyr402 sample was analysed at six concentrations of 0 μM (twice), 5 μM, 10 μM (twice), 19 μM, 29 μM (twice) and 37 μM from bottom to top;

(b) A FH SCR-6/8 His402 sample was analysed at six concentrations of 0 μM, 5 μM, 9 μM, 14 μM, 22 μM and 28 μM from bottom to top, each measured in duplicate;

(c) Binding affinities were fitted using the maximum response values in (a) and (b), however no K_D values were determined because these are greater than 40 μM.

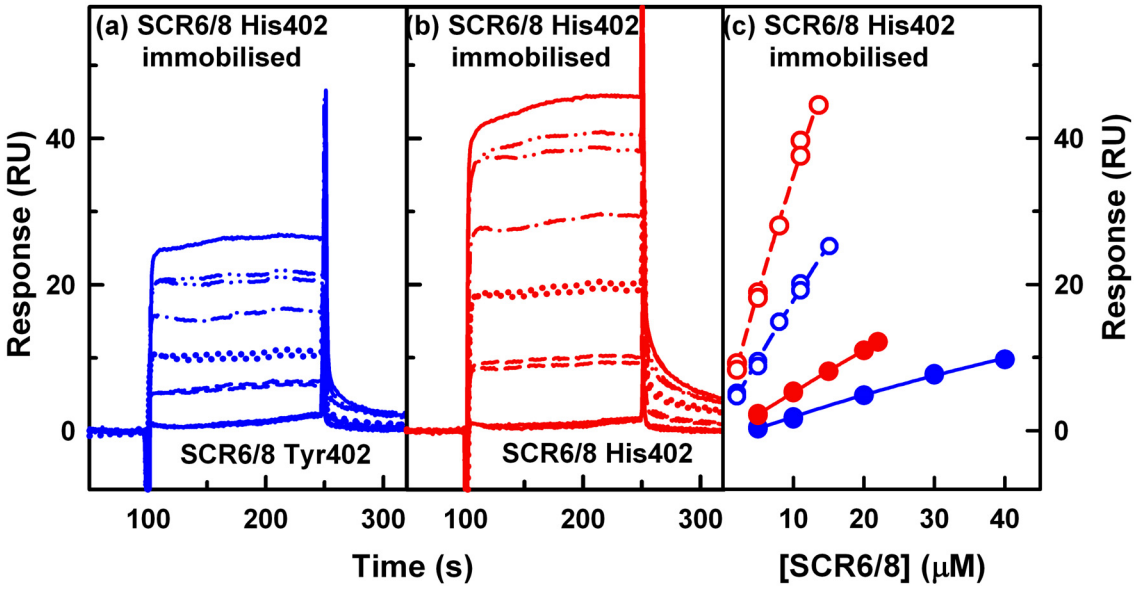

Figure 7.3 Surface plasmon resonance analysis of the FH SCR-6/8 self-association with 400 RU of the His402 allotype of FH SCR-6/8 immobilised on a CM4 chip. The Tyr402 allotype is denoted by blue; the His402 allotype is denoted by red.

(a) A FH SCR-6/8 Tyr402 sample was analysed at concentrations of 0 μM (twice), 2 μM (twice), 5 μM (twice), 8 μM, 11 μM (twice) and 15.1 μM from bottom to top;

(b) A FH SCR-6/8 His402 sample was analysed at six concentrations of 0 μM (twice), 2 μM (twice), 5 μM (twice), 8 μM, 11 μM (twice) and 13.6 μM from bottom to top;

(c) Binding affinities were fitted (open circles) using the maximum response values in (a) and (b), however no K_D values were determined because these are greater than 40 μM. A second experiment with 150 RU of FH SCR-6/8 His402 immobilised on a CM4 chip using six concentrations of His402 at 0 μM, 5 μM, 10 μM, 15 μM, 20 μM and 22 μM and six concentrations of Tyr402 at 0 μM, 5 μM, 10 μM, 20 μM, 30 μM and 40 μM are also shown (filled circles).

7.2.2 Sedimentation velocity analyses of the two FH allotypes

Analytical ultracentrifugation studies the sedimentation behaviour of macromolecules on subjecting these to a high centrifugal force in order to determine their sizes and shapes (Section 4.1; Cole *et al.*, 2008). The oligomers previously observed for heterozygous FH (Chapter Five; Nan *et al.*, 2008a) were now evaluated using sedimentation velocity experiments on five FH Tyr402 and five FH His402 allotypes from ten genotyped donors at three concentrations between 0.5-2.1 mg/ml in HEPES buffers (10 mM HEPES, 137 mM NaCl, pH 7.4). Similar sedimentation boundary profiles were observed for the two allotypes (Figure 7.4, upper panels), and these were fitted using size-distribution analyses *c(s)*. Good fits with low residuals were obtained in all cases. The mean sedimentation coefficient $s_{20,w}$ of monomeric FH (Tyr402) at a rotor speed of 50,000 r.p.m was 5.69 (± 0.03) S, and that for FH (His402) was identical at 5.67 (± 0.04) S (peak 1 in Figures 7.4 a, b). Both values (Table 7.2) agree well with previous $s_{20,w}$ values of 5.3 (± 0.1) S and 5.65 (± 0.05) S for heterozygous monomeric FH in 137 mM NaCl (Chapter Five; Nan *et al.*, 2008a; Aslam & Perkins, 2001). Conversion of the *c(s)* distribution to mass distribution plots *c(M)* showed that the major peak 1 corresponded to a molecular mass of 147 (± 10) kDa for the FH (Tyr402) allotype and 147 (± 11) kDa for FH (His402). Both values agreed with the sequence-calculated molecular mass of 154 kDa for both allotypes, and previous *c(M)* mass determinations of 142 (± 2) kDa for heterozygous FH (Chapter Five; Nan *et al.*, 2008a). Integration of the *c(s)* peaks showed that dimer and trimer comprised 4.0 (± 1.9) % and 2.1 (± 0.7) % respectively for FH Tyr402 samples, and 5.7 (± 1.5) % and 2.5 (± 0.6) % respectively for FH His402 samples at 1.1 mg/ml. Thus the averaged *c(s)* distributions showed similar dimer and trimer formation for the two allotypes (peaks 2 and 3 in Figure 7.4 c). The mean $s_{20,w}$ value of dimeric FH Tyr402 was 7.57 (± 0.36) S, and that for dimeric FH His402 was similar at 7.69 (± 0.40) S (peak 2 in Figure 7.4 a, b). The mean $s_{20,w}$ value of trimeric FH Tyr402 was 9.3 (± 0.7) S, and that for trimeric FH His402 was similar at 9.4 (± 0.8) S (peak 3 in Figure 7.4 a, b). These values also agree well with previous values of 7.3 ± 0.2 S and 9.2 ± 0.2 S for heterozygous FH dimers and trimers respectively (Chapter Five; Nan *et al.*, 2008a). These dimer peaks were reproducibly seen for heterozygous FH in a range of NaCl concentrations and pH values, and their size increases with increase in FH concentration (Okemefuna *et al.*, 2009). The present study now shows that these reversible peaks also exist in

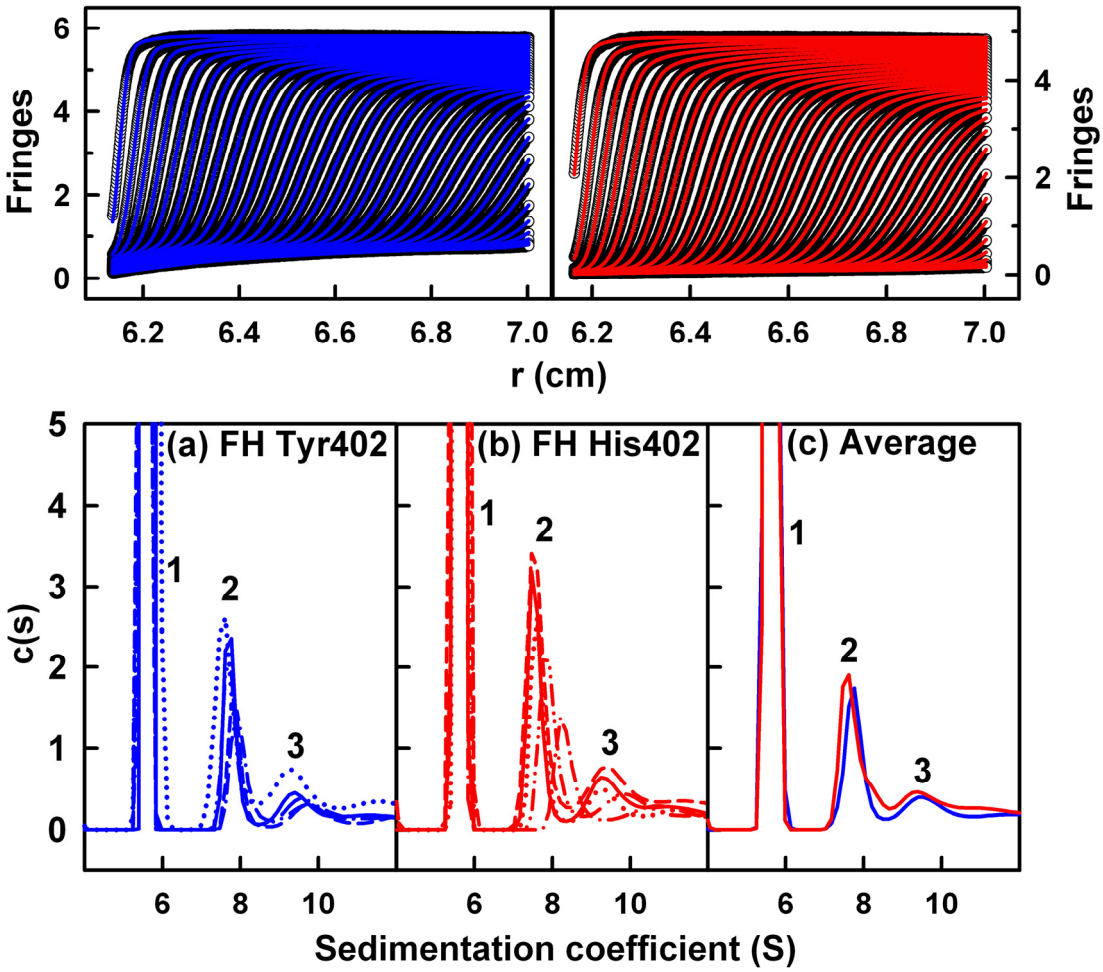

Figure 7.4 Sedimentation velocity *c(s)* size-distribution analyses for the two FH allotypes. All analyses correspond to 1.1 mg/ml FH. In the upper panels, the sedimentation boundary fits corresponding to the FH Tyr402 (blue) and FH His402 (red) allotypes are shown in the upper panels, where only every tenth scan is shown for reason of clarity. In the lower panels, the intensity of the major monomer peak at approximately 5.7 S is normalised to 100 for reason of clarity.

(a) The *c(s)* analyses are shown for five Tyr402 FH samples (___, 002CW; _ _ _, 004EE; ....., 026II; _._._, 020FM; _ . . _, 022LM);

(b) The *c(s)* analyses are shown for five His402 FH samples (___, 011KY; _ _ _, 023SK; ....., 027BA; _._._, 028EL; _ . . _, 032KO).

(c) The averaged *c(s)* plots for Tyr402 FH (blue) and His402 FH (red) from (a,b) are overlaid for comparison.

Table 7.2 Experimental X-ray and ultracentrifugation data and modelling fits for the FH Tyr402 and His402 allotypes.

	Filter	Models	Dry spheres	Hydrated spheres	R_G (nm)	R_{XS-1} (nm)	R_{XS-2} (nm)	D_{max} (nm)	R factor (%)	$s^0_{20,w}$ (S)
Experimental data										
FH Tyr402 (020FM)					7.54 ± 0.24; 8.03 ± 0.04 [a]	2.35 ± 0.11	1.77 ± 0.04	28		5.67 ± 0.02
FH Tyr402 (022LM)					7.97 ± 0.42; 8.14 ± 0.05 [a]	2.36 ± 0.05	1.75 ± 0.03	29		5.66 ± 0.08
FH His402 (028EL)					7.45 ± 0.34 7.93 ± 0.05 [a]	2.15 ± 0.08	1.77 ± 0.02	28		5.71 ± 0.02
FH His402 (032KO)					7.91 ± 0.70 7.50 ± 0.05 [a]	2.25 ± 0.12	1.76 ± 0.02	26		5.69 ± 0.02
Modelling of FH										
Library of 5,000 FH models	None	5,000	1434 - 1619	1948-2284	4.88 - 13.0	0.06 - 6.02	0.03 - 2.82	n.a	2.8 - 25.3	n.a.
FH Tyr402 (020FM)	R_G, R_{XS-1} and R factor	8	1476 - 1556	2087-2170	7.45 -8.18	2.25-2.46	1.48-1.87	26 - 29	3 - 4.5	5.08 -5.54
	Best fit	1	1494	2070	7.54	2.36	1.86	28	3	5.45
FH Tyr402 (022LM)	R_G, R_{XS-1} and R factor	8	1476 - 1556	2042 -2181	7.45 - 8.28	2.25 -2.44	1.57 - 1.86	24 - 30	2.8 - 4.3	5.08 - 5.54
	Best fit	1	1494	2070	7.54	2.36	1.86	28	2.8	5.45
FH His402 (028EL)	R_G, R_{XS-1} and R factor	8	1476 - 1561	2042 - 2180	7.45 - 8.32	1.96 -2.36	1.57-2.07	24 - 31	3.2 - 4.8	5.08 -5.54
	Best fit	1	1494	2070	7.54	2.36	1.86	28	3.2	5.45
FH His402 (032KO)	R_G, R_{XS-1} and R factor	8	1476 - 1556	2042 - 2181	6.91 - 7.65	2.18 - 2.43	1.48 -2.13	23 - 28	3.1 - 5.7	5.30 - 5.54
	Best fit	1	1494	2070	7.54	2.36	1.86	28	3.1	5.45
Four best-fit FH models (Figure 9)	R_G, R_{XS-1} and R factor	4	1476 -1511	2042 - 2096	7.45 - 7.57	2.25 - 2.36	1.57 - 1.86	24 - 28	2.8 - 4.7	5.38 - 5.54

[a] Both R_G values correspond to 0.4 mg/ml; likewise the R_{XS} values. The first correspond to the Guinier fits; the second correspond to the *P(r)* fits.

homozygous FH. Reaction boundaries are *c(s)* peaks that correspond to the co-sedimentation of two different species, and exhibit well-defined sedimentation coefficients between the values of the two different species (Dam & Schuck, 2005). The dimer and trimer peaks do not correspond to reaction boundaries because these are separately observed from that of the FH monomer peak, thus they correspond to slow equilibria between the monomer, dimer and trimer on the timescale of sedimentation.

In heterozygous FH, variable amounts of further oligomers from tetramers to nonamers with lower intensities have been observed (Chapter Five; Nan *et al.*, 2008a; Okemefuna *et al.*, 2009). For the FH Tyr402 allotype, the $s_{20,w}$ values of peaks 4-9 (Figure 7.5 a) were 11.9 (± 1.0) S, 14.7 (± 0.8) S, 17.1 (± 0.7) S, 19.4 (± 1.0) S, 22.1 (± 1.0) S and 25.0 (± 0.7) S in that order. For the FH His402 allotype, the $s_{20,w}$ values of peaks 4-9 (Figure 7.5 b) were in close agreement at 11.9 (± 0.9) S, 14.3 (± 0.5) S, 16.7 (± 0.4) S, 18.7 (± 0.6) S, 21.3 (± 0.5) S and 24.8 (± 0.7) S in that same order. The percentages of the FH Tyr402 and His402 oligomers at concentrations from 0.5 to 2.1 mg/ml were derived by integration of the peaks 2-9 between 6.8 S to 28 S in the five *c(s)* analyses for each allotype (Figure 7.5 c). A mean value of 11.7 (± 2.0) % of oligomers was seen for FH Tyr402 while a mean of 12.8 (± 2.7) % of oligomers were seen for FH His402 FH. Both percentages agree well with that of 12% observed for heterozygous FH at 1 mg/ml, and are comparable with an estimate of 17% of dimer predicted from a simple reversible monomer-dimer self-association K_D value of 28 μM (Chapter Five; Nan *et al.*, 2008a). The variability in quantifying the proportion of higher FH oligomers is attributable to two factors. First, the amount of higher oligomers is not consistently observed in all cases, as exemplified by the NaCl concentration and pH study of heterozygous FH (Okemefuna *et al.*, 2009). Second, slight misalignments of the ultracentrifugation cells in the rotor relative to the centre of rotation can result in the observation of pseudo-oligomeric peaks (Arthur *et al.*, 2009). Overall, larger FH oligomers appear to form irreversibly by a different mechanism to that for the FH dimer and trimer.

7.2.3 Mass spectrometry of the two FH allotypes

Because the direct evidence for discrete FH oligomers in solution has been observed up to now only by analytical ultracentrifugation, mass spectrometry of homozygous FH

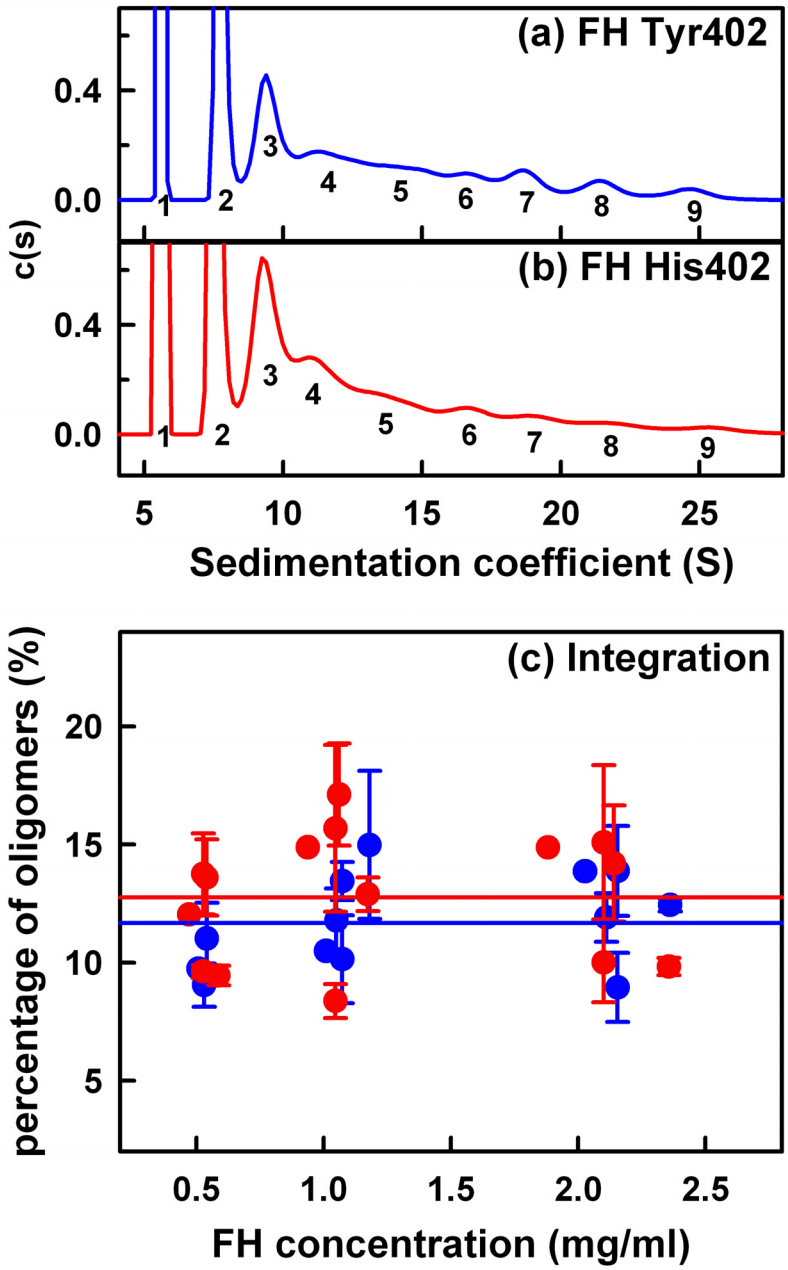

Figure 7.5 Integration of the homozygous FH oligomers in *c(s)* analyses. FH samples were analysed by sedimentation velocity at rotor speeds up to 60,000 r.p.m. (a,b) Representative analyses of the Tyr402 and His402 allotypes are shown at 50,000 r.p.m., where the numbers represent the FH oligomers starting with monomer (peak 1) and dimer (peak 2) and extending to nonamers (peak 9). (c) The proportion of oligomers present was derived by integration of the *c(s)* analyses for peaks 2-9 for the five different samples of each FH allotype (Tyr402, blue; His402, red) at concentrations of approximately 0.5 mg/ml, 1.1 mg/ml and 2.1 mg/ml. Statistical error bars are shown where visible. The mean proportion of oligomers is shown as a straight line.

was employed as a further means of detecting oligomers. Mass spectrometry is able to observe macromolecular assemblies and determine their stoichiometry (Benesch & Robinson, 2009). Caution in data interpretation is required because the presence of oligomeric forms may not reflect the solution composition, but instead result from non-specific protein-protein interactions formed during the electrospray process during the evaporation of nanodroplets inside the instrument (Lane *et al.*, 2009). One pair of the FH Tyr402 and His402 allotypes was studied shortly after concentration to about 4 mg/ml in order to promote the formation of reversible oligomers. Buffers with either 140 mM or 1 M ammonium acetate (pH 7.0) were used in order to evaluate two ionic strengths, given the known decrease of oligomer formation with increase in NaCl concentration (Okemefuna *et al.*, 2009). Ammonium acetate was used because this is volatile in the gas phase used for measurements, unlike the HEPES buffer used for SPR and ultracentrifugation. The mass spectrometry experiments were performed by Dr. Adam MacKay in the Department of Chemistry at UCL. In all four cases, a major signal with five to six components were seen at mass/charge (*m/z*) ratios that corresponded to the monomer of FH with different charge states of +23 to +27 (Figure 7.6). For the FH Tyr402 allotype, the monomer molecular masses were determined to be 150 kDa in 140 mM ammonium acetate and 157 kDa in 1 M ammonium acetate (Figure 7.6 a, b). These results were replicated for the FH His402 allotype, where the masses were determined to be 156 kDa in 140 mM ammonium acetate, and 150 kDa in 1 M ammonium acetate (Figure 7.6 c, d). These masses agree well with those masses obtained from sedimentation velocity analyses for both FH allotypes (Figure 7.4), and for heterozygous FH (Chapter Five; Nan *et al.*, 2008a; Okemefuna *et al.*, 2009). The masses also agree well with the sequence-calculated value of 154 kDa for FH that was based on the glycosylation of eight of the nine sites in FH determined by mass spectrometry of FH peptides (Fenaile *et al.*, 2007). The variability of the individual mass determinations is attributed to the relatively large peak width that results from the comparatively high level of glycosylation in FH at eight locations (Fenaile *et al.*, 2007).

Dimer and trimer forms of FH were also observed in the spectra (Figure 7.6). For the FH Tyr402 allotype, the dimer and small amounts of the trimer were observed in 140 mM ammonium acetate, while only the dimer was observed in 1 M ammonium acetate. Their molecular masses were determined to be 307 kDa and 457 kDa, and 309 kDa respectively (Figure 7.6 a, b). The FH His402 allotype showed similar masses of 306

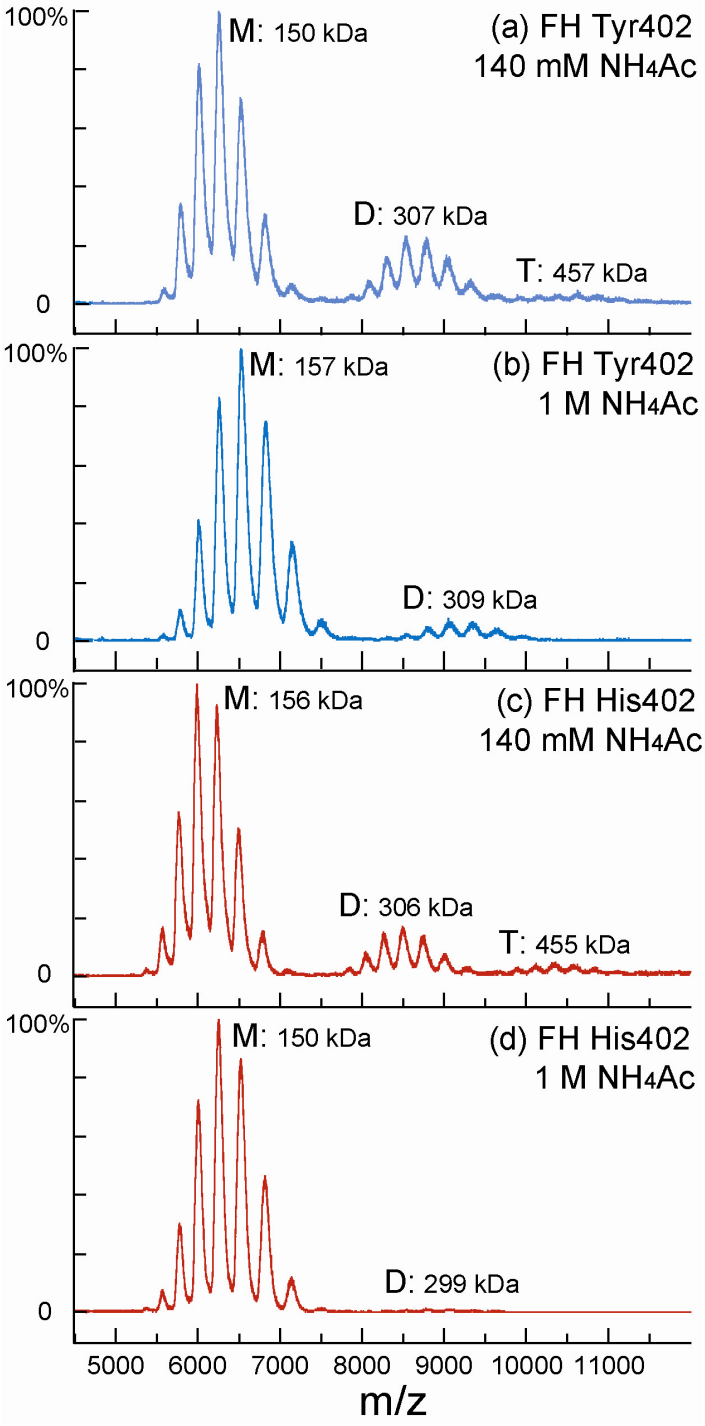

Figure 7.6 Mass spectrometry of the Tyr402 and His402 FH allotypes. The FH monomer, dimer and trimer peaks are marked by M, D and T followed by the measured molecular weight. (a) FH Tyr402 sample 013HH at 3.9 mg/ml (25.3 µM) in 140 mM ammonium acetate buffer pH 7.0. (b) FH Tyr402 sample 013HH at 4.4mg/ml (28.6 µM) in 1 M ammonium acetate buffer pH 7.0. (c) FH His402 sample 015LT at 3.9 mg/ml (25.3 µM) in 140 mM ammonium acetate buffer pH 7.0. (d) FH His402 sample 015LT at 3.6 mg/ml (23.4 µM) in 1 M ammonium acetate buffer pH 7.0.

kDa and 455 kDa in 140 mM ammonium acetate, and 299 kDa in 1 M ammonium acetate (Figure 7.6 c, d). Peak integrations showed that the proportions of monomer, dimer and trimer were comparable at 73%, 24% and 4% for FH Tyr402 and 76%, 17% and 6% for FH His402 in 140 mM ammonium acetate (Figure 7.6 a, c). At 4 mg/ml, a comparable amount of 37% dimer formation is predicted from the monomer-dimer K_D value of 28 μM in 137 mM NaCl HEPES buffer. The proportions of monomer and dimer were altered to 90% and 10% for FH Tyr402 and 98% and 2% for FH His402 in 1 M ammonium acetate (Figure 7.6 b, d). The relative reduction of dimer and the disappearance of trimer in 1 M ammonium acetate are consistent with the reduced FH self-association when the NaCl concentration is increased (Okemefuna *et al.*, 2009). No significant difference was detectable between the two allotypes, and higher oligomers beyond trimers were not detectable. In conclusion, the observation of dimer and trimer by mass spectrometry confirm the reversible existence of discrete monomer, dimer and trimer species of FH in solution, even with the concerns over possible non-specific interactions by mess spectrometry (Lane *et al.*, 2009).

7.2.4 Size-exclusion gel filtration of the two FH allotypes

Ultracentrifugation showed that heterozygous FH that was exposed to concentrations above 2 mg/ml forms irreversible high oligomers (Chapter Five; Nan *et al.*, 2008a). In order to evaluate FH oligomer formation with the homozygous proteins, size-exclusion chromatography was performed at the end of sedimentation velocity experiments after the proteins had sedimented to the bottom of the ultracentrifuge cell. The FH allotypes were resuspended into solution by gentle shaking. Size-exclusion chromatography on resuspended FH showed that the single homogenous FH peak between 65-75 ml was supplemented by additional peaks corresponding to FH oligomers that eluted earlier between 55-65 ml in all cases (Figure 7.7), and this is similar to the previous elution profile of heterozygous FH (Figure 5.6 a). Similar elution profiles were obtained at FH concentrations of 1.7 mg/ml (Figure 7.7 a) decreasing to 0.3 mg/ml (Figure 7.7 d). The main monomer peak was eluted at the same position in each case, indicating that no structural differences between allotypes were detectable by size-exclusion chromatography. The early elution between 55-65 ml showed that both FH allotypes formed oligomers. Even though the His402 allotype eluted slightly earlier in three loading concentrations (Figure 7.7 a, b, c), and the Tyr402 allotype eluted earlier in only

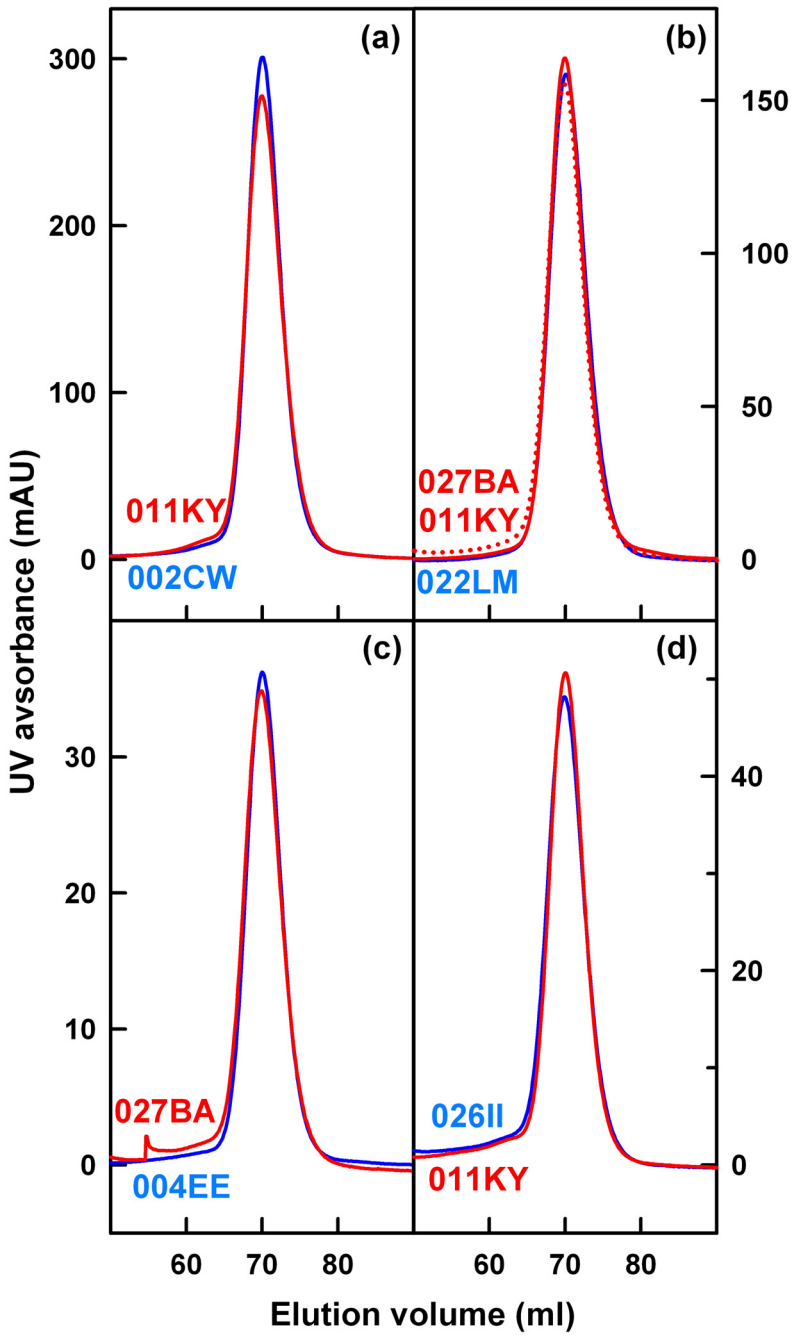

Figure 7.7 Size-exclusion gel filtration of nine homozygous FH preparations. Purified samples of the Tyr402 and His402 allotypes of FH at different concentrations were loaded onto a Superose™ 6 prep grade XK 16/60 column after sedimentation velocity experiments. Pairs of elution profiles for the two allotypes are overlaid at the same concentration of (a) 1.7 mg/ml; (b) 0.9 mg/ml; (c) 0.2 mg/ml; and (d) 0.3 mg/ml. The homozygous FH samples were identified by five-letter codes adjacent to their elution profiles (Table 7.1), and corresponded to the ultracentrifugation samples. The Tyr402 allotype is shown in blue and the His402 allotype is shown in red.

one loading concentration (Figure 7.7 d), the differences are too small to be significant. This approach also showed that both FH allotypes form similar amounts of oligomers.

7.2.5 X-ray scattering of the two FH allotypes

X-ray scattering is a diffraction method used to determine solution structures of macromolecules in random orientations (Section 4.2; Perkins *et al.*, 2008). Here, scattering was used to compare the overall structures of FH Tyr402 and FH His402. Two pairs of FH Tyr402 and FH His402 (Table 7.1) were freshly prepared and studied in two different beam sessions at the ESRF in five concentrations between 0.4 mg/ml (2.6 μM) and 3.3 mg/ml (21.4 μM) in HEPES buffer. Excellent signal-noise ratios were obtained with no detectable effect from radiation damage. Linear Guinier fits at low Q values (where $Q = 4\pi \sin\theta / \lambda$; 2θ = scattering angle; λ = wavelength) gave the radius of gyration R_G in satisfactory $Q.R_G$ ranges below 1.1 (Figure 7.8 a). R_G is the root mean square radius of scattering density. At larger Q values, the cross-sectional Guinier R_{XS} fits monitor the structural proximity between non-neighbouring SCR domains (denoted as $R_{XS\text{-}1}$) and neighbouring SCR domains (denoted as $R_{XS\text{-}2}$) (Aslam & Perkins, 2001). Both the $R_{XS\text{-}1}$ and $R_{XS\text{-}2}$ parameters were likewise obtained from linear fits within satisfactory $Q.R_{XS}$ ranges (Figure 7.8 b, c). This permitted comparative data analyses with errors for the four FH Tyr402 and FH His402 samples. In Guinier analyses, At 0.4 mg/ml, the R_G values were 7.54 nm and 7.97 nm for the two FH Tyr402 samples, and were 7.45 nm and 7.91 nm for the two FH His402 samples (Table 7.2). The $R_{XS\text{-}1}$ values were 2.35 nm and 2.36 nm for FH Tyr402, and 2.15 nm and 2.25 nm for FH His402. The $R_{XS\text{-}2}$ values were 1.77 nm and 1.76 nm for FH Tyr402, and 1.77 nm and 1.75 nm for FH His402. In conclusion, these comparisons showed that the R_G, $R_{XS\text{-}1}$ and $R_{XS\text{-}2}$ parameters at 0.4 mg/ml were similar for both allotypes, thus no conformational changes between the allotypes were detectable.

Both FH Tyr402 and FH His402 showed concentration dependences which were similar for the Guinier $I(0)/c$, R_G and $R_{XS\text{-}1}$ parameters, but no dependence was seen for the $R_{XS\text{-}2}$ parameter (Figure 7.9). These concentration dependences showed that reversible oligomerisation had occurred for both FH allotypes, the extent of which was similar to heterozygous FH. The $I(0)/c$ value is proportional to molecular mass for protein samples measured within a single beam time session. If the slopes in the linear fits of the $I(0)/c$

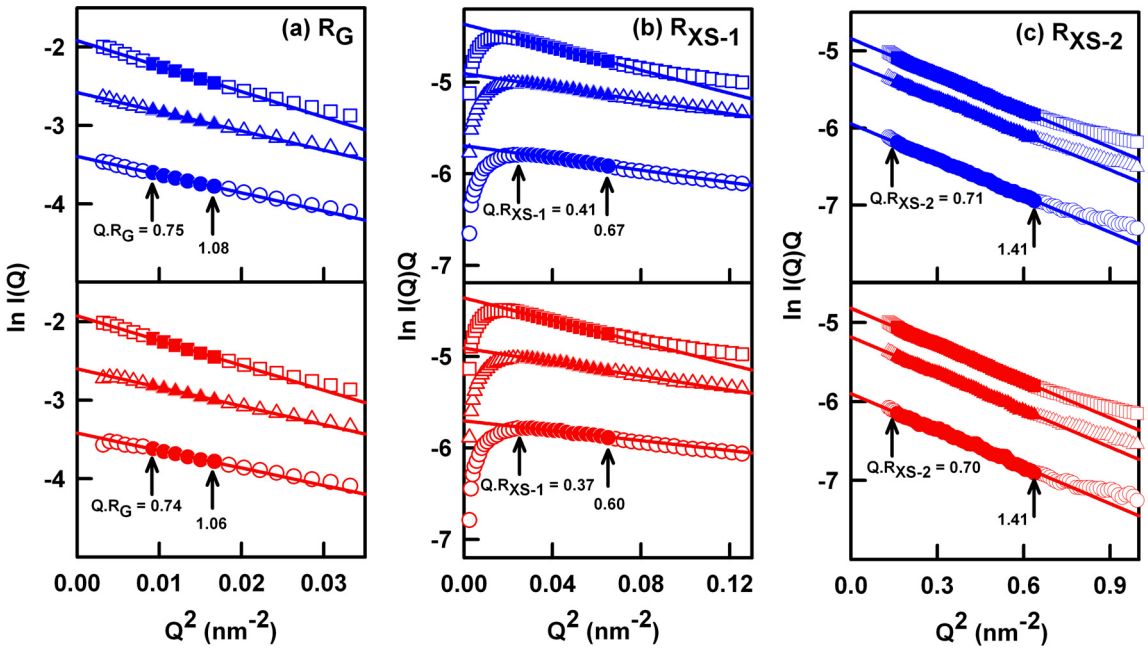

Figure 7.8 Guinier analyses for the X-ray scattering data of the FH Tyr402 and His402 allotypes. In the R_G and R_{XS} Guinier analyses, the open symbols represent the *I(Q)* data, the filled symbols correspond to the *I(Q)* data used to determine the R_G or R_{XS} values, and the straight line correspond to the best fit through those points. The fit ranges are arrowed. Data are shown for one Tyr402 allotype (020FM – blue) and one His402 allotype (028EL – red).

(a) R_G plots of ln I(Q) vs. Q^2 at low Q values for FH at concentrations of 1.1 mg/ml (O), 2.2 mg/ml (Δ) and 3.2 mg/ml (□). The *Q* fit range was 0.09 - 0.13 nm^{-1}.

(b) The corresponding cross-sectional R_{XS-1} fits of ln I(Q).Q vs. Q^2 are shown using a *Q* fit range of 0.16 - 0.26 nm^{-1}.

(c) The R_{XS-2} fits of ln I(Q).Q vs. Q^2 are shown using a *Q* range of 0.4 - 0.8 nm^{-1}.

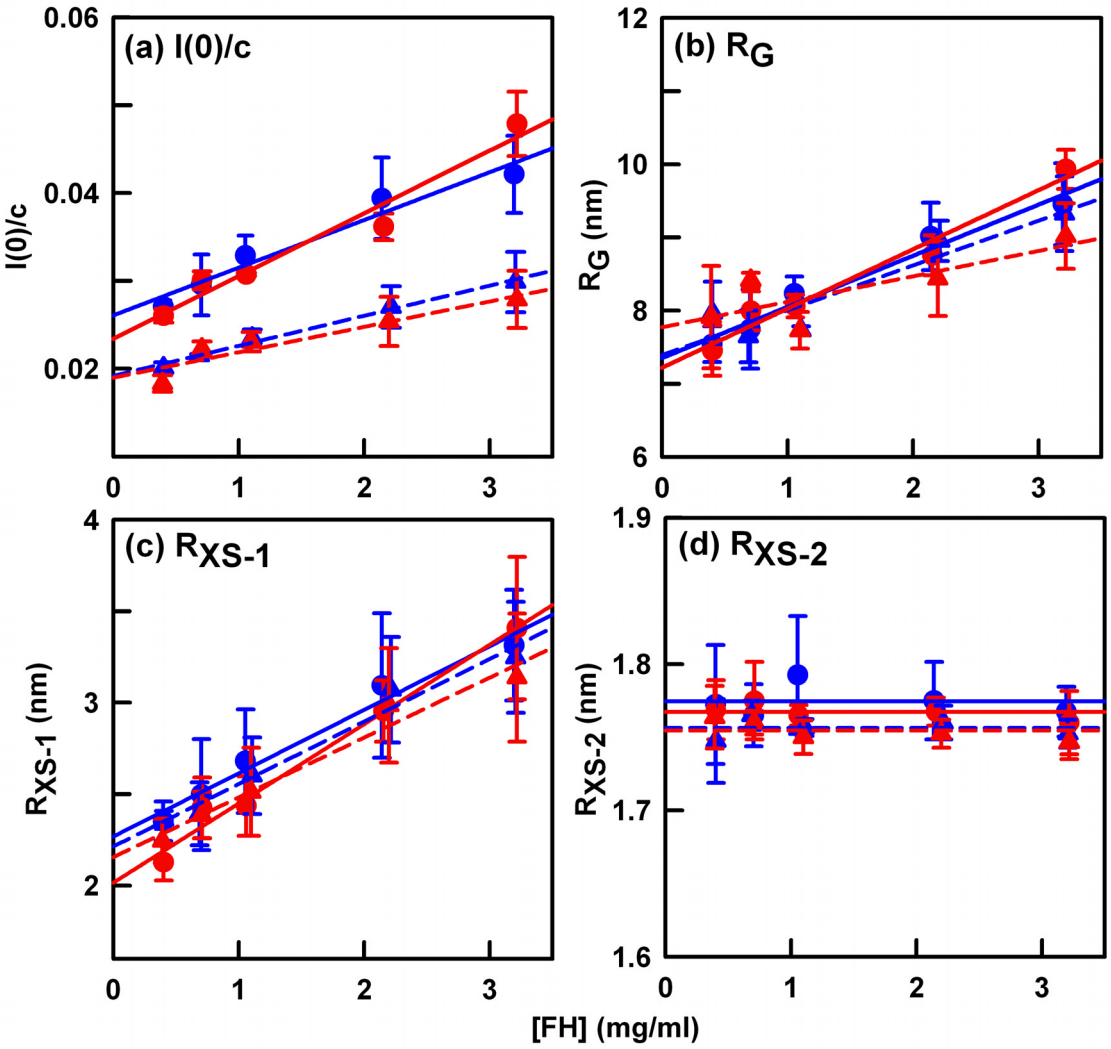

Figure 7.9 Concentration dependence of the Guinier parameters for the FH Tyr402 and His402 allotypes. The *I(0)/c*, R_G, R_{XS-1}, and R_{XS-2} data are shown for two different pairs of each of two allotypes of FH from 0.4 mg/ml to 3.3 mg/ml (Tyr402, 020FM ● and 022LM ▲; His402, 028EL ● and 032KO ▲). Each value was measured in quadruplicate, then averaged and fitted by linear regression except for panel (d) when the mean values were shown. Statistical error bars are shown where visible. In (a), the pairs of *I(0)/c* intensities were measured in two beam sessions, resulting in two different pairs of lines. In (b), the R_G values at zero concentration were 7.39 ± 0.25 nm and 7.35 ± 0.13 nm (Tyr402), and 7.22 ± 0.15 nm and 7.77 ± 0.27 nm (His402). In (c), the R_{XS-1} values at zero concentration were 2.21 ± 0.06 nm and 2.27 ± 0.06 nm (Tyr402), and 2.02 ± 0.06 nm and 2.15 ± 0.06 nm (His402). In (d), the averaged R_{XS-2} values were 1.77 nm and 1.77 nm (Tyr402), and 1.76 nm and 1.75 nm (His402).

parameters are assumed to reflect a monomer-dimer equilibrium (Figure 7.9 a), the resulting K_D values were estimated to be 16 (± 4) μM and 18 (± 2) μM for the two FH Tyr402 samples, and 11 (± 3) μM and 22 (± 8) μM for the two FH His402 samples. These K_D values are comparable with that of 28 μM for heterozygous FH from sedimentation equilibrium (Chapter Five; Nan *et al.*, 2008a), and the K_D values of 8 μM and 7 μM respectively for FH Tyr402 and FH His402 binding to heterozygous immobilised FH (Figure 7.1). Because the K_D values from scattering and ultracentrifugation are higher than those determined by SPR, this suggests that full-length FH dimerises more weakly when free in solution than when immobilised on a surface. The extrapolation of the R_G values to zero concentration resulted in R_G values of 7.22-7.77 nm for the allotypes (Figure 7.9 b). These values were lower than that of 8.90 ± 0.19 nm for heterozygous FH when extrapolated to zero concentration (Chapter Five; Nan *et al.*, 2008a). The $R_{XS\text{-}1}$ values at zero concentration were 2.02-2.27 nm, which is lower when compared to the previous extrapolated $R_{XS\text{-}1}$ value of 2.51 ± 0.06 nm for heterozygous FH (Chapter Five; Nan *et al.*, 2008a). The mean $R_{XS\text{-}2}$ value is 1.75-1.77 nm which is similar to the previous mean $R_{XS\text{-}2}$ value of 1.79 ± 0.01 nm for heterozygous FH (Chapter Five; Nan *et al.*, 2008a). The further reduction in R_G is attributed to reduced oligomerisation in the homozygous FH preparations; this most probably resulted from improved protein handling, and the use of a slightly increased Q range of fit to reduce the contribution of FH oligomers. The new R_G values are even lower than the originally-reported high R_G value of 11.1-11.3 nm for heterozygous FH, where the high values are attributed to the presence of aggregated FH (Aslam & Perkins, 2001). Overall, the lower R_G value of 7.22-7.77 nm for the two allotypes indicated that FH is even more folded-back in its SCR domain arrangement than previously thought.

The distance distribution function $P(r)$ is calculated from the full scattering curve *I(Q)* and reports the distances between all pairs of atoms within full-length FH (Figure 7.10; Section 4.2.5.2). The $P(r)$ curves gave another calculation of the R_G and *I(0)* values for full-length FH Tyr402 and FH His402 (Table 7.2) for comparison with the Guinier analyses at low Q. At 0.4 mg/ml, the Guinier and $P(r)$ R_G values showed good agreement, indicating self-consistency of the scattering curve across the measured Q range. The maximum dimension L of FH is deduced from the intercept of the *P(r)* curves with zero at large r. The r value of the maximum M in the $P(r)$ curve gives the

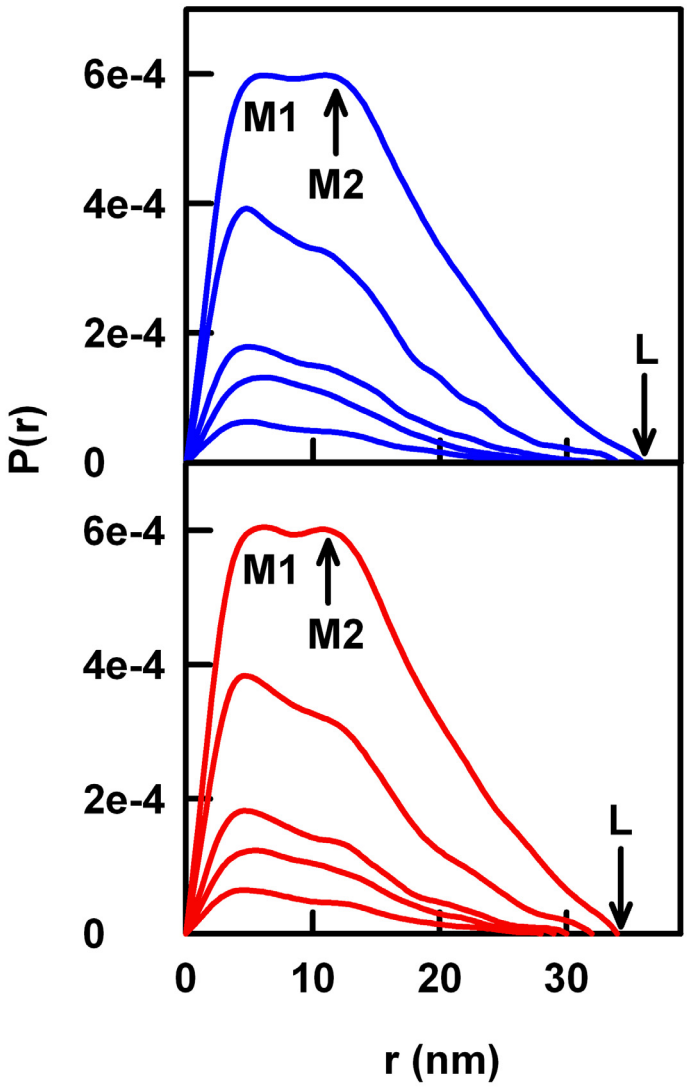

Figure 7.10 Distance distribution function *P(r)* analyses for the X-ray scattering data of the FH Tyr402 and His402 allotypes. The *P(r)* analyses are shown for one Tyr402 allotype (020FM – blue) and one His402 allotype (028EL – red) at five concentrations of 0.4 mg/ml, 0.7 mg/ml, 1.1 mg/ml, 2.2 mg/ml and 3.3 mg/ml from bottom to top.

most commonly occurring distance within the macromolecule. The two allotypes of FH between 0.4 mg/ml and 3.3 mg/ml showed similar concentration dependences in the appearances of their *P(r)* curves and *L* values (Figure 7.10). These appearances were comparable with that for heterozygous FH shown in Figure 5.3 (Chapter Five; Nan *et al.*, 2008a), and indicated the similar solution structures of the two allotypes. For the FH Tyr402 allotype, the *P(r)* curves show a concentration-independent peak *M1* at $r = 5.3 \pm 0.7$ nm, and a concentration-dependent second peak *M2* which was observed at $r = 11$ nm at 3.3 mg/ml. For the FH His402 allotype, *M1* was unchanged at 4.9 ± 0.4 nm and *M2* was likewise unchanged at 11 nm at 3.3 mg/ml. The dependence of peak *M2* on concentration showed that *M2* corresponds to FH oligomer formation. At 0.4 mg/ml, the *L* values were 28 nm and 29 nm for FH Tyr402, and 28 nm and 26 nm for FH His402 (Table 7.2). These *L* values were lower than that of 32 nm determined previously for heterozygous FH at 0.9 mg/ml in Figure 5.3 (Chapter Five; Nan *et al.*, 2008a), and this is attributable to a reduced level of FH oligomerisation at the lower concentrations. In conclusion, the *P(r)* curves confirm the reversible formation of FH oligomers in the concentration range up to 3.3 mg/ml, and that these oligomers were significantly reduced at 0.4 mg/ml.

7.2.6 Constrained scattering modelling of the two FH allotypes

Solution structures for the FH Tyr402 and FH His402 allotypes in 137 mM NaCl were determined by constrained scattering modelling. This procedure optimises the arrangement of 20 SCR domains joined by 19 conformationally-randomised linkers against the X-ray scattering curve. To be consistent, the same randomly generated 5,000 FH models used previously to model ionic strength effects on the FH conformation (Okemefuna *et al.*, 2009) were used here to evaluate the FH allotypes. This FH library was based on nine SCR homology models and 11 crystal or NMR structures for the SCR domains, which were linked together by randomised peptide linker conformations (Materials and Methods). Best-fit monomer conformations for FH Tyr402 and FH His402 were identified from trial-and-error searches of these 5,000 structures. The experimental X-ray curves used for fits corresponded to the lowest measured concentration of 0.4 mg/ml in order to reduce the estimated proportion of dimer to 8% (K_D = 28 μM). The comparisons of the R_G values with the *R*-factor (goodness of curve fit) (Figure 7.11) and $R_{XS\text{-}1}$ values (Figure 7.12) using two experimental curves for each

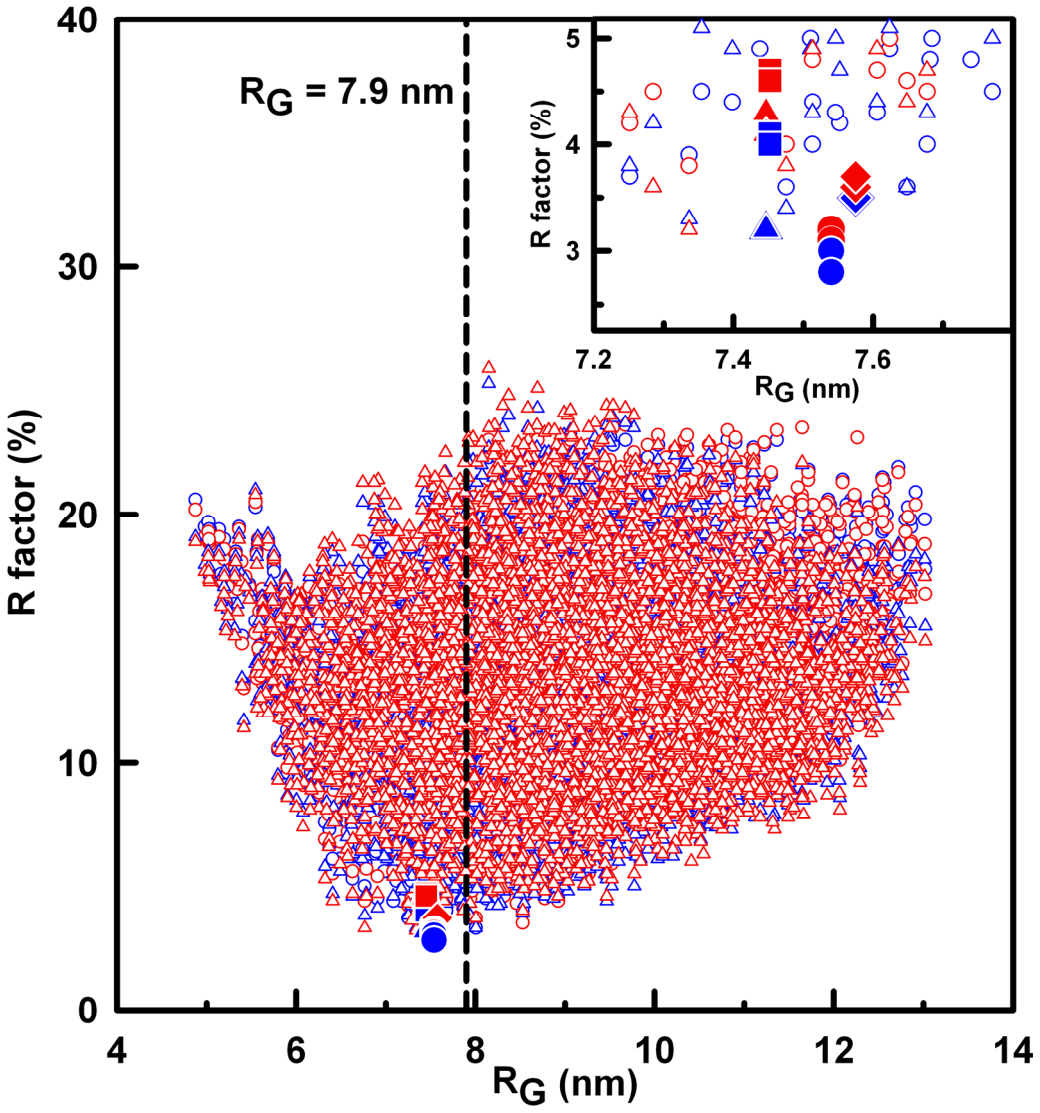

Figure 7.11 Constrained modelling searches to determine the solution structures of the FH Tyr402 and His402 allotypes by comparing of the 5,000 *R*–factor goodness-of-fit values with the R_G values. For each structure of 5,000 conformationally-randomised FH models, a R_G value was calculated, and a *R*-factor was generated by fitting the structure to two scattering curves for each of the Tyr402 (020FM, ○; 022LM, Δ; blue) and His402 (028EL, ○; 032KO, Δ; red) allotypes measured at 0.4 mg/ml. The vertical dashed line shows the averaged experimental R_G value. The fittings of the four best-fit models at the bottom are shown using filled symbols (Model 1, ●; Model 2, ▲; Model 3, ◆; Model 4, ■; Red for Tyr402 and blue for His402 allotype). These best-fit models are shown in more detail in the magnified view at the upper right corner.

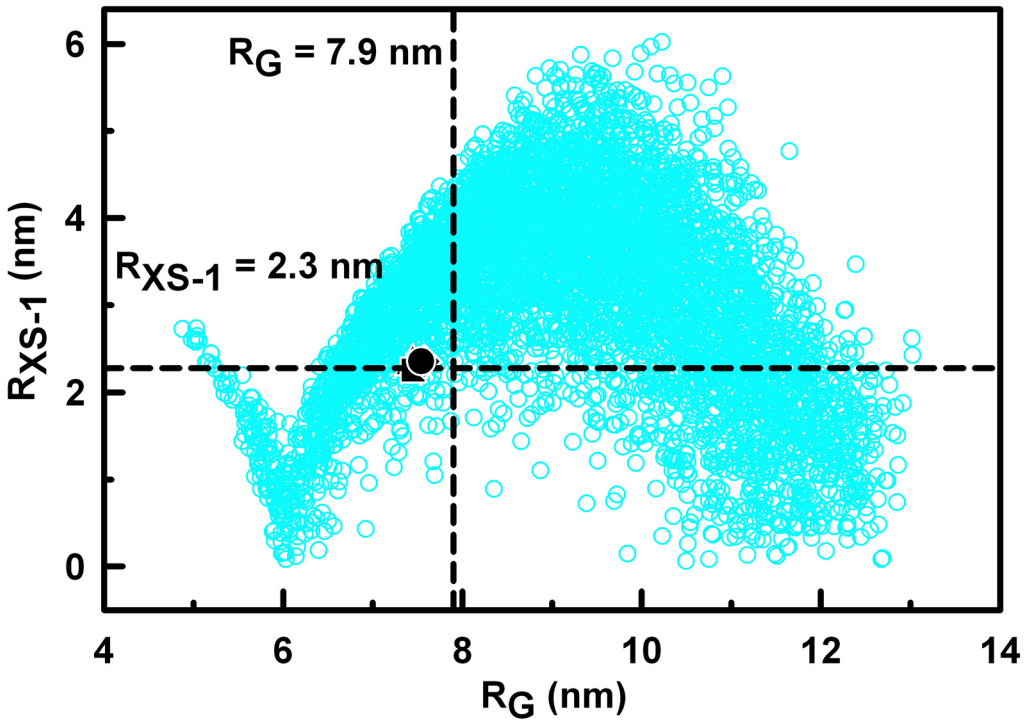

Figure 7.12 Constrained modelling searches to determine the solution structures of the FH Tyr402 and His402 allotypes by comparing of the 5,000 R_{XS-1} and R_G values**.** For each structure of 5,000 conformationally-randomised FH models, a R_G value and a R_{XS-1} value was calculated (denoted by cyan open symbol). The vertical dashed line indicates the average experimental R_G value, and the horizontal dashed line indicates the average experimental R_{XS-1} value measured at 0.4 mg/ml. The four best-fit models (Model 1, ●; Model 2, ▲; Model 3, ◆; Model 4, ■) are high-lighted in black.

FH allotype showed that the 5,000 models satisfactorily encompassed the mean experimental *P(r)* R_G of 7.90 nm and the mean Guinier $R_{XS\text{-}1}$ value of 2.28 nm (Table 7.2). The final best-fit structures for each FH experimental curve were selected using the criteria that they were within 10% of the experimental R_G and $R_{XS\text{-}1}$ values, and showed the lowest *R*-factor values. A family of eight best-fit structures were identified for each of the four FH curves (Table 7.2). Interestingly, four of these FH models occurred in all four fit analyses (Figure 7.13). The close similarity of the four best-fit families showed that the solution structures of the FH Tyr402 and FH His402 allotypes were indistinguishable.

The four best-fit models were all partially folded-back and bent in appearance. It is stressed that the best-fit models correspond to structures in which the 20 SCR domains are free to reorientate themselves. Because the method does not correspond to high resolution structure determinations, no specific inter-SCR proximity arrangements can be deduced. Unlike the 2001 fits (Aslam & Perkins, 2001) which revealed 31 best-fit structures with R-factors of 19 ± 3% and the 2009 fits (Okemefuna *et al.*, 2009) which revealed 17 best-fit with R-factors between 4.5-9.6%, the four best-fit structures now exhibited even lower *R*-factors between 2.8-4.7%. This reduction was attributed to improvements in experimental data acquisitions and a reduced level of FH oligomerisation. The R_G values of the four best-fit models were slightly lower than the observed R_G values. This difference is attributed to the effect of trace amount of FH dimer in the curve fit procedure that assumed a fully monomeric structure (Figure 7.11). The visual comparison between the experimental *I(Q)* curves for the best-fit Model 1 showed excellent visual agreements out to a *Q* value up to 1.5 nm^{-1} (Figure 7.13). Likewise the *P(r)* curves showed maxima *M* and maximum dimensions *L* that were in excellent agreements with the experimental values (Figure 7.13). These visual agreements were improved over the curve fitting of heterozygous FH in 2001 and 2009 (Figure 7.14) (Aslam & Perkins, 2001; Okemefuna *et al.*, 2009).

The $s^o_{20,w}$ values of the four best-fit FH models were calculated using HYDROPRO as an independent check of the scattering modelling (Table 7.2). The calculated $s^o_{20,w}$ values for the four common best fitting models (Figure 7.13) ranged between 5.38-5.54 S, where Model 1 gave a calculated $s^o_{20,w}$ values of 5.45 S. The calculated values agree well with the experimental values of 5.67 S, 5.66 S, 5.71 S, and 5.69 S for the two

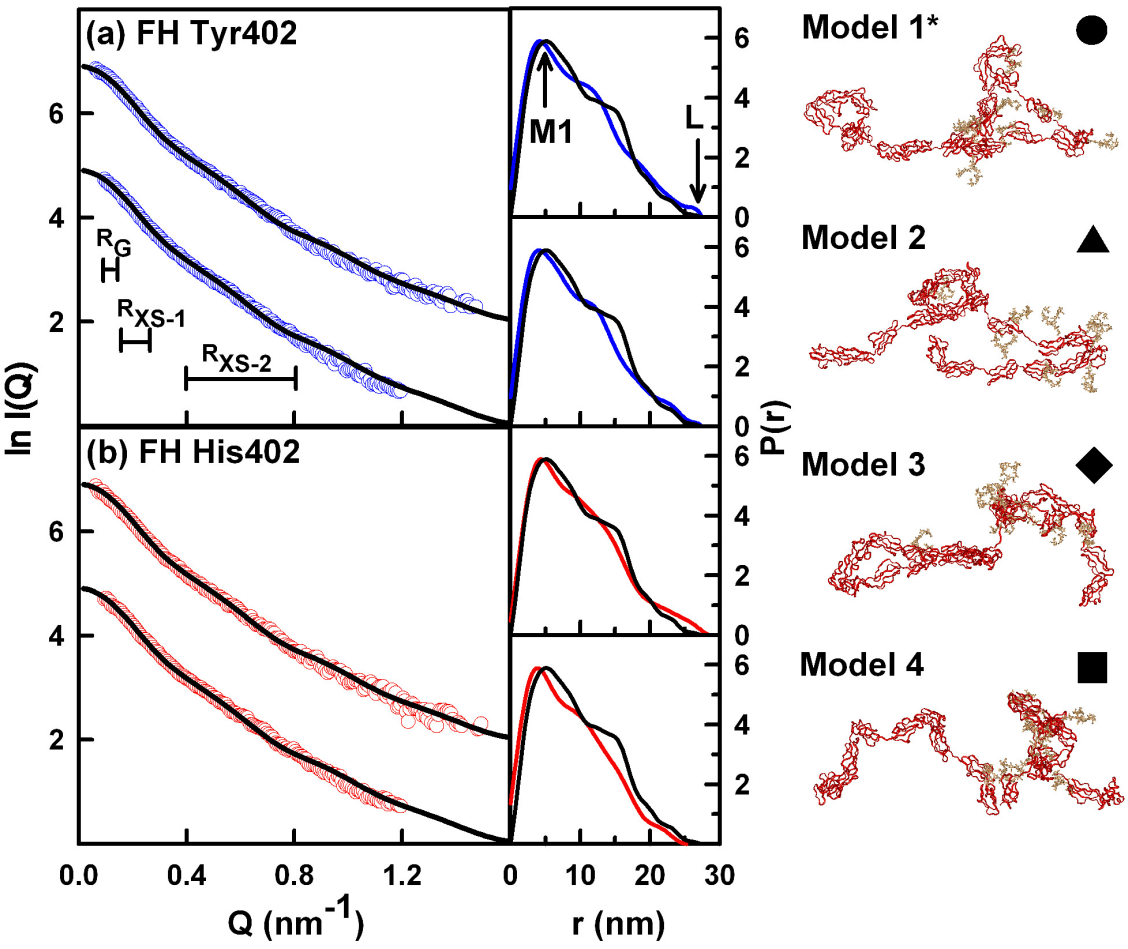

Figure 7.13 Four best-fit FH models for the X-ray scattering curve fit analyses. The left panel shows the X-ray scattering curve modelling fits, with the modelled curves in black and the experimental data in blue or red. The central panels compare the modelled *P(r)* curve (black) with the experimental *P(r)* curves (blue; red). The right panels show ribbon views of the four best-fit FH models that fit the curves for both allotypes and correspond to those highlighted in Figure 7.11 (Model 1, ●; Model 2, ▲; Model 3, ◆; Model 4, ■). The oligosaccharides are shown in orange. (a) Tyr402 FH at 0.4 mg/ml (upper, 020FM; lower, 022LM). (b) His402 FH at 0.4 mg/ml (upper, 028EL; lower, 032KO). The modelled curves in black in (a, b) are all calculated from Model 1.

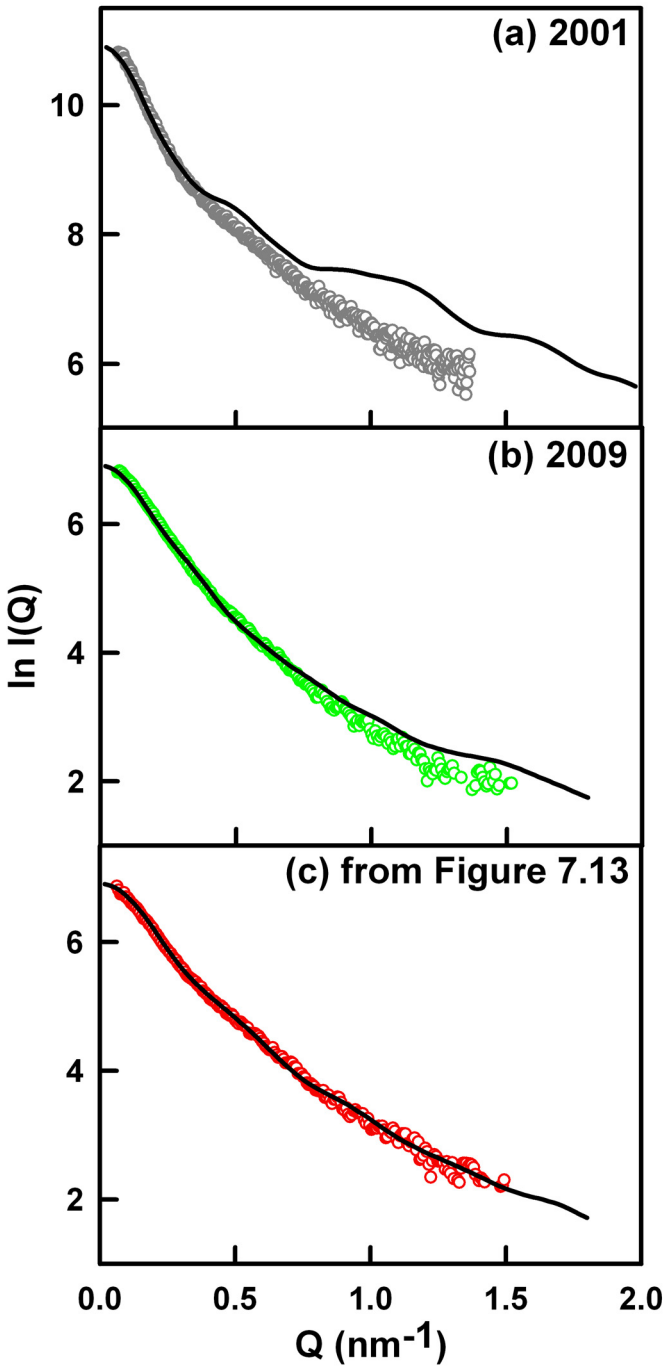

Figure 7.14 Comparison of the visual agreements between the experimental *I(Q)* curves for the best-fit model in the analyses for heterozygous FH in 2001 (a) (Aslam & Perkins, 2001), in 2009 (b) (Okemefuna *et al.*, 2009), and for homozygous FH from Figure 7.13 b (His402 FH sample 028EL at 0.4 mg/ml).

allotypes (Table 7.2). This agreement is acceptable given that the mean difference between the modelled and experimental values should be ± 0.21 S (Perkins *et al.*, 2009). The discrepancy between the calculated and experimental values is much reduced compared to the 2001 best-fit model that gave predicted $s^{o}_{20,w}$ values of 5.0 ± 0.1 S (Aslam & Perkins, 2001) and the 2009 fits that gave predicted $s^{o}_{20,w}$ values of 4.85–5.18 S (Okemefuna *et al.*, 2009). This better agreement is attributable to the reduced level of FH oligomers in the experimental X-ray scattering curves. The resulting scattering curve fits identified more compact FH models, which in turn resulted in the calculation of larger $s^{o}_{20,w}$ values that agreed better with experiment.

The improved FH monomer models permitted the sedimentation modelling of the dimer, trimer and tetramer forms of FH (Figure 7.15). Previous $s^{o}_{20,w}$ models for the FH oligomers had been based on too elongated a FH monomer model from the analyses in 2001 (Aslam & Perkins, 2001), and conformational changes in this model had been required in order to achieve agreement between the experimental and modelled $s^{o}_{20,w}$ values (Figure 5.8; Nan *et al.*, 2008a). Here, $s^{o}_{20,w}$ models were prepared from the Model 1 structure of Figure 7.13, in which the putative locations of SCR-7 and SCR-20 were assumed to comprise dimerisation sites (Fernando *et al.*, 2007; Okemefuna *et al.*, 2008). The K_D of 16 μM for SCR-16/20 self-association corresponds to stronger binding than the K_D of 40 μM for SCR-6/8 self-association, hence full-length FH is expected to dimerise at SCR-20 before SCR-7. The association of two SCR-20 domains gave a dimer with a modelled $s^{o}_{20,w}$ value of 7.60 S in good agreement with the experimental values of 7.57 S (Tyr402) and 7.69 S (His402), and no conformational change in the monomer structure was required (Figure 7.15). The addition of further conformationally-unmodified FH monomers at SCR-7 to this dimer gave trimer and tetramer models with modelled $s^{o}_{20,w}$ values of 9.42 S and 11.2 S respectively. These agreed well with the experimental values of 9.35 S (Tyr402) and 9.45 S (His402) for the trimer, and with the experimental values of 11.9 S (Tyr402) and 11.2 S (His402) for the tetramer (although the tetramer is less readily observed in Figure 7.5 a, b). These agreements support the observation of reversible FH equilibria that involve the SCR-6/8 and SCR-16/20 fragments.

Sedimentation modelling also supported the deduction of irreversible oligomer forms of FH (Figure 7.16). The addition of further reversibly-bound FH monomers at SCR-7 and

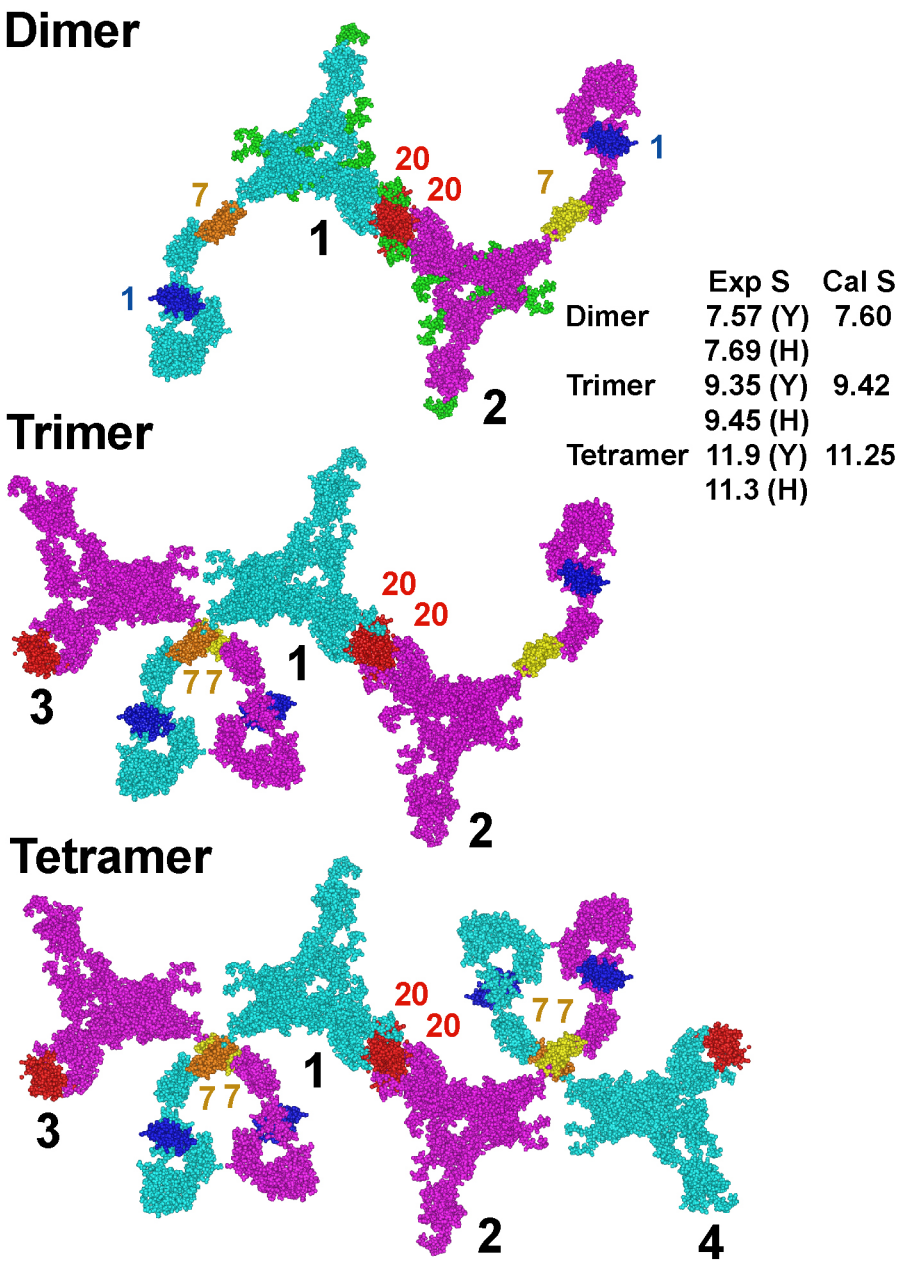

Figure 7.15 Sedimentation modelling of FH dimer, trimer and tetramer. The models were based on Model 1 from Figure 7.13. The reversible association of FH monomers is depicted, first to form the dimer by contacts at two SCR-20 domains (red), then followed by trimer and tetramer formation by contacts at two SCR-7 domains (orange/yellow). The experimental and modelled sedimentation coefficient values are shown to the right.

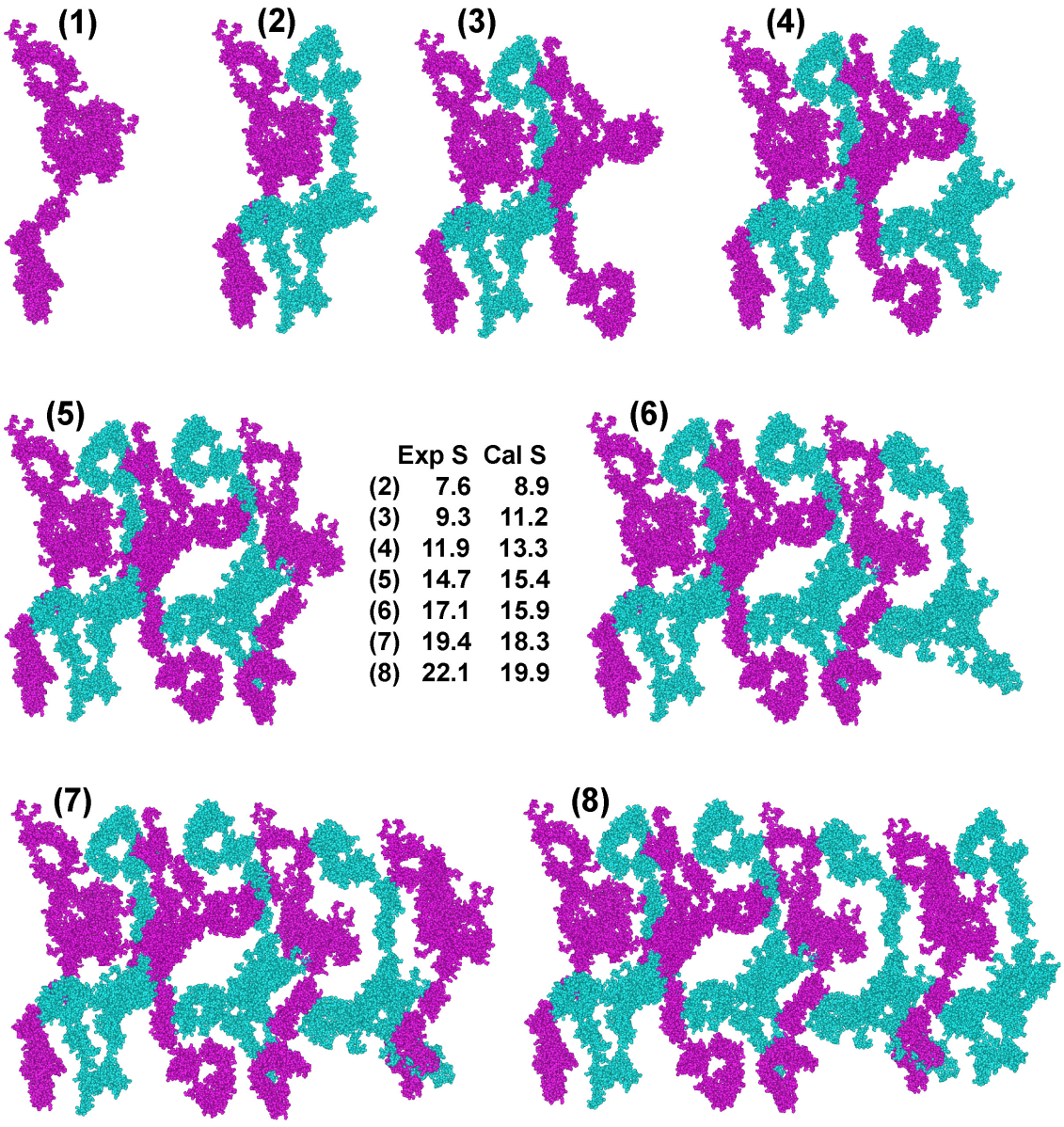

Figure 7.16 Sedimentation modelling of the irreversible higher oligomers of FH. The models were based on Model 1 from Figure 7.13. The irreversible association of FH monomers is depicted in side-by-side models that show more extensive contacts between the FH monomers (alternating cyan and purple). The experimental and modelled sedimentation coefficient values are tabulated at the centre.

SCR-20 to the models of Figure 7.15 gave models with $s^{o}_{20,w}$ values of 12–15 S that were too low compared to the observed values of 15–22 S. These "reversible" models were too elongated in shape. If irreversibility is the result of extra contacts between FH monomers, the FH oligomers are expected to become more compact in shape when forming aggregates. Modelling with conformationally-unmodified monomer structures that are arranged side-by-side to form aggregated structures resulted in modelled $s^{o}_{20,w}$ values of 8.9 S and 11.2 S for compact dimer and trimer structures respectively, up to 19.9 S for a compact octamer structure (Figure 7.16). This showed that the compact dimer and trimer peaks overlap with the reversible trimer and tetramer peaks respectively, and this would account for the intensity increase between 9-11 S in Figure 7.5 a, b. At larger S values, the peaks become more clearly resolved (Chapter Five; Nan *et al.*, 2008a; Okemefuna *et al.*, 2009). Given that the error in the experimental $s^{o}_{20,w}$ values are as large as 1 S, the agreement to within 1 S between the experimental and modelled values is considered to be satisfactory.

7.2.7 Fluid-phase activity assay of the two FH allotypes

In order compare the regulatory role of Tyr402 and His402 allotype of FH in solution, assays of fluid-phase haemolytically inactive C3 (C3u) cleavage by factor I and two allotypes of FH were performed (Section 6.2.4; Nan *et al.*, 2008b; Crossley & Porter, 1980). As mentioned in Section 2.3.5, previous fluid-phase activity assays were performed at significantly lower concentrations of FH than the 0.235-0.81 mg/ml (1.5–5.3 μM) observed *in vivo* (Crossley & Porter, 1980; Day & Sim, 1986; Bloom *et al.*, 2003; Tsiftsoglou & Sim, 2004). The assays in this chapter were performed with both allotypes of FH at a concentration of 0.3 mg/ml (1.9 μM) which is comparable with the physiological concentration and the concentration of heterozygous native FH used for previous activity assays (Section 6.2.4; Nan *et al.*, 2008b). The α-chain of C3u was cleaved by factor I in the presence of 0.3 mg/ml of each FH allotype to produce two major degradation fragments at apparent sizes of 45 kDa and 75 kDa (Figure 7.17 a). The cleavage rates of inactive C3 were not distinguishable between the Tyr402 and His402 allotypes of FH (Figure 7.17 b), and were similar to that of heterozygous FH (Figure 6.17). Therefore, the Tyr402His polymorphism does not affect the C3u cleavage function of FH in fluid phase. This result agrees well with the previous observation by

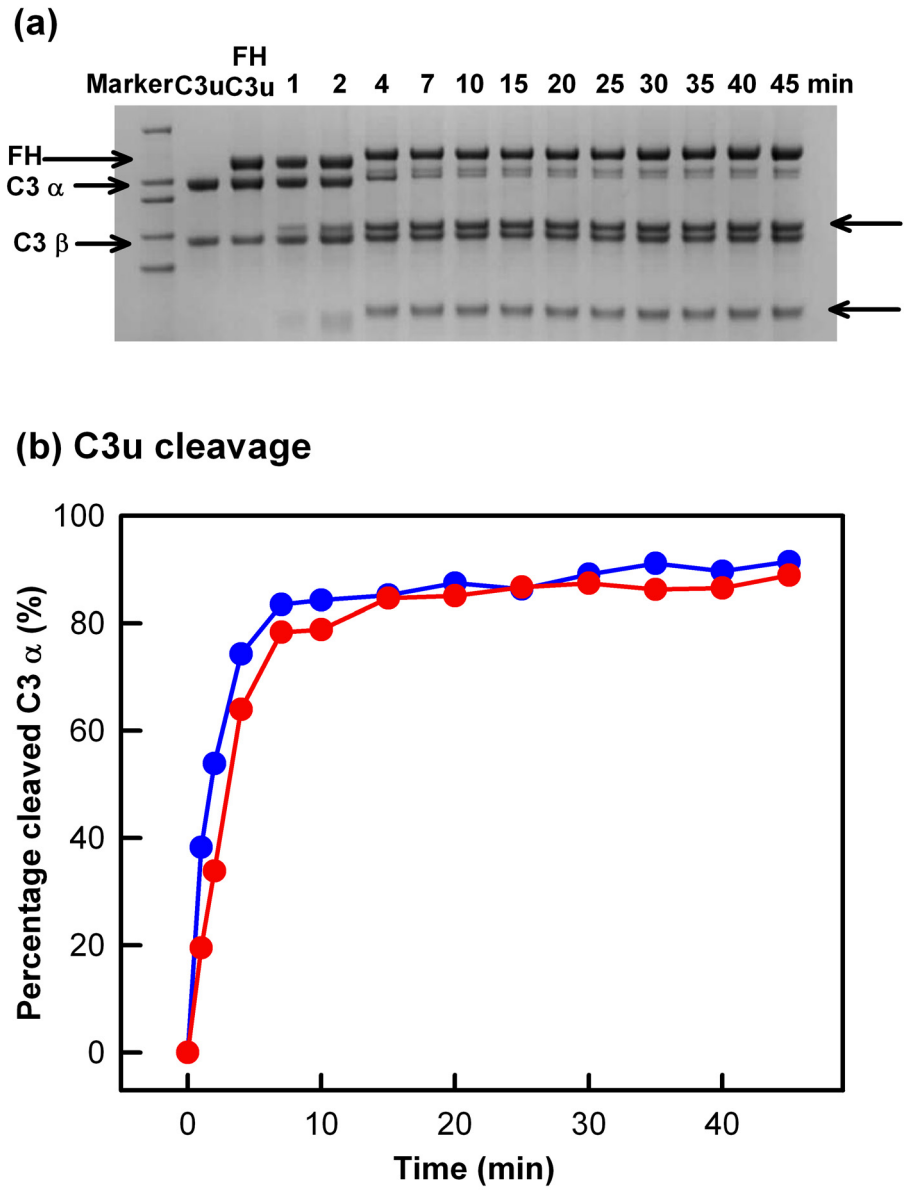

Figure 7.17 Cleavage of fluid phase C3u by FI and the two FH allotypes. (a) Reducing SDS-PAGE analysis of C3u cleavage by FI and FH Tyr402 allotype (013 HH). Lane 1, High Mark™ Prestained High Molecular Weight Standard; Lane 2, 0.3 mg/ml C3u as a control; Lane 3, 0.3 mg/ml C3u added with 0.3 mg/ml of FH Tyr402 allotype as another control; Lane 4-15 correspond to the reaction mixture that contains 0.3 mg/ml C3u, 0.3 mg/ml of FH Tyr402 allotype and 0.003mg/ml FI with the reaction time labelled. FH and the α-chain and β-chain of C3u are arrowed on the left, whereas the cleavage products of the C3u α-chain are arrowed on the right. (b) Comparison of the C3u α-chain cleavage rate by 0.003 mg/ml FI and 0.3 mg/ml FH Tyr402 allotype or His402 allotype. The percentage cleavage is shown as a function of time. The FH Tyr402 allotype (013HH) (Table 7.1) is denoted in blue, and the His402 allotype (015LT) (Table 7.1) is denoted in red.

SPR of the similar weak affinities to C3b for the two allotypes of FH SCR-6/8 (Schmidt *et al.*, 2008b), and the observation by ELISA of the similar bindings to C3b for the two allotypes of FH and FHL1 (Skerka *et al.*, 2007).

7.3 Materials and Methods

7.3.1 Protein purifications

Human blood was obtained from 48 genotyped healthy volunteers following ethical approval. The common Tyr402His and Ile62Val FH polymorphisms were genotyped by direct DNA sequencing of their PCR product by Dr Naushin Waseem and Prof. Shomi Bhattacharya. The PCR was performed with Extensor Hi-Fidelity PCR® Master Mix from ABgene following the manufacturer's protocol. Bidirectional sequencing of the PCR product was carried out with Big Dye Terminator v3.1 on a 3730 DNA Analyzer (Applied Biosystems, Cheshire, UK) at the UCL Institute of Ophthalmology. A total of seven homozygous FH Tyr402 and seven FH His402 allotypes were purified from appropriate genotyped plasma (Table 7.1), while wild-type FI was purified from a pool of just-outdated anonymised human plasma. Purifications utilised monoclonal affinity chromatography with MRC-OX23 Sepharose columns for FH and MRC-OX21 Sepharose columns for FI (Section 6.3.1; Nan *et al.*, 2008; Sim *et al.*, 1993). Bound homozygous FH and native FI were each eluted from the column using 3 M $MgCl_2$, pH 6.9, then each was dialysed into HEPES buffer (10 mM HEPES, 137 mM NaCl, pH 7.4) in the presence of 0.5 mM EDTA to remove Mg^{2+}. To avoid cross-contamination between different FH samples, the MRC-OX23 column was washed with guanidine (0.2 M Tris, 4 M guanidine-HCl, pH 8.0) between each preparation. Each FH and FI sample was passed through a Hitrap™ Protein G HP column to remove residual IgG contaminant. Non-specific aggregates and human serum albumin were removed by gel filtration on a Superose™ 6 prep grade XK 16/60 column. Protein concentrations were determined using absorption coefficients of 16.2 for FH (Tyr402) and 16.1 for FH (His402) (1%, 280 nm, 1 cm path length), revised in the light of its known glycosylation (Okemefuna *et al.*, 2009), and that of 12 for FI (Ullman *et al.*, 1998). After sedimentation velocity experiments on the purified FH allotypes, the proteins were re-passed through the Superose™ 6 prep grade XK 16/60 column in order to analyse the presence of FH oligomers (Figure 7.1).

Native C3 was purifed from fresh plasma from the author using slightly modified methods described previously (Dodds *et al.*, 1993). The purification utilised a 20 ml Q-Sepharose^{TM} fast flow anion-exchange column (Amersham Biosciences, GE Healthcare, Uppsala, Sweden), followed by a MonoQ 5/50 GL anion-exchange column (Pharmacia GE Healthcare, Uppsala, Sweden) with better resolution. Haemolytically inactive C3 (C3u) was obtained by incubating native C3 in 200 mM hydrazinc at 37°C for 1 h (Section 6.3.1; Dodds *et al.*, 1993). The purity of C3u was checked by using reducing SDS-PAGE (Figure 7.17 a), and the protein concentration was determined using the absorption coefficient of 9.4 for C3u (1%, 280 nm, 1 cm path length) (Li *et al.*, 2010).

FH SCR-6/8 was expressed and purified following previous procedures (Fernando *et al.*, 2007) (A. Miller and S. J. Perkins, unpublished data). The recombinant SCR-6/8 Tyr402 was expressed in BL21 (DE3) *E. coli* cells using a pET21ab vector system, while SCR-6/8 His402 was expressed in BL21 (DE3)pLysS *E. coli* cells using a pET14b vector system. The protein was extracted from inclusion bodies and solubilised, and the refolded protein was passed through a Hitrap^{TM} 5 ml Heparin HP column equilibrated in Tris buffer (50 mM Tris, 150 mM NaCl, 1 mM EDTA, pH 7.4). The bound protein was washed with Tris buffer and was eluted with up to 1 M NaCl in Tris buffer. The protein concentration of FH SCR-6/8 was determined using absorption coefficients of 22.7 for SCR-6/8 Tyr402, and 22.1 for SCR-6/8 His402 (1%, 280 nm, 1 cm path length). Proteins were dialysed into HEPES buffer for experiments, and their integrity was routinely checked by SDS-PAGE before and after scattering and ultracentrifugation.

7.3.2 Surface plasmon resonance data

The binding of one pair of FH Tyr402 and His402 allotypes (Table 7.1) to immobilised heterozygous FH and of the FH SCR-6/8 Tyr402 and His402 allotypes to immobilised FH SCR-6/8 were performed using a Biacore X100 instrument with version 1.1 of its evaluation software (GE Healthcare, Uppsala, Sweden). Heterozygous FH was coupled to a carboxymethylated dextran (CM5) research grade sensor chip (Okemefuna *et al.*, 2010). Each of the FH SCR-6/8 allotypes were coupled to a carboxymethylated dextran (CM4) research grade sensor chip with a lower degree of carboxymethylation. Both

procedures utilised a standard amine coupling procedure according to the manufacturer's protocol. Heterozygous FH (20 µg/ml) or FH SCR-6/8 (10 µg/ml) in 10 mM acetate buffer, pH 5.5 (FH) was injected over flow cell 2 to reach a maximum response of 150 or 400 resonance units (RU) immobilised on the surface. A control surface cell was prepared identically on flow cell 1 but without protein immobilisation. Equilibrium analyses were performed at 25º C using the appropriate Biacore X100 wizards at a flow rate of 30 µl/min. The running buffer was HEPES buffer. FH Tyr402 was injected for 180 sec at six concentrations between 0.1-1.5 mg/ml (0.65-9.74 µM). FH His402 was injected at six concentrations between 0.1-1.8 mg/ml (0.65-11.69 µM). FH SCR-6/8 Tyr402 was injected for 150 sec over the CM4 chip immobilised with 150 RU of either the Tyr402 or the His402 allotype at concentrations of 0.1-0.8 mg/ml (5-40 µM), and over the CM4 chip bound with 400 RU of His402 at concentrations of 0.04-0.32 mg/ml (5-15 µM). FH SCR-6/8 His402 was injected over the Tyr402 CM4 chip at concentrations of 0.1-0.6 mg/ml (5-28 µM), and over the CM4 chip immobilised with 150 RU His402 at concentrations of 0.1-0.5 mg/ml (5-22 µM), and over the CM4 chip with 400 RU His402 at 0.04-0.32 mg/ml (2-14 µM). For the FH SCR-6/8 analyses, the CM4 chips were used with 0.3 mg/ml non-specific binding (NSB) reducer added to each sample to reduce the non-specific binding to dextran surfaces. Regeneration after each run was achieved by pulsing with 10 mM sodium acetate buffer, 5 M NaCl, 0.05 mM EDTA, pH 7.0 across both flow cells twice for 45 sec. The maximum binding response value in each run was fitted to a steady state 1:1 affinity model.

7.3.3 Sedimentation velocity data

FH data were obtained on two Beckman XL-I instruments equipped with AnTi50 and AnTi60 rotors. Sedimentation velocity experiments were performed at 20^{o}C at rotor speeds of at rotor speeds of 50,000 r.p.m and 60,000 r.p.m. in two-sector cells with column heights of 12 mm for five FH Tyr402 samples at 0.5 mg/ml, 1.1 mg/ml and 2.1 mg/ml (3.2-13.6 µM), and again for five FH His402 samples, all in HEPES buffer (Table 7.1). Data analyses were performed using SEDFIT (version 11.71) (Schuck, 1998; Schuck, 2000). The size-distribution analyses *c(s)* that provided shape and size data were performed using direct boundary Lamm fits of up to 300 scans using a fixed resolution of 200, and floated the meniscus, the bottom of the cell, the baseline and the average frictional ratio *f/fo* (initial value 1.781), until the overall root mean square

deviation and agreement between the observed and calculated sedimentation boundaries were satisfactory (Figure 7.2). The percentage fraction of oligomers in the total loading concentration was derived using the *c(s)* integration function. Other details are described elsewhere (Section 4.1.2; Nan *et al.*, 2008; Okemefuna *et al.*, 2009).

7.3.4 Mass spectrometry data

Mass spectra were acquired on a LCT orthogonal time-of-flight instrument modified for high mass operation and equipped with a Z-spray nanoflow source (Waters, Manchester, UK). The following instrumental parameters were used: capillary voltage 1.7 kV, cone voltage 80 – 120 V, cone gas 100 L/h. Mass spectra were analysed using Mass Lynx and Data-Explorer software. Purified FH samples were concentrated to a final concentration of about 4 mg/ml (26 μM), and then dialysed overnight into 140 mM or 1 M ammonium acetate at pH 7.0 for measurement the next day. One pair of FH Tyr402 and one FH His402 allotype (Table 7.1) were analysed in both buffers. These mass spectrometry experiments were performed by Dr Adam MacKay in the Department of Chemistry at UCL.

7.3.5 X-ray scattering data

X-ray scattering data were acquired in two beam sessions on Instrument ID02 (Narayanan & Bosecke, 2001) at the European Synchrotron Radiation Facility (Grenoble, France) with a ring energy of 6.0 GeV and operating in four-bunch mode. Storage ring currents were 30-44 mA and 68-89 mA. The sample-detector distances were 2 m and 3 m respectively. Potential radiation damage was eliminated by the continuous movement of the sample in its capillary flow cell during beam exposure, the use of 10 time frames of duration between 0.1 sec and 0.5 sec each during each acquisition, and on-line checks for the absence of radiation damage at low Q. Two FH Tyr402 and two FH His402 allotypes were each studied at five concentrations between 0.4 mg/ml (2.6 μM) and 3.3 mg/ml (21.4 μM) to compare their self-association properties. All measurements were done in HEPES buffer. Other details including the data reduction are described elsewhere (Section 4.2; Fernando *et al.*, 2007; Okemefuna *et al.*, 2008).

In a given solute-solvent contrast, the radius of gyration R_G is the root mean square radius of scattering density if the internal inhomogeneity of scattering densities within the protein has no effect. Guinier analyses at low Q gives the R_G, and the forward scattering at zero angle $I(0)$ (Glatter & Kratky, 1982):

$$\ln I(Q) = \ln I(0) - R_G^2 Q^2/3.$$

This expression is valid in a $Q.R_G$ range up to 1.5. If the structure is elongated, the mean radius of gyration of cross-sectional structure R_{XS} and the mean cross-sectional intensity at zero angle $[I(Q)Q]_{Q\to 0}$ is obtained from:

$$\ln [I(Q)Q] = \ln [I(Q)Q]_{Q\to 0} - R_{XS}^2 Q^2/2.$$

The R_G and R_{XS} analyses lead to the triaxial dimensions of the macromolecule if the structure can be represented by an elliptical cylinder, where $L = \sqrt{12 \cdot (R_G^2 - R_{XS}^2)}$ and L is its length (Glatter & Kratky, 1982). The R_G and R_{XS} analyses were performed using an interactive PERL script program SCTPL7 (J. T. Eaton and S. J. Perkins, unpublished software) on Silicon Graphics OCTANE Workstations. Indirect transformation of the scattering data $I(Q)$ in reciprocal space into real space to give the distance distribution function $P(r)$ was carried out using the program GNOM (Semenyuk & Svergun, 1991):

$$P(r) = \frac{1}{2\pi^2} \int_o^\infty I(Q)\, Qr \sin(Qr)\, dQ$$

$P(r)$ corresponds to the distribution of distances r between volume elements. For this, the X-ray $I(Q)$ curve utilised up to 207 data points for Q between 0.06 nm^{-1} and 1.50 nm^{-1} for 0.4 mg/ml FH, and increasing up to 308 data points for Q between 0.06 nm^{-1} and 2.10 nm^{-1} for 3.3 mg/ml FH. Other details are described elsewhere (Nan *et al.*, 2008; Fernando *et al.*, 2007; Okemefuna *et al.*,2008; Aslam & Perkins, 2001).

7.3.6 Constrained modelling procedure

The original constrained modelling of the 20 SCR domains in FH used NMR structures for three SCR domains and homology models for the remaining 17 SCR domains (Aslam & Perkins, 2001). Here the remodelling of FH for this study and its accompanying study was based on NMR and crystal structures for 11 SCR domains and 9 improved SCR homology models for the remainder. NMR structures were used for SCR-5 (Barlow, *et al.*, 1992), SCR-15 (PDB codes 1hfi), SCR-16 (PDB codes 1hcc)

(Barlow, *et al.*, 1993) and SCR-1/3 (PDB codes 2rlp and 2rlq) (Hocking, *et al.*, 2008). Crystal structures were used for SCR-19/20 (PDB code 2g7i) (Jokiranta, *et al.*, 2006) and SCR-6/8 (PDB code 2uwn) (Prosser, *et al.*, 2007). The homology models for the remaining SCR domains were taken from the website http://www.fh-hus.org (Saunders, *et al.*, 2006). The FH sequence numbering starts from the N-terminus of the 18-residue signal peptide, and not that of the mature protein. Eight biantennary disialylated glycans were added to Asn529 in SCR-9, Asn719 in SCR-12, Asn802 in SCR-13, Asn822 in SCR-14, Asn882 and Asn911 in SCR-15, Asn1029 in SCR-17 and Asn1095 in SCR-19 (Fenaille *et al.*, 2007). Libraries of 1,000 randomised conformations were generated in extended β-strand conformations for each of the twenty peptides that corresponded to the N-terminus (19-ED-20) and the 19 inter-SCR linkers using INSIGHT II 98.0 molecular graphics software (Accelrys, San Diego, CA, USA) on Silicon Graphics OCTANE Workstations. This procedure followed Randomized-3 search in the original constrained modelling of FH which gave satisfactory results (Aslam & Perkins, 2001). One conformation was randomly selected from each library for each linker in order to join the 20 SCR domains to assemble 5,000 full FH models. Further details are given elsewhere (Aslam & Perkins, 2001; Gilbert *et al.*, 2005).

Each full FH molecular model was used to calculate its X-ray scattering curve for comparison with two different experimental curves for each FH allotype (Table 7.1). A cube side length of 0.498 nm in combination with a cutoff of 3 atoms was used to convert the coordinates into Debye sphere models with 1554 spheres that corresponded to the unhydrated structure, and the addition of the hydration shell gave an optimal total of 2074 hydrated spheres. The X-ray scattering curve *I(Q)* was calculated using the Debye equation adapted to spheres. Details are given elsewhere (Okemefuna *et al.*, 2009). Steric overlap between the SCR domains in the models was used to filter out unacceptable models, where models showing less than 95% of the required total *N* of 1554 unhydrated spheres and 2074 hydrated spheres were discarded. Next, the X-ray R_G and $R_{XS\text{-}1}$ values calculated from the modelled curves in the same *Q* ranges used for the experimental Guinier fits were used to select models that were within 10% of the experimental R_G and $R_{XS\text{-}1}$ parameters. Models that passed the *N*, R_G and $R_{XS\text{-}1}$ filters were then ranked using a goodness-of-fit *R* factor defined by analogy with protein crystallography. Sedimentation coefficients $s^0_{20,w}$ were calculated directly from the atomic coordinates in the HYDROPRO shell modelling program using the default value

of 0.31 nm for the atomic element radius for all atoms to represent the hydration shell (Garcia de la Torre *et al.*, 2000).

7.3.7 Protein Data Bank accession number

The four best-fit FH models have been deposited in the Protein Data Bank with the accession codes 3n0j.

7.3.8 Fluid-phase activity assays

The reaction mixtures contained 0.3 mg/ml of Tyr402 or His402 allotype of FH, 0.3 mg/ml C3u and 0.003 mg/ml factor I were incubated in a water bath at 37 °C. The functions of one FH Tyr402 allotype sample (013HH) and one FH His402 allotype sample (015LT) were tested. At timed intervals, 5 µl aliquots were removed for reducing SDS-PAGE analyses using NuPAGE® Novex® 4-12% Bis-Tris Mini Gel. Two controls were used, namely 0.3 mg/ml C3u; and 0.3 mg/ml C3u and 0.3 mg/ml FH. The C3 α-chain band densities from SDS-PAGE were measured using the gel analysis system SYNGENE (Synoptics Ltd., Cambridge, UK). The C3 α-chain cleavage was referenced to the averaged density of the uncleaved bands in the controls.

7.4 Conclusions

A functional understanding of FH is complicated by its multivalency, its relative abundance in serum, and its weak interactions with ligands (Perkins *et al.*, 2010a; Perkins *et al.*, 2010b). The major human physiological and pathophysiological ligands of FH include (i) its self-association properties, and its interactions with (ii) C3b and C3d, (iii) heparin, (iv) CRP, and (v) zinc. The unravelling of these five interactions requires knowledge of the K_D values in combination with the use of appropriate buffers and protein concentrations. The study in Chapter Seven clarifies the self-association properties of FH using purified homozygous proteins (Table 7.1). This study showed that the full-length FH Tyr402 and FH His402 allotypes show similar self-association properties both at surfaces and in solution, and indistinguishable structures in solution. However surface-immobilized SCR-6/8 His402 shows a higher level of self association

than SCR-6/8 Tyr402. There is no indication that the Ile62Val polymorphism (Table 7.1), another AMD-associated polymorphism in SCR-1, is relevant for self-association or the FH structure. The formation of FH dimer and trimer is shown to be reversible, together with the presence of irreversible higher oligomers. The folded-back FH solution structure of its monomer is more compact than previously believed, as the maximum length of monomeric FH was determined to be 28 nm. A relatively inflexible monomer structure is able to account for the FH oligomers seen by ultracentrifugation. The biological meaning of FH self-association in terms of sub-RPE deposit formation and AMD is discussed below. For example, an understanding of FH self-association was essential to show that heterozygous FH and native CRP interacted with each other. Ultracentrifugation showed that the FH oligomers were eliminated when native CRP was added (Okemefuna *et al.*, 2010). In the present study, the K_D value of 7-8 μM measured for the self-association of the two FH allotypes by SPR is larger than the corresponding K_D value of 4.2 μM for the FH-CRP interaction by SPR (Okemefuna *et al.*, 2010). This difference confirms that the FH-CRP interaction is stronger and will block FH oligomer formation.

FH oligomer formation is relevant for a proper interpretation of functional assays and the physiological role of FH. The weak self-association of FH is now established through a series of investigations. The dimerisation of heterozygous FH was originally proposed from molecular weights of 250-320 kDa that were determined by X-ray and neutron scattering Guinier fits at high 1-11 mg/ml concentrations, although these Guinier analyses were approximate ones (Perkins *et al.*, 1991). Initial electron microscopy, gel filtration and ultracentrifugation studies suggested that FH is only monomeric (DiScipio, 1992). Further X-ray and neutron scattering of heterozygous FH showed that this was largely monomeric and its folded-back solution structure could be modelled by constrained scattering modelling, although the final Q range of the curve fit was quite limited (Figure 7.14) (Aslam & Perkins, 2001). However FH fragments revealed dimeric bands by SDS-PAGE, and FH self-interactions were observed by SPR (Jokiranta *et al.*, 2000; Oppermann *et al.*, 2006). In addition, ultracentrifugation showed that the SCR-6/8 and SCR-16/20 fragments displayed monomer-dimer equilibria with K_D values of 40 μM for SCR-6/8 His402 and 16 μM for SCR-16/20 (Fernando *et al.*, 2007; Okemefuna *et al.*, 2008). The presence of at least two different dimer sites within FH suggested that FH molecules could form “daisy-chains” at alternating pairs of dimer

sites at high concentrations (Figure 7.15). This hypothesis was initially verified by ultracentrifugation and scattering studies of heterozygous FH, when oligomers that contained 2-9 subunits were observed in *c(s)* distribution analyses at high FH concentrations (Chapter Five; Nan *et al.*, 2008a). In the present study, the availability of homozygous FH Tyr402 and FH His402 showed that FH oligomers with 2-9 subunits existed for each of these by ultracentrifugation, and did not depend on Tyr402His or Ile62Val, the two major AMD-associated polymorphisms (Figure 7.5 a). The existence of FH dimer and trimer forms was supported independently by mass spectrometry (Figure 7.6). Given the reversibility of the dimer and trimer forms of FH with its monomer (Chapter Five; Nan *et al.*, 2008a), their sedimentation coefficients could be modelled on the basis of previously-observed reversible associations at SCR-7 and SCR-20 (Figure 7.15). The observation of small amounts of irreversible higher oligomers is best explained by the indefinite compact self-association of FH monomers (Figure 7.16).

The AMD-risk Tyr402His polymorphism corresponds to a surface residue located in the SCR-7 domain. Previously, ultracentrifugation showed that FH SCR-6/8 His402 dimerises slightly more than FH SCR-6/8 Tyr402 (Fernando *et al.*, 2007), and this result was confirmed in this chapter by SPR (Figure 7.3). This difference indicates that the SCR-6/8 dimerisation site is close to residue 402. Because SCR-7 also possesses the heparin and CRP binding sites in FH, the Tyr402His polymorphism is implicated with these FH interactions. For the full-length FH allotypes, four different comparisons consistently indicated no significant difference in their self-association. This lack of difference in full-length FH is explained by the somewhat greater strength of dimer formation at SCR-20 and not at SCR-7 (Fernando *et al.*, 2007; Okemefuna *et al.*, 2008). For the two FH allotypes, the K_D values for a monomer-dimer equilibrium model were 7-8 μM by SPR, and 11-22 μM by scattering. The lower K_D values by SPR than by scattering indicated a strengthened self-association for immobilised FH, presumably for reason of local concentration effects and a more complex self-association process than that represented by a monomer-dimer equilibrium. Given that FH occurs in serum at 0.235-0.810 mg/ml (Saunders *et al.*, 2006), the scattering K_D values indicate that 8-21% of the FH allotypes in serum will be dimeric if no other factors are involved. These percentages correspond well to the observed oligomerisation of 12-13% at 1.1 mg/ml and 23-28% at *ca.* 4 mg/ml of the FH allotypes seen by sedimentation velocity and mass

spectrometry respectively (Figures 7.5 b and Figure 7.6), and 5-14% calculated from the K_D of 28 μM for heterozygous FH from sedimentation equilibrium (Chapter Five; Nan *et al.*, 2008a). A more detailed comparison between full-length FH and the SCR-6/8 fragment is instructive. Because SPR and ultracentrifugation revealed a clearer difference between the His402 and Tyr402 allotypes for only the fragment and not for full-length FH, the effect of this will only become biologically significant under relevant conditions. For example, if FH is immobilised on cell surfaces through SCR-20 and reaches a sufficient density, the closer packing of FH molecules will provide more opportunities for SCR-6/8 to interact, and SCR-6/8 dimerisation may become more important. This aspect may be important for RPE surface-bound FH and the development of sub-RPE deposits in Bruch's membrane in the early stages of AMD. The resulting impairment of C3b control may facilitate the early stages of AMD. If comparative fluorescent microscopy studies of full length FH Tyr402 and FH His402 binding to RPE cell surfaces are performed (Hageman *et al.*, 2005), controls will be required to show that any observed differential binding of the two allotypes is independent of potential FH self-association effects.

Indistinguishable solution structures for FH Tyr402 and FH His402 were determined by constrained modelling. The replacement of neutral Tyr402 by a positively charged His402 residue increases the predicted isoelectric point of the SCR-7 domain from 9.04 to 9.14. The Tyr402His replacement did not lead to an altered FH domain arrangement, and this was confirmed by the similarity of the $R_{XS\text{-}1}$ values within error (Table 7.2) and by the similar curve fits for the two allotypes (Figure 7.13). The similarity of the structures for the full-length FH allotypes complements the similar solution structures of the two SCR-6/8 allotypes and the subsequent similar crystal structure of SCR-6/8 His402 (Clark *et al.*, 2006; Prosser *et al.*, 2007). The NMR structures for SCR-7 Tyr402 and SCR-7 His402 in 20 mM sodium acetate at pH 5.2 are also similar (Herbert *et al.*, 2007). All these structures show that, even though Tyr402His is solvent exposed at the SCR-7 surface, the residue change has no effect. The lack of structural change in full-length FH by the Tyr402His substitution suggests that the domain arrangement in full-length FH may be less flexible than previously thought. The view that the FH structure possesses limited inter-SCR flexibility is suggested also by the sedimentation modelling of the FH dimer, trimer and tetramer that started from a FH monomer without

conformational change in this (Figure 7.15). Overall it can be concluded that the reduced binding affinity of FH His402 to ligands such as CRP (Okemefuna *et al.*, 2010) is attributable to the residue change itself, and not through changes in the similar overall FH structures.

In summary, we found that while the overall structure and self-association of the two full-length FH allotypes are not affected by the Tyr402His polymorphism, there is a measurable increase in self-association involving the SCR-6/8 His402 allotype, especially when this is surface bound. FH accumulates at surfaces such as that of the basal membrane of the RPE (Hageman *et al.*, 2005), therefore this process might be relevant *in vivo*. The consequence of FH enrichment at surfaces has been associated with increased sub-RPE deposit formation in the Bruch's membrane and inflammation (Hageman *et al.*, 2005) that may lead to AMD. Several decades elapse between early deposit formation and the development of blindness, a slow process perhaps explained by the low affinity interactions described above. Sub-RPE deposit formation is part of a natural ageing process and yet how sub-RPE deposit formation accelerates and leads to AMD is not understood. Together with the previous study on the FH-CRP interaction (Okemefuna *et al.*, 2010), this study provides evidence for a mechanistic model for how the Tyr402His polymorphism in FH might connect sub-RPE deposit formation with inflammatory processes and the development of blindness in AMD.

Chapter Eight

Localisation of zinc binding sites in the wild-type Tyr402 and disease-related His402 allotypes of homozygous complement factor H: implications for age-related macular degeneration

8.1 Introduction

The complement system of the innate immune system is activated by the alternative pathway through the low level spontaneous hydrolysis of C3 to form C3u (also known as $C3_{H2O}$), which leads to a positive-feedback amplification of C3 cleavage to form activated C3b (Law & Reid, 1995; Walport, 2001). While complement is targeted against pathogenic bacteria, complement-mediated host cell damage is prevented by the complement regulator factor H, which acts as a cofactor for factor I to cleave C3b, competes with factor B to inhibit the formation of the C3 convertase C3bBb, and accelerates the decay of C3bBb (Ferreira *et al.*, 2010). FH is constructed from 20 short complement regulator (SCR) domains, each of length about 61 residues (Soares & Barlow, 2005). The SCR domains in heterozygous and homozygous FH form a partially-folded back structure in solution (Aslam & Perkins, 2001; Okemefuna *et al.*, 2009; Chapter Seven). FH binds to glycosaminoglycans on the host cell surface through its C-terminal region and to SCR-7, and this is followed by the decay accelerating and co-factor activity of FH against C3b through the N-terminal region (Sharma & Pangburn, 1996; Pangburn, 2000; Oppermann *et al.*, 2006). FH binds to C3b at SCR-1/4 and SCR-19/20 (Schmidt *et al.*, 2008b). FH also binds to other ligands such as C-reactive protein, M-protein of Streptococci bacterium, and FH binding protein of Neisseria meningitides (Okemefuna *et al.*, 2010; Horstmann *et al.*, 1988; Giannakis *et al.*, 2003; Schneider *et al.*, 2009). FH also self-associates to form dimer, trimer and higher oligomers (Fernando *et al.*, 2007; Okemefuna *et al.*, 2008; Nan *et al.*, 2008a, Chapter Seven). FH oligomerisation is strongly promoted by transition metals, of which zinc has the strongest effect, followed by copper (Perkins *et al.*, 1991; Chapter Six; Nan *et al.*, 2008b). X-ray scattering and analytical ultracentrifugation (AUC) experiments showed that pooled heterozygous FH aggregates strongly in the presence of ≥ 20 μM of zinc or copper, and this is matched by the decrease of fluid-phase activity of heterozygous FH (Chapter Six; Nan *et al.*, 2008b).

FH is genetically associated with age-related macular degeneration (AMD), the most common cause of blindness in the elderly in the Western population (Hageman *et al.*, 2001; Klein *et al.*, 2005; Haines *et al.*, 2005; Edwards *et al.*, 2005; Hageman *et al.*, 2005). FH is also involved with atypical haemolytic uraemic syndrome (aHUS), membranoproliferative glomerulonephritis type II (MPGN), and Alzheimer's disease

(AD) (Strohmeyer *et al.*, 2002; Saunders *et al.*, 2007; Zetterberg *et al.*, 2008). Even with the analysis of over 100 genetic alterations, the molecular role of FH in these diseases is still unclear (Saunders *et al.*, 2007). This lack of knowledge is attributed to the multivalent weak affinities of FH for its ligands, which makes experimental studies difficult (Perkins *et al.*, 2010a; Perkins *et al.*, 2010b). A hallmark of early AMD is the drusen deposits that develop within Bruch's membrane, an extracellular matrix layer interposed between the retinal pigment epithelium (RPE) and the choroidal vasculature (Bird, 1992; Bird *et al.*, 1995; Guymer & Bird, 1998). Drusen contains oxidized lipids, carbohydrates, cellular materials and over 200 aggregated proteins including FH and other complement components. FH is secreted by RPE cells or is delivered by the choroidal blood circulation (Hageman *et al.*, 2001; Crabb *et al.*, 2002; Hageman *et al.*, 2005; Bok, 2005). Complement activation-related inflammation has been linked with the formation of drusen (Hageman et al, 2001; Anderson *et al.*, 2002; Hageman *et al.*, 2005). A Tyr402His polymorphism in FH SCR-7 is associated with 50% of AMD cases (Klein *et al.*, 2005; Haines *et al.*, 2005; Edwards *et al.*, 2005; Hageman *et al.*, 2005). The SCR-6/8 His402 allotype shows slightly greater self-association than the Tyr402 allotype (Fernando *et al.*, 2007; Section 7.2.1). While the binding of C-reactive protein to FH was recently disputed, the most recent study confirmed that the proteins interact with each other, and that the SCR-6/8 His402 allotype binds more weakly to C-reactive protein than the Tyr402 allotype (Okemefuna *et al.*, 2010; Perkins *et al.*, 2010b; Ferreira *et al.*, 2010). The two FH allotypes showed similar cofactor activity in C3b degradation (Skerka *et al.*, 2007; Schmidt *et al.*, 2008b). However the effect of glycosaminoglycans on these two FH allotypes presently remains unclear (Clark *et al.*, 2006).

Zinc is abundant in human retina (Galin *et al.*, 1962). It is vital for retinal cell survival, and the functioning of antioxidant enzymes and the visual cycle, while an excess of zinc can be detrimental and exacerbate neuronal damage (Ugarte & Osborne, 2001). Under oxidative stress during light exposure, the secretion of zinc from the zinc-rich RPE cells is elevated (Ugarte & Osborne, 2001). Millimolar concentrations of zinc have been found in sRPEds and Bruch's membrane, suggesting that the pathological release of zinc from surrounding tissues like the RPE-choroid complex might be involved in sRPEd formation (Galin *et al.*, 1962; Lengyel *et al.*, 2007). Studies of the effect of zinc supplements on reducing the development of AMD gave different results. Based on the premise that zinc is an antioxidant, the large Age-Related Eye Disease Study (AREDS)

indicated that supplements with zinc alone or with zinc together with vitamins C and E and β carotene reduces the risk for progression to advanced AMD (AREDS Research Group, 2001a; AREDS Research Group, 2001b). Interestingly, a follow-up study found that the treatment response to the AREDS-recommended zinc supplement was influenced by the Tyr402His FH polymorphism. A smaller reduction in the progression to AMD to advanced stage disease was found in patients with the FH His402 allotype than in those with the FH Tyr402 allotype (Klein *et al.*, 2008). Zinc binding sites between two protein surfaces show a tetrahedral coordination geometry at which the binding site is often formed from surface His, Asp, Glu and Cys residues (Auld, 2001). The Tyr402His polymorphism is of great interest because this potentially provides a new His zinc-binding ligand. In this chapter, to clarify whether the two allotypes exhibit different zinc binding properties, the homozygous FH Tyr402 and His402 allotypes and the two allotypes of recombinant SCR-6/8 in zinc titrations were studied. By analytical ultracentrifugation and synchrotron X-ray scattering, this study showed that zinc interacts with the two homozygous allotypes of FH, hence ruling out heterogeneity effects, and the major zinc binding sites are most likely to be within the SCR-6/8 fragment. The analyses were confirmed by bioinformatics predictive strategies which were performed by Miss Irene Farabella and Mr Felix F. Schumacher. The molecular implications of these results for complement regulation and sRPEd formation in AMD are discussed in this chapter.

8.2 Results and discussion

8.2.1 Sedimentation velocity of the complexes of the two FH and SCR-6/8 allotypes with zinc

Homozygous FH and recombinant SCR-6/8 were purified (Materials and Methods). The two homozygous FH allotypes were studied at 0.9 mg/ml (5.8 μM) in order to be comparable in concentration with the physiological FH range of 0.235-0.810 mg/ml in serum (Saunders *et al.*, 2007). The SCR-6/8 allotypes were studied at 0.2-0.3 mg/ml (9.7-14.6 μM) which was the lowest concentration that produced analysable data. Both proteins were studied in Hepes buffer (Materials and Methods). PBS buffer was not used, in order to avoid the precipitation of zinc with phosphate. Both were titrated with

0-600 μM $ZnSO_4$ in ultracentrifugation (section 8.2.1) and scattering experiments (Section 8.2.2).

Analytical ultracentrifugation studies the sedimentation behaviour of macromolecules on subjecting these to a high centrifugal force in order to determine their sizes and shapes (Section 4.1; Cole *et al.*, 2008). Sedimentation velocity experiments were performed using speeds up to 60,000 r.p.m on two Tyr402 and two His402 FH allotypes at concentrations of 0.7-0.8 mg/ml, each being titrated with zinc from 0.2 μM to 200 μM. Similar sets of rapidly-moving sedimentation boundaries were observed for both allotypes when [Zn] increased. Good fits to the sedimentation boundaries were obtained in all cases using sedimentation coefficient distribution analyses *c*(*s*) (Figures 8.1). At all [Zn] values, the FH monomer was observed at a mean value of 5.67 ± 0.05 S for the Tyr402 allotype, and at 5.74 ± 0.07 S for the His402 allotype at 50,000 r.p.m. These values agree well with the previous determined values for homozygous FH monomer (Section 7.2.2). This indicated the presence of zinc-free FH even with a 40-fold excess of zinc, meaning that the binding of zinc is weak. For both allotypes with [Zn] between 0.2-20 μM, additional peaks that corresponded to similar small amounts of oligomers from dimers to nonamers were visible from 7 S to 30 S that resembled those for zinc-free FH (Chapter Five; Nan *et al.*, 2008a; Okemefuna *et al.*, 2009; Chapter seven). For both allotypes with [Zn] between 60-200 μM, sizeable amounts of rapidly sedimenting species were observed with increased $s_{20,w}$ values up to 100 in the *c(s)* distributions (Figure 8.2). The proportions of oligomers of the Tyr402 and His402 allotypes were derived by integration of the *c(s)* size-distribution analyses. No differences in proportions were seen between the allotypes. Like heterozygous pooled native FH (Chapter Six; Nan *et al.*, 2008b), both the Tyr402 and His402 allotypes form heavy oligomers with zinc and share similar dependences on [Zn] (Figure 8.3).

The sedimentation boundaries showed that differential amounts of zinc-induced FH oligomers were formed with the two allotypes. For the Tyr402 allotype, the oligomers ranged in S values in excess of 100 S, indicating a larger proportion of more compact or high molecular mass species (Figure 8.2 a). For the His402 allotype, the oligomers peaked in the region of 20-80 S, indicating a larger proportion of more extended or lower molecular mass oligomers (Figure 8.2 b). These differences were reflected in Figure 8.1, where the upper part of the boundaries sedimented more rapidly for the

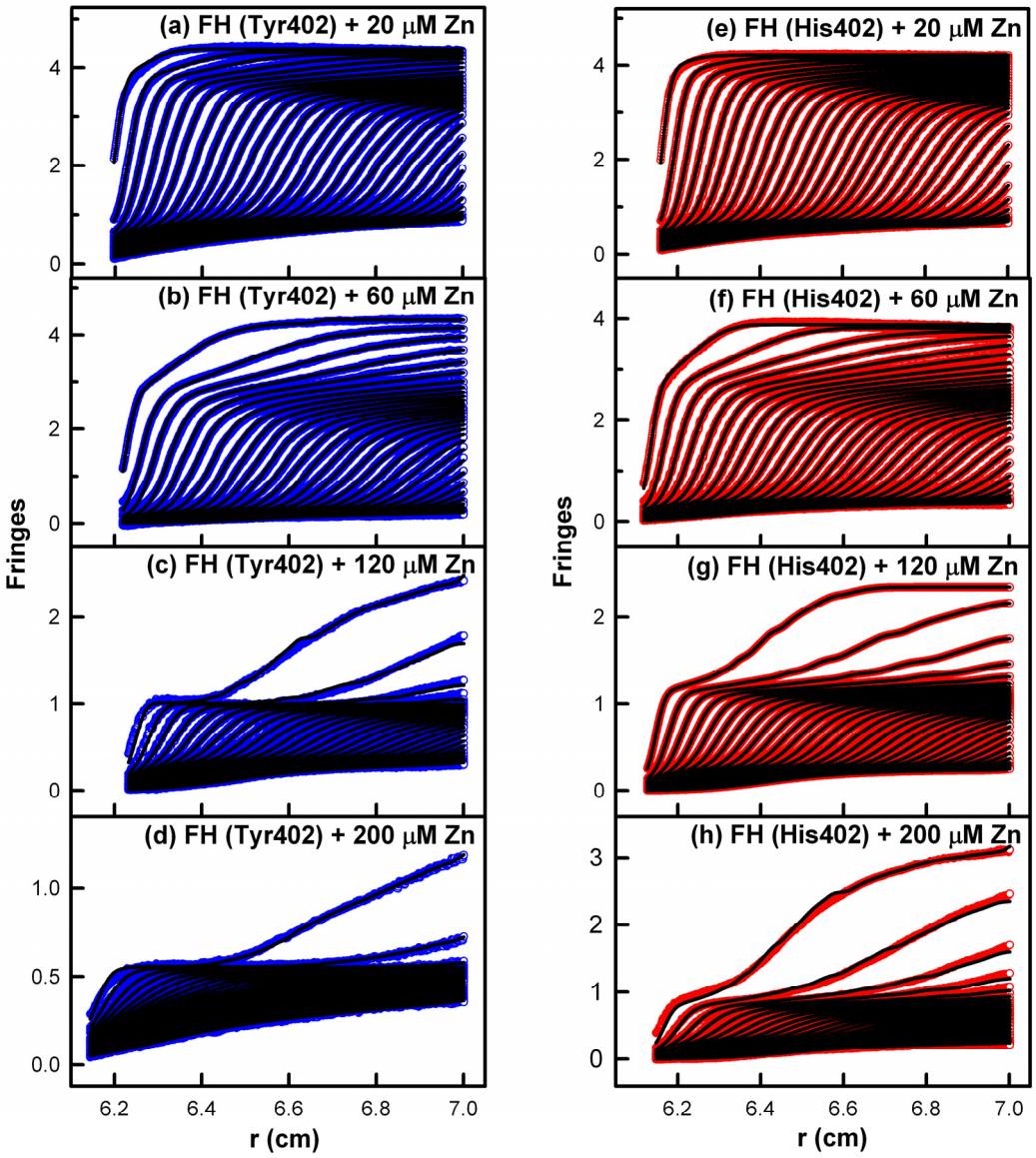

Figure 8.1 Sedimentation boundary fits of the two FH allotypes titrated with zinc. Both allotypes were studied at 0.7 mg/ml. Only every tenth scan is shown for clarity. (a, b, c, d) The fits corresponding to the FH Tyr402 allotype (026II; blue) was titrated with zinc concentrations of 20 μM, 60 μM, 120 μM and 200 μM in that order. (e, f, g, h) The fits corresponding to the FH His402 allotype (027BA; red) was titrated with the same zinc concentrations.

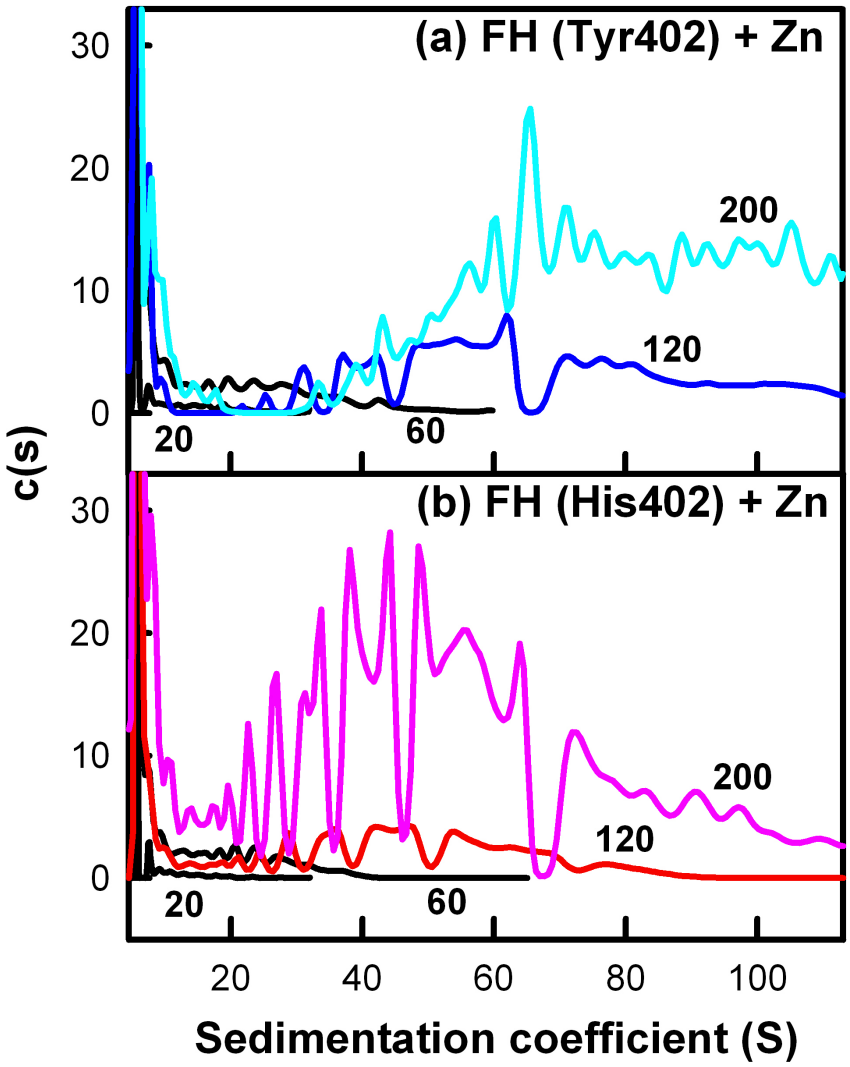

Figure 8.2 *c(s)* sedimentation coefficient distribution analyses of the two FH allotypes titrated with zinc. (a) *c(s)* analyses for FH Tyr402 titrated with 20 μM, 60 μM, 120 μM and 200 μM zinc from the boundary fits in Figure 8.1 a, b, c, d; (b) corresponding *c(s)* analyses for FH His402 with zinc from the boundary fits in Figure 8.1 e, f, g, h. The height of the FH monomer peak at 5.7 S is normalised to 100 for clarity. The zinc concentrations (μM) are denoted numerically. The sedimentation boundary fits of the same homozygous FH samples are shown in Figure 8.1.

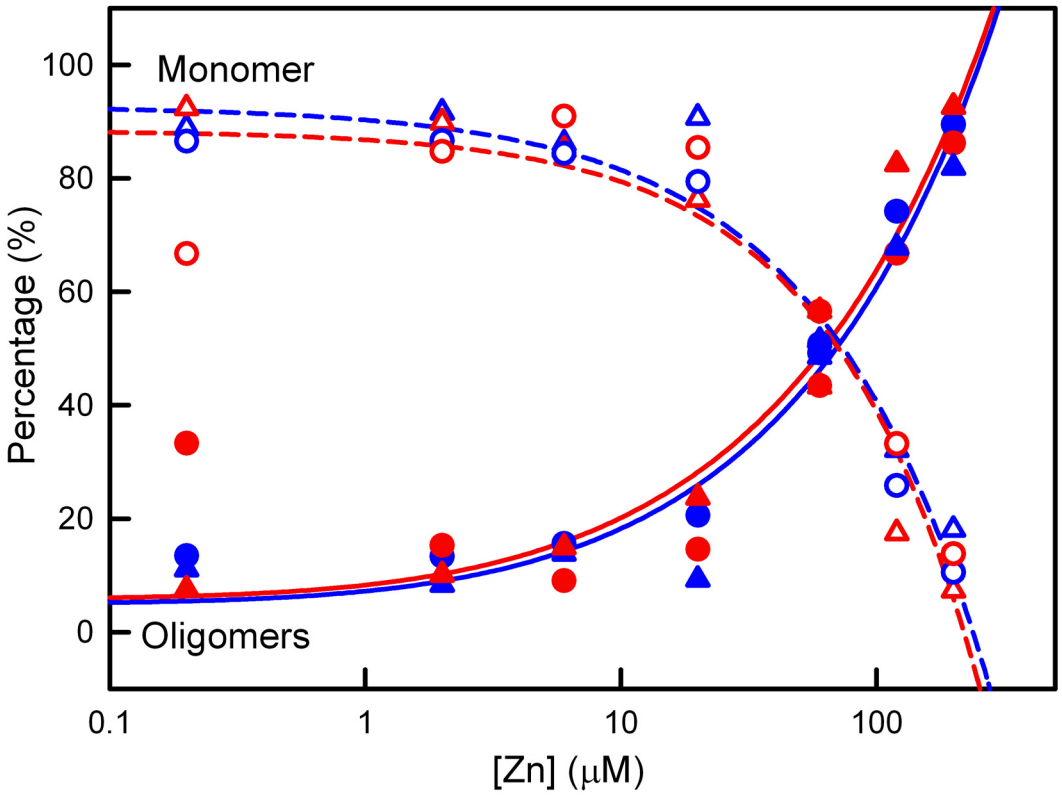

Figure 8.3 Dependence of the monomer and oligomers of homozygous FH on zinc concentrations. The values from *c(s)* integrations correspond to the averages obtained at 50,000 r.p.m. and 60,000 r.p.m. The oligomer data were fitted to a two-parameter power function $y=a*(1 + x)^b$, and the monomer data were fitted to the function $f=y0+a*x^b$. Oligomers are denoted by filled symbols and monomers by open symbols for four experiments with two FH Tyr402 (026II, 022LM, blue, ●, ○, ▲, Δ) and two FH His402 (027BA, 032KO, red, ●, ○, ▲, Δ) allotypes.

Tyr402 allotype compared to the His402 allotype at all zinc concentrations. These features were not reproducible for another pair of the two FH allotypes, although differential effects were again observed (data not shown). Therefore, the difference between the zinc-induced oligomers of FH Tyr402 allotype and that of His402 allotype shown in Figure 8.2 is not considered significant. In addition, even with the homozygous FH proteins whose heterogeneity is much reduced compared to the pooled FH used in earlier studies, the *c(s)* peaks show no sequence of peaks with well-resolved progression of S values similar to the peaks 2-9 seen in zinc-free FH (Chapter Five; Nan *et al.*, 2008a; Okemefuna *et al.*, 2009; Chapter Seven). Overall, these observations suggested that a range of zinc-induced FH oligomers of different sizes had formed through the cross-linking of different weak zinc-binding sites at the surface of FH.

In order to clarify the molecular basis for zinc-induced FH oligomers, sedimentation velocity experiments were performed at 50,000 r.p.m on the Tyr402 and His402 allotypes of the SCR-6/8 fragment at 0.3 mg/ml (14.6 μM) titrated with zinc from 0.2 μM to 600 μM. Similar sedimentation boundaries were observed for the two allotypes of SCR-6/8 at each [Zn] (Figure 8.4 a, b, c, d). In contrast to full-length FH, no rapidly sedimenting larger species were detected in the size distribution *c(s)* fits at any [Zn]. The *c*(*s*) analyses consistently showed a major monomer peak at 2.12 ± 0.09 S and a minor dimer peak at 4.03 ± 0.20 S for the Tyr402 allotype, and likewise two peaks at 2.19 ± 0.08 S and 3.95 ± 0.16 S for the His402 allotype (Figure 8.4 e). This agrees with the previous observation of SCR-6/8 monomer and dimer by sedimentation velocity (Fernando *et al.*, 2007). However, with [Zn] above 60 μM, the signal intensity of the monomer peak for both allotypes decreased significantly with increase in [Zn] (Figure 8.4 e; Figure 8.5). This indicates that, at [Zn] above 60 μM, zinc induced the formation of aggregated SCR-6/8 which were sufficiently large to precipitate and sediment to the bottom of the sample cell before the first boundary scan was recorded. While the His402 allotype showed slightly greater precipitation than the Tyr402 allotype, this may result from experimental variability in quantifying the different sedimenting species. Overall, it was noteworthy that SCR-6/8 precipitated at the same [Zn] value that caused large FH oligomers to form. This indicated that the major binding sites for zinc in full-length FH were located within SCR-6/8.

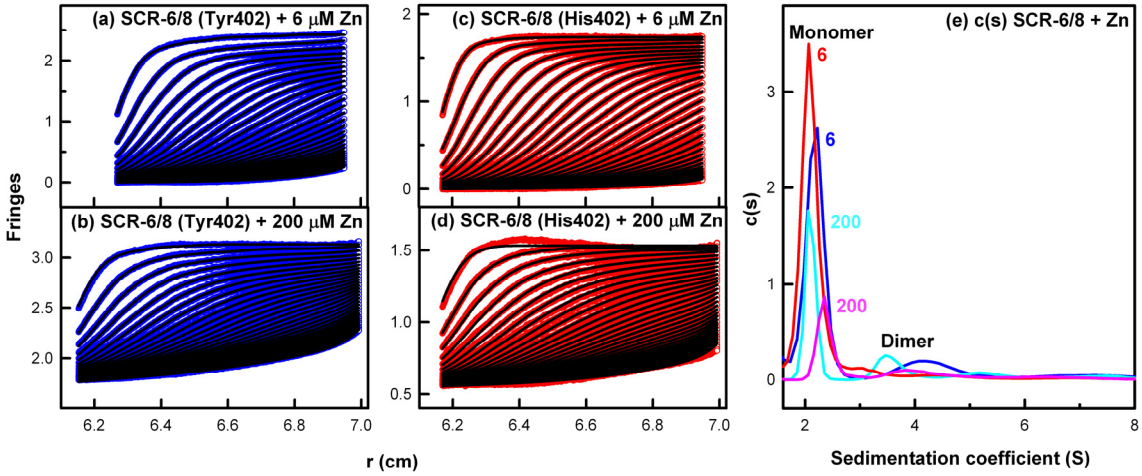

Figure 8.4 Sedimentation velocity analyses of the two SCR-6/8 allotypes titrated with zinc. Both allotypes were studied at 0.3 mg/ml. In the sedimentation boundary fits, only every tenth scan is shown for clarity. (a,b) The fits for the SCR-6/8 Tyr402 allotype (blue) titrated with zinc at 6 μM and 200 μM. (c,d) The fits for the SCR-6/8 His402 allotype (red) titrated with zinc at 6 μM and 200 μM. (e) The *c(s)* sedimentation coefficient distribution analyses for the Tyr402 allotype with 6 μM (blue) and 200 μM (cyan) zinc, and the His402 allotype with 6 μM (red) and 200 μM (pink) zinc. The *c(s)* distributions are labelled with their zinc concentration values (μM). The peak at about 2.1 S corresponds to the monomer, and that at about 4.0 S is the dimer.

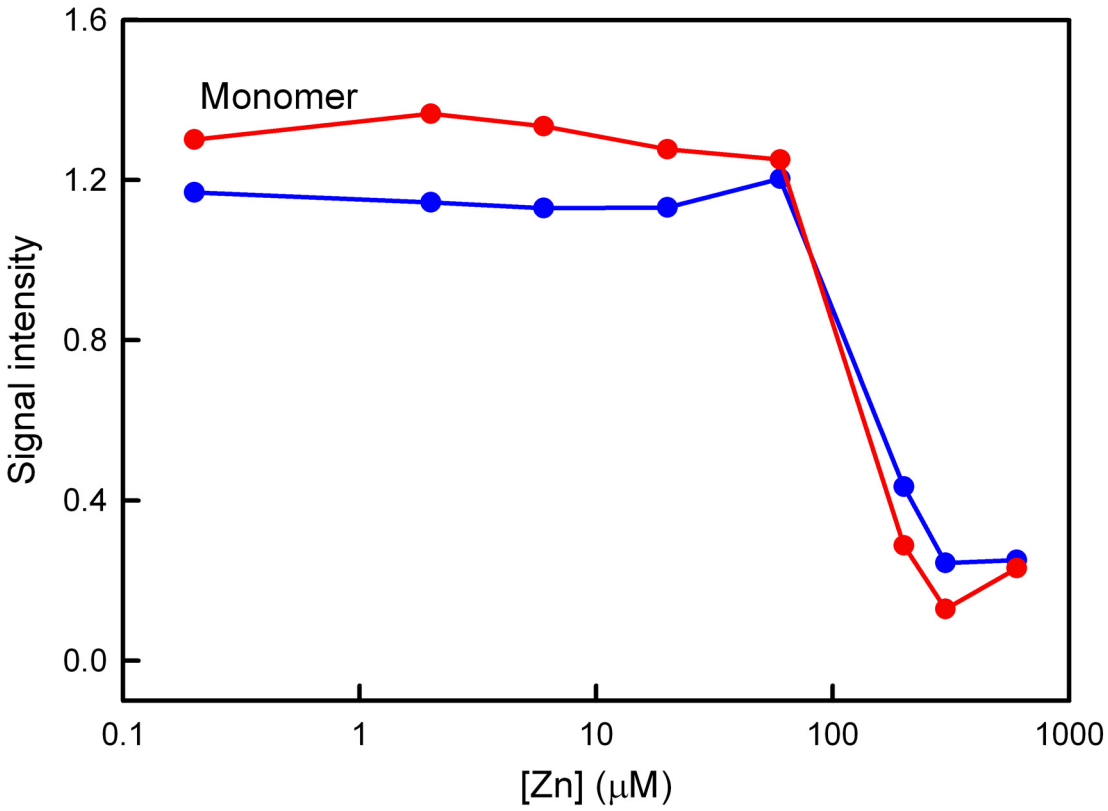

Figure 8.5 Dependence of the monomer and oligomers of FH and SCR-6/8 on zinc concentrations. The signal intensities of the monomer of SCR-6/8 fragment titrated with zinc are obtained from the integration function of the *c(s)* analyses (Tyr402 allotype, blue; His402 allotype, red).

The reversibility of the zinc-induced precipitation of the SCR-6/8 allotypes was studied by adding 2 mM EDTA to the ultracentrifuge cell contains 0.3 mg/ml SCR-6/8 and 300 μM of zinc. After mixing, the sedimentation velocity experiment was immediately re-run at 50,000 r.p.m on this cell again. Even though the size distribution *c(s)* analyses showed that the monomer peak for both allotypes of SCR-6/8 with 300 μM of zinc was much reduced, the addition of EDTA caused a significant increase of the monomer peak intensity for both allotypes (Figure 8.6). This showed that the zinc-induced precipitation of SCR-6/8 was reversible, in good agreement with the reversibility of the zinc-induced oligomers of heterozygous pooled FH by adding EDTA (Chapter Six; Nan *et al.*, 2008b).

Additional ultracentrifugation experiments with the SCR-1/5 and SCR-16/20 fragments in the presence of zinc were performed as controls of the SCR-6/8 experiments. The control experiments were performed by Mr Felix F. Schumacher and Miss Irene Farabella. SCR-1/5 is less soluble at 0.2 mg/ml when expressed, compared to SCR-6/8 and SCR-16/20. As [Zn] increased, SCR-1/5 precipitated in the same manner as SCR-6/8 at a similar [Zn] value to that for SCR-6/8. This was visible from both the reduced intensities of the fringes as [Zn] increased and the marked reduction of the monomer peak intensity in the *c(s)* plot (Figure 8.7 a, b, c, d). In contrast to this, SCR-16/20 is more soluble than SCR-1/5 and SCR-6/8, and SCR-16/20 remained in solution as [Zn] increased with a smaller reduction in the number of observed fringes at 600 μM. Here, the *c(s)* plot showed a smaller reduction in the sizes of the monomer and dimer peaks, while at the same time as many as three other species were observed (Figure 8.7 e, f, g, h). These experiments showed that other different types of zinc-induced oligomers formed at other regions of FH. Unlike SCR-6/8, both SCR-1/5 and SCR-16/20 possessed His_6-tags which may comprise potential zinc binding sites (Okemefuna *et al.*, 2008). This was evaluated by further zinc titrations in which a 2:1 molar ratio of nickel (17 μM) was present to saturate its binding site at the His_6-tag, to which nickel binds more tightly with a dissociation constant of 1 μM (Nieba *et al.*, 1997). The resulting *c(s)* plots showed that no SCR-1/5 or SCR-16/20 precipitated, and that only the monomer or monomer/dimer peaks were seen similar to those observed for zinc-free protein. These control experiments indicate either that the His_6-tag represented an oligomeric zinc-binding site which is eliminated by the stronger binding of nickel, or that nickel competes with zinc for weak interaction sites in FH. The first explanation is preferred,

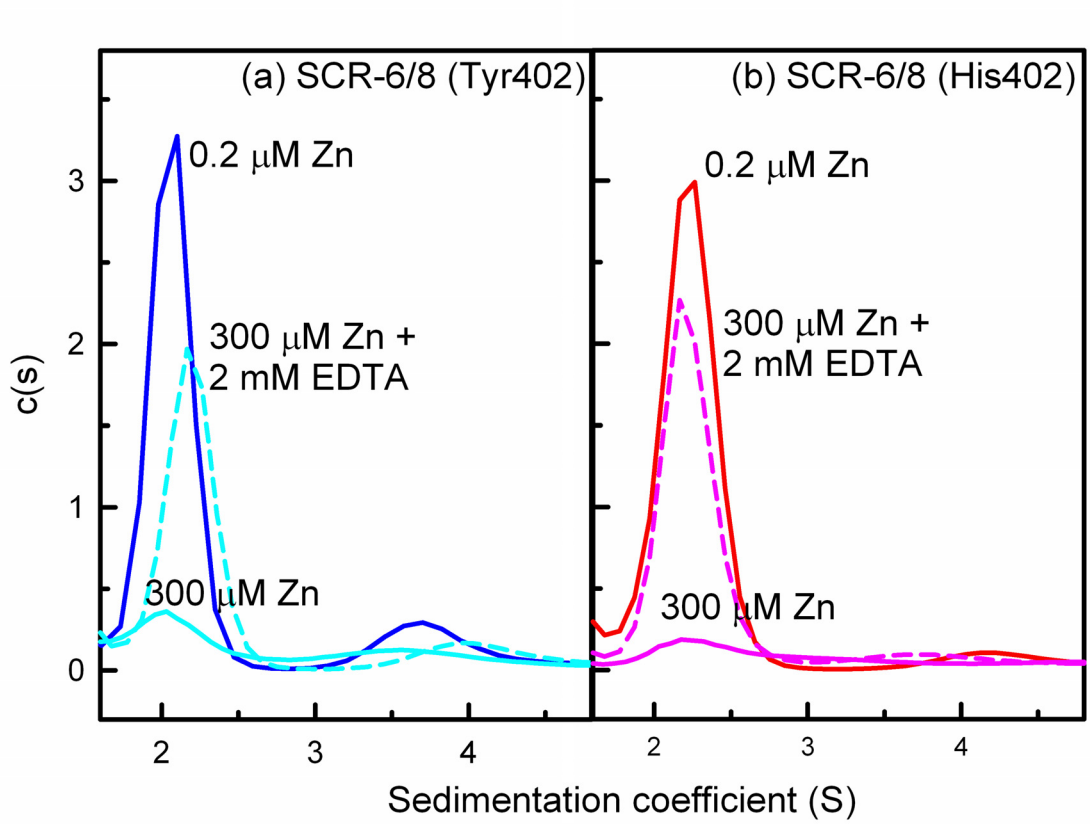

Figure 8.6 Effects of EDTA on the interactions between the SCR-6/8 allotypes and zinc using sedimentation velocity.

(a) The *c(s)* distribution analyses are shown for the Tyr402 allotype in the presence of 0.2 μM zinc (blue solid line), 300 μM zinc (cyan solid line), and 300 μM zinc and 2 mM EDTA (cyan dashed line).

(b) The *c(s)* distribution analyses are shown for the His402 allotype in the presence of 0.2 μM zinc (red solid line), 300 μM zinc (pink solid line), and 300 μM zinc and 2 mM EDTA (pink dashed line).

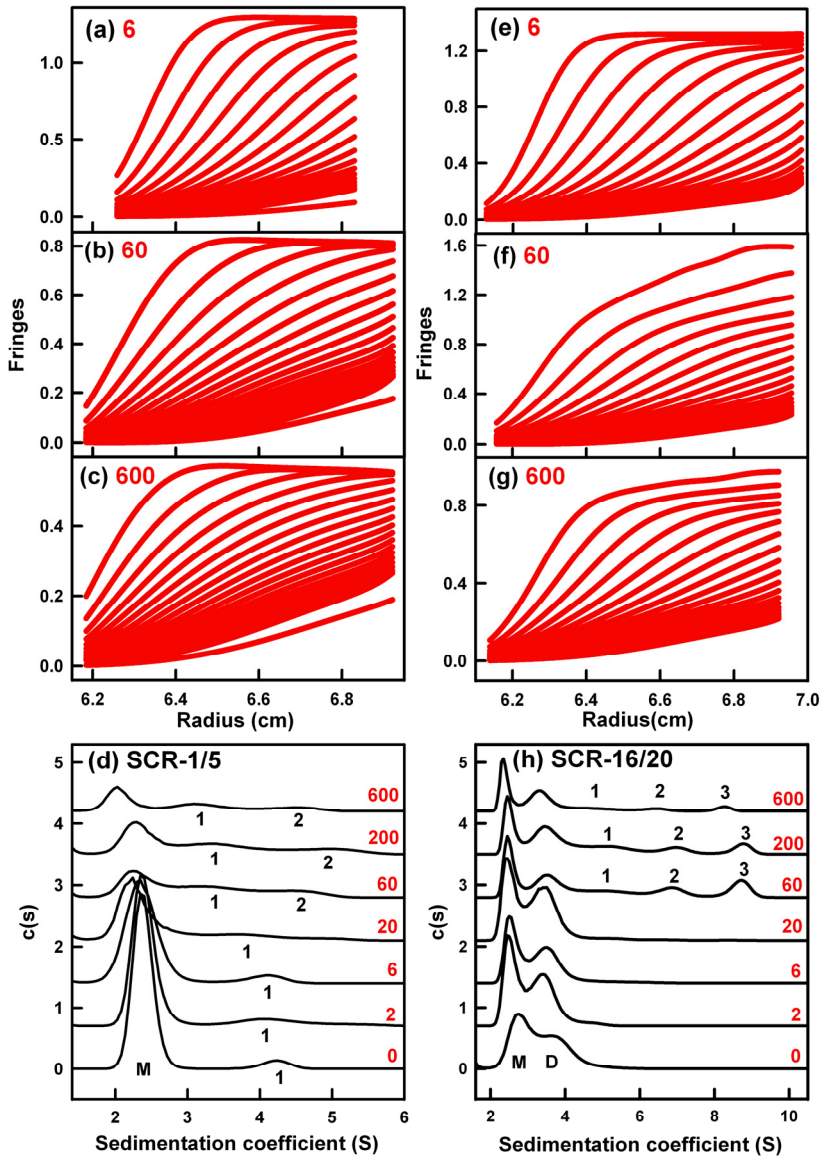

Figure 8.7 Sedimentation velocity analysis of SCR-1/5 and SCR-16/20 titrated with zinc. Red numbers indicate zinc concentrations (μM) (adapted from Rotation 1 report of Mr Felix F. Schumacher, 2009). (a-c) For SCR-1/5, the boundary fits at three zinc concentrations are shown for only every 24th scan out of 480 for reason of clarity. (d) Size-distribution *c(s)* analyses for SCR-1/5 at seven zinc concentrations are shown. M indicates the monomer position, and two weak emerging zinc-induced signals are denoted by 1 and 2. The graphs were displaced vertically in units of 0.5 for reason of clarity. (e-g) For SCR-16/20, the boundary fits at three zinc concentrations are shown for only every 22nd scan out of 440. (h) Size-distribution *c(s)* analyses for SCR-16/20 at seven zinc concentrations are shown. M and D indicates the monomer and dimer peaks. Weak emerging signals are denoted by 1, 2 and 3. Graphs are displaced vertically in units of 0.5 for reason of clarity.

because nickel has no strong effect on FH oligomer formation (Chapter Six; Nan *et al.*, 2008b). Control experiments with full-length FH in the presence of 200 μM zinc and 20 μM nickel were performed to complete these studies. These experiments showed that zinc still causes FH to aggregate, indicating that while other possible zinc-binding sites in FH apart from those in SCR-6/8 may require consideration, no major sites were detected within SCR-1/5 and SCR-16/20.

8.2.2 X-ray scattering of the two allotypes of FH and SCR-6/8 with zinc

X-ray scattering is a diffraction method used to study solution structures of macromolecules in random orientations (Perkins *et al.*, 2008). The effect of zinc on the structures of freshly-purified two Tyr402 and two His402 allotypes of full-length FH and the two allotypes of FH fragment SCR-6/8 were investigated by synchrotron X-ray scattering. FH was studied at 0.9 mg/ml (5.8 μM) in order to be comparable with physiological FH concentrations, while SCR-6/8 was studied at 0.2 mg/ml (9.7 μM), this being the lowest concentration of SCR-6/8 that produced analysable data. Each FH or SCR-6/8 sample was titrated with 0 μM to 600 μM $ZnSO_4$. The scattering data $I(Q)$ showed excellent signal-noise ratios and no detectable effect from radiation damage.

Guinier fits at low Q values (where $Q = 4\pi \sin\theta / \lambda$; 2θ = scattering angle; λ = wavelength) gives the radius of gyration (R_G) which monitors the degree of elongation of the protein, and the *I(0)/c* value which is proportional to the relative molecular mass (Figure 8.8 a, b) (Glatter & Kratky, 1982; Perkins *et al.*, 2008). At larger Q values, Guinier fits give the cross-sectional radius of gyration R_{XS} which monitors the structural proximity relationships between non-neighbouring SCR domains ($R_{XS\text{-}1}$) and neighbouring SCR domains ($R_{XS\text{-}2}$) (Figure 8.8 c, d, e, f) (Aslam & Perkins, 2001). In our previous study of heterozygous and homozygous FH, the presence of oligomers caused concentration-dependent increases in the values of R_G and $R_{XS\text{-}1}$ (Chapter Five; Nan *et al.*, 2008a; Chapter Six). Here, at the lowest zinc concentration of 0.2 μM, the mean R_G and $R_{XS\text{-}1}$ values were 8.91 ± 0.17 nm and 3.03 ± 0.17 nm respectively for the Tyr402 FH allotype, and 9.23 ± 0.72 nm and 3.15 ± 0.39 nm respectively for the His402 FH allotype (Figure 8.9 b, c). Both the R_G and $R_{XS\text{-}1}$ values were similar to those for heterozygous FH at 0.9 mg/ml without zinc (Figure 5.2 a, c) (Nan *et al.*, 2008a). Both

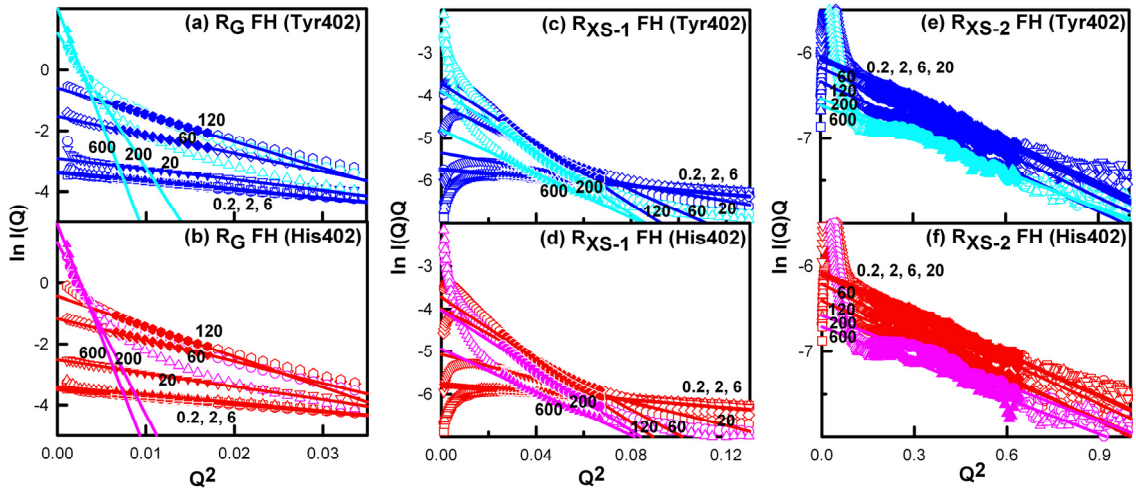

Figure 8.8 X-ray Guinier analyses of the two full-length FH allotypes titrated with zinc. In all panels, the open symbols correspond to the experimental data and the filled symbols correspond to those used for the R_G and R_{XS} straight line fits. Data correspond to one FH Tyr402 allotype (018DK) in (a,c,e) and one FH His402 allotype (030TJ) in (b,d,f), both at 0.9 mg/ml. Data for the Tyr402 allotype of FH are shown in blue from 0.2 μM to 120 μM of $ZnSO_4$, and in cyan from 200 μM to 600 μM of $ZnSO_4$. Data for the His402 allotype of are shown in red from 0.2 μM to 120 μM of $ZnSO_4$, and in pink from 200 μM to 600 μM of $ZnSO_4$.

(a,b) Guinier R_G plots of ln $I(Q)$ vs. Q^2 for FH Tyr402 and FH His402 allotypes titrated with $ZnSO_4$ concentrations of 0.2 μM (O), 2 μM (□), 6 μM (Δ), 20 μM (▽), 60 μM (◇), 120 μM (⬡), 200 μM (O) and 600 μM (Δ). The Q fit range was 0.08 - 0.13 nm^{-1} for 0.2 μM to 120 μM $ZnSO_4$, and 0.03 - 0.16 nm^{-1} for 200 μM to 600 μM $ZnSO_4$. The zinc concentrations are numerically labelled as shown.

(c,d) The corresponding Guinier cross-sectional R_{XS-1} fits of ln $I(Q).Q$ vs. Q^2 for the two FH allotypes with zinc using a Q range of 0.16 - 0.26 nm^{-1}.

(d,e) The corresponding Guinier cross-sectional R_{XS-2} fits for the two FH allotypes with zinc using a Q range of 0.4 - 0.8 nm^{-1}.

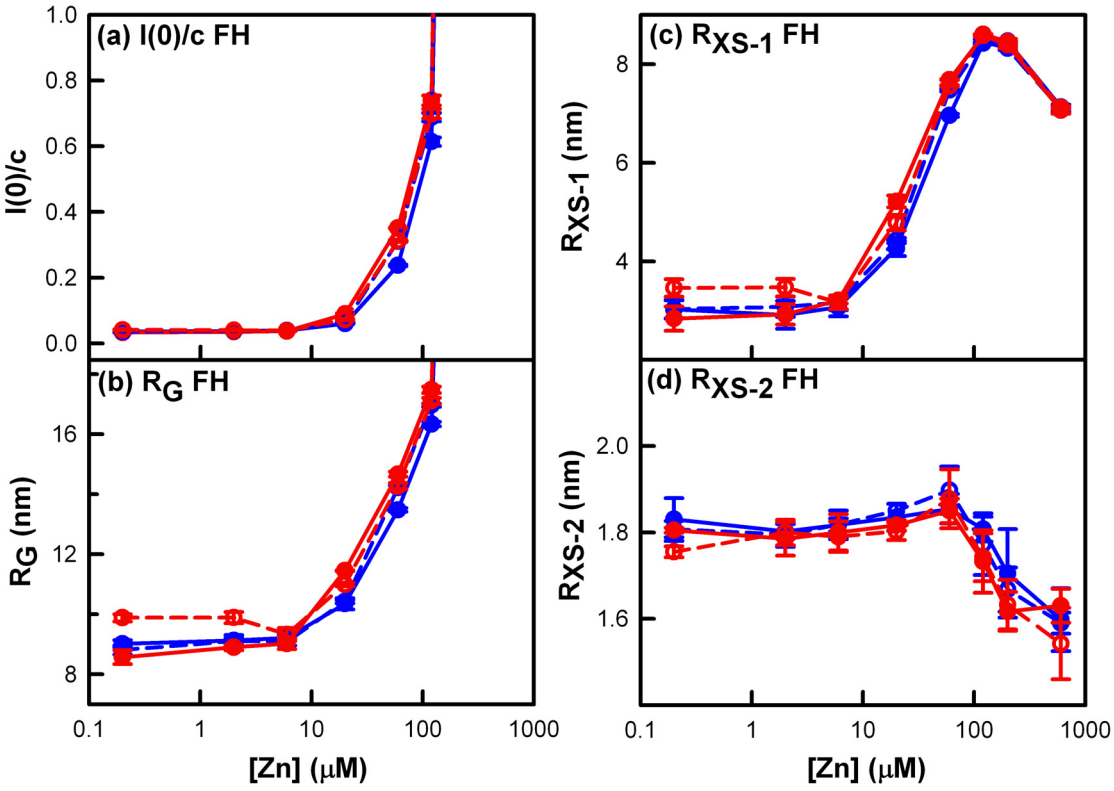

Figure 8.9 Dependence of the *I(0)/c*, R_G and R_{XS} values of the two allotypes of FH on the zinc concentration. In all cases, the Tyr402 allotype is shown in blue and the His402 allotype is shown in red. Each value was measured in quadruplicate and averaged, and statistical error bars are shown where visible. The four titrations correspond to two pairs of FH Tyr402 allotypes (018DK, ● with solid line; 016CC, ○ with dashed line) and FH His402 allotypes (030TJ, ● with solid line; 033NV, ○ with dashed line) at 0.9 mg/ml titrated with zinc from 0.2 to 600 μM.

R_G and R_{XS-1} values were the same within error of the corresponding values for zinc-free homozygous FH at 1.1 mg/ml (Figure 7.9). When both the Tyr402 and His402 FH allotypes were titrated with zinc up to 6 μM, the scattering curves $I(Q)$ remained unchanged (Figure 8.8 a, b), and the Guinier values remained unchanged (Figure 8.9). For [Zn] from 20 μM to 600 μM, the $I(Q)$ intensities increased significantly at low Q and decreased at high Q as the result of oligomer formation (Figure 8.8). The Guinier $I(0)/c$ and R_G values increased significantly (Figure 8.9 a, b), although the R_{XS-1} and R_{XS-2} valued decreased at [Zn] above 200 μM as the result of the decrease in the intensity of $I(Q)$ in the Q ranges used for the R_{XS} determinations (Figures 8.8 c, d, e, f and Figure 8.9 c, d). The changes for both homozygous FH allotypes are comparable with previous observations for heterozygous native FH (Figure 6.2) (Nan *et al.*, 2008b), indicating again that FH heterogeneity is not responsible for these observations. For [Zn] between 20 μM and 120 μM, the two His402 allotypes showed slightly higher Guinier $I(0)/c$, R_G and R_{XS-1} values than the two Tyr402 allotype (Figure 8.9 a, b, c), which if true would indicate that the His402 allotype formed more oligomers than the Tyr402 allotype, however the difference is not considered to be significant.

To test whether the Tyr402 and His402 allotypes of SCR-6/8 formed zinc-induced oligomers, both were titrated with [Zn] from 0.2 to 600 μM. For SCR-6/8 at 0.2 mg/ml with 0.2 μM zinc, the Guinier R_G and R_{XS} values were 2.63 ± 0.46 nm and 0.88 ± 0.29 nm respectively for the Tyr402 allotype, which were similar to values of 2.79 ± 0.47 nm and 1.00 ± 0.27 nm for the His402 allotype. Those Guinier values are slightly less but within error of the experimental R_G and R_{XS} values of 3.26-3.35 nm and 1.04 nm respectively for the zinc-free Tyr402 allotype, and 3.12-3.21 nm and 1.15 nm (± 0.06-0.20 nm) for the zinc-free His402 allotype (Fernando *et al.*, 2007). For [Zn] between 0.2 μM to 6 μM, the scattering curves $I(Q)$ were unchanged for both allotypes (Figure 8.10 a, b and Figure 8.11). At 20 μM [Zn], the $I(Q)$ curves of both allotypes underwent dramatic changes in which the intensities sharply increased at low Q and decreased rapidly at large Q (Figure 8.10 c, d), and these changes resulted in much increased Guinier $I(0)/c$ and R_G values (Figure 8.11 a, b). Above 20 μM [Zn], the $I(Q)$ intensities continued to rise at very low Q (Figure 8.10 a, b). The Guinier $I(0)/c$ and R_G values peaked at [Zn] of 60 μM and declined at higher [Zn] values (Figure 8.11 a, b). These changes showed that both allotypes of SCR-6/8 interacted with zinc starting from 20

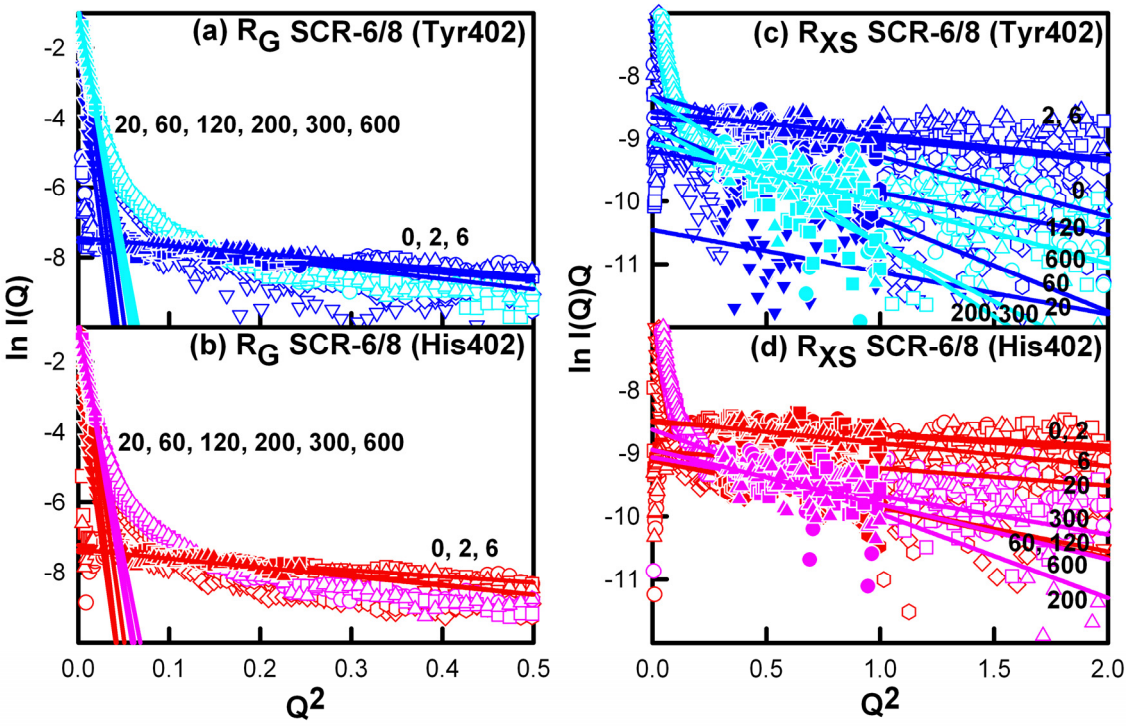

Figure 8.10 X-ray Guinier analyses of the two SCR-6/8 allotypes titrated with zinc. In all panels, the open symbols correspond to the experimental data and the filled symbols correspond to those used for the R_G and R_{XS} straight line fits. Data correspond to SCR-6/8 Tyr402 (g,i) and SCR-6/8 His402 (h,j), both at 0.2 mg/ml. Data for the SCR-6/8 Tyr402 are shown in blue from 0.2 μM to 120 μM of $ZnSO_4$, and in cyan from 200 μM to 600 μM of $ZnSO_4$. Data for SCR-6/8 His402 are shown in red from 0.2 μM to 120 μM of $ZnSO_4$, and in pink from 200 μM to 600 μM of $ZnSO_4$.

(a, b) Guinier R_G plots for the SCR-6/8 Tyr402 and His402 allotypes at 0.2 mg/ml titrated with $ZnSO_4$ at concentrations of 0 μM (O), 2 μM (□), 6 μM (Δ), 20 μM (▽), 60 μM (◇), 120 μM (⬡), 200 μM (O), 300 μM (□) and 600 μM (Δ). The Q fit range was 0.16 - 0.5 nm^{-1} for 0.2 μM to 120 μM $ZnSO_4$, and 0.06 - 0.11 nm^{-1} for 200 μM to 600 μM $ZnSO_4$.

(c, d) The corresponding Guinier cross-sectional R_{XS} fits for the SCR-6/8 allotypes using a Q range of 0.55 – 1.0 nm^{-1}.

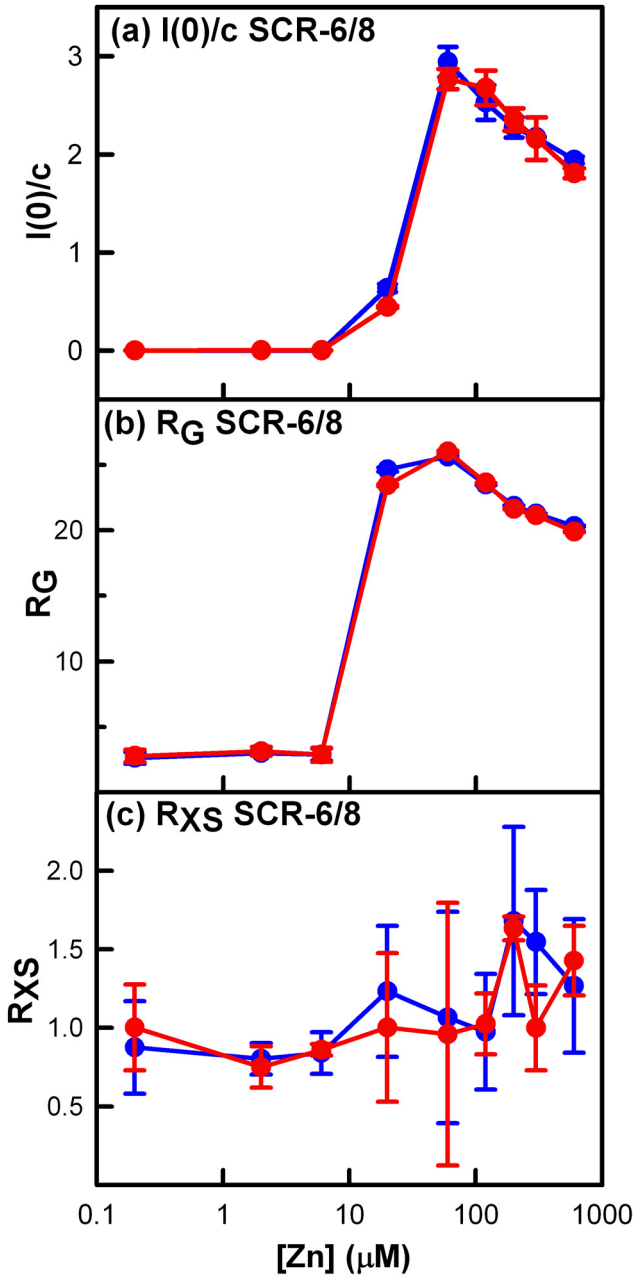

Figure 8.11 Dependence of the *I(0)/c*, R_G and R_{XS} values of SCR-6/8 on the zinc concentration. The titrations correspond to the two SCR-6/8 allotypes titrated with the same zinc concentration range from 0.2 to 600 μM. The Tyr402 allotype is shown in blue and the His402 allotype is shown in red. Each value was measured in quadruplicate and averaged, and statistical error bars are shown where visible.

μM, which is the same starting concentration as the FH interaction with zinc. Unlike the FH-zinc oligomers which remained in solution, the changes observed for SCR-6/8 caused this to precipitate, and this accounted for the apparent decline in the *I(0)/c* and R_G above 60 μM. Like full-length FH, no significant difference was observed for the zinc-induced oligomerisation of the Tyr402 and His402 allotypes.

The distance distribution function *P*(*r*) of the two FH allotypes provided shape information in real space on the zinc-induced FH oligomers. The *P*(*r*) curve summarises the distances between all pairs of atoms within FH, and gives the most frequently occurring distance *M* from the position of the peak maximum, the maximum length *L* from the point at which *P(r)* becomes zero at large *Q*, and an independent calculation of the R_G and *I(0)* values for comparison with the Guinier determinations (Perkins *et al.*, 2008). At [Zn] up to 6 μM, the shape of the *P*(*r*) curves remained unchanged with increase in [Zn], and was indistinguishable between the Tyr402 and His402 FH allotypes (Figure 8.12). The length *L* of both allotypes was 32 nm, and the maximum *M* was at 5.36 ± 0.11 nm and 5.20 ± 0.11 nm for the Tyr402 and His402 allotypes. These values are in good agreement with previous observations for heterozygous FH with zinc (Section 6.2.2; Nan *et al.*, 2008b). Also similar to previous, the intensity of the *P*(*r*) curves and the *L* and *M* values for both allotypes increased with increase in [Zn] above 6 μM, which indicates that zinc-induced oligomerisation occurred with both the Tyr402 and His402 allotypes and was not dependent on heterogeneity (Figure 8.12). For [Zn] at 20 μM, 60 μM and 120 μM, the shapes of the *P(r)* curves were similar between the two allotypes, indicating that similar-sized oligomers had formed under these conditions (Figure 8.12). The *P(r)* intensities and *M* values were slightly higher for the His402 allotype than the Tyr402 allotype, which is consistent with the Guinier analyses, however the difference is not considered to be significant (Figure 8.12). When the *P(r)* analyses were repeated for the SCR-6/8 allotypes with [Zn] up to 6 μM, *L* was determined to be 9 nm for both allotypes, and the curves were indistinguishable between the two allotypes. The *P*(*r*) curves were similar in appearance to those for SCR-6/8 without zinc (Fernando *et al.*, 2007). Above 6 μM zinc, the precipitation of SCR-6/8 made further *P*(*r*) impossible. The lack of difference between the SCR-6/8 allotypes indicated that His402 had no effect on zinc-induced oligomerisation compared to Tyr402.

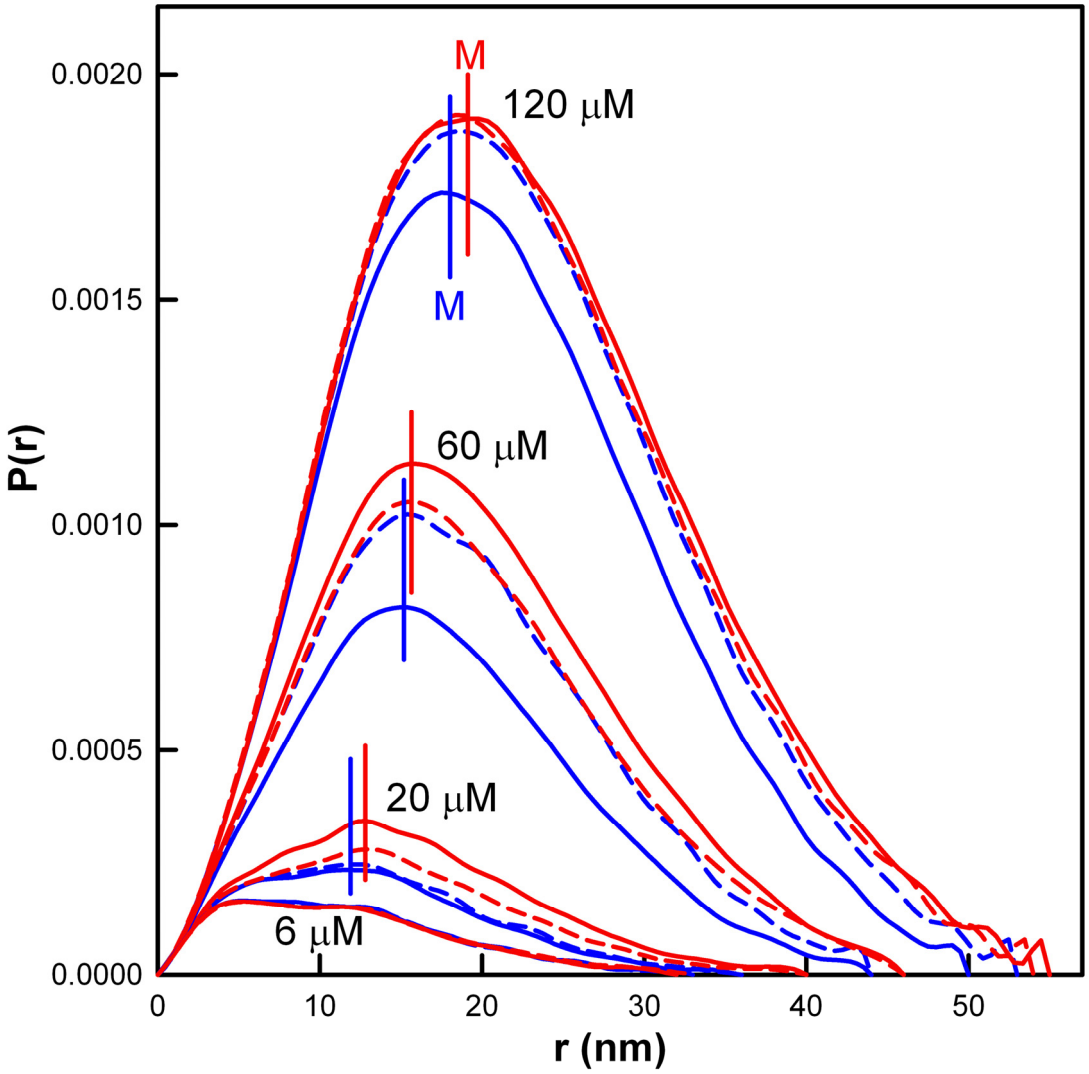

Figure 8.12 Dependence of the distance distribution function *P(r)* of the FH allotypes on zinc concentration. The *P(r)* curves were calculated from the scattering curves of the two FH Tyr402 allotypes (018DK, 016CC; blue) and two FH His402 allotypes (030TJ, 033NV; red). From bottom to top, the zinc concentrations were 6 μM, 20 μM, 60 μM and 120 μM (labelled). The average value of the most frequently occurring distance *M* for each allotype at each zinc concentration is marked by vertical straight lines.

8.2.3 Fluid-phase activity assays of the two allotypes of FH complexes with zinc

In order to test the impact of zinc on the regulatory role of the Tyr402 and His402 FH allotypes, assays of fluid-phase ammonium-inactivated C3 (C3u) cleavage by factor I and two allotypes of FH were performed by zinc titration (Crossley & Porter, 1980). As mentioned in Section 2.3.5, previous fluid-phase activity assays had been performed at significantly lower FH concentrations that included 45 μg/ml (Crossley & Porter, 1980), 3 μg/ml (Day & Sim, 1986), 30 μg/ml (Blom *et al.*, 2003) and 0.3 μg/ml (Tsiftsoglou & Sim, 2004) than the 0.235-0.81 mg/ml (1.5–5.3 μM) observed *in vivo*. Our assays with the FH allotypes were performed at 0.3 mg/ml (1.9 μM) which is comparable with both its physiological range and the heterozygous FH concentrations used previously (Chapter Six; Nan *et al.*, 2008b). Thus the α-chain of C3u was cleaved by factor I in the presence of the FH Tyr402 allotype without zinc to produce two major degradation fragments at apparent sizes of 45 kDa and 75 kDa (Figure 8.13 a), and the cleavage rate was significantly reduced in the presence of 200 μM zinc (Figure 8.13 b). The influence of zinc on this reaction for both FH allotypes was investigated at concentrations of 0 μM, 120 μM and 200 μM (Figure 8.14). This revealed that the C3u cleavage rate was decreased by zinc, in good agreement with the decrease seen previously for heterozygous FH (Chapter Six; Nan *et al.*, 2008b). No difference between the Tyr402 and His402 allotypes was seen (Figure 8.14). If similar levels of FH oligomerisation with both allotypes accounted for the decrease of FH activity by blocking FH access to C3u and/or factor I (Chapter Six; Nan *et al.*, 2008b), this would account for the observed reduced rate of C3u cleavage.

8.2.4 Bioinformatics prediction of zinc-binding sites on full-length FH

Two bioinformatics strategies were developed in order to assess potential zinc-binding sites in FH. The first approach utilised a distance-dependent knowledge-based method that was based on known zinc-binding sites, and was performed by Miss Irene Farabella. A total of 3705 proteins with Zn-binding sites were identified in the Protein Data Bank, which were screened to identify the residues that were within 0.3 nm of the metal site. Zinc binding sites at the interface between two protein surfaces generally contain Asp, His and Glu sidechains as zinc-coordination sites (Auld, 2001). Cys

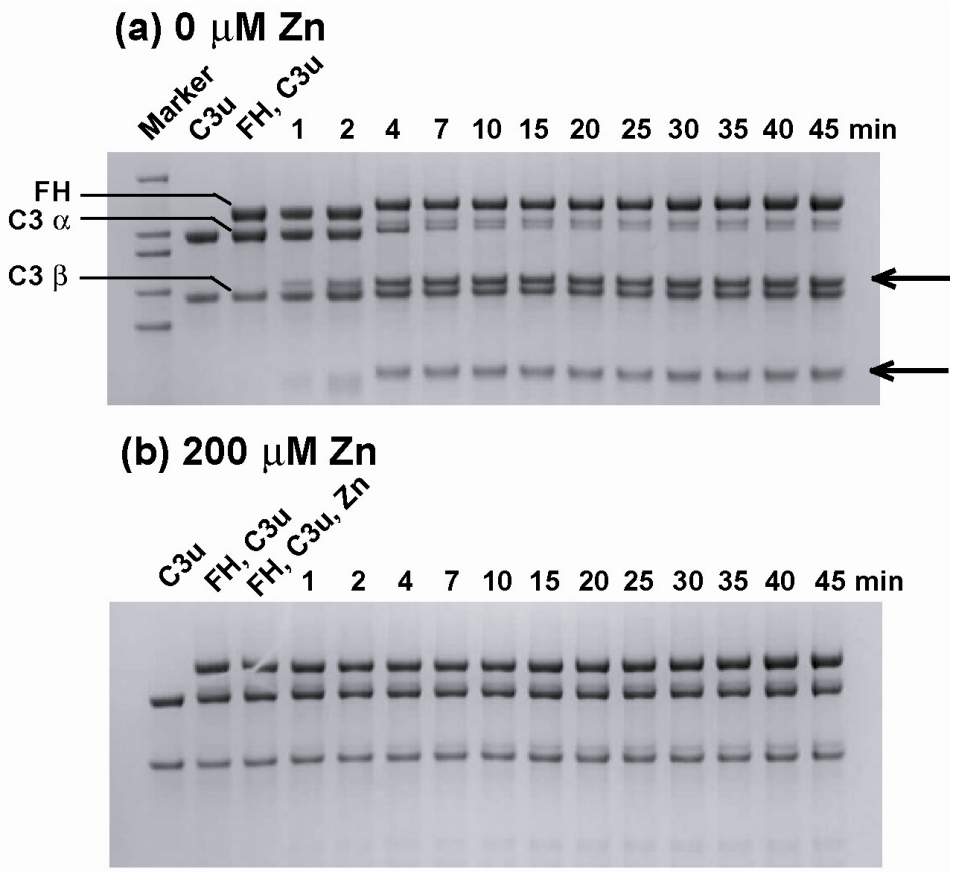

Figure 8.13 Comparison of the reducing SDS-PAGE analyses of C3u cleaved by FI and the FH Tyr402 allotype in the absence and the presence of zinc.

(a) Reducing SDS-PAGE of C3u cleavage by FI and the FH Tyr402 allotype (013HH) in the absence of zinc (from Figure 7.17 a). Lane 1, High Mark™ Prestained High Molecular Weight Standard; Lane 2, 0.3 mg/ml C3u; Lane 3, 0.3 mg/ml C3u and 0.3 mg/ml FH; Lanes 4-15 correspond to Lane 3 with 0.003 mg/ml factor I added with the reaction times in min as labelled. FH and the α-chain and β-chain of C3u are arrowed on the left, and the α-chain cleavage products are arrowed on the right.

(b) Reducing SDS-PAGE of C3u cleavage by FI and the FH Tyr402 allotype (013HH) with 200 μM zinc. Lane 1, 0.3 mg/ml C3u; Lane 2, 0.3 mg/ml C3u and 0.3 mg/ml FH; Lane 3, 0.3 mg/ml C3u, 0.3 mg/ml FH and 200 μM of zinc; Lanes 4 – 15 correspond to Lane 3 with the reaction times in min as labelled.

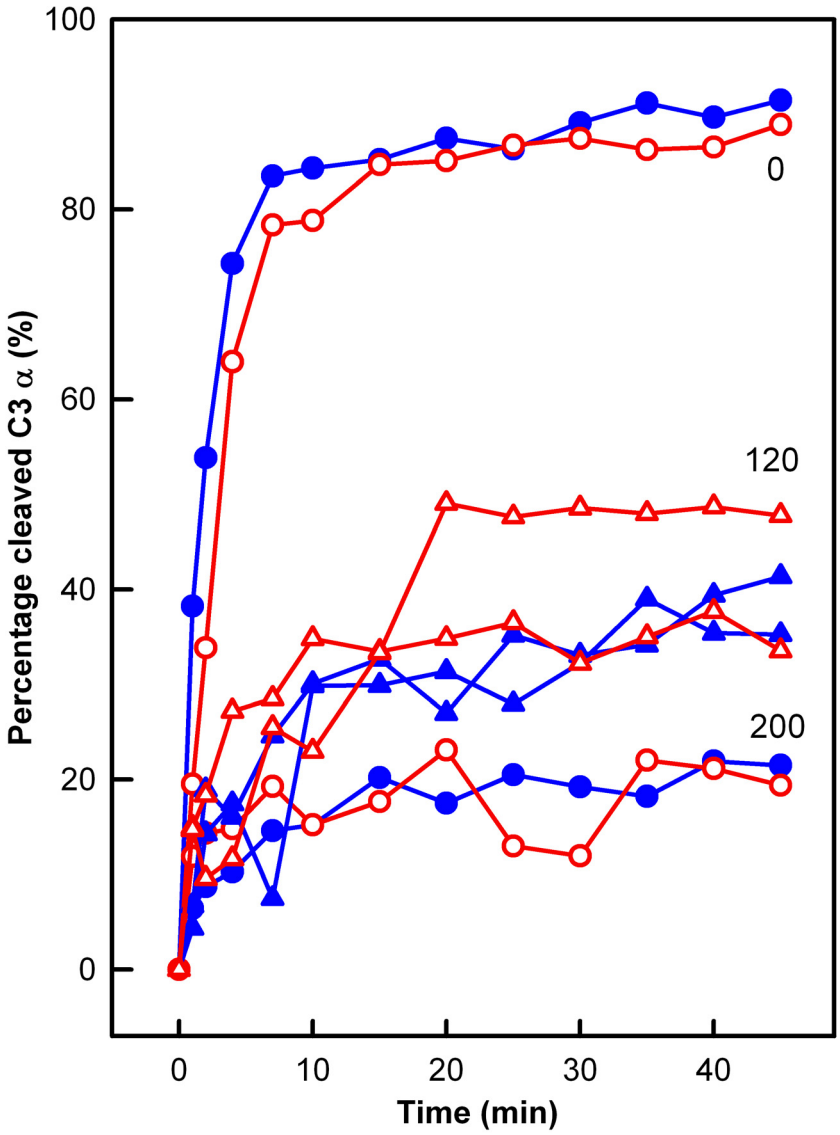

Figure 8.14 Quantification of the cleavage of fluid phase C3u by FI and the two FH allotypes in the presence of zinc. The percentage cleavages of the C3 α-chain are shown as a function of reaction time. The [Zn] values are labelled as shown. The Tyr402 allotypes are in blue (013HH, ●; 022LM, ▲) and the His402 allotypes are in red (015LT, ○; 032KO, Δ).

residues were not included in this survey, because there are no exposed Cys residues in full-length FH. Accordingly a total of 830 zinc-binding sites composed of His, Glu and /or Asp residues only were indentified and classified into 33 subgroups based on their compositions. A contact matrix was defined for each subgroup that is based on the mean separation ± standard deviation between the α-carbon atoms and that between the β-carbon atoms (Materials & Methods). This matrix was used to screen the FH domains in order to predict potential interface zinc-binding sites. For this, crystal and NMR structures for 11 SCR domains and nine homology-modelled structures available at the time of this work were used (Table 8.1) (Barlow *et al.*, 1993; Jokiranta *et al.*, 2006; Saunders *et al.*, 2007; Prosser *et al.*, 2007; Hocking *et al.*, 2008). A total of 202 possible zinc binding sites were identified as residue pairs or triplets that could act as one-half of a zinc-interface binding site. In some cases, a pair or triplet of residues could form a partial zinc binding site with more than one coordination geometry (Table 8.2). In order of probability, 31% of these sites were identified in SCR-6 which had 62.5 sites, followed by 12% in SCR-3, 10% in SCR-16, 7% sites in SCR-2 and 7% sites in SCR-14. Two or less predicted zinc–binding sites were found in five SCR domains (Table 8.1). All the triplets were located in SCR-6 or between SCR-6 and SCR-7 (Table 8.2). The predicted highest number of zinc binding sites in SCR-6 agrees with the similar effect of zinc on the aggregation of full-length FH and SCR-6/8. The predicted involvement of SCR-2, SCR-3 and SCR-16 concurs with the ultracentrifugation experiments with SCR-1/5 and SCR-16/20 that suggest that other weak binding sites may be present. Even though the disease-related His402 residue may be a potential zinc-binding residue, His402 occurred in only two out of the 202 zinc binding sites predicted in FH. The His402 polymorphism thus has a low probability of altering the interaction with zinc, and this agrees with the observed lack of difference between the Tyr402 and His402 allotypes of FH and SCR-6/8.

The second bioinformatics approach was based on submitting the 20 crystal, NMR and homology SCR structures to web servers that predict metal binding sites in proteins (Materials and Methods). The second approach was performed by Mr Felix F. Schumacher. METSITE was developed using relative residue position and does not require side-chain atoms to be present, therefore this is applicable to low resolution structures (Sodhi *et al.*, 2004). It has a high sensitivity of 94.6% and a medium selectivity of 47.8% for zinc. This detected all residues containing a main chain atom

Table 8.1 Distribution of predicted zinc coordination sites in 20 SCR domains (adapted from Rotation 1 report of Miss Irene Farabella, 2009). [a]

Domain	SCR-1	SCR-2	SCR-3	SCR-4	SCR-5
Structure	2RLP	2RLP, 2RLQ	2RLQ	homology	NMR structure
Sites	6	14.5	23.5	2	0

Domain	SCR-6	SCR-7	SCR-8	SCR-9	SCR 10
Structure	2UWN	2UWN	2UWN	homology	homology
Sites	62.5	8.5	1	5	4

Domain	SCR 11	SCR 12	SCR 13	SCR 14	SCR-15
Structure	homology	homology	homology	homology	1HFH
Sites	14	9	8	4	7.5

Domain	SCR-16	SCR 17	SCR 18	SCR-19	SCR-20
Structure	1HFH	homology	homology	2G7I	2G7I
Sites	19.5	0	1	7.5	4.5

[a] Zinc coordination sites that are shared between two adjacent SCR domains are counted as 0.5 per domain.

Table 8.2 Possible predicted zinc binding sites in the FH SCR-6/8 fragment (adapted from Rotation 1 report of Miss Irene Farabella, 2009). [a]

Residues	Location	Possible zinc coordination
D326-D329	SCR-6	DDH, DDHH
D329-H332	SCR-6	DDHH, DHHH
H332-D358	SCR-6	DDDH, DDHH, DEHH, DH, DHH, DHHH
H332-D358-E359	SCR-6	DEHH
H332-D358H360	SCR-6	DDHH, DEHH, DHH, DHHH
H332-D358-E362	SCR-6	DDHH, DEHH
H332-E359	SCR-6	EH, EHH, EHHH
H332-H360	SCR-6	DDHH, DEHH, DHH, DHHH, EHH, HH, HHH
H332-H360-E362	SCR-6	DEHH
H332-H360-E433	SCR-6/7	DEHH
H332-E362	SCR-6	DEHH, EHH, EHHH
H332-E433	SCR-6/7	EHHH, DEH, DEHH
H337-E338	SCR-6	EH, EHHH
D358-E359	SCR-6	DE
D358-H360	SCR-6	DDHH, DH, DHH, DHHH
D358-H360-E362	SCR-6	DEHH
H360-E362	SCR-6	DEHH, EEEH, EEHH, EH, EHHH
H360-E433	SCR-6/7	EHH, DEHH, EHHH
D370-H371	SCR-6	DDHH, DEHH, DHH
D370-H371-H373	SCR-6	DDHH, DHH, DHHH
D370-H373	SCR-6	DDHH, DHH, DHHH
H371-H373	SCR-6	DHHH, EEHH, EHH, HHH, HHHH
H373-D377	SCR-6	DHHH, DDHH
E395-H402	SCR-7	EHH, EHHH
E395-H417	SCR-7	DEHH, EHH,EHHH
D454-E456	SCR-8	DDH, DDE

[a] His402 occurred in 2 of the 76 possible zinc coordinations in SCR-6/8. Zinc coordinations that contain two or three residues also contain two or one H_2O molecules respectively to form the required tetrahedral geometry with zinc.

within 0.7 nm or 0.4 nm of a putative zinc atom position as a seed, then this calculated the residue solvent accessibility in order to achieve the prediction. Using a 0.4 nm threshold, METSITE predicted that a total of 26 out of 175 His, Asp and Glu residues in FH are candidates for 13 predicted interaction sites with zinc. SCR-6 with five residues gave the highest total among the 20 SCR domains, followed by SCR-15 and SCR-20 with three each. A ranking based on the number of residues per zinc binding site (between 1.3 to 1.4) showed that SCR-6, SCR-7, SCR-8, SCR-15 and SCR-20 were the most likely to contain zinc binding sites. Given this outcome, the crystal structure of SCR-6/8 (PDB code 2UWN) was used to create 195 possible homodimeric structures for SCR-6/8 using four different protein docking servers (Materials and Methods). All 195 dimeric structures were subjected to zinc binding site prediction using the web servers METSITE and CHED (Materials and Methods). METSITE identified possible zinc binding sites in 193 out of 195 structures, while CHED with no activated filters identified possible zinc binding sites in 91 structures. The difference is attributed to the higher sensitivity but lower selectivity of METSITE compared to CHED (Sodhi *et al.*, 2004; Babor *et al.*, 2008). The ten most frequent possible zinc binding site residues in the 195 dimeric structures were Glu359, His360, His371, Asp370, Asp485, His332, His417, Glu462, Glu487 and Asp497 in order of frequency. Interestingly, His402 was not included in those ten residues, which is consistent with the experimental observations of no difference seen between the two SCR-6/8 allotypes in the presence of zinc. In order to rationalise the outcome of these searches, the 195 putative dimeric structures were submitted to RMSDCLUST (Materials and Methods) to group together the most similar structures. Nine different zinc binding sites were found in seven clusters that each contained 18, 15, 4, 2, 3, 4 and 5 SCR-6/8 dimer structures, together with a single outlier that did not belong to any cluster. Only two out of the nine possible zinc binding sites possessed all the residues identified as the ten most frequent possible zinc binding residues. One of these binding sites involved Glu359 and His360 on each of two SCR-6/8 monomers (Figure 8.15 a), and the other involved His371 on one SCR-6/8 monomer and Asp485 and Glu487 on the other monomer (Figure 8.15 b). If zinc cross-links pairs of SCR domains, the predictions of Figure 8.15 leads to a schematic cross-linking cartoon in which adjacent pairs of two SCR-6 domains or SCR-6 and SCR-8 domains form contact with each other. The indefinite self-association suggested in Figure 8.16 shows how zinc may cross link SCR-6/8 molecules to form large aggregates that precipitate. As a control of this predictive approach, the same procedure

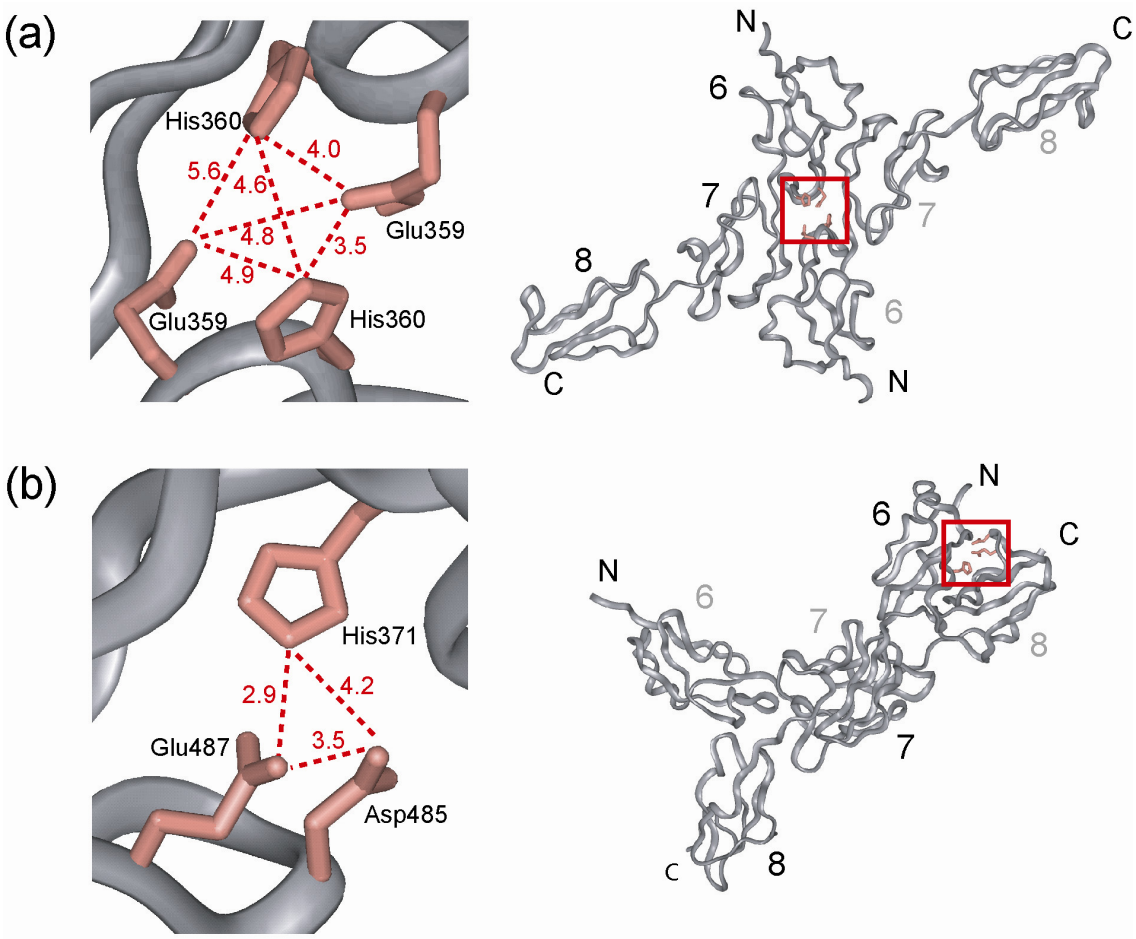

Figure 8.15 Two most likely predicted zinc binding sites to FH SCR-6/8 (taken from Rotation 2 report of Mr Felix F. Schumacher, 2009).

(a) One of the two sites is composed of two Glu359 and His360 sidechains at the surface interface between two SCR-6 domains in the docked dimer. The left panel shows a close-up view of the zinc binding residues, whilst the right panel shows the overall structure of the putative dimer. The distances between each zinc ligand atom (nitrogen or oxygen) are displayed in nm.

(b) The other site is composed of a His371 sidechain in SCR-6 of the first SCR-6/8 monomer and the Asp485 and Glu487 sidechains in SCR-8 of the second SCR-6/8 monomer. Other details follow (a).

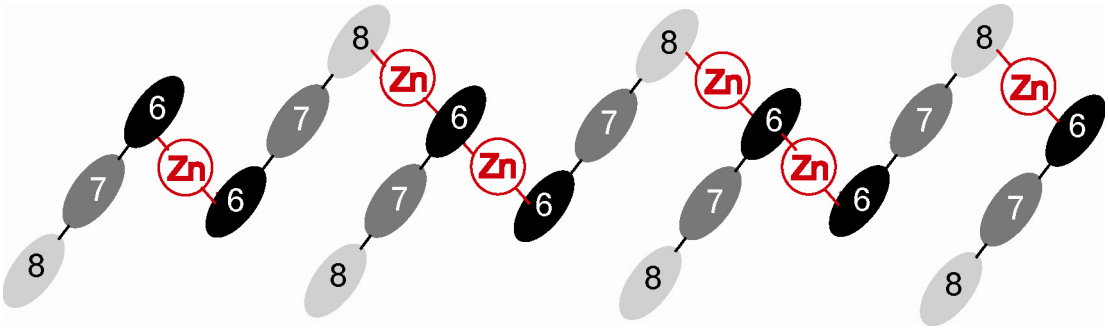

Figure 8.16 Cartoon of the putative zinc-induced SCR-6/8 aggregation. The mechanistic model for the zinc-induced aggregation of SCR-6/8 based on the two possible zinc binding sites shown in Figure 8.15 a, b shows how the two zinc sites may form a daisy-chain of SCR-6/8 that leads to aggregation and precipitation.

was performed with three protein structures with known zinc binding sites (Materials and Methods). All the known zinc binding residues were included in the top ten most frequently occurring residues in the three known protein structures; this outcome supports the credibility of this predictive method.

8.3 Materials and Methods

8.3.1 Protein purification

Human blood was obtained from 48 anonymous genotyped healthy volunteers following ethical approval. Direct DNA sequencing of the PCR product of the FH gene was used to identify the Tyr402His and Val62Ile FH polymorphisms in each volunteer (Table 7.1). Four homozygous FH Tyr402 allotypes (coded 026II, 022LM, 018DK and 016CC), and four FH His402 allotypes (coded 027BA, 032KO, 030TJ and 033NV) were purified using monoclonal affinity chromatography with an MRC-OX23 Sepharose column (Section 6.3.1; Sim *et al.*, 1993; Nan *et al.*, 2008b). The four Tyr402 allotypes were homozygous for Ile62, homozygous for Val62, heterozygous for Val62/Ile62, and homozygous for Val62 in that order, while all four His402 allotypes were homozygous for Val62. Native FI was purified from a pool of just-outdated anonymised human plasma using another monoclonal affinity MRC-OX21 Sepharose column for FI (Section 6.3.1; Sim *et al.*, 1993; Nan *et al.*, 2008b). Bound homozygous FH and native FI were each eluted from the columns using 3 M $MgCl_2$, pH 6.9, then each was dialysed into HEPES buffer (10 mM HEPES, 137 mM NaCl, pH 7.4) in the presence of 0.5 mM EDTA to remove Mg^{2+}. The MRC-OX23 column was washed with guanidine (0.2 M Tris, 4 M guanidine-HCl, pH 8.0) after each FH preparation to avoid allotype cross-contamination. IgG contaminants were removed by passing the FH and FI purifications through a Hitrap™ Protein G HP. Non-specific aggregates and human serum albumin were removed by gel filtration on a Superose™ 6 prep grade XK 16/60 size-exclusive column. Native C3 was purified from fresh plasma by ion-exchange chromatography, and haemolytically inactive C3 in which the reactive thioester is hydrolysed (C3u) was prepared by incubating native C3 in 200 mM hydrazine at 37 °C for 1 h (Section 6.3.1; Dodds, 1993). The DNA constructs for FH SCR-6/8 Tyr402 and His402 allotypes were kindly provided by Miss Ami Miller. The recombinant FH fragment SCR-6/8 Tyr402 was expressed in BL21 (DE3) *E. coli* cells using a pET21ab

vector system, while SCR-6/8 His402 was expressed in BL21 (DE3)pLysS *E. coli* cells using a pET14b vector system. SCR-6/8 was extracted from inclusion bodies, solubilised and refolded. The refolded SCR-6/8 was purified by using ion-exchange chromatography with a Hitrap^{TM} 5 ml Heparin HP column (Fernando *et al.*, 2007; A. Miller and S. J. Perkins, unpublished data). The purification of FH SCR-1/5 and SCR-16/20 fragments were performed by Mr Felix F. Schumacher and Miss Irene Farabella. The fragments FH SCR-1/5 and SCR-16/20 were expressed in the yeast strain P. pastoris, and then purified using a 5 ml nickel affinity columns (Amersham Biosciences), according to the previously described methods (Okemefuna *et al.*, 2008). Both the recombinant fragments FH SCR-1/5 and SCR-16/20 were designed to contain His_6-tag at the C-terminal.

Proteins were dialysed into HEPES buffer for zinc experiments because HEPES does not interact with zinc. Protein concentrations were determined from absorption coefficients of 16.2 for full-length FH Tyr402, 16.1 for full-length FH His402, 12 for FI, 9.4 for C3u, 22.7 for SCR-6/8 Tyr402, 22.1 for SCR-6/8 His402, 17.2 for SCR-1/5, and 15.7 for SCR-16/20 (1%, 280 nm, 1 cm path length) (Perkins & Sim, 1986; Ullman *et al.*, 1998; Aslam & Perkins, 2001; Okemefuna *et al.*, 2009). The integrity of protein samples were routinely checked by SDS-PAGE before and after scattering and ultracentrifugation experiments.

8.3.2 Sedimentation velocity data collection and analyses

Analytical ultracentrifugation data were obtained on two Beckman XL-I instruments equipped with AnTi50 or AnTi60 rotors, using two-sector cells with column heights of 12 mm at rotor speeds of 50,000 r.p.m and 60,000 r.p.m. Sedimentation velocity experiments at 20^{o}C were performed for the two FH allotypes Tyr402 (026II and 022LM) and the two His402 allotypes (027BA and 032KO) at 0.7 – 0.8 mg/ml which were titrated with $ZnSO_4$ at concentrations of 0.2 μM, 2 μM, 6 μM, 20 μM, 60 μM, 120 μM and 200 μM,. The Tyr402 and His402 allotypes of SCR-6/8 at 0.3 mg/ml were titrated with $ZnSO_4$ at concentrations of 0.2 μM, 2 μM, 6 μM, 20 μM, 60 μM, 200 μM, 300 μM and 600 μM. FH SCR-1/5 at 0.3 mg/ml was titrated with of 0 μM, 2 μM, 6 μM, 20 μM, 60 μM, 200 μM and 600 μM zinc, and FH SCR-16/20 at 0.1 mg/ml was titrated

with 0 μM, 2 μM, 20 μM, 200 μM and 600 μM zinc. Data analyses were performed using SEDFIT software (version 11.71) (Schuck, 1998; Schuck, 2000). The distribution analyses *c(s)* provided size and shape data by directly fitting the boundary Lamn equation to 350 scans for FH, 480 scans for SCR-1/5, 440 scans for SCR-16/20, and 640 scans for SCR-6/8. The *c(s)* analyses were based on a fixed resolution of 200, and floated the meniscus, the bottom of the cell, the baseline and the average frictional ratio *f/fo* starting from 1.781 for FH and from 1.200 for SCR-6/8, until the overall root mean square deviation and fits between the observed and calculated sedimentation boundaries were satisfactory. The frictional ratio *f/fo* values were kept un-floated at 1.45 for SCR-1/5, 1.35 for SCR-16/20 monomer, and 1.58 for SCR-16/20 dimer (Okemefuna *et al.*, 2008). Monomer and oligomers were quantitated using the integration function in the *c(s)* analyses. The percentage fraction of monomer and oligomers of FH was derived by assuming that the sum of the signal intensities of monomer and oligomer was 100%. Other details are described elsewhere (Section 4.1.2; Nan *et al.*, 2008a; Okemefuna *et al.*, 2008).

8.3.3 X-ray scattering data collection and analysis

X-ray scattering data was acquired for the FH allotypes in one beam session, and for the SCR-6/8 allotypes in a second beam session on Beamline ID02 at the European Synchrotron Radiation Facility (Grenoble, France) operating with a ring energy of 6.0 GeV in 4-bunch mode and 16-bunch mode in the two beam session respectively to reduce the incident flux (Narayanan & Bosecke, 2001). Storage ring currents were 29 - 43 mA in the first beam session, and 56 - 91 mA in the second beam session. The sample-detector distance was 3 m for the first beam session, and 1.5 m for the second beam session. Potential radiation damage was eliminated by the continuous movement of the sample in a flow cell during beam exposure, the use of 10 time frames of duration between 0.1 sec and 0.25 sec each during each acquisition, and on-line checks for the absence of radiation damage at low *Q*. In the first beam session, the FH Tyr402 allotypes 018DK and 016CC and the His402 allotypes 030TJ and 033NV were studied at 0.9 mg/ml (5.8 μM) with $ZnSO_4$ at concentrations of 0.2 μM, 2 μM, 6 μM, 20 μM, 60 μM, 120 μM, 200 μM and 600 μM. In the second beam session, the Tyr402 and His402 allotypes of SCR-6/8 were studied at 0.2 mg/ml (9.7 μM) with $ZnSO_4$ at concentrations of 0.2 μM, 2 μM, 6 μM, 20 μM, 60 μM, 120 μM, 200 μM, 300 μM and 600 μM. All the

measurements were done in HEPES buffer (10mM HEPES, 137mM NaCl, pH 7.4). Other details including data reduction are described elsewhere (Section 4.2; Fernando *et al.*, 2007; Okemefuna *et al.*, 2008).

In a given solute-solvent contrast, the radius of gyration R_G corresponds to the mean square distance of scattering elements from their centre of gravity, and is a measure of structural elongation. Guinier analyses at low Q gives the R_G value and the forward scattering at zero angle $I(0)$ from the expression (Glatter & Kratky, 1986):

$$\ln I(Q) = \ln I(0) - R_G^2 Q^2/3.$$

This expression is valid in a $Q.R_G$ range up to 1.5. The $I(0)/c$ value (c is the protein concentration in mg/ml) is proportional is the relative molecular mass Mr. If the structure is elongated, the mean cross-sectional radius of gyration R_{XS} and the cross-sectional intensity at zero angle $[I(Q)Q]_{Q\to 0}$ are determined from Guinier analyses in a Q range larger than that used for the R_G determination (Glatter & Kratky, 1986):

$$\ln [I(Q)Q] = \ln [I(Q)Q]_{Q\to 0} - R_{XS}^2 Q^2/2.$$

The Guinier analyses were performed using an interactive PERL script program SCTPL7 (J. T. Eaton and S. J. Perkins, unpublished software) on Silicon Graphics OCTANE Workstations.

Indirect transformation of the $I(Q)$ curve measured in reciprocal space into real space gives the distance distribution function $P(r)$ and was carried out using the program GNOM (Semenyuk & Svergun, 1991):

$$P(r) = \frac{1}{2\pi^2}\int_o^\infty I(Q)\, Qr \sin(Qr)\, dQ$$

$P(r)$ corresponds to the distribution of distances r between volume elements. This offers an alternative calculation of the R_G and $I(0)$ values that is based on the full scattering curve $I(Q)$, and not that at low Q. It also gives the most frequently occurring distance M and the maximum dimension of the macromolecule L. For FH at 0.9 mg/ml titrated with zinc, the X-ray curves utilised up to 344 data points for Q between 0.08 nm^{-1} and 1.60 nm^{-1}. Other details are described elsewhere (Section 4.2; Nan *et al.*, 2008a; Aslam & Perkins, 2001; Fernando *et al.*, 2007; Okemefuna *et al.*, 2008).

8.3.4 Fluid-phase activity assays

To determine activities, the reaction mixtures containing 0.3 mg/ml FH, 0.3 mg/ml C3u and 0.003 mg/ml factor I were incubated in a water bath at 37 °C in three concentrations of $ZnSO_4$ (0 μM, 120 μM and 200 μM). The functions of two pairs of the two allotypes of FH were tested. The FH Tyr402 allotype 013HH and the FH His402 allotype 015LT were tested with 0 μM and 200 μM of zinc, and the FH Tyr402 allotype 022LM and the His402 allotype 032KO were tested with 120 μM of zinc. At timed intervals, 5 μl aliquots were removed for reducing SDS-PAGE analyses. Three blank controls were used, namely 0.3 mg/ml C3u; 0.3 mg/ml C3u and 0.3 mg/ml FH; and 0.3 mg/ml C3u, 0.3 mg/ml FH and zinc. The C3 α-chain band densities from SDS-PAGE were measured using the gel analysis system SYNGENE (Synoptics Ltd., Cambridge, UK). The C3 α-chain cleavage was referenced to the averaged density of the uncleaved bands in the controls.

8.3.5 Molecular prediction of surface zinc binding sites

Structural database analyses were used to predict protein-interface-type zinc binding sites on protein surfaces. A dataset of 3705 Zn-binding protein crystal structures with resolutions better than 0.3 nm was identified from the Protein Data Bank. Residues that were located within 0.3 nm distance of the zinc atom were assigned as putative zinc coordinating residues using a PERL script to scan the Protein Data Bank. Of the 4883 putative zinc binding sites that were identified, a total of 830 zinc-binding sites composed of His, Glu and /or Asp as zinc coordination residues were analysed and classified into 33 subgroups based on the amino acid composition of each site. In each subgroup, the distance x between the Cα atoms and that between the Cβ atoms of each zinc-coordinating residue j were calculated as a residue pair type (x,j), and stored in a contact matrix CM. For each residue pair in CM, the average distance $\bar{x}$ and its standard deviation σ was calculated. An algorithm was implemented to screen each protein structure of interest for residues that form putative partial Zn binding sites. For a given protein structure, solvent-exposed Asp, His and Glu side-chains were identified. A residue is considered exposed if its side-chain has a relative surface accessibility greater than 20%. The geometric distances between pairs and triplets of Cα atoms and Cβ atoms

of the putative zinc-coordinating residues were calculated. If these distances fall within the distance cut-off $\bar{x} \pm \sigma$, then the pair or triplet of residues became considered as possible zinc coordinating residues. Using this algorithm, 11 experimental SCR crystal or NMR structures for SCR-1/2, SCR-2/3, SCR-5, SCR-6/8, SCR-15/16 and SCR-19/20 (Barlow *et al.*, 1993; Jokiranta *et al.*, 2006; Saunders *et al.*, 2007; Prosser *et al.*, 2007), and nine homology-modelled SCR structures for SCR-4, SCR-9, SCR-10, SCR-11, SCR-12, SCR-13, SCR-14, SCR-17 and SCR-18 (Saunders *et al.*, 2007) were screened. This bioinformatics analysis was done by Miss Irene Farabella.

Further predictions of metal binding sites in FH were carried out using web servers. First, the 20 experimental and homology SCR structures in FH were evaluated using METSITE (http://bioinf.cs.ucl.ac.uk/metsite) (Sodhi *et al.*, 2004) which uses a set of neural network classifiers trained to identify potential cation sites. Second, to form FH dimer structures, the SCR-6/8 His402 crystal structure (PDB code 2UWN) was docked using four different docking approaches available as web servers including CLUSPRO (http://cluspro.bu.edu/login.php), HEX (http://www.csd.abdn.ac.uk/hex_sever/), PATCHDOCK (http://bioinfo3d.cs.tau.ac.il/PatchDock/) and ROSETTADOCK (http://rosettadock.graylab.jhu.edu/) (Comeau *et al.*, 2003; Gray *et al.*, 2003; Ritchie, 2003; Schneiderman-Duhovny *et al.*, 2005; Gray, 2006). These four docking programs were selected according to their performance in the Critical Assessment of Predicted Interactions surveys (Mendez *et al.*, 2005; Lyskov and Gray, 2008). Third, the possible biological relevant dimeric structures were tested again by METSITE and another web server CHED (Babor *et al.*, 2008) to detect the possible zinc binding sites at the protein interface of the dimeric structures. The CHED web server searches for Cys, His, Glu and Asp residues with atoms within several specified distances to each other and a 0.27 nm distance to the putative zinc atom position, and if the distances do not match, a independent rotamer library was used to find an appropriate fit configuration. The sites found in CHED are filtered by a decision tree and a support vector machine to verify their suitability. Fourth, the dimeric structures that possess zinc binding sites predicted by METSITE and CHED were clustered by using the program RMSDCLUST to group similar structures. RMSDCLUST computes the centre of gravity of every dimeric structure and finds the lowest root mean square deviation (r.m.s.d) between each structure, and the clusters are formed by the structures within a r.m.s.d limit of 0.6 nm. To validate the methods, the same predictions were performed with three zinc binding

structures as benchmarks, namely human interferon-β (PDB code 1AU1), human growth hormone (PDB code 1BP3) and thermophilic cytochrome P450 from *S. solfataricus* (PDB code 1F4T) (Karpusas *et al.*, 1997; Somers *et al.*; Yano *et al.*, 2000).

8.4 Conclusions

Even though metals have not generally been considered as FH ligands, the study in Chapter Six showed that heterozygous FH aggregated strongly in the presence of zinc, and that five transition metals caused FH to aggregate at physiological FH concentrations and pathophysiological zinc and copper concentrations of ≥ 20 μM (Perkins *et al.*, 1991; Nan et al 2008b; Lengyel *et al.*, 2007). Zinc has the strongest effect on FH. In this study, using ultracentrifugation and X-ray scattering, we have shown that this aggregation occurs for the major homozygous forms of FH with either Tyr402 or the disease-related His402 allotypes, and including the Val62 or Ile62 allotypes. This provides the key result that zinc-induced aggregation does not result from FH heterogeneity. We have also identified SCR-6/8 as a major locus for this process from ultracentrifugation and scattering studies that showed that SCR-6/8 precipitated with zinc. Bioinformatics modelling predictions confirmed that SCR-6/8 has the highest propensity to form partial zinc binding sites at its surface, which become indefinitely cross-linked in the presence of zinc (Figure 8.16). Control experiments with SCR-1/5 and SCR-16/20 showed that SCR-1/5 also precipitated with zinc, while SCR-16/20 remained soluble but formed some oligomers with zinc. The bioinformatics predictions indicated that additional weak zinc binding sites may be present in SCR-1/5 and SCR-16/20, although the involvement of the His_6-tag on our two recombinant fragments in facilitating zinc binding cannot be ruled out. Overall, this work now explains the zinc-induced formation of large compact FH oligomers in terms of multiple weak surface zinc-binding sites, primarily within the SCR-6/8 region. Interestingly, the Tyr402 or His402 allotypes have no significant influence on zinc-induced aggregation, even though His402 might be considered as a zinc-chelating residue.

FH is a major complement regulator in blood, and is expressed and secreted by many different cell types including the RPE (An *et al.*, 2006). The major physiological ligands of FH include C3b and its C3d fragment, heparin and other glycososaminoglycans, C-

reactive protein and FH self-association, in addition to zinc binding (Perkins *et al.*, 2010a; Perkins *et al.*, 2010b). All these ligands bind weakly to FH with μM affinities, and this is consistent with the relative abundance of FH in serum. The FH-zinc interaction has already been discussed previously (Chapter Six; Nan *et al.*, 2008b). Recent studies show that C3b and C3d bind with K_D values of 3.5-14 μM and 2.6 μM respectively (Schmidt *et al.*, 2008; Okemefuna et al 2009), C-reactive protein binds with a K_D value of 4-15 μM (Okemefuna *et al.*, 2010), and FH dimerises with a K_D value of 28 μM (Chapter Five; Nan *et al.*, 2008a). If FH is found at 0.6 mg/ml in serum, this means that 11% of FH exists as dimers. If C3b is found at 1 mg/ml, this means that 29% of FH is bound to C3b if the K_D value is 3.5 μM. If C-reactive protein is at the acute-phase level of 0.4 mg/ml, this means that 32% of FH is bound to C-reactive protein if the K_D value is 4.2 μM. This calculation assumes that no other factors in serum influence these equilibria, and that the three equilibria are considered separately from each other for purpose of illustration here. In comparison to these physiological interactions, the pathophysiological interaction between FH and zinc is characterised by comparable K_D values in the region of 6-20 μM, implying that FH will be 50% bound to zinc if bioavailable zinc is present at 13 μM. This concentration agrees with the total serum zinc concentration of 12.5 μM (AREDS Research Group, 2002). However most of the zinc in plasma is bound to proteins such as serum albumin, and only 2-8% of this zinc is bioavailable (Lu *et al.*, 2008). The zinc level remains low at 14.7 μM even after a daily diet supplement with 80 mg zinc in the AREDS trials (AREDS Research Group, 2002). Therefore, normal zinc levels in plasma are too low to induce FH oligomerisation. Interestingly, because two of the most frequently predicted zinc binding residues His360 and His371 have been implicated in glycosaminoglycan binding to FH (Prosser *et al.*, 2007), it is possible that zinc binding to FH can perturb the binding of glycosaminoglycans to FH.

Human ocular tissues contain unusually high concentrations of zinc, where the zinc concentration is 472 μg/g of dry tissue in the RPE-choroid complex, and 464 μg/g in the neurosensory retina (Galin *et al.*, 1962). Zinc in the RPE-choroidal complex is mostly bound to melanin, metallothionein and other zinc binding proteins, and it has been proposed that 10% of zinc in retina is free or chelatable (Galin *et al.*, 1962; Ugarte & Osborne, 2001; Newsome *et al.*, 1992). Zinc is essential for the normal function of the

retina, being suggested to act as an antioxidant. Zinc appears to be essential for the normal function of the retina, but its exact role is not clear (Section 3.2.2). RPE cells can accumulate zinc following oral supplementation and retain it longer than any other tissues in the body (Newsome *et al.,* 1992). This zinc might be released through photo oxidative damage but the mechanism for this is not known (Ugarte & Osborne, 2001; Lengyel et al., 2007). High millimolar concentrations of zinc are present in drusen (Lengyel *et al.*, 2007). Even if a small fraction of the zinc in drusen becomes bioavailable, this level will be sufficient to induce the localised aggregation of FH. The above comparison with the K_D values for FH interactions with its other ligands (above) shows that the regulatory balance of FH activity in terms of interactions with C3b, heparin and C-reactive protein can be disturbed. The likelihood that zinc mostly interacts with the SCR-6/8 regions, which is a locus for heparin and C-reactive protein interactions, indicates that FH function can be perturbed if sufficient excess zinc is available. Such a mechanism can contribute to both the formation of drusen deposits and the inhibition of the regulatory function of FH to cause host cell damage. Daily supplements with 80 mg zinc, 2 mg copper, vitamins C and E, and β carotene are recommended by AREDS as a means of reducing the risk for progression to advanced AMD (AREDS Research Group, 2001a; AREDS Research Group, 2001b). Interestingly, the AREDS-recommended zinc supplements with antioxidants correlated with a greater reduction in progression to advanced AMD in patients (34% of cases) who are homozygous for the FH Tyr402 allotype compared to patients (11% of cases) who are homozygous for the FH His402 allotype (Klein *et al.*, 2008). Our current study offers no direct explanation for this observation because no significant difference in zinc-induced FH aggregation was seen between the Tyr402 and His402 allotypes of FH and SCR-6/8.

The most common coordination geometry of zinc binding sites is tetrahedral (Auld, 2001). Here, the bioinformatics analyses indicated the availability of 3705 zinc binding co-ordinations in the Protein Data Bank for evaluation. Protein interface zinc binding sites are primarily supplied by His, Glu and Asp residues, but sites containing Cys are also found (not relevant to FH), and β-sheet secondary structures predominately contribute to zinc binding sites. Zinc binding is able to induce protein self-association or link two different proteins (Auld, 2001). The previous discussion of potential FH zinc binding sites (Figure 6.18) (Nan *et al.*, 2008b) is now clarified by the abundance of

potential zinc sites that were predicted using a distance-based algorithm, suggesting that multiple weak zinc binding sites exist in FH. This outcome predicts that a range of different zinc-induced oligomers will form, which is in good agreement with the observation of many overlapping peaks in the ultracentrifugation *c(s)* size distribution analyses (i.e. the opposite of the formation of fewer well-resolved signals such as those observed for FH alone (Figure 5.7 and Figure 7.5) and also with the formation of indefinite oligomers at high zinc concentrations. The prediction of multiple sites also explains better why different types of FH oligomers were observed with different metals such as copper (Chapter Six; Nan *et al.*, 2008b). Finally the predictions were also informative in that they explained the lack of difference seen between the SCR-6/8 Tyr402 and His402 allotypes, because His402 was not predicted to be a significant zinc-binding ligand. These analyses provide insight into the weak binding of zinc to other plasma proteins. It is possible that the outcome of this FH-zinc study will be applicable to other plasma proteins. For example, the zinc-induced oligomer formation in C3 has been observed (K. Li & S. J. Perkins, unpublished data).

Chapter Nine

Conclusions

9.1 Prologue

In the innate immune system, factor H (FH) is a major regulator of complement alternative pathway activation. It is composed of 20 short complement regulator (SCR) domains arranged in tandem, and 19 peptide linkers between the SCR domains. Over the years, high resolution structures have been resolved for small SCR domain fragments (Section 2.1.2), and homology structures have been generated for the remainder (Section 2.1.3). A high resolution structure for full-length FH has never been determined due to its large size, flexibility and glycosylation, and the conformation of full-length FH cannot be obtained by joining the known SCR domains structures together. The combination of constrained X-ray solution scattering modelling and analytical ultracentrifugation offers an approach to reveal the medium-resolution folded back structure of full-length FH in solution. However, the self-association properties of FH have complicated the modelling curve fits (Figure 7.14). In this thesis, an improved solution structure for full-length FH was obtained in which self-association issues were minimized (Chapter Seven).

FH binds to multiple ligands such as C3b, heparin and C-reactive protein, and the binding sites for different ligands are located in different SCR domains (Section 2.3). The studies of the affinities between FH and its ligands showed micromolar K_D values which indicate weak binding. Although some dimerisation of FH fragments has been observed before (Section 2.3.4), the self-association properties of full-length FH have not previously been analysed, and most of the previous studies of FH are based on the assumption that FH is monomeric in solution. In this thesis, the weak self-association of full-length FH has been clarified systematically by using improved X-ray solution scattering and analytical ultracentrifugation analyses (Chapter Five; Chapter Seven). This process needs to be taken into account for interpreting the physiological interaction of FH. Metals have not been generally considered as FH ligands. Previous studies showed that zinc causes FH to aggregate, and this inhibits the regulatory function of FH in the fluid-phase (Section 2.3.5). The K_D of zinc binding and the domain interaction sites have now been clarified by the work in this thesis (Chapter Six; Chapter Eight).

FH is genetically related to several human diseases (Section 2.5). For example, it is related to age-related macular degeneration (AMD), a leading cause of blindness in the

elderly in the western world, through a Tyr402His polymorphism in domain SCR-7 where binding sites for multiple ligands locate. Many studies have been done on comparing the binding affinities of the wild-type Tyr402 allotype and the disease-related His402 allotype of FH with ligands such as heparin, C3b and C-reactive protein. Few studies have been focussed on the self-association properties of FH and its metal binding. Millimolar concentrations of zinc are found in drusen which is a hallmark of early AMD (Section 3.3.1). The work in this thesis presented a detailed comparison of these properties of the two allotypes of FH, and characterised the similar weak self-association and zinc-induced oligomerisation of the two allotypes.

9.2 Solution structure of FH

In this thesis, in relation to FH solution structures, X-ray scattering showed that the maximum length is 28 nm for both monomeric FH Tyr402 and His402 allotypes. Constrained scattering modelling fits gave similar best-fit structures of monomeric FH for the two allotypes, with an improved goodness-of-fit than the previous models for heterozygous FH monomer (Figure 7.13; Figure 7.14). These new results were due to the improvements in X-ray scattering instrumentation and a minimised level of FH oligomerisation. These best-fit structures were more folded-back than those previously determined, and have calculated sedimentation coefficient values that agreed well with the experimental values obtained by ultracentrifugation. The Tyr402His polymorphism is solvent exposed on the surface of SCR-7, where the previously determined solution structures for SCR-6/8 and the NMR structures for SCR-7 are similar between the Tyr402 allotype and His402 allotype. In this thesis, the similarity between the structures of the two allotypes of full-length FH monomer complements the structures for these fragments to show that the polymorphism has no effect on the overall FH structure even through it changes the surface charge of SCR-7. This result suggests that the inter-SCR flexibility of FH is limited, and that the reduced binding affinity of FH His402 to ligands such as CRP is due to the residue change itself rather than an altered FH structure.

9.3 Self-association of FH

Prior to this thesis, FH was known to form dimers, however the basis for these

observations was unclear (Section 2.3.4). In this thesis, the study of self-association properties of FH started with a combination of solution X-ray scattering and analytical ultracentrifugation analyses of heterozygous FH (Chapter Five). The dimerisation of FH had firstly been reported in a previous X-ray scattering study of FH at high concentrations that was necessary for data collection at that time (Section 2.3.4). The updated X-ray scattering study presented in Chapter Five utilised heterozygous FH at lower concentrations with improved signal-noise ratios, and revealed clear dependences of the Guinier parameters R_G, $I(0)/c$ and $R_{XS\text{-}1}$ values on FH concentration that corresponded to the weak self-association of FH (Figure 5.2). From sedimentation equilibrium analyses, the self-association of heterozygous FH below 1.36 mg/ml can be best fitted to a reversible monomer-dimer equilibrium with a dissociation constant K_D value of 28 μM. Less reversible higher oligomers formed at increased concentrations (Figure 5.5). At physiological concentrations of FH (0.235 – 0.810 mg/ml) in serum, the K_D value of 28 μM suggests that 85% to 95 % of FH will be monomeric in serum without considering other factors that might affect this ratio. This K_D value is comparable with that of 40 μM for the dimerisation of the SCR-6/8 His402 allotype, and that of 16 μM for the dimerisation of SCR-16/20 previously determined by ultracentrifugation (Section 2.3.4). Sedimentation coefficient distribution analyses in sedimentation velocity experiments revealed that monomeric FH was the major species, together with small amount of as many as six different higher oligomeric forms of FH (Figure 5.7). These observations suggest a progressive mechanism for FH self-association.

A previous study showed that the disease-related His402 allotype of FH SCR-6/8 exhibits slightly higher self-association than the lower-risk Tyr402 allotype of FH SCR-6/8 (Fernando *et al.*, 2007). This observation triggered the study in this thesis of the self-association properties of the two homozygous allotypes of full-length FH (Chapter Seven). In this study, surface plasmon resonance analyses confirmed that the SCR-6/8 His402 self-associates more than SCR-6/8 Tyr402 does (Figure 7.3). However, the two allotypes of full-length FH showed similar 12 % amounts of oligomeric forms in surface plasmon resonance and analytical ultracentrifugation analyses (Figure 7.5). The similar self-associations of the two allotypes of full-length FH were confirmed in mass spectrometry analyses which indicated that both FH allotypes exhibited monomer,

dimer and possibly trimer forms, and X-ray scattering analyses which showed that similar concentration dependences of the Guinier parameters. The observed FH dimer, trimer and tetramer in sedimentation-coefficient distribution analyses can be well explained by the "daisy-chains" oligomer formation of FH best-fit monomeric structure by alternating dimerisation sites at SCR-7 and SCR-20. Since the bindings of FH with ligands such as CRP and C3b are weak interactions with micromolar level K_D values, the self-association properties may compete with these physiological interactions of FH.

9.4 Zinc-induced oligomerisation of FH

Prior to this thesis, FH was known to aggregate strongly with zinc (Section 2.3.5). In this thesis, the interaction between FH and zinc was first investigated using heterozygous FH using a more quantitative approach (Chapter Six). Heterozygous FH at 2.8 – 7.0 μM was titrated with 0.2 – 200 μM of zinc. By performing X-ray scattering experiments, heterozygous FH was shown to be unaffected by [Zn] lower than 20 μM. With [Zn] ≥ 20 μM, the Guinier parameters R_G, $I(0)/c$ and $R_{XS\text{-}1}$ values showed significant increases as [Zn] increased (Figure 6.2), which indicates the formation of large oligomers of FH with a K_D of about 20 μM. The distance distribution analyses of the scattering data showed that the maximum dimension of FH increased from 32 nm to 50 nm, indicating that the large oligomers of FH are compact in conformation. In the sedimentation coefficient distribution analyses of the sedimentation velocity experiments, monomeric FH at 5.57 S was the major species at [Zn] up to 60 μM. A series of large oligomers in solution with sedimentation coefficient value up to 100 S were observed at [Zn] above 60 μM (Figure 6.9). These zinc-induced oligomers of FH can be disassembled by chelation using EDTA. Control experiments were performed with other metals. Copper can induce FH to form structurally distinct oligomers, while Ni, Cd and Fe exhibited small amounts of oligomers, and Ca and Mg showed no effects (Figure 6.14). The oligomerisation of heterozygous FH induced by zinc and copper was matched with reduced FH regulatory functions in fluid-phase. Therefore, zinc and copper should be considered as inhibitory ligands of FH when the metal concentrations are high enough to trigger the oligomerisation of FH.

The locations of the zinc binding sites in FH were unknown prior to this thesis. The common residues for zinc binding at protein interface include His, Asp, Glu and Cys residues, and the most frequently observed coordination geometry is tetrahedral (Section 2.3.5). The AMD-related polymorphism Tyr402His in SCR-7 introduces a solvent-exposed His402 side chain that may leads to increased zinc binding. This raised the question of whether the zinc interactions with FH Tyr402 allotype and FH His402 allotype are different (Chapter Eight). Similar to heterozygous FH, large amounts of oligomers were formed by each of the Tyr402 and His402 allotypes of full-length FH in the presence of zinc observed by analytical ultracentrifugation. By X-ray scattering, the Guinier parameters R_G, $I(0)/c$ and $R_{XS\text{-}1}$ values for both two allotypes of full-length FH showed the same dependences on [Zn] as for heterozygous FH. The same experiments were performed on the two allotypes of FH SCR-6/8, and the two SCR-6/8 allotypes strongly precipitated in a similar manner with zinc at [Zn] $\geq$ 20 μM. Thus the Tyr402His polymorphism does not lead to different interactions with zinc. Since the zinc-binding properties of full-length FH and that of SCR-6/8 share similar K_D values (about 20 μM), the main interacting domains within FH are most likely located in SCR-6/8 (Figure 8.9; Figure 8.11). Bioinformatics predictions of zinc binding sites revealed multiple zinc binding sites at several SCR domains, of which the most abundant were within SCR-6/8. These predictions agreed well with the experimental results. Interestingly, multiple binding sites for FH ligands such as CRP and heparin are located in SCR-7, thus the binding of zinc may inhibit other ligands binding where [Zn] is sufficient and affect the regulatory role of FH.

9.5 Implications for AMD

In serum, the physiological [Zn] is 12.7 μM, however only 2-8 % of zinc is bio-available. Therefore [Zn] is too low to induce the formation of FH oligomers in serum. However in the RPE-choroid complex, [Zn] is unusually high (472 μg/g). As in serum, most of zinc in the RPE-choroid complex is bound to proteins. Under conditions such as light stimuli, zinc can be released from the RPE, and become bio-available in the extracellular space (Section 3.2). High millimolar concentrations of zinc are present in drusen (Section 3.3). Even only 10 % of zinc in drusen is bio-available, [Zn] would be sufficient to induce the strong oligomerisation of FH locally. FH was found in drusen,

and complement activation-related inflammation has been suggested in relation to drusen formation. The RPE is a local source for FH (Section 2.5.3). Thus the interaction between zinc and FH may play a role in the formation of drusen, through a metal-induced aggregation mechanism or a metal-induced complement mis-regulation mechanism. The AREDS trials found that a supplement with zinc alone, or with zinc together with vitamins C and E and β carotene reduces the risk for progression to advanced AMD. Interestingly, a follow-up study suggested that this treatment has a much weaker response in patients with FH His402 allotype than in those with FH Tyr402 allotype (Section 3.3.2). Because the results from this thesis showed very similar zinc binding of the two FH allotypes (Chapter Eight), the different responses to zinc supplementation are not due to direct effects of the Tyr402His polymorphism on the interactions between FH and zinc.

References

Abdul Ajees, A., Gunasekaran, K., Volanakis, J. E., Narayana, S. V., Kotwal, G. J. & Murthy, H. M. (2006). The structure of complement C3b provides insights into complement activation and regulation. *Nature,* **444**, 221–225.

Abrera-Abeleda, M. A., Nishimura, C., Smith, J. L., Sethi, S., McRae, J. L., Murphy, B. F., Silvestri, G., Skerka, C., Józsi, M., Zipfel, P. F., Hageman, G. S. & Smith, R. J. (2006). Variations in the complement regulatory genes factor H (CFH) and factor H related 5 (CFHR5) are associated with membranoproliferative glomerulonephritis type II (dense deposit disease). *J. Med. Genet.* **43**, 582-589.

Alsenz, J., Lambris, J. D., Schulz, T. F. & Dierich, M. P. (1984). Localization of the complement-component-C3b-binding site and the cofactor activity for factor I in the 38kDa tryptic fragment of factor H. *Biochem. J.* **224**, 389–398.

An, E., Lu, X., Flippin, J., Devaney, J. M., Halligan, B., Hoffman, E. P., Strunnikova, N., Csaky, K. & Hathout, Y. (2006). Secreted proteome profiling in human RPE cell cultures derived from donors with age related macular degeneration and age matched healthy donors. *J. Proteome Res.* **5**, 2599-2610.

Anderson, D. H., Mullins, R. F., Hageman, G. S. & Johnson, L. V. (2002). A role for local inflammation in the formation of drusen in the aging eye. *Am. J. Ophthalmol.* **134**, 411-431.

An introduction to Biacore®'s SPR technology. (2001). GE Healthcare Bio-Sciences AB, Uppsala, Sweden.

Arthur, K. K., Gabrielson, J. P., Kendrick, B. S. & Stoner, M. R. (2009). Detection of protein aggregates by sedimentation velocity analytical ultracentrifugation (SV-AUC): sources of variability and their relative importance. *J. Pharm. Sci.* **98**, 3522-3539.

Age-Related Eye Disease Study Research Group. (2001a). A randomized, placebo-controlled, clinical trial of high-dose supplementation with vitamins C and E, beta carotene, and zinc for age-related macular degeneration and vision loss: AREDS report no. 8. *Arch. Ophthalmol.* **119**, 1417-1436.

Age-Related Eye Disease Study Research Group. (2001b). A randomized, placebo-controlled, clinical trial of high-dose supplementation with vitamins C and E and beta carotene for age-related cataract and vision loss: AREDS report no. 9. *Arch. Ophthalmol.* **119**, 1439-1452.

Age-Related Eye Disease Study Research Group. (2002). The effect of five-year zinc supplementation on serum zinc, serum cholesterol and hematocrit in persons randomly assigned to treatment group in the Age-Related Eye Disease Study. *J. Nutr.* **132**, 687–702.

Atkinson, J. P. & Goodship, T. H. (2007). Complement factor H and the hemolytic uremic syndrome. *J. Exp. Med.* **204**, 1245-1248.

Aslam, M. & Perkins, S. J. (2001). Folded back solution structure of monomeric factor H of human complement by synchrotron X-ray and neutron scattering, analytical ultracentrifugation and constrained molecular modelling. *J. Mol. Biol.* **309**, 1117-1138.

Auld, D. S. (2001). Zinc coordination sphere in biochemical zinc sites. *Biometals.* **14**, 271-313.

Babor, M., Gerzon, S., Raveh, B., Sobolev, V. & Edelman, M. (2008) Prediction of transition metal-binding sites from apo protein structures. *Proteins,* **70**, 208-217.

Balbo, A., Minor, K. H., Velikovsky, C. A., Mariuzza, R. A., Peterson, C. B. & Schuck, P. (2005). Studying multiprotein complexes by multisignal sedimentation velocity analytical ultracentrifugation. *Proc. Natl. Acad. Sci. U. S. A.* **102**, 81-86.

Barlow, P. N., Norman, D. G , Steinkasserer, A., Horne, T. J., Pearce, J., Driscoll, P. C., Sim, R. B. & Campbell, I. D. (1992). Solution structure of the fifth repeat of factor H: a second example of the complement control protein module. *Biochemistry*, **31**, 3626-3634.

Barlow, P. N., Steinkasserer, A., Norman, D. G., Kieffer, B., Wiles, A. P., Sim, R. B. & Campbell, I. D. (1993). Solution structure of a pair of complement modules by nuclear magnetic resonance. *J. Mol. Biol.* **232**, 268-284.

Beckman, Model XL-A/XL-I Analytical Ultracentrifuge Optima^{TM} Series Training Guide, (1998).

Beckman, Coulter$_{TM}$ ProteomeLab^{TM} XL-A/XL-I Protein Characterization System Instruction Manual, (2003).

Beckman Analytical Ultracentrifuge Fluorescence Detection System and Advanced Operating System User Manual, (2009).

Benesch, J. L. P. & Robinson, C. V. (2009). Dehydrated but unharmed. *Nature*, **462**, 575-576.

Bhakdi, S., Kaflein, R., Halstensen, T. S., Hugo, F., Preissner, K. T. & Mollnes, T. E. (1988). Complement S-protein (vitronectin) is associated with cytolytic membrane-bound C5b−9 complexes. *Clin. Exp. Immunol.* **74**, 459–464.

Bhattacharjee, A., Lehtinen, M. J., Kajander, T., Goldman, A. & Jokiranta, T. S. (2010). Both domain 19 and domain 20 of factor H are involved in binding to complement C3b and C3d. *Mol. Immunol.* **47**, 1686-1691.

Biacore™ concentration analysis handbook, version AA (2001). GE Healthcare Bio-Sciences AB, Uppsala, Sweden.

Biacore® Sensor Surface Handbook. (2003). GE Healthcare Bio-Sciences AB, Uppsala, Sweden.

Biacore™ X100 handbook, edition AB (2008). GE Healthcare Bio-Sciences AB, Uppsala, Sweden.

Bird, A. C. (1992). Bruch's membrane change with age. *Brit. J. Ophthalmol.* **76**, 166-168.

Bird, A. C., Bressler, N. M., Bressler, S. B., Chisholm, I. H., Coscas, G., Davis, M. D., de Jong, P. T., Klaver, C. C., Klein, B. E., Klein, R., *et al.* (1995). An international classification and grading system for age-related maculopathy and age-related macular degeneration. *Surv. Ophthalmol.* **39**, 367-374.

Bird, A. C. (2010). Therapeutic targets in age-related macula disease. *J. Clin. Invest.* In press.

Bíró, A., Rovó, Z., Papp, D., Cervenak, L., Varga, L., Füst, G., Thielens, N. M., Arlaud, G. J. & Prohászka, Z. (2007). Studies on the interactions between C-reactive protein and complement proteins. *Immunology,* **121**, 40-50.

Blackmore, T. K., Sadlon, T. A., Ward, H. M., Lublin, D. M. & Gordon, D. L. (1996). Identification of a heparin binding domain in the seventh short consensus repeat of complement factor H. *J. Immunol.* **157**, 5422–5427.

Blackmore, T. K., Hellwage, J., Sadlon, T. A., Higgs, N., Zipfel, P. F., Ward, H. M. & Gordon, D. L. (1998). Identification of the second heparin-binding domain in human complement factor H. *J. Immunol.* **160**, 3342–3348.

Blom, A. M., Villoutreix, B. O. & Dahlback, B. (2004). Complement inhibitor C4b-binding protein-friend or foe in the innate immune system? *Mol. Immunol.* **40**, 1333–1346.

Blom, A. M., Kask, L., Ramesh, B. & Hillarp, A. (2003). Effects of zinc on factor I cofactor activity of C4b-binding protein and factor H. *Arch. Biochem. Biophys.* **418**, 108-118.

Bok, D. (2005). Evidence for an inflammatory process in age-related macular degeneration gains new support. *Proc. Natl. Acad. Sci. U .S. A.* **102**, 7053-7054.

Bonner, A., Perrier, C., Corthésy, B. & Perkins, S. J. (2007). Solution structure of human secretory component and implications for biological function. *J. Biol. Chem.* **282**, 16969-16980.

Bonner, A., Furtado, P. B., Almogren, A., Kerr, M. A. & Perkins, S. J. (2008). Implications of the near-planar solution structure of human myeloma dimeric IgA1 for mucosal immunity and IgA nephropathy. *J. Immunol.* **180**, 1008-1018.

Bordet, J. (1909). *In Studies in Immunity.* J. Wiley & Sons, New York.

Chamberlain, D., Ullman, C. G. & Perkins, S. J. (1998). Possible arrangement of the five domains in human complement factor I as determined by a combination of X-ray and neutron scattering and homology modeling. *Biochemistry,* **37**, 13918-13929.

Chen, M., Forrester, J. V. & Xu, H. (2007). Synthesis of complement factor H by retinal pigment epithelial cells is down-regulated by oxidized photoreceptor outer segments. *Exp. Eye. Res.* **84**, 635–645.

Chopdar, A., Chakravarthy, U. & Verma, D. (2003). Age related macular degeneration. *Brit. Med. J.* **326**, 485-488.

Clark, S. J., Higman, V. A., Mulloy, B., Perkins, S. J., Lea, S. M., Sim, R. B. & Day, A. J. (2006). His-384 allotypic variant of factor H associated with age-related macular degeneration has different heparin binding properties from the non-disease-associated form. *J. Biol. Chem.* **281**, 24713-24720.

Crabb, J. W., Miyagi, M., Gu, S., Shadrach, K., West, K. A., Sakaguchi, H., Kamei, M., Hasan, A., Yan, L., Rayborn, M. E., et al. (2002). Drusen proteome analysis: an approach to the etiology of age-related macular degeneration. *Proc. Natl. Acad. Sci. U. S. A.* **99**, 14682-14687.

Coffey, P. J., Gias, C., McDermott, C. J., Lundh, P., Pickering, M. C., Sethi, C., Bird, A., Fitzke, F. W., Maass, A., Chen, L. L., Holder, G. E., Luthert, P. J., Salt, T. E., Moss, S. E. & Greenwood, J. (2007). Complement factor H deficiency in aged mice causes retinal abnormalities and visual dysfunction. *Proc. Natl. Acad. Sci. U. S. A.* **104**, 16651-16656.

Cole, J. L. & Hansen, J. C. (1999). Analytical ultracentrifugation as a contemporary biomolecular research tool. *J. Biomolec. Techniques*, **10**, 163-176.

Cole, J. L., Lary, J. W., Moody, T. & Laue, T. M. (2008). Analytical ultracentrifugation: sedimentation velocity and sedimentation equilibrium. *Meth. Cell Biol.* **84**, 143-179.

Coleman, H. R., Chan, C. C., Ferris, F. L. & Chew, E. Y. (2008). Age-related macular degeneration. *Lancet.* **372**, 1835-1845.

Comeau, S. R., Gatchell, D. W., Vajda, S. & Camacho, C. J. (2004). ClusPro: an automated docking and discrimination method for the prediction of protein complexes. *Bioinformatics,* **20**, 45-50.

Crossley, L. G. & Porter, R. R. (1980). Purification of the human complement control protein C3b inactivator. *Biochem. J.* **191**, 173-182.

Dam, J. and Schuck, P. (2005). Sedimentation velocity analysis of heterogeneous protein-protein interactions: Sedimentation coefficient distributions c(s) and asymptotic boundary profiles from Gilbert-Jenkins theory. *Biophys. J.* **89**, 651–666.

Davis, A. E., Mejia, P. & Lu, F. (2008). Biological activities of C1 inhibitor. *Mol. Immunol.* **45**, 4057–4063.

Davis, M. D., Gangnon, R. E., Lee, L. Y., Hubbard, L. D., Klein, B. E., Klein, R., Ferris, F. L., Bressler, S. B., Milton, R. C. & Age-Related Eye Disease Study Group.

(2005).The Age-Related Eye Disease Study severity scale for age-related macular degeneration: AREDS Report No. 17. *Arch. Ophthalmol.* **123**, 1484-1498.

Day, A. J. & Sim, R. B. (1986). Inhibitory effect of Zn^{2+} ion on the degradation of the complement activation fragment C3b. *Biochem. Soc. Transact.* **14**, 73-74.

de Córdoba, S. R. & de Jorge, E. G. (2008). Translational mini-review series on complement factor H: genetics and disease associations of human complement factor H. *Clin. Exp. Immunol.* **151**, 1-13.

DiScipio, R. G. (1992). Ultrastructures and interactions of complement factors H and I. *J. Immunol.* **149**, 2592-2599.

DiScipio, R. G., Daffern, P. J., Schraufstätter, I. U. & Sriramarao, P. (1998). Human polymorphonuclear leukocytes adhere to complement factor H through an interaction that involves alphaMbeta2 (CD11b/CD18). *J. Immunol.* **160**, 4057-4066.

Dodds, A. W. (1993). Small-scale preparation of complement components C3 and C4. *Meth. Enzymol.* **223**, 46-61.

Donin, N., Jurianz, K., Ziporen, L., Schultz, S., Kirschfink, M. & Fishelson, Z. (2003). Complement resistance of human carcinoma cells depends on membrane regulatory proteins, protein kinases and sialic acid. *Clin. Exp. Immunol.* **131**, 254-263.

Dragon-Durey, M. A. & Frémeaux-Bacchi, V. (2005). Atypical haemolytic uraemic syndrome and mutations in complement regulator genes. *Springer Semin. Immunol.* **27**, 359-374.

Edwards, A. O., Ritter, R. III, Abel, K. J., Manning, A., Panhuysen, C. & Farrer, L. A. (2005). Complement factor H polymorphism and age-related macular degeneration. *Science*, **308**, 421-424.

Esparza-Gordillo, J., Soriam, J. M., Buil, A., Almasy, L., Blangero, J., Fontcuberta, J. & Rodríguez de Córdoba, S. (2004). Genetic and environmental factors influencing the human factor H plasma levels. *Immunogenetics,* **56**, 77–82.

Farabella, I. (2009). Prediction of the zinc binding sites in complement factor H. *Rotation 1 report. Department of structural and molecular biology. University College London.*

Farries, T. C., Seya, T., Harrison, R. A. & Atkinson, J. P. (1990). Competition for binding sites on C3b by CR1, CR2, MCP, factor B and Factor H. *Complement Inflamm.* **7**, 30-41.

Federman, J. L., Gouras, P., Schubert, H., Slusher, M. M. & Vrabec, T. R. (1994). *Retina and Vitreous.* Mosby-year book Europe, London. pp. 2.1-3.15.

Fenaille, F., Le Mignon, M., Groseil, C., Ramon, C., Riandé, S., Siret, L & Bihoreau, N. (2007). Site-specific N-glycan characterization of human complement factor H. *Glycobiol.* **17**, 932-944.

Feng, X., Tonnesen, M. G., Peerschke, E. I. & Ghebrehiwet, B. (2002). Cooperation of C1q receptors and integrins in C1q-mediated endothelial cell adhesion and spreading. *J. Immunol.* **168**, 2441-2448.

Ferreira, V. P., Herbert, A. P., Hocking, H. G., Barlow, P. N. & Pangburn, M. K. (2006). Critical role of the C-terminal domains of factor H in regulating complement activation at cell surfaces. *J. Immunol.* **177**, 6308-6316.

Ferreira, V. P., Pangburn, M. K. & Cortés, C. (2010). Complement control protein factor H: The good, the bad, and the inadequate. *Molec. Immunol.* **47**, 2187-2197.

Ferris, F. L., Davis, M. D., Clemons, T. E., Lee, L. Y., Chew, E. Y., Lindblad, A. S., Milton, R. C., Bressler, S. B., Klein, R. & Age-Related Eye Disease Study (AREDS) Research Group. (2005). A simplified severity scale for age-related macular degeneration: AREDS Report No. 18. *Arch. Ophthalmol.* **123**, 1570-1574.

Fernando, A. N., Furtado, P. B., Clark, S. J., Gilbert, H. E., Day, A. J., Sim, R. B. & Perkins, S. J. (2007). Associative and structural properties of the region of complement Factor H encompassing the Tyr402His disease-related polymorphism and its interactions with heparin. *J. Mol. Biol.* **368,** 564-581.

Flinn, J. M., Cano, K., Gideons, E., Koscho, J., Ablett, J., Jones, B. F., van Kuyk, E. & Lengyel, I. (2008). Trace metal distribution and concentration in sub-RPE deposits and Bruch´s membrane in post mortem human tissues. *Invest. Ophthalmol. Vis. Sci.* **49**, E-Abstract 1756.

Fonseca, M. I., Carpenter, P. M., Park, M., Palmarini, G., Nelson, E. L & Tenner, A. J. (2001). C1qR(P), a myeloid cell receptor in blood, is predominantly expressed on endothelial cells in human tissue. *J. Leukoc. Biol.* **70**, 793-800.

Forrester, J. V., Dick, A. D., McMenamin, P. G. & Lee, W. R. (2002). *The eye: basic sciences in practice.* Edinburgh: W. B. Saunders. (2nd Edition). pp. 15-59.

Frederickson, C. J., Giblin, L. J., Krezel, A., McAdoo, D. J., Muelle, R. N., Zeng, Y., Balaji, R. V., Masalha, R., Thompson, R. B., Fierke, C. A., Sarvey, J. M., de Valdenebro, M., Prough, D. S. & Zornow, M. H. (2006). Concentrations of extracellular free zinc $(pZn)_e$ in the central nervous system during simple anesthetization, ischemia and reperfusion. *Exp. Neuro.* **198**, 285-293.

Friese, M. A., Hellwage, J., Jokiranta, T. S., Meri, S., Peter, H. H., Eibel, H. & Zipfel, P. F. (1999). FHL-1/reconectin and factor H: two human complement regulators which are encoded by the same gene are differently expressed and regulated. *Mol. Immunol.* **36**, 809-818.

Furtado, P. B., Whitty, P. W., Robertson, A., Eaton, J. T., Almogren, A., Kerr, M. A., Woof, J. M. & Perkins, S. J. (2004). Solution structure determination of monomeric human IgA2 by X-ray and neutron scattering, analytical ultracentrifugation and constrained modelling: A comparison with monomeric human IgA1. *J. Mol. Biol.*, **338**, 921-941.

Galin, M. A., Nano, H. D. & Hall, T. (1962). Ocular zinc concentration. *Investig. Ophthalmol.* **1**, 142-148.

Garcia de la Torre, J., Huertas, M. L. & Carrasco, B. (2000). Calculation of hydrodynamic properties of globular proteins from their atomic-level structure. *Biophys. J.* **78**, 719-730.

Gehrs, K. M., Anderson, D. H., Johnson, L. V. & Hageman, G. S. (2006). Age-related macular degeneration-emerging pathogenetic and therapeutic concepts. *Ann. Med.* **38**, 450-471.

Giannakis, E., Male, D. A., Ormsby, R. J., Mold, C., Jokiranta, T. S., Ranganathan, S., & Gordon, D. L. (2001). Multiple ligand binding sites on domain seven of human complement factor H. *Int. Immunopharmacol.* **1**, 433-443.

Giannikis, E., Jokiranta, T. S., Male, D. A., Ranganathan, S., Ormsby, R. J., Fischetti, V. A., Mold, C. & Gordon, D. L. (2003). A common site within factor H SCR7 responsible for binding heparin, c-reactive protein and streptococcal M protein. *Eur. J. Immunol.* **33**, 962-969.

Gilbert, H. E. (2006). Structural Studies of SCR Domains in Complement Receptor Type Two. *Ph.D Thesis. Department of Biochemistry and Molecular Biology. University College London.*

Glatter, O. & Kratky, O. (Editors) (1982). *Small angle X-ray scattering.* Academic Press, New York.

Gold, B., Merriam J. E., Zernant, J., Hancox, L. S., Taiber, A. J., Gehrs, K., Cramer, K., Neel, J., Bergeron, J., Barile, G. R., Smith, R.T., AMD Genetics Clinical Study Group, Hageman, G. S., Dean, M. & Allikmets, R. (2006). Variation in factor B (BF) and complement component 2 (C2) genes is associated with agerelated macular degeneration. *Nat. Genet.* **38**, 458–462.

Goldsby, R. A., Kindt, T. J. & Osborne, B. A. (Editors) (2000). *Kuby Immunology.* W. H. Freeman and Company, New York.

Goodship, T. H. (2006). Factor H genotype-phenotype correlations: lessons from aHUS, MPGN II, and AMD. *Kidney Int.* **70**, 42-50.

Grahn, B. H., Paterson, P. G., Gottschall-Pass, K. T. & Zhang, Z. (2001). Zinc and the eye. *J. Am. Coll. Nutr.* **20**, 106-118.

Gray, J. J., Moughon, S., Wang, C., Schueler-Furman, O., Kuhlman, B., Rohl, C. A. & Baker, D. (2003). Protein-protein docking with simultaneous optimization of rigid-body displacement and side-chain conformations. *J. Mol. Biol.* **331**, 281-299.

Gray, J. J. (2006). High-resolution protein-protein docking. *Curr. Opin. Struct. Biol.* **16**, 183-193.

Gros, P., Milder, F. J. & Janssen, B. J. (2008). Complement driven by conformational changes. *Nat. Rev. Immunol.* **8**, 48-58.

Guymer, R. & Bird, A. C. (1998). Bruch's membrane, drusen, and age-related macular degeneration. In "*The retinal pigment epithelium"* (eds.) Marmor, M. & Wolfensberger, T. Oxford University Press, Oxford, pp. 693-705.

Guyton, A. C. & Hall, J. E. (2006*). Textbook of medical physiology.* Elsevier Saunders, Philadelphia, pp. 631-639.

Hageman, G. S., Luthert, P. J., Victor Chong, N. H., Johnson, L. V., Anderson, D. H. & Mullins, R. F. (2001). An integrated hypothesis that considers drusen as biomarkers of immune-mediated processes at the RPE-Bruch's membrane interface in aging and age-related macular degeneration. *Progr. Retin. Eye Research,* **20**, 705-732.

Hageman, G. S., Anderson, D. H., Johnson, L. V., Hancox, L. S., Taiber, A. J., Hardisty, L. I., Hageman, J. L., Stockman, H. A., Borchardt, J. D., Gehrs, K. M., Smith, R. J., Silvestri, G., Russell, S. R., Klaver, C. C., Barbazetto, I., Chang, S., Yannuzzi, L. A., Barile, G. R., Merriam, J. C., Smith, R. T., Olsh, A. K., Bergeron, J., Zernant, J., Merriam, J. E., Gold, B., Dean, M. & Allikmets, R. (2005). A common haplotype in the complement regulatory gene factor H (HF1/CFH) predisposes individuals to age-related macular degeneration. *Proc. Natl. Acad. Sci. U. S. A.* **102**, 7227-7232.

Hageman, G. S., Hancox, L. S., Taiber, A. J., Gehrs, K. M., Anderson, D. H., Johnson, L. V., Radeke, M. J., Kavanagh, D., Richards, A., Atkinson, J., Meri, S., Bergeron, J., Zernant, J., Merriam, J., Gold, B., Allikmets, R., Dean, M & AMD Clinical Study Group. (2006). Extended haplotypes in the complement factor H (CFH) and CFH-related (CFHR) family of genes protect against age-related macular degeneration: characterization, ethnic distribution and evolutionary implications. *Ann. Med.* **38**, 592-604.

Haines, J. L., Hauser, M. A., Schmidt, S., Scott, W. K., Olson, L. M., Gallins, P., Spencer, K. L., Kwan, S. Y., Noureddine, M., Gilbert, J. R., Schnetz-Boutaud, N., Agarwal, A., Postel, E. A. & Pericak-Vance, M. A. (2005). Complement factor H variant increases the risk of age-related macular degeneration. *Science,* **308**, 419-421.

Hakobyan, S., Harris, C. L., van den Berg, C. W., Fernandez-Alonso, M. C., de Jorge, E. G., de Cordoba, S. R., Rivas, G., Mangione, P., Pepys, M. B. & Morgan, B. P. (2008). Complement factor H binds to denatured rather than to native pentameric C-reactive protein. *J. Biol. Chem.* **283**, 30451-30460.

Harding, S. E. & Winzor, D. J. (2001). Sedimentation velocity analytical ultracentrifugation. *In "Protein-ligand Interaction: hydrodynamics and calorimetry" (eds.)* Harding, S. E. & Chowdhry B. Z. Oxford University Press, New York. Chapter 4, pp. 75-103.

He, J. Q., Wiesmann, C. & van Lookeren Campagne, M. (2008). A role of macrophage complement receptor CRIg in immune clearance and inflammation. *Mol. Immunol.* **45**, 4041–4047.

Heinen, S., Hartmann, A., Lauer, N., Wiehl, U., Dahse, H. M., Schirmer, S., Gropp, K., Enghardt, T., Wallich, R., Hälbich, S., Mihlan, M., Schlötzer-Schrehardt, U., Zipfel, P. F. & Skerka, C. (2009). Factor H-related protein 1 (CFHR-1) inhibits complement C5 convertase activity and terminal complex formation. *Blood,* **114**, 2439-2447.

Hellwage, J., Jokiranta, T. S., Friese, M. A. Wolk, T. U., Kampen, E., Zipfel, P. F.& Meri, S. (2002). Complement C3b/C3d and cell surface polyanions are recognized by overlapping binding sites on the most carboxyl-terminal domain of complement factor H. *J. Immunol.* **169**, 6935–6944.

Herbert, A. P., Uhrin, D., Lyon, M., Pangburn, M. K. & Barlow, P. N. (2006). Disease-associated sequence variations congregate in a polyanion recognition patch on human factor H revealed in three-dimensional structure. *J.Biol.Chem.* **281,**16512-16520.

Herbert, A. P., Deakin, J. A., Schmidt, C. Q., Blaum, B. S., Egan, C., Ferreira, V. P., Pangburn, M. K., Lyon, M., Uhrín, D. & Barlow, P. N. (2007). Structure shows that a glycosaminoglycan and protein recognition site in factor H is perturbed by age-related macular degeneration-linked single nucleotide polymorphism. *J. Biol. Chem.* **282**, 18960-18968.

Hocking, H. G., Herbert, A. P., Kavanagh, D., Soares, D. C., Ferreira, V. P., Pangburn, M. K., Uhrin, D. & Barlow, P. N. (2008). Structure of the N-terminal region of complement factor H and conformational implications of disease-linked sequence variations. *J. Biol. Chem.* **283**, 9475-9487.

Homola, J. (2003). Present and future of surface plasmon resonance biosensors. *Anal Bioanal. Chem.* **377**, 528-539.

Horstmann, R. D., Sievertsen, H. J., Knobloch, J. & Fischetti, V. A. (1988). Antiphagocytic activity of streptococcal M protein: selective binding of complement control protein factor H. *Proc. Natl. Acad. Sci. U. S. A.* **88**, 1657–1661.

Hourcade, D. E. (2008). Properdin and complement activation: a fresh perspective. *Curr. Drug Targets,* **9**, 158–164.

Howlett, G. J., Minton, A. P. & Rivas, G. (2006). Analytical ultracentrifugation for the study of protein association and assembly. *Curr. Opin. Chem. Biol.* **10**, 430-436.

Huber, R., Scholze, H., Paques, E. P. & Deisenhofer, J. (1980). Crystal structure analysis and molecular model of human C3a anaphylatoxin. *Hoppe Seylers Z. Physiol. Chem.* **361**, 1389–1399.

Hughes, A. E., Orr, N., Esfandiary, H., Diaz-Torres, M., Goodship, T. & Chakravarthy, U. (2006). A common CFH haplotype, with deletion of CFHR1 and CFHR3, is associated with lower risk of age-related macular degeneration. *Nat. Genet.* **38**,1173–1177.

Ibel, K. & Stuhrmann, H. B. (1975). Comparison of neutron and X-ray scattering of dilute myoglobin solutions. *J. Mol. Biol.* **93**, 255-265.

Isaák, A., Prechl, J., Gergely, J. & Erdei, A. (2006). The role of CR2 in autoimmunity. *Autoimmunity*, **39**, 357-366.

Jager, R. D., Mieler, W. F. & Miller, J. W. (2008). Age-related macular degeneration. *New Engl. J. Med.* **358**, 2606-2617.

Jarva, H., Jokiranta, T. S., Hellwage, J., Zipfel, P. F. & Meri, S. (1999). Regulation of complement activation by C-reactive protein: targeting the complement inhibitory activity of factor H by an interaction with short consensus repeat domains 7 and 8-11. *J. Immunol.* **163**, 3957-3962.

Janssen, B. J., Huizinga, E. G., Raaijmakers, H. C., Roos, A., Daha, M. R., Nilsson-Ekdahl, K., Nilsson, B. & Gros, P. (2005). Structures of complement component C3 provide insights into the function and evolution of immunity. *Nature,* **437**, 505-511.

Janssen, B. J., Christodoulidou, A., McCarthy, A., Lambris, J. D. & Gros, P. (2006). Structure of C3b reveals conformational changes that underlie complement activity. *Nature,* **444**, 213–216.

Johnson, P. T., Betts, K. E., Radeke, M. J., Hageman, G. S., Anderson, D. H. & Johnson, L. V. (2006). Individuals homozygous for the age-related macular degeneration risk-conferring variant of complement factor H have elevated levels of CRP in the choroid. *Proc. Natl. Acad. Sci. U. S. A.* **103**, 17456-17461.

Jokiranta, T. S., Hellwage, J., Koistinen, V., Zipfel, P. F & Meri, S. (2000). Each of the three binding sites on complement factor H interacts with a distinct site on C3b. *J. Biol. Chem.* **275,** 27657-27662.

Jokiranta, T. S., Jaakola, V. P., Lehtinen, M. J., Parepalo, M., Meri, S. & Goldman, A. (2006). Structure of complement factor H carboxyl-terminus reveals molecular basis of atypical haemolytic uremic syndrome. *EMBO J.* **25**, 1784-1794.

Józsi, M., Heinen, S., Hartmann, A., Ostrowicz, C. W., Hälbich, S., Richter, H., Kunert, A., Licht, C., Saunders, R. E., Perkins, S. J., Zipfel, P. F. & Skerka, C. (2006). Factor H and atypical hemolytic uremic syndrome: mutations in the C-terminus cause structural changes and defective recognition functions. *J. Am. Soc. Nephrol.* **17**, 170-177.

Józsi, M. & Zipfel, P. F. (2008). Factor H family proteins and human diseases.*Trends Immunol.* **29**, 380-387.

Kang, Y. S., Do, Y., Lee, H. K., Park, S. H., Cheong, C., Lynch, R. M., Loeffler, J. M., Steinman, R. M & Park, C. G. (2006). A dominant complement fixation pathway for pneumococcal polysaccharides initiated by SIGN-R1 interacting with C1q. *Cell,* **125**, 47-58.

Karcioglu, Z. A. (1982). Zinc in the eye. *Surv. Ophthalmol.* **27**, 114–122.

Karpusas, M., Nolte, M., Benton, C. B., Meier, W., Lipscomb, W. N. & Goelz, S. (1997). The crystal structure of human interferon beta at 2.2-A resolution. *Proc. Natl. Acad. Sci. U. S. A.* **94**, 11813-11818.

Khera, R. & Das, N. (2009). Complement receptor 1: disease associations and therapeutic implications. *Mol. Immunol.* **46**, 761–772.

Kim, D. D. & Song, W. C. (2006). Membrane complement regulatory proteins. *Clin. Immunol.* **118**, 127-36.

Kinoshita, C. M., Ying, S. C., Hugli, T. E., Siegel, J. N., Potempa, L. A., Jiang, H., Houghten, R. A. & Gewurz, H. (1989). Elucidation of a protease-sensitive site involved in the binding of calcium to C-reactive protein. *Biochemistry,* **28**, 9840-9848.

Klein, R. J., Zeiss, C., Chew, E. Y., Tsai, J. Y., Sackler, R. S., Haynes, C., Henning, A. K., Sangiovanni, J. P., Mane, S. M., Mayne, S. T., Bracken, M. B., Ferris, F. L., Ott, J., Barnstable, C. & Hoh, J. (2005). Complement factor H polymorphism in age-related macular degeneration. *Science,* **308**, 385-389.

Klein, M. L., Francis, P. J., Rosner, B., Reynolds, R., Hamon, S. C., Schultz, D. W., Ott, J. & Seddon, J. M. (2008). CFH and LOC387715/ARMS2 genotypes and treatment with antioxidants and zinc for age-related macular degeneration. *Ophthalmology,* **115**, 1019-1025.

Klos, A., Tenner, A. J., Johswich, K. O., Ager, R. R., Reis, E. S. & Köhl, J. (2009). The role of the anaphylatoxins in health and disease. *Mol. Immunol.* **46**, 2753-2766.

Kotarsky, H., Hellwage, J., Johnson, E., Skerka, C., Svensson, H. G., Lindahl, G., Sjöbring, U. & Zipfel, P. F. (1998). Identification of a domain in human factor H and factor H-like protein 1 required for interaction with streptococcal M protein. *J. Immunol.* **160**, 3349–3354.

Krushkal, J., Bat, O. & Gigli, I. (2000). Evolutionary relationships among proteins encoded by the regulator of complement activation gene cluster. *Mol. Biol. Evol.* **17**, 1718-1730.

Kühn, S. & Zipfel, P. F. (1996). Mapping of the domains required for decay acceleration activity of the human factor H-like protein 1 and factor H. *Eur. J. Immunol.* **26**, 2383-2387.

Kumar, V., Abbas, A. K., Fausto, N. & Aster, J. (2010). *Robbins and Cotran Pathologic Basis of Disease.* Saunders Elsevier, Philadelphia. (8th Edition). pp. 1345-1368.

Lane, L. A., Ruotolo, B. T., Robinson, C. V., Favrin, G. & Benesch, J. L. P. (2009). A Monte Carlo approach for assessing the specificity of protein oligomers observed in nano-electrospray mass spectra. *Int. J. Mass Spectrometry*, **283**, 169–177.

Laue, T. M. (1996). Choosing which optical system of the optima XL-I analytical centrifuge to use. Beckman Coulter Technical Report A-1821-A.

Law, S. K. A & Reid, K. B. M. (1995). *Complement.* Oxford University Press. (2nd Edition).

Lebowitz, J., Lewis, M. S. & Schuck, P. (2002). Modern analytical ultracentrifugation in protein science: a tutorial review. *Protein Sci.* **11**, 2067-2079.

Lehtinen, M. J., Meri, S. & Jokiranta, T. S. (2004). Interdomain contact regions and angles between adjacent short consensus repeat domains. *J. Mol. Biol.* **344**,1385-1396.

Lengyel, I., Tufail, A., Heba, A. H., Luthert, P., Bird A. C. & Jeffery. G. (2004). Association of drusen deposition with choroidal intercapillary pillars in the aging human Eye. *Invest. Ophthalmol Vis. Sci.* **45**, 2886–2892.

Lengyel, I., Flinn, J. M., Peto, T., Linkous, D. H., Cano, K., Bird, A. C., Lanzirotti, A., Frederickson, C. J. & van Kuijk, F. J. G. M. (2007). High concentration of zinc in sub-retinal pigment epithelial deposits. *Exp. Eye Res.* **84**, 772-780.

Lengyel, I. & Peto, T. (2008). Cure or cause: the opposing roles for zinc in age-related macular degeneration. *Expert Rev. Ophthalmol.* **3**, 1-4.

Li ,K., Gor, J. & Perkins, S. J. (2010). Self-association and domain rearrangements between complement C3 and C3u provide insight into the activation mechanism of C3. *Biochem. J.* **431**, 63-72.

Li, M., Atmaca-Sonmez, P., Othman, M., Branham, K. E. H., Khanna, R., Wade, M. S., Li, Y., Liang, L., Zareparsi, S., Swaroop, A. & Abecasis, G. R. (2006). CFH haplotypes without the Y402H coding variant show strong association with susceptibility to age-related macular degeneration. *Nature Genetics*, **38,** 1049-1054.

Lu, J., Stewart, A. J., Sadler, P. J., Pinheiro, T. J. & Blindauer, C. A. (2008). Albumin as a zinc carrier: properties of its high-affinity zinc-binding site. *Biochem. Soc. Trans.* **36**, 1317-1321.

Lyskov, S. & Gray, J. J. (2008). The RosettaDock server for local protein-protein docking. *Nucleic. Acids. Res.* **36**, W233-238.

Maller, J. B., George, S., Purcell, S., Fagerness, J. A., Altshuler, D., Daly, M. J. & Seddon, J. M. (2006). Common variation in three genes, including a noncoding variant in CFH, strongly influences risk of age-related macular degeneration. *Nat. Genet.* **38,** 1055-1059.

Maller, J. B., Fagerness, J. A., Reynolds, R. C., Neale, B. M., Daly, M. J., Seddon, J. M. (2007). Variation in complement factor 3 is associated with risk of age-related macular degeneration. *Nat. Genet.* **39**, 1200–1201.

Manuelian, T., Hellwage, J., Meri, S., Caprioli, J., Noris, M., Heinen, S., Jozsi, M., Neumann, H. P., Remuzzi, G. & Zipfel, P. F. (2003). Mutations in factor H reduce binding affinity to C3b and heparin and surface attachment to endothelial cells in hemolytic uremic syndrome. *J. Clin. Invest.* **111**, 1181-1190.

McRorie, D. K. & Voelker, P. J. (1993). *Self-associating systems in the analytical ultracentrifuge*. Beckman Instruments, Fullerton, California.

Mendez, R., Leplae, R., Lensink, M. F. & Wodak, S. J. (2005). Assessment of CAPRI predictions in rounds 3-5 shows progress in docking procedures. *Proteins,* **60**, 150-169.

Mold, C., Gewurz, H. & Du Clos, T. W. (1999). Regulation of complement activation by C-reactive protein. *Immunopharmacology,* **42**, 23-30.

Monteferrante, G., Brioschi, S., Caprioli, J., Pianetti, G., Bettinaglio, P., Bresin, E., Remuzzi, G. & Noris, M. (2007). Genetic analysis of the complement factor H related 5 gene in haemolytic uraemic syndrome. *Mol. Immunol.* **44**, 1704-1708.

Morikis, D. & Lambris, J. D. (2005). *Structural biology of the complement system.* CRC Press, Boca Raton, FL. pp. 1-18.

Morris, K. M., Aden, D. P., Knowles, B. B. & Colten, H. R. (1982). Complement biosynthesis by the human hepatoma-derived cell line HepG2. *J. Clin. Invest.* **70**, 906–913.

Mullins, R. F., Russell, S. R., Anderson, D. H. & Hageman, G. S. (2000). Drusen associated with aging and age-related macular degeneration contain proteins common to extracellular deposits associated with atherosclerosis, elastosis, amyloidosis, and dense deposit disease. *FASEB J.* **14**, 835-846.

Murphy, K., Travers, P. & Walport, M. (2008). *Janeway's Immunobiology.* Garland Science, New York. (7th Edition). pp. 61-82.

Nagar, B., Jones, R. G., Diefenbach, R. J., Isenman, D. E. & Rini, J. M. (1998). X-ray crystal structure of C3d: a C3 fragment and ligand for complement receptor 2. *Science,* **280**, 1277–1281.

Nan, R., Gor, J. & Perkins, S. J. (2008a). Implications of the progressive self-association of wild-type human Factor H for complement regulation and disease. *J. Mol. Biol.* **375**, 891-900.

Nan, R., Gor, J., Lengyel, I. & Perkins, S. J. (2008b). Uncontrolled zinc- and copper-induced oligomerisation of the human complement regulator Factor H and its possible implications for function and disease. *J. Mol. Biol.* **384**, 1341-1352.

Narayanan, T., Diat, O. & Bosecke, P. (2001). SAXS and USAXS on the high brilliance beamline at the ESRF. *Nucl. Instrum. Methods Phys. Res. A.* **467-468**, 1005-1009.

Neumann, H. P., Salzmann, M., Bohnert-Iwan, B., Mannuelian, T., Skerka, C., Lenk, D., Bender, B. U., Cybulla, M., Riegler, P., Königsrainer, A., Neyer, U., Bock, A., Widmer, U., Male, D. A., Franke, G. & Zipfel, P. F. (2003). Haemolytic uraemic syndrome and mutations of the factor H gene: a registry-based study of German speaking countries. *J. Med. Genet.* **40**, 676-681.

Newsome, D. A., Oliver, P. D., Deupree, D. M., Miceli, M. V. & Diamond, J. G. (1992). Zinc uptake by primate retinal pigment epithelium and choroid. *Curr. Eye Res.* **11**, 213–217.

Newsome, D. A., Miceli, M. V., Tate, D. J., Alcock, N. W. & Oliver, P. D. (1995). Zinc content of human retinal pigment epithelium decrease with age and macular degeneration while superoxide dismutase activity increases. *J. Trace Elem. Exp. Med.* **8**, 193–199.

Ngampasutadol, J., Ram, S., Gulati, S., Agarwal, S., Li, C., Visintin, A., Monks, B., Madico, G. & Rice, P. A. (2008). Human factor H interacts selectively with Neisseria gonorrhoeae and results in species-specific complement evasion. *J. Immunol.* **180**, 3426-3435.

Nieba, L., Nieba-Axmann, S. E., Persson, A., Hämäläinen, M., Edebratt, F., Hansson, A., Lidholm, J., Magnusson, K., Karlsson, A. F. & Plückthun, A. (1997). BIACORE analysis of histidine-tagged proteins using a chelating NTA sensor chip. *Anal. Biochem.* **252**, 217-228.

Nishida, N., Walz, T. & Springer, T. A. (2006). Structural transitions of complement component C3 and its activation products. *Proc. Natl. Acad. Sci. U. S. A.* **103**, 19737–19742.

Norman, D. G., Barlow, P. N., Baron, M., Day, A. J., Sim, R. B. & Campbell, I. D. (1991). Three-dimensional structure of a complement control protein module in solution. *J. Mol. Biol.* **219**, 717-725.

Oppermann, M., Manuelian, T., Józsi, M., Brandt, E., Jokiranta, T. S., Heinen, S., Meri, S., Skerka, C., Götze, O. & Zipfel, P. F. (2006). The C-terminus of complement regulator Factor H mediates target recognition: evidence for a compact conformation of the native protein. *Clin. Exp. Immunol.* **144**, 342-352.

Ormsby, R. J., Jokiranta, T. S., Griggs, K., Giannakis, E., Sadlon, T. & Gordon, D. L. (2004). Localisation of the third heparin binding domain in human complement factor H. *Mol. Immunol.* **41**, 289-290.

Ormsby, R. J., Jokiranta, T. S., Duthy, T. G., Griggs, K. M., Sadlon, T. A., Giannakis, E. & Gordon, D. L. (2006). Localization of the third heparin-binding site in the human complement regulator factor H. *Mol. Immunol.* **43**, 1624-1632.

Okemefuna, A. I., Gilbert, H. E., Griggs, K. M., Ormsby, R. J., Gordon, D. L. & Perkins, S. J. (2008). The regulatory SCR-1/5 and cell surface-binding SCR-16/20 fragments of factor H reveal partially folded-back solution structures and different self-associative properties. *J .Mol. Biol.* **375**, 80-101.

Okemefuna, A. I., Nan, R., Gor, J. & Perkins, S. J. (2009). Electrostatic interactions contribute to the folded-back conformation of wild type human factor H. *J. Mol. Biol.* **391**, 98-118.

Okemefuna, A. I., Nan, R., Miller, A., Gor, J. & Perkins, S. J. (2010). Complement factor H binds at two independent sites to C-reactive protein in acute phase concentrations. *J. Biol. Chem.* **285**, 1053-1065.

Oyster, C. W. (1999). *The human eye: structure and function.* Sinauer Associates, Inc. Sunderland, MA. pp. 323-752.

Pangburn, M. K., Schreiber, R. D. & Muller-Eberhard, H. J. (1977). Human complement C3b inactivator: isolation, characterization, and demonstration of an absolute requirement for the serum protein beta1H for cleavage of C3b and C4b in solution. *J. Exp. Med.* **146**, 257-270.

Pangburn, M. K., Atkinson, M. A. & Meri, S. (1991). Localization of the heparin-binding site on complement factor H. *J. Biol. Chem.* **266**, 16847-16853.

Pangburn, M. K. (2000). Host recognition and target differentiation by factor H, a regulator of the alternative pathway of complement. *Immunopharmacology,* **49**, 149-157.

Pangburn, M. K. (2002). Cutting edge: localization of the host recognition functions of complement factor H at the carboxyl-terminal: implications for hemolytic uremic syndrome. *J. Immunol.* **169**, 4702–4706.

Pangburn, M. K., Rawal, N., Cortes, C., Alam, M. N., Ferreira, V. P. & Atkinson, M. A. (2009). Polyanion-induced self-association of complement factor H. *J. Immunol.* **182**, 1061-1068.

Perkins, S. J. & Sim, R. B. (1986). Molecular modelling of human complement component C3 and its fragments by solution scattering. *Eur. J. Biochem.* **157**, 155-168.

Perkins, S. J. (1988). X-ray and neutron solution scattering. *New Comprehen. Biochem.* **11B**, 143-265.

Perkins, S. J., Nealis, A. S. & Sim, R. B. (1991). Oligomeric domain structure of human complement factor H by X-ray and neutron solution scattering. *Biochemsitry,* **30**, 2847-2857.

Perkins, S. J. (1994). High-flux X-ray and neutron solution scattering. *Meth. Mol. Biol.* **22**, 39-60.

Perkins, S. J., Ashton, A. W., Boehm, M. K. & Chamberlain, D. (1998). Molecular structures from low angle X-ray and neutron scattering studies. *Int. J. Biol. Macromol.* **22,** 1-16.

Perkins, S. J. (2001a). High-flux X-ray and neutron solution scattering. *In "Protein-ligand Interaction: hydrodynamics and calorimetry" (eds.)* Harding, S. E. & Chowdhry B. Z. Oxford University Press, New York. Chapter 9, pp. 223-262.

Perkins, S. J. (2001b). X-ray and neutron scattering analyses of hydration shells: a molecular interpretation based on sequence predictions and modelling fits. *Biophys. Chem.* **93**, 129-139.

Perkins, S. J. & Goodship, T. H. J. (2002). Molecular modeling of the C-terminal domains of factor H of human complement: a correlation between haemolytic uraemic syndrome and a predicted heparin binding site. *J. Mol. Biol.* **316**, 217-224.

Perkins, S. J., Gilbert, H. E., Lee, Y. C., Sun, Z. & Furtado, P. B. (2005). Relating small angle scattering and analytical ultracentrifugation in multidomain proteins. *In "Modern Analytical Ultracentrifugation: Techniques and Methods"* (eds.) Scott, D. J., Harding, S. E. & Rowe, A. J. Royal Society of Chemistry, London, U.K. Chapter 15, pp. 291-319.

Perkins, S. J., Okemefuna, A. I., Fernando, A. N., Bonner, A., Gilbert, H. E. & Furtado, P. B. (2008). X-ray and neutron scattering data and their constrained molecular modeling. *Meth. Cell Biol.* **84**, 375-423.

Perkins, S. J., Okemefuna, A. I., Nan, R., Li, K. & Bonner, A. (2009). Constrained solution scattering modelling of human antibodies and complement proteins reveals novel biological insights. *J. R. Soc. Interface.* **6**, S679-S696.

Perkins, S. J., Nan, R., Okemefuna, A. I., Li, K., Khan, S. & Miller, A. (2010a). Multiple interactions of complement factor H with its ligands in solution: a progress report. Current Topics on Complement and Eye Diseases (Ed. J.D. Lambris and A. Adamis). *Adv. Exp. Med. Biol.* **703**, 25-47.

Perkins, S. J., Okemefuna, A. I. & Nan, R. (2010b). Unravelling protein-protein interactions between complement factor H and C-reactive protein by a multidisciplinary strategy. *Biochem. Soc. Transact.* **38**, 894-900.

Philo, J. S. (2000). A method for directly fitting the time derivative of sedimentation velocity data and an alternative algorithm for calculating sedimentation coefficient distribution functions. *Anal. Biochem.* **279**, 151-163.

Preissner, K. T. & Seiffert, D. (1998). Role of vitronectin and its receptors in haemostasis and vascular remodeling. *Thromb. Res.* **89**, 1–21.

Prosser, B. E., Johnson, S., Roversi, P., Herbert, A. P., Blaum, B. S., Tyrrell, J., Jowitt, T. A., Clark, S. J., Tarelli, E., Uhrin, D., Barlow, P. N., Sim, R. B., Day, A. J. & Lea, S. M. (2007). Structural basis for complement factor H linked age-related macular degeneration. *J. Exp. Med.* **204**, 2277-2283.

Ram, S., Sharma, A. K., Simpson, S. D., Gulati, S., McQuillen, D. P., Pangburn, M. K & Rice, P. A. (1998). A novel sialic acid binding site on factor H mediates serum resistance of sialylated Neisseria gonorrhoeae. *J. Exp. Med.* **187**, 743-752.

Rich, R. L. & Myszka, D. G. (2000). Advances in surface plasmon resonance biosensor analysis. *Curr. Opin. Biotechnol.* **11**, 54-61.

Ritchie, C. W., Bush, A. I., Mackinnon, A., Macfarlane, S., Mastwyk, M., MacGregor, L., Kiers, L., Cherny R., Li, Q.-X., Tammer, A., Carrington, D., Mavros, C., Volitakis, I., Xilinas, M., Ames, D., Davis, S.,Beyreuther, K., Tanzi, R. E. & Masters, C. L. (2003). Metal-protein attenuation with iodochlorhydroxyquin (Clioquinol) targeting Aβ amyloid deposition and toxicity in Alzheimer disease. *Arch. Neurol.* **60**, 1685-1691.

Ritchie, D. W. (2003). Evaluation of protein docking predictions using Hex 3.1 in CAPRI rounds 1 and 2. *Proteins,* **52**, 98-106.

Ripoche, J., Day, A. J., Harris, T. J. R. & Sim, R. B. (1988). The complete amino acid sequence of human complement factor H. *Biochem. J.* **249**, 593-602.

Rosengard, A. M., Liu, Y., Nie, Z. & Jimenez, R. (2002). Variola virus immune evasion design: expression of a highly efficient inhibitor of human complement. *Proc. Natl. Acad. Sci. U. S. A.* **99**, 8808-8813.

Ross, G. D. (2000). Regulation of the adhesion versus cytotoxic functions of the Mac-1/CR3/alphaMbeta2-integrin glycoprotein. *Crit. Rev. Immunol.* **20**, 197-222.

Rother, K. Till, G. O., & Hansch, G. M. (Editors) (1998). *The complement sytem.* Springer-Verlag Berlin Heidelberg New York. (2nd Edition).

Rulísek, L. & Vondrásek, J., (1998). Coordination geometries of selected transition metal ions (Co^{2+}, Ni^{2+}, Cu^{2+}, Zn^{2+}, Cd^{2+}, and Hg^{2+}) in metalloproteins. *J. Inorg. Biochem.* **71**, 115-27.

Saunders, R. E., Goodship, T. H. J., Zipfel, P. F. & Perkins, S. J. (2006). Factor H associated haemolytic uraemic syndrome: a web database of the structural consequences of disease-associated mutations. *Hum. Mutat.* **27**, 21-30.

Saunders, R. E. Abarrategui-Garrido, C., Frémeaux-Bacchi, V., Goicoechea de Jorge, E., Goodship, T. H. J., López Trascasa, M., Noris, M., Ponce Castro, I. M., Remuzzi, G., Rodríguez de Córdoba, S., Sánchez-Corral, P., Zipfel, P. F. & Perkins, S. J. (2007). The interactive factor H-atypical haemolytic uraemic syndrome mutation database and website: Update and integration of membrane cofactor protein and factor I mutations with structural models. *Hum. Mutat.* **28**, 222-234.

Schlaf, G., Demberg, T., Beiselm, N., Schieferdecker, H. L. & Götze, O. (2001). Expression and regulation of complement factors H and I in rat and human cells: some critical notes. *Mol. Immunol.* **38**, 31-39.

Schmidt, C. Q., Herbert, A. P., Hocking, H. G., Uhrín, D. & Barlow, P. N. (2008a). Translational mini-review series on complement factor H: structural and functional correlations for factor H. *Clin. Exp. Immunol.* **151**, 14-24.

Schmidt, C. Q., Herbert, A. P., Kavanagh, D., Gandy, C., Fenton, C. J., Blaum, B. S., Lyon, M., Uhrín, D. & Barlow, P. N. (2008b). A new map of glycosaminoglycan and C3b binding sites on factor H. *J. Immunol.* **181**, 2610-2619.

Schmidt, C. Q., Herbert, A. P., Mertens, H. D. T., Guariento, M., Soares, D. C., Uhrin, D., Rowe, A. J., Svergun, D. I. & Barlow, P. N. (2010). The central portion of factor H (modules 10-15) is compact and contains a structurally deviant CCP module. *J. Mol. Biol.* **395**, 105-122.

Schneider, M. C., Prosser, B. E., Caesar, J. J. E., Kugelberg, E., Li, S., Zhang, Q., Quoraishi, S., Lovett, J. E., Deane, J. E., Sim, R. B., Roversi, P., Johnson, S., Tang, C. M. & Lea, S. M. (2009). Neisseria meningitidis recruits factor H using protein mimicry of host carbohydrates. *Nature,* **458**, 890-893.

Schneidman-Duhovny, D., Inbar, Y., Nussinov, R. & Wolfson, H. J. (2005). PatchDock and SymmDock: servers for rigid and symmetric docking. *Nucleic. Acids. Res.* **33**, W363-367.

Scholl, H. P. N., Issa, P. C., Walier, M., Janzer, S., Pollok-Kopp, B., Borncke, F., Fritsche, L. G., Chong, N. V., Fimmers, R., Wienker, T., Holz, F. G., Weber, B. H. F. & Oppermann, M. (2008). Systematic complement activation in age-related macular degeneration. *PloS ONE,* **3**, e2593.

Schuck, P. (1998). Sedimentation analysis of non-interacting and self-associating solutes using numerical solutions to the Lamm equation. *Biophys. J.* **75**, 1503-1512.

Schuck, P. (2000). Size-distribution analysis of macromolecules by sedimentation velocity ultracentrifugation and Lamm equation modeling. *Biophys. J.* **78**, 1606-1619.

Schuck, P. (2003). On the analysis of protein self-association by sedimentation velocity analytical ultracentrifugation. *Anal. Biochem.* **320**, 104-124.

Schuck, P. (2005). Diffusion-deconvoluted sedimentation coefficient distributions for the analysis of interacting and non-interacting protein mixtures. *In "Modern Analytical Ultracentrifugation: Techniques and Methods"* (eds.) Scott, D. J., Harding, S. E. & Rowe, A. J. Royal Society of Chemistry, London, U.K. Chapter 1, pp. 26-50.

Schumacher, F. F. (2009). Localisation of the zinc binding SCR domains in complement factor H (FH). *Rotation 1 report. Department of structural and molecular biology. University College London.*

Schumacher, F. F. (2009). Prediction of zinc binding sites in complement factor H. *Rotation 2 report. Department of structural and molecular biology. University College London.*

Schwarz, M., Spath, L., Lux, C. A., Paprotka, K., Torzewski, M., Dersch, K., Koch-Brandt, C., Husmann, M. & Bhakdi, S. (2008). Potential protective role of apoprotein J (clusterin) in atherogenesis: binding to enzymatically modified low-density lipoprotein reduces fatty acid-mediated cytotoxicity. *Thromb. Haemost.* **100**, 110-118.

Scott, D. J. & Schuck, P. (2005). A brief introduction to the analytical ultracentrifugation of proteins for beginners. *In "Modern Analytical Ultracentrifugation: Techniques and Methods"* (eds.) Scott, D. J., Harding, S. E. & Rowe, A. J. Royal Society of Chemistry, London, U.K. Chapter 1, pp 1-25.

Semenyuk, A. V. & Svergun, D. I. (1991). GNOM - a program package for small-angle scattering data-processing. *J. Appl. Crystallogr.* **24,** 537-540.

Sharma, A. K. & Pangburn, M. K. (1996). Identification of three physically and functionally distinct binding sites for C3b in human complement factor H by deletion mutagenesis. *Proc. Natl. Acad. Sci. U. S. A.* **93**, 10996-11001.

Sim, R. B. & DiScipio, R. G. (1982). Purification and structural studies on the complement-system control protein beta 1H (Factor H). *Biochem. J.* **205**, 285-293.

Sim, R. B. Day, A. J., Moffatt, B. E. & Fontaine, M. (1993). Complement factor I and cofactors in control of complement system convertase enzymes. *Meths. Enzymol.* **223**, 13-35.

Sjöberg, A. P., Trouw, L. A., Clark, S. J., Sjölander, J., Heinegård, D., Sim, R. B., Day, A. J. & Blom, A. M. (2007). The factor H variant associated with age-related macular degeneration (His-384) and the non-disease-associated form bind differentially to C-reactive protein, fibromodulin, DNA, and necrotic cells. *J. Biol. Chem.* **282**, 10894-10900.

Skidgel, R. A. & Erdös, E. G. (2007). Structure and function of human plasma carboxypeptidase N, the anaphylatoxin inactivator. *Int. Immunopharmacol.* **7**, 1888-1899.

Skerka, C., Lauer, N., Weinberger, A. A., Keilhauer, C. N., Sühnel, J., Smith, R., Schlötzer-Schrehardt, U., Fritsche, L., Heinen, S., Hartmann, A., Weber, B. H. & Zipfel, P. F. (2007). Defective complement control of factor H (Y402H) and FHL-1 in age-related macular degeneration. *Mol. Immunol.* **44**, 3398-3406.

Soares, D. & Barlow, P. N. (2005). Complement control protein modules in the regulators of complement activators. In "Structural Biology of the Complement System" (eds.) Morikis, D & Lambris, J. D. Taylor & Francis, Boca Raton, USA. Chapter 2, pp. 19-62.

Sodhi, J. S., Bryson, K., McGuffin, L. J., Ward, J. J., Wernisch, L. & Jones, D. T. (2004). Predicting metal-binding site residues in low-resolution structural models. *J. Mol. Biol.* **342**, 307-320.

Somers, W., Ultsch, M., De Vos, A. M. & Kossiakoff, A. A. (1994). The X-ray structure of a growth hormone-prolactin receptor complex. *Nature,* **372**, 478-481.

Spencer, K. L., Hauser, M. A., Olson, L. M., Schmidt, S., Scott, W. K., Gallins, P., Agarwal, A., Postel, E. A., Pericak-Vance, M. A. & Haines, J. L. (2007). Protective effect of complement factor B and complement component 2 variants in age-related macular degeneration. *Hum. Mol. Genet.* **16**, 1986–1992.

Strohmeyer, R., Ramirez, M., Cole, G. J., Mueller, K. & Rogers, J. (2002). Association of factor H of the alternative pathway of complement with agrin and complement receptor 3 in the Alzheimer's disease brain. *J. Neuroimmunol.* **131**, 135-146.

Svergun, D. I. & Stuhrmann, H. B. (1991). New developments in direct shape determination from small-angle scattering. 1. Theory and model calculations. *Acta. Crystallogr.* **A47**, 736-744.

Tanious, F. A., Nguyen, B. & Wilson, W. D. (2008). Biosensor-surface plasmon resonance methods for quantitative analysis of biomolecular interactions. *Meth. Cell Biol.* **84**, 53-77.

Tate, D. J., Jr, Newsome, D. A. & Oliver, P. D. (1993). Metallothionein shows an aged-related decrease in human macular retinal pigment epithelium. *Invest. Ophthalmol. Vis. Sci.* **34**, 2348–2351.

Torreri, P., Ceccarini, M., Macioce, P. & Petrucci, T. C. (2005). Biomolecular interactions by surface plasmon resonance technology. *Ann. Ist Super Sanita.* **41**, 437-441.

Tortajada, A., Montes, T., Martínez-Barricarte, R., Morgan, B. P., Harris, C. L. & de Córdoba, S. R. (2009). The disease-protective complement factor H allotypic variant Ile62 shows increased binding affinity for C3b and enhanced cofactor activity. *Hum. Mol. Genet.* **18**, 3452-3461.

Truedsson, L., Bengtsson, A. A. & Sturfelt, G. (2007). Complement deficiencies and systemic lupus erythematosus. *Autoimmunit*y, **40**, 560–566.

Tschopp. J., Chonn. A., Hertig, S. & French, L. E. (1993). Clusterin, the human apolipoprotein and complement inhibitor, binds to complement C7, C8 beta, and the b domain of C9. *J. Immunol*. **151**, 2159– 2165.

Tsiftsoglou, S. A. & Sim, R. B. (2004). Human complement factor I does not require cofactors for cleavage of synthetic substrates. *J. Immunol.* **173**, 367-375.

Ugarte, M. & Osborne, N. N. (2001). Zinc in the retina. *Prog. Neurobiol.* **64**, 219-249.

Ullman, C. G., Chamberlain, D., Emery, V. C., Haris, P. I., Sim, R. B. & Perkins, S. J. (1998). Human complement factor I: its expression by insect cells and its biochemical and structural characterisation. *Mol. Immunol.* **35**, 503-512.

Van Der Merwe, P. A. (2001). Surface plasmon resonance. *In "Protein-ligand Interaction: hydrodynamics and calorimetry"* (eds.) Harding, S. E. & Chowdhry B. Z. Oxford University Press, New York. Chapter 6, pp. 137-170.

Venables, J. P., Strain, L., Routledge, D., Bourn, D., Powell, H. M., Warwicker, P., Diaz-Torres, M. L., Sampson, A., Mead, P., Webb, M., Pirson, Y., Jackson, M. S., Hughes, A., Wood, K. M., Goodship, J. A. & Goodship, T. H. (2006). Atypical haemolytic uraemic syndrome associated with a hybrid complement gene. *PLoS Med.* **3**, e431.

Walport, M. J. (2001). Complement. First of two parts. *N. Engl. J. Med.* **344**, 1058-1066.

Weiler, J. M., Daha, M. R., Austen, K. F. & Fearon, D. T. (1976). Control of the amplification convertase of complement by the plasma protein beta1H. *Proc. Natl. Acad. Sci. U. S. A.* **73**, 3268-3272.

Whaley, K. & Ruddy, S. (1976). Modulation of the alternative complement pathways by beta 1 H globulin. *J. Exp. Med.* **144**, 1147-1163.

Wiesmann, C., Katschke, K. J., Yin, J., Helmy, K. Y., Steffek, M., Fairbrother, W. J., McCallum, S. A., Embuscado, L., DeForge, L. & Hass, P. E., van Lookeren Campagne, M. (2006). Structure of C3b in complex with CRIg gives insights into regulation of complement activation. *Nature,* **444**, 217–220.

Wills, N. K., Ramanujam, V. M., Kalariya, N., Lewis, J. R. & van Kuijk, F. J. (2008). Copper and zinc distribution in the human retina: relationship to cadmium accumulation, age, and gender. *Exp. Eye. Res.* **87**, 80-88.

Wu, J., Wu, Y., Ricklin, D., Janssen, B. J. C., Lambris, J. D. & Gros, P. (2009). Structure of complement fragment C3b-factor H and implications for host protection by complement regulators. *Nat. Immunol.* **10**, 728-733.

Yano, J. K., Koo, L. S., Schuller, D. J., Li, H., Ortiz de Montellano, P. R. & Poulos, T. L. (2000). Crystal structure of a thermophilic cytochrome P450 from the archaeon Sulfolobus solfataricus. *J. Biol. Chem.* **275**, 31086-31092.

Yates, J. R., Sepp, T., Matharu, B. K., Khan, J. C., Thurlby, D. A., Shahid, H., Clayton, D. G., Hayward, C., Morgan, J., Wright, A. F., Armbrecht, A. M., Dhillon, B., Deary, I. J., Redmond, E., Bird, A. C., Moore, A. T. & Genetic Factors in AMD Study Group. (2007). Complement C3 variant and the risk of age-related macular degeneration. *N. Engl. J. Med.* **357**, 553–561.

Young, R. W. (1987). Pathophysiology of age-related macular degeneration. *Surv. Ophthalmol.* **31**, 291-306.

Zetterberg, M., Landgren, S., Andersson, M. E., Palmér, M. S., Gustafson, D. R., Skoog, I., Minthon, L., Thelle, D. S., Wallin, A., Bogdanovic, N., Andreasen, N., Blennow, K. & Zetterberg, H. (2008). Association of complement factor H Y402H gene polymorphism with Alzheimer's disease. *Am. J. Med. Genet. B. Neuropsychiatr. Genet.* **147**, 720-726.

Zipfel, P. F. & Skerka, C. (1999). FHL-1/reconectin: a human complement and immune regulator with cell-adhesive function. *Immunol. Today,* **20**, 135–140.

Zipfel, P. F., Heinen, S., Jozsi, M., & Skerka, C., (2006). Complement and disease: Defective alternative pathway control results in Kidney and eye diseases. *Mol Immunol.* **43**, 97-106.

Zipfel, P. F., Edey, M., Heinen, S., Józsi, M., Richter, H., Misselwitz, J., Hoppe, B., Routledge, D., Strain, L., Hughes, A. E., Goodship, J. A., Licht, C., Goodship, T. H. & Skerka, C. (2007). Deletion of complement factor H-related genes CFHR1 and CFHR3 is associated with atypical hemolytic uremic syndrome. *PLoS Genet.* **3**, e41.

Zipfel, P. F. & Skerka, C., (2009). Complement regulators and inhibitory proteins. *Nat. Rev. Immunol.* **9**, 729-740.

Publications

Nan, R., Gor, J. & Perkins, S. J. (2008a). Implications of the progressive self-association of wild-type human Factor H for complement regulation and disease. *J. Mol. Biol.* **375**, 891-900.

Nan, R., Gor, J., Lengyel, I. & Perkins, S. J. (2008b). Uncontrolled zinc- and copper-induced oligomerisation of the human complement regulator Factor H and its possible implications for function and disease. *J. Mol. Biol.* **384**, 1341-1352.

Okemefuna, A. I., Nan, R., Gor, J. & Perkins, S. J. (2009). Electrostatic interactions contribute to the folded-back conformation of wild type human factor H *J. Mol. Biol.* **391**, 98-118.

Okemefuna, A. I., Li, K., Nan, R., Ormsby, R. J., Sadlon, T., Gordon, D. L. & Perkins, S. J. (2009). Multimeric interactions between complement factor H and its C3d ligand provide new insight on complement regulation. *J. Mol. Biol.* **391**, 119-135.

Perkins, S. J., Okemefuna, A. I., Nan, R., Li, K. & Bonner, A. (2009). Constrained solution scattering modelling of human antibodies and complement proteins reveals novel biological insights. *J. R. Soc. Interface.* **6**, S679-S696.

Okemefuna, A. I., Nan, R., Miller, A., Gor, J. & Perkins, S. J. (2010). Complement factor H binds at two independent sites to C-reactive protein in acute phase concentrations. *J. Biol. Chem.* **285**, 1053-1065.

Perkins, S. J., Nan, R., Okemefuna, A. I., Li, K., Khan, S. & Miller, A. (2010a). Multiple interactions of complement factor H with its ligands in solution: a progress report. Current Topics on Complement and Eye Diseases (Ed. J.D. Lambris and A. Adamis). *Adv. Exp. Med. Biol.* **703**, 25-47.

Perkins, S. J., Okemefuna, A. I. & Nan, R. (2010b). Unravelling protein-protein interactions between complement factor H and C-reactive protein by a multidisciplinary strategy. *Biochem. Soc. Transact.* **38**, 894-900.

Pulications in preparation

Nan, R., Ward, G., Gavigan, L., Miller, A., Gor, J., McKay, A. R., Lengyel, I. & Perkins, S. J. Self-association and folded-back solution structures of the wild-type Tyr402 and the disease-related His402 allotypes of complement Factor H.

Nan, R., Farabella, I., Schumacher, F. F., Miller, A., Gor, J., Martin, A. C. R., Jones, D. T., Lengyel, I. & Perkins, S. J. Localisation of zinc binding sites in the wild-type Tyr402 and disease-related His402 allotypes of complement factor H: implications for age-related macular degeneration.

Presentations and abstracts

Nan, R., Gor, J., Sim, R. B. & Perkins, S. J. Evidence for a monomer-dimer equilibrium in native human Factor H. 11TH European Meeting on Complement in Human Diseases, Cardiff, 8-11 Sep 2007 (Poster).

Nan, R., Gor, J., Lengyel, I. & Perkins, S. J. Uncontrolled zinc- and copper-induced oligomerisation of native human complement Factor H and its implications for age-related macular degeneration. XXII International Complement Workshop, Basel, Switzerland, 28 Sep–2 Oct 2008 (Poster).

Nan, R., Ward, G., Gor, J., Lengyel, I. & Perkins, S. J. Self-association of the Tyr402 and His402 allotypes of complement factor H in the absence and presence of zinc. 1st International Conference on Inflammation and Retinal Disease: Complement Biology and Pathology, Crete, Greece, 26 Jun-1 Jul 2009 (Oral).

Nan, R., Ward, G., Gavigan, L., Miller, A., Gor, J., Lengyel, I. & Perkins, S. J. The His402 allotype of complement Factor H show similar self-association to the Tyr402 allotype but exhibits greater self-association in the presence of zinc. XXIII International Complement Workshop, New York, US, 1-5 Aug 2010 (Poster).

Nan, R., Ward, G., Gavigan, L., Miller, A., Gor, J., McKay, A. R., Lengyel, I. & Perkins, S. J. Comparison of the self-association and folded-back solution structure of

the wild-type Tyr402 and the disease-related His402 allotypes of complement Factor H. 19th International AUC Conference, Nottingham, UK, 12-16 Sep 2010 (Oral).

doi:10.1016/j.jmb.2007.11.015 J. Mol. Biol. (2008) 375, 891–900

JMB

Available online at www.sciencedirect.com

ScienceDirect

ELSEVIER

COMMUNICATION

Implications of the Progressive Self-association of Wild-type Human Factor H for Complement Regulation and Disease

Ruodan Nan, Jayesh Gor and Stephen J. Perkins*

Department of Biochemistry and Molecular Biology, Darwin Building, University College London, Gower Street, London WC1E 6BT, UK

Received 2 October 2007; received in revised form 1 November 2007; accepted 6 November 2007
Available online
13 November 2007

Factor H (FH) is a major regulator of complement alternative pathway activation. It is composed of 20 short complement regulator (SCR) domains and is genetically associated as a risk factor for age-related macular degeneration. Previous studies on FH suggested that it existed in monomeric and dimeric forms. Improved X-ray scattering and analytical ultracentrifugation methodology for wild-type FH permitted a clarification of these oligomeric properties. Data at lower concentrations revealed a dependence of the X-ray radius of gyration values on concentration that corresponded to the weak self-association of FH. Global sedimentation equilibrium fits indicated that a monomer–dimer equilibrium best described the data up to 1.3 mg/ml with a fitted dissociation constant K_D of 28 μM and that higher oligomers formed at increased concentrations. The K_D showed that about 85–95% of serum FH will be monomeric in the absence of other factors. Size-distribution analyses in sedimentation velocity experiments showed that monomeric FH was the major species but that as many as six oligomeric forms co-existed with it. The data were explained in terms of two weak dimerisation sites recently identified in the SCR-6/8 and SCR-16/20 fragments of FH with similar K_D values. These observations indicate a mechanism for the progressive self-association of FH and may be relevant for complement regulation and the formation of drusen deposits that are associated with age-related macular degeneration.

Keywords: factor H; oligomerisation; X-ray scattering; analytical ultracentrifugation; age-related macular degeneration

Edited by R. Huber

In the human innate immune defence system, the central complement component C3 is activated to C3b by the cleavage and removal of the small anaphylatoxin C3a to initiate the alternative pathway in serum. C3b is regulated by factor H (FH) in order to prevent complement-mediated host cell damage, in which FH acts as a co-factor for factor I cleavage of C3b to form iC3b,[1–3] accelerating the decay of the C3 convertase C3bBb[2,4] and competing with factor B for binding to C3b.[5] FH is composed of 20 short complement regulator (SCR) domains, each of about 61 residues in length. SCR domains, also known as short consensus repeats, Sushi or complement control protein domains,[6] constitute the most abundant domain type in complement proteins. There are multiple binding sites for C3b within the 20 SCR domains,[7,8] and likewise there are multiple binding sites for heparin.[9–12] FH regulates surface-bound C3b activity by recognising charge (anionic) clusters on the surfaces of host cells that are mimicked by heparin. The initial contact with host cells is made through its C-terminal end, which is followed by N-terminal regulatory activity.[13,14] Polymorphisms and mutations in FH have been associated with age-related macular degeneration (AMD),[15–19] the most common cause of blindness in the elderly in the Western world, and with atypical haemolytic uraemic syndrome (aHUS),[19,20] a rare

*Corresponding author. E-mail address: s.perkins@medsch.ucl.ac.uk.

Abbreviations used: FH, factor H; SCR, short complement regulator; R_G, radius of gyration; AMD, age-related macular degeneration; aHUS, atypical haemolytic uraemic syndrome.

disease leading to renal failure that affects individuals of all ages but primarily children and young adults†. The involvement of FH indicates that complement activation and regulation in the retina and the kidney endothelium have been impaired.

Intact FH has not been crystallised to date for reasons of its size, glycosylation and inter-SCR flexibility. Thus, solution scattering and electron microscopy methods have been applied to show that the FH SCR domain structure is not fully extended in solution.[21–23] X-ray scattering and ultracentrifugation, in combination with constrained scattering modelling, are powerful approaches[24,25] that resulted in the first molecular structures for FH and its SCR-6/8, SCR-1/5 and SCR-16/20 fragments.[23,26,27] Homology models for the SCR domains provided many of the first structural explanations for AMD and aHUS.[23,28,29] Thus, AMD was associated with a common Tyr402-His polymorphism, which is located at the surface of SCR-7 and close to a heparin binding site. The aHUS-related mutations cluster at the surface of SCR-20 and to a lesser degree in SCR-16 to SCR-19, and they are associated with another heparin binding site. The distribution of more than 100 genetic alterations† showed that the observed clinical phenotype is correlated with their structural location.[19] NMR and crystal structures, starting with those for SCR-5 and SCR-15/16 and more recently extended to those for SCR-6/8 and SCR-19/20, have confirmed and extended these predictions.[6,12,30–33] Even with these structures, there is no clear indication of a molecular mechanism involving FH that leads to AMD.

One of the hallmarks of AMD is the appearance of drusen, an amyloid plaque-like deposition in Bruch's membrane, a layer interposed between the retinal pigment epithelium and the choroidal vasculature.[34,35] The deposits contain oxidized lipids and many aggregated proteins, including FH.[36] The self-association properties of FH are thus relevant to drusen formation. FH was originally shown to be monomeric by ultracentrifugation.[37] Dimeric FH was demonstrated by scattering, but this observation could not be subsequently replicated.[21,23] Partial FH SCR-15/18 and SCR-15/20 dimers were however observed by non-reducing SDS-PAGE, and SCR-1/7 was observed to interact with SCR-1/20 by surface plasmon resonance.[8,13] Our recent ultracentrifugation and scattering studies showed that SCR-6/8 and SCR-16/20 (but not SCR-1/5) exhibit weak monomer–dimer associations.[26,27] These studies indicate at least two potential dimerisation sites in FH. In combination, the two sites would constitute a mechanism for the continual self-association of FH that would lead ultimately to aggregate formation. In this study, we re-investigated the oligomerisation properties of native FH. Through the use of improved scattering and ultracentrifugation instrumentation and analyses, we found and here show that FH exhibits a monomer–dimer equilibrium at physiological concentrations and multiple oligomers at higher concentrations. We discuss the implications of this result for complement regulation and AMD.

† http://www.fh-hus.org

X-ray scattering of FH oligomers

The purification of wild-type FH for X-ray scattering and analytical ultracentrifugation experiments utilised a 3-l pool of just-outdated anonymised human plasma from the Royal Free Hospital Blood Bank with an anti-FH monoclonal antibody Sepharose MRC-OX23 column as previously described.[23,38] The final column eluate in 3 M $MgCl_2$ was dialysed into Hepes buffer [10 mM Hepes, 137 mM NaCl and 0.5 mM ethylenediaminetetraacetic acid (EDTA), pH 7.4]. The FH concentration step at 4 °C employed a gentle centrifugation approach without stirring (Amicon® Ultra-15 centrifugal filter devices with a molecular-mass cutoff of 50 kDa at 2500*g*). Non-specific aggregates of FH and human serum albumin were removed by gel filtration on a Superose™ 6 prep grade XK 16/60 column, and the sample was re-concentrated by centrifugation. All FH samples were checked using SDS-PAGE before and after scattering and ultracentrifugation experiments. An absorption coefficient of 16.7 (1%, 280 nm, 1-cm path length) was used to determine concentrations.[23]

The X-ray scattering radius of gyration (R_G) of FH monitors its degree of elongation. FH prepared 2 days beforehand was studied on Instrument ID02 at the European Synchrotron Radiation Facility[39] in eight concentrations between 8.7 and 0.43 mg/ml in Hepes buffer (Fig. 1). Improved Guinier R_G fits were obtained at lower Q values compared with the previous X-ray measurements at the Synchrotron Radiation Source at Daresbury ($Q=4\pi \sin\theta/\lambda$, 2θ = scattering angle, λ = wavelength).[21,23] For reason of the higher beam intensities at the European Synchrotron Radiation Facility, improved signal–noise ratios were obtained (Fig. 1a and b). There is better control of radiation damage on Instrument ID02 as this is monitored online during data acquisition. The Guinier R_G and its cross-sectional radius of gyration ($R_{XS\text{-}1}$) parameters (but not its $R_{XS\text{-}2}$ parameter: not shown) and the associated intensity $I(0)/c$ parameters showed small but visible concentration dependences (Fig. 1c–e). The $R_{XS\text{-}2}$ parameter differs from SCR protein to protein and generally monitors the averaged short-range degree of bend between two or among three adjacent SCR domains along the length of the protein.[23] An additional medium-range proximity relationship between non-neighbouring SCR domains that are further apart in the sequence leads to the observation of the $R_{XS\text{-}1}$ region.[23] This weak concentration dependence showed that FH oligomerisation had occurred. Data obtained using phosphate-buffered saline (PBS: 137 mM NaCl, 2.7 mM KCl, 8.1 mM Na_2HPO_4 and 1.15 mM KH_2PO_4, pH 7.4) were consistent with the Hepes data (Fig. 1c and e). The R_G value extrapolated to zero concentration is 8.90±0.19 nm, while $R_{XS\text{-}1}$ is 2.51±0.06 nm and $R_{XS\text{-}2}$ is 1.79±0.01 nm. If the slope in Fig. 1d corresponds to a

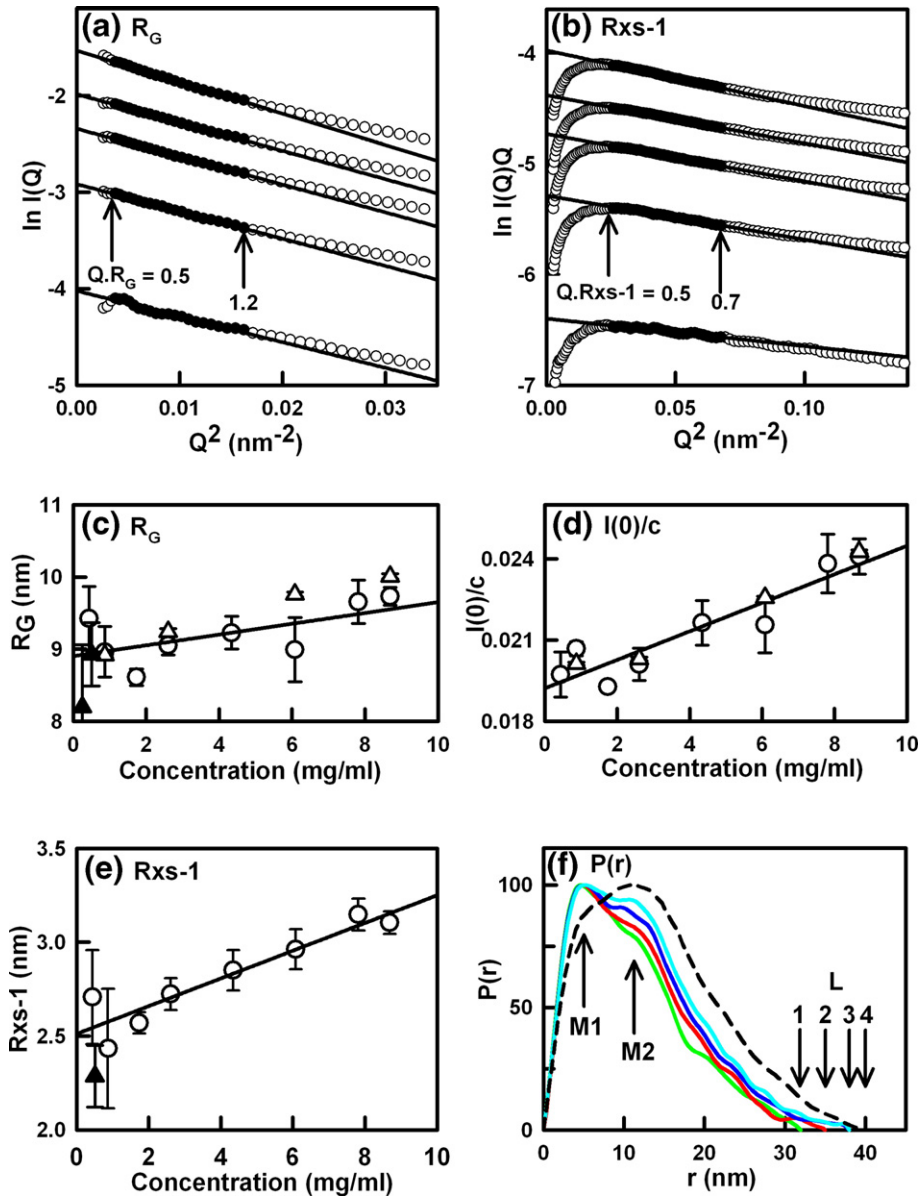

Fig. 1. X-ray scattering analyses of wild-type FH. (a) Guinier R_G plots of ln $I(Q)$ *versus* Q^2 at low Q values for wild-type FH at concentrations of 8.69, 6.08, 4.34, 2.61 and 0.87 mg/ml. The Q fit range was 0.06–0.13 nm^{-1}. The filled circles correspond to the $I(Q)$ data used to determine the R_G values, and the straight line corresponds to the best fit through those points. The $Q{\cdot}R_G$ ranges used in the fits are arrowed. (b) The corresponding Guinier cross-sectional $R_{XS\text{-}1}$ fits of ln $I(Q){\cdot}Q$ *versus* Q^2 for the same five scattering curves in a Q range of 0.16–0.26 nm^{-1} are shown. The $R_{XS\text{-}2}$ fits in a Q range of 0.4–0.8 nm^{-1} are not shown. (c–e) Concentration dependence of the R_G, $I(0)/c$ and $R_{XS\text{-}1}$ values (open circles). Each value was measured in quadruplicate and averaged. Statistical error bars are shown where visible. These data were fitted by linear regression. The open triangles correspond to the R_G and $I(0)/c$ parameters from (f). The filled triangles correspond to data measured in PBS. (f) Distance distribution function $P(r)$ analyses. The four $P(r)$ curves correspond to concentrations of 0.87 mg/ml (green), 2.61 mg/ml (red), 6.08 mg/ml (blue) and 8.69 mg/ml (cyan). The peaks in the $P(r)$ curves are denoted as *M1* at 4.9 nm and as *M2* at 10.3 nm. The maximum length L was determined to be 32, 35 and 38 nm (numbered 1, 2 and 3, respectively). The intensities of the four $P(r)$ curves are normalised using the peak *M1* in order to show the concentration dependence of peak *M2* and L more clearly. The dashed line corresponds to the $P(r)$ curve obtained in 2001 for FH at 3.56 mg/ml in Tris–HCl buffer,[23] for which L was determined to be 40 nm (numbered 4). X-ray scattering data were obtained in three beam time sessions on the Beamline ID02 at the European Synchrotron Radiation Facility (Grenoble, France) operating with a ring energy of 6.0 GeV.[38] Storage ring currents ranged from 63 to 65 mA and 66 to 91 mA (two sessions in 16-bunch mode) and from 170 to 172 mA (one beam session in uniform fill mode). Samples were measured in flow cells to reduce radiation damage by moving the sample continuously during beam exposure in 10 time frames of 0.1- or 0.2-s duration each for the uniform fill mode and those of 1.0- or 2.0-s duration each for the 16-bunch mode, together with online checks for the absence of radiation damage, after which the frames were averaged. Other details, including the data reduction procedure and the Guinier and $P(r)$ analyses, are described elsewhere.[26,27]

monomer–dimer equilibrium, then the resulting dissociation constant K_D is estimated to be 100 μM. This is comparable with the K_D values of 40 and 16 μM observed for the SCR-6/8 and SCR-16/20 fragments, respectively.[26,27]

The present R_G values for FH are lower than previous ones. This was shown by comparisons of Fig. 1 here with Fig. 3 of Ref. 23, reporting a 2001 analysis, and Fig. 2 of Ref. 21, reporting a 1991 analysis. In the 2001 analysis, the apparent R_G value was 11.4±0.4 nm, R_{XS-1} was 4.4±0.2 nm and R_{XS-2} was 1.7±0.1 nm. In the 1991 analysis, the apparent R_G value was 12.4±0.4 nm, R_{XS-1} was 3.6 ±0.4 nm and R_{XS-2} was 1.8±0.3 nm. These earlier values were confirmed by re-analyses of the earlier data files retrieved from archives. The difference is attributed to the presence of minor aggregation in 2001 and to a greater level of aggregation in 1991, together with worsened signal–noise ratios in 2001 and 1991 (data not shown). These issues may have masked the presently observed concentration dependence in FH. Previously, it was thought that alkaline pH values would cause FH to self-associate.[23] This was not confirmed after sample dialysis for 2 days at pH 11.9, followed by X-ray measurement.

The indirect transformation of the scattering data $I(Q)$ in reciprocal space in the Q range between 0.08 and 2.1 nm^{-1} into real space gives the distance distribution function $P(r)$. This summarises all the distances between pairs of atoms within FH. The $P(r)$ function gives an independent calculation of the R_G and $I(0)$ values that is based on the full scattering curve and gives the maximum length of FH, denoted L. The R_G and $I(0)/c$ values from $P(r)$ were in good agreement with the Guinier R_G values (Fig. 1c and d). The eight $P(r)$ curves show a concentration-independent peak *M1* at $r=4.8\pm0.3$ nm. A second peak *M2* was observed at $r=10.2\pm0.6$ nm, and peak *M2* increased in its relative intensity as the concentration increased. L increased from 32 nm at 0.9 mg/ml to 38 nm at 8.7 mg/ml (Fig. 1f). These changes are attributed to oligomer formation in FH. As before,[23] the value of L between 32 and 38 nm is about half the length of 73 nm expected if the 20 SCR domains in FH are in a fully extended arrangement. When compared with the $P(r)$ curve from 2001 at 3.6 mg/ml in 25 mM Tris–HCl, 140 mM NaCl and 0.5 mM EDTA buffer, pH 7.4,[23] peak *M2* is now greater than *M1* and L is 40 nm (Fig. 1f). This difference is consistent with the presence of minor aggregation in FH from 2001. The superimposition of the $I(Q)$ curves from 1991 and 2001 upon the current ones shows increased intensities at low Q that are consistent with aggregation (not shown). Figure 1f shows that the SCR domains in FH are bent or folded back upon themselves in solution, both for the monomer and its oligomeric and aggregated forms.

Sedimentation equilibrium of FH oligomers

Sedimentation equilibrium experiments on an FH sample in Hepes buffer prepared 16 days beforehand were monitored using both absorbance and interference optics. Data were acquired at 4, 20 and 37 °C at 20 concentrations between 0.07 and 7.11 mg/ml and four rotor speeds between 8000 and 20,000 rpm. Absorbance data at 280 nm above 0.7 mg/ml were not fitted because of the saturation of the optics; thus, interference data were fitted. Data at 20 °C were fitted using SEDPHAT v4.10b software,[40] initially using individual fits of 80 equilibrium curves and subsequently using global fits of between 9 and 20 curves. Similar fit outcomes were obtained with the data at 4 and 37 °C. In the individual fits, the fitting of a monomer–dimer model to the 11,000 rpm data at 1.32 mg/ml gave a reduced χ^2 value of 3.7 compared with that of 34.8 from a monomer model using the same data. In global fits up to 1.32 mg/ml and based on a fixed molecular mass of 145 kDa, the monomer–dimer model (reduced χ^2 of 11) gave significantly improved fits compared with a monomer model that gave a high molecular mass of 187 kDa and an increased reduced χ^2 of 22. Low random residuals were obtained (upper nine fits in Fig. 2). This showed that a monomer–dimer equilibrium existed in a physiological concentration range.

At higher FH concentrations, the formation of higher oligomers was detected. Between 2.86 and 7.11 mg/ml, the monomer–dimer model did not result in good fits. Large deviations in the residuals were consistent with aggregate formation (lowest three fits in Fig. 2).[41] Tests with other fit models based on the inclusion of trimers or tetramers gave no improvement in the residuals or reduced χ^2 values. The reduced χ^2 values of between 269 and 980 for these fits at higher concentrations showed that none of the monomer–dimer, monomer–dimer–trimer and monomer–dimer–tetramer self-association models would fit. Hence, these data do not correspond to an equilibrium between monomers and higher oligomers.

Non-reducing SDS-PAGE of the samples at three concentrations after ultracentrifugation showed that a dimer band was observed at the higher concentrations used, and fainter bands corresponding approximately to trimers and tetramers could be observed (Fig. 3b). There is no unpaired Cys residue in FH that would explain this. Size-exclusion gel filtration of the equilibrium samples 78 days after their original purification showed that the single homogenous peak originally obtained between 65 and 75 ml was supplemented by additional peaks that eluted between 50 and 65 ml (Fig. 2a). This showed that oligomers had formed during the ultracentrifugation experiment and the subsequent sample storage at 4 °C.

Sedimentation velocity of higher FH oligomers

The sedimentation coefficient $s^0_{20,w}$ monitors macromolecular elongation and provides an independent monitor of the scattering data through its ability to detect sample polydispersity. Sedimentation velocity experiments were performed at six

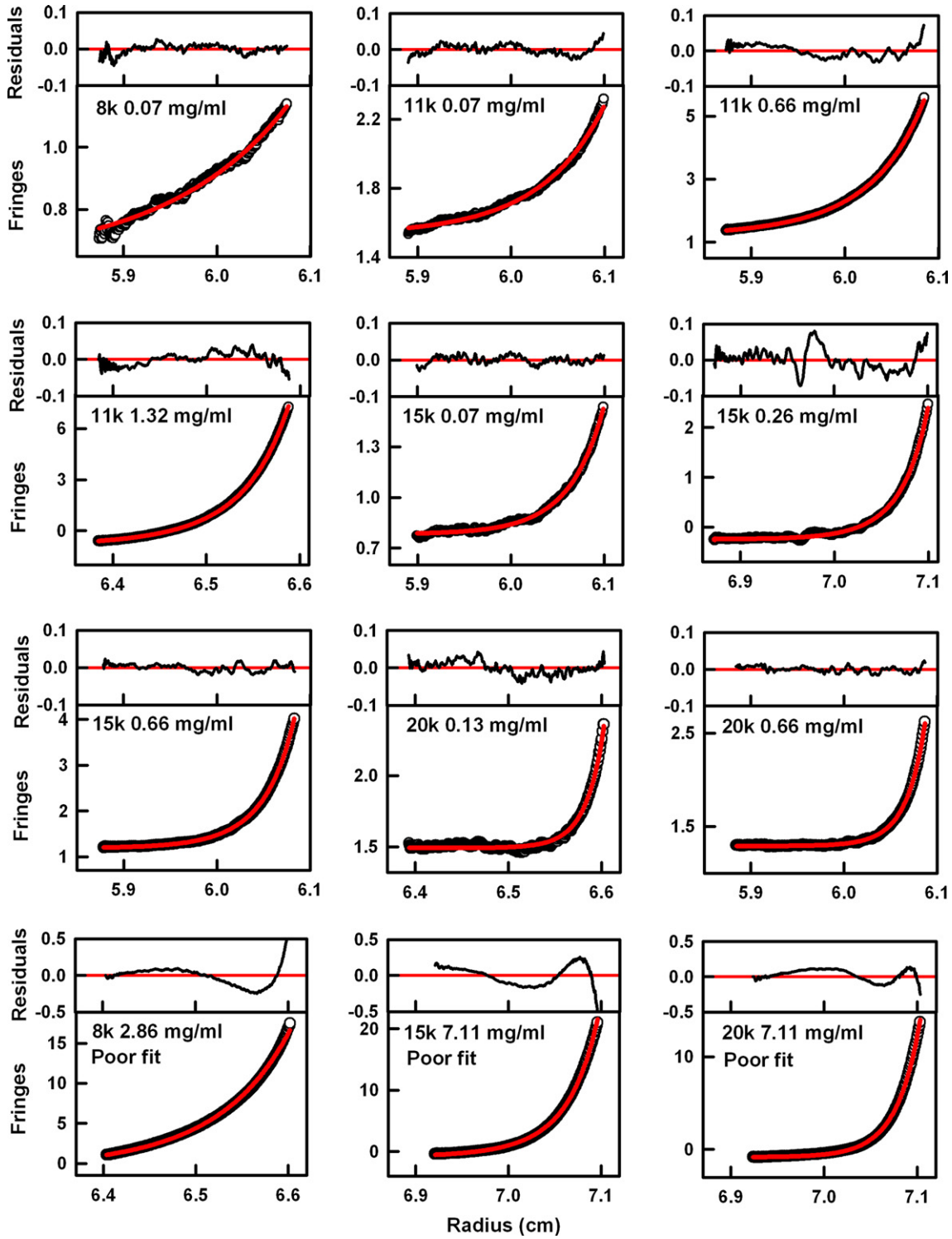

Fig. 2. Sedimentation equilibrium of wild-type FH. Fits for FH in Hepes buffer at 20 °C are shown in a concentration series from 0.07 to 7.1 mg/ml using rotor speeds of 8000, 11,000, 15,000 and 20,000 rpm with two Beckman XL-I analytical ultracentrifuges equipped with AnTi50 and AnTi60 rotors. The upper nine panels show the outcome of a global fit using SEDPHAT when five concentrations between 0.07 and 1.32 mg/ml were fitted to the "monomer–dimer self-association" model using the "M and s" fitting routine. The monomer molecular mass was fixed at 145 kDa, while the baseline and the dissociation constant K_D were floated. The fit residuals are shown above each panel. The lower three panels show the poor fits to the monomer–dimer self-association model when higher concentrations of FH (2.86 and 7.11 mg/ml) were fitted.

rotor speeds between 25,000 and 60,000 rpm using three FH preparations at nine concentrations between 0.07 and 5.9 mg/ml in Hepes buffer and between 0.05 and 0.35 mg/ml in PBS. Data analyses utilised size-distribution $c(s)$ analyses in SEDFIT v9.3b in order to identify species other than

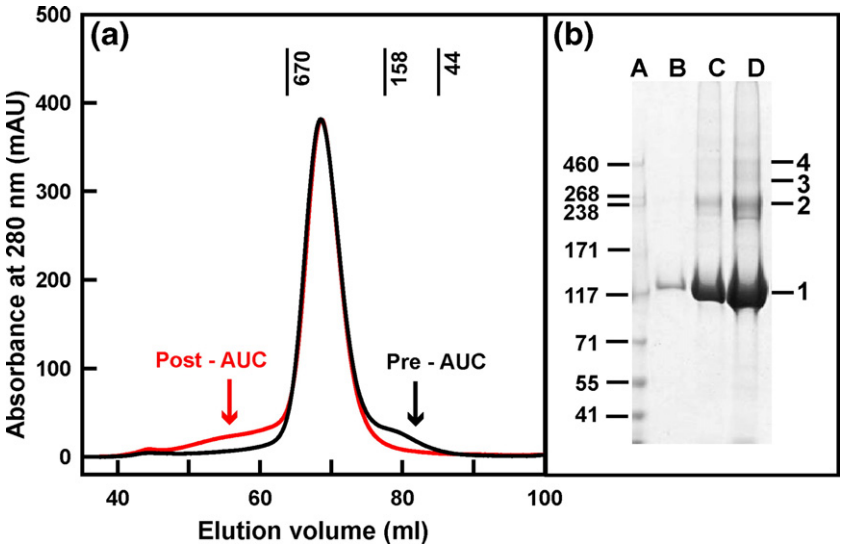

Fig. 3. Size-exclusion gel filtration and non-reducing SDS-PAGE analyses of wild-type FH. (a) FH samples at 3 mg/ml were loaded onto a Superose™ 6 prep grade XK 16/60 column following purification (black) and 78 days after purification (red). The small peak at 80 ml (black) corresponds to residual human serum albumin from the purification. The elution positions of three molecular mass standards are shown. (b) Non-reducing SDS-PAGE analyses of FH after ultracentrifugation. Lane A, Himark™ Prestained High Molecular Weight Standard, labelled to the left; lane B, 0.16 mg/ml of FH; lane C, 1.42 mg/ml of FH; lane D, 2.74 mg/ml of FH. The higher molecular-weight bands seen in FH are labelled on the right by 1, 2, 3 and 4 to denote monomer, dimer, trimer and tetramer, respectively.

monomeric FH.[42,43] The fits were based on a resolution of 200 and a fixed frictional coefficient ratio *f/fo* of 1.78, while allowing both the meniscus and the cell bottom to float within a narrow range of 0.01 cm. At all concentrations, monomeric FH was observed to sediment at $s^0_{20,w} = 5.65 \pm 0.05$ S. This is in good agreement with previous determinations of the $s^0_{20,w}$ value of 5.5 to 5.6 S and 5.3±0.1 S.[2,23,36]

A concentration dependence of the *c*(*s*) distributions was observed. At 0.17 mg/ml, the shape of the boundaries in Fig. 4b indicated a predominantly single sedimentation species. Between 0.05 and 0.63 mg/ml in either Hepes buffer or PBS, a second peak was observed in the *c*(*s*) analyses at 9.2±0.5 S and its relative intensity increased with concentration (Fig. 4c). The *c*(*M*) size-distribution plots showed that the major peak at 5.65 S corresponds to a molecular mass of 142±2 kDa. This is consistent with the global fit of the sedimentation equilibrium data (Fig. 2). At higher FH concentrations between 1.53 and 5.92 mg/ml and with the use of a 1-day-old FH preparation, the boundary fit of Fig. 4a indicated a more complex sedimentation profile. As the concentration increased, six smaller sedimentation species were consistently observed at $s^0_{20,w}$ values of 7.3±0.2, 9.2±0.2, 11.3±0.4, 13.4±0.06, 15.4±0.2 and 17.2±0.4 S at 50,000 rpm. This suggested that FH formed not only dimers but also trimeric to heptameric oligomers in small but significant amounts of about 15% in total.

This interpretation was verified starting from the four best-fit glycosylated FH models previously generated by constrained scattering modelling.[23] The present R_G value of 8.9 nm for monomeric FH (Fig. 1c) meant that these previous models which had an R_G value of 9.9 nm were now too elongated. Thus, linkers in one of the previous four best-fit FH models were adjusted in order to generate a more compact SCR arrangement. In satisfactory agreement with the experimental $s^0_{20,w}$ value of 5.65 S, an $s^0_{20,w}$ value of 5.2 S was obtained from this glycosylated model using HYDROPRO v7c,[44] with the default value of 0.31 nm for the atomic element radius for all atoms in order to represent the hydration shell. The $s^0_{20,w}$ calculations were insensitive to the presence or absence of six biantennary oligosaccharide chains at Asn511, Asn784, Asn804, Asn864, Asn893 and Asn1011 (mature protein numbering).[23] If an FH monomer became spherical in its shape, the maximum possible $s^0_{20,w}$ value would be 9.4 S. Hence, postulating the occurrence of conformational changes in monomeric FH is unable to explain the discrete peaks seen at the larger $s^0_{20,w}$ values in Fig. 4c.

Models to account for oligomer formation were arbitrarily created from dimerisation sites at opposite ends of the FH monomer model. Oligomers

Fig. 4. Sedimentation velocity of wild-type FH. Experiments at 20 °C were performed with FH in Hepes buffer in a concentration series from 0.07 to 5.92 mg/ml at speeds of 25,000, 40,000, 50,000 and 60,000 rpm to confirm reproducibility on two Beckman XL-I analytical ultracentrifuges equipped with AnTi60 rotors. (a) The 200 scan boundaries for FH at 5.92 mg/ml at 50,000 rpm were fitted using Lamm equation fits with SEDFIT. Only every 10th scan is shown for reason of clarity. (b) The corresponding boundary fits are shown for FH at 0.17 mg/ml at 40,000 rpm. Other details follow (a). (c) In the five *c*(*s*) size-distribution analyses, the major sedimentation species at 5.65 S is labelled as 1. Its intensity was normalised in all five analyses for clarity. From bottom to top, the FH concentrations were 0.17, 0.63, 1.53, 2.99 and 5.92 mg/ml. The oligomeric FH peaks in increasing order of S values are labelled from 2 to 7. The five analyses are displaced by 10% of the intensity of peak 1, and in the top *c*(*s*) analysis, peak 2 is 7% of the intensity of peak 1. Underneath, six schematic models for oligomers of FH that yield the predicted $s^0_{20,w}$ values given in brackets are shown. The monomers are denoted by different colours and numbered. Monomers 2 and 3 are viewed in the same orientation in all the models except for the dimer.

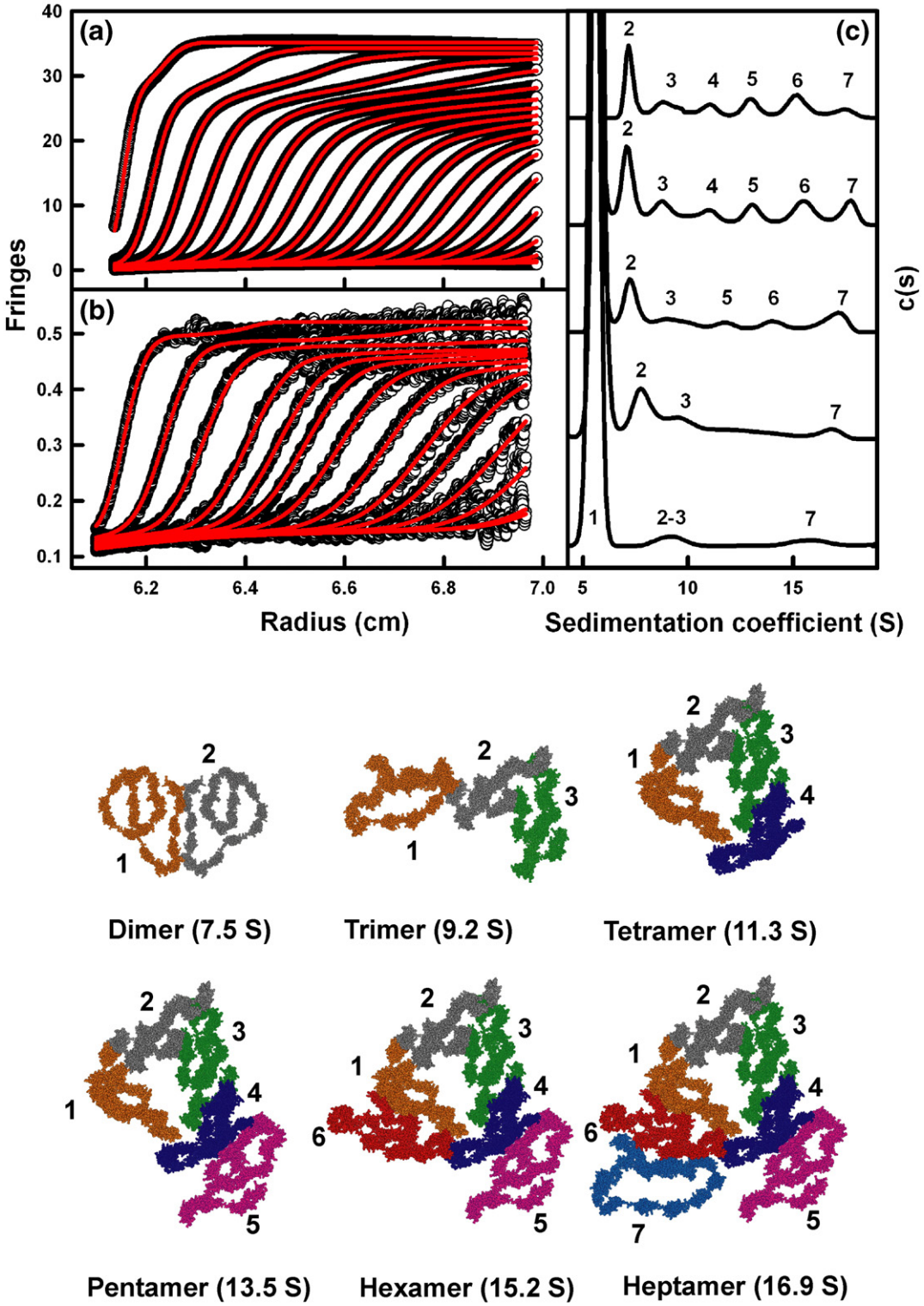

Fig. 4 (*legend on previous page*)

were created using INSIGHT II 98.0 molecular graphics software (Accelrys, San Diego, CA) on Silicon Graphics OCTANE workstations (Fig. 4). The predicted $s^0_{20,w}$ value for a dimer model in an extended conformation was 7.5 S, in good agreement with the observed peak at 7.3 S. The addition of a third monomer to this dimer model resulted in a predicted $s^0_{20,w}$ value of 9.2 S, in good agreement with the observed peak at 9.2 S. Starting with the tetramer, it was found necessary to add further monomers in a more compact arrangement to give models with predicted $s^0_{20,w}$ values that agreed within error of the experimental values. The movement of monomer 1 in the tetrameric model towards the centre of the model gave a predicted value of 11.3 S, in good agreement with the observed peak at

11.3 S. The pentamer, hexamer and heptamer models gave predicted values of 13.5, 15.2 and 16.9 S, respectively, which agreed well with the experimental values of 13.4, 15.4 and 17.2 S, respectively. These agreements support the assignment of the six additional peaks at high S values in the $c(s)$ plots to a series of FH oligomers.

Conclusions

Knowledge of the oligomeric state of FH is crucial for understanding its immunological function in complement regulation and its likely roles in AMD and aHUS. The new data collection in this study clarified that wild-type FH exhibits oligomeric forms after all, as originally proposed.[21] A monomer–dimer equilibrium was identified at the lowest concentrations. Partial FH dimerisation has been reported by two other laboratories.[8,13,32] As the concentration increases, higher oligomeric structures that can be as large as heptamers and are not in equilibrium with each other were identified. Our 2001 and 1991 studies on wild-type FH had reported R_G values that were stated to be approximate for reason of the need to access the lowest Q values, which are difficult to measure with highly elongated proteins. Under these conditions, the aggregation of a highly elongated protein can be difficult to identify. Here, the use of freshly purified FH resulted in a lower R_G value of 8.90 nm, in place of the apparent R_G values of 11.4 and 12.4 nm from before. The sequence-calculated molecular mass of FH is 150,000 Da, assuming six N-linked oligosaccharides. In 2001, the molecular mass of FH was determined as 148,000–182,000 Da, as the result of which FH was deduced to be monomeric.[23] In 1991, its molecular mass was determined to be 250,000–320,000 Da, leading to the deduction that FH was dimeric.[21] The new data suggest that the 1991 result is best explained in terms of the presence of monomeric FH together with sufficient FH oligomers to double its averaged observed molecular mass. Oligomerisation in the 1991 study was favoured by the higher FH concentrations that were necessary for the X-ray data collection at that time.

This study on FH oligomerisation resulted from the unexpected observation of weak monomer–dimer equilibria for two fragments of FH. One equilibrium for the SCR-6/8 fragment of FH has a K_D of about 40 μM. Detailed ultracentrifugation equilibrium and velocity measurements were required to establish this as the compact structure of this SCR-6/8 dimer meant that dimerisation was not readily detected by X-ray scattering.[26] However, the presence of the SCR-6/8 dimer was requisite for good X-ray modelling fits to its structure. The second weak monomer–dimer equilibrium with a K_D of 16 μM for the SCR-16/20 fragment was readily detected by both X-ray scattering and ultracentrifugation because this dimer has an extended structure.[27] Both these K_D values are comparable with the value of 28 μM for wild-type FH from the SEDPHAT global fits below 1.36 mg/ml (Fig. 2). This suggests that the dimerisation of both SCR-6/8 and SCR-16/20 is physiologically relevant, although both were recombinant proteins. As FH concentrations range between 0.235 and 0.810 mg/ml in blood,[19] so long as no other factor requires consideration, this K_D value of 28 μM indicates that about 5–15% of FH in blood will be dimeric. The complement regulatory function of FH will be affected by dimer formation in serum. Thus, ligands may be sterically blocked from approaching their binding sites if they are proximate to either of the two presumed FH dimer sites or may not bind because of aggregate formation. Alternatively, ligand binding may be enhanced if binding sites are distant from the FH dimer sites, because FH would become multivalent in that case. Future studies on FH-ligand binding will be complicated by the observation of dimerisation. Thus, FH-ligand binding studies that disregard dimerisation are open to misinterpretation, as exemplified by a recent SEDPHAT sedimentation equilibrium study on SCR-6/8.[12] Alternative approaches are required to establish 1:1 complex formation with ligands in the presence of dimers, such as that described in Fig. 3 of the original ultracentrifugation study on the SCR-6/8 complex with heparin, where titrations with a range of heparin–protein ratios were analysed using SEDFIT $c(s)$ size-distribution plots.[26]

A mechanistic pathway for oligomer formation is suggested from this work. At higher concentrations, the existence of two weak self-association sites in FH suggests that FH can self-associate continuously by intermolecular contacts that occur alternately through both these sites to form large oligomers. These higher oligomers were indeed directly observed above 2 mg/ml in fresh FH samples by velocity experiments (Fig. 4). At low FH concentrations, the model in Fig. 4 suggests that extended dimer structures were formed, which would explain its reversibility. At higher concentrations, the formation of higher oligomers is predicted to involve more compact associations of the monomer (Fig. 4), and this would explain its lack of reversibility (Fig. 2). The storage of FH samples may facilitate the formation of more stable higher oligomers. Further studies on this are in progress. These results suggest that the use of freshly gel-filtrated FH samples stored below 1-mg/ml concentrations may be required for complement regulatory functional studies. The aggregation of FH is relevant for AMD, for which a risk factor is the observation of drusen deposits at the retinal surface. Currently, there is no detailed knowledge of the mechanism of drusen formation in AMD. It is possible that the localised accumulation of higher FH concentrations within the eye may facilitate the slow formation of protein precipitates within drusen during the course of a lifetime. For such a mechanism to operate, any FH precipitation in drusen would appear to necessitate concentrations of FH much higher than those seen physiologically in serum, and this would occur in the presence of a number of other components that are present. The latter would alter the kinetics and thermodynamics of deposit formation when

compared with a mechanism based only on FH self-association. In this context, it is intriguing that the His402 genetic polymorphism that is a risk factor for AMD showed a slightly higher propensity to self-associate than the lower-risk Tyr402 form when the SCR-6/8 fragment was studied by X-ray scattering and ultracentrifugation.[26]

Acknowledgements

We thank the Biotechnology and Biological Sciences Research Council and the Mercer Fund of the Fight For Sight Charity for a Dorothy Hodgkin Postgraduate Award and equipment grant support. We also thank the Henry Smith Charity for equipment support. We are very grateful to Dr. Robert B. Sim (Medical Research Council Immunochemistry Unit, Oxford, UK) for providing a Sepharose MRC-OX23 matrix and helpful discussions in relation to FH purification, Dr. Pierre Panine and Dr. Emanuela Di Cola (European Synchrotron Radiation Facility, Grenoble) for excellent instrumental support and Mr. Azubuike Okemefuna, Dr. Imre Lengyel and Prof. Alan C. Bird for useful discussions.

References

1. Law, S. K. A. & Reid, K. B. M. (1995). *Complement*, 2nd edit., IRL Press, Oxford, UK.
2. Whaley, K. & Ruddy, S. (1976). Modulation of the alternative complement pathways by beta 1 H globulin. *J. Exp. Med.* **144**, 1147–1163.
3. Pangburn, M. K., Schreiber, R. D. & Muller-Eberhard, H. J. (1977). Human complement C3b inactivator: isolation, characterization, and demonstration of an absolute requirement for the serum protein beta1H for cleavage of C3b and C4b in solution. *J. Exp. Med.* **146**, 257–270.
4. Weiler, J. M., Daha, M. R., Austen, K. F. & Fearon, D. T. (1976). Control of the amplification convertase of complement by the plasma protein beta1H. *Proc. Natl Acad. Sci. USA*, **73**, 3268–3272.
5. Farries, T. C., Seya, T., Harrison, R. A. & Atkinson, J. P. (1990). Competition for binding sites on C3b by CR1, CR2, MCP, factor B and factor H. *Complement Inflammation*, **7**, 30–41.
6. Soares, D. & Barlow, P. N. (2005). Complement control protein modules in the regulators of complement activators. In *Structural Biology of the Complement System* (Morikis, D. & Lambris, J. D., eds), pp. 19–62, Taylor & Francis, Boca Raton, FL.
7. Sharma, A. K. & Pangburn, M. K. (1996). Identification of three physically and functionally distinct binding sites for C3b in human complement factor H by deletion mutagenesis. *Proc. Natl Acad. Sci. USA*, **93**, 10996–11001.
8. Jokiranta, T. S., Hellwage, J., Koistinen, V., Zipfel, P. F. & Meri, S. (2000). Each of the three binding sites of factor H interacts with a distinct site on C3b. *J. Biol. Chem.* **275**, 27657–27662.
9. Blackmore, T. K., Sadlon, T. A., Ward, H. M., Lublin, D. M. & Gordon, D. L. (1996). Identification of a heparin binding domain in the seventh short consensus repeat of complement factor H. *J. Immunol.* **157**, 5422–5427.
10. Blackmore, T. K., Hellwage, J., Sadlon, T. A., Higgs, N., Zipfel, P. F., Ward, H. M. & Gordon, D. L. (1998). Identification of the second heparin-binding domain in human complement factor H. *J. Immunol.* **160**, 3342–3348.
11. Ormsby, R. J., Jokiranta, T. S., Duthy, T. G., Griggs, K. M., Sadlon, T. A., Giannakis, E. & Gordon, D. L. (2006). Localization of the third heparin-binding site in the human complement regulator factor H. *Mol. Immunol.* **43**, 1624–1632.
12. Prosser, B. E., Johnson, S., Roversi, P., Herbert, A. P., Blaum, B. S., Tyrrell, J. *et al.* (2007). Structural basis for complement factor H-linked age-related macular degeneration. *J. Exp. Med.* **204**, 2277–2283.
13. Oppermann, M., Manuelian, T., Jozsi, M., Brandt, E., Jokiranta, T. S., Heinen, S. *et al.* (2006). The C-terminus of complement regulator factor H mediates target recognition: evidence for a compact conformation of the native protein. *Clin. Exp. Immunol.* **144**, 342–352.
14. Ferreira, V. P., Herbert, A. P., Hocking, H. G., Barlow, P. N. & Pangburn, M. K. (2006). Critical role of the C-terminal domains of factor H in regulating complement activation at cell surfaces. *J. Immunol.* **177**, 6308–6316.
15. Klein, R. J., Zeiss, C., Chew, E. Y., Tsai, J. Y., Sackler, R. S., Haynes, C. *et al.* (2005). Complement factor H polymorphism in age-related macular degeneration. *Science*, **308**, 385–389.
16. Haines, J. L., Hauser, M. A., Schmidt, S., Scott, W. K., Olson, L. M., Gallins, P. *et al.* (2005). Complement factor H variant increases the risk of age-related macular degeneration. *Science*, **308**, 419–421.
17. Edwards, A. O., Ritter, R., III, Abel, K. J., Manning, A., Panhuysen, C. & Farrer, L. A. (2005). Complement factor H polymorphism and age-related macular degeneration. *Science*, **308**, 421–424.
18. Hageman, G. S., Anderson, D. H., Johnson, L. V., Hancox, L. S., Taiber, A. J., Hardisty, L. I. *et al.* (2005). A common haplotype in the complement regulatory gene factor H (*HF1/CFH*) predisposes individuals to age-related macular degeneration. *Proc. Natl Acad. Sci. USA*, **102**, 7227–7232.
19. Saunders, R. E., Abarrategui-Garrido, C., Frémeaux-Bacchi, V., Goicoechea de Jorge, E., Goodship, T. H. J., López Trascasa, M. *et al.* (2007). The interactive factor H–atypical haemolytic uraemic syndrome mutation database and website: update and integration of membrane cofactor protein and factor I mutations with structural models. *Hum. Mutat.* **28**, 222–234.
20. Dragon-Durey, M. A. & Frémeaux-Bacchi, V. (2005). Atypical haemolytic uraemic syndrome and mutations in complement regulator genes. *Springer Semin. Immunopathol.* **27**, 359–374.
21. Perkins, S. J., Nealis, A. S. & Sim, R. B. (1991). Oligomeric domain structure of human complement factor H by X-ray and neutron solution scattering. *Biochemistry*, **30**, 2847–2857.
22. DiScipio, R. G. (1992). Ultrastructures and interactions of complement factors H and I. *J. Immunol.* **149**, 2592–2599.
23. Aslam, M. & Perkins, S. J. (2001). Folded-back solution structure of monomeric factor H of human complement by synchrotron X-ray and neutron scattering, analytical ultracentrifugation and constrained molecular modelling. *J. Mol. Biol.* **309**, 1117–1138.

24. Perkins, S. J., Ashton, A. W., Boehm, M. K. & Chamberlain, D. (1998). Molecular structures from low angle X-ray and neutron scattering studies. *Int. J. Biol. Macromol.* **22**, 1–16.
25. Perkins, S. J., Okemefuna, A. I., Fernando, A. N., Bonner, A., Gilbert, H. E. & Furtado, P. B. (2008). X-ray and neutron scattering data and their constrained molecular modelling. *Methods Cell Biol.* **84**, 375–423.
26. Fernando, A. N., Furtado, P. B., Clark, S. J., Gilbert, H. E., Day, A. J., Sim, R. B. & Perkins, S. J. (2007). Associative and structural properties of the region of complement factor H encompassing the Tyr402His disease-related polymorphism and its interactions with heparin. *J. Mol. Biol.* **368**, 564–581.
27. Okemefuna, A. I., Gilbert, H. E., Griggs, K. M., Ormsby, R. J., Gordon, D. L. & Perkins, S. J. (2008). The regulatory SCR-1/5 and cell-surface-binding SCR-16/20 fragments of factor H reveal partially folded-back solution structures and different self-associative properties. *J. Mol. Biol.* **371**, 80–101.
28. Perkins, S. J. & Goodship, T. H. J. (2002). Molecular modelling of the C-terminal domains of factor H of human complement: a correlation between haemolytic uraemic syndrome and a predicted heparin binding site. *J. Mol. Biol.* **316**, 217–224.
29. Saunders, R. E., Goodship, T. H. J., Zipfel, P. F. & Perkins, S. J. (2006). Factor H-associated haemolytic uraemic syndrome: a web database of the structural consequences of disease-associated mutations. *Hum. Mutat.* **27**, 21–30.
30. Barlow, P. N., Norman, D. G., Steinkasserer, A., Horne, T. J., Pearce, J., Driscoll, P. C. *et al.* (1992). Solution structure of the fifth repeat of factor H: a second example of the complement control protein module. *Biochemistry*, **31**, 3626–3634.
31. Barlow, P. N., Steinkasserer, A., Norman, D. G., Kieffer, B., Wiles, A. P., Sim, R. B. & Campbell, I. D. (1993). Solution structure of a pair of complement modules by nuclear magnetic resonance. *J. Mol. Biol.* **232**, 268–284.
32. Jokiranta, T. S., Jaakola, V. P., Lehtinen, M. J., Parepalo, M., Meri, S. & Goldman, A. (2006). Structure of complement factor H carboxyl-terminus reveals molecular basis of atypical haemolytic uremic syndrome. *EMBO J.* **25**, 1784–1794.
33. Herbert, A. P., Deakin, J. A., Schmidt, C. Q., Blaum, B. S., Egan, C., Ferreira, V. P. *et al.* (2007). Structure shows that a glycosaminoglycan and protein recognition site in factor H is perturbed by age-related macular degeneration-linked single nucleotide polymorphism. *J. Biol. Chem.* **282**, 18960–18968.
34. Bird, A. C. (1992). Bruch's membrane change with age. *Br. J. Ophthalmol.* **76**, 166–168.
35. Bird, A. C., Bressler, N. M., Bressler, S. B., Chisholm, I. H., Coscas, G., Davis, M. D. *et al.* (1995). An international classification and grading system for age-related maculopathy and age-related macular degeneration. The International ARM Epidemiological Study Group. *Surv. Ophthalmol.* **39**, 367–374.
36. Hageman, G. S., Luthert, P. J., Victor Chong, N. H., Johnson, L. V., Anderson, D. H. & Mullins, R. F. (2001). An integrated hypothesis that considers drusen as biomarkers of immune-mediated processes at the RPE–Bruch's membrane interface in aging and age-related macular degeneration. *Prog. Retinal Eye Res.* **20**, 705–732.
37. Sim, R. B. & DiScipio, R. G. (1982). Purification and structural studies on the complement system control protein β_1H (factor H). *Biochem. J.* **205**, 285–293.
38. Sim, R. B., Day, A. J., Moffatt, B. E. & Fontaine, M. (1993). Complement factor I and cofactors in control of complement system convertase enzymes. *Methods Enzymol.* **223**, 13–35.
39. Narayanan, T., Diat, O. & Bosecke, P. (2001). SAXS and USAXS on the high brilliance beamline at the ESRF. *Nucl. Instrum. Methods Phys. Res., Sect. A*, **467–468**, 1005–1009.
40. Schuck, P. (2003). On the analysis of protein self-association by sedimentation velocity analytical ultracentrifugation. *Anal. Biochem.* **320**, 104–124.
41. McRorie, D. K. & Voelker, P. J. (1993). *Self-associating Systems in the Analytical Ultracentrifuge.* Beckman Instruments, Fullerton, CA.
42. Schuck, P. (1998). Sedimentation analysis of non-interacting and self-associating solutes using numerical solutions to the Lamm equation. *Biophys. J.* **75**, 1503–1512.
43. Schuck, P. (2000). Size-distribution analysis of macromolecules by sedimentation velocity ultracentrifugation and Lamm equation modeling. *Biophys. J.* **78**, 1606–1619.
44. Garcia de la Torre, J., Huertas, M. L. & Carrasco, B. (2000). Calculation of hydrodynamic properties of globular proteins from their atomic-level structure. *Biophys. J.* **78**, 719–730.

doi:10.1016/j.jmb.2008.10.030 J. Mol. Biol. (2008) 384, 1341–1352

JMB

Available online at www.sciencedirect.com

ScienceDirect

ELSEVIER

Uncontrolled Zinc- and Copper-Induced Oligomerisation of the Human Complement Regulator Factor H and Its Possible Implications for Function and Disease

Ruodan Nan[1], Jayesh Gor[1], Imre Lengyel[2] and Stephen J. Perkins[1]*

[1]*Institute of Structural and Molecular Biology, Division of Biosciences, Darwin Building, University College London, Gower Street, London WC1E 6BT, UK*

[2]*Department of Ocular Biology and Therapeutics, UCL Institute of Ophthalmology, University College London, 11-43 Bath Street, London EC1V 9EL, UK*

Received 20 August 2008; received in revised form 2 October 2008; accepted 8 October 2008
Available online 19 October 2008

Edited by R. Huber

Polymorphisms in factor H (FH), a major regulator of complement activation, and the accumulation of high zinc concentrations in the outer retina are both associated with age-related macular degeneration. FH is inhibited by zinc, which causes FH to aggregate. To investigate this, we quantitatively studied zinc-induced FH self-association by X-ray scattering and analytical ultracentrifugation to demonstrate uncontrolled FH oligomerisation in conditions corresponding to physiological levels of FH and pathological levels of zinc in the outer retina. By scattering, FH at 2.8–7.0 μM was unaffected until [Zn] increased to 20 μM, whereupon the radius of gyration, R_G, values increased from 9 to 15 nm at [Zn] = 200 μM. The maximum dimension of FH increased from 32 to 50 nm, indicating that compact oligomers had formed. By ultracentrifugation, size-distribution analyses showed that monomeric FH at 5.57 S was the major species at [Zn] up to 60 μM. At [Zn] above 60 μM, a series of large oligomers were formed, ranging up to 100 S in size. Oligomerisation was reversed by ethylenediaminetetraacetic acid. Structurally distinct large oligomers were observed for Cu, while Ni, Cd and Fe showed low amounts of oligomers and Mg and Ca showed no change. Fluid-phase assays showed reduced FH activities that correlated with increased oligomer formation. The results were attributed to different degrees of stabilisation of weak self-dimerisation sites in FH by transition metals. The relevance of metal-induced FH oligomer formation to complement regulation and age-related macular degeneration is discussed.

Keywords: complement factor H; X-ray scattering; analytical ultracentrifugation; age-related macular degeneration; inflammation

Introduction

In the innate immune response, C3 is activated to C3b by the cleavage of the small anaphylatoxin C3a, thereby initiating the alternative complement pathway. C3b is regulated by factor H (FH) among other proteins to prevent complement-mediated host cell damage: FH acts as a cofactor for the factor I-mediated cleavage of C3b to form iC3b, C3c and C3dg.[1–3] FH also accelerates the decay of the C3 convertase C3bBb[2,4] and competes with factor B for binding to C3b.[5] FH is composed of a linear arrangement of 20 short complement regulator (SCR) domains, each of about 61 residues in length.[6] FH possesses multiple binding sites for C3b and heparin, the latter being an analogue of heparan sulfate that is found on host cell surfaces, and FH also binds to such other proteins as C-reactive protein.[7–9] FH protects host cells by binding to heparin-like negatively charged clusters on their surfaces through its C-terminal end, which is then followed by N-terminal regulatory activity against C3b.[10,11] FH involvement in uncontrolled inflammation is associated with disease, namely, atypical haemolytic uraemic syndrome and membranoproliferative glomerulonephritis type II[12] and age-related macular degeneration (AMD).[13–16] AMD is the most common cause of blindness in the elderly in the Western world. In 2005, several groups identified a Tyr402His FH polymorphism that increased the risk of

*Corresponding author. E-mail address: s.perkins@medsch.ucl.ac.uk.

Abbreviations used: AMD, age-related macular degeneration; FH, factor H; RPE, retinal pigment epithelium; SCR, short complement regulator; sRPEd, subretinal pigment epithelial deposit.

developing AMD over sevenfold.[13–16] Since then, other FH variants have been shown to modify the risk for AMD.[17–19] Even with the analysis of over 100 genetic alterations in FH,[12] no clear molecular mechanism for diseases based on the involvement of defective forms of FH has been proposed so far.

An early hallmark of AMD is the appearance of subretinal pigment epithelial deposits (sRPEds) that can be focal (drusen) or diffuse (basal linear and laminar). These deposits contain oxidised lipids and over 120 aggregated proteins, including FH and other complement components that are secreted by retinal pigment epithelium (RPE) cells or delivered by choroidal blood circulation.[20,21] These deposits develop within Bruch's membrane, an extracellular matrix layer interposed between the RPE and the choroidal vasculature.[22,23] Recently, millimolar concentrations of zinc have been found in sRPEds and Bruch's membrane, suggesting that the pathological release of zinc from surrounding tissues such as the zinc-rich RPE choroid complex might be involved in sRPEd formation.[24,25] In the context of AMD, the presence of FH and zinc in sRPEd is of interest, because, first, zinc inhibits the factor I-mediated cleavage of C3b leading to uncontrolled inflammation[26] and, second, an initial X-ray scattering study showed that FH aggregates in the presence of high zinc concentrations.[27]

The molecular basis of the self-associative interaction between FH and zinc is unknown. The overall structure of native FH is not straightforward to characterise by methods such as crystallisation and NMR for reason of its large size, glycosylation and inter-SCR flexibility between its 20 domains, although several crystal and NMR structures have been published for small domain fragments of FH. Solution structural methods such as X-ray and neutron scattering and analytical ultracentrifugation have been applied to demonstrate that native FH possesses a partially folded-back SCR structure in solution.[28,29] Recently, we showed that native FH is predominantly monomeric and partly dimeric at physiological concentrations in serum and forms higher oligomers as its concentration increases if no other factor requires consideration.[30] The original X-ray scattering study on FH–zinc complexes was limited by a requirement for relatively high FH concentrations at that time, that only Guinier analyses at low scattering angles were consequently measured and that the resulting averaged FH structure was mostly dimeric.[27] Since that time, the availability of monomeric FH at low concentrations[30] and improvements in X-ray scattering instrumentation at the European Synchrotron Radiation Facility[30] have permitted a more detailed investigation of the role of zinc and FH in a physiological concentration range. By performing quantitative titration studies on FH with a range of different metals by X-ray scattering, supplemented by analytical ultracentrifugation, we show here that monomeric FH aggregates in the presence of zinc. Unexpectedly, not only zinc but also other transition metals such as copper induce different degrees of uncontrolled FH oligomer formation. We correlate these results with FH activity assays in the presence of zinc and copper. We discuss whether the high zinc concentrations associated with Bruch's membrane may drive the aggregation of FH in the environment of the retina; we also discuss the molecular implications of our results for complement regulation and sRPEd formation.

Results and Discussion

Guinier X-ray scattering analyses of FH–metal complexes

Freshly purified FH for scattering and ultracentrifugation studies resulted in a homogeneous peak by gel filtration, which was verified by SDS-PAGE.[30] FH concentrations were generally maintained at 1 mg/ml or lower with storage at 4 °C to avoid irreversible oligomer formation[30] and studied at this or a lower concentration to be comparable with physiological FH concentrations between 0.235 and 0.810 mg/ml in serum.[12] The effect of metals on FH was studied by synchrotron X-ray scattering and analytical ultracentrifugation in Hepes buffer (Materials and Methods). Phosphate buffer was not used in order to avoid precipitation issues.

Solution scattering enabled the overall structure and size of FH to be studied.[28] FH at 0.42 mg/ml (2.8 μM) and that at 1.05 mg/ml (7.0 μM) were titrated with 0–200 μM $ZnSO_4$. Excellent signal–noise ratios were obtained with no detectable effect from radiation damage. Linear Guinier analyses at low Q values (where $Q = 4\pi \sin\theta/\lambda$; 2θ = scattering angle; λ = wavelength) gave the radius of gyration, R_G, in satisfactory $Q \cdot R_G$ ranges below 1.1 (Fig. 1). For native FH without zinc, the mean R_G value was 8.45±0.14 nm at 1.05 mg/ml and 8.28±1.18 nm at 0.42 mg/ml (Fig. 2a). Both values were consistent with the recently reported R_G value of 8.90±0.19 nm for monomeric FH.[30] The present R_G values starting from a monodisperse preparation of FH were consistently lower than the old R_G values for FH that had partially self-aggregated.[27] Here, the R_G values increased significantly when [Zn] ≥ 20 μM (Figs. 1a and 2a). The Guinier $I(0)/c$ value that is proportional to molecular weight also showed a large increase at [Zn] ≥ 20 μM (Fig. 2b). Hence, these changes are attributable to the strong FH oligomer formation previously seen for dimeric FH.[27] Comparison of 200 μM $ZnSO_4$ and 200 μM $ZnCl_2$ with 0.93 mg/ml of FH showed no difference in the Guinier parameters of Fig. 2, hence ruling out any anion effect. The present experiments extend our previous X-ray work by demonstrating that zinc causes monomeric FH to aggregate.

The cross-sectional Guinier analyses monitor the structural proximity relationships between non-neighbouring SCR domains ($R_{XS\text{-}1}$) and neighbouring SCR domains ($R_{XS\text{-}2}$).[31] Linear fits for both parameters were obtained within satisfactory $Q \cdot R_{XS}$

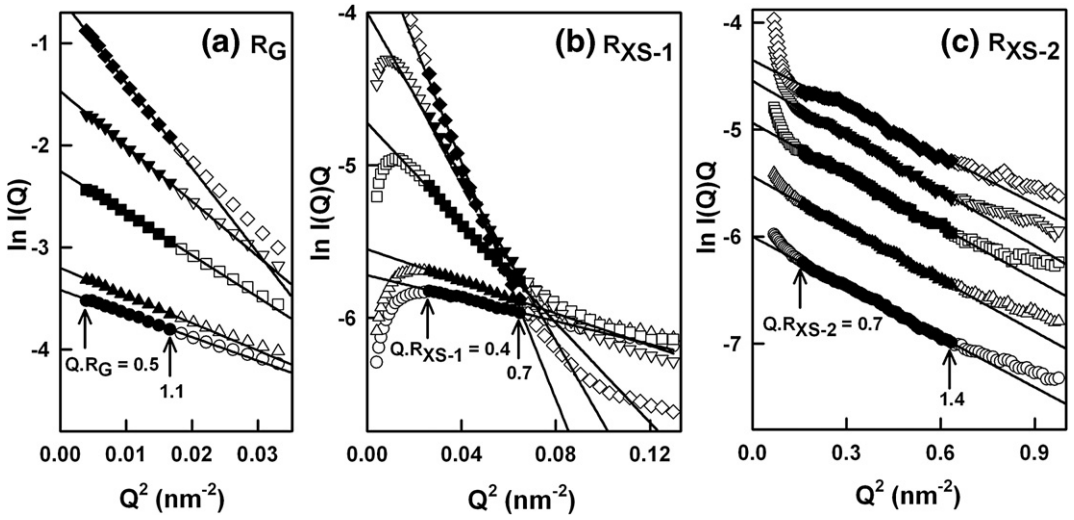

Fig. 1. Guinier analyses for native FH titrated with zinc. The filled symbols correspond to the Q range used to determine the R_G and R_{XS} values. The symbols ○, △, □, ▽, and ◊ represent [Zn]=2, 6, 20, 60 and 200 μM, respectively. The $Q \cdot R_G$ and $Q \cdot R_{XS}$ fit ranges are arrowed. (a) R_G plots of ln $I(Q)$ *versus* Q^2 for 1.05 mg/ml of FH using a Q range of 0.06–0.13 nm^{-1}. (b and c) The corresponding cross-sectional R_{XS-1} and R_{XS-2} plots of ln $I(Q).Q$ *versus* Q^2 for the same five scattering curves in Q ranges of 0.16–0.26 and 0.4–0.8 nm^{-1} are shown. In (c), the five curves are successively displaced in steps of 0.5 ln units for clarity.

ranges (Fig. 1b and c). Without zinc, the R_{XS-1} value was determined to be 2.68±0.08 nm at 1.04 mg/ml and 2.40±0.16 nm at 0.42 mg/ml, in good agreement with the previously determined R_{XS-1} value of 2.51±0.06 nm for the FH monomer.[30] The R_{XS-1} values significantly increased when [Zn]≥20 μM (Fig. 2c). This change showed that the FH oligomers associated in a side-by-side, not end-to-end, manner. Without zinc, the R_{XS-2} value was determined to be 1.78±0.03 nm, in good agreement with the previously reported value of 1.79±0.01 nm.[27,30,31] When zinc was added, the R_{XS-2} value did not alter (Fig. 2d),

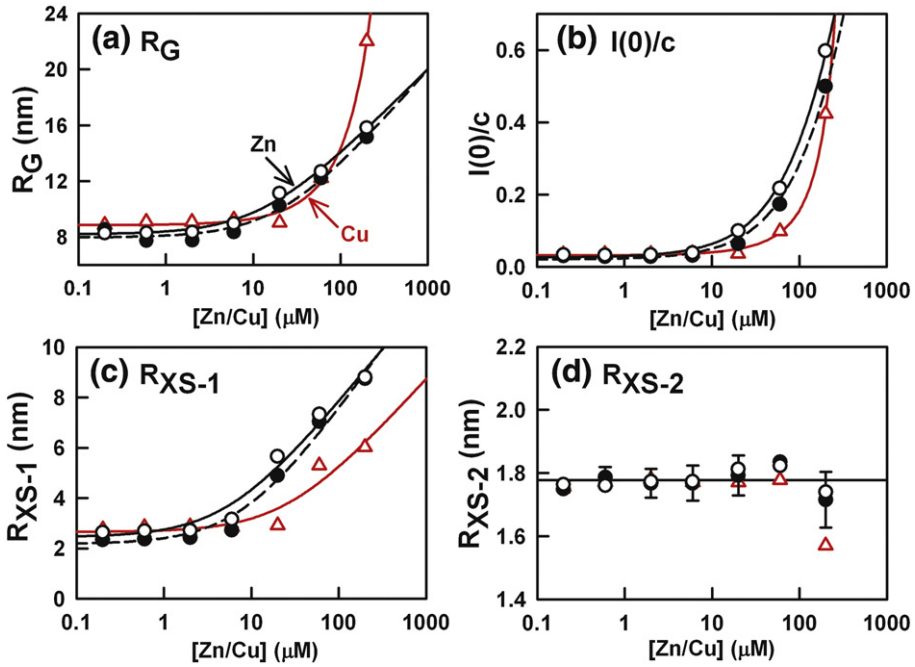

Fig. 2. Dependence of the Guinier parameters on the zinc or copper concentration. Each value was measured in quadruplicate and averaged. The three titrations correspond to 1.05 mg/ml of FH titrated with zinc (○, continuous line), 0.42 mg/ml of FH titrated with zinc (●, dashed line) and 0.93 mg/ml of FH titrated with copper (△, red continuous line). (a and c) The data were fitted to a three-parameter function $y=y_0+a\ln(x-x_0)$. (b) The lines correspond to a two-parameter function $y=\ln(a+bx)$. (d) The straight line indicates the averaged R_{XS-2} values for FH at 0.42 mg/ml, with statistical error bars shown where visible.

indicating that the linear arrangement of neighbouring SCR domains was unchanged.

Control experiments with other metals were performed with 200 μM $CaCl_2$, $MgCl_2$, $NiCl_2$, $CdCl_2$ and $FeSO_4$ with FH at 0.93 mg/ml. No change was detected for $CaCl_2$ and $MgCl_2$. Small increases in the R_G, R_{XS-1} and $I(0)/c$ values compared with zinc were observed for $NiCl_2$, $CdCl_2$ and $FeSO_4$. The result for nickel was unexpected, as 100 μM Ni^{2+} had previously shown no effect,[27] and the difference is attributed to the improved signal–noise ratio available at the European Synchrotron Radiation Facility. Even more unexpected was the large effect caused by $CuSO_4$, which revealed strong FH oligomerisation similar in magnitude to that for $ZnSO_4$ (Fig. 2). Copper had not been tested previously.[26,27] The reversibility of oligomer formation with zinc and copper was demonstrated by the addition of 1.5 mM ethylenediaminetetraacetic acid (EDTA) (final concentration) to FH at 0.93 mg/ml with 200 μM $ZnSO_4$ or $CuSO_4$, Their R_G, R_{XS-1} and $I(0)/c$ values decreased to their metal-free values.

X-ray distance distribution function of FH–metal complexes

The distance distribution function $P(r)$ is calculated from the full scattering curve and reports the distances between all pairs of atoms within FH. The calculation of the R_G and $I(0)$ values from the $P(r)$ curve agreed well with the Guinier R_G and $I(0)$ values above, showing that the scattering curve is self-consistent across the observed Q range. The intensity of the $P(r)$ curve increased significantly with an increase in [Zn] (Fig. 3a). The maximum dimension L is determined when $P(r)=0$ at a large r. When [Zn] was between 0 and 2 μM, the L value of FH was 32 nm, in good agreement with previous data for metal-free FH.[30] When [Zn] increased from 2 to 200 μM, L increased to 50 nm (Fig. 3a and b). The r value of the maximum M in the $P(r)$ curve gives the most commonly occurring distance within the macromolecule. Peak $M1$ at $r=5.2\pm0.6$ nm was observed for [Zn] up to 6 μM, which agrees with the previous $M1$ determination of 4.8 ± 0.3 nm for metal-free FH.[27] Peak $M2$ was previously observed for metal-free FH at 10.2 ± 0.6 nm, but here its position shifted from a starting value of 10.8 nm at [Zn]= 6 μM up to 17.0 nm at [Zn]=200 μM (Fig. 3b). The changes in the $P(r)$ curves with an increase in [Zn] showed that zinc formed relatively compact FH oligomers with maximum dimensions not much larger than those for monomeric metal-free FH. Similar $P(r)$ changes were seen for 200 μM $ZnCl_2$ and in the $CuSO_4$ titration, although the change seen with 200 μM copper differed from that seen with zinc when $M2$ and L both increased by about 10 nm (Fig. 3c). The $P(r)$ curves reverted to the metal-free $P(r)$ curve when EDTA was added (not shown).

Other metals showed divergent effects. The addition of $CaCl_2$ and $MgCl_2$ had no effect (Fig. 3c). The $P(r)$ intensities increased in the presence of 200 μM $NiCl_2$, $CdCl_2$, $FeSO_4$, $CuSO_4$ and $ZnSO_4$, in that order. The L values, however, increased in the presence of 200 μM $FeSO_4$, $CdCl_2$, $NiCl_2$, $ZnSO_4$ and $CuSO_4$, in that order, which is different and

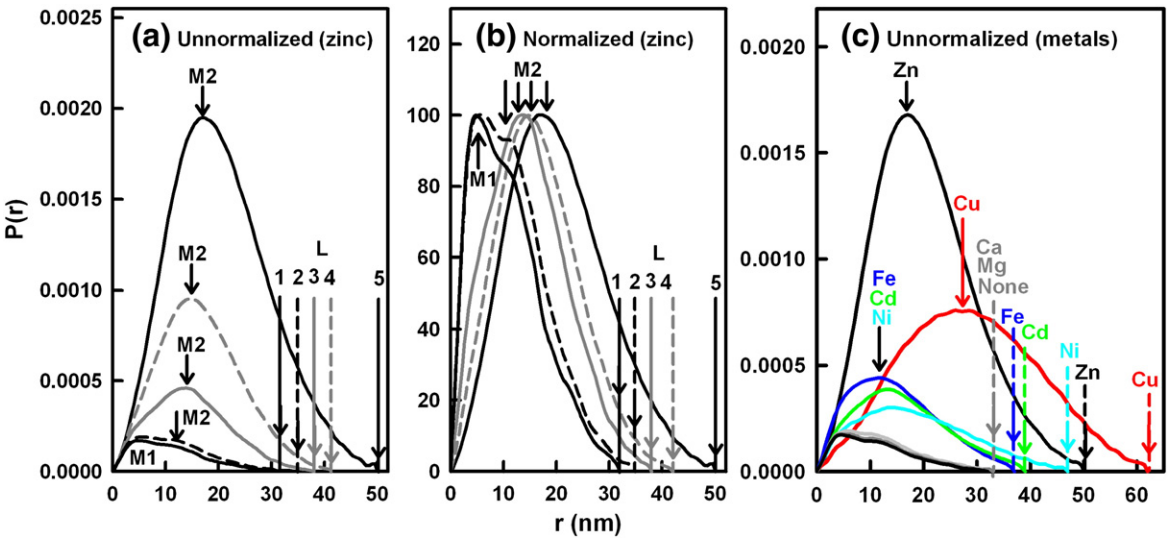

Fig. 3. Dependence of the distance distribution function $P(r)$ on metal. (a) The unnormalised $P(r)$ curves were calculated from the five scattering curves in Fig. 1. From bottom to top, the [Zn] values are 2, 6, 20, 60 and 200 μM, represented by alternate continuous and dashed lines in gray and black. The two maxima occur at $M1$ and $M2$. The maximum length L values were determined to be 32, 35, 38, 42 and 50 nm (numbered 1, 2, 3, 4 and 5, respectively) with an increase in [Zn]. (b) The five $P(r)$ curves in (a) are normalised to 100 to show that $M1$ is unchanged at 5.2 ± 0.6 nm while $M2$ increases from 10.8 to 17.0 nm with an increase in [Zn]. The alternate continuous and dashed lines correspond to those in (a). (c) The eight $P(r)$ curves for 0.93 mg/ml of FH in the presence of seven metals at 200 μM are shown. The $M2$ and L values are arrowed for each curve. The L values were 32 nm (no metal, Mg, Ca), 37 nm (Fe, blue), 39 nm (Cd, green), 47 nm (Ni, cyan), 50 nm (Zn, black) and 62 nm (Cu, red).

shows that different metals caused different structural effects on FH.

Sedimentation velocity analyses of FH–metal complexes

Analytical ultracentrifugation follows the sedimentation behaviour of FH on subjecting this to a high centrifugal force.[29] The sedimentation coefficient $s^{o}_{20,w}$ monitors macromolecular elongation and is analogous to the R_G value. Velocity experiments were performed at four rotor speeds up to 60,000 rpm for FH at 0.35 and 0.87 mg/ml, each titrated with zinc at eight concentrations between 0 and 200 μM. In comparison with the run at 6 μM zinc, rapidly sedimenting species were observed at 60 μM zinc, and even more so at 200 μM zinc (Fig. 4a–c). The observed sedimentation boundaries were fitted using size-distribution analyses $c(s)$ in which the frictional ratio f/fo was held fixed (Materials and Methods), and good fits were obtained in all cases (Fig. 4a–c). These revealed the presence of distinct FH oligomers through the appearance of resolved, stable multiple peaks (Fig. 4d and e). At all zinc concentrations, an FH monomer peak was observed at $s^{o}_{20,w}=5.57\pm0.12$ S (Fig. 4e). A $c(M)$ mass distribution plot showed that this corresponded to a molecular mass of 138±7 kDa. This value agreed well with the sequence-determined molecular mass of 155 kDa, previous $s^{o}_{20,w}$ determinations of 5.65±0.12 S and 5.3±0.1 S and mass determinations of 142±2 and 145 kDa for FH monomers.[30,31] At all zinc concentrations, the $c(s)$ distributions showed additional peaks that correspond to larger FH oligomers as [Zn] increased. For [Zn] between 0 and 20 μM, dimers were visible at an $s^{o}_{20,w}$ value of 7.7±0.3 S. In addition, smaller amounts of trimers to nonamers of FH were consistently observed at $s^{o}_{20,w}$ values of 10.0±0.6, 11.8±0.7, 14.2±0.7, 16.1±0.8, 18.5±0.9, 22.6±1.5 and 27.0±0.5 S (Fig. 4e).[27] At 0 μM zinc, 12% oligomers were seen in agreement with previous data.[30] At [Zn]=60 μM, sizeable amounts of larger FH oligomers with $s^{o}_{20,w}$ values up to 50 S were observed in the $c(s)$ distribution (Fig. 4d and e). At [Zn]=200 μM, the size of the FH oligomers reached 100 S, together with an increase in their intensities (Fig. 4d). Integration of the $c(s)$ size-distribution analyses showed that, at 0.35 and 0.87 mg/ml of FH, 50% oligomer formation occurred at approximately 35 and 50 μM [Zn], respectively (Fig. 5). The slight difference is attributed to the larger zinc/FH ratio at the lower FH concentration, meaning that more FH oligomers were formed at 0.35 mg/ml of FH for a given zinc concentration.

Control experiments were performed. The reversibility of the zinc-induced FH oligomers was tested by sedimentation velocity on 0.87 mg/ml of FH with 120 μM zinc, to which a final concentration of 1.5 mM EDTA was added. The large zinc-induced FH oligomers in the $c(s)$ plot reverted back to the level of oligomers seen for 0.87 mg/ml of native FH (Fig. 6). The percentage of FH oligomers decreased from 62% to 16%. The comparison of 200 μM $ZnSO_4$ and $ZnCl_2$ on 0.93 mg/ml of FH showed no difference in the $c(s)$ distributions; hence, oligomer formation is not dependent on the anion. As for X-rays, the effect of 2 to 200 μM $CuSO_4$ on 0.81 mg/ml of FH caused significant oligomer formation to take place, for which 50% oligomer formation occurred

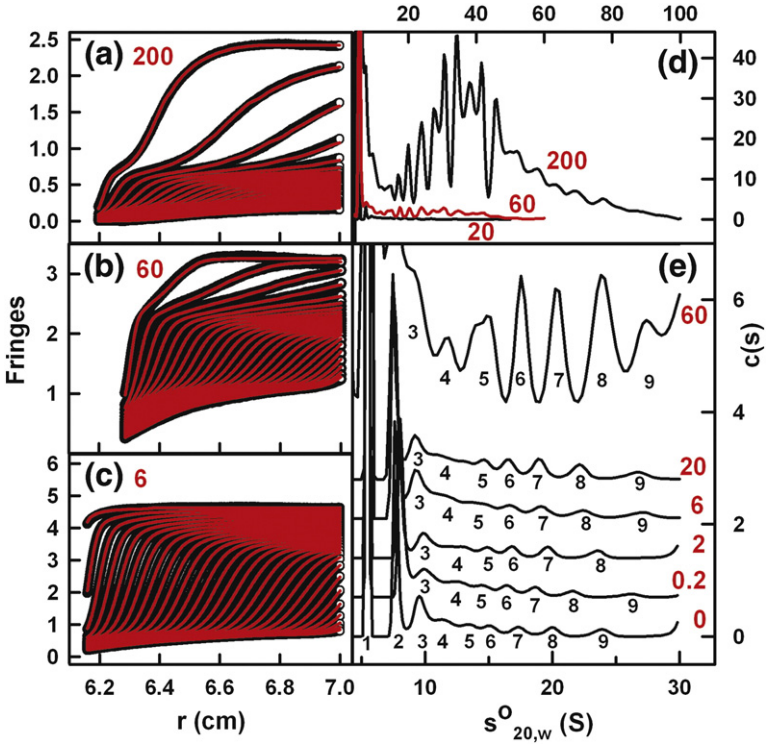

Fig. 4. Size-distribution $c(s)$ analyses of native FH titrated with zinc. The [Zn] values in micromolar are denoted by red numbers. The experimental runs were performed at 50,000 rpm with 0.87 mg/ml of FH (black), and the boundary fits are shown in red. (a) Every 6th scan boundary for 200 μM zinc was fitted. (b) Every 15th scan boundary for 60 μM zinc was fitted. (c) Every 6th scan boundary for 6 μM zinc was fitted. (d) The $c(s)$ size-distribution analyses for 20, 60 and 200 μM zinc are shown. Here and in (e), the intensity of the monomer peak at 5.57 S was set to 100 for clarity. (e) The $c(s)$ size-distribution analyses for 0, 0.2, 2, 6, 20 and 60 μM zinc are shown. The FH oligomers are numbered from 2 to 9 in increasing order of S values.[27] The six analyses are displaced vertically in steps of 0.7 U for clarity.

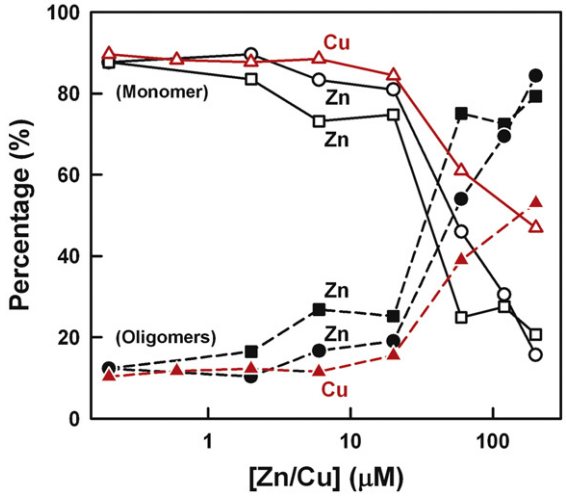

Fig. 5. Comparison of the proportions of FH monomer and oligomers in titrations with zinc and copper. The percentages were derived by integration of the *c*(*s*) analyses and correspond to the mean value obtained at 50,000 and 60,000 rpm. Monomers are denoted by filled symbols; oligomers, by open symbols (0.87 mg/ml of FH with zinc: black ●, ○; 0.35 mg/ml of FH with zinc: black ■, □; 0.81 mg/ml of FH with copper: red ▲, △).

at approximately 150 μM [Cu] (Fig. 5). FH at 0.93 mg/ml was also studied with 200 μM $CaCl_2$, $MgCl_2$, $NiCl_2$, $CdCl_2$, $FeSO_4$, $CuSO_4$ and $ZnSO_4$. The *c*(*s*) plots for $NiCl_2$, $CdCl_2$ and $FeSO_4$ showed an increase in oligomer formation from 12% to 20% when compared with those of FH alone and with $CaCl_2$ or $MgCl_2$ (Fig. 6b and c). Oligomer formation increased further with $CuSO_4$ and $ZnSO_4$ (Fig. 6c).

Fluid-phase activity assays of FH–metal complexes

Assays of fluid-phase ammonium-inactivated C3 cleavage by factor I were performed in the presence and in the absence of metals in order to test whether the formation of FH oligomers is correlated with the regulatory cofactor role of FH.[26] Previous complement functional assays routinely employed FH concentrations that were significantly lower than the 0.235–0.81 mg/ml (1.6–5.4 μM) observed *in vivo* (e.g., 45 μg/ml,[26] 3 μg/ml, [32] 30 μg/ml[33] and 75 μg/ml[34]). Accordingly, our assays were performed at 0.3 mg/ml of FH (2 μM) for direct comparison with the analytical ultracentrifugation data and to be more comparable with serum levels. Figure 7a showed that the α-chain of haemolytically inactive C3 was cleaved by factor I in the presence of FH to produce two major degradation fragments at apparent sizes of 45 and 75 kDa. The influence of zinc or copper on this reaction was investigated at the concentrations of 0, 2, 20, 60, 120 and 200 μM. The cleavage rate was decreased by both metals, and this became noticeable with zinc at 120 and 200 μM (Fig. 7b) and to a lesser extent with copper at 200 μM (Fig. 7c). This matched the growth of oligomers illustrated in Fig. 5, indicating that the oligomerisation of FH is able to account for the decrease of activity of FH by blocking FH access to C3u and/or factor I. Factor I

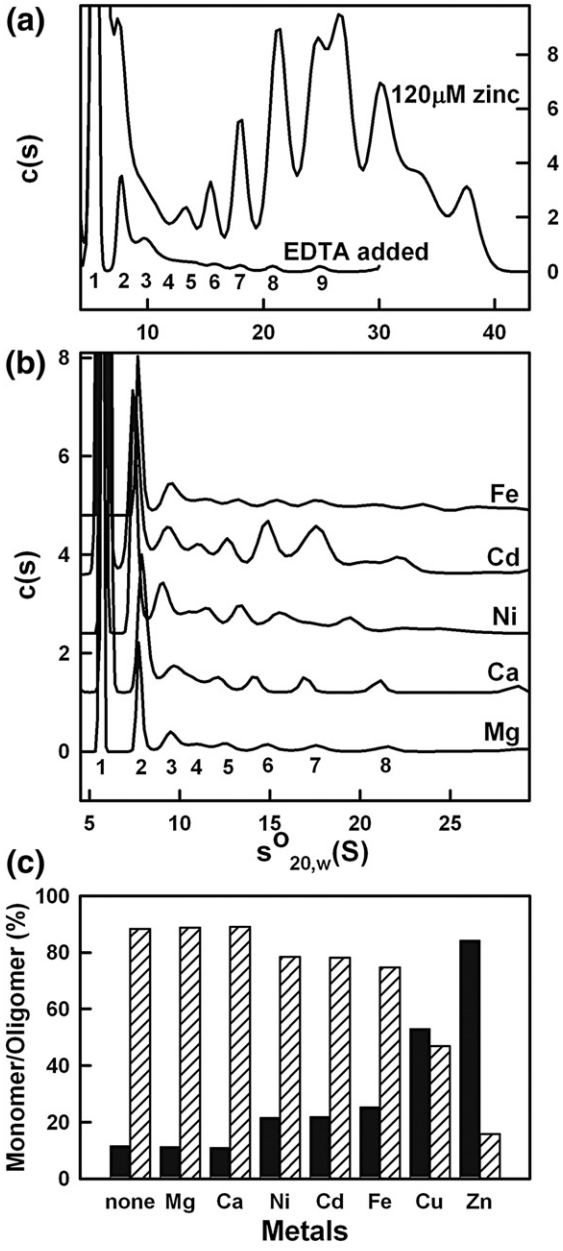

Fig. 6. The comparative effects of different metals on FH oligomerisation. The sedimentation velocity data were obtained at 50,000 rpm. The intensity of the monomer peak at 5.57 S was set to 100 for clarity. The oligomer peaks are labelled from 2 to 9 to follow Fig. 4. (a) The *c*(*s*) distribution analyses for 0.87 mg/ml of FH with 120 μM zinc and after the addition of EDTA to a final concentration of 0.22 mg/ml of FH, 30 μM zinc and 1.5 mM EDTA. (b) The *c*(*s*) distribution analyses for 0.93 mg/ml of FH for five metals at 200 μM (labelled). (c) Proportions of FH monomer and oligomers in the presence of different metals at a concentration of 200 μM. The hatched columns correspond to FH monomer, and the solid columns correspond to FH oligomers.

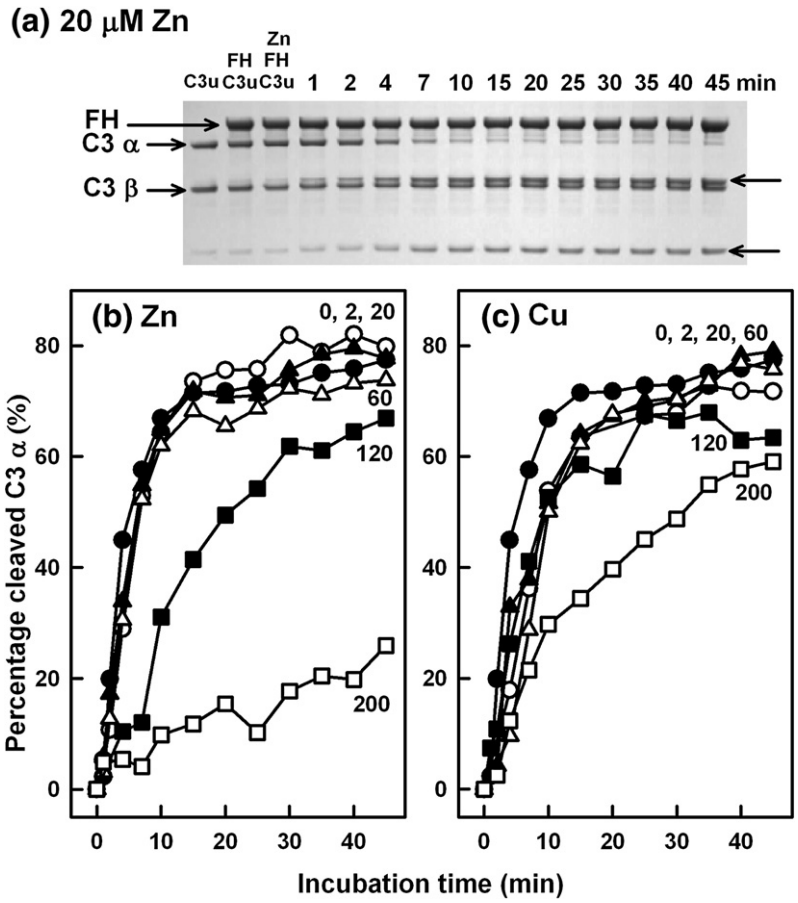

Fig. 7. Cleavage of fluid-phase inactive C3 (C3u) in the presence of zinc or copper. (a) Reducing SDS-PAGE analysis of C3u cleavage in 20 μM zinc (lanes 4–15 correspond to the reaction times in minutes as labelled). Lane 1, 0.3 mg/ml of C3u; lane 2, 0.3 mg/ml of C3u and 0.3 mg/ml of FH; lane 3, 0.3 mg/ml of C3u, 0.3 mg/ml of FH and zinc. FH, C3 α-chain and C3 β-chain are arrowed on the left, and the C3 α-chain cleavage products are arrowed on the right. (b) The percentage cleavage of C3 α-chain is shown as a function of [Zn], with their values shown as labels (0 μM, ●; 2 μM, ○; 20 μM, ▲; 60 μM, △; 120 μM, ■; 200 μM, □). (c) As with (b) except that copper was used instead of zinc.

activity is unaffected by zinc,[34] while C3b binds to zinc with little change in activity.[32,33]

Conclusions

Metals have not been generally considered as FH ligands. In distinction to our original study,[27] we have shown here that five transition metals cause monomeric FH to form large oligomers at the FH concentration seen in serum. Zinc and copper have the most significant effects, followed by other transition metals, while calcium and magnesium have no effect. We also show that zinc- and copper-induced FH oligomerisation is matched by loss of activity. Therefore, zinc and copper should be considered as newly identified inhibitory FH ligands at pathological metal concentrations above 60 μM. Zinc and copper promote uncontrolled FH oligomer formation; in addition, the preformed oligomers can be disassembled by chelation using EDTA.

FH is a major complement regulator in blood and is expressed and secreted by many cell types, including the RPE.[35] Many functional studies on FH binding to its major ligand C3b, and to others such as heparin and C-reactive protein, have been performed. In distinction, surprisingly little attention has been given to FH self-association and its effect on its regulatory function. The originally reported inhibition of C3b cleavage in 1000 μM zinc[26] could be explained in terms of the non-specific aggregation of FH first reported by X-ray scattering, because the protein aggregates would block accessibility to the functionally active regions in FH.[27] While FH is often considered to be monomeric, several groups have reported its ability to dimerise.[9,10,36] To date, two dimerisation sites have been located within the FH SCR-6/8 and SCR-16/20 fragments, with K_d values of about 40 and 16 μM, respectively.[37,38] Ultracentrifugation showed that native FH exists in a reversible monomer–dimer equilibrium with a dissociation constant K_d of 28 μM up to 1.36 mg/ml, indicating that about 5%–15% of FH in serum is reversibly dimeric and that non-reversible higher oligomers form at higher concentrations, presumably through an alternating chain of dimerisation events at the two dimer sites.[30] The effect of dimerisation on regulatory function is not known. Here, with the use of physiological concentrations of native FH from pooled serum, our scattering data showed the formation of large but compact oligomers of FH in the presence of zinc and copper, while our ultracentrifugation data showed that FH is 85% oligomeric in 200 μM zinc and 50% oligomeric in 200 μM copper. FH activity was proportionately reduced by oligomer formation (Fig. 7).

In a physiological scenario, because this metal binding is weak, the zinc- or copper-induced uncontrolled oligomerisation of FH can only occur in tissues where a sufficient amount of zinc or copper is

present. For example, the total zinc concentration of 12.5 μM in serum is clearly too low to induce FH oligomerisation according to our data (Figs. 2 and 5). This level remains low at 14.7 μM even after a daily diet supplement with 80 mg of zinc in the AREDS trials.[39,40] Few tissues have total zinc concentrations high enough to release biologically reactive zinc in the range of 20–200 μM.[41] The retina appears to be an exception, as this has the highest concentration of zinc per gram of tissue.[42] Retinal zinc is concentrated mostly in the RPE–choroidal complex, where sRPEds are formed, bound to melanin, metallothionein and other zinc binding proteins.[24,43] Cellular damage to the RPE, which may occur through stress factors such as excessive light, smoking or oxidative processes during ageing, is one of the first pathological events leading to AMD. Damage to RPE cells may trigger the release of pathological levels of zinc from protein complexes into extracellular regions, and the local bioavailable zinc level may reach >60 μM, which will be sufficient to initiate FH oligomerisation (Fig. 2) and its precipitation into sRPEds.[41] The concept that zinc might be involved in the initiation of AMD appears to contradict the clinical observation that zinc supplements are able to slow the development of blindness in patients.[39,40] However, AMD is a progressive disease, and decades elapse between the appearance of sRPEds and the degeneration that eventually leads to blindness. Therefore, it is possible that too much bioavailable zinc in the early stages of the disease can trigger the problem by facilitating the formation of sRPEds, while decades later zinc supplementation can be beneficial if much of the zinc in the tissues is trapped in sRPEds and the surrounding tissues are relatively depleted.[44]

At present, there is no simple mechanistic understanding of the formation of sRPEds and the slow progression to AMD over several decades of a life span. In the absence of metal, FH self-association involving probably SCR-7 and SCR-20 may lead to the formation of higher oligomers of FH through a set of alternating dimeric interactions between FH molecules.[30,37,38] It is intriguing that the SCR-6/8 fragment with the His402 allotype that is a risk factor for AMD shows a slightly higher propensity to self-associate than the wild-type Tyr402 allotype,[37] and this by itself could enhance the deposition of FH into sRPEds over several decades. However, if the alternative pathway is involved in AMD, as suggested from the involvement of FH polymorphisms[13–16] (and not the classic pathway that is regulated by membrane-bound regulators, including membrane cofactor protein and decay-acceleration factor), and if FH–metal complexes contribute to the onset of AMD, a pathway for zinc-induced oligomer formation is suggested by our results. Zinc is tetrahedrally coordinated in proteins.[45] Given that zinc ligands at protein interfaces often include pairs of surface Asp and His residues and that Tyr402 is exposed at the surface of SCR-7,[37] it is also intriguing that the AMD-risk Tyr402His polymorphism involves the introduction of a His residue.[13–16] This raises the possibility that an Asp–His pair on the surface of an SCR domain forms half a zinc binding site, and zinc may pair these two SCR domains together in a symmetric arrangement. Other scenarios based on other metal coordinations are possible. Possible zinc binding sites in FH are currently being investigated to clarify this. Irrespective of whether zinc interacts with specific residues on the surface of SCR domains or promotes the previously observed self-association dimer sites in SCR-6/8 and SCR-16/20, it is clear that, in the presence of zinc, FH will form indefinite oligomers more readily than in its absence. Different metals will cause different oligomerisation properties depending on their relative affinity for different self-association sites. For example, the more compact zinc-promoted oligomers seen in Fig. 3c may be formed through a stronger pairing of two central SCR domains of FH, while the more extended copper-induced oligomers may result from a stronger pairing of SCR domains at one end of FH (Fig. 8). As zinc is more abundant in sRPEds than any other metal,[46] a compact association mechanism might be more relevant. While such an aggregation mechanism may be directly relevant to AMD, it is not known whether this proposed aggregation mechanism may act as a trigger for sRPEd formation or facilitates the growth of sRPEd into larger and clinically relevant sizes over several decades of a life span. An aggregation mechanism will be distinct from that in which excessive complement activation and uncontrolled inflammation caused by reduced FH regulation will generate the slow buildup of protein and lipids after complement attack of host cells.[13–16,47]

The molecular effect of dimerisation on FH function is not known presently, but Fig. 7 indicates that complement regulation by FH will be diminished by oligomer formation. The C3b or factor I ligands may be sterically blocked from interaction with FH aggregates by zinc. Alternatively, or simultaneously, zinc may enhance the deposition of FH binding proteins, together with FH, into sRPEds contributing to the accelerated protein built up in Bruch's membrane. This process might be slow, given that it could be triggered by the gradual decline of RPE cells that may happen without relevant visual impairment of the peripheral retina.[48] However, the process might be accelerated by the several environmental, cellular and genetic factors associated with AMD, especially when the damage affects the macula.[49] If FH–metal complexes contribute to the onset of AMD, a pathway for zinc-induced oligomer formation is suggested by analogy with our recent work.[37,38] By this, two weak dimer sites will initiate FH dimer formation at either site. As shown in Fig. 8, these are arbitrarily postulated to be in the vicinity of SCR-7 and SCR-20. In the absence of metal, these sites will lead to higher oligomers of FH at a high concentration through a set of alternating dimeric interactions between FH molecules.[30] If the process of self-association at two dimer sites is enhanced by the presence of zinc (not necessarily at SCR-7 and

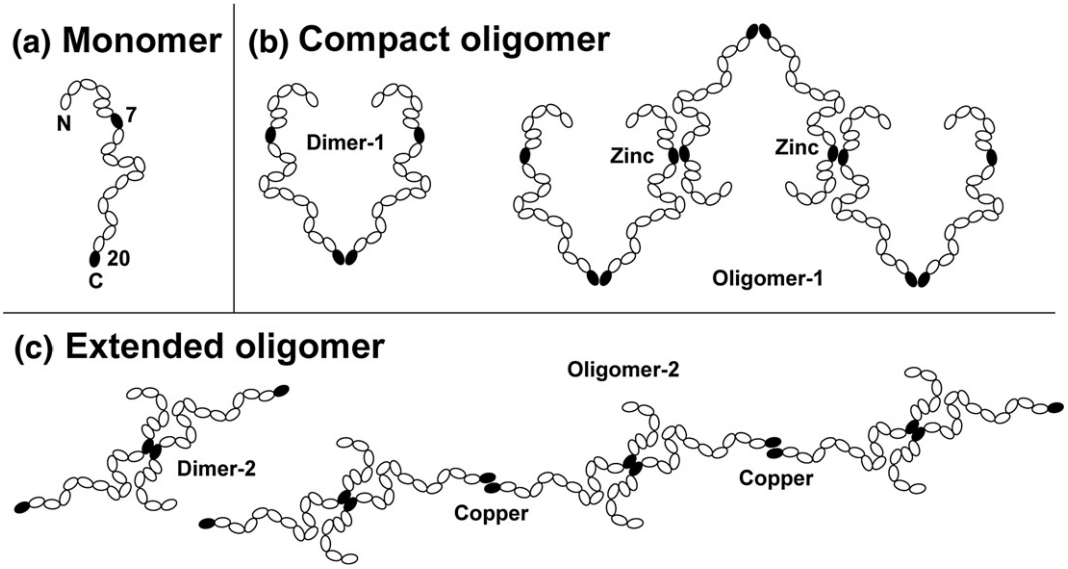

Fig. 8. Hypothetical cartoon of the differential effects of metals on FH oligomerisation. (a) A partially folded-back FH monomer structure is depicted, with SCR-7 and SCR-20 highlighted in black as possible dimerisation sites in native FH. It is stressed that the FH monomer is more compact in its folded-back structure than that shown, which is drawn for clarity. (b) A putative compact oligomer is formed, initially as a dimer, through contacts in the region near SCR-20. The presence of zinc promotes further dimerisation in a central region of FH near but not necessarily at SCR-7, and this leads to a set of compact oligomers (Fig. 3c). (c) More extended oligomers can be formed if a different metal promotes a different pattern of oligomer formation. In the schematic view shown, dimers are initially formed near SCR-7, and the presence of copper leads to further dimerisation near one end of FH, not necessarily at SCR-20. More extended oligomers are formed in the presence of copper (Fig. 3c).

SCR-20), FH will form indefinite oligomers more readily (Fig. 8). The varied effect of different transition metals on the FH oligomer structure is explained schematically in Fig. 8, depending on which of the two dimer sites is more strongly promoted by metal. For example, the more compact zinc-promoted oligomers of Fig. 3c may be formed through a stronger dimerisation effect at a central SCR domain of FH (Fig. 8b), while the more extended copper-induced oligomers may result from a stronger effect at a C-terminal region of FH (Fig. 8c). Note that zinc is more abundant in the retina than copper.[50] While such an aggregation mechanism for FH may be directly relevant to AMD, it is possible that the high bioavailability of zinc in the retina may exert a pathogenic effect by this route. Given that zinc ligands at protein interfaces often include surface Asp and His residues and that Tyr402 is exposed at the surface of SCR-7,[37] it is also intriguing that the AMD-risk polymorphism in FH replaces Tyr402 with His402.[13–16]

Given the unambiguous association between complement activation and AMD, the presence of FH and other complement-related proteins in sRPEds[21] and the indication that FH plays a role in the age-related thickening of Bruch's membrane,[51] an improved understanding of the role of FH may lead to novel therapies for AMD. For example, if a metal-induced aggregation mechanism or metal-induced complement dysregulation proves to be significant, then the reversibility of FH oligomerisation with EDTA offers the possibility of capturing this oligomerisation before the irreversible cross-linking of proteins with photo-oxidised lipids takes place.[20] Similar arguments may be relevant to other deposit-forming diseases in which trace metals are involved, such as Alzheimer's disease, for which a zinc buffering compound is already in clinical trials.[52]

Materials and Methods

Protein purification

Native FH and factor I were purified from a pool of just-outdated anonymised human plasma using monoclonal affinity chromatography with MRC-OX23 and MRC-OX21 Sepharose columns.[53] Bound FH and factor I were each eluted from the column using 3 M $MgCl_2$, pH 6.9, and then each was dialysed into Hepes buffer (10 mM Hepes and 137 mM NaCl, pH 7.4) in the presence of 0.5 mM EDTA to remove Mg^{2+}, and then each was passed through a HiTrap Protein G HP column to remove the contaminant immunoglobulin G. Non-specific aggregates and human serum albumin were removed using Superose 6 gel filtration. Native C3 was purified from the eluate after the MRC-OX23 column stage by ion-exchange chromatography. Haemolytically inactive C3 (C3u) was prepared by incubating native C3 in 200 mM hydrazine at 37 °C for 1 h.[54] Protein concentrations were determined from absorption coefficients of 16.7 for FH, 12 for factor I and 9.4 for C3u (1%; 280 nm; 1 cm path length).[31,55,56] Proteins were dialysed into Hepes buffer for experiments, and their integrity was routinely checked by SDS-PAGE before and after scattering, ultracentrifugation and assays.

X-ray scattering data collection and analysis

X-ray scattering is a diffraction method used to study solution structures of macromolecules in random orientations.[28] The X-ray data $I(Q)$ as a function of the scattering vector Q were acquired in two beam sessions on beamline ID02 at the European Synchrotron Radiation Facility (Grenoble, France) with a ring energy of 6.0 GeV and operating in 4- and 16-bunch modes to reduce the incident flux. Storage ring currents ranged from 22 to 41 mA for the 4-bunch mode and from 67 to 92 mA for the 16-bunch mode. Potential radiation damage was eliminated by continuous movement of the sample in a flow cell during beam exposure, use of 10 time frames of 0.2- or 0.5-s duration each during each acquisition and online checks for the absence of radiation damage at low Q. FH was studied at concentrations of 1.05 mg/ml (7.0 μM) and 0.42 mg/ml (2.8 μM), with $ZnSO_4$ concentrations between 0 and 200 μM and 0.93 mg/ml (6.2 μM) with $CuSO_4$ in the same concentration range as well as 200 μM $ZnCl_2$, $CaCl_2$, $MgCl_2$, $NiCl_2$, $CdCl_2$ and $FeSO_4$. Other details, including data reduction, are described elsewhere.[37,38]

In a given solute–solvent contrast, Guinier analyses of ln $I(Q)$ *versus* Q^2 at low Q give the R_G and the forward scattering at zero angle $I(0)$. The R_G is a measure of overall FH structural elongation, and $I(0)/c$ (c = concentration) is a measure of its molecular weight. For elongated structures, the cross-sectional radius of gyration R_{XS} and cross-sectional intensity at zero angle $[I(Q)\cdot Q]_{Q\rightarrow 0}$ are obtained from analyses at larger Q ranges. These provide information on the structural relationship between adjacent SCR domains. Indirect transformation of the scattering data $I(Q)$ in reciprocal space to give the distance distribution function $P(r)$ in real space was carried out using GNOM. The $P(r)$ curve reports the distribution of distances r between all volume elements within the protein. This offers an alternative calculation of the R_G and $I(0)$ values that is based on the full scattering curve $I(Q)$, and not that at low Q. It also gives the maximum dimension of the macromolecule L. The X-ray curve utilised up to 211 data points for Q between 0.06 and 1.50 nm^{-1} for 0.42 mg/ml of FH, up to 309 data points for Q between 0.06 and 2.10 nm^{-1} for 1.05 mg/ml of FH and up to 599 data points for Q between 0.09 and 2.10 nm^{-1} for 0.93 mg/ml of FH. Other details are described elsewhere.[30,31,37,38]

Sedimentation velocity data collection and analyses

Analytical ultracentrifugation studies the sedimentation behaviour of macromolecules on subjecting these to a high centrifugal force in order to determine their sizes and shapes.[29] Data were obtained on a Beckman XL-I instrument using AnTi50 or AnTi60 rotors at 20 °C. Sedimentation velocity experiments were performed at rotor speeds up to 60,000 rpm in two-sector cells with a column height of 12 mm for 0.87 and 0.35 mg/ml of FH titrated with $ZnSO_4$ at eight concentrations between 0 and 200 μM, 0.81 mg/ml of FH titrated with $CuSO_4$ at eight concentrations from 0 to 200 μM and 0.93 mg/ml of FH with 200 μM $ZnCl_2$, $CaCl_2$, $MgCl_2$, $NiCl_2$, $CdCl_2$ and $FeSO_4$. Data analyses were performed using SEDFIT (version 9.4). The size-distribution analyses $c(s)$ that provided size and shape data were based on a fixed resolution of 200 and a frictional ratio f/fo of 1.78 and floated on the meniscus, the bottom of the cell and the baseline until the overall rmsd and fits between the observed and calculated sedimentation boundaries were satisfactory. The percentage fraction of oligomers in the total loading concentration was derived using the $c(s)$ integration function. Other details are described elsewhere.[30,38]

Fluid-phase activity assays

The reaction mixtures contained 0.3 mg/ml of FH, 0.3 mg/ml of C3u and 0.003 mg/ml of factor I in six concentrations of $ZnSO_4$ or $CuSO_4$ (0, 2, 20, 60, 120 and 200 μM) and were incubated in a water bath at 37 °C. At timed intervals, 5-μl aliquots were removed for reducing SDS-PAGE analyses. Three controls were used: 0.3 mg/ml of C3u, 0.3 mg/ml of C3u and 0.3 mg/ml of FH; and 0.3 mg/ml of C3u, 0.3 mg/ml of FH and zinc or copper. The C3 α-chain band densities from SDS-PAGE were measured using the gel analysis system SYNGENE (Synoptics, Ltd., Cambridge, UK). The C3 α-chain cleavage was referenced to the averaged density of the uncleaved bands in the controls.

Acknowledgements

We thank the Biotechnology and Biological Sciences Research Council and the Mercer Fund of the Fight For Sight Charity for a Dorothy Hodgkin Postgraduate Award and equipment grant support as well as the Henry Smith Charity for equipment support. We also thank Dr. R. B. Sim and Dr. A. Dodds (MRC Immunochemistry Unit, Oxford) for the provision of MRC-OX21 and MRC-OX23 Sepharose and advice on C3 purifications as well as Ms. Keying Li for useful discussions. We are very grateful to Dr. Anuj Shukla and Dr. Emanuela Di Cola (European Synchrotron Radiation Facility, Grenoble, France) for excellent instrumental support as well as Prof. Alan C. Bird for useful discussions. I.L. thanks the Mercer Fund, the Special Trustees of Moorfields Eye Hospital and the Bill Brown Charitable Trust for support.

References

1. Law, S. K. A. & Reid, K. B. M. (1995). Complement (Second Edition). IRL Press, Oxford, UK.
2. Whaley, K. & Ruddy, S. (1976). Modulation of the alternative complement pathways by beta1H globulin. *J. Exp. Med.* **144**, 1147–1163.
3. Pangburn, M. K., Schreiber, R. D. & Muller-Eberhard, H. J. (1977). Human complement C3b inactivator: isolation, characterization, and demonstration of an absolute requirement for the serum protein beta1H for cleavage of C3b and C4b in solution. *J. Exp. Med.* **146**, 257–270.
4. Weiler, J. M., Daha, M. R., Austen, K. F. & Fearon, D. T. (1976). Control of the amplification convertase of complement by the plasma protein beta1H. *Proc. Natl Acad. Sci. USA*, **73**, 3268–3272.
5. Farries, T. C., Seya, T., Harrison, R. A. & Atkinson, J. P. (1990). Competition for binding sites on C3b by CR1, CR2, MCP, factor B and factor H. *Complement Inflammation*, **7**, 30–41.
6. Soares, D. & Barlow, P. N. (2005). Complement control protein modules in the regulators of complement

activators. In *Structural Biology of the Complement System* (Morikis, D. & Lambris, J. D., eds), pp. 19–62, Taylor & Francis, Boca Raton, FL.
7. Ormsby, R. J., Jokiranta, T. S., Duthy, T. G., Griggs, K. M., Sadlon, T. A., Giannakis, E. & Gordon, D. L. (2006). Localization of the third heparin-binding site in the human complement regulator factor H. *Mol. Immunol.* **43**, 1624–1632.
8. Sharma, A. K. & Pangburn, M. K. (1996). Identification of three physically and functionally distinct binding sites for C3b in human complement factor H by deletion mutagenesis. *Proc. Natl Acad. Sci. USA*, **93**, 10996–11001.
9. Jokiranta, T. S., Hellwage, J., Koistinen, V., Zipfel, P. F. & Meri, S. (2000). Each of the three binding sites of factor H interacts with a distinct site on C3b. *J. Biol. Chem.* **275**, 27657–27662.
10. Oppermann, M., Manuelian, T., Jozsi, M., Brandt, E., Jokiranta, T. S., Heinen, S. *et al.* (2006). The C-terminus of complement regulator factor H mediates target recognition: evidence for a compact conformation of the native protein. *Clin. Exp. Immunol.* **144**, 342–352.
11. Ferreira, V. P., Herbert, A. P., Hocking, H. G., Barlow, P. N. & Pangburn, M. K. (2006). Critical role of the C-terminal domains of factor H in regulating complement activation at cell surfaces. *J. Immunol.* **177**, 6308–6316.
12. Saunders, R. E., Abarrategui-Garrido, C., Frémeaux-Bacchi, V., Goicoechea de Jorge, E., Goodship, T. H. J., López Trascasa, M. *et al.* (2007). The interactive factor H-atypical haemolytic uraemic syndrome mutation database and website: update and integration of membrane cofactor protein and factor I mutations with structural models. *Hum. Mutat.* **28**, 222–234.
13. Klein, R. J., Zeiss, C., Chew, E. Y., Tsai, J. Y., Sackler, R. S., Haynes, C. *et al.* (2005). Complement factor H polymorphism in age-related macular degeneration. *Science*, **308**, 385–389.
14. Haines, J. L., Hauser, M. A., Schmidt, S., Scott, W. K., Olson, L. M., Gallins, P. *et al.* (2005). Complement factor H variant increases the risk of age-related macular degeneration. *Science*, **308**, 419–421.
15. Edwards, A. O., Ritter, R., III, Abel, K. J., Manning, A., Panhuysen, C. & Farrer, L. A. (2005). Complement factor H polymorphism and age-related macular degeneration. *Science*, **308**, 421–424.
16. Hageman, G. S., Anderson, D. H., Johnson, L. V., Hancox, L. S., Taiber, A. J., Hardisty, L. I. *et al.* (2005). A common haplotype in the complement regulatory gene factor H (HF1/CFH) predisposes individuals to age-related macular degeneration. *Proc. Natl Acad. Sci. USA*, **102**, 7227–7232.
17. Li, M., Atmaca-Sonmez, P., Othman, M., Branham, K. E. H., Khanna, R., Wade, M. S. *et al.* (2006). CFH haplotypes without the Y402H coding variant show strong association with susceptibility to age-related macular degeneration. *Nat. Genet.* **38**, 1049–1054.
18. Maller, J., George, S., Purcell, S., Fagerness, J., Altshuler, D., Daly, M. J. & Seddon, J. M. (2006). Common variation in three genes, including a noncoding variant in CFH, strongly influences risk of age-related macular degeneration. *Nat. Genet.* **38**, 1055–1059.
19. Hughes, A. E., Orr, N., Esfandiary, H., Diaz-Torres, M., Goodship, T. & Chakravarthy, U. (2006). A common CFH haplotype, with deletion of CFHR1 and CFHR3, is associated with lower risk of age-related macular degeneration. *Nat. Genet.* **38**, 1173–1177.
20. Crabb, J. W., Miyagi, M., Gu, X., Shadrach, K., West, K. A., Sakaguchi, H. *et al.* (2002). Drusen proteome analysis: an approach to the etiology of age-related macular degeneration. *Proc. Natl Acad. Sci. USA*, **99**, 14682–14687.
21. Hageman, G. S., Luthert, P. J., Victor Chong, N. H., Johnson, L. V., Anderson, D. H. & Mullins, R. F. (2001). An integrated hypothesis that considers drusen as biomarkers of immune-mediated processes at the RPE–Bruch's membrane interface in aging and age-related macular degeneration. *Prog. Retinal Eye Res.* **20**, 705–732.
22. Bird, A. C. (1992). Bruch's membrane change with age. *Br. J. Ophthalmol.* **76**, 166–168.
23. Bird, A. C., Bressler, N. M., Bressler, S. B., Chisholm, I. H., Coscas, G., Davis, M. D. *et al.* (1995). An international classification and grading system for age-related maculopathy and age-related macular degeneration. *Surv. Ophthalmol.* **39**, 367–374.
24. Galin, M. A., Nano, H. D. & Hall, T. (1962). Ocular zinc concentration. *Invest. Ophthalmol.* **1**, 142–148.
25. Lengyel, I., Flinn, J. M., Peto, T., Linkous, D. H., Cano, K., Bird, A. C. *et al.* (2007). High concentration of zinc in sub-retinal pigment epithelial deposits. *Exp. Eye Res.* **84**, 772–780.
26. Crossley, L. G. & Porter, R. R. (1980). Purification of the human complement control protein C3b inactivator. *Biochem. J.* **191**, 173–182.
27. Perkins, S. J., Nealis, A. S. & Sim, R. B. (1991). Oligomeric domain structure of human complement factor H by X-ray and neutron solution scattering. *Biochemistry*, **30**, 2847–2857.
28. Perkins, S. J., Okemefuna, A. I., Fernando, A. N., Bonner, A., Gilbert, H. E. & Furtado, P. B. (2008). X-ray and neutron scattering data and their constrained molecular modelling. *Mol. Cell. Biol.* **84**, 375–423.
29. Cole, J. L., Lary, J. W., Moody, T. P. & Laue, T. M. (2008). Analytical ultracentrifugation: sedimentation velocity and sedimentation equilibrium. *Mol. Cell. Biol.* **84**, 143–211.
30. Nan, R., Gor, J. & Perkins, S. J. (2008). Implications of the progressive self-association of wild-type human factor H for complement regulation and disease. *J. Mol. Biol.* **375**, 891–900.
31. Aslam, M. & Perkins, S. J. (2001). Folded-back solution structure of monomeric factor H of human complement by synchrotron X-ray and neutron scattering, analytical ultracentrifugation and constrained molecular modelling. *J. Mol. Biol.* **309**, 1117–1138.
32. Day, A. J. & Sim, R. B. (1986). Inhibitory effect of Zn^{2+} ion on the degradation of the complement activation fragment C3b. *Biochem. Soc. Trans.* **14**, 73–74.
33. Blom, A. M., Kask, L., Ramesh, B. & Hillarp, A. (2003). Effects of zinc on factor I cofactor activity of C4b-binding protein and factor H. *Arch. Biochem. Biophys.* **418**, 108–118.
34. Tsiftsoglou, S. A. & Sim, R. B. (2004). Human complement factor I does not require cofactors for cleavage of synthetic substrates. *J. Immunol.* **173**, 367–375.
35. An, E., Lu, X., Flippin, J., Devaney, J. M., Halligan, B., Hoffman, E. P. *et al.* (2006). Secreted proteome profiling in human RPE cell cultures derived from donors with age related macular degeneration and age matched healthy donors. *J. Proteome Res.* **5**, 2599–2610.
36. Jokiranta, T. S., Jaakola, V. P., Lehtinen, M. J., Parepalo, M., Meri, S. & Goldman, A. (2006). Structure of complement factor H carboxyl-terminus reveals molecular basis of atypical haemolytic uremic syndrome. *EMBO J.* **25**, 1784–1794.
37. Fernando, A. N., Furtado, P. B., Clark, S. J., Gilbert,

H. E., Day, A. J., Sim, R. B. & Perkins, S. J. (2007). Associative and structural properties of the region of complement factor H encompassing the Tyr402His disease-related polymorphism and its interactions with heparin. *J. Mol. Biol.* **368**, 564–581.
38. Okemefuna, A. I., Gilbert, H. E., Griggs, K. M., Ormsby, R. J., Gordon, D. L. & Perkins, S. J. (2008). The regulatory SCR-1/5 and cell-surface-binding SCR-16/20 fragments of factor H reveal partially folded-back solution structures and different self-associative properties. *J. Mol. Biol.* **375**, 80–101.
39. AREDS Research Group. (2002). The effect of five-year zinc supplementation on serum zinc, serum cholesterol and hematocrit in persons randomly assigned to treatment group in the Age-Related Eye Disease Study. *J. Nutr.* **132**, 687–702.
40. AREDS Research Group. (2001). A randomized, placebo-controlled, clinical trial of high-dose supplementation with vitamins C and E, beta carotene, and zinc for age-related macular degeneration and vision loss. *Arch. Ophthalmol.* **119**, 1417–1436.
41. Frederickson, C. J., Giblin, L. J., Krezel, A., McAdoo, D. J., Muelle, R. N., Zeng, Y. *et al.* (2006). Concentrations of extracellular free zinc $(pZn)_e$ in the central nervous system during simple anesthetization, ischemia and reperfusion. *Exp. Neurol.* **198**, 285–293.
42. Ugarte, M. & Osborne, N. N. (2001). Zinc in the retina. *Prog. Neurobiol.* **64**, 219–249.
43. Newsome, D. A., Oliver, P. D., Deupree, D. M., Miceli, M. V. & Diamond, J. G. (1992). Zinc uptake by primate retinal pigment epithelium and choroid. *Curr. Eye Res.* **11**, 213–217.
44. Lengyel, I. & Peto, T. (2008). Cure or cause: the opposing roles for zinc in age-related macular degeneration. *Expert Rev. Ophthalmol.* **3**, 1–4.
45. Auld, D. S. (2001). Zinc coordination sphere in biochemical zinc sites. *BioMetals*, **14**, 271–313.
46. Flinn, J. M., Cano, K., Gideons, E., Koscho, J., Ablett, J., Jones, B. F. *et al.* (2008). Trace metal distribution and concentration in sub-RPE deposits and Bruch's membrane in post-mortem human tissues. *Invest. Ophthalmol. Visual Sci.* **49**, E–1756; Abstract.
47. Scholl, H. P. N., Issa, P. C., Walier, M., Janzer, S., Pollok-Kopp, B., Borncke, F. *et al.* (2008). Systematic complement activation in age-related macular degeneration. *PLoS ONE*, **3**, e2593.
48. Lengyel, I., Tufail, A., Hosaini, H. A., Luthert, P., Bird, A. C. & Jeffery, G. (2004). Association of drusen deposition with choroidal intercapillary pillars in the aging human eye. *Invest. Ophthalmol. Visual Sci.* **45**, 2886–2892.
49. Jager, R. D., Mieler, W. F. & Miller, J. W. (2008). Age-related macular degeneration. *New Engl. J. Med.* **358**, 2606–2617.
50. Wills, N. K., Sadagopa Ramanujum, V. M., Kalariya, N., Lewis, J. R. & van Kuijk, F. J. G. M. (2008). Copper and zinc distribution in the human retina: relationship to cadmium accumulation, age and gender. *Exp. Eye Res.* **87**, 80–88.
51. Coffey, P. J., Gias, C., McDermott, C. J., Lundh, P., Pickering, M. C., Sethi, C. *et al.* (2007). Complement factor H deficiency in aged mice causes retinal abnormalities and visual dysfunction. *Proc. Natl Acad. Sci. USA*, **104**, 16651–16656.
52. Ritchie, C. W., Bush, A. I., Mackinnon, A., Macfarlane, S., Mastwyk, M., MacGregor, L. *et al.* (2003). Metal–protein attenuation with iodochlorhydroxyquin (clioquinol) targeting Aβ amyloid deposition and toxicity in Alzheimer disease. *Arch. Neurol.* **60**, 1685–1691.
53. Sim, R. B., Day, A. J., Moffatt, B. E. & Fontaine, M. (1993). Complement factor I and cofactors in control of complement system convertase enzymes. *Methods Enzymol.* **223**, 13–35.
54. Dodds, A. W. (1993). Small-scale preparation of complement components C3 and C4. *Methods Enzymol.* **223**, 46–61.
55. Ullman, C. G., Chamberlain, D., Emery, V. C., Haris, P. I., Sim, R. B. & Perkins, S. J. (1998). Human complement factor I: its expression by insect cells and its biochemical and structural characterisation. *Mol. Immunol.* **35**, 503–512.
56. Perkins, S. J. & Sim, R. B. (1986). Molecular modelling of human complement component C3 and its fragments by solution scattering. *Eur. J. Biochem.* **157**, 155–168.